Lecture Notes in Mechanical Engineering

Damodar Maity
Pradeep G. Siddheshwar
Sunanda Saha *Editors*

Advances in Fluid Mechanics and Solid Mechanics

Proceedings of the 63rd Congress of ISTAM 2018

Springer

Lecture Notes in Mechanical Engineering

Lecture Notes in Mechanical Engineering (LNME) publishes the latest developments in Mechanical Engineering - quickly, informally and with high quality. Original research reported in proceedings and post-proceedings represents the core of LNME. Volumes published in LNME embrace all aspects, subfields and new challenges of mechanical engineering. Topics in the series include:

- Engineering Design
- Machinery and Machine Elements
- Mechanical Structures and Stress Analysis
- Automotive Engineering
- Engine Technology
- Aerospace Technology and Astronautics
- Nanotechnology and Microengineering
- Control, Robotics, Mechatronics
- MEMS
- Theoretical and Applied Mechanics
- Dynamical Systems, Control
- Fluid Mechanics
- Engineering Thermodynamics, Heat and Mass Transfer
- Manufacturing
- Precision Engineering, Instrumentation, Measurement
- Materials Engineering
- Tribology and Surface Technology

To submit a proposal or request further information, please contact the Springer Editor in your country:

China: Li Shen at li.shen@springer.com
India: Priya Vyas at priya.vyas@springer.com
Rest of Asia, Australia, New Zealand: Swati Meherishi at swati.meherishi@springer.com
All other countries: Dr. Leontina Di Cecco at Leontina.dicecco@springer.com

To submit a proposal for a monograph, please check our Springer Tracts in Mechanical Engineering at http://www.springer.com/series/11693 or contact Leontina.dicecco@springer.com

Indexed by SCOPUS. The books of the series are submitted for indexing to Web of Science.

More information about this series at http://www.springer.com/series/11236

Damodar Maity · Pradeep G. Siddheshwar ·
Sunanda Saha
Editors

Advances in Fluid Mechanics and Solid Mechanics

Proceedings of the 63rd Congress of ISTAM 2018

Springer

Editors
Damodar Maity
Indian Institute of Technology Kharagpur
Kharagpur, West Bengal, India

Pradeep G. Siddheshwar
Bangalore University
Bengaluru, Karnataka, India

Sunanda Saha
Dayananda Sagar University
Bengaluru, Karnataka, India

ISSN 2195-4356 ISSN 2195-4364 (electronic)
Lecture Notes in Mechanical Engineering
ISBN 978-981-15-0771-7 ISBN 978-981-15-0772-4 (eBook)
https://doi.org/10.1007/978-981-15-0772-4

This Springer imprint is published by the registered company Springer Nature Singapore Pte Ltd.
The registered company address is: 152 Beach Road, #21-01/04 Gateway East, Singapore 189721, Singapore

Editorial Board

Contents

About the Editors

Prof. Dr. Damodar Maity is currently Professor in the Department of Civil Engineering, Indian Institute of Technology, Kharagpur. After graduating from Jadavpur University, Kolkata in Civil Engineering, he obtained Ph.D. from IIT Kharagpur in the area of fluid-structure interaction. Prof. Maity has more than 150 research publications in journals and conference proceedings of national and international repute. His research interests include computation mechanics, structural health monitoring, fluid-structure interaction. He has received two best paper awards from The Institution of Engineers (India). Prof. Maity is author of a book titled "Computer Analysis of Framed Structures". He was joint convener of the 2nd International Congress in Computational Mechanics and Simulation held in 2006 at IIT Guwahati. He has served as scientific/advisory board member of several international conferences. He served as secretary for The Indian Society of Theoretical and Applied Mechanics for three consecutive years. Prof. Maity has developed a video course on "Design of Steel Structures" and a web course on "Finite Element Analysis" under NPTEL, MHRD.

Prof. Dr. Pradeep G. Siddheshwar F.I.M.A (U.K.), F.N.A.Sc., is Professor in the Department of Mathematics and Director Planning, Monitoring and Evaluation Board Bangalore University. He has 35 years of teaching experience and nearly 40 years of research experience. He has guided 24 students for their Ph.D. degree. He has over 150 research papers in international journals of repute. He has 2237 google scholar citations, h-index of 28 and i10-index of 60. He was President of the Indian Society of Theoretical and Applied Mechanics, IIT, Kharagpur. He has visited over 30 countries on research assignments. He is a recipient of the Royal Society Incoming Fellowship, London, William Mong Fellowship, Hong Kong and a number of other Fellowships.

Dr. Sunanda Saha is currently Assistant Professor in the Department of Mathematics, Dayananda Sagar University, Bangalore. After graduating from IIT Madras in Mathematics she obtained her Ph.D. from IIT Guwahati in the area of water wave theory. She has published several research papers in reputed international journals. Her research interests include shallow water wave theory, flow in porous media, special functions, integral transform and cardiovascular modelling and simulations. She has received early career research grant for 3 years from SERB-DST and for 1 year from VGST for working on "Mathematical modelling and numerical simulation of blood flow in arteries". She was the convener of the 62nd International Conference of ISTAM held in 2018 at Dayananda Sagar University. She is the Vice-President for The Indian Society of Theoretical and Applied Mechanics, IIT Kharagpur, for the year 2019.

Sun Gravity-Assist to Trans-Lunar Injection Orbits

Harishkumar Sellamuthu, Subramanian Arumugam and Ram Krishan Sharma

Abstract Solar gravity propelled highly elliptical resident Earth orbits have been utilized to improve lunar mission performance. A regularized orbit propagator has been used to perform linear search for initial conditions that produce energy-saving pre-trans-lunar injection exo-atmospheric highly elliptical orbits. Additional propellant mass margin or smaller piggyback payloads to the Moon/high altitude orbits may be enabled by such transfers.

Keywords Solar gravity · Regularization · Lunar transfer · Highly elliptical orbits

1 Introduction

With the reinvigorated global interests toward the cislunar space, energy-efficient lunar transfers are being preferred by the stakeholders. The lunar transfers are rendered through highly elliptical orbits (HEO), with eccentricity (e) > 0.4, whose dynamics are predominantly governed by the third-body gravity perturbations from the Sun and the Moon. When perigee altitude (h_p > 600 km) is high (HPHEO), the orbit geometry of HEO is influenced by the variation in apsidal lines of the Sun and the Moon. Nodal regression consequently apsidal precession of the orbit are caused by the Earth's oblateness (J_2). Lunisolar perturbation maintains constant semimajor axis and varies the eccentricity of such orbits which causes the oscillation of perigee

H. Sellamuthu (✉) · S. Arumugam · R. K. Sharma
Department of Aerospace Engineering, Karunya Institute of Technology and Sciences, Coimbatore 641114, Tamil Nadu, India
e-mail: hari251086@gmail.com

S. Arumugam
e-mail: asubramanian.astrosci@gmail.com

R. K. Sharma
e-mail: ramkrishansharma@gmail.com

H. Sellamuthu
Institute of Computational Engineering and Sciences, The University of Texas, Austin, USA

D. Maity et al. (eds.), *Advances in Fluid Mechanics and Solid Mechanics*, Lecture Notes in Mechanical Engineering,
https://doi.org/10.1007/978-981-15-0772-4_1

altitude. The short periodicity of the oscillation is driven by the orbital periods of the Sun and the Moon, whose phases are sensitive to the initial angles of the Sun and the Moon with respect to the orbital plane of the spacecraft [1–3].

Although several types of low-energy and low-thrust orbit designs to the Moon were already flight-rated [4, 5], traditional high energy transfers are still being considered in view of mission reliability and sustainable technological developments in upcoming space programs. For high energy transfers to the Moon via direct transfer orbit, popularly known as trans-lunar injection (TLI), phasing through multiple HEO is utilized to improve the mission performance for characterizing the propulsion system and operational flexibility [6, 7]. During the phasing in HEO, the change in the perigee and the apogee can be viewed as a naturally induced maneuver and may come handy for fuel-saving transfer trajectories. Such naturally induced fuel-saving trajectories are sensitive to initial conditions such as launch time and day, initial orbital parameters, etc. Precise force models should be used with suitable formulation of governing equations to obtain good trajectory estimates. Numerical errors are seldom fully avoided in trajectory generation, and it is critical to minimize the errors which may otherwise steer to false conclusions leading to wrong science and even failure of a mission.

The nonlinear Newtonian differential equations of motion are unstable, are singular at collision of two bodies, and are not an ideal choice for low-order numerical propagation. The theoretical and physical difficulties of singular differential equations can be overcome by regularization which is a set of mathematical transformations that can produce a suitable formulation of the equations of motion. Transforming time as well as space coordinates produces regular equations, and one such regularization technique is called Kustaanheimo–Stiefel (KS) regularization [8] where they transformed the nonlinear Kepler motion and reduced it to linear differential equations of a harmonic oscillator of constant frequency. Stiefel and Scheifele [9] extended the application of KS transformation to perturbed motion. These equations are less sensitive to round–off and truncation errors in the numerical integration algorithm. The orbital frequency based on the total energy gives more accuracy to the in orbit position calculations. The equations are regular everywhere and they are smoothed for eccentric orbits as generalized eccentric anomaly is the independent variable.

KSROP is a regularized numerical orbit propagator package based on KS regular elements. KSROP contains lunisolar perturbations, Earth's oblateness, atmospheric drag, and solar radiation pressure perturbations. A fixed step-size fourth-order Runge–Kutta numerical scheme with Gill's variation is used for propagation. In this study, we have run numerical simulations with varying initial conditions for HPHEO using KSROP constraining to lunisolar and J_2 perturbations and computed energy-saving pre-TLI orbits.

2 KS—Regular Orbit Propagator

The mapping of four-dimensional space onto the three-dimensional physical space in Cartesian coordinates is called KS transformation [9], which is defined by

$$\boldsymbol{x} = L(\boldsymbol{u})\boldsymbol{u},$$

where $\boldsymbol{x}$ is supplemented by a vanishing fourth component and $r = \|\boldsymbol{x}\|$ is the magnitude of the position with $\boldsymbol{x}$ as the position vector with (x, y, z) as its components in km in inertial geocentric coordinate frame, $\boldsymbol{u}$ is the KS position vector with (u_1, u_2, u_3, u_4) as its components and

$$L(\boldsymbol{u}) = \begin{pmatrix} u_1 & -u_2 & -u_3 & u_4 \\ u_2 & u_1 & -u_4 & -u_3 \\ u_3 & u_4 & u_1 & u_2 \\ u_4 & -u_3 & u_2 & -u_1 \end{pmatrix}$$

is the generalized Levi–Civita matrix commonly known as KS matrix. With t being the physical time, s (fictitious time) is defined by Sundman in the classical time transformation [10]. The raised dimension would allow an additional degree of freedom to the solution in parametric space. To achieve robust regularization of equations of orbital motion using KS transformation, it is necessary to use generalized eccentric anomaly (E) as the independent variable which is related to fictitious time (s) by

$$E = 2ws, \tag{1}$$

where w is the orbital frequency obtained by

$$w = \sqrt{\left[\frac{\mu}{2r} - \frac{|\dot{\boldsymbol{x}}|^2}{4} - \frac{V}{2}\right]}. \tag{2}$$

μ, $\dot{\boldsymbol{x}}$, and V are the standard gravitational parameter of the Earth in $\mathrm{km^3 s^{-2}}$, velocity vector with $(\dot{x}, \dot{y}, \dot{z})$ as its components in $\mathrm{kms^{-1}}$, and perturbing potential, respectively. The velocity transformation is done through

$$\dot{\boldsymbol{x}} = \frac{4w}{r} L(\boldsymbol{u})\boldsymbol{u}^*,$$

where * represents derivative with respect to E.

The usage of E as independent variable, through Eq. (1), will render the solutions more meaningful than s, for practical purposes. The perturbed KS regular elements equations of motion [9] are

$$\frac{\mathrm{d}w}{\mathrm{d}E} = -\frac{r}{8w^2}\frac{\partial V}{\partial t} - \frac{1}{2w}\left(\frac{\mathrm{d}\boldsymbol{u}}{\mathrm{d}E}\cdot L^T\boldsymbol{P}\right), \tag{3}$$

$$\frac{\mathrm{d}\tau}{\mathrm{d}E} = \frac{1}{8w^3}(\mu - 2rV) - \frac{r}{16w^3}\left(\boldsymbol{u}\cdot\frac{\partial V}{\partial \boldsymbol{u}} - 2L^T\boldsymbol{P}\right) - \frac{2}{w^2}\frac{\mathrm{d}w}{\mathrm{d}E}\left(\boldsymbol{u}\cdot\frac{\mathrm{d}\boldsymbol{u}}{\mathrm{d}E}\right), \tag{4}$$

$$\frac{\mathrm{d}\boldsymbol{\alpha}}{\mathrm{d}E} = \left\{\frac{1}{2w^2}\left[\frac{V}{2}\boldsymbol{u} + \frac{r}{4}\left(\frac{\partial V}{\partial \boldsymbol{u}} - 2L^T\boldsymbol{P}\right)\right] + \frac{2}{w}\frac{\mathrm{d}w}{\mathrm{d}E}\frac{\mathrm{d}\boldsymbol{u}}{\mathrm{d}E}\right\}\sin\frac{E}{2}, \tag{5}$$

$$\frac{\mathrm{d}\boldsymbol{\beta}}{\mathrm{d}E} = \left\{\frac{-1}{2w^2}\left[\frac{V}{2}\boldsymbol{u} + \frac{r}{4}\left(\frac{\partial V}{\partial \boldsymbol{u}} - 2L^T\boldsymbol{P}\right)\right] + \frac{2}{w}\frac{\mathrm{d}w}{\mathrm{d}E}\frac{\mathrm{d}\boldsymbol{u}}{\mathrm{d}E}\right\}\cos\frac{E}{2}, \tag{6}$$

where $\boldsymbol{P}$ is the representation for the sum of nonconservative forces, namely, atmospheric drag, solar radiation pressure, spacecraft thrust, etc.; V is the perturbing potential which is the summation of all conservative forces such as non-sphericity of the central body, third-body gravity attraction, etc.; τ is the time element which computes the physical time through

$$t = \tau - \frac{1}{w}(\boldsymbol{u}\cdot\boldsymbol{u}^*),$$

$\boldsymbol{\alpha}$ and $\boldsymbol{\beta}$ are the KS regular elements arising from the KS elements $\boldsymbol{u}$ and $\boldsymbol{u}^*$. The vector dimension in KS space is four. The integration of Eqs. (3)–(6) is carried out using a fixed step-size fourth-order Runge–Kutta numerical scheme with Gill's variation.

The gravitational perturbations are indicated by perturbing potential V which is expanded in terms of Legendre polynomial (P_n) of degree n. The third-body perturbing potential is

$$V_{n\kappa} = -\frac{\mu_\kappa}{r_\kappa}\sum_{n=2}^{\infty}\left(\frac{r}{r_\kappa}\right)^n P_n(\cos\varphi_\kappa), \tag{7}$$

with

$$\cos\varphi_\kappa = \frac{x_\kappa x + y_\kappa y + z_\kappa z}{r_\kappa r},$$

φ_κ is the angle between the third-body and the spacecraft in inertial geocentric equatorial coordinates in degrees, $\boldsymbol{r}_\kappa = (x_\kappa, y_\kappa, z_\kappa)$ is the position vector and its components of the third-body in the inertial geocentric equatorial coordinate frame in km, R is the equatorial radius of the Earth in km and μ_κ is the standard gravitational parameter of the third-body in $\mathrm{km^3 s^{-2}}$. κ is "M" for the Moon and is "S" for the Sun. The perturbing potential term with Earth's oblateness is

$$V_n = \frac{\mu}{r}\sum_{n=2}^{\infty} J_n\left(\frac{R}{r}\right)^n P_n(\cos\psi), \tag{8}$$

with

$$\cos\psi = \frac{z}{r},$$

where ψ is the argument of latitude in degrees and J_n is the nth order coefficient of the zonal harmonic. When only V is considered and $\boldsymbol{P} = 0$, Eq. (3) becomes

$$\frac{\mathrm{d}w}{\mathrm{d}E} = 0, \tag{9}$$

and rest of the equations are simplified. Plataforma Solar de Almería (PSA) [11] and Fourier series algorithm [12] compute the geocentric lunar and solar position vectors. The state and time elements equations are computed with the lunisolar perturbing potential chosen up to third- and fourth-order expansion, respectively. The initial conditions are obtained as in [9].

3 Numerical Study

The change in the perigee and the apogee altitudes, after a number of orbits, caused by lunisolar gravity tends to change the eccentricity. Eccentricity change (Δe) can be directly translated to velocity change (Δv_e in ms^{-1}) and mass change (Δm) as

$$\Delta v_\mathrm{e} = \frac{n_\mathrm{mean} a}{2\sqrt{1-e^2}}\Delta e,\ \Delta m = m_0\left(1 - e^{-\frac{\Delta v_\mathrm{e}}{g_0 I_\mathrm{sp}}}\right), \tag{10}$$

where n_mean is the mean motion in s^{-1}, a is the semimajor axis in km, m_0 is initial mass in kg, $g = 9.80665$ is the acceleration due to gravity in ms^{-2}, and $I_\mathrm{sp} = 400$ is the specific impulse of the engine in s. A contour map of Δm is plotted in Fig. 1 with Δv_e ranging from 1 to 10 ms^{-1} and m_0 from 1000 to 15000 kg. For a Δv_e gain of 5 ms^{-1} for m_0 of 6000 kg, the mass gain is up to 10 kg.

To achieve a good mass gain margin, the sensitivity of the initial orbital parameters (time and day, inclination, argument of perigee, and the Sun azimuth angle with respect to the spacecraft orbital plane) on the pre-TLI orbits should be considered. Using KSROP, naturally propelled pre-TLI orbits are designed and their physics is studied purview of the initial orbital parameters in respect to reachability to sphere of influence of the Moon.

Three test cases with a fixed perigee altitude and different apogee altitudes (h_a0), as shown in Table 1, are considered with varying initial inclination, argument of perigee, right ascension of ascending node and initial epoch. The initial inclination and epoch are varied in steps of 1 degree and day, respectively. The initial argument of perigee and right ascension of the ascending node are varied in steps of 5 degree. The propagation is done for up to 50 revolutions and maximum Δv_e gain ($\Delta v_\mathrm{egain+}$) is computed for each initial condition from Eq. (10). Only the initial conditions that

can reach within the lunar sphere of influence after an impulsive maneuver at perigee with $\Delta v_{\text{egain+}}$ are obtained and rest of the initial conditions are deemed invalid.

If Δv_{e} is found to be negative, then it is not a suitable solution. The number of valid initial conditions exceeds 70,000 in each case. Taking the maximization of the mission performance into consideration, the maximum $\Delta v_{\text{egain+}}$ obtained at the end of 10, 30 and 50 revolutions for each case is tabulated in Table 2.

The magnitude of the $\Delta v_{\text{egain+}}$ values for each case resonates with the initial apogee altitude and the number of revolutions. Cases A and B have relatively more difference

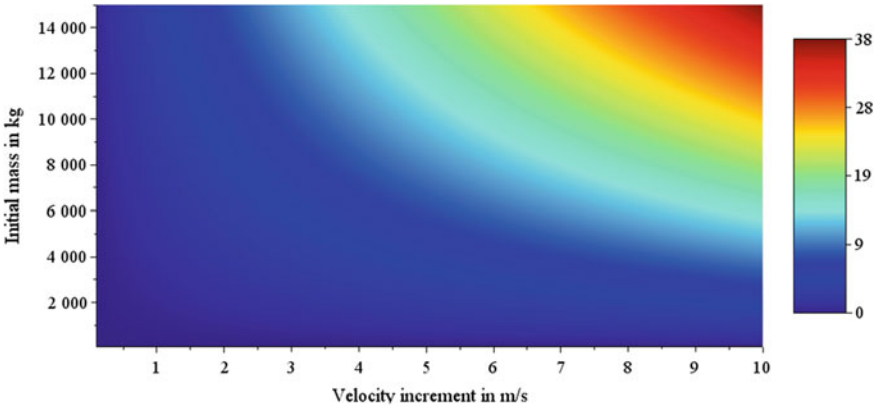

Fig. 1 Mass gain (Δm) map in kg for fixed I_{sp}= 400 s and $g = 9.80665$ ms^{-2}

Table 1 Initial osculating elements for numerical simulation

Case		A	B	C
h_{p0} in km		800		
h_{a0} in km		60,000	70,000	80,000
I_0	in degrees	17:1:28		
Ω_0		0:5:360		
ω_0		0:5:360		
M_0		0.0		
Initial epoch	dd-mm-yyyy hh:min:ss	01-01-2019 00:00:00		

Table 2 Maximum $\Delta v_{\text{egain+}}$ (ms^{-1}) for each case

Number of revolutions	Case		
	A	B	C
10	1.26336	1.41931	1.45219
30	2.3057	3.40331	4.152255
50	3.60427	5.07808	5.8561736

than cases B and C. It is mainly due to the initial epoch, argument of perigee and right ascension of the ascending node are found to be in the same neighborhood for cases B and C.

To further understand the dynamics of the solar gravity on the velocity increment, it is necessary to impose a limit on the lowest $\Delta v_{\text{egain+}}$ mainly because there exists solutions with $\Delta v_{\text{egain+}}$ of the order 10^{-3} ms^{-1} which is not a very good margin. The total number of solutions that can be sequestered between the lower limit and maximum $\Delta v_{\text{egain+}}$ is the number of good solutions with relatively better $\Delta v_{\text{egain+}}$ values. With these constraints, the points are plotted with the initial epoch against the varied initial orbital parameters in Figs. 2, 3 and 4. For simulations up to 10 revolutions, the lower limit is set at 1.25, 1.40 and 1.44 ms^{-1} for cases A, B, and C, respectively, and depicted in Fig. 2. The total number of obtained solutions are 73, 12, and 27, respectively. It is noticed that good solutions exist only near the solstices for $\omega_0 < 90°$ or $\omega_0 > 90°$ and few are observed near the start of the year before the equinox. With inclination variation, case A is noted only at inclinations above 20° during summer solstice and during start of the year. A similar trend is observed in B and C. Before the spring equinox, there are few solutions for the Sun azimuth angle between 100° and 150° and around summer solstice for the Sun azimuth angle above 300°. Similar seasonal trend as the inclination variation is found for Ω_0 variation.

For the cases up to 30 revolutions, the lower limit for $\Delta v_{\text{egain+}}$ is set at 2.3, 3.0, and 4.0 ms^{-1} in cases A, B, and C, respectively, where the total number of obtained solutions are 23, 5, and 150. From Fig. 3, it is inferred that solutions exist near equinoxes for $\omega_0 > 180°$ and near solstices for $\omega_0 < 180°$. They show increasing trend as the initial epoch varies. Cases A and B have very limited distribution but case C is spread throughout except for the gaps between solstice and equinox. The Sun azimuth angle configuration for the solutions is found where it is clear that there

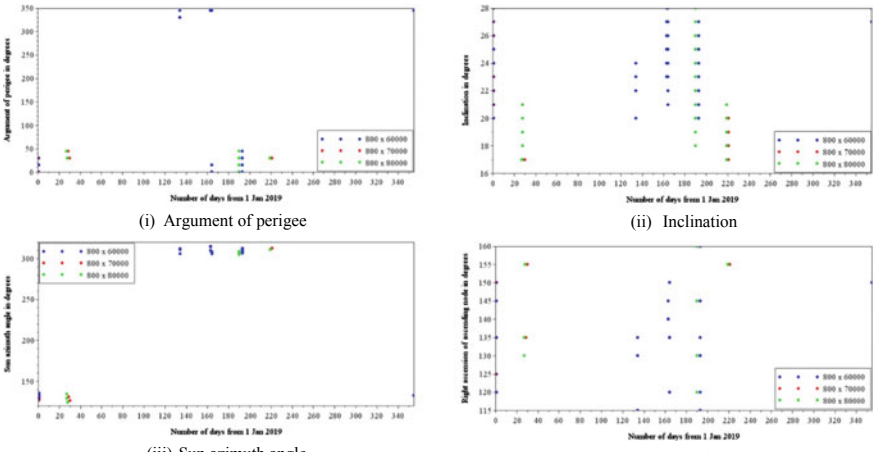

(i) Argument of perigee (ii) Inclination

(iii) Sun azimuth angle (iv) Right ascension of ascending node

Fig. 2 Initial epoch versus (selected orbital elements) for solutions found up to 10 revolutions with cases A (blue), B (red), and C (green)

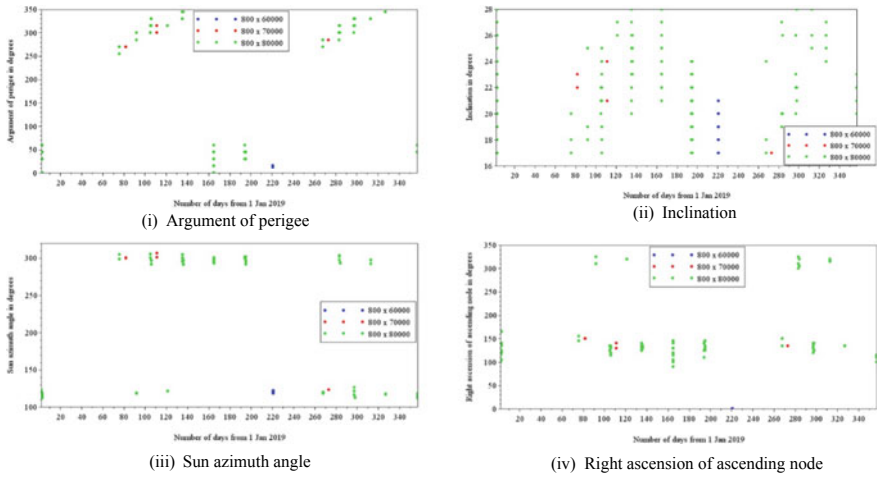

(i) Argument of perigee (ii) Inclination

(iii) Sun azimuth angle (iv) Right ascension of ascending node

Fig. 3 Initial epoch versus (selected orbital elements) for solutions found up to 30 revolutions with cases A (blue), B (red), and C (green)

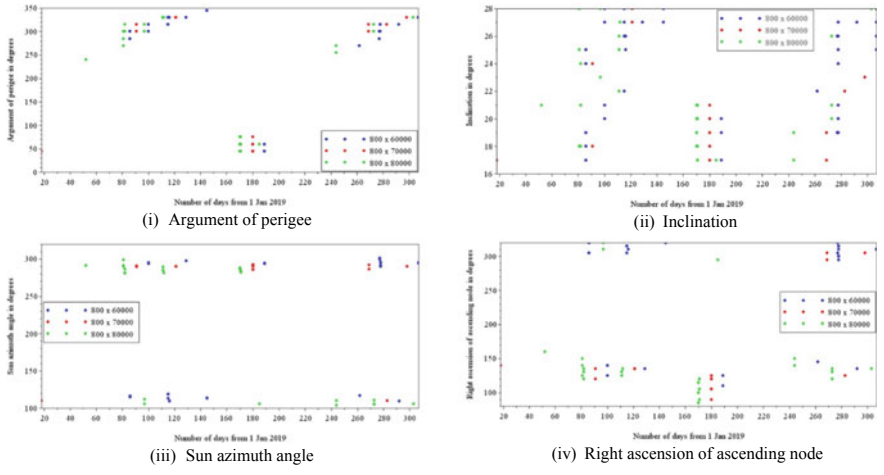

(i) Argument of perigee (ii) Inclination

(iii) Sun azimuth angle (iv) Right ascension of ascending node

Fig. 4 Initial epoch versus (selected orbital elements) for solutions found up to 50 revolutions with cases A (blue), B (red), and C (green)

is no solution below 90° and between 150° and 250°. Solutions are found between the two equinoxes for $\Omega_0 < 180°$ and $> 90°$ in cases A and C. For $\Omega_0 > 180°$, the solutions in case B are found between two solstices and in case C between the two equinoxes.

A lower limit is set on Δv_{egain+} at 3.5, 5.0, and 5.75 ms^{-1} for cases A, B, and C with 50 revolutions, respectively. The number of solutions obtained from these settings is 37, 18, and 31, respectively. It is observed in Fig. 4 that the initial argument of

perigee is found above 180° during equinoxes and below 180° during solstices. The number of solutions decrease as the equinox season fades into solstice but the initial argument of perigee increases in all cases. Summer solstice has relatively higher number of points than the winter solstice. Similarly, seasonal dynamics are seen with respect to inclination as well. For all inclinations during equinoxes, the trend is similar to the argument of perigee for all the three cases. It is inferred that the seasonal dynamics of the initial Sun azimuth angle is more pronounced when it is in the range of (90°–150°) and (250°–320°). Equinox seasons contains more good solutions than solstices. Case B is not very prominent in the lower angles of the Sun azimuth. The right ascension of the ascending node is found with similar distribution and range as in Sun azimuth distribution. In the higher range, relatively there are less number of solutions than lower range, especially it can be noticed during solstice. In general, no good solution exists for the Sun azimuth angle in first quadrant and in the range of (150°–250°) which is due to the positive change in perigee altitude thereby reducing the eccentricity. The large gaps in the distribution of the solutions are mainly because of the higher steps in the varying parameters considered for the simulation. The primary reason for choosing higher steps is the computational time. For generating the solution set for a single case up to 50 orbits, the simulation time was about 6 days with an Intel FORTRAN compiler run in a Red Hat Linux Server with 32 GB RAM and 8-core i7-4790 processors @3.6 GHz. The majority of the seasonal dynamics is captured here which can improve the knowledge on multiple orbit raising from pre-TLI orbits for achieving better efficiency in future high energy lunar transfers.

4 Conclusion

The efficacy of the medium-fidelity KSROP is demonstrated through mission planning applications. The physics of the sun gravity propelled pre-TLI orbits and its advantage in improving the mission performance is studied. It is found that such orbits are extremely sensitive to the initial conditions. Delta-V gain up to 6 ms^{-1} is obtained from the computations reaching up to 50 pre-TLI revolutions using linear search algorithm. The gain in delta-V can be represented as gain in the propellant mass thereby providing an opportunity for additional margin or for mounting piggyback smaller payloads such as lunar cubesats. Future studies shall use a variant of genetic algorithm with better KSROP model to obtain finer solutions for real-time applications.

Acknowledgements We would like to extend our gratitude to Padma Shri Dr. V. Adimurthy for the fruitful discussion. We extend our thanks to the IBM Centre of Excellence for Big Data Software at Karunya Institute of Technology and Sciences. The first author acknowledges Dr. Moriba Jah and the Texas Advanced Computing Centre at UTAustin.

References

1. Sharma RK, Bandyopadhyay P, Adimurthy V (2004) Consideration of lifetime limitation for spent stages in GTO. Adv Space Res 34(5):1227–1232. https://doi.org/10.1016/j.asr.2003.10.044
2. Wang Y, Gurfil P (2016) Dynamical modeling and lifetime analysis of geostationary transfer orbits. Acta Astronaut 128:262–276. https://doi.org/10.1016/j.actaastro.2016.06.050
3. Wang Y, Gurfil P (2017) The role of solar apsidal resonance in the evolution of geostationary transfer orbits. Adv Space Res 59(8):2101–2116. https://doi.org/10.1016/j.asr.2017.01.038
4. Koon WS, Lo MW, Marsden JE, Ross SD (2001) Low energy transfer to the Moon. Celest Mech Dyn Astron 81(1):63–73. https://doi.org/10.1023/A:1013359120468
5. Hatch SJ, Roncoli RB, Sweetser TH (2010) GRAIL trajectory design: lunar orbit insertion through science. In: AIAA/AAS astrodynamics specialist conference, Toronto, Canada
6. Adimurthy V, Ramanan RV, Tandon SR, Ravikumar C (2005) Launch strategy for Indian lunar mission and precision injection to the Moon using genetic algorithm. J Earth Syst Sci 114(6):711–716. https://doi.org/10.1007/BF02715954
7. Ramanan RV, Adimurthy V (2006) Precise lunar gravity assist transfers to geostationary orbits. J Guid Control Dyn 29(2):500–502. https://doi.org/10.2514/1.17469
8. Kustaanheimo P, Stiefel EL (1965) Perturbation theory of Kepler motion based on Spinor regularization. J Reine Angew Math 218:204–219. https://doi.org/10.1515/crll.1965.218.204
9. Stiefel EL, Scheifele G (1971) Linear and regular celestial mechanics. Springer, Berlin
10. Sundman KF (1913) Mémoire sur le problème des trois corps. Acta Math 36(1):105–179. https://doi.org/10.1007/BF02422379
11. Blanco-Muriel M, Alarcón-Padilla DC, López-Moratalla T, Lara-Coira M (2001) Computing the solar vector. Sol Energy 70(5):431–441. https://doi.org/10.1016/S0038-092X(00)00156-0
12. Simpson DG (1999) An alternative lunar ephemeris model for on-board flight software use. In: NASA/GSFC flight mechanics symposium, pp 175–184

On the Recurrence Signatures of Flapping Wings Exposed to Gusty Simple Shear Flow

Manabendra M. De, J. S. Mathur and S. Vengadesan

Abstract The primary aim of the research reported in this paper was to understand the effect of change of gusty simple shear inflow's gradient on the force and moment patterns of a flapping wing in the 3D reference frame. A wing undergoing one degree of freedom asymmetric flapping and rectangular planform shape was considered. The gradient of the gusty simple shear inflow profile, V_{grad}, was varied from –10 to +10 in steps of 5 and corresponding vertical and horizontal forces and moment about the flapping axis were computed. Time series of these forces and moment were used to plot the global recurrence plots and were compared. Quantitative analysis of the findings was carried out by the windowed recurrence quantification analysis of the force and moment patterns. Eight recurrence parameters, viz. recurrence rate, determinism, laminarity, trapping time, ratio, entropy, maximum line and trend were calculated and compared. Numerical investigations revealed that negative gusty shear gradient induced a considerable increase in vertical force and moment and marginally decreased the horizontal forces. Positive gusty shear gradient induced a marginal increase in horizontal forces but caused a substantial decrement in vertical force and moment.

Keywords 1 DoF asymmetric flapping · Gusty shear flow · Pico aerial vehicle · Global recurrence plots · Windowed recurrence quantification analysis

1 Introduction

Flapping wings have been studied by academicians, scientists and engineers over past decades to decode the fluid dynamics that drive the magnificent flight of birds and insects. Various approaches like analytical, experimental and computational fluid dynamics have been employed to understand the science. Attempts are underway

M. M. De (✉) · J. S. Mathur
CSIR-National Aerospace Laboratories, Bengaluru, India
e-mail: manav@nal.res.in

S. Vengadesan
Indian Institute of Technology Madras, Chennai, India

D. Maity et al. (eds.), *Advances in Fluid Mechanics and Solid Mechanics*,
Lecture Notes in Mechanical Engineering,
https://doi.org/10.1007/978-981-15-0772-4_2

to employ this scientific understanding to design and develop artificial flyers and use them for civilian and military applications. However, due to their small size and less mass, when these artificial flyers operate outdoor, they are subjected to the gusty atmospheric conditions. In order to optimally operate in such gusty conditions, it becomes important to understand the effect of these destabilizing atmospheric conditions on the forces generated by the flapping wings and then find out measures to ensure stable and controlled flight. Researchers like Lian and Shyy [1], Viswanath and Tafti [2], Prater and Lian [3], Sarkar et al. [4], Zhu et al. [5] and Jones and Yamaleev [6] studied effects of gusty inflow conditions on the flapping wing. Most of them dealt with inflow conditions represented by a temporally varying sinusoidal function or a Heaviside function. However, a real-life inflow condition has wind shear also. Keeping in mind these aspects, 2D [7] and 3D [8] simulations were carried out to understand the effect of various inflow conditions on the force and moment patterns of flapping wings. It was observed in the previous study [8] that the inflow with a gusty simple shear inflow condition induced a relatively higher disturbance on the force and moment patterns generated by a flapping wing.

In light of the above-mentioned observations and the previously reported studies [7, 8], the present work focused on the numerical investigation of a rectangular wing with 1 DoF asymmetric flapping kinematics subjected to a gusty simple shear inflow profile in the 3D reference frame. The gradient of the gusty simple shear velocity inflow profile, V_{grad}, was varied and the effects on the force and moment patterns were studied. Gusty simple shear inflow model was represented by a mathematical expression with a non-zero mean inflow velocity term, a sinusoidally fluctuating temporal term and a 1D shear gradient term. Reynolds number of the simulation was limited to 150.

2 Methodology

3D unsteady Navier–Stokes equations were solved using finite volume formulation, assuming incompressible and laminar flow for Re = 150. Mass and momentum equations were solved in a fixed inertial reference frame by the ALE formulation. Spatial discretization was second-order upwind and the temporal discretization was second-order implicit. PISO scheme was used for pressure–velocity coupling. The convergence of the iterative method was considered to be satisfied when mass and momentum residues decreased below $O(10^{-6})$ in magnitude. Finite volume formulation based-CFD code ANSYS Fluent was used to solve the 3D time-dependent unsteady Reynolds averaged Navier–Stokes equations. Dynamic meshing was used for simulating wing flapping.

Flow domain is shown in Fig. 1. Flow domain consisted of a spherical domain containing the wing. This domain moved with the wing. The grid inside this domain did not deform during the simulation. The spherical domain was bounded by a cubical flow domain. The grids in this domain deformed and re-gridded and adjusted their shapes and sizes as the wing marched in time and flapped. Face ABCD was attributed

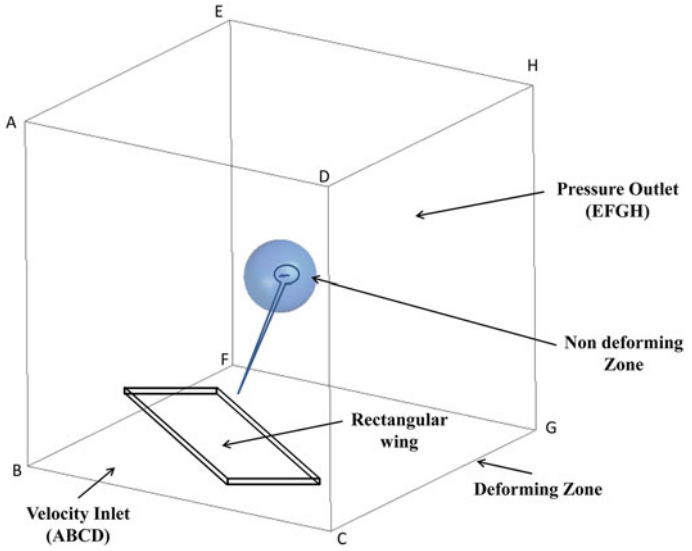

Fig. 1 Domain details

with inlet velocity boundary condition. The gusty simple shear inflow condition was specified on this face. Face EFGH was attributed to pressure outlet boundary condition. The rest of the four faces, bounding the cubical domain, were attributed with symmetric boundary conditions.

Wing kinematics is shown in Fig. 2. As depicted in the schematic, the kinematics was asymmetric 1 DoF flapping. Similar kinematics is reported in the literature [9]. Wing planform was rectangular in shape with an aspect ratio of 4, wing half-span of 155 mm and thickness of 0.3 mm. The flapping axis coincided with the X-axis. The simulation was carried out for the flapping frequency of 250 Hz. Mean free stream velocity, U_∞, and fluid properties like density and viscosity were specified to

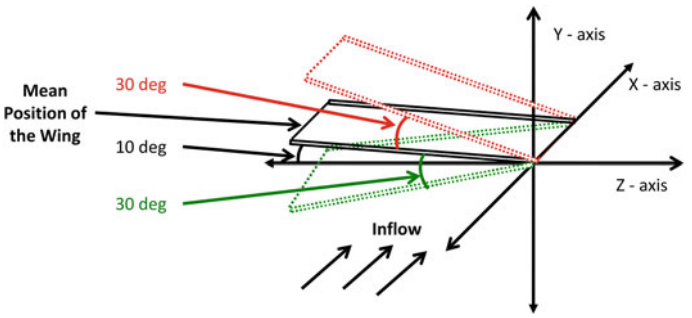

Fig. 2 Wing kinematics (looking from upstream)

maintain simulation Re = 150. This Re falls in the operating regime of natural flyers like the fruit fly and man-made flyers like pico aerial vehicles (PAVs).

The spatiotemporal frontal gust model, reported in this paper, was of the form $U_{inlet} = U_\infty + U_g \sin(2\pi f_g t) + V_{grad} \cdot y$. Here, U_{inlet} is the inlet velocity, U_∞ is mean free stream velocity, U_g is gust amplitude, V_{grad} is the spatial velocity gradient per unit length along Y-axis, y is the spatial location along Y-axis, f_g is gust frequency in Hz and t is time in seconds. For the simulation reported in this paper, V_{grad} was varied from -10 to $+10$ in steps of 5. Gust amplitude was of the same order as wingtip velocity and gust frequency was an order of magnitude lesser than the flapping frequency.

Global recurrence plots, derived from the phase plots of the forces and moments for positive and negative shear gradients, were compared to qualitatively examine the change in their signatures. Windowed recurrence quantification analysis using eight recurrence parameters were carried out to quantitatively examine the effect of change in the gradient of the gusty simple shear inflow profile on the force and moment patterns.

3 Results and Discussions

Findings of the present study are reported in this section. These include plots of instantaneous and gust cycle averaged force and moment coefficients, global recurrence plots and windowed recurrence quantification analysis.

3.1 Instantaneous Force and Moment Coefficients

Variations in instantaneous force and moment coefficient during a flapping cycle over a period of one gust cycle are shown in Fig. 3a–c. The expressions to calculate these force and moment coefficients are as follows:

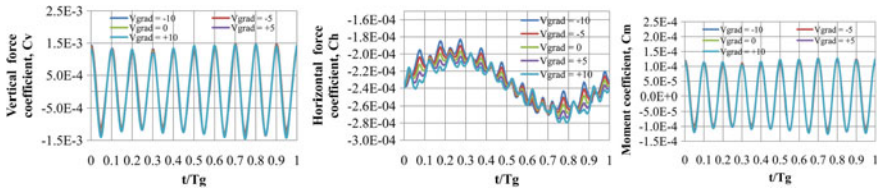

(a) Vertical force coefficient (b) Horizontal force coefficient (c) Moment coefficient

Fig. 3 Variation of instantaneous coefficients

$$C_V = \frac{F_V}{\frac{1}{2} \times \rho \times A_{wing} \times U_\infty}, \; C_H = \frac{F_H}{\frac{1}{2} \times \rho \times A_{wing} \times U_\infty} \; \& \; C_M = \frac{M_{Pivot}}{\frac{1}{2} \times \rho \times A_{wing} \times U_\infty \times r'} \quad (1)$$

Here, ρ is the fluid density in kg/m^3, A_{wing} is wing planform area in m^2 and U_∞ is free stream velocity in m/s. F_V and F_H are instantaneous vertical and horizontal forces generated by the wing during flapping in Newton, respectively, and M_{Pivot} is the aerodynamic moment about wing's flapping pivot axis in N-m. *r'* is the characteristic distance and is considered as the distance between the pivot point and the centroid of the wing planform. C_V, C_H and C_M are the non-dimensionalized vertical and horizontal force and moment coefficients, respectively. The instantaneous force and moment coefficients are plotted against non-dimensionalized time. The reference timescale considered here is the period of one gust cycle, T_g.

It was observed from the plots of the instantaneous force and moment coefficients that the shear gradient affected the force and moment patterns throughout the gust cycle. The effect of shear gradient on the vertical force and moment was similar in nature. The effect was observed to be more prominent during the wing reversals for the vertical force and moment coefficients. The shear gradient altered the horizontal force pattern throughout the gust cycle.

3.2 *Gust Cycle Averaged Forces and Moment Coefficient*

Variations in gust cycle averaged forces and moment coefficients with respect to V_{grad} are shown in Fig. 4a–c.

It was observed from these plots that as the shear gradient, V_{grad} varied from –10 to +10, the gust cycle averaged vertical force coefficient as well as moment coefficient reduced in magnitude. The gust cycle averaged horizontal force coefficient, on the other hand, increased as the shear gradient, V_{grad} varied from –10 to +10. The decrement in vertical force and moment were significant. Increment in the horizontal force due to the variation of the shear gradient from –10 to +10 was marginal. Also, the variation of the force and moment coefficients was nonlinear in nature. In the

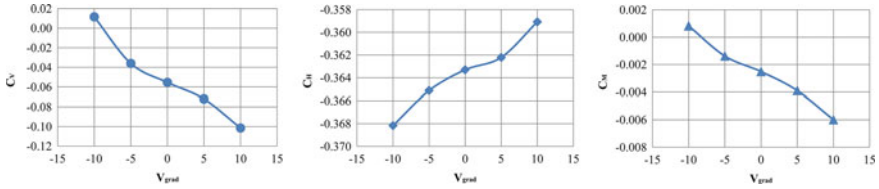

(a) Vertical force coefficient (b) Horizontal force coefficient (c) Moment coefficient

Fig. 4 Variation of gust cycle averaged coefficients w.r.t V_{grad}

present studies, two shear gradients on either side of the zero shear gradient were considered. In order to understand the nonlinear behaviours, further detailed studies can be pursued.

3.3 Global Recurrence Plots [10]

Global recurrence plots (GRP) are 2D graphical representation of the temporal instances when the state of a dynamic system recurs. The plot represents the distances of every point g(a) to all the other points g(b) in the 2D phase space plot. The mathematical expression for GRP is shown below:

$$G(a, b) = c(\|g(a) - g(b)\|) \tag{2}$$

Here, a and b = 1, 2, 3, …, M, $\|\cdot\|$ is the Euclidean norm and c(·) correlates the distance to the colour code. GRPs of vertical and horizontal force coefficients and moment coefficient for $V_{grad} = \pm 10, \pm 5$ and 0 were plotted and are shown in Fig. 5a–c, respectively.

From these studies, it was observed that GRP patterns of the force and moment coefficients exhibited a checkerboard pattern for all the shear gradient inflow conditions. This indicated that their variation was periodic in nature and was a superposition of harmonic oscillations. Checkerboard patterns for the vertical force and moment coefficients were similar in nature. This implied that the effect of a change in the gradient of gusty simple shear inflow was similar in nature on these two parameters. Secondary checkerboard patterns were observed apart from the primary patterns in the GRPs of the horizontal force coefficient. This prominently indicated the presence of a periodic temporal change in the force pattern. These secondary checkerboard patterns differed in accordance with the variation in the gradient of the gusty simple shear flow. It implied that higher positive and negative shear gradient induced a possible onset of instability in the horizontal force pattern.

3.4 Windowed Recurrence Quantification Analysis [10]

Windowed recurrence quantification analysis (WRQA) is a quantitative recurrence paradigm which inspects whether a dynamic system has a tendency or trend to move to an unstable state. In the present study, eight parameters proposed by Webber and Marwan [10] have been used. The eight parameters are recurrence rate, determinism, laminarity, trapping time, ratio, entropy, maximum line and trend. One window period width was equal to the period of one flapping cycle. This choice was governed by the thought process that the frontal gust induced a change in the inflow conditions for consecutive flapping cycles. The focus of the study was to examine whether the difference in the frontal gusty inflow conditions induced uneven fluctuations in the

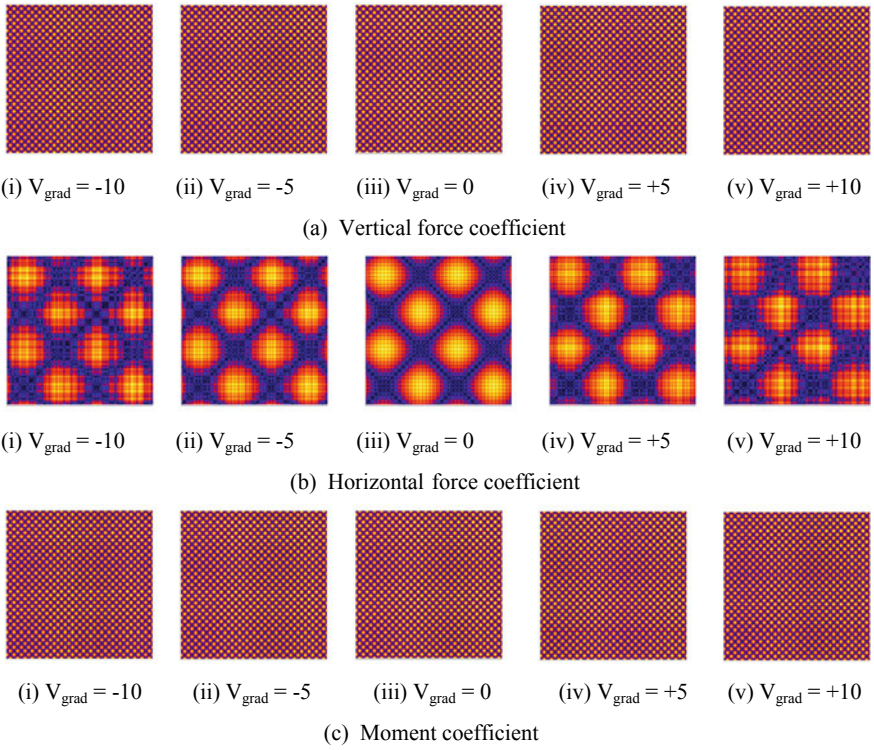

Fig. 5 Global recurrence plots

recurrence parameter series. A visible fluctuation in the recurrence parameter series would imply a possible onset of instability. Standard deviations of these recurrence parameter series were calculated to examine the extent of fluctuations. The threshold for the WRQA calculations was chosen as five times the standard deviation to avoid the effect of spurious local spikes. Dimension equal to 1 was considered. Euclidean norm was adopted for calculating neighbourhood radius.

3.4.1 Recurrence Rate

Recurrence rate quantifies the concentration of recurrence instances in a dynamic system. The mathematical expression to calculate it is as shown below:

$$\text{Recurrence Rate} = \frac{1}{M^2} \sum_{a,b=1}^{M} R_{a,b}^{d,r} \times 100 \tag{3}$$

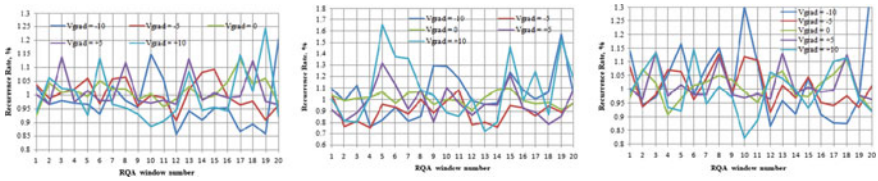

(a) Vertical force coefficient (b) Horizontal force coefficient (c) Moment coefficient

Fig. 6 Recurrence rate series

Here M is the data series length and $R_{a,b}^{d,r}$ is the d-dimensional recurrence matrix and r is the neighbourhood radius. For the reported study, d is equal to 1, and the value of r is set in a manner such that the value of recurrence rates in the WRQA approximates to 1% [10]. Recurrence rate series for force and moment coefficients are shown in Fig. 6a–c.

3.4.2 Determinism

Determinism is the measure of the diagonal pattern of length $l_{\min}$ in a GRP. A stochastic natured dynamic system has a small value of determinism. A periodically natured dynamic system has higher values of determinism. Mathematical expression to calculate determinism is as below:

$$\text{Determinism} = \frac{\sum_{l=l_{\min}}^{M} l\,P^r(l)}{\sum_{a,b}^{M} R_{a,b}^{d,r}} \times 100 \tag{4}$$

Here $P^r(l)$ represents frequency distribution of the diagonal pattern of length l, r is the neighbourhoods radius and $l_{\min}$ is the minimum threshold of diagonal pattern. For the present studies, $l_{\min} = 2$ was considered. Determinism series for force and moment coefficients are shown in Fig. 7a–c.

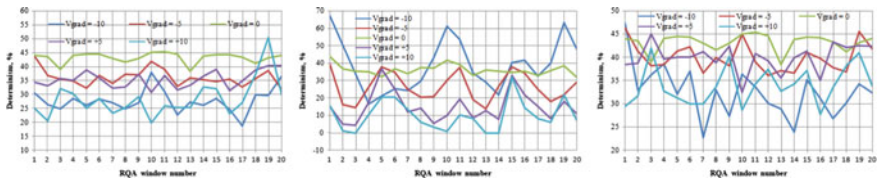

(a) Vertical force coefficient (b) Horizontal force coefficient (c) Moment coefficient

Fig. 7 Determinism series

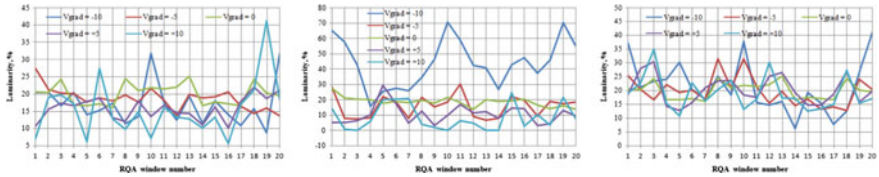

(a) Vertical force coefficient (b) Horizontal force coefficient (c) Moment coefficient

Fig. 8 Laminarity series

3.4.3 Laminarity

Laminarity is the measure of the vertical line of length v_{min} in a GRP. It is the representation of the laminar state of a dynamic system and is independent of the laminar phase length. Laminarity reduces when the proportion of recurrence singularities is higher. Laminarity is calculated as below:

$$\text{Laminarity} = \frac{\sum_{v=v_{\min}}^{M} v P^r(v)}{\sum_{a,b}^{M} R_{a,b}^{d,r}} \times 100 \tag{5}$$

Here $P^r(v)$ is the frequency distribution of the vertical pattern's length v in the recurrence plot, r is the neighbourhood radius, and v_{min} is the minimum threshold of vertical pattern. For the present studies, $v_{min} = 2$ was considered. Laminarity series for force and moment coefficients are shown in Fig. 8a–c.

3.4.4 Trapping Time

Trapping time is derived based on the vertical patterns of GRP. It contains details of the quantity and magnitude of vertical patterns. It represents the temporal trapping information of the state of a dynamic system. Trapping time is calculated as below:

$$\text{Trapping Time} = \frac{\sum_{v=v_{\min}}^{M} v P^r(v)}{\sum_{v=v_{\min}}^{M} P^r(v)} \tag{6}$$

Trapping time series for force and moment coefficients are shown in Fig. 9a–c.

3.4.5 Ratio

Ratio is the WRQA parameter derived from determinism and recurrence rate. This parameter helps to detect transitions in the nature of a dynamic system. Ratio is calculated as below:

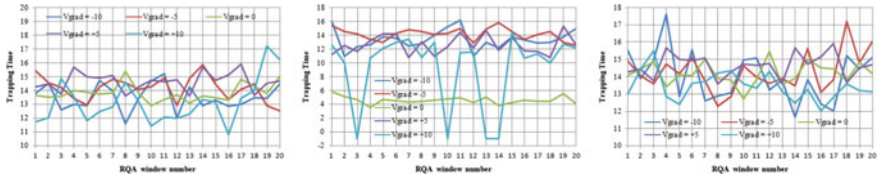

(a) Vertical force coefficient (b) Horizontal force coefficient (c) Moment coefficient

Fig. 9 Trapping time series

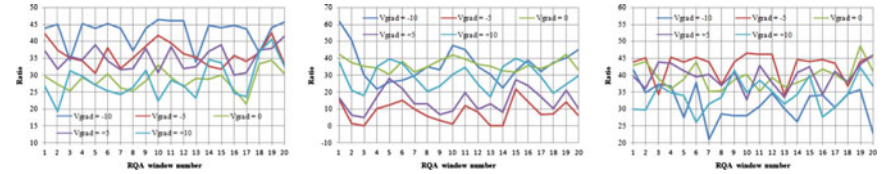

(a) Vertical force coefficient (b) Horizontal force coefficient (c) Moment coefficient

Fig. 10 Ratio series

$$\text{Ratio} = M^2 \frac{\sum_{l=l_{\min}}^{M} l P^r(l)}{\left(\sum_{a,b}^{M} R_{a,b}^{d,r}\right)^2} \tag{7}$$

Ratio series for force and moment coefficients are shown in Fig. 10a–c.

3.4.6 Entropy

Entropy is the Shannon entropy associated with the diagonal line lengths in the GRP. It represents the complications of the deterministic patterns. Entropy is calculated as below:

$$\text{Entropy} = -\sum_{l=l_{\min}}^{M} p(l) ln p(l);\ p(l) = \frac{P^r(l)}{\sum_{l=l_{\min}}^{M} P^r(l)} \tag{8}$$

Here, the value of $l_{\min}$ is considered as 2. Entropy series for force and moment coefficients are shown in Fig. 11a–c.

3.4.7 Maximum Line

Maximum line is associated with the mutual divergence of the trajectory patterns in a GRP. It represents the limits of the closeness of each trajectory pattern with their neighbouring patterns. It is linked to the largest positive Lyapunov exponent. It

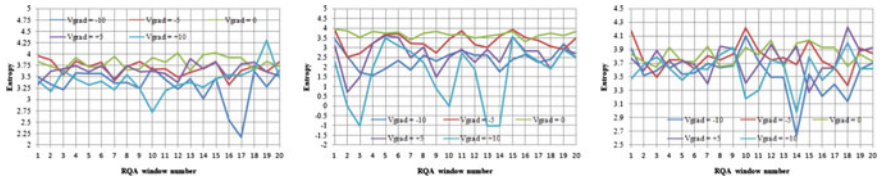

(a) Vertical force coefficient (b) Horizontal force coefficient (c) Moment coefficient

Fig. 11 Entropy series

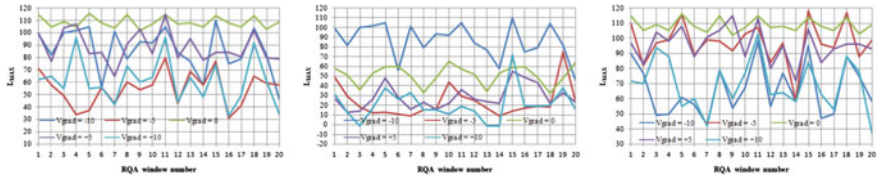

(a) Vertical force coefficient (b) Horizontal force coefficient (c) Moment coefficient

Fig. 12 Maximum line series

contains information about the rate of divergence of the trajectories. Maximum line is calculated as below:

$$\text{Maximum Line} = max(\{l_i; i = 1 \ldots M\}) \tag{9}$$

Maximum Line series for force and moment coefficients are shown in Fig. 12a–c.

3.4.8 Trend

Trend represents the linear regression coefficient associated with the diagonal patterns along the line of identity (LoI). It measures the time distance between the diagonal patterns and the LoI. It is useful to detect drifts or such non-stationary events. Trend is calculated as below:

$$\text{Trend} = \frac{\sum_{a=1}^{M}(a - M/2)(RR_a - \langle RR_a \rangle)}{\sum_{a=1}^{M}(a - M/2)^2} \tag{10}$$

Here, $\langle \text{RR}_\text{a} \rangle$ represents average recurrence rate of the ath diagonal pattern. Trend series for force and moment coefficients are shown in Fig. 13a–c.

Standard deviations of all the recurrence parameters based on forces and moment coefficients were computed and are reported in Tables 1, 2, and 3.

All the WRQA series quantitatively implied that the fluctuation of the windowed series varied with the variation in the shear gradient. As compared to the fluctuations in the WRQA parameters of the force and moment patterns for the flapping wing

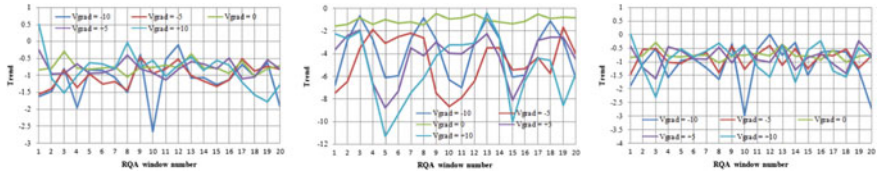

(a) Vertical force coefficient (b) Horizontal force coefficient (c) Moment coefficient

Fig. 13 Trend series

with a gusty simple shear inflow gradient of zero, the higher positive and negative gradient flows induced more fluctuations. Also, it was observed that the fluctuations of the force and moment patterns corresponding to positive and negative gusty simple shear flow grading had phase differences among them. From the tables of standard deviations of the WRQA parameter series, it was observed that the standard deviation was less for the shear gradient of zero. As the shear gradient varied on either side (positive and negative), the standard deviations of the series increased. This implied that the presence of a gradient in the inflow induced fluctuations in the series of WRQA parameter. It is interpreted from these observations that the increase of shear gradient can induce instability in the force patterns of the flapping wing system with a 1 DoF asymmetric flapping kinematics.

4 Conclusion

Findings of the numerically investigate of flapping wings with Re = 150 undergoing asymmetric 1 DoF flapping kinematics under the influence of gusty simple shear inflow condition were reported in this paper. Effects of positive and negative shear inflow profile on forces and moment patterns were assessed. It was observed that variation of the gradient from negative to positive shear inclination reduced the vertical force and moments and increased the horizontal force. From the application point of view, this know-how would lead to improvement of the existing control algorithms for kinematics of flapping wings and hence perk up their performance. For example, if the pico aerial vehicle needs more lift force during a vertical take-off mode, the stroke plane angle can be modulated such that a negative shear gradient V_{grad} within an acceptable limit is maintained, thus improving the lift force pattern. Similarly, when the need for higher thrust arises, the stroke plane angle can be modulated to maintain a positive shear gradient V_{grad} within an acceptable limit. This would help to the realization of man-made aerial vehicles with better flight stability, longer flight endurance and enhanced manoeuvrability. Higher magnitude of relative shear velocity inflow gradient would lead to the onset of instability. Hence too much of relative shear velocity inflow gradient should be avoided for a wing exhibiting a 1 DoF asymmetric flapping kinematics.

Table 1 Standard deviation of RQA parameter series based on vertical force coefficient

Shear gradient, V_{grad}	Recurrence rate	Determinism	Laminarity	Trapping time	Ratio	Entropy	Maximum line	Trend
−10	0.09	4.31	6.09	0.95	3.93	0.37	18.02	0.60
−5	0.05	3.02	3.16	0.89	3.51	0.16	13.77	0.32
0	0.04	1.85	3.05	0.63	3.09	0.14	4.53	0.18
+5	0.06	3.01	3.36	0.68	3.47	0.15	12.70	0.24
+10	0.09	6.72	8.23	1.62	5.33	0.29	18.26	0.53

Table 2 Standard deviation of RQA parameter series based on horizontal force coefficient

Shear gradient, V_{grad}	Recurrence rate	Determinism	Laminarity	Trapping time	Ratio	Entropy	Maximum line	Trend
−10	0.19	14.70	15.54	1.42	10.02	0.48	18.02	2.22
−5	0.10	8.35	7.28	0.89	6.22	0.41	16.20	2.17
0	0.05	3.02	3.16	0.54	3.51	0.16	10.23	0.32
+5	0.14	8.84	6.27	1.39	6.98	0.75	12.08	2.03
+10	0.27	8.70	8.51	5.41	7.66	1.52	16.60	2.98

Table 3 Standard deviation of RQA parameter series based on moment coefficient

Shear gradient, V_{grad}	Recurrence rate	Determinism	Laminarity	Trapping Time	Ratio	Entropy	Maximum line	Trend
−10	0.15	5.50	9.49	1.48	5.26	0.30	17.21	0.78
−5	0.07	3.07	5.29	1.15	3.93	0.20	13.79	0.34
0	0.05	1.85	3.05	0.65	3.45	0.14	4.53	0.18
+5	0.06	2.97	5.13	0.68	3.65	0.23	11.14	0.38
+10	0.09	4.15	6.27	0.82	4.37	0.24	17.11	0.59

References

1. Lian Y, Shyy (2007) Aerodynamics of low Reynolds number plunging airfoil under gusty environment. In: 45th AIAA aerospace sciences meeting and exhibit, AIAA paper 2007-70. https://doi.org/10.2514/6.2008-523
2. Viswanath K, Tafti DK (2010) Effect of frontal gusts on forward flapping flight. AIAA J 48(9):2049–2062. https://doi.org/10.2514/1.J050263
3. Prater R, Lian Y (2012) Aerodynamic response of stationary and flapping wings in oscillatory low Reynolds number flows. In: 50th AIAA aerospace science meeting including the new horizons forum and aerospace exposition, AIAA paper 2012-0418. https://doi.org/10.2514/6.2012-418
4. Sarkar S, Chajjed S, Krishnan A (2013) Study of asymmetric hovering in flapping flight. Eur J Mech B Fluids 37:72–89. https://doi.org/10.1016/j.euromechflu.2012.07.002
5. Zhu J, Jiang L, Zhao H, Tao B, Lei B (2015) Numerical study of a variable camber plunge airfoil under wind gust condition. J Mech Sci Technol 29(11):4681–4690. https://doi.org/10.1007/s12206-015-1015-z
6. Jones M, Yamaleev NK (2016) Effect of lateral, downward and frontal gusts on flapping-wing performance. Comput Fluids 140:175–190. https://doi.org/10.1016/j.compfluid.2016.08.016
7. De MM, Mathur JS, Vengadesan S (2016) Numerical investigation of insect-sized flapping wings in inclined-stroke plane under the influence of spatio-temporally varying frontal gust, 61-istam-fm-fp-386. In: 61st Congress of the Indian society of theoretical and applied mechanics (an international conference), 11th–14th Dec 2016. VIT, Vellore
8. De MM, Mathur JS, Vengadesan S (2018) Recurrence perspective of forces generated by flapping wing under different frontal inflow conditions. In: NAFEMS Indian regional conference on engineering modelling, analysis, simulation and 3D printing (NIRC-2018), 20th–21st July 2018, Bengaluru
9. Hong YS, Altman A (2008) Lift from spanwise flow in simple flapping wings. J Aircr 45:1206–1216. https://doi.org/10.2514/1.34100
10. Webber Jr CL, Marwan N (2015) Recurrence quantification analysis: theory and best practices. Springer, Switzerland

Unsteady Heat Transfer from a Non-isothermal Axisymmetric Body Immersed in Porous Media Saturated by Nanofluid

Shobha Bagai and Mridu Sharma

Abstract The intent of this paper is to present the numerical results for transient heat transfer across an axisymmetric non-isothermal body embedded in porous media saturated by nanofluid. A non-linear coupled PDE is reduced using dimensionless similarity variables and is solved using Keller Box method. Buoyancy ratio *Nr*, Brownian motion *Nb* and thermophoresis *Nt* are the parameters considered in this study. The effect of Lewis number *Le* and non-Newtonian parameter *N* on reduced Nusselt number and reduced Sherwood number is recorded in tabular form for isothermal as well as for non-isothermal bodies. The heat flux for different values of non-Newtonian parameter *N* is plotted in the case of sphere and cylinder at different time levels.

Keywords Porous media · Nanofluid · Transient · Non-Newtonian fluid · Non-isothermal axisymmetric body · Keller Box method

1 Introduction

Nanofluids possesses novel properties that make them useful in geophysics and geothermal engineering, cooling of electronic systems, thermal insulation system, groundwater pollution, and petroleum recovery. The field of heat transfer from a heated body immersed in porous media saturated by nanofluids has been an area of great interest to researchers across the globe due to its wide-scale applications. Nanofluids play a crucial role as they enhance the thermal conductivity of a fluid and are better than microfluids as they do not clog the pores. Mahdi et al. [1] and Kasaeian et al. [2] in their review papers discussed latest developments in the field of porous media and nanofluid. Some of the theory on this topic was also documented in ([3–6]). The study of convection in porous media is done for different types of

S. Bagai (✉)
Cluster Innovation Center, University of Delhi, New Delhi, India
e-mail: shobhabagai@gmail.com

M. Sharma
Department of Mathematics, University of Delhi, New Delhi, India

D. Maity et al. (eds.), *Advances in Fluid Mechanics and Solid Mechanics*,
Lecture Notes in Mechanical Engineering,
https://doi.org/10.1007/978-981-15-0772-4_3

geometries immersed in porous media saturated with nanofluid has been studied by different researchers. Nield and Kuznetsov [7] and Noghrehabadi et al. [8] have investigated the problem for a flat vertical plate for constant viscosity and variable viscosity, respectively. Gorla and Kumari [9] have solved free convection problem for a non-Newtonian fluid for a horizontal plate. Tham and Nazar [10] and Gorla et al. [11] have studied the problem for a sphere and a vertical cone, respectively.

Due to computational complexities of transient problems, the work carried out by researchers in this field is mostly restricted to steady state. There are variety of methods available to solve transient problems. For example, Degan et al. [12] investigated transient boundary-layer flow along a vertical surface embedded in an anisotropic porous medium using method of characteristics. Amin et al. [13] worked on Darcy–Brinkman–Forchheimer model using explicit finite differencing scheme etc. Chamkha et al. [14] presented a study of steady, laminar, natural convection boundary-layer flow over a permeable vertical cone embedded in a porous medium saturated with a nanofluid in the presence of uniform lateral mass flux. An analysis was carried out by Loganathan et al. [15] to study the effects of heat generation and nanoparticle volume concentration on an unsteady free convective flow of a nanofluid past an impulsively started infinite vertical plate. Finite difference method was used by Sheremet et al. [16] to solve unsteady free convection heat transfer in porous cavity filled with nanofluid using Buongiorno's mathematical model. Rajesh et al. [17] worked on the effects of transverse magnetic field on transient free convective flow of nanofluid past an impulsively started infinite vertical porous plate with viscous dissipation.

The present study focuses on transient free convection heat transfer from an axisymmetric body immersed in a porous media saturated by nanofluid for different values of non-Newtonian parameter N. In this study, the system of coupled PDEs has been solved using the Keller Box method.

2 Physical Model and Governing Equations

Consider Fig. 1 where the axes are fixed as x-axis along the surface of the body and the y-axis normal to the surface of the body. The initial temperature of the body $T = T_\infty$, where T_∞ is the ambient temperature, is increased to $T = T_w(x)$ which is thereafter maintained at the same level, when time t is greater than zero. The wall geometry $r^*(x)$ is equal to 1, for plane flow and to $r(x)$, for axisymmetric flow.

Consider the following governing equations which involves equation of continuity, equation of momentum, equation of energy and equation of nanoparticle volume fraction together with the boundary conditions. Introducing Darcy law and Boussinesq approximations, we get

$$\frac{\partial(r^*u)}{\partial x} + \frac{\partial(r^*v)}{\partial y} = 0 \tag{1}$$

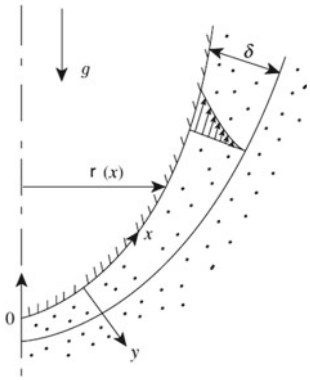

Fig. 1 Physical model

$$u^N = \frac{(1-\phi_\infty)k\beta g_x(T-T_\infty)}{\nu} - \frac{(\rho_p/\rho_{f\infty}-1)g_x k(\phi-\phi_\infty)}{\nu} \tag{2}$$

$$\sigma\frac{\partial T}{\partial \tau} + u\frac{\partial T}{\partial x} + v\frac{\partial T}{\partial y} = \alpha\frac{\partial^2 T}{\partial y^2} + \tau\left[D_B\frac{\partial \phi}{\partial y}\frac{\partial T}{\partial y} + \frac{D_T}{T_\infty}\left(\frac{\partial T}{\partial y}\right)^2\right] \tag{3}$$

$$\Phi\frac{\partial \phi}{\partial \tau} + u\frac{\partial \phi}{\partial x} + v\frac{\partial \phi}{\partial y} = \frac{\partial^2 \phi}{\partial y^2} + \frac{D_T}{T_\infty}\frac{\partial^2 T}{\partial y^2} \tag{4}$$

$$\text{At } \tau = 0: \quad u = 0,\ v = 0,\ T = T_\infty \tag{5}$$

$$\tau > 0:\ v = 0,\ T = T_w(x), \phi = \phi_w \text{ at } y = 0$$
$$u \to 0,\ T \to T_\infty, \phi \to \phi_\infty \text{ as } y \to \infty \tag{6}$$

The acceleration due to gravity is given by $g_x = g[1-(dr/dx)^2]^{\frac{1}{2}}$. We introduce the following similarity transformations to non-dimensionalize Eqs. (2)–(4):

$$f(\eta, t) = \frac{\psi}{\alpha r^*\left(Ra_x I(x)\right)^{\frac{1}{2}}} \tag{7}$$

$$\theta(\eta, t) = \frac{T-T_\infty}{\Delta T_w(x)} \tag{8}$$

$$\omega(\eta, t) = \frac{\phi-\phi_\infty}{\Delta\phi_w} \tag{9}$$

where η is the dimensionless space variable and t is the dimensionless time variable given by

$$\eta = \frac{y}{x}\left(\frac{Ra_x}{I(x)}\right)^{\frac{1}{2}} \text{ and } t = \frac{\alpha}{\sigma x^2}\frac{Ra_x}{I(x)}\tau \tag{10}$$

The streamfunction ψ is defined as

$$u = \frac{1}{r^*}\frac{\partial \psi}{\partial y} \text{ and } v = -\frac{1}{r^*}\frac{\partial \psi}{\partial x}$$

which satisfies the equation of continuity (1). The modified Rayleigh number is defined by

$$Ra_x = \frac{x}{\alpha}\left(\frac{(1-\phi_\infty)k\beta g_x \Delta T_w}{\nu}\right)^{1/N} \tag{11}$$

and

$$I(x) = \frac{\int_0^x (g_x \Delta T_w)^{\frac{1}{N}} r^{*2} dx}{(g_x \Delta T_w)^{\frac{1}{N}} r^{*2} x} \tag{12}$$

is a non-dimensional function of x.
Substitution of the similarity variables given by Eqs. (7)–(10) in Eqs. (2)–(4) yields

$$\left(\frac{\partial f}{\partial \eta}\right)^N = \theta - Nr\frac{\Delta T_{wr}}{\Delta T_w(x)}\omega \tag{13}$$

$$\frac{\partial \theta}{\partial t} - \frac{1}{2}f\frac{\partial \theta}{\partial \eta} + \delta\frac{\partial f}{\partial \eta}\theta = \frac{\partial^2 \theta}{\partial \eta^2} + Nb\frac{\partial \theta}{\partial \eta}\frac{\partial \omega}{\partial \eta} + Nt\frac{\Delta T_w(x)}{\Delta T_{wr}}\left(\frac{\partial \theta}{\partial \eta}\right)^2 \tag{14}$$

$$\frac{\partial^2 \omega}{\partial \eta^2} + \frac{Nt}{Nb}\frac{\Delta T_w(x)}{\Delta T_{wr}}\frac{\partial^2 \theta}{\partial \eta^2} = CLe\frac{\partial \omega}{\partial t} - \frac{1}{2}Lef\frac{\partial \omega}{\partial \eta} \tag{15}$$

where C is the ratio of heat capacity and porosity. The initial and boundary conditions in non-dimensional form are written as

$$\begin{aligned} &\text{At } t = 0: \quad f = 0, \theta = 0, \omega = 0 \\ &\text{for } t > 0: \quad f = 0,\ \theta = 1, \omega = 1 \quad \text{at } \eta = 0 \\ &\qquad\qquad f' \to 0,\ \theta \to 0, \omega \to 0 \ \text{ as } \eta \to \infty \end{aligned}$$

3 Solution Procedure

The lumped parameter δ and the wall temperature defined as in [18]

$$\delta = \frac{dln\Delta T_w}{dlnx}\frac{\int_0^x r^{*2}(g_x \Delta T_w)^{\frac{1}{N}} dx}{r^{*2}(g_x \Delta T_w)^{\frac{1}{N}} x} \text{ and } \Delta T_w \propto \xi^\lambda \tag{16}$$

Also, ΔT_{wr} is defined as the average wall temperature

$$\Delta T_{wr} = \frac{1}{\xi}\int_0^{\xi} \Delta T_w d\xi \tag{17}$$

where the variable ξ is given as $\xi = \int_0^x r^{*2} g_x^{\frac{1}{N}} dx$.
Hence, δ will turn out to be

$$\delta = \frac{N\lambda}{\lambda + N} \tag{18}$$

For the plane flow, $r^* = 1$ and $g_x = g$, ξ is proportional to the distance measured from the lower stagnation point. The variable ξ for the horizontal cylinder is given by $\xi = g^{\frac{1}{N}} R \int_0^{\Phi} sin^{\frac{1}{N}} \Phi \, d\Phi$ and for the sphere is given by $\xi = g^{\frac{1}{N}} R^3 \int_0^{\Phi} sin^{2+1/N} \Phi \, d\Phi$, where R is the radius of the horizontal cylinder (or the sphere) and Φ is the angle measured from the lower stagnation point.

4 Keller Box Method

We will use Keller Box method to solve Eqs. (13)–(15) together with initial and boundary conditions. The method is an extension of Crank–Nicolson method and is second-order accurate in both time and space. This method is unconditionally stable. The detailed discussion of this method can be found in Cebeci and Bradshaw [19] and Keller [20]. The method can be described in three steps:

Step 1 Convert the system of higher order PDEs into the system of first-order PDEs.

$$\theta' = \theta_1 \tag{19}$$

$$\omega' = \omega_1 \tag{20}$$

$$(f')^N = \theta - \frac{Nr}{\lambda + 1}\omega \tag{21}$$

$$\frac{\partial \theta}{\partial t} - \frac{1}{2} f\theta_1 + \frac{N\lambda}{N + \lambda} f'\theta = \theta_1' + Nb\omega_1\theta_1 + Nt(\lambda + 1)(\theta_1)^2 \tag{22}$$

$$\omega_1' + \frac{Nt(\lambda + 1)}{Nb}\theta_1' = CLe\frac{\partial \omega}{\partial t} - \frac{Le}{2} f\omega_1 \tag{23}$$

where prime in the above equations is with respect to η.

Step 2 The finite difference scheme is applied to first-order PDEs to obtain corresponding difference equations.

For Eqs. (19)–(21), central differencing is applied with midpoint at $(\eta_{j-1/2}, t^n)$,

$$\frac{\theta_j^n - \theta_{j-1}^n}{h} = \frac{(\theta_1)_j^n + (\theta_1)_{j-1}^n}{2} \tag{24}$$

$$\frac{\omega_j^n - \omega_{j-1}^n}{h} = \frac{(\omega_1)_j^n + (\omega_1)_{j-1}^n}{2} \tag{25}$$

$$\left(\frac{f_j^n - f_{j-1}^n}{h}\right)^N = \frac{(\theta_j^n + \theta_{j-1}^n)}{2} - \frac{Nr}{\lambda+1}\frac{\omega_j^n + \omega_{j-1}^n}{2} \tag{26}$$

The remaining first-order Eqs. (22) and (23) are solved by using central difference about the midpoint $(\eta_{j-1/2}, t^{n-1/2})$.

$$\frac{\theta_{j-1/2}^n - \theta_{j-1/2}^{n-1}}{\Delta t} = \frac{1}{2}(f)_{j-1/2}^{n-1/2}(\theta_1)_{j-1/2}^{n-1/2} - \frac{N\lambda}{N+\lambda}(\theta)_{j-1/2}^{n-1/2}\frac{f_j^{n-1/2} - f_{j-1}^{n-1/2}}{h} + \frac{(\theta_1)_j^{n-1/2} - (\theta_1)_{j-1}^{n-1/2}}{h} + Nb(\omega_1)_{j-1/2}^{n-1/2}(\theta_1)_{j-1/2}^{n-1/2} + Nt(\lambda+1)\frac{({\theta_1}_{j-1/2}^{n-1/2})^2 + ({\theta_1}_{j-1/2}^{n-1/2})^2}{2} \tag{27}$$

$$\frac{(\omega_1)_j^{n-1/2} - (\omega_1)_{j-1}^{n-1/2}}{h} + \frac{Nt(\lambda+1)}{Nb}\frac{(\theta_1)_j^{n-1/2} - (\theta_1)_{j-1}^{n-1/2}}{h} = CLe\frac{(\omega)_{j-1/2}^n - (\omega)_{j-1/2}^{n-1}}{\Delta t} - \frac{1}{2}(f)_{j-1/2}^{n-1/2}(\omega_1)_{j-1/2}^{n-1/2} \tag{28}$$

Step 3 Linearise the discretized equations using Newton's Method.

We will substitute the following linearising equations in Eqs. (24)–(28) and ignore the higher order terms of δ to obtain system of linear PDEs:

$$\begin{aligned}
\theta_j^{n+1} &= \theta_j^n + \delta\theta_j^n \\
{\theta_1}_j^{n+1} &= {\theta_1}_j^n + \delta{\theta_1}_j^n \\
\omega_j^{n+1} &= \omega_j^n + \delta\omega_j^n \\
{\omega_1}_j^{n+1} &= {\omega_1}_j^n + \delta{\omega_1}_j^n \\
f_j^{n+1} &= f_j^n + \delta f_j^n
\end{aligned}$$

The boundary conditions are also linearised using the same set of linearising equations to obtain following transformed boundary conditions:

$$\begin{aligned}
&\delta\theta_0 = 0, \quad \delta\omega_0 = 0 \text{ and } \delta f_0 = 0 \\
&\delta\theta_M = 0, \quad \delta\omega_M = 0.
\end{aligned} \tag{29}$$

The system of linearised equations together with boundary conditions takes the form of $AX = B$ where A is a block tridiagonal matrix and B is a column vector. This system of equations in matrix form together with appropriate initial guess, satisfying boundary conditions, can be solved using Matlab or Mathematica to obtain the values of X. In this paper, the solution is accepted when tolerance error reaches 10^{-3}.

5 Results and Discussions

The non-dimensional heat flux for a vertical flat plate at $x = L_r$ is given by [18]

$$q_v{}^* = [-\theta'(0)]\left(\frac{\lambda + N}{N}\right)^{\frac{1}{2}}.$$

Table 1 contains the values of the reduced Nusselt number $(-\theta'(0))$ and reduced Sherwood number $(-\omega'(0))$ at steady state by solving the system of difference equations using Keller Box method. $Nr = 0.5$, $Nt = 0.5$ and $Nb = 0.5$ are assumed to be constants and variation is done with respect to Lewis number Le and non-Newtonian parameter N. The solutions $(-\theta'(0))$ and $(-\omega'(0))$ were independent of the choice of Δt and h, which confirms the stability of the method used for the problem under study. The values are presented for $\Delta t = 0.05$ and $h = 0.02$. Also, as the value of N increases from 0.5 to 2, the value of $(-\theta'(0))$ and $(-\omega'(0))$ increases. As the parameter Le occurs only in the equation for the nanoparticle fraction (28), the effect of the Lewis number Le is visible in the values of reduced Sherwood number $-\omega'(0)$ whereas it does not alter the values of reduced Nusselt number. Sherwood number increases significantly as Le increases. The values at steady state are independent of constant C, for calculation purpose we have assumed $C = 0.1$.

The profiles of temperature function versus η are plotted in Figs. 2, 3, and 4 for pseudoplastic fluids $(N = 0.5)$, Newtonian fluids $(N = 1)$, and dilatant fluids $(N = 2)$. Figures 5, 6, and 7 illustrate the heat flux variations for the three types of fluids under consideration. For all the three cases, the heat flux oscillates near the boundary $(\eta = 0)$. The oscillations are smooth for non-isothermal body and are more significant in the transient state. These oscillations die down as we reach the steady state. The streamfunction profiles are given in Figs. 8, 9, and 10. Because $u \to 0$ as $\eta \to \infty$, the streamfunction f tends to a constant value as $\eta \to \infty$.

Table 1 Values of reduced Nusselt number $-\theta'(0)$ and reduced Sherwood number$-\omega'(0)$ for different values of λ and Le at steady state for vertical plate

λ	Le	$N = 0.5$		$N = 1$		$N = 2$	
		$-\theta'(0)$	$-\omega'(0)$	$-\theta'(0)$	$-\omega'(0)$	$-\theta'(0)$	$-\omega'(0)$
0	10	0.1688	1.0768	0.2191	1.3876	0.2513	1.5783
	50	0.1818	2.6416	0.2217	3.2541	0.2485	3.6253
	100	0.1860	3.7893	0.2234	4.6222	0.2489	5.1247
1	10	0.2750	1.1809	0.3885	1.3054	0.4848	1.3650
	50	0.2681	3.1939	0.3628	3.5341	0.4466	3.7243
	100	0.2671	4.6247	0.3568	5.0987	0.4361	5.3649

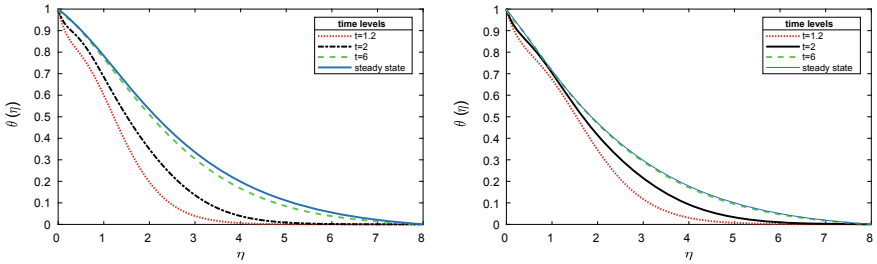

(a) $\lambda = 0$ (b) $\lambda = 1$

Fig. 2 Temperature profile for pseudoplastic fluid ($N = 0.5$)

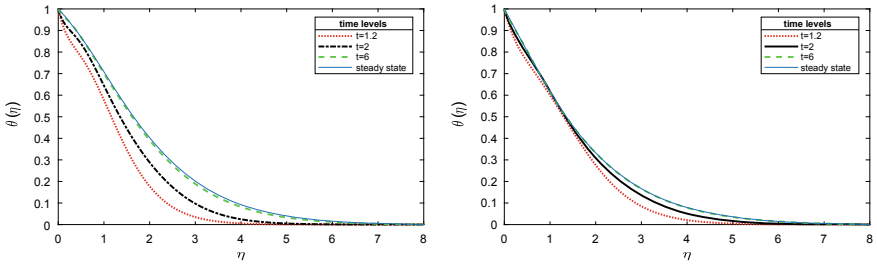

(a) $\lambda = 0$ (b) $\lambda = 1$

Fig. 3 Temperature profile for Newtonian fluid ($N = 1$)

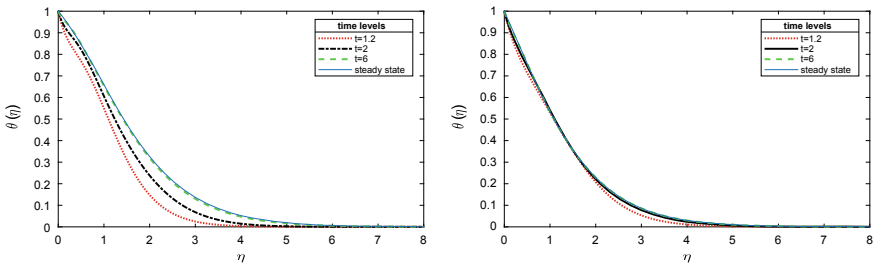

(a) $\lambda = 0$ (b) $\lambda = 1$

Fig. 4 Temperature profile for dilatant fluid ($N = 2$)

The local heat flux for the case of cylinder is given by

$$q_c{}^* = q_v{}^*(sin\phi)^{\frac{1}{N}}\left[\frac{(\int_0^{\phi}(sinx)^{\frac{1}{N}}dx)^{\frac{(2N+1)\lambda-N}{2N}}}{(\int_0^{\pi}(sinx)^{\frac{1}{N}}dx)^{\frac{(2N+1)\lambda}{2N}}}\right]$$

and for the case of sphere is

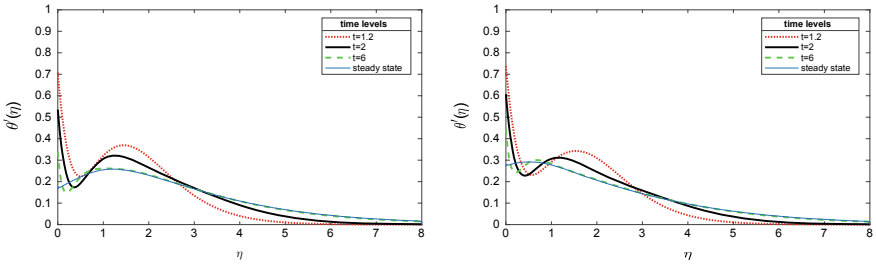

(a) $\lambda = 0$ (b) $\lambda = 1$

Fig. 5 Heat flux profile for pseudoplastic fluid

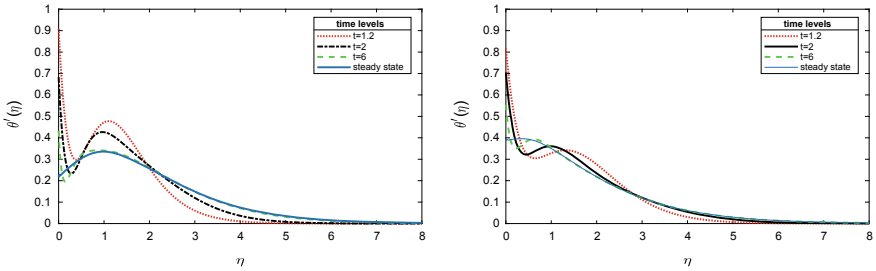

(a) $\lambda = 0$ (b) $\lambda = 1$

Fig. 6 Heat flux profile for Newtonian fluid

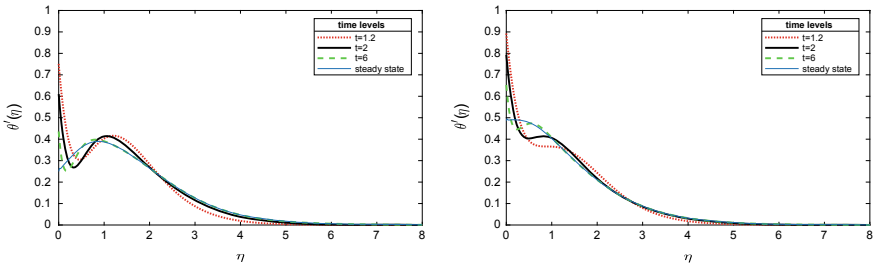

(a) $\lambda = 0$ (b) $\lambda = 1$

Fig. 7 Heat flux profile for dilatant fluid

$$q_s{}^* = q_v{}^*(sin\phi)^{\frac{N+1}{N}}\left[\frac{(\int_0^{\phi}(sinx)^{\frac{2N+1}{N}}dx)^{\frac{(2N+1)\lambda-N}{2N}}}{(\int_0^{\pi}(sinx)^{\frac{2N+1}{N}}dx)^{\frac{(2N+1)\lambda}{2N}}}\right]$$

The heat flux profiles with respect to ϕ are given by Figs. 11 and 12. In these figures, black curves are of isothermal bodies and green ones are for non-isothermal bodies. The limiting value for isothermal as well non-isothermal cases for both sphere and cylinder are calculated at the two stagnation point $\phi = 0, \pi$ and this value turns out

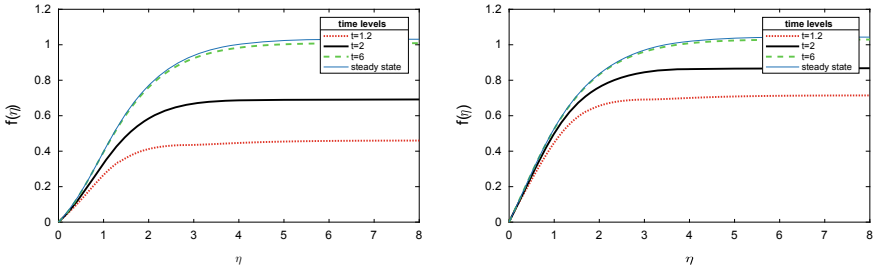

(a) $\lambda = 0$ (b) $\lambda = 1$

Fig. 8 Profile of streamfunction f for pseudoplastic fluid

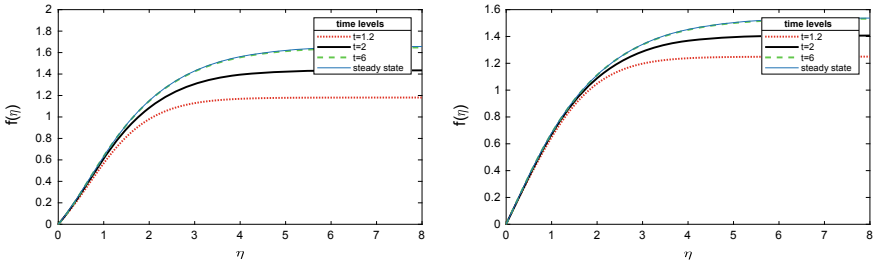

(a) $\lambda = 0$ (b) $\lambda = 1$

Fig. 9 Profile of streamfunction f for Newtonian fluid

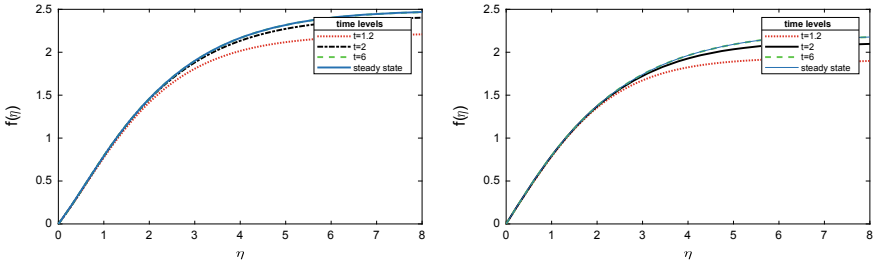

(a) $\lambda = 0$ (b) $\lambda = 1$

Fig. 10 Profile of streamfunction f for dilatant fluid

to be zero except for the case of isothermal bodies at $\phi = 0$ which is 0 for $N = 0.5$, $q_v{}^*$ for $N = 1$ and ∞ for $N = 2$. Using the concept of critical points and double derivative, the maxima value for $N = 1$ is obtained at $\frac{2\pi}{3}$ in case of cylinder and at $\frac{3\pi}{5}$ approximately for sphere. From the figures, we also observe that for a cylinder at $N = 0.5$, the maxima are obtained at $\phi < \frac{2\pi}{3}$ and for $N = 2$, $\phi > \frac{2\pi}{3}$ whereas for sphere, maxima are at the same point.

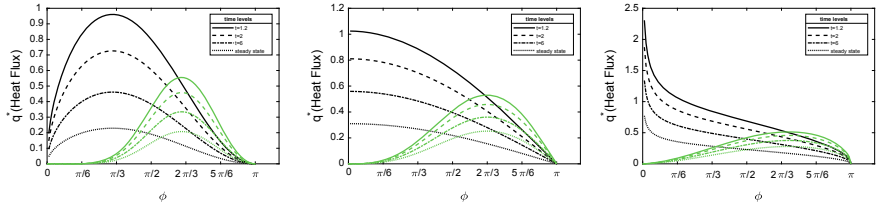

(a) Pseudoplastic Fluid (b) Newtonian Fluid (c) Dilatant Fluid

Fig. 11 Cylinder

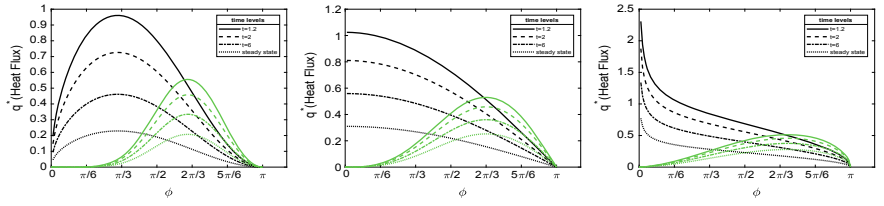

(a) Pseudoplastic fluid (b) Newtonian Fluid (c) Dilatant Fluid

Fig. 12 Sphere

6 Conclusion

The present study investigates transient free convection flow for an axisymmetric body immersed in a porous media saturated by nanofluid. The model incorporates the effect of Brownian motion, buoyancy and thermophoresis. The following conclusions can be made from the above study:

I. The solutions $(-\theta'(0))$ and $(-\omega'(0))$ were independent of the choice of Δt and h. Hence, the stability of the method is assured.
II. As the value of N increases, the heat flux will increase.
III. The effect of the Lewis number Le is insignificant on the reduced Nusselt number $-\theta'(0)$ whereas the effect is significantly visible in the values of reduced Sherwood number $-\omega'(0)$.
IV. The value of reduced Sherwood number increases as Le increases.
V. The limiting value for isothermal as well non-isothermal cases for both sphere and cylinder are calculated at the two stagnation points $\Phi = 0, \pi$, and these values turn out to be zero except for the case of isothermal bodies at $\Phi = 0$ which is 0 for $N = 0.5$, q_v for $N = 1$ and ∞ for $N = 2$.
VI. The point of maxima is observed for non-isothermal body in case of both sphere and cylinder.

References

1. Mahdi RA, Mohammed HA, Munisamy KM, Saeid NH (2015) Review of convection heat transfer and fluid flow in porous media with nanofluid. Renew Sustain Energy Rev 41:715–734. https://doi.org/10.1016/j.rser.2014.08.040
2. Kasaeian A, Daneshazarian R, Mahian O, Kolsi L, Chamkha AJ, Wongwises S, Pop I (2017) Nanofluid flow and heat transfer in porous media: a review of the latest developments. IJHMT 107:778–791. https://doi.org/10.1016/j.ijheatmasstransfer.2016.11.074
3. Pop I, Ingham D (2001) Convective heat transfer
4. Nield DA, Bejan A (2017) Convection in porous media
5. Wafai K (2015) Handbook of porous media
6. Dass SK, Choi SUS, Yu W, Pradeep T (2008) Nanofluids science and technology
7. Kuznetsov AV, Nield DA (2010) Natural convective boundary-layer flow of a nanofluid past a vertical plate. Int J Therm Sci 49(2):243–247. https://doi.org/10.1016/j.ijthermalsci.2009.07.015
8. Noghrehabadi A, Ghalambaz M, Ghanbarzadeh A (2014) Effects of variable viscosity and thermal conductivity on natural-convection of nanofluids past a vertical plate in porous media. J Mech 30(3):265–275. https://doi.org/10.1017/jmech.2013.61
9. Gorla RSR, Kumari M (2003) Free convection in non-Newtonian fluids along a horizontal plate in a porous medium. Heat Mass Transf 39:101–106. https://doi.org/10.1007/s00231-002-0351-6
10. Tham L, Nazar R (2012) Numerical solution of mixed convection flow about a sphere in a porous medium saturated by a nanofluid. J Sci Technol 4:35–46
11. Gorla RSR, Chamkha AJ, Ghodeswar K (2014) Natural convective boundary layer flow over a vertical cone embedded in a porous medium saturated with a nanofluid. J Nanofluids 3:65–71. https://doi.org/10.4236/jmp.2011.22011
12. Degan G, Akowanou C, Awanou N (2007) Transient natural convection of non-Newtonian fluids about a vertical surface embedded in an anisotropic porous medium. Int J Heat Mass Trans 50:4629–4639. https://doi.org/10.1016/j.ijheatmasstransfer.2007.03.023
13. Amin MEl, Salama A, Suna S (2012) A conditionally stable scheme for a transient flow of a non-Newtonian fluid saturating a porous medium. Procedia Comput Sci 9:651–660. https://doi.org/10.1016/j.procs.2012.04.070
14. Chamkha AJ, Rashad AM (2012) Natural convection from a vertical permeable cone in a nanofluid saturated porous media for uniform heat and nanoparticles volume fraction fluxes. Int J Numer Methods Heat Fluid Flow 22(8):1073–1085. https://doi.org/10.1108/09615531211271871
15. Loganathan P, Chand PN, Ganesan P (2015) Transient natural convective flow of a nanofluid past a vertical plate in the presence of heat generation. J Appl Mech Tech Phy 56:433. https://doi.org/10.1134/S002189441503013X
16. Sheremet MA, Pop I, Shenoy A (2015) Unsteady free convection in a porous open wavy cavity filled with a nanofluid using Buongiorno's mathematical model. Int Commun Heat and Mass 67:66–72. https://doi.org/10.1016/j.icheatmasstransfer.2015.07.007
17. Rajesh V, Mallesh MP, Bég OA (2015) Transient MHD free convection flow and heat transfer of nanofluid past an impulsively started vertical porous plate in the presence of viscous dissipation. Procedia Mater Sci 10:80-89. https://doi.org/10.1016/j.mspro.2015.06.028
18. Bagai S, Nishad C (2014) Buoyancy induced flow past a non-isothermal arbitrary shaped axisymmetric body immersed in a non-Newtonian porous medium saturated by a nanofluid. J Nanofluids 3:287–295. https://doi.org/10.1166/jon.2014.1106
19. Cebeci T, Bradshaw P (1988) Physical and computational aspects of convective heat transfer. Springer, New York
20. Keller HB (1992) Numerical methods for two-point boundary value problems. Dover, New York, USA

Nevanlinna Theory for Finding Meromorphic Solutions of Cubic-Quintic Ginzburg–Landau Equation Arising in Nonlinear Dynamics

Adaviswamy Tanuja

Abstract Research on meromorphic solution of complex differential equations using Nevanlinna theory has become a subject of great interest. This paper is devoted to finding meromorphic solutions of the cubic-quintic Ginzburg–Landau equation which arises in problems of dynamics, especially fluid dynamics. We consider the complex differential equation corresponding to cubic-quintic Ginzburg–Landau equation with coefficients being small functions of meromorphic functions. The problem has been mainly studied under the condition that meromorphic function and its first derivative share one value of the type counting multiplicity or ignoring multiplicity.

Keywords Complex differential equations · Ginzburg–Landau equation · Meromorphic functions · Nevanlinna theory

1 Introduction

In this article, we find meromorphic solution of the cubic-quintic Ginzburg–Landau equation using Nevanlinna theory which is a leading tool for obtaining the existence of entire or meromorphic functions as solution of complex differential equations. Recently, many researchers [1–9] have focused attention on complex differential equations and several others [10–13] have concentrated on entire or meromorphic functions sharing one value.

In the rest of this paper, we use standard notations and basic results of Nevanlinna theory [14–17]. The aim of this paper is to find meromorphic solution, $H(z)$, of the following type of differential equation:

$$H' = c_1 H + c_3 H^3 + c_5 H^5, \tag{1}$$

A. Tanuja (✉)
Department of Mathematics, Siddaganga Institute of Technology,
Tumkur 572 103, India
e-mail: a.tanuja1@gmail.com

D. Maity et al. (eds.), *Advances in Fluid Mechanics and Solid Mechanics*,
Lecture Notes in Mechanical Engineering,
https://doi.org/10.1007/978-981-15-0772-4_4

where c_1, c_3 , *and* c_5 are small functions of H. Equation (1) typically arises in a nonlinear stability analysis. One could also have higher degree terms of odd nature in the equation. We consider $H' - 1$ and $H' - H$ to share 0 CM(counting multiplicity) with $\overline{N}_{=5}(r, H) \neq S(r, H)$. In this case H and H' share 1 CM(counting multiplicity). This kind of sharing value plays a cardinal role in finding the solution of complex differential equations. We introduce the even degree terms knowing fully well that they do not exist. This is just for the ease of proof. With the introduction of such terms, Eq. (1) may be written as

$$H' = c_0 + c_1 H + c_2 H^2 + c_3 H^3 + c_4 H^4 + c_5 H^5, \tag{2}$$

it is understood that $c_0 = c_2 = c_4 = 0$ which does not violate the assumption of c_i 's being small functions.

To prove the existence of meromorphic solution for the differential equation (2) we make use of the following lemmas.

2 Required Lemmas

Lemma 1 *Suppose H is a meromorphic function so that H' is not a constant then either*

$$\left(H''\right)^5 = a\left(H' - \mu\right)^6, \tag{3}$$

for some nonconstant a, or

$$N_{4)}(r, H) \leq \overline{N}_{(5}(r, H) + N_{4)}\left(r, \frac{1}{H' - \mu}\right) + \overline{N}\left(r, \frac{1}{H''}\right) + S(r, H), \tag{4}$$

where μ is a constant.

Proof Consider

$$\Phi = 2\frac{H'''}{H''} - 3\frac{H''}{H' - \mu}. \tag{5}$$

Let z_∞ be a pole of H of order 4 and from Eq. (5) we arrive at the following expression:

$$\Phi(z) = O((z - z_\infty)^5).$$

This shows that Φ has zero z_∞ with multiplicity 5. Therefore, Eq. (3) is not true which implies that $\Phi \not\equiv 0$, then

$$\begin{aligned} N_{4)}(r, H) &\leq N(r, \frac{1}{\Phi}) \\ &\leq T(r, \Phi) + O(1). \end{aligned} \tag{6}$$

Note that Φ can have poles of order 4 at zeros of H'' or $H' - \mu$ or multiple poles of H. Hence from Eq. (5), we can write

$$N(r, \Phi) \leq \overline{N}_{(5}(r, H) + N_{4)}\left(r, \frac{1}{H' - \mu}\right) + \overline{N}\left(r, \frac{1}{H''}\right). \tag{7}$$

Again from Eq. (5), we have

$$m(r, \Phi) = S(r, H). \tag{8}$$

Adding Eqs. (7) and (8) and substituting the resulting equation in Eq. (6), we get Eq. (4).

Lemma 2 *Consider meromorphic function H which is nonconstant then either Eq. (4) holds or*

$$H(z) = \frac{3125}{4a[z + 5B_1]^4} + \mu z + B_2, \tag{9}$$

where $a \neq 0$, B_1, B_2 and μ are constants.

Proof Let H be a nonconstant and H' be a constant. Then H is a polynomial of degree at most 1 and so $N_{4)}(r, H) = S(r, H)$. From this case Eq. (4) is true. Now we consider H' is not a constant then by Lemma 1 if Eq. (4) is not true then Eq. (3) must be true. We now rewrite Eq. (3) as

$$\left(\frac{H''}{H' - \mu}\right)^5 = a(H' - \mu). \tag{10}$$

Differentiating Eq. (10), we obtain

$$5\left(\frac{H''}{H' - \mu}\right)^4 \left(\frac{H''}{H' - \mu}\right)' = aH''. \tag{11}$$

Combining Eqs. (10) and (11) yields

$$\left(\frac{H''}{H' - \mu}\right)^{-2} \left(\frac{H''}{H' - \mu}\right)' = \frac{1}{5}. \tag{12}$$

Integrating Eq. (12) once and then using Eq. (10), we get

$$H' - \mu = \frac{1}{a}\left[\frac{-5}{z + 5B_1}\right]^5. \tag{13}$$

By integrating Eq. (13) once and rearranging the resulting equation, we arrive at Eq. (9).

3 Main Results

We now prove two main results in this section one each on functions involving counting multiplicity(CM) and ignoring multiplicity(IM).

Theorem 1 *Suppose meromorphic function H which is nonconstant satisfying Eq. (2). Let $H' - 1$ and $H' - H$ sharing 0 CM, then we have H and H' sharing 1 CM and H will satisfy the equation*

$$H(z) = \frac{z + B_1}{1 - ae^{-z}}, \tag{14}$$

where B_1 and $a \neq 0$ are constants.

Proof From Eq. (2), we can easily infer that $N_{(5}(r, H) + m(r, H) = S(r, H)$ which implies that $T(r, H) = N_{4)}(r, H) + S(r, H)$. Therefore $N_{4)}(r, H) \neq S(r, H)$, i.e., $N_{=4}(r, H) \neq S(r, H)$. Following [18] we can get Eq. (14). Substituting Eq. (14) in Eq. (2), we get

$$\begin{aligned}\left[\frac{z + B_1}{1 - ae^{-z}}\right]' &= c_0 + c_1\left(\frac{z + B_1}{1 - ae^{-z}}\right) + c_2\left(\frac{z + B_1}{1 - ae^{-z}}\right)^2 + c_3\left(\frac{z + B_1}{1 - ae^{-z}}\right)^3 \\ &\quad + c_4\left(\frac{z + B_1}{1 - ae^{-z}}\right)^4 + c_5\left(\frac{z + B_1}{1 - ae^{-z}}\right)^5.\end{aligned} \tag{15}$$

If $c_0 \not\equiv 0$, now using Eq. (15) we get $T(r, e^{-z}) = S(r, e^{-z})$ this is not possible. Hence, we conclude that $c_0 \equiv 0$. Substituting $c_0 \equiv 0$ in Eq. (15) and equating the coefficients of like powers of ae^{-z}, we can obtain $c_1(z),\ c_3(z)\ and\ \ c_5(z)$.

Having proved a theorem on a meromorphic solution of the Ginzburg–Landau equation (2) sharing one CM, in what follows we prove an analogous theorem for one IM.

Theorem 2 *Suppose meromorphic function H which is nonconstant satisfying the Eq. (2). Let H and H' sharing 1 IM, now we have either*

$$H' - 1 = -c_5(H - 1)\left[\left(1 + \frac{c_1}{c_5} + \frac{c_3}{c_5}\right)(H^4 + H^3) + \left(1 + \frac{c_1}{c_5}\right)(H^2 + H) + 1\right], \tag{16}$$

or

$$\begin{aligned}H' - 1 = c_5(H - 1)\Bigg[&\left(B_1 - z - \frac{c_1}{c_5} - \frac{c_3}{c_5} + 1\right)(H^4 + H^3) \\ &+ \left(B_1 - z - \frac{c_1}{c_5} + 1\right)(H^2 + H) + B_1 - z + 1\Bigg],\end{aligned} \tag{17}$$

where B_1 is a constant.

Proof Let z_5 be a zero of $H' - 1$ and $c_j(z_5) \not\equiv 0, \infty (j = 0, 1, 3, 5)$ with H and H' sharing 1 IM along with z_5 being a zero of $H - 1$ of order 4. Now using Eq. (2), we can obtain

$$(c_0 + c_1 + c_3 + c_5)(z_5) \equiv 1. \tag{18}$$

If $c_0 + c_1 + c_3 + c_5 \not\equiv 1$, we obtain

$$\begin{aligned}\overline{N}\left(r, \frac{1}{H'-1}\right) = N\left(r, \frac{1}{H-1}\right) &\leq N\left(r, \frac{1}{c_0+c_1+c_3+c_5-1}\right) + S(r, H),\\ &\leq T(r, c_0 + c_1 + c_3 + c_5) + S(r, H),\\ &\leq T(r, c_0) + T(r, c_1) + T(r, c_3) + T(r, c_5) + S(r, H),\\ &= S(r, H). \end{aligned} \tag{19}$$

From Eq. (2), we get

$$N_{(5}(r, H) + m(r, H) = S(r, H). \tag{20}$$

Combining Eqs. (19) and (20), and using result from Yang and Yi [17], we get

$$\begin{aligned} T(r, H) &\leq N\left(r, \frac{1}{H-1}\right) + \overline{N}\left(r, \frac{1}{H'-1}\right) + \overline{N}(r, H) - N_0\left(r, \frac{1}{H''}\right) + S(r, H),\\ &= \overline{N}_{(5}(r, H) + N_{4)}(r, H) - N_0\left(r, \frac{1}{H''}\right) + S(r, H). \end{aligned}$$

Also, we get the following expression:

$$N_0\left(r, \frac{1}{H''}\right) = S(r, H). \tag{21}$$

Using Eqs. (4) and (9), with $\mu = 1$, we get either

$$N_{4)}(r, H) \leq \overline{N}_{(5}(r, H) + N_{4)}\left(r, \frac{1}{H'-1}\right) + \overline{N}\left(r, \frac{1}{H''}\right) + S(r, H), \tag{22}$$

or

$$H = \frac{3125}{4a[z + 5B_1]^4} + z + B_2, \tag{23}$$

where B_1, B_2, and $c \neq 0$ are constants. From Eqs. (19), (20), and (22), we get

$$T(r, H) \leq \overline{N}\left(r, \frac{1}{H''}\right) + S(r, H). \tag{24}$$

Equation (24) together with Eq. (21) yields the following result:

$$T(r, H) \leq \overline{N}_{(5}\left(r, \frac{1}{H'-1}\right) + S(r, H). \tag{25}$$

Equations (25) and (19) yield the condition $T(r, H) = S(r, H)$, and this is a contradiction. Therefore, Eq. (22) does not hold. From Eq. (23), we find that

$$H - 1 = \frac{24a[z + 5B_1]^4[z + B_2] + 18750}{24a[z + 5B_1]^4} \tag{26}$$

and

$$H' - 1 = \frac{-3125}{a[z + 5B_1]^5}. \tag{27}$$

Now H and H' cannot share 1 IM this is not possible. Therefore

$$c_0 + c_1 + c_3 + c_5 \equiv 1. \tag{28}$$

Substituting Eq. (28) into the differential equation (2), we get

$$H' - 1 = c_5(H - 1)\left[\left(\frac{c_1}{c_5} + \frac{c_3}{c_5} + 1\right) + \left(\frac{c_3}{c_5} + 1\right)(H + H^2) + H^3 + H^4\right]. \tag{29}$$

If $1 + \frac{c_1}{c_5} + \frac{c_3}{c_5} = -1$ or $1 + \left(\frac{c_1}{c_5}\right)' + \left(\frac{c_3}{c_5}\right)' = 0$, then we, respectively, arrive at the conclusion (16) or (17). Otherwise, we infer that

$$N\left(r, \frac{1}{\left(\frac{c_1}{c_5} + \frac{c_3}{c_5} + 1\right) + \left(\frac{c_3}{c_5} + 1\right)(H + H^2) + H^3 + H^4}\right) = S(r, H).$$

Suppose $\left(\frac{c_1}{c_5} + \frac{c_3}{c_5} + 1\right) + \left(\frac{c_3}{c_5} + 1\right)(H + H^2) + H^3 + H^4$ has a zero of multiplicity l at z_0, say, such that $\frac{1}{c_5}\frac{H'-1}{H-1}$ has a zero of multiplicity l at z_0. Now let us consider the following cases:

(i) $H(z_0) = \infty$ or
(ii) $H(z_0) = H^2(z_0) = H^3(z_0) = H^4(z_0) = H'(z_0) = 1$ or
(iii) $c_5(z_0) = \infty$.
If $H(z_0) = \infty$, then c_5 has a pole of multiplicity $l + 1$ at z_0, while if $H'(z_0) = H^4(z_0) = H^3(z_0) = H^2(z_0) = H(z_0) = 5$, then $\frac{c_1}{c_5} + 3\frac{c_3}{c_5} + 5$ has a zero of multiplicity 10 at z_0 and $1 + \left(\frac{c_1}{c_5}\right)' + \left(\frac{c_3}{c_5}\right)'$ has a zero of multiplicity $\min\{l - 1, l + 1 - t\}$ at z_0, here t represents the possible multiplicity of the pole of c_5 at z_0. From case (iii), c_5 will have a pole of multiplicity l at z_0. Hence we have

$$N\left(r, \frac{1}{\left(\frac{c_1}{c_5}+\frac{c_3}{c_5}+1\right)+\left(\frac{c_3}{c_5}+1\right)(H+H^2)+H^3+H^4}\right) \leq N(r, c_5)$$
$$+N\left(r, \frac{1}{\frac{c_1}{c_5}+3\frac{c_3}{c_5}+5}\right)+N\left(r, \frac{1}{1+\left(\frac{c_1}{c_5}\right)'+\left(\frac{c_3}{c_5}\right)'}\right),$$

$$N\left(r, \frac{1}{\left(\frac{c_1}{c_5}+\frac{c_3}{c_5}+1\right)+\left(\frac{c_3}{c_5}+1\right)(H+H^2)+H^3+H^4}\right) \leq S(r, H). \quad (30)$$

Equation (29) may now be written as

$$\frac{\left[\left(\frac{c_1}{c_5}+\frac{c_3}{c_5}+1\right)+\left(\frac{c_3}{c_5}+1\right)(H+H^2)+H^3+H^4\right]'-\left[1+\left(\frac{c_1}{c_5}\right)'+\left(\frac{c_3}{c_5}\right)'\right]}{\left[\left(\frac{c_1}{c_5}+\frac{c_3}{c_5}+1\right)+\left(\frac{c_3}{c_5}+1\right)(H+H^2)+H^3+H^4\right]}$$
$$= c_5(H-1). \quad (31)$$

From Eqs. (20) and (31), it follows that, if $1+\left(\frac{c_1}{c_5}\right)'+\left(\frac{c_2}{c_5}\right)' \neq 0$, then

$$m\left(r, \frac{1}{\left(\frac{c_1}{c_5}+\frac{c_3}{c_5}+1\right)+\left(\frac{c_3}{c_5}+1\right)(H+H^2)+H^3+H^4}\right) = S(r, H). \quad (32)$$

From Eqs. (30) and (32), we can obtain $T(r, H) = S(r, H)$ which is not possible. Therefore, we have

$$1+\left(\frac{c_1}{c_5}\right)'+\left(\frac{c_3}{c_5}\right)' \equiv 0. \quad (33)$$

By integrating Eq. (33) w.r.t. "z", we have

$$\frac{c_1}{c_5}+\frac{c_3}{c_5} = B_1 - z. \quad (34)$$

From Eqs. (29) and (34), we arrive at Eq. (17).

4 Conclusions

Ginzburg–Landau differential equation is a frequently used nonlinear differential equation with algebraic nonlinearities in nonlinear stability problems. In this article, we have shown that Nevanlinna theory can be used to obtain meromorphic solution

of Ginzburg–Landau differential equation with sharing one counting multiplicity or ignoring multiplicity between meromorphic function and its derivative. If nonlinearities appear beyond the cubic term, then this meromorphic solution is most useful since there is no known analytical solution of such equations.

Acknowledgements The author thanks the referees for useful comments that improved the paper.

References

1. Cao TB, Xu JF, Chen ZX (2010) On the meromorphic solutions of linear differential equations on the complex plane. J Math Anal Appl 364:130–142. https://doi.org/10.1016/j.jmaa.2009.11.018
2. Li P (2008) Entire solutions of certain type of differential equations. J Math Anal Appl 344:253–259. https://doi.org/10.1016/j.jmaa.2010.09.026
3. Tang JF, Liao LW (2007) The transcendental meromorphic solutions of a certain type of nonlinear differential equations. J Math Anal Appl 334:517–527
4. Hu PC, Wang QY (2019) Growth on meromorphic solutions of non-linear delay differential equations. Bull Belg MathSoc Simon Stevin 26:131–147
5. Siddheshwar PG, Tanuja A (2019) Existence of meromorphic solution of Riccati-Abel differential equation. Appl Math Sci Comput. 21–28. https://doi.org/10.1007/978-3-030-01123-9_3
6. Siddheshwar PG, Tanuja A, Bhoosnurmath SS, Mahesh B (2019) Meromorphic solution of a class of non-linear differential equations with sharing one value. J Anal 1–16. https://doi.org/10.1007/s41478-019-00176-2
7. Siddheshwar PG, Tanuja A, Bhoosnurmath SS, Mahesh B (2019) Meromorphic solutions of nonlinear ordinary differential equations. Tbilisi Math J 12(2):77–88
8. Yuan WJ, Shang YD, Huang Y, Wang H (2013) The representation of meromorphic solutions of certain ordinary differential equations and its applications. Sci Sin Math 43(6):563–575. https://doi.org/10.1360/012012-159
9. Zhang J, Liao LW (2011) On entire solutions of a certain type of nonlinear differential and difference equations. Taiwan J Math 15:2145–2157
10. Fang ML (2002) Uniqueness and value-sharing of entire functions. Comput Math Appl 44:828–831
11. Gundersen GG (1983) Meromorphic functions that share two finite values with their derivative. Pac J Math 105:299–309
12. Lin XQ, Lin WC (2011) Uniqueness of entire functions sharing one value. J Math Anal Appl 31B(3):1062–1076
13. Zhang XY, Chen JF, Lin WC (2008) Entire or meromorphic functions sharing one value. Comput Math Appl 56:1876–1883. https://doi.org/10.1016/j.camwa.2008.04.008
14. Cherry W, Ye Z (2001) Theory of value distribution. Springer monographs in mathematics. Springer, Berlin https://www.springer.com/in/book/9783540664161
15. Hayman WK (1964) Meromorphic functions. Clarendon Press, Oxford
16. Laine I (1993) Nevanlinna theory and complex differential equations. Walter de Gruyter, Berlin https://www.degruyter.com/viewbooktoc/product/173583
17. Yang CC, Yi HX (2004) Uniqueness theory of meromorphic functions. Kluwer, Dordrecht
18. Al-Khaladi AHH (2013) Meromorphic functions that share one value and the solution of Riccati differential equation. Arab J Math 2:129–137. https://doi.org/10.1007/s40065-012-0057-7

Geometry of Variably Inclined Inviscid MHD Flows

Anirban Roy and R. Hari Baskar

Abstract A steady plane variably inclined magnetohydrodynamic flow of an inviscid incompressible fluid of infinite electrical conductivity studied. Introducing the vorticity, magnetic flux density, and energy functions along with the variable angle between magnetic field and velocity vector, governing equations are reformulated. The resulting equations are solved to analyze the geometry of the fluid flow. Considering streamlines to be parallel, stream function approach is applied to obtain the pattern for magnetic lines and the complete solution to the flow variables. Next considering parallel magnetic lines, magnetic flux function approach is applied to obtain streamlines and the complete solution of the flow. A graphical analysis of pressure variation is made in all the cases.

Keywords MHD · Incompressible · Vorticity · Magnetic flux density · Streamlines · Magnetic lines

1 Introduction

A fluid motion is generally described by giving the flow pattern that is streamlines and magnetic lines. In this article, we consider a steady plane variably inclined MHD flow of an inviscid incompressible fluid of infinite electrical conductivity. Steady plane variably inclined flow means a flow where the velocity of the fluid and magnetic vector fields are coplanar, and the angle between these vector fields is variable, a function of two space coordinates in the flow region. We use the concept given by Martin [1] where the order of the governing equations reduced.

Garg and Chandna [2], studied MHD flows of a viscous fluid having infinite electrical conductivity where magnetic and velocity fields are orthogonal. Chandna and Garg [2] used the concepts from differential geometry to study a constantly inclined

A. Roy (✉) · R. H. Baskar
Christ University, Bengaluru, India
e-mail: anirban.roy@christuniversity.in

R. H. Baskar
e-mail: hari.baskar@christuniversity.in

D. Maity et al. (eds.), *Advances in Fluid Mechanics and Solid Mechanics*,
Lecture Notes in Mechanical Engineering,
https://doi.org/10.1007/978-981-15-0772-4_5

MHD flow for a viscous fluid with infinite electrical conductivity. Nath and Chandna [3] extended the work of Martin [1] further for steady incompressible orthogonal MHD flows of viscous fluid with infinite electrical conductivity. Chandna et al. [4] also studied a plane MHD flow of an incompressible viscous fluid having finite electrical conductivity where they have considered that the magnetic field vector is variably inclined with the velocity vector. Bagewadi and Bhagya [5] considered variably inclined MHD flows for an incompressible viscous fluid having infinite electrical conductivity. Applying hodograph transformation and using differential geometry techniques, Bagewadi and Bhagya [6] studied the behavior of streamlines in aligned flow. Solutions for steady plane orthogonal flow of second grade fluid are obtained by Bagewadi and Bhagya [7] using curvilinear coordinate system where one curve represents the streamlines and the other curve is left arbitrary. Manoj et al. [8] applied transformation technique to constantly inclined steady, plane, two-phase MFD flows of viscous, incompressible fluid, through porous media. They used hodograph transformation in particular and obtained partial differential equation of second order which they used to find the solution for vortex flow. Ramesh et al. [9] have analyzed the effect of radiation on the flow near the two-dimensional stagnation point of an incompressible, viscous, electrically conducting dusty fluid toward stretching sheet. They converted non-linear equations into similarity equations and then solving numerically they analyzed the thermal results. Manjunatha and Gireesha [10] have observed the effect of variable viscosity and the thermal conductivity on an MHD flow for a dusty fluid. Manjunatha et al. [11] have analyzed theoretically a free convective MHD flow of an unsteady rotating dusty fluid. They solved governing equations analytically using perturbation technique for viscous, incompressible electrically conducting fluid flow in the porous media under the influence of periodic pressure gradient with uniform distribution of dust particles.

In this article, we write the governing equations in the convenient form introducing vorticity, current density, and energy function. Then by considering the parallel streamlines, we use the stream function approach to obtain the pattern for magnetic lines and obtain the complete solution to the flow variables. Next using magnetic flux function approach when magnetic lines are considered parallel, streamlines are obtained and then we derive the complete solution of the flow. In all the cases, the variation of pressure is plotted in graphs and hence an analysis is made on pressure function.

2 Governing Equations

The governing equations of a steady magnetohydrodynamic two-dimensional flow of an inviscid incompressible fluid of infinite electrical conductivity are given by

$$\operatorname{div} \vec{v} = 0 \tag{1}$$

$$\rho\left(\overrightarrow{v}\ .\mathrm{grad}\right)\overrightarrow{v} + \mathrm{grad}\, p = \mu\, \mathrm{curl}\, \overrightarrow{H} \times \overrightarrow{H} \tag{2}$$

$$\mathrm{curl}\left(\overrightarrow{v} \times \vec{H}\right) = \vec{0} \tag{3}$$

$$\mathrm{div}\, \vec{H} = 0 \tag{4}$$

where $\overrightarrow{v}$ denotes the velocity, ρ the constant fluid density, p the fluid pressure, μ the constant magnetic permeability of flow, and $\overrightarrow{H}$ the magnetic field vector.

For a two-dimensional flow with $\overrightarrow{H}$ in the plane, we take $\overrightarrow{v} = (v_1, v_2)$ and $\overrightarrow{H} = (H_1, H_2)$ with $v = \left|\overrightarrow{v}\right| = \sqrt{v_1^2 + v_2^2}$ and $H = \left|\overrightarrow{H}\right| = \sqrt{H_1^2 + H_2^2}$.

We now reduce Eqs. (1)–(4) in Cartesian form by introducing the vorticity function, current density function and the energy function. Thus, the system of Eqs. (1)–(4) is now replaced by the following system:

$$\frac{\partial v_1}{\partial x} + \frac{\partial v_2}{\partial y} = 0 \tag{5}$$

$$-\rho v_2 \xi + \mu\, \delta H_2 = -\frac{\partial h}{\partial x} \tag{6}$$

$$-\rho v_1 \xi + \mu\, \delta H_1 = \frac{\partial h}{\partial y} \tag{7}$$

$$v_1 H_2 - v_2 H_1 = k, \text{ where } k \text{ is an arbitrary non-zero constant.} \tag{8}$$

$$\frac{\partial H_1}{\partial x} + \frac{\partial H_2}{\partial y} = 0 \tag{9}$$

$$\frac{\partial v_2}{\partial x} - \frac{\partial v_1}{\partial y} = \xi \tag{10}$$

$$\frac{\partial H_2}{\partial x} - \frac{\partial H_1}{\partial y} = \delta \tag{11}$$

The above system of seven equations are having seven unknown functions v_1, v_2, H_1, H_2, ξ, δ, and h, each of them are functions of x and y.

3 Variably Inclined MHD Flows

Let the variable angle $\alpha(x, y)$, between velocity vector and the magnetic field be such that $\alpha(x, y) \neq 0$ for every $\alpha(x, y)$ in the flow region. So we get $\overrightarrow{v}.\overrightarrow{H} = VH\cos\alpha$ and $\left|\overrightarrow{v} \times \overrightarrow{H}\right| = VH\sin\alpha$

Therefore,

$$v_1 H_1 + v_2 H_2 = V\,H\,\cos\,\alpha \tag{12}$$

And by (8), the Cartesian form of the diffusion Eq. (3), we have

$$v_1 H_2 - v_2 H_1 = VH\,\sin\,\alpha = k \tag{13}$$

Equations (12) and (13) can be used for solving H_1 and H_2 as well v_1 and v_2. Here

$$H_1 = \frac{k(v_1 \cot\alpha - v_2)}{v^2},\; H_2 = \frac{k(v_2 \cot\alpha + v_1)}{v^2} \tag{14}$$

Eliminating H_1 and H_2 from Eqs. (6), (7), (9) and (11) using (14), we get the following system of six partial differential equations:

$$\frac{\partial v_1}{\partial x} + \frac{\partial v_2}{\partial y} = 0 \tag{5}$$

$$-\rho v_2 \xi + k\mu \frac{(v_2 \cot\alpha + v_1)}{v^2}\delta = -\frac{\partial h}{\partial x} \tag{15}$$

$$-\rho v_1 \xi + k\mu \frac{(v_1 \cot\alpha - v_2)}{v^2}\delta = \frac{\partial h}{\partial y} \tag{16}$$

$$\frac{\partial}{\partial x}\left(\frac{v_1 \cot\alpha - v_2}{v^2}\right) + \frac{\partial}{\partial y}\left(\frac{v_2 \cot\alpha + v_1}{v^2}\right) = 0 \tag{17}$$

$$\frac{\partial v_2}{\partial x} - \frac{\partial v_1}{\partial y} = \xi \tag{10}$$

$$k\left[\frac{\partial}{\partial x}\left(\frac{v_2 \cot\alpha + v_1}{v^2}\right) - \frac{\partial}{\partial y}\left(\frac{v_1 \cot\alpha - v_2}{v^2}\right)\right] = \delta \tag{18}$$

The above system of six equations has six unknown functions v_1, v_2, α, ξ, δ, and h. Once a solution of this system is determined, we can find pressure, velocity, and magnetic field.

4 Streamlines Parallel to the *X*-Axis

The equation of continuity (5) implies the existence of a stream function $\psi\ (x, y)$ such that

$$\mathrm{d}\psi = -v_2\,\mathrm{d}x + v_1\,\mathrm{d}y \text{ or } \frac{\partial \psi}{\partial x} = -v_2, \quad \frac{\partial \psi}{\partial y} = v_1$$

Then from Eqs. (15)–(18) and (10), we get

$$\rho\left(\frac{\partial\psi}{\partial x}\frac{\partial\xi}{\partial y}-\frac{\partial\psi}{\partial y}\frac{\partial\xi}{\partial x}\right)+k\mu\left[\frac{\left(\frac{\partial\psi}{\partial y}-\frac{\partial\psi}{\partial x}\cot\alpha\right)\frac{\partial\delta}{\partial y}+\left(\frac{\partial\psi}{\partial x}+\frac{\partial\psi}{\partial y}\cot\alpha\right)\frac{\partial\delta}{\partial x}}{\left(\frac{\partial\psi}{\partial x}\right)^2+\left(\frac{\partial\psi}{\partial y}\right)^2}\right]=0 \tag{19}$$

Finally obtaining a solution of (19), we can find velocity field, vorticity, current density, magnetic field, and energy, and thus can determine the pressure.

When the streamlines are straight lines parallel to the x-axis, we consider the stream function $\psi(x, y)$ in the form

$$\psi(x, y) = N(y),\ N'(y) \neq 0 \tag{20}$$

Then

$$v_1 = \frac{\partial\psi}{\partial y} = N'(y)\,, \qquad v_2 = -\frac{\partial\psi}{\partial x} = 0$$

Thus

$$\xi = -N''(y) \tag{21}$$

$$\delta = -k\frac{\partial}{\partial y}\left(\frac{\cot\alpha}{N'(y)}\right) \tag{22}$$

$$\cot\alpha = \frac{N''(y)}{N'(y)}x + M(y),\ \text{where}\ M(y)\ \text{is an arbitrary function of y.} \tag{23}$$

In order to solve for $M(y)$ and $N(y)$, we now discuss the following two cases:

$$\text{(i)}\ N''(y) = 0 \quad \text{(ii)}\frac{\partial}{\partial y}\left(\frac{N''(y)}{N'(y)}\right) = 0$$

Case I:

$$N''(y) = 0 \quad \Rightarrow \quad N(y) = N_1(y) + N_2$$

$$\therefore\ N(y) = N_1 y + N_2\ \text{where}\ N_1(\neq 0)\ \text{and}\ N_2\ \text{are arbitrary constants.}$$
$$M(y) = N_3 y + N_4\ \text{where}\ N_3(\neq 0)\ \text{and}\ N_4\ \text{are arbitrary constants.}$$

Then

$$\vec{v} = (N_1, 0),\ \alpha = \cot^{-1}(N_3 y + N_4),\ \xi = -k\frac{N_3}{N_1},\ \vec{H} = \left(\frac{k(N_3 y + N_4)}{N_1}, \frac{k}{N_1}\right)$$

Then the pattern of magnetic lines are given by

$$N_3 y^2 + 2N_4 y - 2x = -\frac{N_4^2}{N_3} + 2k_1, \text{ where } k_1 \text{is an arbitrary constant.}$$

i.e.,

$$N_3 y^2 + 2N_4 y - 2x = \text{constant} \tag{24}$$

Magnetic lines pattern for different values of the arbitrary constants is plotted below.

Then the energy function $h(x, y)$ is given by

$$h = \frac{k^2\mu}{N_1^2}\left[N_3 x - \frac{(N_3 y + N_4)^2}{2}\right]$$

And hence, the pressure function is given by

$$p = \frac{k^2\mu}{N_1^2}\left[N_3 x - \frac{(N_3 y + N_4)^2}{2}\right] - \frac{1}{2}\rho N_1^2 \tag{25}$$

Now we plot the graphs for variation of pressure corresponding to different values of density and magnetic permeability. We have taken arbitrary values for the constants as $k = 1, N_1 = 0.6, N_3 = 2, N_4 = 0.5$.

We now use the following non-dimensional quantities to avoid the arbitrary constants:

$$X = \frac{x}{L},\quad Y = \frac{y}{L},\quad P = \frac{p}{\rho U^2},\quad N_1 = U,\quad L = \frac{1}{N_3} = \frac{N_4}{N_3},\quad \mu = \frac{\rho U^4}{k^2},\quad k_1 = L$$

where L is the characteristic length and U is the characteristic speed of the flow motion. Then the non-dimensional expression is

$$Y^2 + 2Y - 2X = 3 \text{ and } P = X - Y - \frac{1}{2}Y^2 - 1$$

The above two non-dimensional expressions give an overview of the geometry of the magnetic lines and the pressure variation, given below in Figs. 9 and 10.

Case II:

$$\frac{\partial}{\partial y}\left(\frac{N''(y)}{N'(y)}\right) = 0 \Rightarrow \quad N'(y) = c_2 e^{c_1 y}, \quad c_2 \neq 0$$

i.e. $\dfrac{\partial \Psi}{\partial y} = N'(y) = c_2 e^{c_1 y}$ where c_2 ($\neq 0$) and c_1 are arbitrary constants.

$$M(y) = c_3 + c_4 e^{2c_1 y} \text{where } c_3 \text{ and } c_4 \text{ are arbitrary constants.}$$

Then

$$\vec{v} = \left(c_2 e^{c_1 y}, 0\right), \quad \alpha = cot^{-1}\left(c_1 x + c_3 + c_4 e^{2c_1 y}\right) \quad , \xi = -c_1 c_2 e^{c_1 y},$$

$$\delta = \frac{kc_1}{c_2}\left[(c_1 x + c_3)e^{-c_1 y} - c_4 e^{c_1 y}\right], \quad \vec{H} = \frac{k}{c_2}\left((c_1 x + c_3)e^{-c_1 y} + c_4 e^{c_1 y}, e^{-c_1 y}\right)$$

Then the pattern of magnetic lines are given by

$$c_4 e^{2c_1 y} + c_1 c_5 e^{c_1 y} - c_1 x = c_3, \text{ where } c_5 \text{ is an arbitrary constant.} \tag{26}$$

Magnetic lines pattern for different values of the arbitrary constants is plotted below.

We find the energy function by integration.

$$h = \frac{\rho}{2} c_2^2 e^{2c_1 y} - \frac{k^2 \mu\, c_1}{2c_2^2}\left[(c_1 x + c_3)^2 e^{-2c_1 y} + c_4^2 e^{2c_1 y}\right] + \frac{k^2 \mu}{2c_2^2}\left[2c_1 c_4 x - 2c_1\left(\frac{c_1}{2}x + c_3\right)x\, e^{-2c_1 y}\right]$$

And hence, the pressure function is given by

$$p = \frac{k^2 \mu}{2c_2^2}\left[2c_1 c_4 x - 2c_1\left(\frac{c_1}{2}x + c_3\right)x\, e^{-2c_1 y} - (c_1 x + c_3)^2 e^{-2c_1 y} - c_4^2 e^{2c_1 y}\right] \tag{27}$$

We now plot graphs for the variation of pressure for different values of magnetic permeability. We take $k = 1$, $c_1 = 1$, $c_2 = 2$, $c_3 = 1$, and $c_4 = 1$.

We now substitute the following non-dimensional quantities:

$$X = \frac{x}{L}, \; Y = \frac{y}{L}, \; P = \frac{2U^2}{k^2 \mu} p, \; c_1 = \frac{1}{L}, \; c_2^2 e^{2c_1 y} = U^2, \; c_3 = c_4 = 1, \; c_5 = L$$

where L is the characteristic length and U is the characteristic velocity of the flow motion.

Then the non-dimensional expression for magnetic lines and pressure are

$$e^{2Y} + e^{Y} - X = 1 \text{ and } P = 2Xe^{2Y} - e^{4Y} - 2X^2 - 4X - 1$$

The above two non-dimensional expression give an overview of the geometry of the magnetic lines and the pressure variation, given below in Figs. 15 and 16.

Theorem 1 *In the steady plane MHD flow of an incompressible inviscid fluid of infinite electrical conductivity, when streamlines are parallel to the x-axis and inclined variably to the magnetic lines in the flow plane, then magnetic lines pattern are either* $N_3y^2 + 2N_4y - 2x = \text{constant}$ *or* $c_4e^{2c_1y} + c_1c_5e^{c_1y} - c_1x = c_3$.

5 Magnetic Lines Parallel to the *X*-Axis

Now

$$v_1 = \frac{k(H_2 + H_1 \cot\alpha)}{H^2}, \quad v_2 = \frac{k(H_2 \cot\alpha - H_1)}{H^2} \tag{28}$$

Eliminating v_1 and v_2 from Eqs. (5), (6), (7) and (10) using (28) we obtain a system of six equations having six unknown functions H_1, H_2, h, ξ, δ and α as functions of x, y. Once a solution of this system is determined, we can find pressure, velocity, and magnetic field.

The solenoidal Eq. (9) implies the existence of magnetic flux function $\varphi(x, y)$ such that

$$\mathrm{d}\phi = -H_2\,\mathrm{d}x + H_1\,\mathrm{d}y \text{ or } \frac{\partial\phi}{\partial x} = -H_2, \quad \frac{\partial\phi}{\partial y} = H_1$$

Then we obtain,

$$\mu\left(\frac{\partial\phi}{\partial y}\frac{\partial\delta}{\partial x} - \frac{\partial\phi}{\partial x}\frac{\partial\delta}{\partial y}\right) + \rho k\left[\frac{\left(\frac{\partial\phi}{\partial x} - \frac{\partial\phi}{\partial y}\cot\alpha\right)\frac{\partial\xi}{\partial x} + \left(\frac{\partial\phi}{\partial x}\cot\alpha + \frac{\partial\phi}{\partial y}\right)\frac{\partial\xi}{\partial y}}{\left(\frac{\partial\phi}{\partial x}\right)^2 + \left(\frac{\partial\phi}{\partial y}\right)^2}\right] = 0 \tag{29}$$

Finally obtaining a solution of (29), we can find velocity field, vorticity, current density, the magnetic field and energy and thus can determine the pressure.

When the magnetic lines are straight lines parallel to the x-axis and are variably inclined to the streamlines in the flow plane, then we assume

$$\phi(x, y) = G(y) \text{ with } G'(y) \neq 0 \tag{30}$$

so that

$$H_1 = \frac{\partial \phi}{\partial y} = G'(y)\,, \quad H_2 = -\frac{\partial \phi}{\partial x} = 0$$

Applying the expression of φ, we get the following equations in reduced form:

$$\cot\alpha = -\frac{G''(y)}{G'(y)}x + F(y), \text{ where } F(y) \text{ is an arbitrary function of } y. \tag{31}$$

$$\xi = -k\frac{\partial}{\partial y}\left[\frac{\cot\alpha}{G'(y)}\right] \tag{32}$$

$$\delta = -G''(y) \tag{33}$$

In order to solve for $F(y)$ and $G(y)$, we have now the following two cases:

$$\text{(i) } G''(y) = 0 \quad \text{(ii)} \frac{\partial}{\partial y}\left(\frac{G''(y)}{G'(y)}\right) = 0$$

Case III:

$$G''(y) = 0 \quad \Rightarrow \quad G(y) = b_1 y + b_2$$

i.e. $\Phi(x, y) = b_1 y + b_2$ where $b_1 (\neq 0)$ and b_2 are arbitrary constants.

$F(y) = b_3 y + b_4$ where $b_3 (\neq 0)$ and b_4 are arbitrary constants.

Then

$$\vec{H} = (b_1, 0), \alpha = \cot^{-1}(b_3 y + b_4),\ \xi = -k\frac{b_3}{b_1},\ \delta = 0, \vec{v} = \left(\frac{k(b_3 y + b)}{b_1}, -\frac{k}{b_1}\right)$$

So the streamlines are given by

$$b_3 y^2 + 2b_4 y + 2x = \frac{b_4^2}{b_3} + 2k_4, \text{ where } k_4 \text{ is an arbitrary constant.}$$

$$\text{i.e. } b_3 y^2 + 2b_4 y + 2x = \text{constant.} \tag{34}$$

Using the above solutions, we find the energy function by integration.

$$h = \frac{\rho k^2}{b_1^2} b_3 x + \frac{\rho k^2}{2b_1^2}(b_3 y + b_4)^2$$

And hence, the pressure function is given by

$$p = \frac{\rho k^2}{2b_1^2}(2b_3 x - 1) \tag{35}$$

We now plot the graph for the variation of pressure for different densities. While plotting the graph, we take $b_1 = 2$ and $b_3 = 2$.

For the characteristic length, L and the characteristic velocity, U using the following non-dimensional quantities: $X = \frac{x}{L},\ P = \frac{2b_1^2}{\rho k^2} p,\ b_3 = \frac{1}{L},\ b_4 = 1,\ k_4 = L$

We get the non-dimensional expression for magnetic lines and pressure in the following form:

$$Y^2 + 2Y + 2X = 3 \text{ and } P = 2X - 1$$

These non-dimensional expressions give an overview of the geometry of the streamlines and the pressure variation.

Case IV:

$$\frac{\partial}{\partial y}\left(\frac{G''(y)}{G'(y)}\right) = 0 \quad \Rightarrow \quad G'(y) = d_2\, e^{d_1 y}$$

And so

$$G(y) = \frac{d_2}{d_1} e^{d_1 y} + d_3, \text{ where } d_1 \text{ and } d_2 \text{ are non-zero constants.}$$

$$F(y) = d_4 + d_5 e^{2d_1 y} \text{ where } d_4 \text{ and } d_5 \text{ are arbitrary constants.}$$

Then

$$\vec{H} = \left(d_2 e^{d_1 y}, 0\right), \quad \alpha = \cot^{-1}\left(-d_1 x + d_4 + d_5 e^{2d_1 y}\right),$$

$$\xi = -k\left(\frac{d_1^2}{d_2} x e^{-d_1 y} - \frac{d_1 d_4}{d_2} e^{-d_1 y} + \frac{d_1 d_5}{d_2} e^{d_1 y}\right),\ \delta = -d_1 d_2 e^{d_1 y},$$

$$\vec{v} = \frac{k}{d_2}\left(\left(-d_1 x e^{-d_1 y} + d_4 e^{-d_1 y} + d_5 e^{d_1 y}, -e^{-d_1 y}\right)\right)$$

So the streamlines are given by

$$d_5 e^{2d_1 y} - d_1 d_6 e^{d_1 y} + d_1 x = d_4, \text{ where } d_6 \text{ is an arbitrary constant.} \tag{36}$$

We find the energy function by integration.

$$h = \rho \frac{k^2}{2d_2^2}\left(2d_1^2 x^2 e^{-2d_1 y} - 4d_1 d_4 x e^{-2d_1 y} + 2d_1 d_5 x + d_4^2 e^{-2d_1 y} + d_5^2 e^{2d_1 y}\right)$$

And hence, the pressure function is given by

$$p = \rho \frac{k^2}{2d_2^2}\left[3d_1^2 x^2 e^{-2d_1 y} - 6d_1 d_4 x e^{-2d_1 y} + 2d_4^2 e^{-2d_1 y} + 2d_5^2 e^{2d_1 y} + 2d_4 d_5 + e^{-2d_1 y}\right] \quad (37)$$

We now plot the variation of pressure for different values of densities. While plotting we consider y as constant and assign $y = 2$.

Using the following non-dimensional quantities for L, the characteristic length

$$X = \frac{x}{L}, \quad Y = \frac{y}{L}, \quad P = \frac{2d_2^2 e^{2d_1 y}}{k^2 \rho} p, \quad d_1 = \frac{1}{L}, \quad d_4 = d_5 = 1, \quad d_6 = L$$

Non-dimensional expression for streamlines and pressure are

$$e^{2Y} - e^Y + X = 1 \text{ and } P = 3(X-1)^2 + 2e^{4Y}\left(e^{2Y} + 1\right)$$

Theorem 2 *In the steady plane MHD flow of an incompressible inviscid fluid of infinite electrical conductivity, if the magnetic lines are parallel to the x-axis and inclined variably to the streamlines in the flow plane, then streamlines are either* $b_3 y^2 + 2b_4 y + 2x =$ constant *or* $d_5 e^{2d_1 y} - d_1 d_6 e^{d_1 y} + d_1 x =$ constant.

6 Conclusions

We have studied variably inclined MHD flow problems, for two cases when streamlines as well magnetic lines are parallel to the x-axis.

When the streamlines are parallel to the x-axis, magnetic lines are found to be either parabolic or spiral in nature, given by Eqs. (24) and (26), respectively. Pattern of the magnetic lines is presented graphically in Figs. 1, 2, 3, 4, and 11. While plotting magnetic lines given by Eq. (24), we take $k_1 = -3, -0.5, 0.9, 4$ in every graph and observe the change of pattern for four set of combinations of the arbitrary constants N_1 and N_2, by taking their values as (1, 1), (1, −1), (−1, 1), and (−1–1). Parabolic behavior of the magnetic lines is exhibited in all the four Figs. 1, 2, 3, and 4. For case II, magnetic lines given by Eq. (26), graph is plotted in Fig. 11. Magnetic lines are spiral and by taking different values of c_1, c_3, c_4, and c_5, the pattern is exhibited (Figs. 5, 6, 7, 8, 9, 10, 12, 13, 14, 15, 16).

Streamlines are found to be either parabolic or spiral in nature, given by Eqs. (34) and (36), respectively, when the magnetic lines are parallel to the x-axis. Pattern of

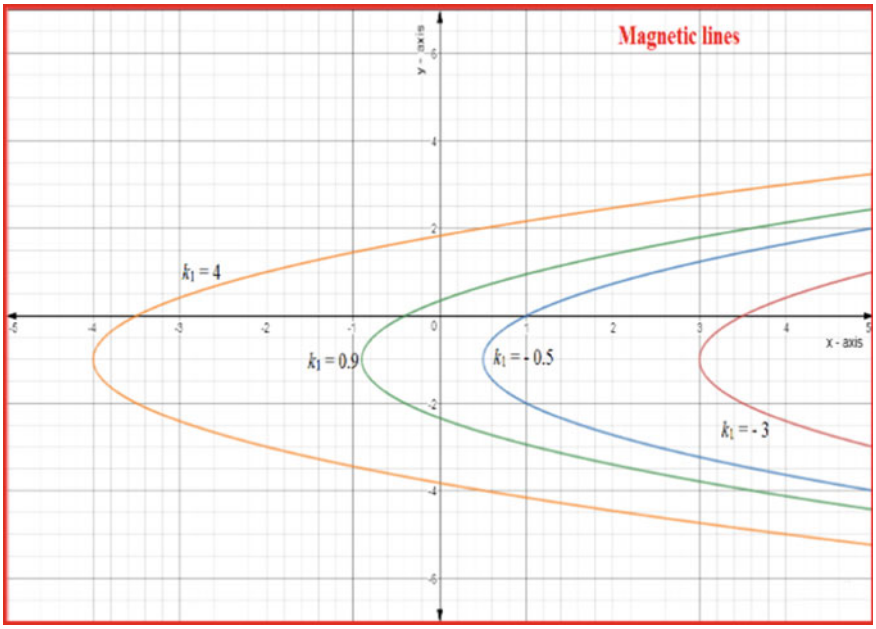

Fig. 1 Magnetic lines when $N_3 = 1$ and $N_4 = 1$

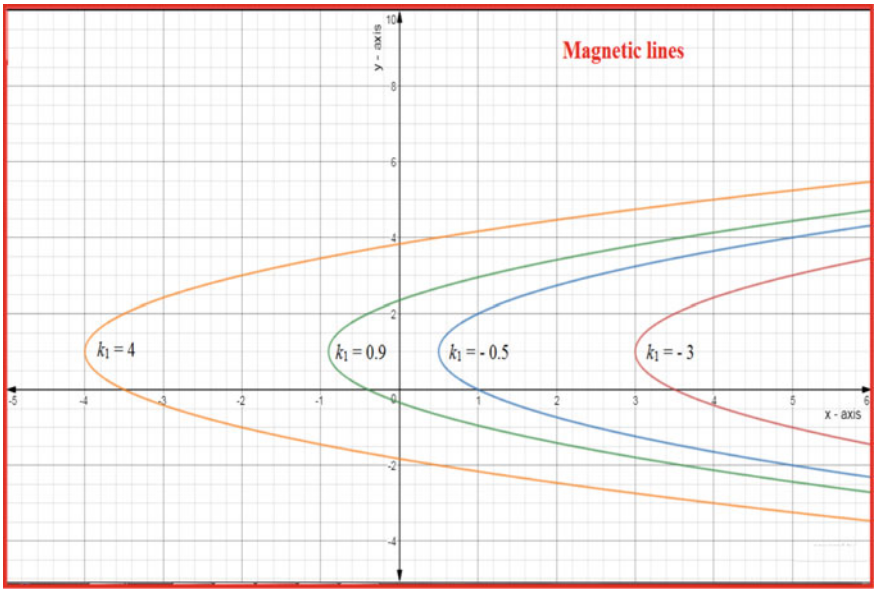

Fig. 2 Magnetic lines when $N_3 = 1$ and $N_4 = -1$

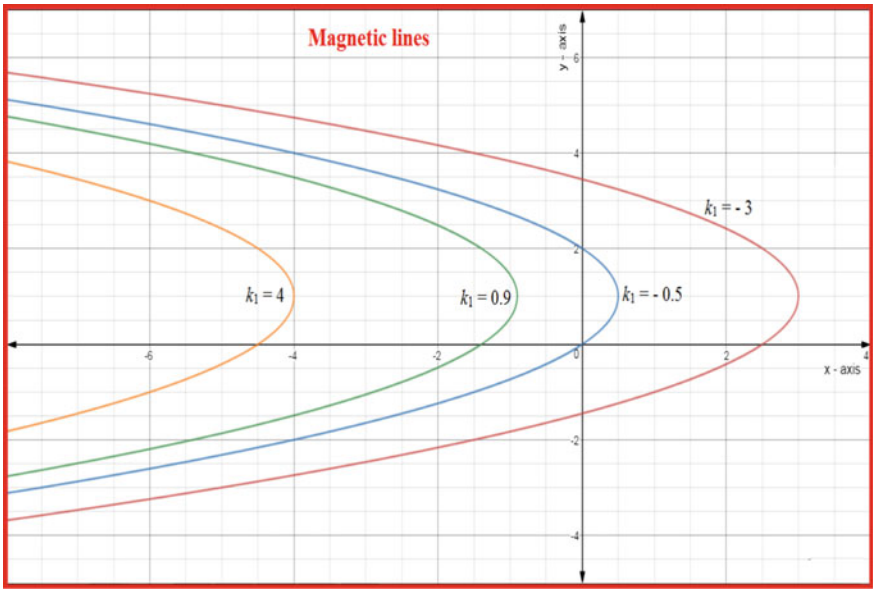

Fig. 3 Magnetic lines when $N_3 = -1$ and $N_4 = 1$

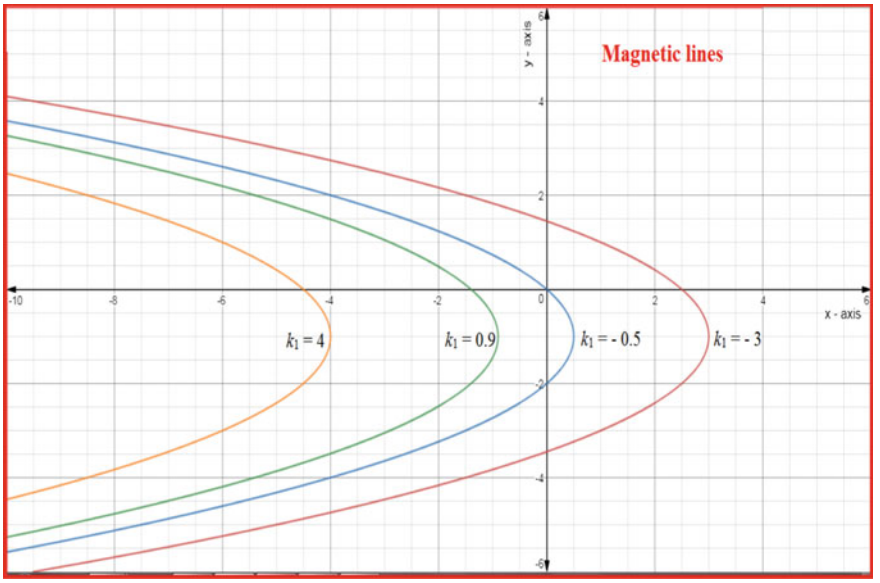

Fig. 4 Magnetic lines when $N_3 = -1$ and $N_4 = -1$

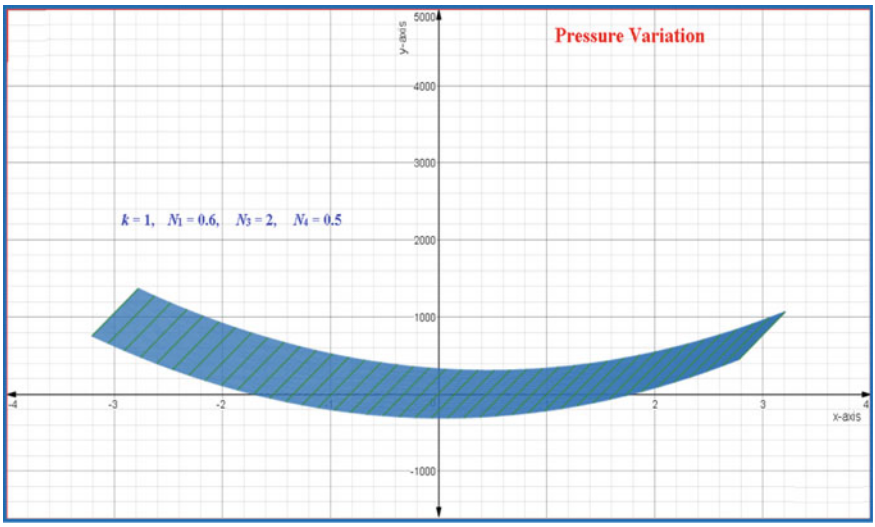

Fig. 5 Pressure variation $\mu = 50$

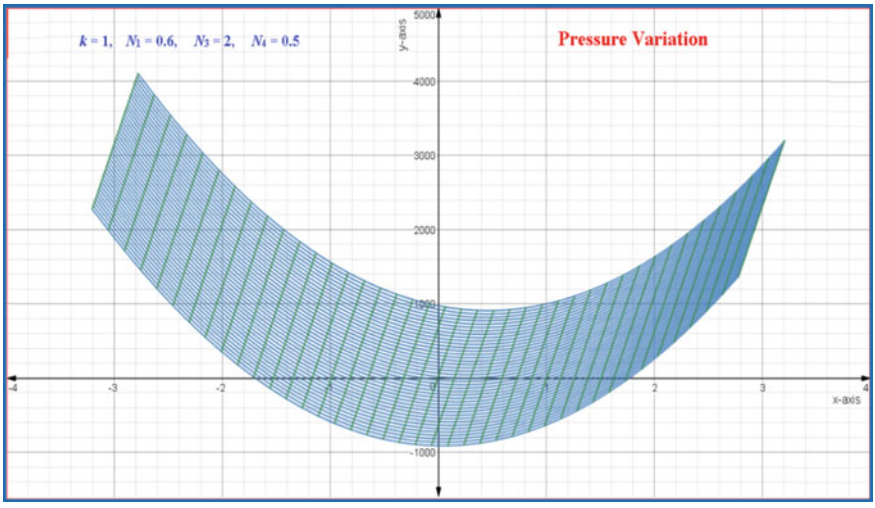

Fig. 6 Pressure variation for $\mu = 150$

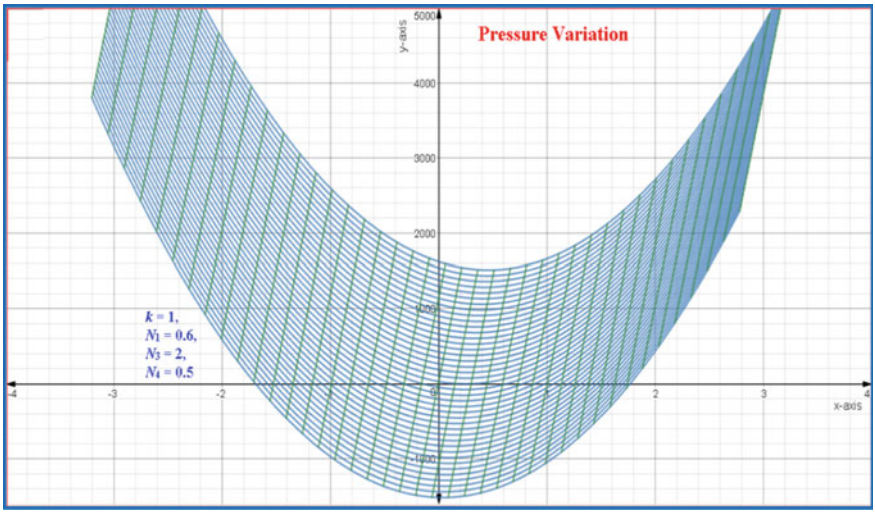

Fig. 7 Pressure variation for $\mu = 250$

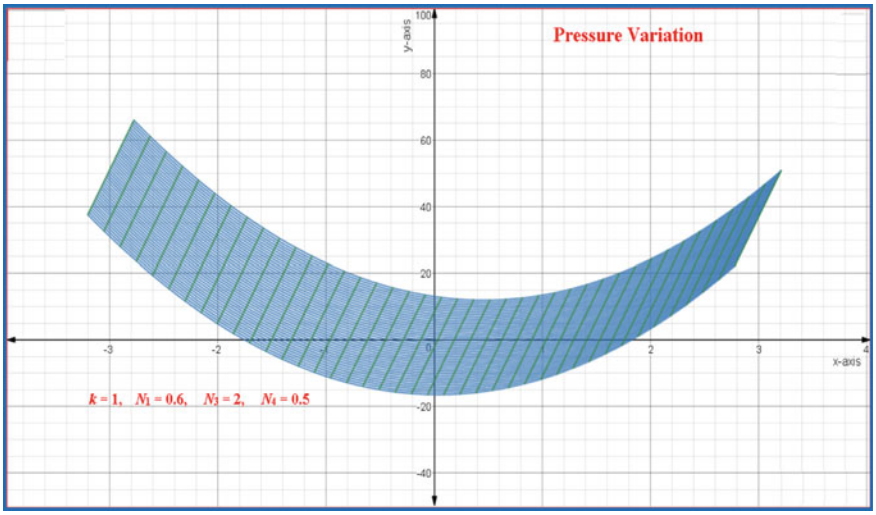

Fig. 8 Pressure variation for high density and low permeability

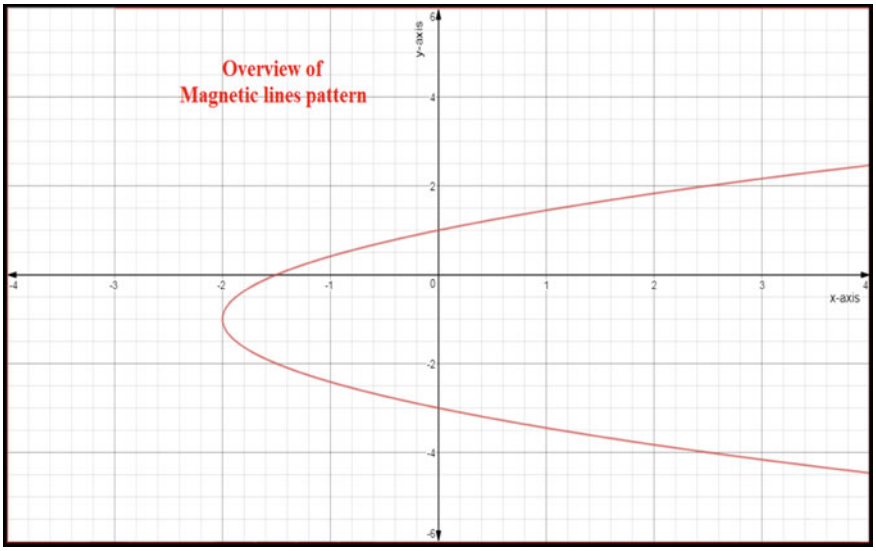

Fig. 9 Overview of magnetic lines pattern (case I)

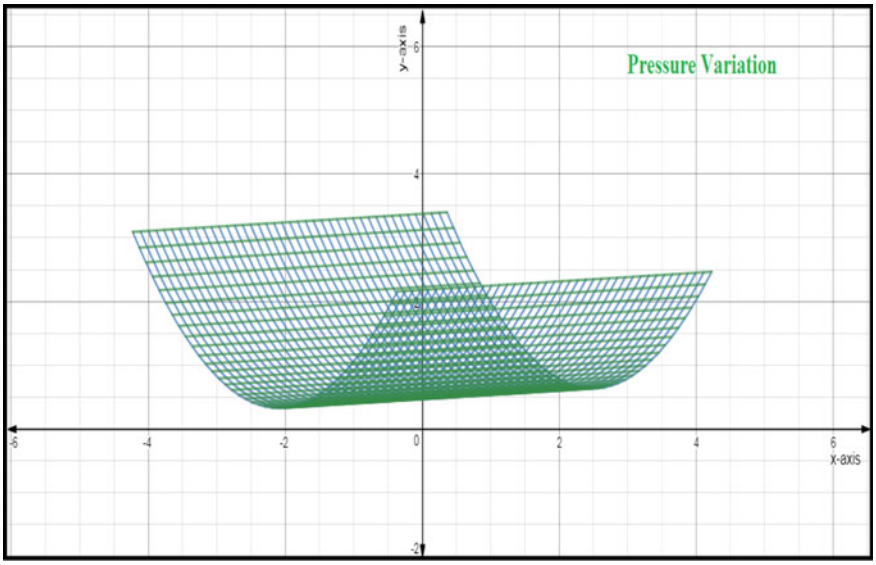

Fig. 10 Overview of pressure variation (case I)

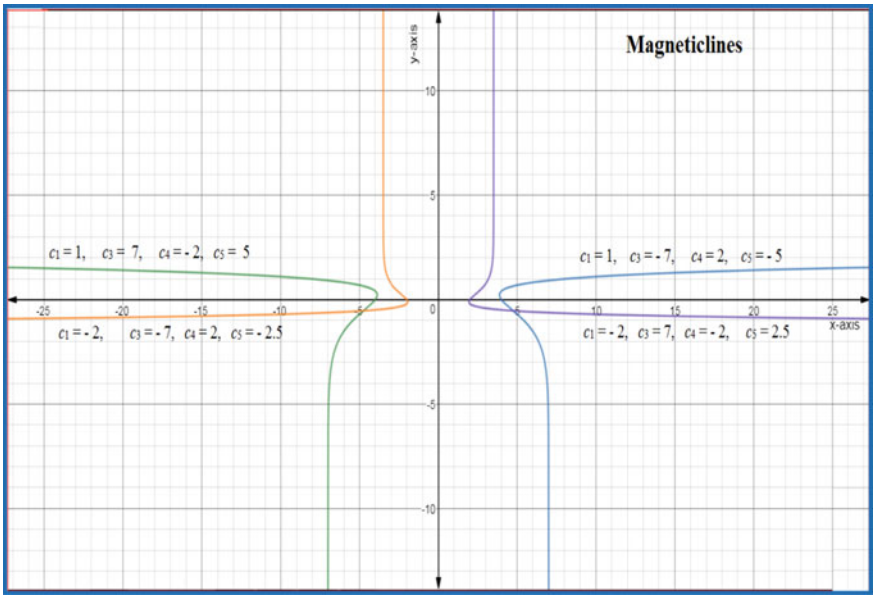

Fig. 11 Magnetic lines for different arbitrary constants

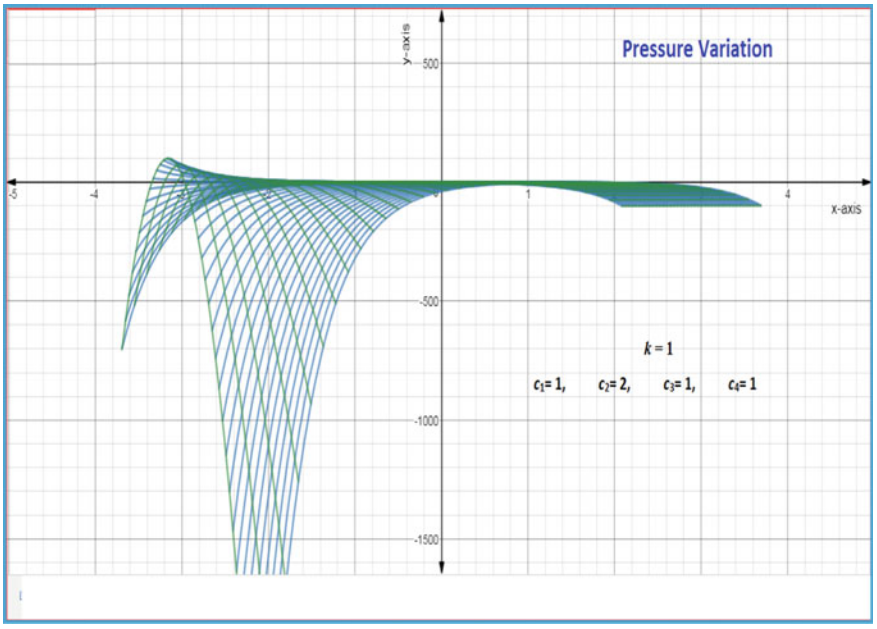

Fig. 12 Pressure variation for $\mu = 2$

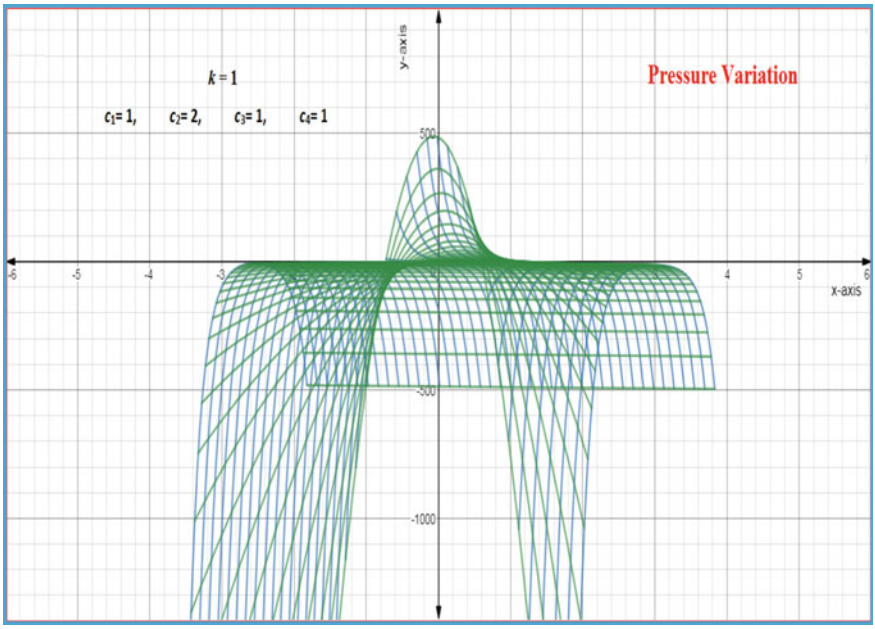

Fig. 13 Pressure variation for $\mu = 10$

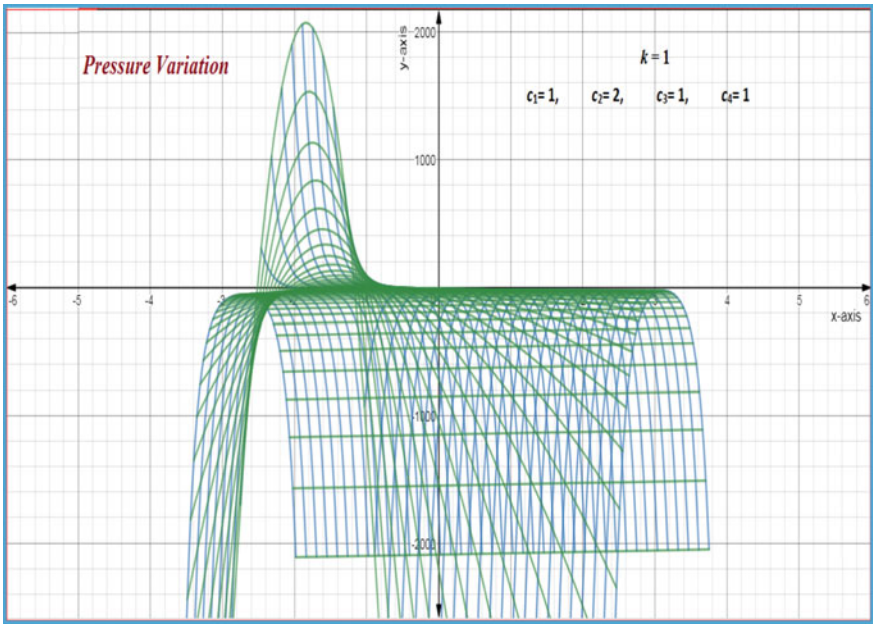

Fig. 14 Pressure variation for $\mu = 50$

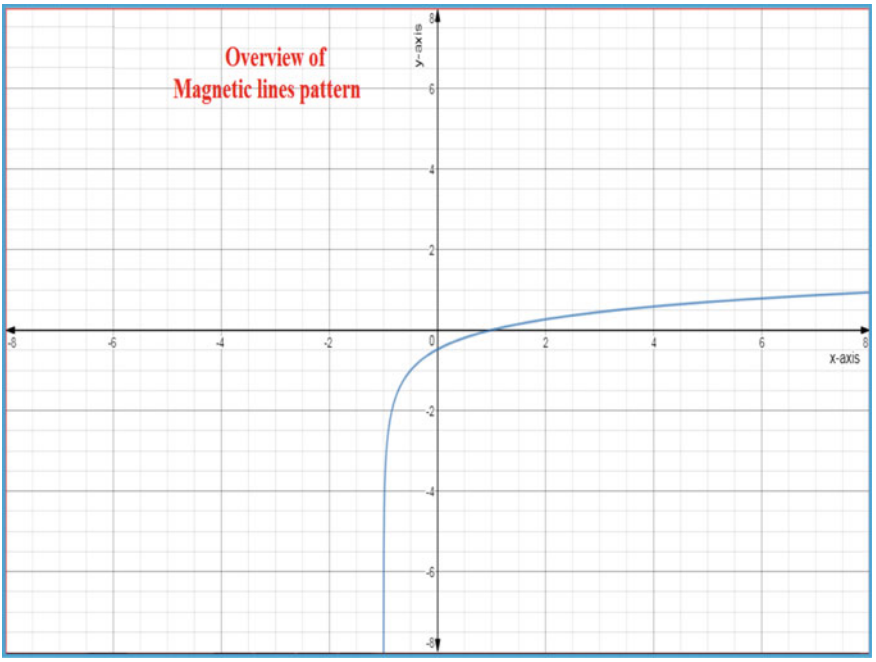

Fig. 15 Overview of magnetic lines pattern (case II)

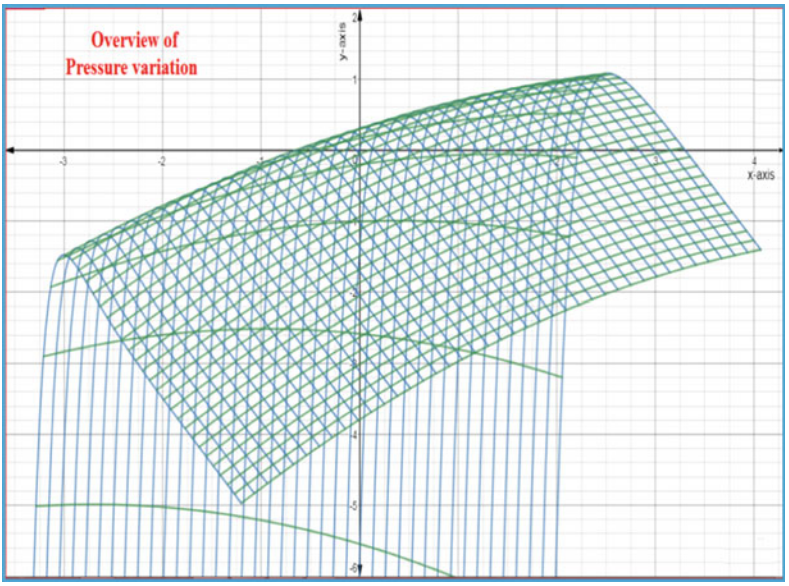

Fig. 16 Overview of pressure variation (case II)

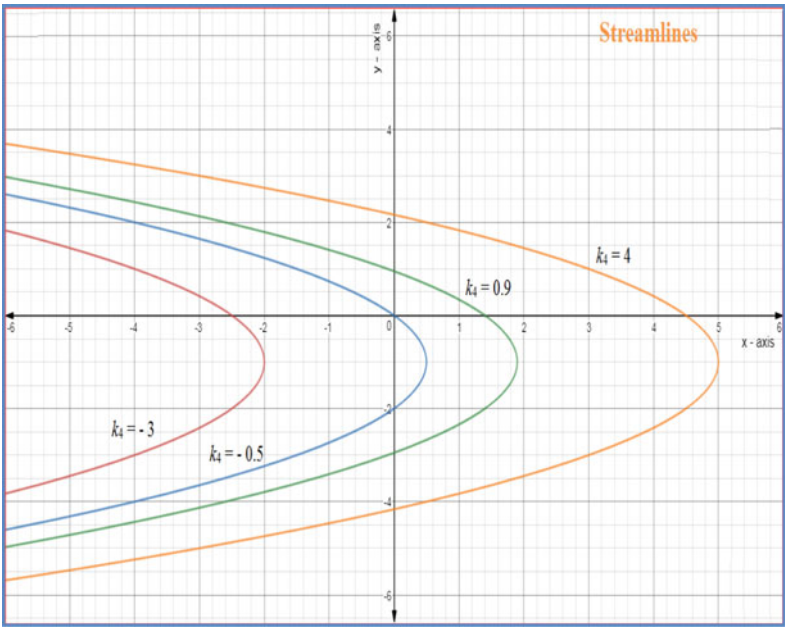

Fig. 17 Streamlines when $b_3 = 1$ and $b_4 = 1$

the streamlines is presented graphically in Figs. 17, 18, 19, 20, and 24. Similar to the last case, the parabolic behavior and spiral pattern of the streamlines are represented graphically by considering different values of the arbitrary constants. While plotting streamlines given by Eq. (34), we take the previous values for the arbitrary constant k_4 in every graph and observe the change of pattern for four set of combinations of the arbitrary constants b_3 and b_4, by taking their values as (1, 1), (1, −1), (−1, 1), and (−1–1). Parabolic behavior of the streamlines is exhibited in all the four Figs. 17, 18, 19, and 20. For the case IV, streamlines pattern is found as spiral, given by Eq. (36), and is plotted for different combinations of values of the arbitrary constants d_1, d_4, d_5, and d_6. All the variations are represented in Fig. 24 (Figs. 21, 22 and 23).

Finally, pressure is calculated and given by Eqs. (25), (27), (35), and (37). Moreover, the variation of the pressure in every cases being analyzed by plotting graphs.

When the streamlines are straight lines and parallel to the x-axis, we observe from Figs. 5, 6, and 7 that the pressure increases when the magnetic permeability increases. And variation of density does not affect the pressure variation in a significant manner. Density makes a considerable influence on the pressure when permeability is less and the density value is very large. Graphical representation is given in Fig. 8. In another case also, we observe from Figs. 12, 13, and 14 that pressure increases along with the increase in permeability.

For the other two cases where magnetic lines are parallel to the x-axis, we observe from Fig. 21 and from Figs. 25, 26, 27 and 28 that pressure increases when density increases.

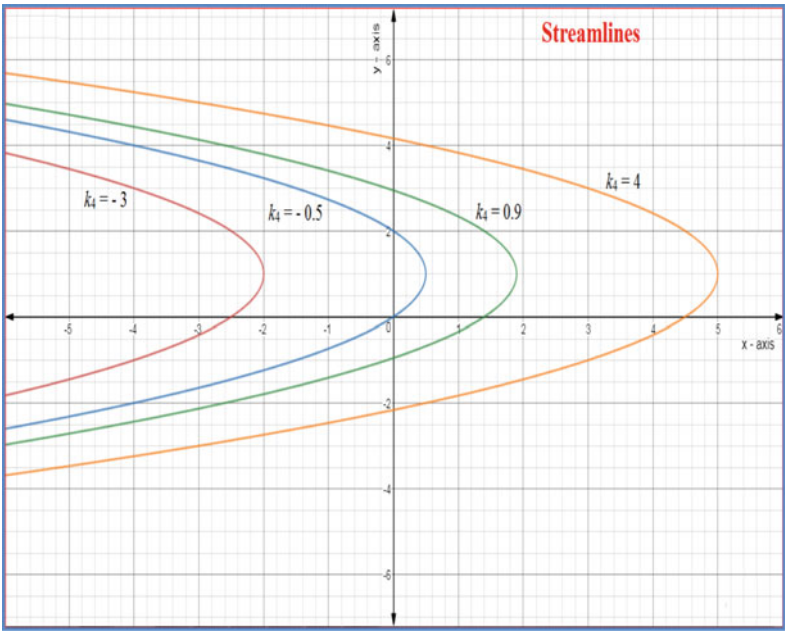

Fig. 18 Streamlines when $b_3 = 1$ and $b_4 = -1$

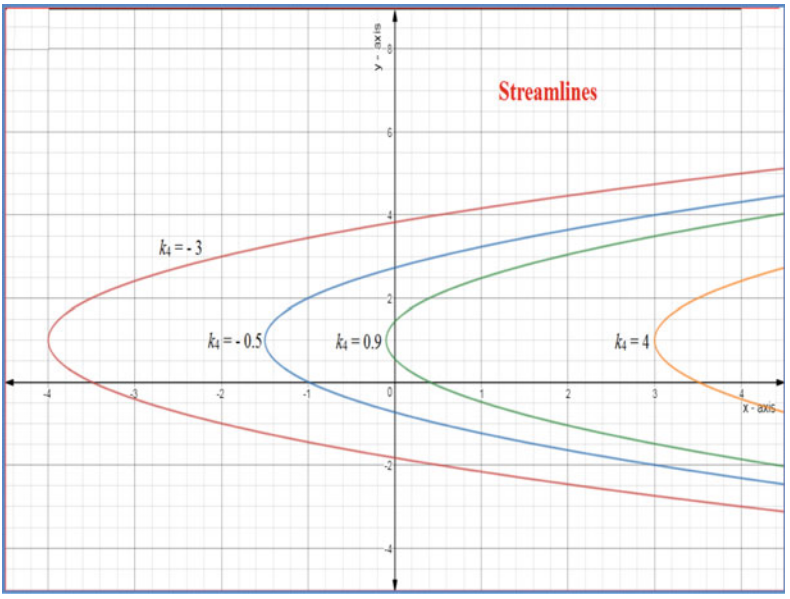

Fig. 19 Streamlines when $b_3 = -1$ and $b_4 = 1$

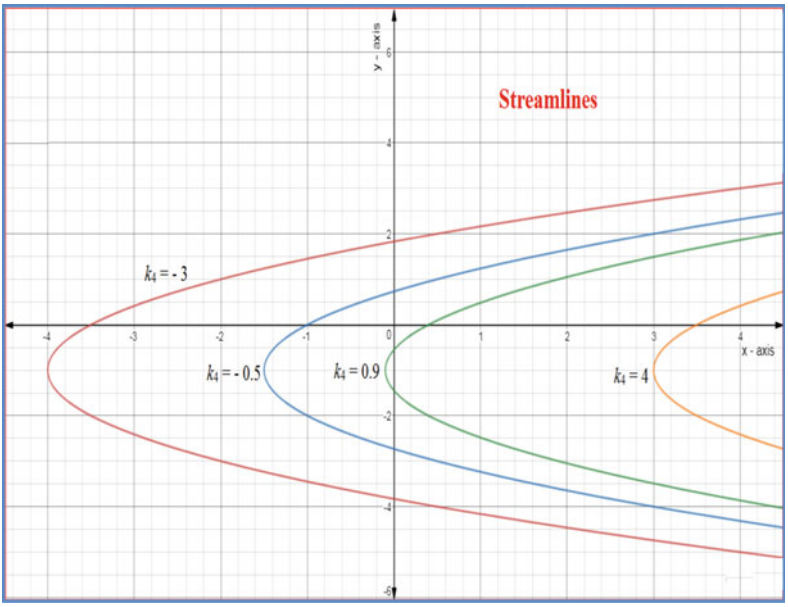

Fig. 20 Streamlines when $b_3 = -1$ and $b_4 = -1$

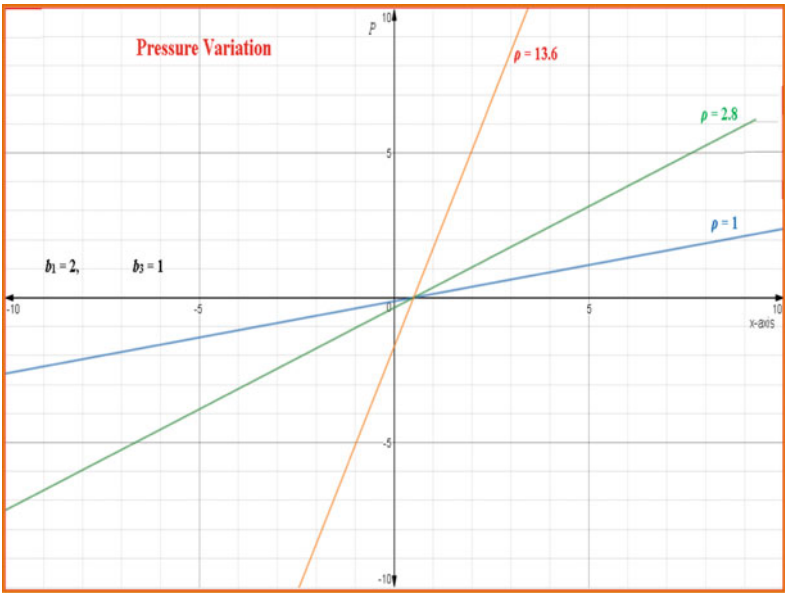

Fig. 21 Pressure variation for different densities

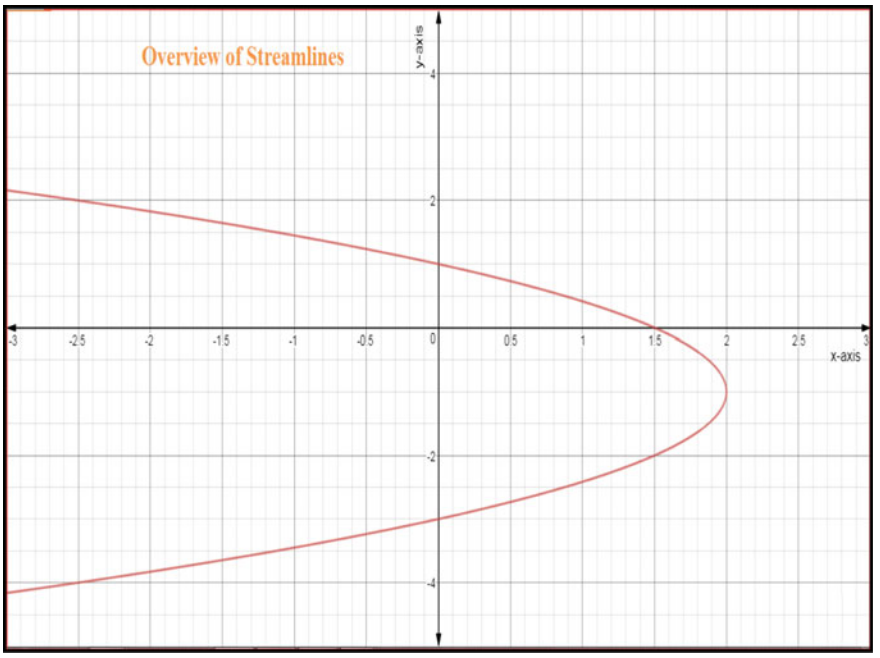

Fig. 22 Overview of streamlines (case III)

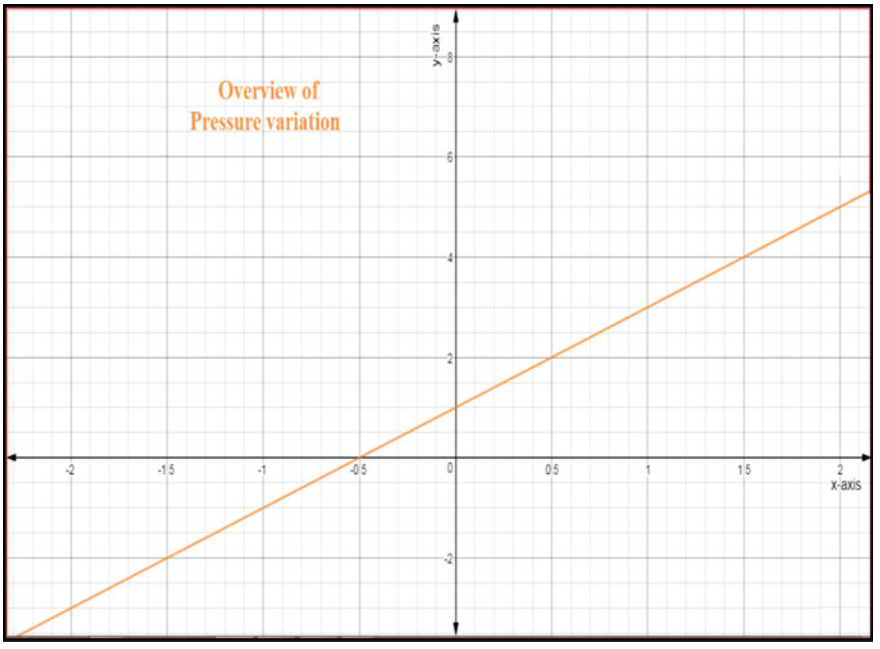

Fig. 23 Overview of variation of pressure (case III)

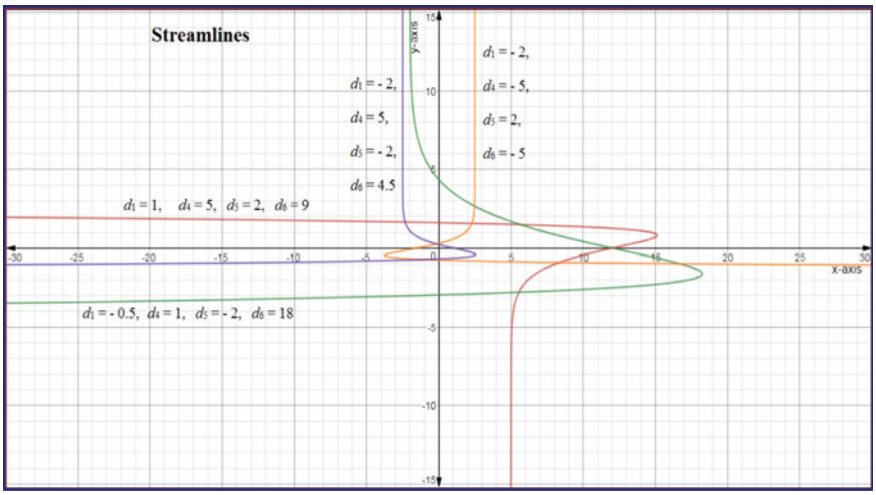

Fig. 24 Streamlines for different arbitrary constants

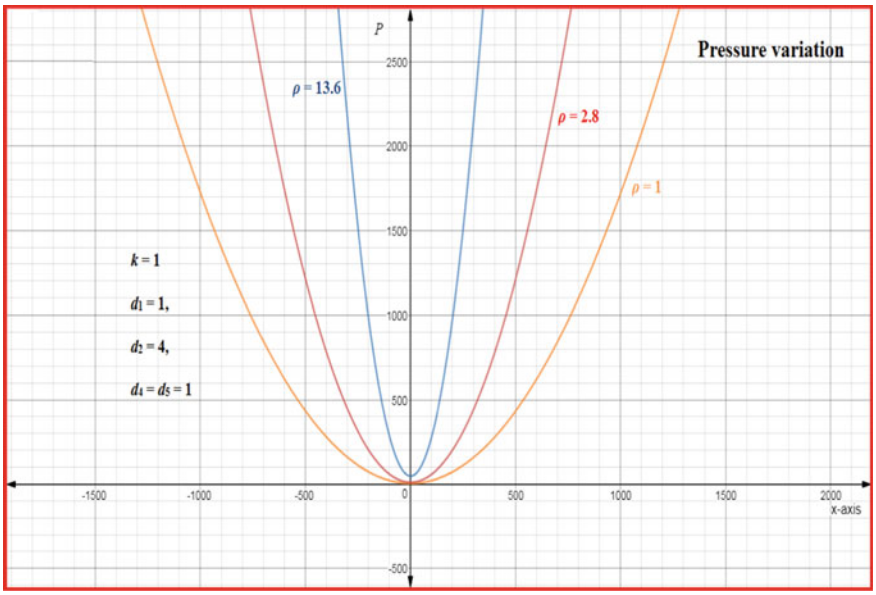

Fig. 25 Pressure variation with density versus x keeping y constant

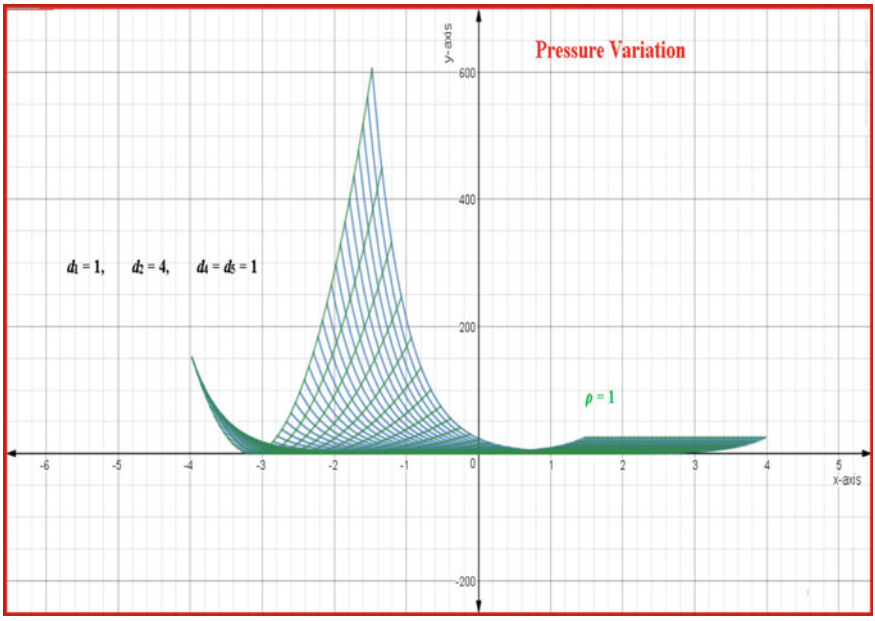

Fig. 26 Pressure variation for density equal to 1

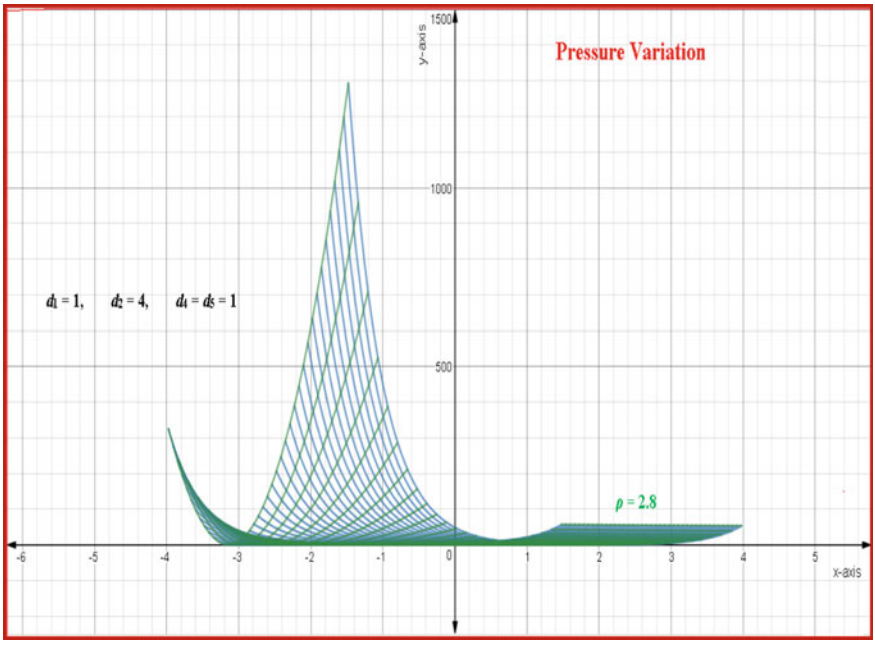

Fig. 27 Pressure variation for density equal to 2.8

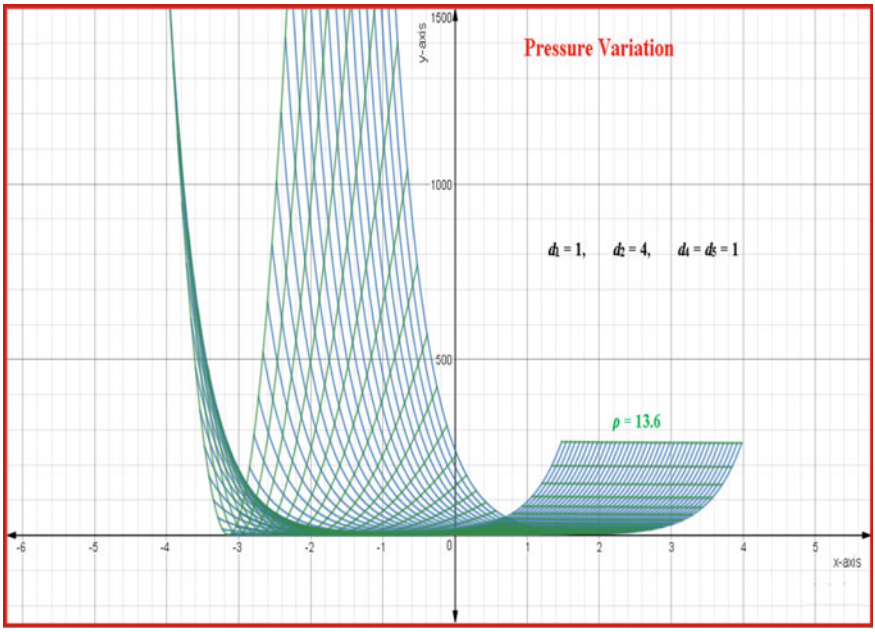

Fig. 28 Pressure variation for density equal to 13.6

We have applied non-dimensional substitution on magnetic lines or streamlines and the pressure expressions to get rid of arbitrary constants and plotted the graph consequently. These graphs give an overview of the flow pattern and the variation of pressure. Figures 9 and 15 give an overview of the magnetic lines pattern, and Figs. 22 and 29 give the same for streamlines. Figures 10, 16, 23, and 30 give the overview of pressure variations in all the cases.

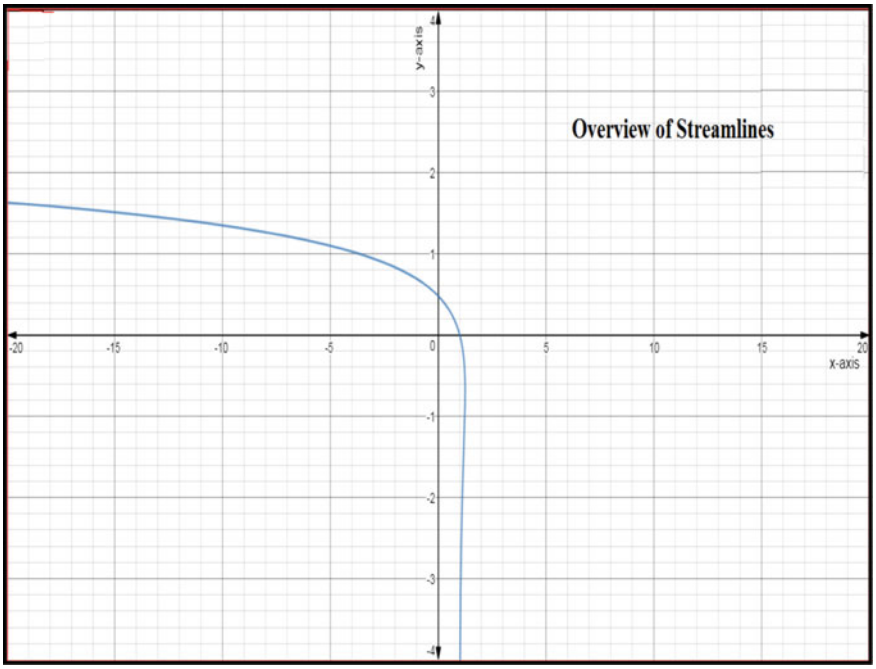

Fig. 29 Overview of streamlines (case IV)

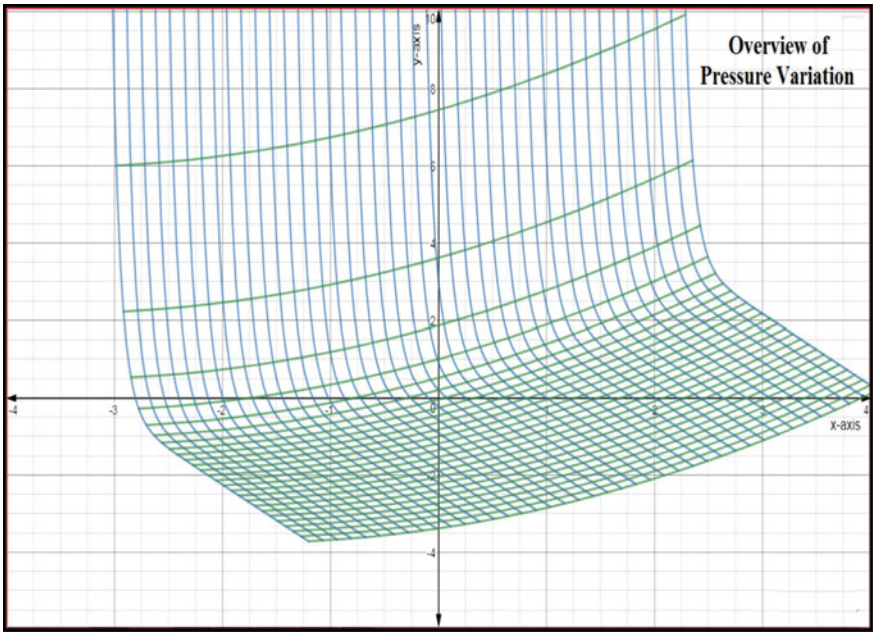

Fig. 30 Overview of pressure variation (case IV)

References

1. Martin MH (1971) The flow of a viscous fluid. I. Arch Rat Mech Anal 41:266–286
2. Chandna OP, Garg MR (1976) The flow of a viscous MHD fluid. Q Appl Math 34(3):287–299
3. Chandna OP, Nath VI (1973) Two-dimensional steady magneto-fluid-dynamic flows with orthogonal magnetic and velocity field distributions. Can J Phys 51:772–778
4. Chandna OP, Soteros CE, Swaminathan MK (1984) Some solutions for finitely conducting viscous MHD plane flows. Q Appl Math 42(2):143–158
5. Bagewadi CS, Bhagya S (2011) Solutions in variably inclined MHD flows. J Appl Math 4:77–83
6. Bagewadi CS, Bhagya S (2004) Behavior of streamlines in aligned flow. Far East J Appl Math 17(2):121–138
7. Bagewadi CS, Bhagya S (2007) A study of streamlines in second grade fluid flows. Mapana J Sci 5(1):5–20
8. Manoj K, Sayantan S, Thakur C (2013) Hodograph transformation in constantly inclined two phase MFD flows through porous media. Int J Math Arch 4(7):42–47
9. Ramesh GK, Gireesha BJ, Bagewadi CS (2014) Stagnation point flow of a MHD dusty fluid towards a stretching sheet with radiation. Afr Mat 25(1):237–249
10. Manjunatha S, Gireesha BJ (2016) Effects of variable viscosity and thermal conductivity on MHD flow and heat transfer of a dusty fluid. Ain Shams Eng J 7:505–515
11. Manjunatha S, Gireesha BJ, Bagewadi CS (2017) Series solutions for an unsteady flow and heat transfer of a rotating dusty fluid with radiation effect. Acta Math Univ Comenianae LXXXVI(1):111–126

Kinematic Analysis of Theo Jansen Mechanism-Based Eight-Leg Robot

Keval Bhavsar, Dharmik Gohel, Pranav Darji, Jitendra Modi and Umang Parmar

Abstract This paper presents the design analysis of an intellectual model of an autonomous surveillance robot. The principle objective is to do surveillance in the muddy or desert area or on that region where the surface is less grippy. This spider is having EIGHT legs controlled by two DC servo motors. The mechanism which is used to make those legs is THEO JANSEN MECHANISM, which is one of the animal walking patterns. To do the surveillance, a 360° rotating camera is used which is having its own working module. All the electronics are controlled by Arduino and that Arduino takes power to run itself as well as all other systems by 12 V DC battery. As this is the first spider robot which is made by Polylactic Acid (PLA) material, it gives comparison between Conventional Theo Jansen Mechanism and Modified Theo Jansen Mechanism.

Keywords Theo Jansen mechanism · Animal walking pattern · 360 camera · Surveillance device · PLA material

1 Introduction

This paper presents the design and development of an intellectual model of an autonomous surveillance robot known as Spider—A Security Device. The principle objective is to do surveillance in the muddy or desert area or on that region where the surface is less grippy. This spider is having EIGHT legs controlled by two DC servo motors. The mechanism which is used to make those legs is THEO JENSON MECHANISM, which is one of the animal walking patterns. To do the surveillance, a 360-degree rotating camera is used which is having its own working module. All the electronics are controlled by Arduino and that Arduino takes power to run itself as well as all other systems by 12 V DC battery, as this is the first spider robot which is made by Polylactic Acid (PLA) material.

K. Bhavsar (✉) · D. Gohel · P. Darji · J. Modi · U. Parmar
Aditya Silver Oak Institute of Technology, Ahmedabad, India
e-mail: kevalbhavsar42@gmail.com

D. Maity et al. (eds.), *Advances in Fluid Mechanics and Solid Mechanics*,
Lecture Notes in Mechanical Engineering,
https://doi.org/10.1007/978-981-15-0772-4_6

2 Literature Review

The Klann linkage offers a considerable lot of guides of further developed strolling cars without a portion of their limitations. It fits into the specialized void among the strolling gadgets and axel-driven wheels. While Theo Jansen Mechanism uses 11 little bars, Dutch active stone carver Theo Jansen has made a planar instrument that, when utilized pair with numerous others indistinguishable from it, can stroll in a smooth forward movement.

Qu et al. [1] present the structure and advancement of an applied model of a self-sufficient self-propelled inline examination robot, called Smart Spider. The essential goal is to utilize this kind of robot for seaward oil and gas pipeline review, particularly for those pipelines where the traditional astute pigging framework could not or be hard to be conveyed. Deepak D, Pathma sharma S [2] proposed two six-legged walker connected by utilizing a connection system and by coupling two kinematic walkers with a different engine for every walker. By utilizing the different engine, we can run every walker in the ideal position like front and back, and consequently we can be ready to control the walker to turn left and right movements. Patnaik [3] presents the Study of Theo Jansen Mechanism for burden conveying limit. It gives the outcome for pressure study. Parekh et al. [4] present to automatize the errand of pitch checking. Theo Jansen's component displays better portability while proceeding onward unpleasant territory over wheeled robots. The enhancement is set up to limit the vitality input and boost the throughput. The outcomes which were gotten depended on a four-legged strolling model; in any case, the exactness can be improved by expanding the quantity of legs. Nansai et al. [5] present unique study of a four-legged Theo Jansen linkage instrument utilizing projection technique that outcomes in requirement power and proportional Lagrange's standard of movement essential for any suggestive expansion or potential improvement of this NICHE system. Numerical recreations utilizing MA TX are displayed in mix with the dynamic study Kazuma Komoda, H.W. [6]. The connection is valuable to emulate creature development, and they accepted that an extra here and there movement in the linkage focus gives assorted movement designs from the first inward cycle. Amir AF, Nassiraei KI [7] present the possibility of IMD to approve how a mechanical gathering can be intended to boost robot controllability, universalization, and errand execution. Lokhande NG, Emche VB [8] present a robot that can venture over asphalts, climb staircases, or travel into regions that are at present not reachable with wheels but rather does not require microchip control or huge numbers of inciting instruments. Celaya E, Porta JM [9] set up a hearty controller for a six-legged robot that enables it to stroll over horrid territories in an independent way, with restricted utilization of tangible information. Blair [10] examine a ROTAB produced for improving the work envelope of an SIR-I robot in an adaptable assembling cell. The cell contains six terminals, four of which are served by the robot.

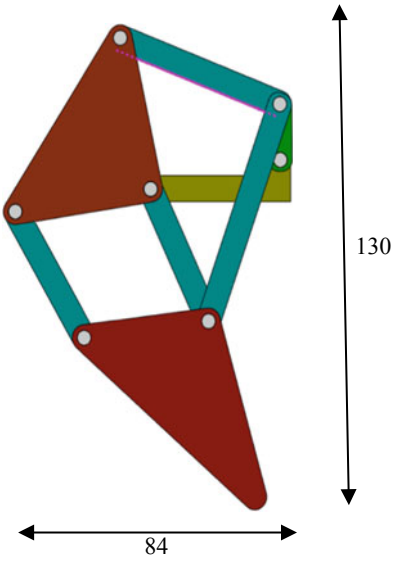

Fig. 1 Modified Theo Jansen mechanism

3 Research Gap

After doing literature review on many research papers as well as patents on Theo Jansen mechanism, we found that no one had used plastic material till now in making the robot. This study sets a theoretic basis for upcoming study into Theo Jansen mechanism. Till now, Theo Jansen mechanism is used only for transportation robots and walking robots. We are using this Theo Jensen mechanism for the surveillance. In all the previous mechanisms, no ternary link is used in place of binary link. This is the first spider robot which will made by Polylactic Acid (PLA) material (Figs. 1 and 2).

4 Design and Analysis

Here, Conventional Theo Jansen Mechanism has 12 links includes 2 binary joints, 4 ternary joints, and 4 quaternary joints, while the Modified Theo Jansen Mechanism has 6 links of which 2 are ternary links and 4 are binary links (Figs. 3 and 4; Table 1).

When we did the path analysis in SOLIDWORKS 2017, we came to know that we are getting almost the same path when we compared it with conventional Theo Jansen mechanism (Figs. 5 and 6).

In Displacement Analysis, doing comparison with the Conventional Theo Jansen Mechanism, we get minor difference in both the graphs (Figs. 7 and 8).

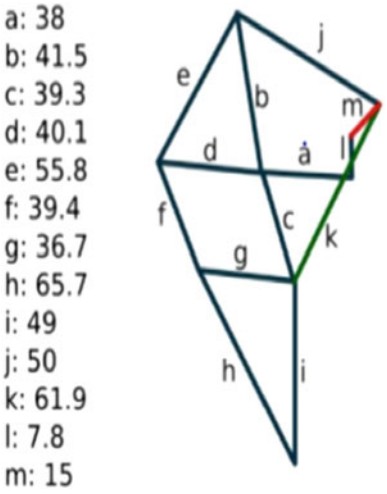

Fig. 2 Conventional Theo Jansen mechanism

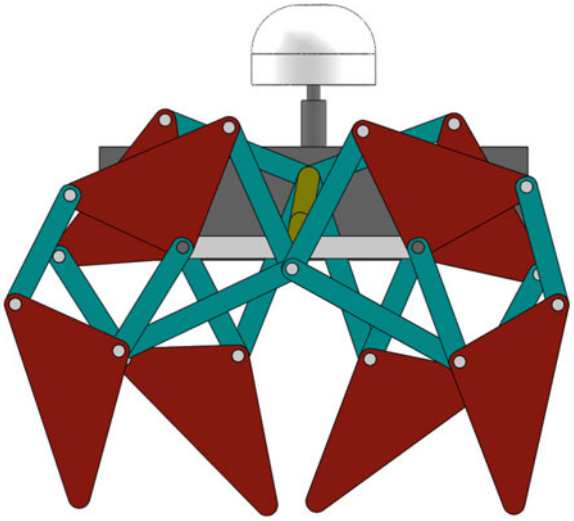

Fig. 3 Side view of the robot

Linear Velocity Analysis, comparing with conventional design, we get slight better velocity (Figs. 9 and 10).

In Acceleration Analysis, Modified Theo Jansen Mechanism, we get more acceleration in starting and then it becomes constant which means that new design is not jerky (Figs. 11 and 12).

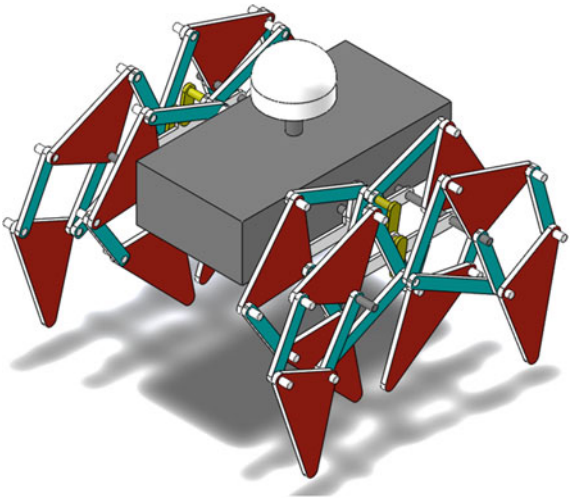

Fig. 4 Isometric view of the robot

Table 1 Components of robot with specifications

Component	Specifications
Legs and body of robot	Made from **polylactic acid (PLA)**
Motor	70–90 rpm, high torque
Arduino	Mega
Battery	12 V (4 Unit)
Camera	Camera—360 angle motion-controlled camera module

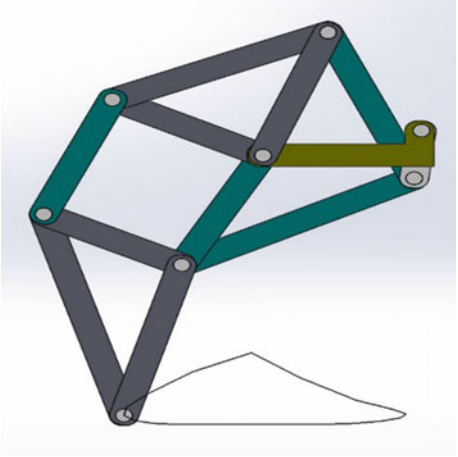

Fig. 5 Conventional design path

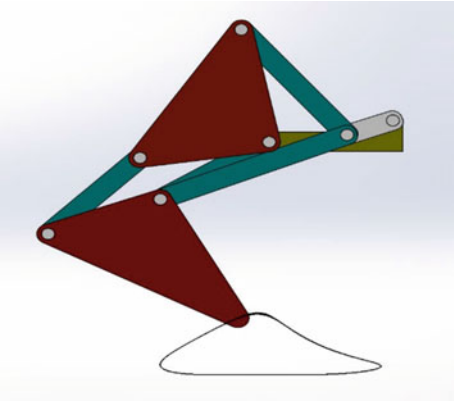

Fig. 6 Modified Theo Jansen path

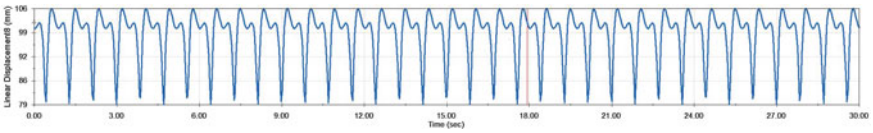

Fig. 7 Conventional Theo Jansen displacement graph

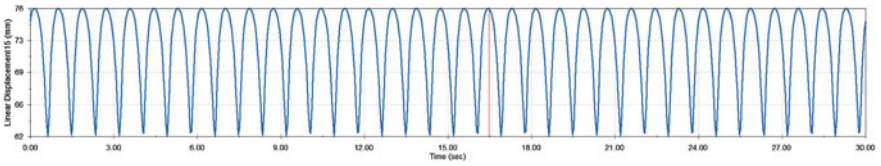

Fig. 8 Modified Theo Jansen displacement graph

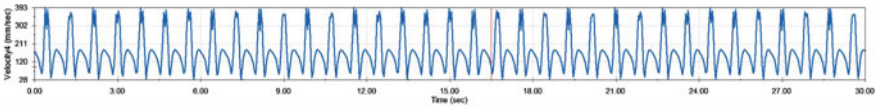

Fig. 9 Conventional Theo Jansen velocity analysis

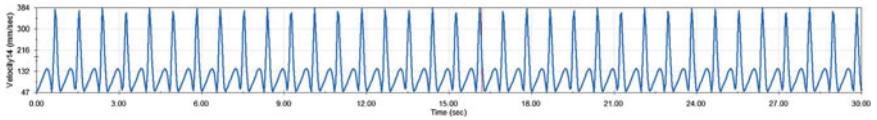

Fig. 10 Modified Theo Jansen velocity analysis

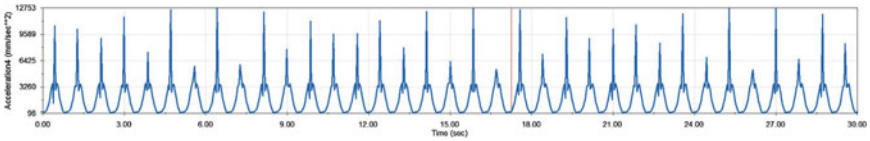

Fig. 11 Conventional Theo Jansen acceleration analysis

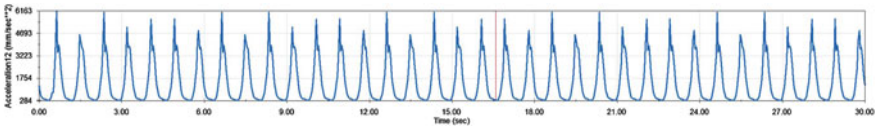

Fig. 12 Modified Theo Jansen acceleration analysis

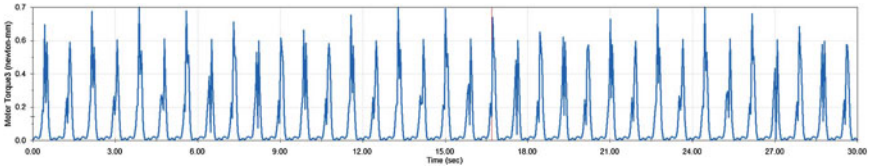

Fig. 13 Conventional Theo Jansen motor torque analysis

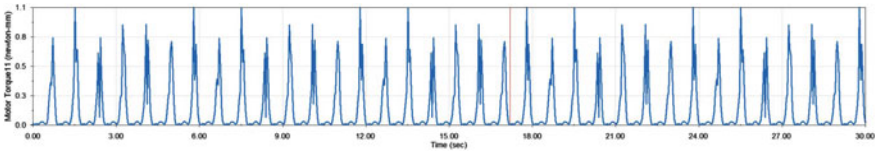

Fig. 14 Modified Theo Jansen motor torque analysis

In Torque Analysis, Modified Theo Jansen Mechanism requires a maximum torque of 0.9 N mm, while the convention mechanism requires 0.6 N mm (Figs. 13 and 14).

Power Consumption in Modified Theo Jansen Mechanism requires about 0.007 W to run while convention mechanism requires 0.006 W (Figs. 15 and 16).

5 Conclusion

The robot uses the Modified Theo Jensen as its walking pattern. It has six links of which two are ternary links and four are binary links. This mechanism satisfies

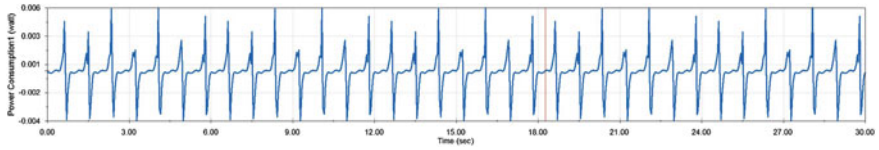

Fig. 15 Conventional Theo Jansen power consumption analysis

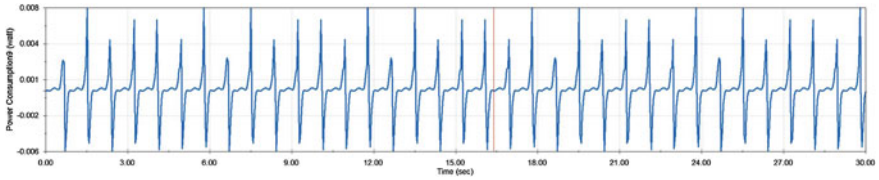

Fig. 16 Modified Theo Jansen power consumption analysis

Grubler's and Kutzbach's criterion. After doing the kinematic analysis of modified Theo Jansen Mechanism, we found that it is jerk free, and by using ternary links it provides us better stability with minor increase of input power.

Acknowledgements We would like to thank R. K. Technology who gave us an opportunity to undertake such a great challenging and innovative work.

References

1. Qu Y, Durdevic P, Yang Z (2018) Smart-spider: autonomous self-driven in-line robot for versatile pipeline inspection. IFAC PapersOnLine 51(8):251–256
2. Deepak D, Pathma sharma S (2017) Design and fabrication of kinematic robotic walker with left and right motion with camera. SSRG Int J Mech Eng 4(4):53–56
3. Patnaik S (2015) Analysis of Theo Jansen mechanism (strandbeest) and its comparative advantages over wheel based mine excavation system. IOSR J Eng 5(7):43–52
4. Parekh BJ, Thakkar PN, Tambe MN (2014) Design and analysis of Theo Jansen's mechanism based ports ground (pitch) marking robot. In: Annual IEEE India conference
5. Nansai S, Elara MR, Iwase M (2013) Dynamic analysis and modeling of Jansen mechanism. Procedia Eng 64:1562–1571
6. Kazuma Komoda HW (2011) A study of availability and extensibility of Theo Jansen mechanism toward. In: The 21st annual conference of the Japanese Neural Network Society, no. 21
7. Amir AF, Nassiraei KI (2007) Concept of intelligent mechanical design for autonomous mobile robots
8. Lokhande NG, Emche VB (2004) Mechanical spider by using Klann mechanism
9. Celaya E, Porta JM (1996) Control of a six-legged robot walking on abrupt terrain. In: International conference on robotics and automation, Minneapolis
10. Blair RM (1989) Enhancement of robot work envelope in a flexible manufacturing cell

Wave Trapping by Trapezoidal Porous Breakwater

Santanu Koley

Abstract The trapping of normally incident free surface water waves by a porous trapezoidal breakwater is studied in the context of two-dimensional linearized and potential water wave theory. The trapezoidal porous breakwater is situated at a finite distance away from the leeward rigid wall. The mathematical solution of the related boundary value problem is obtained using the well-known boundary element method. The flow of the water through the porous medium is modeled using Sollitt and Cross model for thick porous structure (see [13]). A number of important physical parameters such as wave loads on the rigid wall, reflection coefficient, and free surface elevations are calculated and discussed in detail.

Keywords Porosity · Breakwater · Boundary element method

1 Introduction

Breakwaters generally constructed at ports and harbor to protect various marine infrastructures from incoming waves coming from the open sea. The traditional shapes of these breakwaters are trapezoidal in nature. Generally, these breakwaters are placed at a suitable distance apart from a marine sea wall to create a calm or tranquil region in the leeside of the breakwater. Earlier days, rigid breakwater was constructed in ports and harbors (see [8] for details). The disadvantages of a rigid breakwater are that incoming wave forces acting on these structures are very high and due to that, these structures often got collapsed. Therefore, to increase the durability of these structures, often porous breakwaters are constructed. These porous breakwaters can dissipate a huge amount of wave energy (see [8] for details). In this way, the incoming wave loads will get reduced drastically. Significant research was carried out in the past to study the wave transmission through porous breakwaters

S. Koley (✉)
Birla Institute of Technology and Science—Pilani, Hyderabad Campus, Hyderabad, India
e-mail: santanukoley1989@gmail.com

D. Maity et al. (eds.), *Advances in Fluid Mechanics and Solid Mechanics*,
Lecture Notes in Mechanical Engineering,
https://doi.org/10.1007/978-981-15-0772-4_7

(see [8, 11, 12]). The widely used model for porous flow through the breakwater is based on the Sollitt and Cross [13]. This model is extended and modified by [10] for linear long wave theory. Reference [9] used an analytic solution method based on expansion of velocity potentials in terms of eigenfunctions to study the scattering of obliquely incident and non-breaking surface gravity waves by a bottom-mounted finite width porous breakwater. Model test was performed extensively by [4] to study the characteristics of the wave reflection of oblique surface gravity waves by a rubble mound porous breakwater. Reference [14] studied the transmission of water waves over submerged breakwater analytically using eigenfunction expansion method. Reference [3] studied the flow pattern of the water waves above a submerged trapezoidal rigid breakwater in the long wave approximation. Reference [15] studied the wave transformation due to the presence of rigid trapezoidal breakwater or channel using the modified mild slope model. Reference [2] studied oblique incoming waves interaction with porous structures having finite width of different structural shapes and configurations in two-layer fluid system. Reference [5] investigated the oblique water wave trapping in presence of bottom-standing and surface-piercing thick porous structures placed near a rigid sea wall. They have used solution method based on eigenfunction expansion technique for semi-analytical solution and boundary element method to get numerical solution. This aforementioned problem was further extended by [7] for sloping water bed and in presence of trapezoidal multilayered porous breakwater. Further, [1] studied the trapping of water waves by porous breakwater in two-layered fluid system. Recently, [6] used a coupled method based on eigenfunction expansion and boundary element method to study the surface gravity wave trapping and scattering by a permeable semicircular breakwater placed near to a sloping porous sea wall.

In the present manuscript, the trapping of normally incident water waves by a trapezoidal porous breakwater placed near a rigid wall is investigated. The overall structure of the paper is as follows. In Sect. 2, the mathematical formulation of the associated boundary value problem is provided. Section 3 contains details of boundary element method-based numerical solution technique. Following the same, the results for various physical parameters are provided in Sect. 4. Finally, Sect. 5 contains the summary of the study.

2 Mathematical Formulation

In the present context, it is assumed that trapezoidal porous thick breakwater is placed in finite water depth (see Fig. 1). The flow of the water is of potential kind. The incident wave is propagating from $-x$ to x direction and impinges on the breakwater in normal direction. The trapezoidal-shaped surface-piercing structure (as in Fig. 1) made up of porous materials such as interlocking armor units with the two-sides slopes $1:10$ and $1:5$, respectively. Further, the leeside vertical rigid wall is located at a finite distance away from the breakwater. The water depth is assumed to be uniform in nature. It is to be noted that the left-hand region of the breakwater is semi-infinite

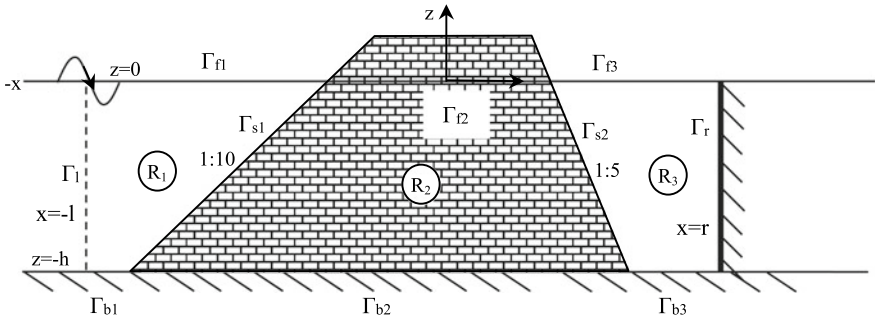

Fig. 1 Schematic diagram of the physical problem

and so to use numerical solution method, a fictitious boundary Γ_l is constructed at a finite distance away from the breakwater. The requirement and utility for the same are discussed subsequently. For the sake of modeling, the total region is divided into three regions, namely regions R_j for $j = 1, 2, 3$. It is also assumed that the water flow is simple harmonic having angular frequency ω. Therefore, the velocity potentials in each region can be written in the form $\Phi(x, z, t) = \Re\{\phi(x, z)e^{-i\omega t}\}$. So, the spatial component of the velocity potentials $\phi_j(x, z)$ for $j = 1, 2, 3$ satisfies the well-known Laplace equation

$$\left(\frac{\partial^2}{\partial x^2} + \frac{\partial^2}{\partial z^2}\right)\phi_j = 0. \tag{1}$$

Now, the boundary conditions at the bottom and at the free surface are

$$\frac{\partial \phi_j}{\partial \boldsymbol{n}} = 0 \quad \text{on } \Gamma_{bj} \quad \text{for } j = 1, 2, 3, \tag{2}$$

$$\frac{\partial \phi_j}{\partial \boldsymbol{n}} - K\left(m_j + \mathrm{i} f_j\right)\phi_j \quad \text{on } \Gamma_{fj} \quad \text{for } j = 1, 2, 3, \tag{3}$$

where $K = \omega^2/g$, $g = 9.81\ m/s$. It is to be noted that $\partial/\partial \boldsymbol{n}$ represent the normal derivative and $m_j = 1$, $f_j = 0$ for $j = 1, 3$. The boundary conditions on Γ_{sj} are given by

$$\phi_j = (m_2 + \mathrm{i} f_2)\,\phi_2, \quad \text{and} \quad \frac{\partial \phi_j}{\partial \boldsymbol{n}} = -\epsilon_2 \frac{\partial \phi_2}{\partial \boldsymbol{n}}, \quad \text{on } \Gamma_{sj} \quad \text{for } j = 1, 3, \tag{4}$$

where ϵ represents the porosity, and m and f are the inertial and linearized friction coefficients, respectively. The boundary condition on the rigid wall gives

$$\frac{\partial \phi_3}{\partial \boldsymbol{n}} = 0, \quad \text{on } \Gamma_{\mathrm{r}}. \tag{5}$$

Finally, the boundary condition at the far-field is given by

$$\frac{\partial(\phi_1 - \phi_I)}{\partial \boldsymbol{n}} - \mathrm{i}k_0(\phi_1 - \phi_I) = 0, \quad \text{on } \Gamma_1, \tag{6}$$

where $\phi_I = e^{\mathrm{i}k_0(x+l)} \dfrac{\cosh(k_0(z+h))}{\cosh k_0 h}$ is the incident wave potential with k_0 is the real and positive root of the dispersion relation $K = k \tanh kh$. Here, Γ_l is taken four times water depth away from the breakwater to ensure that the effect of local or evanescent wave modes will vanish on Γ_1. This also requires to ensure the uniqueness of the solution.

In the next section, the aforementioned mathematical problem will be transformed into a system of integral equations and will be solved using the boundary element method (see [5] for details).

3 Boundary Element Method-Based Solution Procedure

Using the Green's function $G(x, z; \xi, \eta)$ and the velocity potential $\phi(x, z)$ as two arguments in the Green's second identity over the domain Ψ which is bounded by Γ, we get the following Fredholm integral equation of second kind:

$$\begin{pmatrix} \frac{1}{2}\phi(\xi,\eta) \\ \phi(\xi,\eta) \end{pmatrix} = \int_{\Gamma} \left(\phi \frac{\partial G}{\partial \boldsymbol{n}} - G \frac{\partial \phi}{\partial \boldsymbol{n}} \right) \mathrm{d}\Gamma(x, z), \quad \begin{pmatrix} \text{if } (\xi,\eta) \in \Gamma \\ \text{if } (\xi,\eta) \in \Psi \text{ but } \notin \Gamma \end{pmatrix}. \tag{7}$$

where

$$G(x, z; \xi, \eta) = \frac{1}{2\pi} \ln \sqrt{(x-\xi)^2 + (z-\eta)^2}, \qquad r = \sqrt{(x-\xi)^2 + (z-\eta)^2}. \tag{8}$$

Now, using the boundary condition Eqs. (2)–(6), the following integral equations will be obtained:

$$\begin{aligned} -0.5\phi_1 + \int_{\Gamma_l} \phi_1 \left(\frac{\partial G}{\partial \boldsymbol{n}} - \mathrm{i}k_0 G \right) \mathrm{d}\Gamma + \int_{\Gamma_{b1}} \phi_1 \frac{\partial G}{\partial \boldsymbol{n}} \mathrm{d}\Gamma + \int_{\Gamma_{f1}} \left(\frac{\partial G}{\partial \boldsymbol{n}} - KG \right) \phi_1 \mathrm{d}\Gamma \\ + \int_{\Gamma_{s1}} \left((m_2 + \mathrm{i}f_2)\phi_2 \frac{\partial G}{\partial \boldsymbol{n}} + \epsilon_2 G \frac{\partial \phi_2}{\partial \boldsymbol{n}} \right) \mathrm{d}\Gamma = \int_{\Gamma_l} \phi_I \left(\frac{\partial G}{\partial \boldsymbol{n}} - \mathrm{i}k_0 G \right) \mathrm{d}\Gamma, \end{aligned} \tag{9}$$

$$-0.5\phi_2 + \int\limits_{\Gamma_{s1}} \left(\phi_2 \frac{\partial G}{\partial \boldsymbol{n}} - G\frac{\partial \phi_2}{\partial \boldsymbol{n}}\right)\mathrm{d}\Gamma + \int\limits_{\Gamma_{f2}} \left(\frac{\partial G}{\partial \boldsymbol{n}} - K(m_2 + \mathrm{i}f_2)G\right)\phi_2 \mathrm{d}\Gamma + \int\limits_{\Gamma_{b2}} \phi_2 \frac{\partial G}{\partial \boldsymbol{n}}\mathrm{d}\Gamma + \int\limits_{\Gamma_{s2}} \left(\phi_2 \frac{\partial G}{\partial \boldsymbol{n}} - G\frac{\partial \phi_2}{\partial \boldsymbol{n}}\right)\mathrm{d}\Gamma = 0, \tag{10}$$

$$-0.5\phi_3 + \int\limits_{\Gamma_{s2}} \left((m_2 + \mathrm{i}f_2)\phi_2 \frac{\partial G}{\partial \boldsymbol{n}} + \epsilon_2 G\frac{\partial \phi_2}{\partial \boldsymbol{n}}\right)\mathrm{d}\Gamma + \int\limits_{\Gamma_{f3}} \left(\frac{\partial G}{\partial \boldsymbol{n}} - KG\right)\phi_3 \mathrm{d}\Gamma = 0, + \int\limits_{\Gamma_{b2}+\Gamma_{\mathrm{r}}} \phi_3 \frac{\partial G}{\partial \boldsymbol{n}}\mathrm{d}\Gamma \tag{11}$$

Now, the integral equations (9)–(11) are discretized to get system of linear algebraic equations which involve ϕ and $\partial\phi/\partial\boldsymbol{n}$ and solve these to get the required unknowns. The detailed procedure was given in [8].

4 Results and Discussions

In this section, a code is written in MATLAB for the sake of numerical computation as discussed in the previous section. The structural and wave parameters will assume the following values: $m_2 = 1.0$, $h = 20$ m and $T = 10$ s (T is the incident wave time period) are kept fixed unless otherwise stated explicitly. The reflection coefficient is given by

$$K_{\mathrm{r}} = |R_0|. \tag{12}$$

The vertical and horizontal wave loads/forces F_{v} and F_{h} acting on the front side Γ_{s1} of the breakwater is given by

$$F_{\mathrm{v}} = \Re\left\{\mathrm{i}\rho\sigma \int_{\Gamma_{s1}} \phi_1 n_z \mathrm{d}\Gamma\right\}, \qquad F_{\mathrm{h}} = \Re\left\{\mathrm{i}\rho\sigma \int_{\Gamma_{s1}} \phi_1 n_x \mathrm{d}\Gamma\right\}, \tag{13}$$

where n_x and n_z are the components along the x and z-directions, respectively, of the unit normal vector $\mathbf{n}$ on Γ_{s1}.

Figure 2 shows the changes of reflection coefficient with the change in non-dimensional wave number k_0h for a number of values of friction coefficient f_2 of the porous material. It is observed in Fig. 2 that for $k_0h < 1/10$, i.e., for long wave approximation, the reflection coefficient K_{r} decreases for higher values of wave number k_0h. This happens because most of the wave energy in case of long waves passes through the breakwater and again reflects back by the leeside rigid wall. However, for higher and moderate values of the wave number k_0h, the reflection coefficient K_{r} changes in an oscillatory manner. This is due to the combined effect of wave

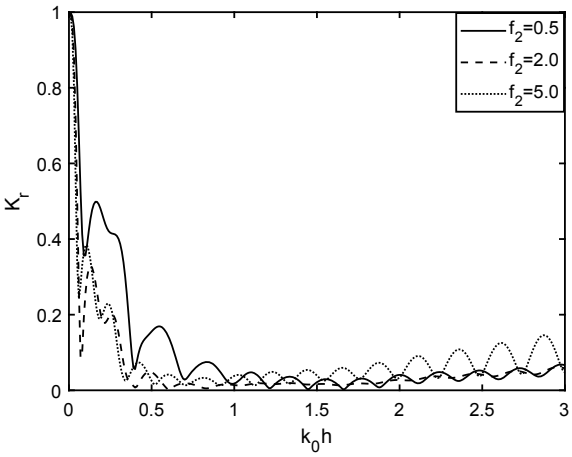

Fig. 2 K_r versus k_0h for various f_2

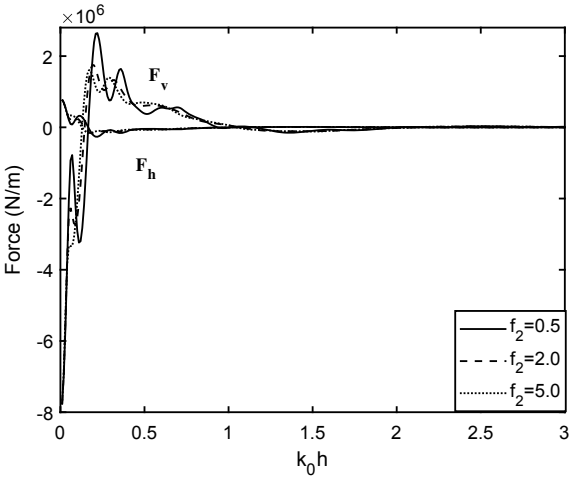

Fig. 3 F_h and F_v versus k_0h for various f_2

reflection and wave energy dissipation due to the porous materials of the breakwater. Moreover, it is seen that the wave reflection decreases for higher values of friction coefficient f_2. This is due to the higher amount of wave energy dissipation with an increase in friction coefficient.

Figure 3 shows the variation in the horizontal and vertical wave forces F_h and F_v as a function of k_0h for different values of friction coefficient f_2. The occurrences of phase lag between the two wave forces are clearly visible. For higher wave number k_0h, both the wave forces take the same values. However, for smaller values of k_0h, the vertical wave loads/forces acting on the seaside of the breakwater takes maximum and minimum values.

Figure 4 depicts the changes in free surface elevation η/h for different possible values of friction coefficient f_2. It is observed that there is a huge decrease in the

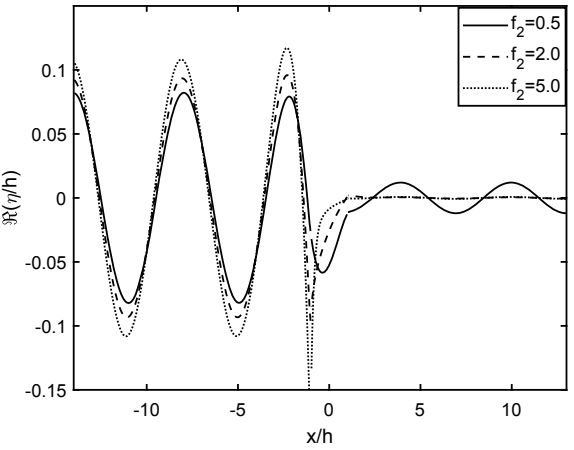

Fig. 4 η/h for various f_2

free surface elevation amplitude at the leeside of the trapezoidal porous breakwater. This shows that by suitably placing breakwater at a finite distance away from the rigid sea wall will helps to create a calm zone in the confined region between the breakwater and the sea wall. Moreover, the figure shows that the amplitude of the surface elevation diminishes for higher values of the friction coefficient f_2. The reason is that a significant portion of the wave energy is dissipated when the incoming wave passes through the porous structure.

5 Conclusion

The present study provides a boundary element method-based efficient numerical solution technique to study wave past a trapezoidal shape porous breakwater. The results clearly indicate that the trapezoidal porous breakwater is very effective to create a tranquility region in between the rigid sea wall and the porous structure. This will certainly reduces the wave force which is acting on the sea wall and various marine infrastructures to a great extent. As a result, the durability of the sea wall will increase significantly. The present methodology can be extended easily to handle similar problems arise in mathematical physics and other engineering branches.

References

1. Behera H, Koley S, Sahoo T (2015) Wave transmission by partial porous structures in two-layer fluid. Eng Anal Bound Elements 58:58–78
2. Behera H, Sahoo T (2014) Gravity wave interaction with porous structures in two-layer fluid. J Eng Math 87(1):73–97

3. Chang H-K, Liou J-C (2007) Long wave reflection from submerged trapezoidal breakwaters. Ocean Eng 34(1):185–191
4. Isaacson M, Papps D, Mansard E (1996) Oblique reflection characteristics of rubble-mound structures. J Waterw Port Coast Ocean Eng 122(1):1–7
5. Koley S, Behera H, Sahoo T (2014) Oblique wave trapping by porous structures near a wall. J Eng Mech 141(3):04014122
6. Koley S, Sahoo T (2017) Wave interaction with a submerged semicircular porous breakwater placed on a porous seabed. Eng Anal Bound Elements 80:18–37
7. Koley S, Sarkar A, Sahoo T (2015) Interaction of gravity waves with bottom-standing submerged structures having perforated outer-layer placed on a sloping bed. Appl Ocean Res 52:245–260
8. Koley S (2016) Integral equation and allied methods for wave interaction with porous and flexible structures. Ph.D. thesis, IIT, Kharagpur
9. Losada IJ, Silva R, Losada MA (1996) 3-d non-breaking regular wave interaction with submerged breakwaters. Coast Eng 28(1–4):229–248
10. Madsen OS, Shusang P, Hanson SA (1978) Wave transmission through trapezoidal breakwaters. In: Coastal engineering 1978, pp 2140–2152
11. Madsen OS, White SM (1977) Wave transmission through trapezoidal breakwaters. In: Coastal engineering 1976, pp 2662–2676
12. Rojanakamthorn S, Isobe M, Watanabe A (1991) Modeling of wave transformation on submerged breakwater. Coast Eng 1990:1060–1073
13. Sollitt CK, Cross RH (1973) Wave transmission through permeable breakwaters. In: Coastal engineering 1972, pp 1827–1846
14. Twu S-W, Liu C-C, Hsu W-H (2001) Wave damping characteristics of deeply submerged breakwaters. J Waterw Port Coast Ocean Eng 127(2):97–105
15. Xie J-J, Liu H-W (2013) Analytical study for linear wave transformation by a trapezoidal breakwater or channel. Ocean Eng 64:49–59

Heat and Mass Transfer Due to Double-Diffusion Convection in a Square Porous Enclosure Occupied by Casson Fluid

Madhu Aneja and Sapna Sharma

Abstract Heat and mass transfer in a porous cavity filled with Casson fluid are analyzed. The flow behavior of Casson fluid in a porous cavity is investigated due to the realization that most of the fluids exhibiting non-Newtonian behavior come in contact with porous media, particularly, in ceramic processing, enhanced oil recovery, production of glass float, and processing of nuclear waste. The mathematical model of the physical problem consisting of continuity, momentum, energy, and concentration equations is converted into finite element equations and solved by penalty finite element method. The bottom wall of the cavity is hotter than the side walls ($T_h > T_c$). The top wall of the cavity is adiabatic. On the other hand, concentration is more on the top wall compared to the bottom ($C_h > C_c$) wall. The side walls are taken to be impermeable to concentration flux. The physical parameters governing the fluid flow are Rayleigh number (Ra), Prandtl number (Pr), Darcy number (Da), Lewis number (Le), buoyancy ratio parameter (N), and Casson fluid parameter (γ). It is observed from the obtained results that with the rise in Casson fluid parameter in porous medium leads to enhancement in heat transfer rate, mass transfer rate, and fluid flow intensification.

Keywords Porous media · Casson fluid · Penalty finite element method · Square cavity · Free convection

1 Introduction

In recent years, natural convective flow in porous cavities has gained much attention from researchers. This phenomenon has numerous applications in the industries and engineering such as fluid flow in geothermal reservoirs, processes involved in chemical separation, removal of moisture from stored grain system, production of crude

M. Aneja · S. Sharma (✉)
Thapar Institute of Engineering & Technology, Patiala 147004, Punjab, India
e-mail: sapna2002@gmail.com

M. Aneja
e-mail: madhu.aneja28@gmail.com

D. Maity et al. (eds.), *Advances in Fluid Mechanics and Solid Mechanics*,
Lecture Notes in Mechanical Engineering,
https://doi.org/10.1007/978-981-15-0772-4_8

oil, etc. The convection mode takes place when the temperature and concentration gradient creates due to transfer of heat and species within the fluid layer. This phenomenon is known as convection due to double diffusion. Numerous researchers [1–3] have extensively examined the natural convection in a porous saturated medium. In recent years, the double-diffusive flow in a porous medium has given some attention. Bourich et al. [4] used the scale analysis method to investigate the two-dimensional double-diffusive natural convection. The heat and mass transfer characteristics in a multi-porous cavity were examined by Saghir [5]. They studied the impact of solutal Rayleigh number on double diffusion and found that saltiness produces convection which is stronger than thermal ones. Azeem et al. [6] analyzed the influence of small solid wall on diffusion due to temperature and concentration gradient in a square porous cavity. These authors' research was confined to double diffusion in porous cavities filled with viscous fluids which obey Newton's law of viscosity. However, non-Newtonian fluids also played an important role in many industrial and engineering processes. These are chyme movement in the intestine, blood flows in arteries, foodstuff, and many more. To understand the flow behavior of these fluids, various rheological models are developed. Some of these are power-law fluids [7], Jeffrey fluids [8], micro-polar fluids [9], Maxwell fluids [10], viscoplastic fluids [11], Casson fluids [12], etc. The characteristic behavior of materials like mud/melts, ink, soaps, shampoos are not detected by the theory of Newtonian fluids. The Casson fluid is one such model which helps in studying the characteristic behavior of these fluids. The flow behavior of Casson fluid between two rotating cylinders was studied by Eldabe et al. [13]. In the problems related to biology, Casson fluid model is studied by Mernone et al. [14], Boyd et al. [15].

In the above mentioned literature, numerous researchers considered free convective flow with Casson fluid over stretching/shrinking surfaces, square cavity, etc. To our best knowledge, Casson fluid flow in a square porous cavity has not been analyzed yet. Thus, the aim of the present investigation is to analyze the heat and mass transfer characteristics of a Casson fluid in a porous square enclosure. Streamlines, isotherms, iso-concentration lines, average Nusselt number, average Sherwood number, and fluid flow rate are analyzed for various pertinent parameters obtained in the nondimensional form of the mathematical model and discussed in detail.

2 Mathematical Formulation of the Flow Problem

A saturated porous cavity is assumed to be filled with Casson fluid is demonstrated in Fig. 1. The wall is heated with uniform temperature and denotes as T_h from below. On the other hand, both the side walls are symmetrical cooled, their temperature is designated as T_c. The concentration at the top wall is higher than the bottom wall, i.e., $C_h > C_c$. The side walls are impermeable to concentration flux.

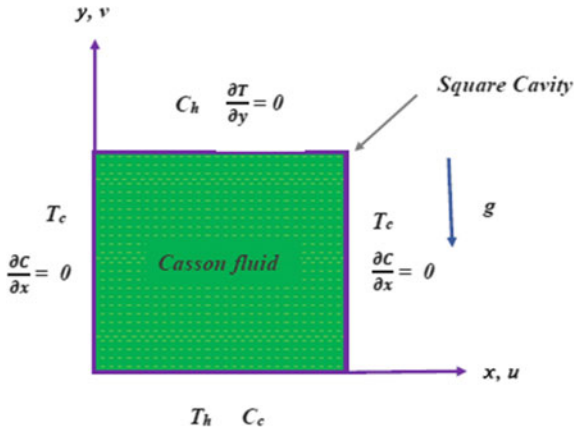

Fig. 1 Physical model and coordinate system

The rheological condition of state for the Cauchy stress tensor [16] of Casson fluid is given by

$$\tau_{ij} = \begin{cases} 2\left(\mu_B + \frac{p_y}{\sqrt{2\pi}}\right)e_{ij}, & \pi > \pi_c \\ 2\left(\mu_B + \frac{p_y}{\sqrt{2\pi_c}}\right)e_{ij}, & \pi < \pi_c \end{cases}.$$

Here $\pi = e_{ij}e_{ij}$ and e_{ij} are the (i, j)th component of the deformation rate, π designated as the components of the product of deformation rate itself, π_c denotes the critical value of this product for the particular non-Newtonian fluid, μ_B represents the plastic dynamic viscosity, and p_y is the yield stress of the fluid. It is considered that non-Newtonian fluid satisfies Boussinesq's approximation and other physical properties are assumed to be invariant. Moreover, the assumption here taken that the fluid and porous medium possess homogeneity. Under these assumptions, the mathematical model of the physical phenomenon is represented by nondimensional continuity, conservation of momentum, energy, and concentration equations.

2.1 Governing Equations

$$\frac{\partial U}{\partial X} + \frac{\partial V}{\partial Y} = 0, \tag{1}$$

$$U\frac{\partial U}{\partial X} + V\frac{\partial U}{\partial Y} = -\frac{\partial P}{\partial X} + Pr\left(\frac{\partial^2 U}{\partial X^2} + \frac{\partial^2 U}{\partial Y^2}\right) - \frac{Pr}{Da}U, \tag{2}$$

$$U\frac{\partial V}{\partial X} + V\frac{\partial V}{\partial Y} = -\frac{\partial P}{\partial Y} + Pr\left(\frac{\partial^2 V}{\partial X^2} + \frac{\partial^2 V}{\partial Y^2}\right) - \frac{Pr}{Da}V - RaPr(\theta + N\varphi), \tag{3}$$

$$U\frac{\partial\theta}{\partial X}+V\frac{\partial\theta}{\partial Y}=\left(\frac{\partial^2\theta}{\partial X^2}+\frac{\partial^2\theta}{\partial Y^2}\right), \tag{4}$$

$$U\frac{\partial\varphi}{\partial X}+V\frac{\partial\varphi}{\partial Y}=\frac{1}{Le}\left(\frac{\partial^2\varphi}{\partial X^2}+\frac{\partial^2\varphi}{\partial Y^2}\right). \tag{5}$$

The following are the transformation used for conversion of equations into dimensionless form:

$$X=\frac{x}{L},\quad Y=\frac{y}{L},\quad U=\frac{uL}{\alpha},\quad V=\frac{vL}{\alpha},\quad \theta=\frac{T-T_c}{T_h-T_c},\quad Pr=\frac{\vartheta}{\alpha},\quad \gamma=\frac{\sqrt{2\pi_c}}{\frac{\partial P}{\partial Y}},$$

$$Ra=\frac{g\beta(T_h-T_c)L^3Pr}{\vartheta^2},\varphi=\frac{C-C_c}{C_h-C_c},Le=\frac{\alpha}{D},N=\frac{\beta_c(C_h-C_c)}{\beta_T(T_h-T_c)},Da=\frac{K}{L^2}.$$

The corresponding boundary conditions are

$$U(X,0)=U(X,1)=U(0,Y)=U(1,Y)=0,$$

$$V(X,0)=V(X,1)=V(0,Y)=V(1,Y)=0,$$

$$\theta(X,0)=1,\quad \frac{\partial\theta}{\partial Y}(X,1)=0,\quad \theta(0,Y)=\theta(1,Y)=0,$$

$$\varphi(X,0)=0,\ \varphi(X,1)=1\frac{\partial\varphi}{\partial X}(0,Y)=\frac{\partial\varphi}{\partial X}(1,Y)=0. \tag{6}$$

3 Methodology

The governing equations of the flow problem are solved by highly efficient penalty finite element method [17, 18]. To accommodate the pressure in the momentum equations, a penalty parameter Γ and incompressibility criteria are used, which results in $P=-\Gamma\left(\frac{\partial U}{\partial X}+\frac{\partial V}{\partial Y}\right)$. The continuity equation is satisfied automatically for large values of Γ. For stable solutions, Γ is taken as 10^7. By using this assumption, the pressure is eliminated and corresponding momentum equations take the form:

$$U\frac{\partial U}{\partial X}+V\frac{\partial U}{\partial Y}=\Gamma\frac{\partial}{\partial X}\left(\frac{\partial U}{\partial X}+\frac{\partial V}{\partial Y}\right)+Pr\left(\frac{\partial^2U}{\partial X^2}+\frac{\partial^2U}{\partial Y^2}\right)-\frac{Pr}{Da}U, \tag{7}$$

$$U\frac{\partial V}{\partial X}+V\frac{\partial V}{\partial Y}=\Gamma\frac{\partial}{\partial Y}\left(\frac{\partial U}{\partial X}+\frac{\partial V}{\partial Y}\right)+Pr\left(\frac{\partial^2V}{\partial X^2}+\frac{\partial^2V}{\partial Y^2}\right)-\frac{Pr}{Da}V-RaPr(\theta+N\varphi). \tag{8}$$

The domain of computation comprises (20×20) biquadratic elements which relate to (41×41) grid points. The nonlinearity in the modeled equations with the lesser number of nodes is easily captured by biquadratic elements as compared to finite difference/finite volume scheme [19].

4 Discussion of Results

The numerical results are obtained by varying key parameters such as Casson fluid parameter ($\gamma = 0.1-5.0$), Darcy number $\left(Da = 10^{-5}-10^{-3}\right)$ while other parameters are kept fixed. Streamlines, isotherms, and iso-concentration profiles for different values of governing parameters are visualized in Figs. 2, 3, 4, 5, 6 and 7. It is observed that the results obtained via streamlines, isotherms, and iso-concentration lines are symmetric about vertical axis due to symmetrical boundary conditions. The symmetric nature forms counter rotating vortices in the two halves of the cavity, i.e., left and right. Due to heating, the fluid moves upward along the symmetric plane in each vortex cell and then moves in the horizontal direction because the upper wall

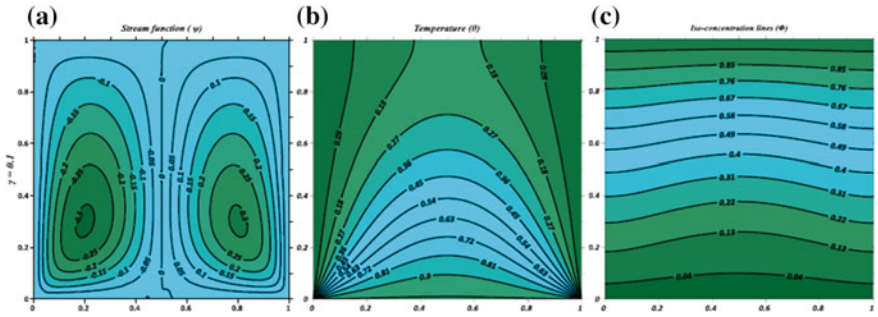

Fig. 2 Contour plots for $\gamma = 0.1,\ Da = 10^{-5},\ Ra = 10^{6},\ N = 0.5,\ Le = 1,\ Pr = 7.0$

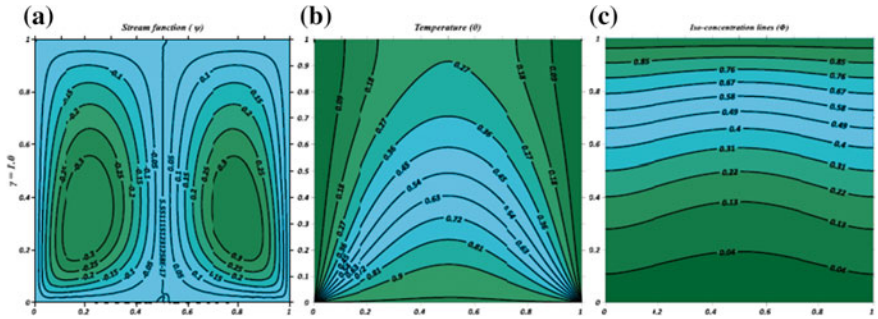

Fig. 3 Contour plots for $\gamma = 1.0,\ Da = 10^{-5},\ Ra = 10^{6},\ N = 0.5,\ Le = 1,\ Pr = 7.0$

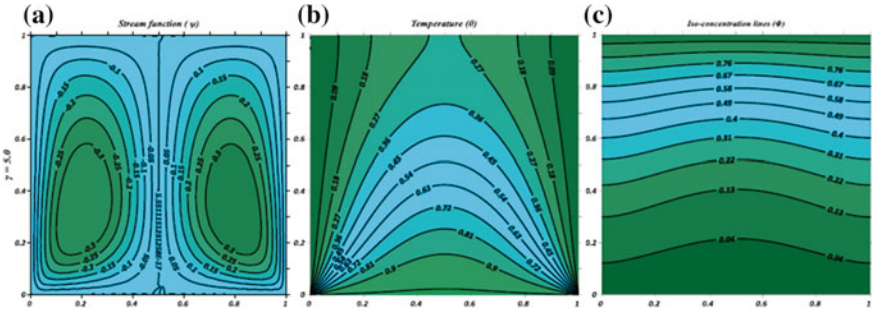

Fig. 4 Contour plots for $\gamma = 5.0,\ Da = 10^{-5},\ Ra = 10^{6},\ N = 0.5,\ Le = 1,\ Pr = 7.0$

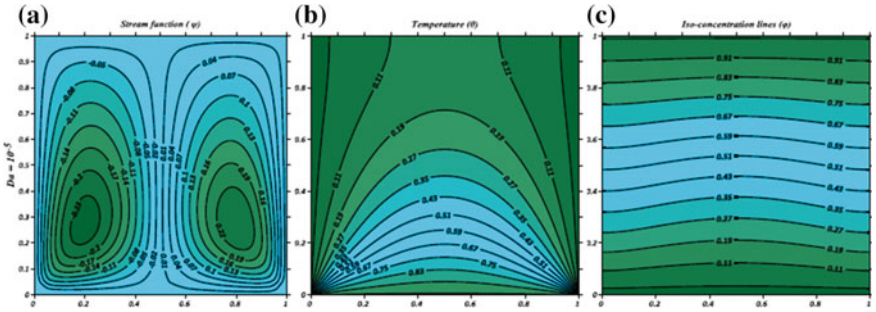

Fig. 5 Contour plots for $\gamma = 0.1,\ Da = 10^{-5},\ Ra = 10^{6},\ N = 0.5,\ Le = 3,\ Pr = 0.71$

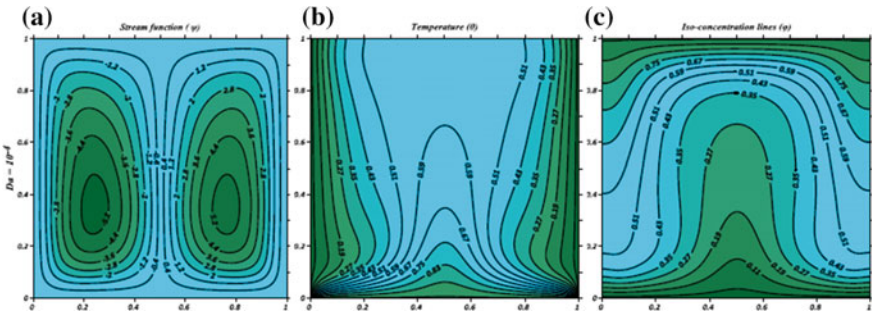

Fig. 6 Contour plots for $\gamma = 0.1,\ Da = 10^{-4},\ Ra = 10^{6},\ N = 0.5,\ Le = 3,\ Pr = 0.71$

is adiabatic. Afterward, the fluid moves downward through cold vertical walls as it is feeling cooling effect and finally lifted by the heated bottom wall.

The present study investigates the influence of one of the important pertinent parameter, i.e., Casson fluid parameter γ that represents the additional viscosity of the fluid. Impact of Casson fluid parameter γ on streamlines, isotherms, and iso-concentration lines is displayed in Figs. 2, 3 and 4. The key point to be noted here that

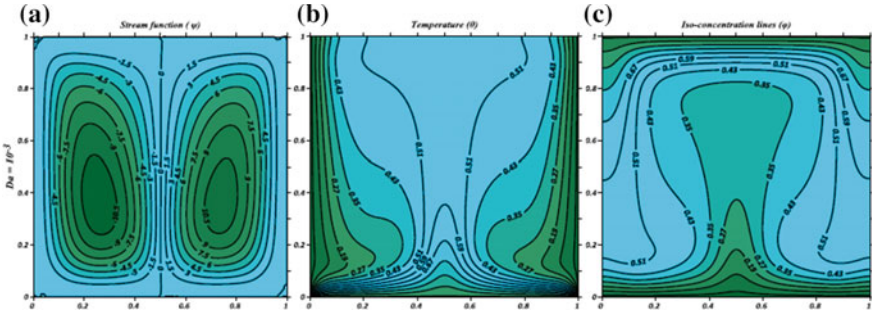

Fig. 7 Contour plots for $\gamma = 0.1,\ Da = 10^{-3},\ Ra = 10^{6},\ N = 0.5,\ Le = 3,\ Pr = 0.71$

with an increase in Casson fluid parameter efficient viscosity of the fluid decreases. Thus, the size of the vortex pair increases. At fixed value of other parameters such as Rayleigh number (heating condition), Darcy number (permeability), Lewis number, Prandtl number, and Buoyancy ratio parameter, the fluid offers more resistance at low value of γ to the movement. Thus, conduction is a dominance heat transfer phenomenon due to reduction in convection current. For $\gamma = 0.1$, one can visualize in Fig. 2a, a formation of a convective cell with a circular core of low intensity in clockwise (positive sign) and anticlockwise (negative sign) directions of streamlines ψ. Also, it is observed that with larger values of γ effective viscosity of fluid reduces. Due to this fact, at higher values of γ convective cell core stretches as depicted in Fig. 3a. For $\gamma = 5.0$, two elongated cores are formed in both the directions described in Fig. 4a. Isotherms illustrated in Figs. 2b and 4b reflect that as the Casson fluid parameter γ increases, heat transfer rate toward cold walls enhances. Similar kind of behavior is depicted for iso-concentration lines and is displayed in Figs. 2c and 4c.

Figures 5, 6, and 7 demonstrate the velocity profile, temperature profile, and concentration profile in terms of stream functions, isotherms and iso-concentration lines with variation in Darcy number Da. It is observed that fluid circulation strongly depends on the Darcy number. The two counterrotating vortex regions of streamlines are observed by varying Darcy number. Even though with different values of Darcy number, the shape of the recirculating region is almost similar but due to the increase in magnitude of buoyant forces, more intensified streamlines anticipate.

In Fig. 5, at $Da = 10^{-5}$ by taking $Ra = 10^{6}$, $Pr = 0.71,\ \gamma = 0.1$ and $Le = 3$. These particular values are taken for fixed parameter as we are considering non-Newtonian fluid. It is seen from the stream functions that the flow is exceptionally frail. For low Darcy number, the temperature distribution is purely due to conduction; hence, fluid behaves as a stationary fluid. Similar behavior is observed for the iso-concentration lines. At $Da = 10^{-4}$, the fluid flow rate increases and as anticipated due to the cold vertical walls, the middle portion of the fluid rises toward the cold vertical walls forming clockwise and anticlockwise symmetric rolls. The more grounded circulation causes the isotherms to be condensed near the side walls and close to the bottom wall resulting in more noteworthy heat exchange by convection and is depicted in Fig. 6.

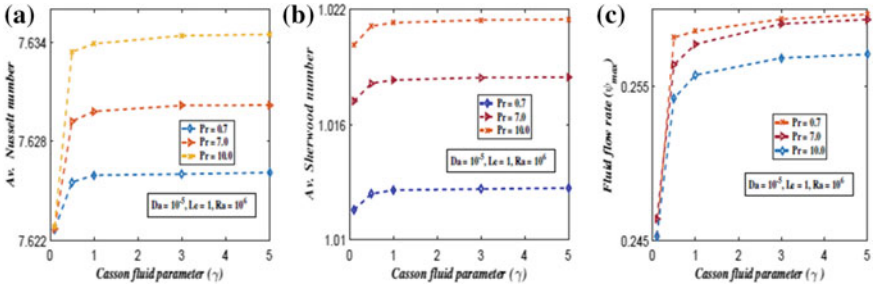

Fig. 8 Heat transfer rate, mass transfer rate, and fluid flow rate for different values of Casson fluid parameter γ and Prandtl number Pr

It is observed in Fig. 7, for $Da = 10^{-3}$ and $Ra = 10^6$, free convective flow inside the cavity takes place which results in the greater magnitude of stream functions. Due to no-slip boundary conditions, circulations are concentrated near the center as compared to side walls. The more noteworthy circulation in each half of the box takes after a progressive wrapping around the centers of revolution, and an increasingly articulated compression of the isotherms and iso-concentration lines toward the boundary surfaces of the enclosures occurs. Thus at $Da = 10^{-3}$, the thermal boundary layer is significantly developed due to temperature gradients near the base and side walls. A thermal boundary layer is almost developed in the entire cavity for $Da = 10^{-3}$ as compared to $Da = 10^{-5}$ at which it develops approximately 75%. Concentration boundary layer thickness is more for $Da = 10^{-3}$, whereas concentration boundary thickness is negligible for $Da = 10^{-5}$.

Heat, mass, and fluid flow rates for variation in Casson fluid parameter and Prandtl number are displayed in Fig. 8. An expansion in Prandtl number prompts the heat transfer, mass transfer while the intensity of flow decreases. On the other hand with a rise in Casson fluid parameter γ, rate of heat transfer, mass transfer, and fluid flow rate increases.

5 Concluding Remarks

1. For Casson fluid parameter $\gamma > 1$, due to a reduction in effective viscosity of fluid leads to an increase in heat transfer, mass transfer, and fluid flow rate.
2. A growth in Darcy number Da and Rayleigh number Ra leads to convection dominant flow which leads to a rise in the thermal boundary layer and concentration boundary layer.
3. The heat transfer and the mass transfer rise whereas fluid flow rate decreases with larger Prandtl number Pr.

Acknowledgements The authors acknowledge Indian Funding Agency: DST for financial support.

References

1. Badruddin IA, Al-Rashed AA, Ahmed NS, Kamangar S (2012) Investigation of heat transfer in square porous-annulus. Int J Heat Mass Transf 55(7–8):2184–2192
2. Prasad V, Kulacki F (1984) Natural convection in a vertical porous annulus. Int J Heat Mass Transf 27(2):207–219
3. Ahmed NS, Badruddin IA, Kanesan J, Zainal Z, Ahamed KN (2011) Study of mixed convection in an annular vertical cylinder filled with saturated porous medium, using thermal non-equilibrium model. Int J Heat Mass Transf 54(17–18):3822–3825
4. Bourich M, Hasnaoui M, Amahmid A (2004) A scale analysis of thermosolutal convection in a saturated porous enclosure submitted to vertical temperature and horizontal concentration gradients. Energy Convers Manag 45(18–19):2795–2811
5. Saghir MZ (1998) Heat and mass transfer in a multi-porous cavity. Int Commun Heat Mass Transf 25(7):1019–1030
6. Azeem A, Idna Idris MY, Nik-Ghazali N, Ahmed NJS, Al Rashed AA (2016) Conjugate heat and mass transfer in square porous cavity. Indian J Pure Appl Phys 54(12):777–786
7. Mishra L, Chhabra RP (2018) Natural convection in power-law fluids in a square enclosure from two differentially heated horizontal cylinders. Heat Transf Eng 39(10):819–842
8. Santhosh N, Radhakrishnamacharya G, Chamkha AJ (2015) Flow of a Jeffrey fluid through a porous medium in narrow tubes. J Porous Media 18(1):71–78
9. Muthtamilselvan M, Periyadurai K, Doh DH (2017) Effect of uniform and non uniform heat source on natural convection flow of micropolar fluid. Int J Heat Mass Transf 115:19–34
10. Aman S, Al-Mdallal Q, Khan I (2018) Heat transfer and second order slip effect on MHD flow of fractional Maxwell fluid in a porous medium. J King Saud Univ Sci
11. Férec J, Perrot A, Ausias G (2015) Toward modeling anisotropic yield stress and consistency induced by fiber in fiber-reinforced viscoplastic fluids. J Nonnewton Fluid Mech 220:69–76
12. Aghighi MS, Ammar A, Metivier C, Gharagozlu M (2018) Rayleigh-Bénard convection of Casson fluids. Int J Therm Sci 127:79–90
13. Eldabe NTM, Saddeck G, El-Sayed AF (2001) Heat transfer of MHD non-Newtonian Casson fluid flow between two rotating cylinders. Mech Mech Eng 5(2):237–251
14. Mernone A, Mazumdar J, Lucas S (2002) A mathematical study of peristaltic transport of a Casson fluid. Math Comput Model 35(7–8):895–912
15. Boyd J, Buick JM, Green S (2007) Analysis of the Casson and Carreau-Yasuda non-Newtonian blood models in steady and oscillatory flows using the lattice Boltzmann method. Phys Fluids 19(9):093–103
16. Nakamura N, Sawada T (1998) Numerical study on the flow of a non-Newtonian fluid through an axisymmetric stenosis. ASME J Biomech Eng 110:137–143
17. Reddy JN, Gartling DK (2010) The finite element method in heat transfer and fluid dynamics. CRC press
18. Reddy JN (2014) An introduction to non linear finite element analysis with applications to heat transfer, fluid mechanics, and solid mechanics. Oxford University Press, Oxford
19. Basak T, Roy S, Paul T, Pop I. Natural convection in a square cavity filled with a porous medium: effects of various thermal boundary conditions. Int J Heat Mass Transf 49(7–8):1430–1441

Convergence of Eigenfunction Expansions for Membrane Coupled Gravity Waves

Santanu Koley, K. Panduranga and Dipak K. Satpathi

Abstract In the present paper, some characteristics of eigenfunctions associated with membrane coupled gravity waves and its convergence are provided for finite water depth. Expansion formulae for velocity potentials and related orthogonal mode coupling relations for Laplace equation subject to the higher order boundary conditions are studied. The spectral representation of eigenfunctions is obtained in terms of Dirac delta function through the Green's function technique. Finally, the convergence of eigenfunction expansion to velocity potential is obtained with the help of spectral representations.

Keywords Spectral representation · Green's function technique · Convergence of eigenfunction expansion

1 Introduction

In recent years, more importance is given to understand the structural mechanics when wave propagates through the structure. The exact mathematical descriptions of the wave structure interaction problems are complex in nature. Hence, some physical assumptions need to be considered for modeling the same mathematically. In many cases, the governing equation in wave structure interaction problem is the Laplace/Helmholtz equation subject to the higher order boundary conditions on the structural boundaries. The associated BVPs are generally non-Sturm–Liouville type in nature. Rhodes-Robinson [1] derived the orthogonal mode coupling relations for water wave structure interaction problems in presence of surface tension in water of both finite and infinite depths. Later, Rhodes-Robinson [2] developed a reduction method to tackle the surface wave interaction with immersed vertical rigid boundaries in finite and infinite water depth cases. Lawrie and Abrahams [3] derived an

S. Koley (✉) · K. Panduranga · D. K. Satpathi
Birla Institute of Technology and Science - Pilani, Hyderabad Campus, Hyderabad, India
e-mail: santanukoley1989@gmail.com

D. Maity et al. (eds.), *Advances in Fluid Mechanics and Solid Mechanics*, Lecture Notes in Mechanical Engineering,
https://doi.org/10.1007/978-981-15-0772-4_9

orthogonality relation for a class of boundary value problems having higher order boundary conditions. Since then, several researchers such as [4–6] solved a number of hydroelastic problems using eigenfunction expansion method. They used appropriate orthogonality relations to get a system of equations in terms of the unknowns. Manam et al. [4] derived expansion formulae of velocity potential for semi-infinite strip as well as quarter plane and also given an equivalent form of orthogonal mode coupling relation for quarter plane. Lawrie and Abrahams [3] presented a new type of orthogonality relation for a general class of wave propagation problems through ducts and pipes. Mondal et al. [7] derived the expansion formulae for velocity potentials for wave structure interaction problems in three dimensions and associated orthogonal mode coupling relations satisfying the higher order boundary conditions. Mondal et al. [5] have developed a modified inner product to study the surface wave scattering by a floating semi-infinite flexible plate and concluded that the eigenfunctions for the plate covered domain are orthogonal with respect to the newly developed inner product.

In the present paper, some characteristics of eigenfunctions associated with membrane coupled gravity waves and its convergence are provided for finite water depth case. To derive the convergence of expansion formulae, first the Green's function corresponding to the associated BVP is obtained and then expressed the same in terms of spectral representations. Finally, using the spectral representation, it is shown that the series of eigenfunction expansions converges to the velocity potential of the physical problem.

2 Mathematical Formulation

The problem is studied in 2D Cartesian coordinate system where x-axis is considered horizontally and y-axis is taken in vertically upward direction. A thin flexible membrane is floating in the region $0 < x < \infty$. The water is occupied in the region $0 < x < \infty$ and $-h < y < 0$ for finite water depth case. The fluid is assumed to be of potential kind and so, there exists a velocity potential $\Phi(x, y, t)$. Further, under the assumption of simple harmonic motion with circular frequency ω, the velocity potential can be expressed as $\Phi(x, y, t) = \Re\{\phi(x, y)e^{-i\omega t}\}$. Therefore, the spatial velocity potential will satisfy the Laplace equation

$$\nabla^2\phi = 0 \tag{1}$$

subject to the linearized membrane covered upper boundary condition and bottom boundary condition

$$T\frac{\partial^3\phi}{\partial y^3} + \frac{\partial\phi}{\partial y} - K'\phi = 0 \quad \text{on} \quad y = 0 \tag{2}$$

and

$$\frac{\partial \phi}{\partial y} \quad \text{on} \quad y = -h \tag{3}$$

with

$$T = \frac{T_1}{\rho g - m\omega^2}, \qquad K' = \frac{\rho \omega^2}{\rho g - m\omega^2}$$

being constants as in [4]. Further, m is the mass of the membrane per unit length, g is the acceleration due to gravity, T_1 is the membrane tension and ρ is the density of water.

3 Eigenfunction Expansion and Its Characteristics

3.1 Eigenfunction Expansion

The spatial component of the velocity potential $\phi(x, y)$ is expressed as (see [4, 5] for details)

$$\phi(x, y) = \sum_{n=0}^{\infty} R_n(x)\psi_n(y) \tag{4}$$

The eigenfunctions ψ_n's are of the form

$$\psi_n = \begin{cases} \dfrac{\cosh\ k_0(h+y)}{\cosh\ k_0 h}, & n = 0. \\ \dfrac{\cos\ k_n(h+y)}{\cos\ k_n h}, & n = 1, 2, \ldots \end{cases} \tag{5}$$

where k_n satisfies the dispersion relation

$$f(k) = 0,$$

with $f(k) = K' - (Tk^2 + 1)k \tanh\ kh$. It has one real positive zero $k = k_0$ and infinite number of imaginary zeros on $k = +ik_n$ on the upper half complex plane. The details of root-finding procedure for the aforementioned dispersion relation are given in the Appendix. It is to be noted that in Eq. (4), the dependency of $R_n(x)$ on x-component is given by $R_n(x) = R_n e^{ik_n x}$ with R_n being

$$R_n = \frac{1}{E_n}\left[\int_{-h}^{0} \phi(x, y)\psi_n(y)dy + \frac{T}{K'}\frac{\partial \phi}{\partial y}\bigg|_{(x,0)} \frac{\partial \psi}{\partial y}\bigg|_{y=0}\right] \tag{6}$$

where $E_n = \dfrac{f'(k)\psi_y(0)}{2K'}$.

3.2 Eigen Value Problem

Writing the eigenfunctions $\psi_n(y)$ as $\psi(y)$ and the same satisfy the equation

$$\frac{\partial^2 \psi}{\partial y^2} - k^2 \psi = 0, \quad -h < y < 0 \tag{7}$$

subject to the boundary conditions

$$T \frac{\partial^3 \psi}{\partial y^3} + \frac{\partial \psi}{\partial y} - K' \psi = 0 \quad \text{on} \quad y = 0 \tag{8}$$

and

$$\frac{\partial \psi}{\partial y} = 0 \quad \text{on} \quad y = -h \tag{9}$$

Here T and K' are same as defined before. Further, we can define orthogonal mode coupling relation for $\psi_n(y)$ (as in Eq. 5) as

$$\langle \psi_m, \psi_n \rangle = \int_{-h}^{0} \psi_m \psi_n dy + \frac{T}{K'} \left(\frac{\partial \psi_m}{\partial y} \frac{\partial \psi_n}{\partial y} \right) \Big|_{y=0} = E_n \delta_{mn} \tag{10}$$

where δ_{mn} is the Kronecker delta.

Next, the Green's function corresponding to the associated BVP as described above is obtained and then expressed the same in terms of spectral representation. The details are provided as different lemmas and theorems in the subsequent sections.

Lemma 1 *The Green's function ξ of the BVP stated in Sect. 3.2 is the solution of*

$$\frac{\partial^2 \xi}{\partial y^2} - k^2 \xi = \delta(y - \eta) \; for \; -h < y, \eta < 0 \tag{11}$$

which satisfies the boundary conditions (2) and (3) along with the following properties:

(i) $\xi(y, \eta)$ is continuous at $y = \eta$
(ii) The first derivative of $\xi(y, \eta)$ has jump discontinuity of magnitude -1 at the point $y = \eta$

is given by

$$\xi(y, \eta) = \begin{cases} \xi_1, \eta < y \leq 0 \\ \xi_2, -h \leq y < \eta \end{cases} \tag{12}$$

where

$$\xi_1 = \frac{[(Tk^3 + k)\cosh\ ky + K'\sinh\ ky]}{k\ f(k)} \frac{\cosh\ k(h+\eta)}{\cosh\ kh}$$

$$\xi_2 = \frac{[(Tk^3 + k)\cosh\ k\eta + K'\sinh\ k\eta]}{k\ f(k)} \frac{\cosh\ k(h+y)}{\cosh\ kh}$$

Lemma 2 *The Spectral representation of ψ_n can be expressed as (see [8] for details)*

$$\delta(y-\eta) = \sum_{n=0}^{\infty} Z_n \psi_n(y)\psi_n(\eta) \tag{13}$$

where δ is the Dirac delta function and $Z_n = \dfrac{K'}{f'(k)\tanh\ k_n h}$.

Proof Proceeding in same manner as discussed in [9], we can express Dirac delta function as

$$\lim_{R\to\infty} \frac{1}{\pi i} \oint \xi(y,\eta;k)k\,dk = -\delta(y-\eta) \tag{14}$$

where ξ is the Green's function as expressed in (12). It has been observed that ξ is an analytic function everywhere except at the poles. Thus, the left-hand side integral in Eq. (14) reduces into sum of residues at poles. It is to be noticed that the Green's function involves $f(k)$ (see Lemma 1), whose zeros are of the form $k = \pm k_0$ lying on the real axis and infinite number of imaginary roots $k = \pm ik_n$, $k_n > 0$ (see Appendix for details). The path of integration being taken along the circular arc of radius $R(\to \infty)$ (Γ_R), and consider semicircle (γ_r) centered at $k = k_0$ having radius r in the upper half complex plane contains all the singular points

$$\frac{1}{\pi i} \oint \xi\ (y,\eta;k)\ k\,\mathrm{d}k = \frac{1}{\pi i} \oint k\,dk(\xi_1(y,\eta;k)H(\eta-y) + \xi_2(y,\eta;k)H(y-\eta)) \tag{15}$$

where ξ_1 and ξ_2 same as in Eq. 12 and H is the Heaviside step function. Using Cauchy's residue theorem and Jordan's lemma, the two integrals on the right-hand side of Eq. 17 can be expressed as

$$\frac{1}{\pi i} \oint \xi_1 k H(\eta-y)\,dk = -\sum_{n=0}^{\infty} Z_n \psi_n(y)\psi_n(\eta)H(\eta-y) \tag{16}$$

$$\frac{1}{\pi i} \oint \xi_2 k H(y-\eta)\,dk = -\sum_{n=0}^{\infty} Z_n \psi_n(y)\psi_n(\eta)H(y-\eta) \tag{17}$$

Substituting the expressions of Eqs. (16) and (17) into Eq. (15), we get

$$\frac{1}{\pi i}\oint \xi\, k\, dk = -\sum_{n=0}^{\infty} Z_n \psi_n(y)\psi_n(\eta)\,(H(\eta - y) + H(y - \eta)) \tag{18}$$

Now, the contour integral in Eq. (18) approaches to $-\delta(y - \eta)$ for R$\rightarrow \infty$.

3.3 Convergence of Eigenfunction Expansion

Theorem 1 *Assume the coefficients*

$$R_n = \frac{1}{E_n}\left[\int_{-\infty}^{0} \phi(x, y)\psi_n(y)dy + \frac{T}{K'}\frac{\partial \phi}{\partial y}\bigg|_{(x,0)}\frac{\partial \psi}{\partial y}\bigg|_{y=0}\right]$$

exist, where the velocity potential $\phi(x, y)$ satisfies the Laplace equation (1) w.r.t to the boundary conditions (2) and (3). The series

$$\sum_{n=0}^{\infty} R_n(x)\psi_n(y)$$

converges to $\phi(x, y)$

Proof

$$\begin{aligned}
&\sum_{n=0}^{\infty} R_n(x)\psi_n(y)\\
&= \sum_{n=0}^{\infty}\frac{1}{E_n}\left[\int_{-\infty}^{0}\phi(x, y)\psi_n(y)dy + \frac{T}{K'}\phi_y(x, 0)\psi_{ny}(0)\right]\psi_n(y)\\
&= \int_{-\infty}^{0}\phi(x, \eta)\delta(y - \eta)\, d\eta\\
&= \phi(x, y)
\end{aligned}$$

Hence, the convergence of the eigenfunction expansion formula is established.

4 Conclusion

The study provides convergence of eigenfunction expansion in coupled membrane gravity waves problem for finite water depth. To prove the convergence of eigenfunctions, Green's function for associated BVP is derived, and also an inner product between eigenfunctions is established. Then this Green's function is integrated over

the complex plane to obtain the spectral representation as Dirac delta function. Using this spectral representation, the convergence of eigenfunction expansion is proved.

Appendix

Here the analysis of the roots of the wave dispersion relation is provided for the sake of easy reference. The dispersion relation

$$f(k) = k(1 + Tk^2) \tanh\ kh - K'$$

will have the zeros of the form $k = \pm k_0$ located on the real axis and infinite number of zeros $k = \pm ik_1, \pm ik_2, \pm ik_3$.... located on imaginary axis. It is also assumed that $k_0 > 0$ and $0 < k_1 < k_2 < ....$

Proof These results can be obtained easily by taking equivalent form of dispersion relation as follows:

$$f(k) = k(1 + Tk^2) \sinh\ kh - K' \cosh\ kh$$

Let

$$g(k) = k(1 + Tk^2) \sinh\ kh$$

which has zeros $k = 0, \pm i/\sqrt{T}$ and $kh = \pm n\pi i, n \in \mathbb{Z}$ on imaginary axis. Consider a closed contour (Ω) as a square with vertices at $(2n - 1)\frac{\pi}{2}(\pm 1 \pm i)$ where n is a large positive integer. Construct the square in such a way that it should contain all the zeros of the dispersion relation and the sides of the square will not go through any zeros on the imaginary axis. On the square $|f(k) - g(k)| < |f(k)|$ is satisfied. Therefore, using Rouch's theorem, both the functions $f(k)$ and $g(k)$ have same number of zeros within Ω. As $n \to \infty$, $f(k)$ has no zeros other than $k = \pm k_0, \pm ik_1, \pm ik_2, ...$

References

1. Rhodes-Robinson PF (1971) On the forced surface waves due to a vertical wave-maker in the presence of surface tension. In: Mathematical proceedings of the Cambridge philosophical society, vol 70, pp 323–337. Cambridge University Press
2. Rhodes-Robinson PF (1979) On surface waves in the presence of immersed vertical boundaries. I. Q J Mech Appl Math 32(2):109–124
3. Lawrie JB, Abrahams ID (1999) An orthogonality relation for a class of problems with high-order boundary conditions; applications in sound-structure interaction. Q J Mech Appl Math 52(2):161–181
4. Manam SR, Bhattacharjee J, Sahoo T (2006) Expansion formulae in wave structure interaction problems. Proc R Soc Lond A Math Phys Eng Sci 462:263–287. The Royal Society
5. Mandal S, Sahoo T, Chakrabarti A (2017) Characteristics of eigen-system for flexural gravity wave problems. Geophys Astrophys Fluid Dyn 111(4):249–281

6. Sahoo T, Yip TL, Chwang AT (2001) Scattering of surface waves by a semi-infinite floating elastic plate. Phys Fluids 13(11):3215–3222
7. Mondal R, Mohanty SK, Sahoo T (2011) Expansion formulae for wave structure interaction problems in three dimensions. IMA J Appl Math 78(2):181–205
8. Mandal S, Sahoo T, Chakrabarti A (2015) A note on convergence of expansion formula for wave structure interaction problems. In: 30th international workshop on the water waves and floating bodies (IWWWFB)
9. Friedman B (1990) Principles and techniques of applied mathematics. Courier Dover Publications

Numerical Analysis of Variations on Design Modifications of Train and Tunnel Geometries to Reduce Aerodynamic Drag on Train

Vaibhav Rastogi and Nityananda Nandi

Abstract The flow of air around the train in a confined space, i.e., tunnel is different than that of the train moving in an open air. As the train passes through a tunnel, there is a large amount of aerodynamic drag force exerted on the body of the train. There is a compression of the air ahead of the train inside a tunnel due to which large pressure is produced ahead of a train while just behind the tail there is a suction of air due to low pressure at the tail end of the train. The train inside a confined space in a tunnel behaves just like a loosely fitted piston inside a cylinder. Thus, in order to reduce the drag force, train head and tail geometries are modified. This analysis has been done on ANSYS Fluent 14.0 and steady Navier–Stokes (N-S) equations for two-dimensional, axi-symmetric, incompressible flow using standard k-ε turbulence modeling was solved with the help of Fluent 14.0 software to simulate the flow around the train passing inside a tunnel. In this analysis, two observations are done: first, tunnel width, i.e., blockage ratio has been changed from 0.25 to 0.36 (tunnel width from 6 to 5 m) and variation of drag force with the blockage ratio is analyzed. Second, train head and tail geometries are changed to see the variation of drag force on blunt and hemispherical head and tail of the train. This paper suggests that a less blockage ratio is responsible for less drag force on the train. A similar investigation has been performed by taking different shapes of head and tail of the train keeping the blockage ratio same.

Keywords Aerodynamic drag force · Blockage ratio · Train geometry · Tunnel · Blunt · Hemispherical

V. Rastogi (✉) · N. Nandi
Department of Aerospace Engineering and Applied Mechanics, Indian Institute of Engineering Science and Technology, Shibpur, West Bengal, India
e-mail: vaibhavrastogi12294@gmail.com

D. Maity et al. (eds.), *Advances in Fluid Mechanics and Solid Mechanics*,
Lecture Notes in Mechanical Engineering,
https://doi.org/10.1007/978-981-15-0772-4_10

1 Introduction

The airflow induced by a train inside a tunnel is different from the train moving in a free stream of air. As the train passes inside a tunnel, huge amount of aerodynamic drag is induced on the body of the train. When a train is moving in open air flow around the train is fully unsteady and turbulent which generates rapidly changing pressure fields around the train called as slipstreams [1]. But when it passes through a tunnel it behaves like a loosely fitted piston in a cylinder [2]. The air ahead of the train gets compressed and induces large pressure at the inlet of the train head. The compressibility of the air around high-speed trains produces what are called "**micro-pressure waves**" as a result of running in a confined space [3]. The air velocity, pressure variation, and direction of the flow inside tunnels are different to the slipstream in the open air. These differences depend on the size of the tunnel (cross section and length of the tunnel) and the shape and speed of the train. As a train is passing through a tunnel, a large aerodynamic drag force is exerted on the body of the train [4, 5]. In order to reduce that drag force, some design modifications of the tunnel and train have been done in order to reduce the drag force on the train body [1]. This is a two-dimensional analysis of the train and tunnel model which is taken from the work of Zhang [6] and certain modifications have been done to see the variations [7–9].

$$\textbf{Blockage ratio} = \frac{\textbf{cross} - \textbf{section area of the train}}{\textbf{cross} - \textbf{section area of the tunnel}}$$

2 Methodology

Basic assumptions:

- The flow inside the tunnel was assumed to be incompressible.
- The flow is viscous, two dimensional, and steady.
- The walls of the train body and tunnel were smooth.
- The pressure inside the tunnel is considered to be atmospheric pressure, i.e., 101,325 Pa.
- The flow was assumed to be turbulent.
- The air inside was perfect.
- Flow field Reynolds number Re was defined as

$$\textbf{Re} = \textbf{rVL}/\textbf{m}$$

Governing equations:

The commercial CFD solver FLUENT was used in the present study to solve the set of incompressible flow N-S equations along with the k-ε turbulence model. The equations used are basically based on the following assumptions:

1. The flow is of a calorically perfect gas.
2. It is a two-dimensional, axi-symmetric, steady, turbulent, and incompressible flow.

Standard k-ε model is the simplest "complete models" of turbulence. It is a two-equations model in which the solution of two separate transport equations allows the turbulent velocity and length scales to be independently determined.

The turbulence kinetic energy, $\boldsymbol{k}$, and its rate of dissipation, $\boldsymbol{\epsilon}$, are obtained from the following transport equations:

$$\frac{\partial(\rho k)}{\partial t} + \frac{\partial(\rho k u_i)}{\partial xi} = \frac{\partial}{\partial xj}\left[\left(\mu + \frac{\mu_t}{\sigma_k}\right)\frac{\partial k}{\partial xj}\right] + G_k + G_b - \rho\epsilon - Y_m + S_k$$

$$\frac{\partial(\rho\varepsilon)}{\partial t} + \frac{\partial(\rho\varepsilon u_i)}{\partial xi} = \frac{\partial}{\partial xj}\left[\left(\mu + \frac{\mu_t}{\sigma_\varepsilon}\right)\frac{\partial \varepsilon}{\partial xj}\right] + C_{1\varepsilon}\frac{\varepsilon}{k}(G_k + C_{3\varepsilon}G_b) - G_{2\epsilon}\rho\frac{\epsilon^2}{k} + S_\varepsilon$$

The continuity equation for the conservation of mass for a 2-D axi-symmetric incompressible flow is given as follows:

$$\frac{\partial(\rho u_x)}{\partial x} + \frac{\partial(\rho v_r)}{\partial r} + \frac{\rho v_r}{r} = 0$$

where x is the axial coordinate and r is the radial coordinate. Generalized momentum conservation equations for the 2-D axi-symmetric body in axial and radial directions are given as

$$\frac{\partial(\rho u_x)}{\partial t} + \frac{\partial(\rho r v_r v_r)}{r\partial r} + \frac{\partial(\rho r v_x v_r)}{r\partial x} = -\frac{\partial \mathrm{p}}{\partial \mathrm{r}} + \frac{1}{\mathrm{r}}\frac{\partial}{\partial \mathrm{r}}\left[\mathrm{r}\mu\left(2\frac{\partial \mathrm{u_r}}{\partial \mathrm{r}}\right)\right] + \frac{1}{\mathrm{r}}\frac{\partial}{\partial \mathrm{x}}\left[\mathrm{r}\mu\left(\frac{\partial \mathrm{u_x}}{\partial \mathrm{r}} + \frac{\partial \mathrm{v_r}}{\partial \mathrm{x}}\right)\right] + \mathrm{F_r}$$

In the above equations, Reynolds time averaging is applied for the turbulent flow. In order to make the problem, simple axi-symmetric swirl is avoided.

For the computation of density of the incompressible gas, i.e., air, perfect gas equation is used and the solver will compute the density as

$$\rho = \frac{P}{\frac{R}{M}T}$$

Model Geometry: The geometry of the model used for validation is shown in Fig. 1. In the model, the train taken has a diameter of 3 m, body length 40 m, and a hemispherical head with a blunt tail. The distance from the head of the train to the inlet

of the tunnel is 80 m, and the distance from the tail of the train to the outlet is also 80 m [6, 10].

After validation, the variation of the drag force on the train was calculated by taking different velocities of the train and with different blockage ratio of the tunnel. At this parameter, different shapes of the train head and tail were taken in order to optimize the drag force on the train.

3 Calculations and Analysis

Validation:

In the present work, results were compared with the work of Zhang [6] for validation. The model taken for present analysis is similar to that of his and discussed earlier (as shown in Fig. 1). Yaoping's work was based on a train in an evacuated tube in which the pressure is ranging from 10.1325 to 10132.5 Pa and a density ranging from 0.0001225 to 0.1225 kg/m^3.

In the present analysis for validation of the proposed work, following parameters are taken:

- Blockage ratio is taken as 0.36.
- Outside diameter of the tube is 5 m.
- The diameter of the train is 3 m (area = $\pi * 1.5^2 = 7.068$).

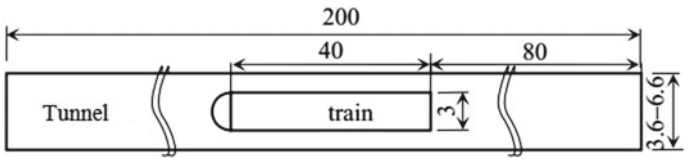

Fig. 1 Schematic model of the train (unit m)

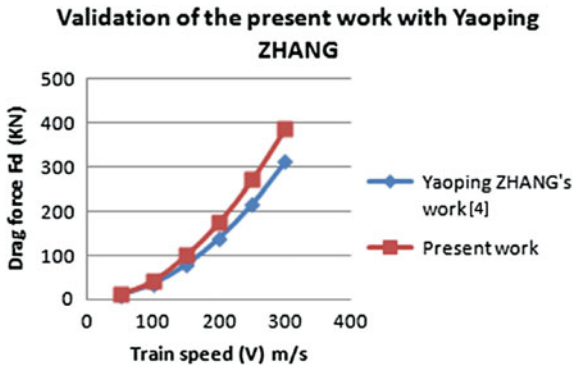

Fig. 2 Aerodynamic drag on the train at blockage ratio 0.36 and pressure = 10132.5

- The half geometry of train is taken for analysis.
- Pressure is 10132.4 Pa and density is 0.1225.

Boundary Conditions:

- Velocity inlet (ranging from 50 to 250 m/s).
- Pressure outlet (0 Pa).
- Train body stationary wall.
- Tunnel body movable wall (in the opposite direction with the same velocity as of air).

Following Fig. 3 compares the drag force and it shows how for an increase in the velocity of the train the drag force increases (Fig. 2).

Results and discussion

In the following analysis, aerodynamic drag force is calculated by taking two shapes of head and tail of the train, i.e., blunt and hemispherical. The drag force is calculated for different velocities of the train ranging between 50 and 100 m/s for blunt shape and hemispherical shape of the train. And also aerodynamic drag force is also calculated for different blockage ratios of the tunnel at different train velocities.

Following Tables 1 and 2 show the variation of drag force at different train velocities for different shapes of the train head and tail at tunnel blockage ratio of 0.25 and 0.36.

From the tables, it can be analyzed that the drag force is more for a blunt shape head and tail of the train as compared to the hemispherical head and tail of the train.

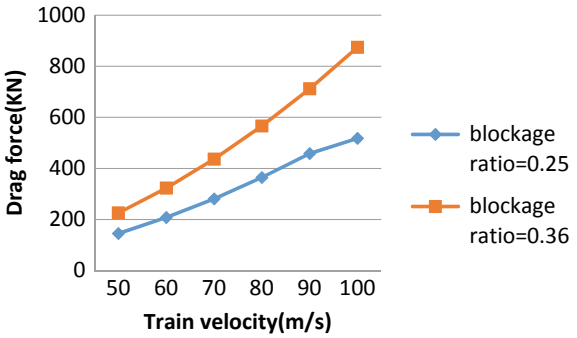

Fig. 3 Curves are shown for blunt head and tail of train at different blockage ratios

Table 1 Drag force at different train velocities for the blunt and hemispherical shape of the train at **blockage ratio = 0.25**

Velocity (m/s)	50	60	70	80	90	100
Drag force (KN) (*blunt head and tail*)	145.095	207.632	280.844	364.413	457.957	517.391
Drag force (KN) (*hemispherical head and tail*)	33.155	46.423	61.739	79.078	98.394	119.654

Table 2 Drag force at different train velocities for the blunt and hemispherical shape of the train at **blockage ratio = 0.36**

Velocity (m/s)	50	60	70	80	90	100
Drag force (KN) (*blunt head and tail*)	226.042	322.790	436.132	566.127	711.84	874.249
Drag force (KN) (*hemispherical head and tail*)	57.610	80.403	106.620	136.204	169.061	205.034

Following curves show that as the blockage ratio increases from 0.25 to 0.36 or as the tunnel width decreases from 6 to 5 m there is a drastic increase in the drag force on the body of the train (Fig. 4).

Contours of velocity magnitude and streamlines in Tecplot

See Figs. 5, 6, 7, and 8.

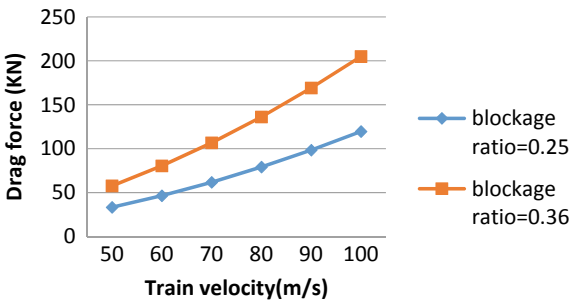

Fig. 4 Curves are shown for hemispherical head and tail of train at different blockage ratios

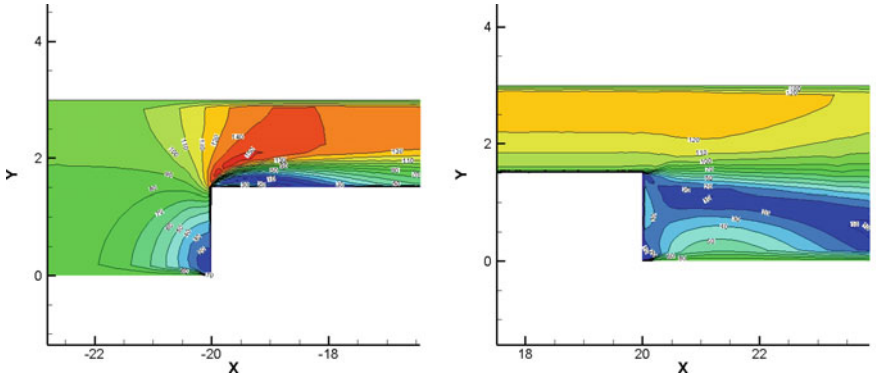

Fig. 5 Velocity contours at V = 90 m/s, α = 0.25 for blunt head and tail

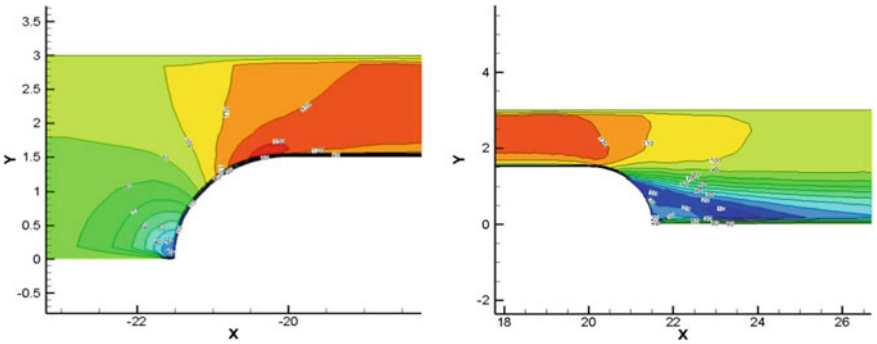

Fig. 6 Velocity contours at V = 90 m/s, α = 0.25 for hemispherical head and tail

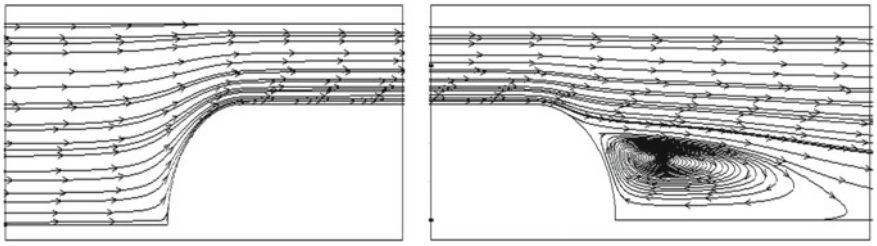

Fig. 7 Stream lines for hemispherical head and tail

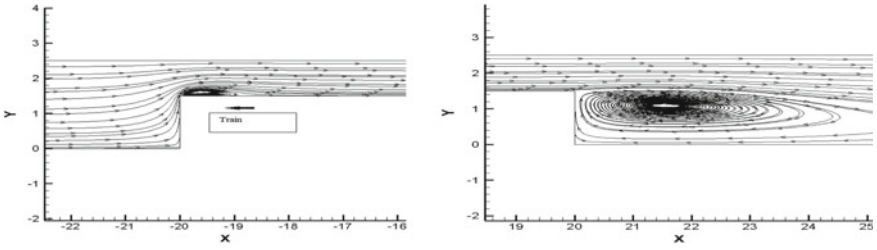

Fig. 8 Stream lines for bunt head and tail

4 Conclusion

From the above results and discussion, it is observed that a less blockage ratio (0.25), i.e., more tunnel width (6 m) is required to reduce the drag force on the body of the train. And it is also observed that a blunt shape of head and tail produces a large amount of drag force as compared to hemispherical head and tail of the train.

It is our concern to reduce the aerodynamic drag on the body of the train because it reduces fuel consumption which in turn reduces the cost of operation of the train. So in accordance with the parameters taken for analysis, less blockage ratio of the tunnel

with hemispherical head and tail of the train is a suitable to design consideration for less drag force on the body of the train.

Acknowledgements The analysis is supported by CAD Laboratory of the Department of Aerospace Engineering and Applied Mechanics of Indian Institute of Engineering Science and Technology, Shibpur, Howrah, West Bengal, 711103, India.

References

1. Baker C, Quinn A, Sima M, Hoefener L, Licciardello R (2013) Full-scale measurement and analysis of train slipstreams and wakes: part 1 ensemble averages. Proc Inst Mech Eng Part F J Rail Rapid Transit
2. Cross D, Hughes B, Ingham D, Ma L (2017) Enhancing the piston effect in underground railway tunnels. Tunn Undergr Space Technol
3. Baron A, Molteni P, Vigevano L (2006) High-speed trains: prediction of micro-pressure wave radiation from tunnel portals. J Sound Vib 296:59–72
4. Mossi M, Sibilla S (2002) Swiss-metro: aerodynamic drag and wave effects in tunnels under partial vacuum
5. Huang Y, Gao W (2010) A numerical study of the train-induced unsteady airflow in a subway tunnel with natural ventilation ducts using the dynamic layering method. J Hydrodyn 22(2):164–172
6. Zhang Y (2012) Numerical simulation and analysis of aerodynamic drag on a subsonic train in evacuated tube transportation. J Mod Transp 20(1):44–48
7. Kim JY, Kim KY (2007) Experimental and numerical analyses of train-induced unsteady tunnel flow in subway. Tunn Undergr Space Technol 22:166–172
8. Xiang X, Xue L (2010) Tunnel hood effects on high speed train compression wave. J Hydrodyn 22(5) Supplement:940–947
9. Baron A, Mossi M, Sibilla S (2001) The alleviation of the aerodynamic drag and wave effects of high-speed trains in very long tunnels. J Wind Eng Ind Aerodyn 89:365–401
10. Pandey BK, Mukherjea SK (2014) Aerodynamic simulation of evacuated tube transport trains with suction at tail. In: Proceedings of the ASME 2014

Analysis of Exact Solutions of Electromagnetohydrodynamic Flow and Heat Transfer of Non-Newtonian Casson Fluid in Microchannel with Viscous Dissipation and Joule Heating

Motahar Reza and Amalendu Rana

Abstract A theoretical investigation is done to study the analytical solutions for the velocity and temperature distribution of non-Newtonian Casson fluid in microchannel associated with combined effects of electromagnetohydrodynamics forces and electrokinematics forces. Heat transfer and flow characteristic of non-newtonian Casson fluid are controlled by the combination of imposed pressure gradients, applied magnetic field, and electrokinematic forces. The interesting features of the electromagnetohydrodynamics flow along with heat transfer characteristic are examined by variation in the nondimensional physical parameter on the velocity and temperate profiles. The effect of Casson parameter on the velocity and temperature distribution has been analyzed. Variation of Nusselt number with applied magnetic field and also Casson parameter has been studied.

Keywords Electroosmotic flow · Electromagnetohydrodynamic flow · Microchannel · Casson fluid · Viscous dissipation · Joule heating · Hartmann number · Nusselt number

1 Introduction

The study of heat transfer characteristics, flow separation, detection, and analysis of chemical and biological samples in microsystem are needed to design the efficient small-scale microfluidics system which is used in many engineering applications. The mechanism to manipulating and controlling the fluid flow in micro-devices, the electrically driven charge particle or fluid flow such as electroosmosis flow is

M. Reza (✉) · A. Rana
School of Computer Science and Engineering, Department of Mathematics, National Institute of Science & Technology, Berhampur 761008, Odisha, India
e-mail: reza@nist.edu

A. Rana
e-mail: amalmath94@gmail.com

D. Maity et al. (eds.), *Advances in Fluid Mechanics and Solid Mechanics*, Lecture Notes in Mechanical Engineering,
https://doi.org/10.1007/978-981-15-0772-4_11

considered instead of pressure-driven flow. This mechanism is used in many engineering applications and technology for better accuracy and other benefits associated with these flow problems [1–3]. The limitation of the strength of axial electric field causes the upper limit in many applications in which axial electric field is employed in the fluid flow to limit the Joule heating effects and associate negative consequences [4, 5]. Further, it is observed from the experiments results by many researchers that the flows in microchannels can be augmented by using the combined effects of electromagnetohydrodynamics (EMHD). It was also experimentally found that the average flow rates in microchannels can be substantially increased by using low-magnitude magnetic fields [6].

In most of engineering applications in microsystem associated with recent and modern technology, transport of non-Newtonian fluid through microchannel is found and this transport mechanism is characterized mathematically considering the material behavior on nonlinear relation between stress and strain rates. The constitutive model is important to describe the physical material properties. Recently, many mathematical models have been studied by many researchers [7, 8] to analyze the non-Newtonian characteristic in microchannel flows. Liu and Yang [9], Liu et al. [10] have examined the electrokinetic-driven flow of Casson fluids in microchannel. Ng [11] investigated the steady electroosmotic (EO) flow of a visco-plastic material, namely, Casson fluid flow through a rectangular microchannel considering pressure forcing.

Aim of the paper is to obtain the analytical solution for the velocity and temperature distribution of the non-Newtonian Casson fluid in microchannel associated with combined effects of electromagnetohydrodynamics forces and electrokinematics forces. The features of the electromagnetohydrodynamics flow along with heat transfer characteristic are investigated by variation of different physical parameters on the nondimensional flow velocity and temperate profiles. The effect of Casson parameter and magnetic field on the velocity and temperature distribution has been examined.

2 Mathematical Model and Problem Description

We consider non-Newtonian Casson fluid flow through a parallel plate microchannel of height 2a, length l, and width W. The electric field and a magnetic field is applied in the fluid flow simultaneously. Figure 1 shows the physical sketch of this problem. Pressure gradient is applied along the axis of the plate which is influence by electric double layer (EDL) which is formed due to applied electric field. The applied magnetic field interacts with applied electric field to control the flow and heat transfer characteristic of the Casson fluid flow in microchannel.

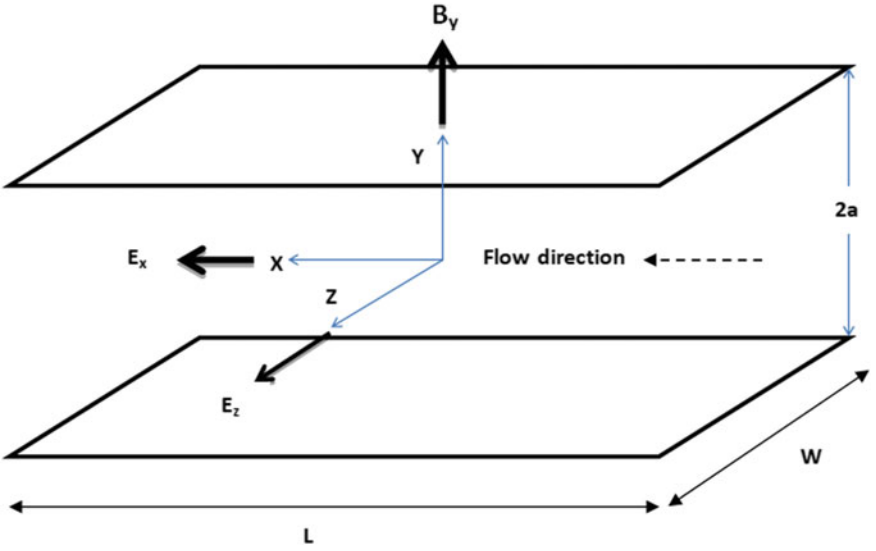

Fig. 1 Physical sketch of the problem

The Casson fluid sample plays both Newtonian and non-Newtonian fluid behaviors. The Casson fluid model proposed by Casson can be followed by

$$\mu\dot{\gamma} = \begin{cases} \left[1 - \sqrt{\frac{\tau}{\tau_0}}\right]^2 \tau & for\ \tau \geq \tau_0 \\ 0 & for\ \tau \leq \tau_0 \end{cases} \tag{1}$$

where τ is the stress tensor, $\gamma = \nabla u + \ [\![\nabla u]\!]\ T$ is the deformation rate tensor, μ is the plastic dynamic viscosity of the fluid, τ_0 is the critical value of Casson yield stress, and the magnitude of the stress is

$$|\tau| = \sqrt{\frac{1}{2}\tau : \tau} \tag{2}$$

when the yield stress vanishes then the model reduces to Newtonian model, by which the plastic dynamic viscosity μ of the fluid becomes Newtonian viscosity.

The governing equations of the flow problem for conservation of mass, conservation of momentum, equation for electric double layer (EDL) potential field and conservation of energy for the electrolyte solute can be expressed as follows:

I. **Mass-conservation equation**:

Let ρ is the density of the fluid and $\vec{V}$ be the fluid velocity, then the mass-conservation equation is written as

$$\frac{\partial \rho}{\partial t} + \nabla \cdot (\rho \overrightarrow{V}) = 0 \tag{3}$$

II. **Linear momentum equation**:

$$\frac{D}{Dt}(\rho \overrightarrow{V}) = \nabla \cdot (\vec{\tau}) + \vec{b} \tag{4}$$

where the stress tensor is $\vec{\tau}$ and due to combined effect of electromagnetohydrodynamic effect the body force $\vec{b}$ per unit volume is described as

$$\vec{b} = \rho_e \overrightarrow{E} + \overrightarrow{F} \tag{5}$$

ρ_e is the net electric charge density, $\overrightarrow{E}$ is the applied external electric field, and $\overrightarrow{F}$ is Lorentz force due to applied magnetic field. The Lorentz force can be written as

$$\overrightarrow{F} = \overrightarrow{J} \times \overrightarrow{B} \tag{6}$$

where $\overrightarrow{J} = \sigma_e(\overrightarrow{E} + \vec{u} \times \overrightarrow{B})$ and σ_e is the electrical conductivity of the medium.

III. **Equation for potential distribution within EDL (Poisson–Boltzmann Equation)**:

In electroosmotic flow, to evaluate the net charge density ρ_e in the EDL, first the EDL potential ψ is determined by solving the Poisson–Boltzmann equation:

$$\nabla \cdot (\nabla \psi) = -\frac{\rho_e}{\varepsilon} \tag{7}$$

where ε is permittivity of the fluid. The relationship between the charge density ρ_e and the electric potential ψ is given by

$$\rho_e = -2n_0 ez \sinh\left(\frac{ez\psi}{k_B T}\right) \tag{8}$$

where n_0 is the ion density (in molar units), e is the electronic charge, z is the valence, k_B is the Boltzmann constant, and T is the absolute temperature. To depict the relationship between the net electric charge density and Debye length, n_0 can be expressed as a function of the Debye length, λ, as follows: $n_0 = \frac{\varepsilon k_B T}{8\pi e^2 z^2 \lambda^2}$.

IV. **Energy conservation equation**:

$$\frac{D}{Dt}(\rho C_P T) = \nabla \cdot (K_{Th} \nabla T) + \vec{\tau}\overrightarrow{D} + \dot{q} \tag{9}$$

where $\overrightarrow{D}$ is the strain rate tensor, K_{Th} be the thermal conductivity of the fluid, and $\dot{q}$ is the heat generation per unit volume due to Joule heating, which is given by

$$\dot{q} = \frac{(\rho_e \overrightarrow{V} + \sigma \overrightarrow{E})(\rho_e \overrightarrow{V} + \sigma \overrightarrow{E})}{\sigma} \tag{10}$$

Here σ is the electric conductivity of the fluid.

3 Momentum Transport for Fully Developed Flow Analysis

The simplified form of the above momentum conservation equation along the x-direction, assuming a hydrodynamically fully developed flow for potential field within the electric double layer (EDL), is written as

$$\mu\left(1 + \frac{1}{\beta}\right)\frac{d^2u}{dy^2} - \frac{dp}{dx} = -\rho_e E_x + \sigma_e B_y^2 u - \sigma_e E_z B_y \tag{11}$$

where β is Casson parameter, σ_e is the electrical conductivity of the medium, ρ_e is the net electric charge density, and $\overrightarrow{E}$ is the applied external electric field.

The boundary conditions are written as

$$u(y = a) = 0; \quad \frac{du}{dy}(y = 0) = 0 \tag{12}$$

Assuming $dp/dx = -(\nabla p/L)$ which is a constant for a fully developed flow.

The nondimensional form of Eq. (11) is given by

$$\left(1 + \frac{1}{\beta}\right)\frac{d^2u^*}{dy^{*2}} + \frac{u_p}{u_{HS}} = -k^2\frac{\cosh(ky^*)}{\cosh(k)} + Ha^2u^* - HaS \tag{13}$$

where

$$Ha = B_y a\sqrt{\frac{\sigma_e}{\mu}}, u_{HS} = -\frac{\varepsilon\psi_0 E_x}{\mu}, u_p = \frac{\nabla p a^2}{\mu L}, S = (E_z a/u_{HS})\sqrt{\sigma_e/\mu}$$

The boundary conditions are reduced as

$$u^*(y^* = 1) = 0 \quad \frac{du^*}{dy^*}(y^* = 0) = 0 \tag{14}$$

Equation (13) is analytically solved using the boundary conditions (14) to obtain exact solution which is written as

$$u^* = \frac{(u_p/u_{HS})\{(1+1/\beta)k^2 - Ha^2\} - Ha^3 S + (1+1/\beta)k^2 SHa - Ha^2k^2}{Ha^2\{Ha^2 - (1+1/\beta)k^2\}\{e^{(Ha/\sqrt{1+1/\beta})} + e^{-(Ha/\sqrt{1+1/\beta})}\}} \{e^{(Hay^*/\sqrt{1+1/\beta})} + e^{-(Hay^*/\sqrt{1+1/\beta})}\}$$
$$+ \frac{(u_p/u_{HS})\{Ha^2 - (1+1/\beta)k^2\} + Ha^3 S - (1+1/\beta)k^2 SHa + Ha^2k^2 \cosh(ky^*)\sec h(k)}{Ha^2\{Ha^2 - (1+1/\beta)k^2\}}$$

4 Heat Transfer Analysis

To investigate the thermal transport characteristics associated with electromagneto-hydrodynamic flows through rectangular microchannel is written to consider viscous dissipation and volumetric heat generation terms which can be written as

$$\rho C_p u \frac{\partial T}{\partial x} = k\left(\frac{\partial^2 T}{\partial x^2} + \frac{\partial^2 T}{\partial y^2}\right) + \mu\left(1 + \frac{1}{\beta}\right)\left(\frac{\partial u}{\partial y}\right)^2 + S_J \tag{15}$$

where C_P is the specific heat of the liquid at constant pressure, T is the local temperature of the liquid, k is the thermal conductivity of the liquid, and $S_J = \sigma(E_x^2 + E_z^2)$ is the volumetric heat generation due to Joule heating effect (on considering weak advective influence on ionic species transport, as consistent with the present formulation). Now, for thermally fully developed flow, the classical nondimensional temperature, $\theta = (T - T_W)/(T_M - T_W)$ is invariant of the axial coordinate (i.e., the x coordinate), where T_W is the channel wall temperature and T_M is the bulk mean temperature.

For investigation, the thermally fully developed analysis, the energy conservation equation is reduced by suitable nondimensional transformation as

$$\frac{d^2\theta}{dy^{*2}} = \frac{Nu}{u^*_{av}}\left[A - B \cdot u^*(y^*) + \left(1 + \frac{1}{\beta}\right)C.F(y^*)\right] \tag{16}$$

where Nu = (ha/k) is the Nusselt number based on half channel height, $u^*_{av} = \frac{u_{av}}{u_{HS}}$, $A = g_1 u^*_{av}$, $B = \left(1 + g_1 + g_2\frac{V}{2}\right)$, $C = g_2 u^*_{av}$, $g_1 = (S_j a/q''_w)$, $g_2 = (\mu u^2_{HS}/aq^2_w)$, $F(y^*) = \left(\frac{du^*}{dy^*}\right)^2$, $V = \int_{-1}^{1} F(y^*)dy^*$

The boundary conditions are given by

$$\theta(y^* = 1) = 0, \quad \frac{d\theta}{dy^*}(y^* = 0) = 0 \tag{17}$$

The nondimensional temperature distribution is obtained to solve Eq. (16) based on boundary conditions Eq. (17) using Mathematics 11.0 package as

$$\theta = \frac{Nu}{u^*_{av}}\{F_1(y^*) - F_1(1)\} = Nu\tilde{\theta} \tag{18}$$

where $\tilde{\theta} = \frac{1}{u^*_{av}}\{F_1(y^*) - F_1(1)\}$.

From Eq. (18), the unknown Nusselt number is derived using the definition of bulk mean temperature as

$$Nu = \frac{2u^*_{av}}{\int_{-1}^{1} u^*\tilde{\theta}dy^*} \tag{19}$$

5 Result and Discussions

The analytical solutions for the velocity and temperature distribution of non-Newtonian Casson fluid in rectangular microchannel have been obtained to solve nonlinear differential equations (11) and (16) subject to the boundary conditions (12) and (17) in the presence of combined effects of applied magnetic force and electrokinematics forces along with pressure-driven force. The characteristics of unknown Nusselt number have been derived by evaluating Eq. (19).

Figure 2 shows that the variation of velocity distribution for different values of Hartmann numbers (Ha) in the absence of applied transverse electric field (S = 0). It is observed from Fig. 2 that the applied magnetic field creates the Lorentz force which causes the retarding effect to opposing fluid particle velocity. So, by increasing the applied magnetic field, the development length of Casson fluid flow decreases and for large value of Hartmann Number, it does not become fully development flow. But it is observed from Fig. 3 that in the presence of transverse applied electric field, for large value of Hartmann number (Ha), fluid flow shows fully developed region. The flow development-length decreases by increasing the applied magnetic field. Figure 4 depicts that variation of velocity distribution for different value of Casson parameter in the absence of applied transverse electric field (see Fig. 4a) and in the presence of applied transverse electrical field, S = 50 (see Fig. 4b). It is noticed that velocity

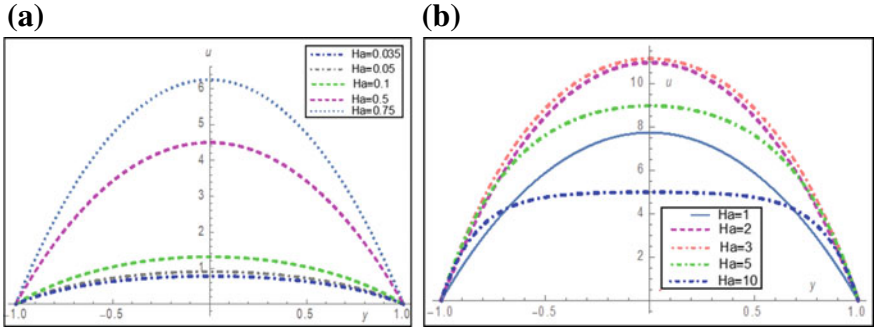

Fig. 2 Variation of velocity distribution for several values of Hartmann number **a** Ha < 1, **b** Ha > 1 for parameter S = 0

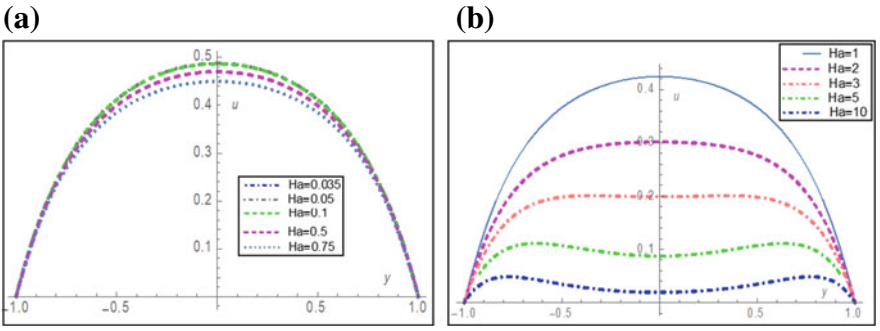

Fig. 3 Variation of velocity distribution for several values of Hartmann number **a** Ha < 1, **b** Ha > 1 for parameter S = 50

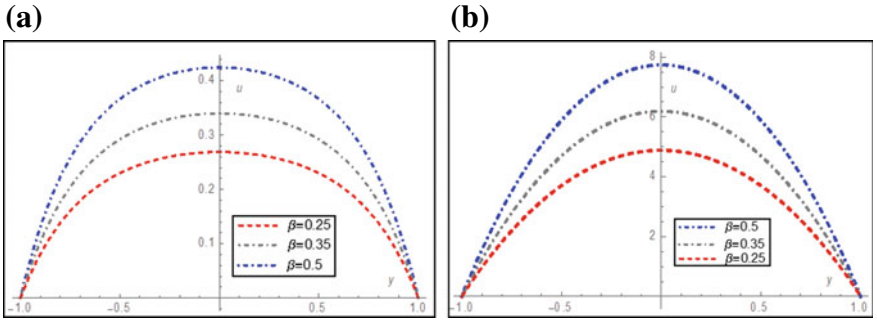

Fig. 4 Variation of velocity distribution for several values of Casson parameter $\boldsymbol{\beta}$. **a** S = 0, **b** S = 50

at point increases with increasing the Casson parameter β. It is interesting to note that development length of flow is more in the presence of transverse electric field than absence of it. Figure 5 shows the effect of applied magnetic field on temperature distribution. It is noted that temperature at fixed point decreases by increasing the applied magnetic field in the absence of electric field. Figure 6 shows the variation of Casson parameter on temperature distribution. It can be remarked from the fact that temperature at a fixed point increases with increasing the Casson parameter.

Effect of the applied magnetic field on the variation of Nusselt number is plotted in Fig. 7. It records that variation of Nusselt number increases with applied magnetic field. It can be explained into two distinct regions in the presence of large applied transverse electric field S = 50. In the small value of Hartmann number, the variation of Nusselt number decreases with increasing the Hartmann number but at certain limit of Hartmann number, i.e., threshold/critical value, variation of Nusselt number increases with increasing magnetic field. Figure 8 displays the variation of Nusselt number with Casson parameter β. It is noticed that variation of Nusselt number decreases with decreasing Casson parameter.

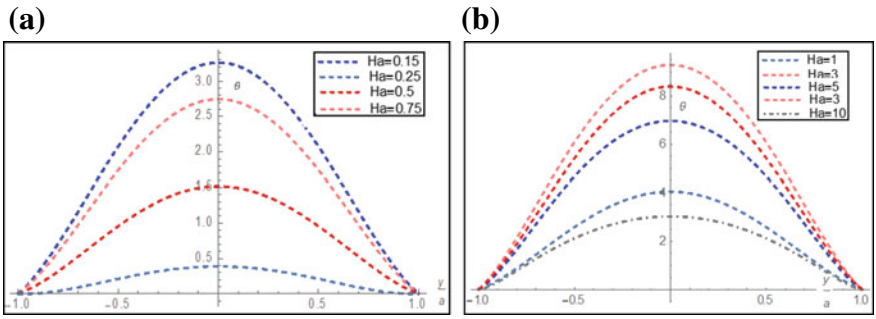

Fig. 5 Variation of temperature distribution for several values of Hartmann number **a** Ha < 1, **b** Ha > 1 for parameter S = 0

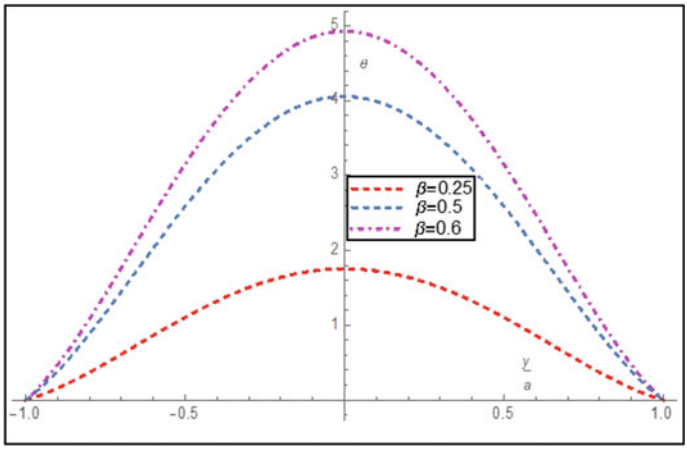

Fig. 6 Variation of temperature distribution for several values of Casson parameter

6 Conclusions

The analytical exact solutions of non-Newtonian Casson fluid flow and thermal transport characteristics under the combined action of EMHD and constant pressure gradient are analyzed in this study. Again, the effects of viscous dissipation and Joule heating are also examined to the heat transfer analysis.

- It is observed that due to the presence and absence transverse electric field in both cases, the flow is always fully developed flow except the presence of transverse electric field with large Hartmann number.
- The temperature distribution at fixed point is decreasing when the applied electric field is increasing. It is noted that the velocity and temperature of the flow both are increasing when the Casson parameter is increasing. From this fact, it can be

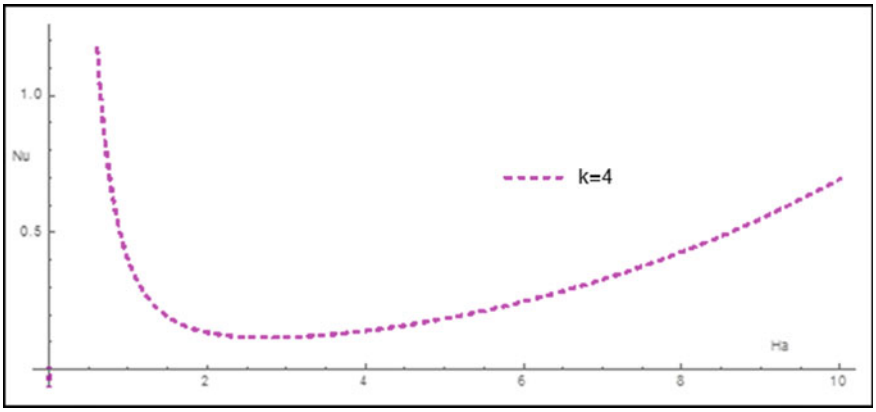

Fig. 7 Variation of Nusselt number with variation of Hartmann number when S = 50, $g_1 = 1$, $g_2 = 0.01$, $\beta = 0.5$, k = 4

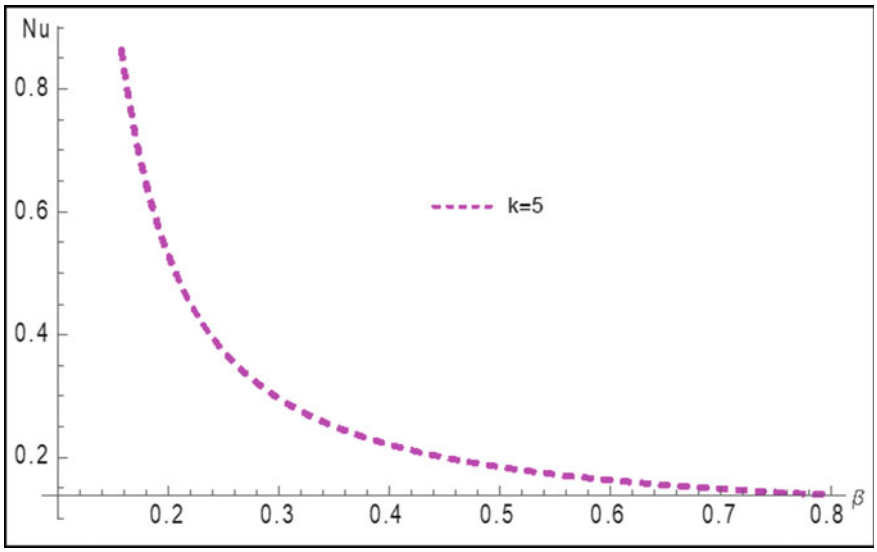

Fig. 8 Variation of Nusselt number with variation of Casson parameter when S = 50, $g_1 = 1$, $g_2 = 0.01$, Ha = 5, k = 5

concluded that the velocity and temperature profiles both are proportional to the Casson parameter.

- The Nusselt number is decreasing gradually with the increasing Casson parameter. The Nusselt number is decreasing with the small value of Hartmann number to a certain limit of Hartmann number.
- After a threshold/critical value of Hartmann number, the Nusselt number increases with increasing the strength of magnetic field.

- Our results will help those researchers who take/investigate more complicated fluid flow model in microchannel for various industrial applications like microfluidic devices.

Acknowledgements This work was supported by SERB, Govt of India (Grant File No. EMR/2016/006383). The authors would like to acknowledge this support.

References

1. Probstein RF (1994) Physicochemical hydrodynamics. Wiley, New York
2. Heller MJ (1996) An active microelectronics device for multiplex DNA analysis. IEEE Eng Med Biol 15:100–103
3. Sosnowski RG, Tu E, Butler WF, O'Connell JP, Heller MJ (1997) Rapid determination of single base mismatch mutations in DNA hybrids by direct electric field control. Proc Natl Acad Sci USA 94(4):1119–1123
4. Xuan X, Li D (2004) Joule heating effects on peak broadening in capillary zone electrophoresis. J Micromech Microeng 14(8):1171–1180
5. Das S, Das T, Chakraborty S (2006) Modeling of coupled momentum, heat and solute transport during DNA hybridization in a microchannel in the presence of electro-osmotic effects and axial pressure gradients. Microfluid Nanofluid 2(1):37–49
6. Jang J, Lee SS (2000) Theoretical and experimental study of MHD (magnetohydrodynamic) micropump. Sens Actuators A Phys 80:84–89
7. Tang GH, Ye PX, Tao WQ (2010) Pressure-driven and electroosmotic non-Newtonian flows through microporous media via lattice Boltzmann method. J Non-Newton Fluid Mech 165:1536–1542
8. Zhao C, Yanga C (2011) Electro-osmotic mobility of non-Newtonian fluids. Biomicrofluidics 5:014110
9. Liu M, Yang J (2009) Electrokinetic effect of the endothelial glycocalyx layer on two-phase blood flow in small blood vessels. Microvasc Res 78(1):14–9
10. Liu M, Liu Y, Guo Q, Yang J (2009) Modeling of electroosmotic pumping of nonconducting liquids and biofluids by a two-phase flow method. J Electroanal Chem 636:86–92
11. Ng C (2013) Combined pressure-driven and electroosmotic flow of Casson fluid through a slit microchannel. J Non-Newton Fluid Mech 198:1–9

Pre-clinical Analysis of Implanted Ankle Joint Using Finite Element Method

Subrata Mondal and Rajesh Ghosh

Abstract Slacken off of the implant component, dislocation, misalignment, fracture, wear in meniscal bearing, etc. are the most important reasons behind the failure of ankle arthroplasty. The study on the effects of implant material on tibia bone stress due to total ankle replacement (TAR) is the prime goal of this paper. Computed tomography (CT) scan data was used to develop the bones, and other soft tissues for the intact and implanted ankle joint. Three implanted FE models were generated having a different combination of implant material. The implanted FE model 1 is having the implant material combination of metal and ultra-high molecular weight polyethylene (UHMWPE). The combination of implant material in FE model 2 was ceramic and UHMWPE, whereas FE model 3 consists of the implant material combination of ceramic and carbon-fiber-reinforced polyetheretherketone (CFR-PEEK), respectively. Three positions during gait such as dorsiflexion, neutral, and plantar flexion positions were considered as applied loading condition, along with muscle force and ligaments. Stress shielding was found in the proximal region of the tibia (i.e., away from the implant neighborhood) due to implantation. Implant material combinations have less impact on tibia bone stress. The present outcome recommended that ceramic can be used as a substitute for metal and CFR-PEEK as an alternate to UHMWPE owing to the high metal release of metal and UHMWPE for long-standing attainment of the prosthetic components.

Keywords Ankle joint · Implant material · Finite element method · Tibia

1 Introduction

The total ankle replacement (TAR) is a preferred used operative surgery for ankle arthritis and fracture. Loosening of the components is one of the leading causes for the early failure of TAR. Extreme bone density resorption due to stress/strain shielding and wear-induced osteolysis is the reason behind the late loosening of the tibia

S. Mondal · R. Ghosh (✉)
School of Engineering, IIT Mandi, Mandi 175005, Himachal Pradesh, India
e-mail: rajesh@iitmandi.ac.in

D. Maity et al. (eds.), *Advances in Fluid Mechanics and Solid Mechanics*,
Lecture Notes in Mechanical Engineering,
https://doi.org/10.1007/978-981-15-0772-4_12

and talar components [1]. The appropriate arrangement of implant material (bearing material) plays a critical role to decrease the stress/strain shielding and wear. Some recent studies stated that carbon-fiber-reinforced polyetheretherketone (CFR-PEEK) and ceramics implant material showed promising results [2–4]. In spite of the current trend of tibial and talar component is made of metal, and meniscal bearing is made of ultra-high molecular weight polyethylene (UHMWPE), ceramic as a substitute to metal and CFR-PEEK as a substitute to UHMWPE might be helpful to reduce the problem associated to the metallic ion release and high volumetric wear.

Numerous studies used the finite element method (FEM) and experimental technique to comprehend the load transmission through the intact and implanted ankle and to assess the performance of TAR prosthesis [5–10]. A study by Reggiani et al. [5] focused on to examine the consequence of kinematics of the foot contact pressure. Misalignment of the TAR components caused higher joint contact pressure [6]. Sopher [7] also examined the effect of prosthetic malpositioning on micromotion at the implant–bone interface and strain distribution. Most recently, Mondal and Ghosh [8] studied the impact of implant orientation and different implant–bone interfaces on strain energy density distribution at the tibia owing to TAR. Wear at the polyethylene component is one of the significant issues of failure of TAR. Putra [9] stated that its radial curvature influences wear in TAR. Most recently, Smyth [10] has also investigated the influence of kinematics on the volumetric wear at the meniscal bearing owing to TAR. The impact of implant material combination (PEEK and its composites) on the wear rate of TAR devices has been investigated by Kerschhofer [11]. Apart from PEEK and its composite combination implant material, no other implant material combination has been examined on the performance of TAR till now. It is hypothesized that the selection of different implant materials might have an effect on stress distribution at the tibia and wear at the meniscal bearing which may eventually affect long-standing survival of the implant. The present study is focused on to have an insight into the effect of implant material combination on stress distribution in tibia bone owing to TAR.

2 Materials and Methods

The computed tomography (CT) scan images which were encoded in the digital imaging and communications in medicine (DICOM) format and were kept in 512 × 512 pixels, having a pixel size of 0.803 mm and slice thickness of 1 mm were used to develop three-dimensional (3D) FE models of intact and implanted ankle joint as similar to an earlier study [8, 12]. The comprehensive description of generation and development of bones and other soft tissues was given in the previous study by the same group of authors [8, 12]. The cortical bone layer was anticipated to have a uniform Young's modulus of 19 GPa and Poisson's ratio of 0.3, respectively [8, 12].

The cancellous bone material properties were considered as heterogeneous, linear, and isotropic. A linear relationship was used between bone density and CT gray value (in Hounsfield unit) to determine the apparent density of cancellous bone.

Table 1 The Young's modulus and Poisson's ratio of bones, cartilage, and prosthetic components. Data adapted from earlier studies [2, 8, 13, 19]

Components	Young's modulus (E), MPa	Poisson's ratio (ν)
Cortical bone	19000	0.3
Cancellous bone	Location depended	0.3
Tibial component (Co-Cr-Mo)	210000	0.3
Tibial component (Ceramic)	350000	0.26
Meniscal bearing (UHMWPE)	1174	0.4
Meniscal bearing (CFR-PEEK)	13000	0.4
Talar component (Co-Cr-Mo)	210000	0.3
Talar component (Ceramic)	350000	0.26
Cartilage	10	0.4

$$\rho = 0.022 + 0.0008456 \times HU \tag{1}$$

A power law among Young's modulus and density of bone was used similar to the previous study to determine Young's modulus after obtaining the density values [13].

$$E = 4778\rho^{1.99} \tag{2}$$

In order to develop the prosthetic components of ankle joint, the Scandinavian Total Ankle Replacement (S.T.A.R$^{@TM}$) prosthesis consists of a flat tibial component (32 mm × 30 mm) with two anchorage bars, meniscal bearing (Thickness of 10 mm), and talar component (34 mm × 35 mm) which were created using design software (Solidworks, DS Solidworks Corp., Concord, MA, USA) conferring to the facts provided by the Small Bone Innovations, Inc. and positioned (optimal position) according to surgical guidelines [14]. Rhinoceros software (Robert McNeel & Associates, Seattle, WA, USA) was used for the virtual operation of implant and bone [14].

In the case of implanted FE model 1, tibial and talar components were assigned with Cobalt–Chromium–Molybdenum, and meniscal bearing was UHMWPE, the FE model 2 was assigned with ceramic and UHMWPE, and FE model 3 was assigned with ceramic and CFR-PEEK to comprehend the consequence of different implant material arrangements on bone stress. Material properties of prosthetic components are shown in Table 1. ANSYS FE software v 17 was used for discretization of all bones and implant components. Mesh convergence study was performed (based on stress value in the tibia bone) with ten-node tetrahedral element to check that the result

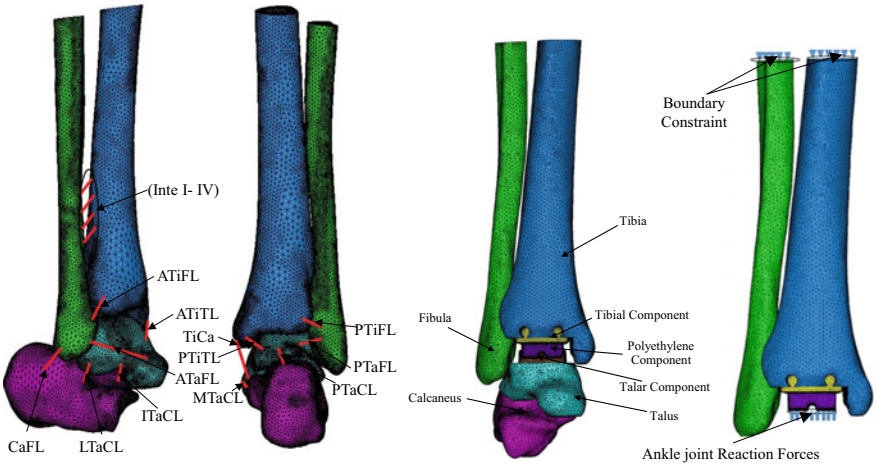

Fig. 1 The intact and implanted FE models showing bones, ligaments, and prosthetic components with applied loading and boundary conditions

does not depend on element size. Three different element sizes (coarse, medium, and fine) were considered for meshing purpose. The coarse, medium, and fine mesh were consisting of 523,871, 723,438, and 965,213 number of elements. On comparing the first (coarse) and the second (medium) FE models, 7% deviation in maximum stress was observed. However, the deviation was reduced to 1.2%, when the results of the second (medium) and the third (fine) models were compared. Therefore, the second FE model contained 723,438 number of elements (maximum edge length of 3 mm) which was considered for the present analysis. Figure 1 shows the intact and implanted FE models. Apart from bones, soft tissues such as ligaments and cartilages were also modeled for this study. Cartilages were developed between the bones by using an offsetting method which was done manually in MIMICS software v 11.1 (Materialise, Leuven, Belgium). Whereas ligaments were modeled using linear spring elements in ANSYS FE software v 17. Totally 16 numbers of ligaments were identified around the ankle joint and inserted according to the earlier study [12, 15–18]. The material properties of bones, cartilages, and prosthetic components were shown in Table 1, whereas the material properties of ligaments are presented in Table 2.

2.1 Applied Loading and Boundary Conditions

The magnitude and direction of ankle joint reaction forces at the three altered locations (dorsiflexion, neutral, and plantarflexion) during the posture stage of gait are presented in Table 3. The magnitude of reaction forces was measured from earlier literature [5, 8, 19, 20] which was equivalently rescaled and applied according to

Table 2 The value of stiffness, Young's modulus, and Poisson's ratio of all the ligaments considered in this study [15–18]

Ligaments represented in models	Stiffness (N/mm)	Young's modulus (E), MPa	Poisson's ratio (ν)
Anterior tibiofibular (ATiFL)	90	160	0.49
Anterior tibiotalar (ATiTL)	70	184.5	0.49
Anterior talofibular (ATaFL)	90	255.5	0.49
Calcaneofibular (CaFL)	70	512	0.49
Interosseous I- IV (Inte I-IV)	400	260	0.4
Interosseous talocalcaneal (ITaCL)	70	260	0.4
Lateral talocalcaneal (LTaCL)	70	260	0.4
Medial talocalcaneal (MTaCL)	70	260	0.4
Posterior tibiofibular (PTiFL)	90	160	0.49
Posterior talofibular (PTaFL)	70	216.5	0.49
Posterior tibiotalar (PTiTL)	80	99.5	0.49
Posterior talocalcaneal (PTaCL)	70	260	0.4
Tibiocalcaneal (TiCa)	122	512	0.49

Table 3 The reaction forces at the ankle joint. Data adapted from earlier studies [5, 8, 19, 20]

Concentrated Force (N) and moment	Position		
	Dorsiflexion (−10°)	Neutral (0°)	Plantarflexion (+15°)
Axial force (Z-component)	1600	600	400
Interior–exterior force (Y-component)	−185	150	100
Anterior–posterior force (X-component)	−185	−280	−245
Interior–exterior torque (Y-component)	−6.2	−2.85	0.1

our present FE coordinate system. These reaction forces were applied underneath the meniscal bearing on the set of nodes restricted in the specific fixed areas. Apart from the joint reaction forces, muscle force (i.e., Achilles tendon) was set at 75% of the total body weight at the extreme posterior position of the calcaneus bone in the present FE model. Applied reaction force and fixed boundary condition are shown in Fig. 1.

2.2 Contact Simulations

The present study assumed the debonded (non-osseointegration) implant–bone interface condition. For the contact simulation, an Augmented Lagrangian contact algorithm was used similar to an earlier study [2, 3, 8]. The contact stiffness and a penetration factor for the intact and the implanted model were selected as per the previous research [8]. The Coulomb friction coefficient of 0.02 was considered between bones and cartilages in case of intact bone as described in earlier studies [8]. Owing to the lubricating nature of the articulating surface, the contact between bone and cartilage is considered to be frictionless.

3 Results

Equivalent stress distribution in the tibia formerly and later the implantation for the different implant material combinations are shown in Fig. 2. Outcomes were attained for all three loading conditions.

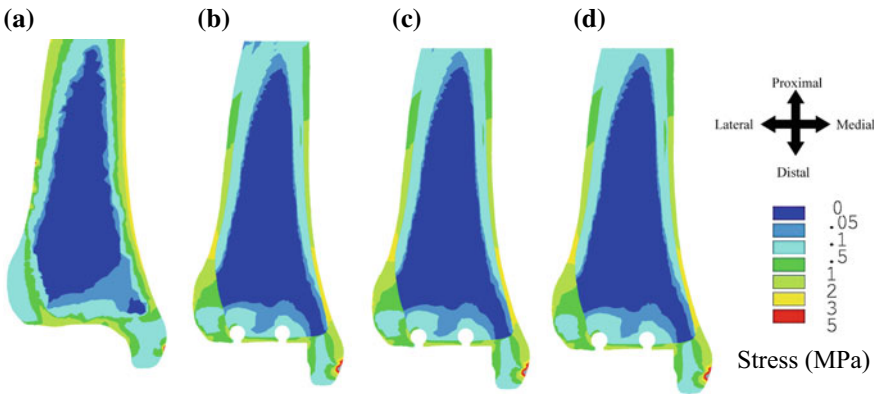

Fig. 2 Equivalent stress distribution (von Mises) in tibia before and after implantation for different implant material combinations in case of debonded implant–bone interface condition

The magnitude of stress was found to be greater in the case of dorsiflexion loading condition as compared to other two loading conditions (neutral and plantarflexion) for all the models considered in this study. However, the stress distribution pattern was found to be similar for all the three loading conditions. Therefore, to comprehend the effect of implantation and different implant materials on stress distribution at the tibia, only the outcomes conforming to the dorsiflexion position were presented in Fig. 2. Considering the debonded implant–bone interface condition, implantation headed for increasing in stress (around 5–30%) in the tibia bone adjacent to the tibial component vicinity (Fig. 2a, b). Whereas away from the region of tibial component, reduction in stress (around 10–50%) was found (Fig. 2a, b). Although the alterations in stress distribution were observed to be nearly alike for prosthetic models 1, 2, and 3 in case of debonded implant–bone interface condition (Fig. 2b–d).

4 Discussions

The FE investigation has been extensively used for pre-clinical analysis and assessment of the orthopedic implants owing to its less financial, computational cost, and high precision. The present study was intended at studying the influence of different implant materials on tibia bone stress due to TAR. For this analysis, CT scan images were used to develop 3D FE models of the intact and implanted ankle joint. S.T.A.R$^{@TM}$ prosthesis was used for this present study. It was not possible to validate this FE model with direct one-to-one experimental data as the present CT scan data were taken on a living subject of a 35-year female. The present FE model of the implanted ankle was substantiated and corroborated with earlier published data by Ozen [21] using the same material properties of bone, boundary, and loading conditions. It was observed that predicted FE stress at the different bones corroborated well with the earlier measured data by Ozen [21]. However, some deviations were found due to the difference in geometry, the age of the patient, and the quality of the CT scan dataset. These validation results are well comparable with the earlier published data and support the present FE model.

The current study detected that implantation has an influence on stress distribution in the tibia. After the implantation, the stress value was increasing near the tibial component, whereas the stress was decreasing toward the proximal region of the tibia bone which was observed from Fig. 2a, b. The decrease in stress at the proximal part of the tibia indicated stress shielding due to implantation for debonded (non-osseointegration) implant–bone interfacial condition (Fig. 2b). It has been mentioned earlier that stress shielding in the bone is causing bone resorption due to bone remodeling and subsequent implant loosening [3]. The result of the present study indicated different implant materials have less effect on stress distribution at tibia due to TAR. Stress distribution was observed at the tibia is found to be almost similar for all the three different implant material models (Fig. 2b–d). Although earlier studies stated that ceramic appeared to be a promising and viable alternative to metal, owing to its better biomechanical properties, such as lower friction, greater wear resistance,

and more biocompatibility [2, 3]. As well as CFR-PEEK can be used in place of UHMWPE due to its less metal ion release and volumetric wear [4]. Modern components of ankle prosthesis are made of metal and UHMWPE which have high wear and metal ion release. Considering almost same stress distribution in the tibia for all the three different implant materials, it can be suggested from the present result that ceramic and CFR-PEEK are alternatives to metal and UHMWPE, respectively.

The study, however, has some limitations and assumptions. The current FE models contained only ligaments and cartilages as soft tissues. Ligaments were modeled as a linear spring element as similar to an earlier study [19]. Cartilages were anticipated as linear elastic, isotropic, and homogeneous for the present study. Only three positions of posture were considered as a loading condition in this study. Only one CT scan data was used for the development of the implanted and intact joint.

5 Conclusions

The 3D FE models of the intact and the implanted ankle have been beneficial in comprehending the deviations in load transfer. Stress shielding was found at the proximal part of the tibia due to implantation which causes the bone density loss owing to bone remodeling and threatens for fixation of the implant. The present study concluded that ceramic could be used in place of metal and CFR-PEEK can be used as a substitute to UHMWPE as metal and UHMWPE has a higher rate of volumetric wear and metallic ion release.

Conflict of Interest None.

Ethical Statement This study is not an experimental one. This is a numerical study where we used the CT scan data of a living subject. Informed consent was obtained from the subject for being included in the study.

References

1. National Joint Registry (2016) National Joint Registry for England and Wales, 13th Annual Report. http://www.njrcentre.org.uk/njrcentre/Reports,PublicationsandMinutes/Annualreports/tabid/86/Default.aspx
2. Ghosh R, Mukharjee K, Gupta S (2013) Bone remodelling around uncemented metallic and ceramic acetabular components. Proc Inst Mech Eng Part H: J Eng Med 227(5):490–502
3. Ghosh R, Gupta S (2014) Bone remodelling around cementless composite acetabular components: the effects of implant geometry and implant-bone interfacial conditions. J Mech Behav Biomed Mater 32:257–269
4. Manley MT, Ong KL, Kurtz SM (2006) The potential for bone loss in acetabular structures following THA. Clin Orthop Relat Res 453:246–253
5. Reggiani B, Leardini A, Corazza F (2006) Finite element analysis of total ankle replacement during the stance phase of gait. J Biomech 39:1435–1443

6. Espinosa N, Walti M, Favre P (2010) Misalignment of total ankle components can induce high joint contact pressures. J Bone Jt Surg 92:1179–1187
7. Sopher SR, Andrew AA, James DC (2017) Total ankle replacement design and positioning affect implant-bone micromotion and bone strains. Med Eng Phys 42:80–90
8. Mondal S, Ghosh R (2018) The effects of implant orientations and implant–bone interfacial conditions on potential causes of failure of tibial component due to total ankle replacement. J Med Biol Eng 1–11. https://doi.org/10.1007/s40846-018-0435-5
9. Putra AMS, Harun MN, Ardiyansyah S (2014) Study of wear prediction on total ankle replacement. Adv Mater Res 845:311–315
10. Smyth A, Fisher J, Suner S (2017) Influence of kinematics on the wear of a total ankle replacement. J Biomech 53:105–110
11. Kerschhofer D, Gundapaneni D, Christof S (2016) Applicability of PEEK and its composites in total ankle replacement devices and wear rate predictions. Biomed Phys Eng Express 2:065012. https://doi.org/10.1088/2057-1976/2/6/065012
12. Mondal S, Ghosh R (2017) A numerical study on stress distribution across the ankle joint: Effects of material distribution of bone, muscle force and ligaments. J Orthop 14:329–335
13. Linde F, Hvid I, Madsen F (1992) The effect of specimen geometry on the mechanical behaviour of trabecular bone specimens. J Biomech 25:359–368
14. STAR Surgical Technique—Small Bone Innovations, Inc. Cited 4 Mar 2013
15. Beumar A, Hemert WLV, Swierstra BA (2003) A biomechanical evaluation of the tibiofibular and tibiotalar ligaments of the ankle. Foot Ankle Int 24:426–429
16. Liacouras PC, Wayne JS (2007) Computational modelling to predict mechanical function of joints: application to the lower leg simulation of two cadaver studies. J Biomech Eng 129:811–817
17. Corazza F, O'Connor JJ, Leardini A (2003) Ligament fibre recruitment and forces for the anterior drawer test at the human ankle joint. J Biomech 36(3):363–372
18. Bekerom VDMP, Raven EE (2007) The distal fascicle of the anterior inferior tibiofibular ligament as a cause of tibiotalar impingement syndrome: a current concepts review. Knee Surg Sports Traumatol Arthrosc 15(4):465–471
19. Mondal S, Ghosh R (2019) Effects of implant orientation and implant material on tibia bone strain, implant–bone micromotion, contact pressure, and wear depth due to total ankle replacement. J Eng Med Proc Inst Mech Eng H 1–14. https://doi.org/10.1177/0954411918823811
20. Seireg A, Arvikar RJ (1975) The prediction of muscular load shearing and joint forces in the lower extremities during walking. J Biomech 8:89–102
21. Ozen M, Sayman O, Havitcioglu H (2013) Modelling and stress analyses of a normal foot-ankle and a prosthetic foot-ankle complex. Acta Bioeng Biomech 15(3):19–27

Dynamic Problem of Fractional Thermoelasticity in Bounded Cylindrical Domain with Relaxation Time

Gaurav Mittal and V. S. Kulkarni

Abstract A fractional heat conduction model of a solid heat conductor is designed in the bounded cylindrical domain. The solid heat conductor under consideration is assumed to be in the form of a thick circular plate. The boundaries of the thick circular plate are traction free and subjected to externally applied axisymmetric heat source. Governing heat conduction equation of this model has been designed in the context of time fractional derivative with one-relaxation time. The solution of fractional heat conduction equation in association with Caputo time fractional derivative has been found by transforming the original boundary value problem into eigenvalue problem through the integral transforms. The inversion of Laplace transforms in terms of infinite series approximations has been achieved numerically using Gaver–Stehfest algorithm. The convergence of infinite series solutions has been discussed. Illustratively, the numerical scheme has been employed to partially distributed heat flux and thermal behavior of a heat conductor has been discussed numerically and studied graphically. Results obtained are compared with coupled thermoelasticity, fractional thermoelasticity, and generalized thermoelasticity.

Keywords Dynamic problem · Fractional thermoelasticity · Finite wave speed · Relaxation time · Integral transforms

G. Mittal (✉)
Department of Applied Mathematics, Thadomal Shahani Engineering College, Mumbai, Maharashtra, India
e-mail: gmsre.1979@gmail.com

V. S. Kulkarni
Department of Mathematics, University of Mumbai, Mumbai, Maharashtra, India
e-mail: drvinayaksk1@gmail.com

D. Maity et al. (eds.), *Advances in Fluid Mechanics and Solid Mechanics*, Lecture Notes in Mechanical Engineering,
https://doi.org/10.1007/978-981-15-0772-4_13

1 Introduction

In thermal mechanics, a novel contribution of fractional calculus has been achieved toward the development of the generalized theory of coupled thermoelasticity from last few years. Povstenko [1, 2]reconstructed the Fourier's law of heat conduction in the context of Caputo [3] time fractional derivative. Sherief et al. [4] proved uniqueness theorem to support the theory of fractional thermoelasticity. Following the fractional theory of thermoelasticity, Hussein [5] solved a one-dimensional half-space problem of the infinite domain for a long solid circular cylinder. The corresponding thermal parameters were obtained analytically and numerically as well. The computed results were compared to existing theories. Tripathi et al. [6] investigated the thermal effects of a thick circular plate in half-space subjected to axisymmetric heat source. Recently, Sherief and Raslan [7] applied Caputo Fabrizio fractional differential operator to discuss a fractional order thermoelastic problem. This problem deals with an infinite elastic space under the influence of a continuous line heat source. Analytically, the problem was solved using asymptotic expansions which were valid for short times. The nature of propagation of thermal waves was also given special attention. Sheiref et al. [8] assumed axisymmetric 2D problems for a viscoelastic half-space where asymptotic expansions were used to study wave propagation in the medium. Mathematically, the problem was solved using integral transforms, and the numerically computed results for temperature, displacement, and thermal stresses were illustrated graphically.

According to a report by Cotterell and Parkes [9], the post-buckling behavior of a circular plate needed to be investigated mainly for two conditions as heating over the center and at the edge. However, in the former case, the plate buckles into the form of a saucer and in the latter into a saddle shape. The plate may be free or it may be subjected to a variety of edge restraints.

This article is an attempt to design a two-dimensional heat conduction model of a perfectly thermoelastic solid heat conductor in the form of a thick circular plate subjected to the axisymmetric heat source with one-relaxation time in the bounded cylindrical domain and thermal deformation effects have been investigated. The lateral surfaces of the plate are traction free and subjected to thermal loading due to the externally applied axisymmetric heat source. The governing equations of the heat conduction model are taken from the generalized fractional theory of thermoelasticity with one-relaxation time. The analytical solutions of the governing equations are obtained by applying Laplace and finite Hankel transforms in time and space variables, respectively. Illustratively, a numerical scheme is applied to a thick circular plate of copper material that is subjected to a partially distributed heat source and distributions of temperature, displacement, and thermal stresses are obtained analytically in Laplace domain. The numerical inversion has been achieved using Gaver–Stehfest algorithm [10, 11]. The numerically computed results were depicted graphically and compared to generalized and classical theories.

The model presented in this article may be helpful to decode and analyze the thermal effects for the micro-level heating process of a thick circular plate, which could

be useful in aerospace engineering, laser technology, fabrication of semiconductor devices [12–14], and other related fields.

To our knowledge, no one has formulated a two-dimensional fractional thermoelastic heat conduction problem associated with one-relaxation time in the bounded cylindrical domain for a thick circular plate subjected to an axisymmetric heat source whose surfaces are traction free. This is the latest and novel contribution to the field of thermal mechanics.

2 The Mathematical Model

A brief description of the mathematical formulation of the governing equations of the problem along with imposed boundary conditions is given below in the context of fractional thermoelasticity is association with one-relaxation time.

2.1 Basic Assumptions and Governing Equations

Assume the axis of symmetry as z-axis and origin of the system of coordinates is at middle plane between upper and lower faces of the plate. Due to rotational symmetry about z-axis, all quantities are independent of the coordinate ϕ. Initially, the solid is kept at zero temperature. The upper and lower plane boundary surfaces $\partial D_{\text{plane}}$ are subjected to convective heat flux $\Phi(r, t), \forall\, t > 0$, described by a continuous integrable function $\Phi : D \times (0, \infty) \longrightarrow \mathbb{R}$. The circular boundary surface $\partial D_{\text{circular}}$ attempts to simulate heat transfer by convection due to dissipation into surrounding media. Assume that the boundary ∂D of heat conductor is free from traction. Under these more realistic generalized boundary conditions, the thermal behavior of solid heat conductor is required to be determined.

For displacement vector $\overrightarrow{u}(r, z, t) = (u_1, 0, u_2)$, the equations of motion can be written as

$$\mu \nabla^2 u_1 - \frac{\mu}{r^2} u_1 + (\lambda + \mu) \frac{\partial e}{\partial r} - \gamma \frac{\partial T}{\partial r} = \rho \frac{\partial^2 u_1}{\partial t^2}, \tag{1}$$

$$\mu \nabla^2 u_2 + (\lambda + \mu) \frac{\partial e}{\partial z} - \gamma \frac{\partial T}{\partial z} = \rho \frac{\partial^2 u_2}{\partial t^2}, \tag{2}$$

$$e = \frac{u_1}{r} + \frac{\partial u_1}{\partial r} + \frac{\partial u_2}{\partial z} = \frac{1}{r} \frac{\partial}{\partial r}(r u_1) + \frac{\partial u_2}{\partial z}. \tag{3}$$

where λ, μ are Lamé constants, $\gamma = \alpha_t(3\lambda + 2\mu)$ is the material constant, and e is dilatation function.

In view of Maxwell–Cattaneo law of heat conduction defined above, the governing time fractional boundary value problem of heat conduction with the mixed boundary conditions on open domain D for $T : D \times (-\infty, \infty) \longrightarrow \mathbb{R}$ has the following form:

$$\kappa \nabla^2 T = \left(\frac{\partial}{\partial t} + \tau_0 \frac{\partial^{1+\alpha}}{\partial t^{1+\alpha}} \right) (\rho c_e T + \gamma T_0 e), \quad \alpha \in (0,\ 1], \tag{4}$$

where T_0 is reference temperature and T is the absolute temperature assumed to be such that $|T - T_0| \ll 1$. Constants κ is thermal conductivity, ρ is material density, c_e is the specific heat capacity, α is the fractional order applied to time derivatives, and τ_0 is relaxation time.

The normal and shear stresses $\sigma_{rr}, \sigma_{zz}, \sigma_{rz}$ constitutive relations in terms of temperature change and displacement supplement the preceding equations as

$$\sigma_{rr} = 2\mu \frac{\partial u_1}{\partial r} + \lambda e - \gamma (T - T_0), \tag{5}$$

$$\sigma_{zz} = 2\mu \frac{\partial u_2}{\partial z} + \lambda e - \gamma (T - T_0), \tag{6}$$

$$\sigma_{rz} = \mu \left(\frac{\partial u_1}{\partial z} + \frac{\partial u_2}{\partial r} \right). \tag{7}$$

Equations (1)–(7) constitute the mathematical formulation of the problem in the context of fractional differentiation.

To convert the dimensionless system of equations, one can make use of the following nondimensional variables

$$r' = c\delta r,\ z' = c\delta z,\ u'_1 = c\delta u_1,\ u'_2 = c\delta u_2,\ t' = c\delta t,\ \tau'_0 = (c^2\delta)^{\alpha} \tau_0,\ \sigma'_{ij} = \frac{\sigma_{ij}}{\mu},$$

$$\theta = \frac{\gamma (T - T_0)}{(\lambda + 2\mu)},\ \epsilon = \frac{\gamma^2 T_0}{\kappa c^2 \delta \rho}, \delta = \frac{\rho c_e}{\kappa}.$$

Using the above nondimensional variables, the governing Equations (1)–(7) take the form (neglecting primes for simplicity)

$$\nabla^2 u_1 - \frac{u_1}{r^2} + (\beta^2 - 1) \frac{\partial e}{\partial r} - \beta^2 \frac{\partial \theta}{\partial r} = \beta^2 \frac{\partial^2 u_1}{\partial t^2}, \tag{8}$$

$$\nabla^2 u_2 + (\beta^2 - 1) \frac{\partial e}{\partial z} - \beta^2 \frac{\partial \theta}{\partial z} = \beta^2 \frac{\partial^2 u_2}{\partial t^2}, \tag{9}$$

$$\nabla^2 \theta = \left(\frac{\partial}{\partial t} + \tau_0 \frac{\partial^{1+\alpha}}{\partial t^{1+\alpha}} \right) (\theta + \epsilon e), \tag{10}$$

$$\sigma_{rr} = 2 \frac{\partial u_1}{\partial r} + (\beta^2 - 2) e - \beta^2 \theta, \tag{11}$$

$$\sigma_{zz} = 2 \frac{\partial u_2}{\partial z} + (\beta^2 - 2) e - \beta^2 \theta, \tag{12}$$

$$\sigma_{rz} = \left(\frac{\partial u_1}{\partial z} + \frac{\partial u_2}{\partial r} \right), \tag{13}$$

where

$$\beta^2 = \frac{\lambda + 2\mu}{\mu}.$$

Combining Eqs. (8), (9), and making use of Eq. (3), one will have the following equation:

$$\nabla^2 e - \nabla^2 \theta = \frac{\partial^2 e}{\partial t^2}. \tag{14}$$

Equations (8)–(14) constitute nondimensional conversion of governing equations.

2.2 Initial and Boundary Conditions

The plane boundaries $\partial D_{\text{plane}}$ are subjected to axisymmetric heat flux $\Phi : \partial D \times [0, \infty) \longrightarrow \mathbb{R}$, which is a continuous and absolutely integrable function that depends on the space variable r and time variable t. The circular boundary $\partial D_{\text{circular}}$ attempts to stimulate the heat transfer between plate and surrounding media. The boundary conditions has the following form:

$$\pm \kappa \frac{\partial \theta}{\partial z} + h_{pl}\theta = \Phi(r, t), \quad \text{for } z = \pm\frac{h}{2}, \tag{15}$$

$$\kappa \frac{\partial \theta}{\partial r} + h_{cr}\theta = 0, \ \text{for } r = a, \tag{16}$$

where h_{pl} and h_{cr} are heat transfer coefficient of plane and circular boundary surface of thick circular plate, respectively. Assuming all the initial conditions are homogeneous boundary conditions for traction-free surfaces are given by

$$\sigma_{zz} = \sigma_{rz} = 0, \quad z = \pm\frac{h}{2}, \tag{17}$$

$$\sigma_{rr} = \sigma_{rz} = 0, \quad r = a. \tag{18}$$

Equations (15)–(18) describe the imposed initial and boundary conditions of the problem.

3 The Mathematical Solution

The mathematical solution of governing dimensionless equations derived in the above section subjected to initial and boundary condition has been achieved using Laplace and Hankel integral transforms applied in time and space variables, respectively.

The inversion of results obtained in the Laplace domain has been carried out by Gaver–Stehfest algorithm to obtain the time-domain solutions.

3.1 Transformation in Laplace Domain

Applying Laplace transforms to nondimensional governing Equations (8)–(14) together with the boundary conditions (15)–(18), one will have the following equations:

$$\nabla^2\overline{u}_1 - \frac{\overline{u}_1}{r^2} + (\beta^2 - 1)\frac{\partial\overline{e}}{\partial r} - \beta^2\frac{\partial\overline{\theta}}{\partial r} = \beta^2 s^2\overline{u_1}, \tag{19}$$

$$\nabla^2\overline{u}_2 + (\beta^2 - 1)\frac{\partial\overline{e}}{\partial z} - \beta^2\frac{\partial\overline{\theta}}{\partial z} = \beta^2 s^2\overline{u}_2, \tag{20}$$

$$(\nabla^2 - s - \tau_0 s^{\alpha+1})\overline{\theta} = \epsilon(1 + \tau_0 s^{\alpha})s\overline{e}, \tag{21}$$

$$(\nabla^2 - s^2)\overline{e} = \nabla^2\overline{\theta}, \tag{22}$$

$$\overline{\sigma}_{rr} = 2\frac{\partial\overline{u}_1}{\partial r} + (\beta^2 - 2)\overline{e} - \beta^2\overline{\theta}, \tag{23}$$

$$\overline{\sigma}_{zz} = 2\frac{\partial\overline{u}_2}{\partial z} + (\beta^2 - 2)\overline{e} - \beta^2\overline{\theta}, \tag{24}$$

$$\overline{\sigma}_{rz} = \left(\frac{\partial\overline{u}_1}{\partial z} + \frac{\partial\overline{u}_2}{\partial r}\right). \tag{25}$$

$$\pm\kappa\frac{\partial\overline{\theta}}{\partial z} + h_{pl}\overline{\theta} = \overline{\Phi}(r,\ s),\quad z = \pm\frac{h}{2}, \tag{26}$$

$$\kappa\frac{\partial\overline{\theta}}{\partial r} + h_{cr}\overline{\theta} = 0,\quad r = a, \tag{27}$$

$$\overline{\sigma}_{zz} = \overline{\sigma}_{rz} = 0,\quad z = \pm\frac{h}{2}, \tag{28}$$

$$\overline{\sigma}_{rz} = \overline{\sigma}_{rr} = 0,\quad r = a, \tag{29}$$

where $\overline{\Phi}(r,\ s)$ is a function of variables r and Laplace parameter s.

Eliminating $\overline{e}$ between Eqs. (21), (22), one has the following equation in $\overline{\theta}$:

$$(\nabla^2 - m_1^2)(\nabla^2 - m_2^2)\overline{\theta} = 0, \tag{30}$$

where m_1^2, m_2^2 are the positive roots of real parts of the following characteristic equation:

$$m^4 - (s^2 + s(1 + \tau_0 s^{\alpha})(1 + \epsilon))m^2 + s^3(1 + \tau_0 s^{\alpha}) = 0. \tag{31}$$

The solution of equation (30) is given by

$$(\nabla^2 - m_i^2)\overline{\theta}_i = 0, \quad i = 1, 2. \tag{32}$$

Equations (19)–(33) represent the conversion of nondimensional governing equations including boundary conditions (8)–(18) in Laplace domain.

3.2 Transformation in Hankel Domain

Following Özisik [15], if $\psi(r, z, t)$ be a function of space variables r, z and time variable t, then the finite Hankel integral transform $\psi^*(\nu_n, z, t)$ and corresponding inverse transform are given by following relations:

$$\psi^*(\nu_n, z, t) = \int_0^a r \cdot S_0(\nu_n, r) \cdot \overline{\psi}(r, z, t) \cdot dr, \tag{33}$$

$$\psi(r, z, t) = \sum_{n=1}^{\infty} S_0(\nu_n, r) \cdot \psi^*(\nu_n, z, t), \tag{34}$$

where the summation is taken over the positive eigenvalues, ν_n, which are positive root of the transcendental equation given as

$$\nu_n J_0'(\nu_n a) + \frac{h_{cr}}{\kappa} J_0(\nu_n a) = 0, \quad n \in N, \tag{35}$$

and $S_0(\nu_n, r)$ denotes the kernel of Hankel transform given by

$$S_0(\nu_n, r) = \frac{\sqrt{2}\kappa \nu_n J_0(\nu_n r)}{a J_0(\nu_n a)\sqrt{[h_{cr}^2 + \kappa^2 \nu_n^2]}}. \tag{36}$$

3.3 Results in Laplace Domain

Practising finite Hankel transform and corresponding inverse transform to the nondimensional Equations (19)–(29), including Eq. (32), one will have the following results for distribution of temperature, displacement, and thermal stresses in Laplace domain:

$$\overline{\theta}(r,\ z,\ s) = \sum_{n=1}^{\infty}\sum_{i=1}^{i=2} S_0(\nu_n,\ r)A_i(\nu_n,\ s)(m_i^2 - s^2)\cosh(l_i z), \tag{37}$$

$$\overline{e}(r,\ z,\ s) = \sum_{n=1}^{\infty}\sum_{i=1}^{i=2} S_0(\nu_n,\ r)A_i(\nu_n,\ s)m_i^2\cosh(l_i z), \quad \text{where } l_i = \sqrt{\nu_n^2 + m_i^2},\ \ i = 1,\ 2, \tag{38}$$

$$\overline{u}_1(r,\ z,\ s) = -\sum_{n=1}^{\infty} S_0(\nu_n,\ r)\left\{B(\nu_n,\ s)l_3\cosh l_3 z + \nu_n^2\sum_{i=1}^{i=2} A_i(\nu_n,\ s)\cosh l_i z\right\}, \tag{39}$$

$$\overline{u}_2(r,\ z,\ s) = \sum_{n=1}^{\infty} S_0(\nu_n,\ r)\left\{B(\nu_n,\ s)\sinh l_3 z + \sum_{i=1}^{i=2} A_i(\nu_n,\ s)l_i\sinh l_i z\right\},$$

$$\text{where } l_3 = \sqrt{\nu_n^2 + \beta^2 s^2}, \tag{40}$$

$$\overline{\sigma}_{rr}(r,\ z,\ s) = \sum_{n=1}^{\infty}\sum_{i=1}^{i=2} S_0(\nu_n,\ r)A_i(\nu_n,\ s)\cosh l_i z[\beta^2 s^2 - 2m_i^2]$$

$$-2\sum_{n=1}^{\infty} S_1(\nu_n,\ r)\left\{B(\nu_n,\ s)l_3\cosh l_3 z + \nu_n^2\sum_{i=1}^{i=2} A_i(\nu_n,\ s)\cosh l_i z\right\}, \tag{41}$$

$$\text{where } S_1(\nu_n,\ r) = \frac{d}{dr}S_0(\nu_n,\ r),$$

$$\overline{\sigma}_{zz}(r,\ z,\ s) = \sum_{n=1}^{\infty} S_0(\nu_n,\ r)\left\{(\nu_n^2 + l_3^2)\sum_{i=1}^{i=2} A_i(\nu_n,\ s)\cosh l_i z + 2B(\nu_n,\ s)l_3\cosh l_3 z\right\}, \tag{42}$$

$$\overline{\sigma}_{rz}(r,\ z,\ s) = \sum_{n=1}^{\infty} S_1(\nu_n,\ r)\left\{B(\nu_n,\ s)\sinh l_3 z + \sum_{i=1}^{i=2} A_i(\nu_n,\ s)l_i\sinh l_i z\right\}$$

$$-\sum_{n=1}^{\infty} S_0(\nu_n,\ r)\left\{B(\nu_n,\ s)l_3^2\sinh l_3 z + \nu_n^2\sum_{i=1}^{i=2} l_i A_i(\nu_n,\ s)\sinh l_i z\right\}. \tag{43}$$

Applying the prescribed boundary conditions to the results obtained in Laplace domain, one will have the following simultaneous equations in unknowns $A_i(\nu_n, s)$, $B(\nu_n, s)$:

$$\sum_{i=1}^{i=2} A_i(\nu_n,\ s)(m_i^2 - s^2)\left[\kappa l_i\sinh l_i\left(\frac{h}{2}\right) + h_{s_p}\cosh l_i\left(\frac{h}{2}\right)\right] = \overline{\Phi}^*(\nu_n,\ s), \tag{44}$$

$$(\nu_n^2 + l_3^2)\sum_{i=1}^{i=2} A_i(\nu_n,\ s)\cosh\left(l_i\frac{h}{2}\right) + 2l_3 B(\nu_n,\ s)\cosh\left(l_3\frac{h}{2}\right) = 0, \tag{45}$$

$$J_0(\nu_n a)\left\{B(\nu_n,\ s)l_3^2\sinh\left(l_3\frac{h}{2}\right)+\nu_n^2\sum_{i=1}^{i=2}l_iA_i(\nu_n,\ s)\sinh\left(l_i\frac{h}{2}\right)\right\}$$
$$+\nu_nJ_1(\nu_n a)\left\{B(\nu_n,\ s)\sinh\left(l_3\frac{h}{2}\right)+\sum_{i=1}^{i=2}A_i(\nu_n,\ s)l_i\sinh\left(l_i\frac{h}{2}\right)\right\}=0. \quad (46)$$

Equations (37)–(43) describe the analytical solutions of thermal parameters $\overline{\theta}$, $\overline{u}$, $\overline{\sigma}_{rr}$, $\overline{\sigma}_{zz}$, $\overline{\sigma}_{rz}$, respectively, in Laplace domain, where unknown constants $A_1(\nu_n,\ s)$; $A_2(\nu_n,\ s)$; $B(\nu_n,\ s)$ can be obtained on solving Equations (44)–(46) simultaneously.

3.4 Gaver–Stehfest Algorithm

Definition: The Gaver–Stehfest algorithm [10, 11] has been applied to approximate the time-domain solution using the iteration scheme illustrated by following equation:

$$f(t)\approx f_M(t)$$
$$=\frac{\ln(2)}{t}\sum_{k=1}^{2M}\left[(-1)^{M+k}\left[\sum_{j=\lfloor\left(\frac{k+1}{2}\right)\rfloor}^{j=\min(k,M)}\frac{j^{M+1}}{M!}\binom{M}{j}\binom{2j}{j}\binom{j}{k-j}\right]\cdot\overline{f}\left(\frac{k\ln(2)}{t}\right)\right], \quad (47)$$

where $\lfloor x\rfloor$ is the flooring function and $2M$ is an even integer whose value depends on the word length of the computer used.

3.5 The Convergence Criterion

Convergence Theorem: Following Kuznetsov [16], assume that $f:(0,\ \infty)\longrightarrow\mathbb{R}$ is a locally integrable function such that its Laplace transform $\overline{f}(s)$ exists for all $s>0$ and the sequence $f_M(t)$ is defined by Eq. (47), then the convergence of sequence $f_M(t)$ depends on the values of the function f in the neighborhood of t. If f has bounded variation in the neighborhood of t then $f_n(t)\rightarrow\dfrac{f(t+0)+f(t-0)}{2}$ as $n\rightarrow\infty$.

4 The Numerical Scheme

Following fractional theory of thermoelasticity by Sherief et al. [4], the thermal variations are studied by numerical values of thermal properties of heat conductor by considering various order (α) of fractional differential coefficient in time variable. As a special case for coupled thermoelasticity ($\alpha \to 0$), Cattaneo approach to generalized fractional thermoelasticity ($\alpha = 0.5,\ 0.98$) and generalized theory of thermoelasticity ($\alpha = 1.0$) are discussed numerically.

4.1 Illustrative Example

Assume that thick circular plate under consideration is subjected to partially distributed axisymmetric heat flux defined for $0 < r_1 < r < a$ and $z = \pm\frac{h}{2}$, described in terms of Heaviside unit step function as follows:

$$\Phi(r,\ t) = \theta_0 H(r - r_1) H(t),\ \text{ for } z = \pm\frac{h}{2} \text{ and } r_1 \in (0,\ a), \tag{48}$$

$$\overline{\Phi}^*(\nu_n,\ s) = \frac{\theta_0}{s\nu_n}\left[a J_1(a\nu_n) - r_1 J_1(r_1\nu_n)\right], \tag{49}$$

where θ_0 is strength of partially distributed heat flux.

4.2 Dimensions and Material Properties

Assuming following dimensions for numerical computations:
The radius $a = 1.0$ m,
The radius of inner annular region $r_1 = 0.5$ m.
The thickness of the circular plate $h = 0.3$ m.
Following Hussein [5], the numerical scheme has been applied for **copper material** with physical properties (with **SI-units**) given as

$$\alpha_t = 1.78 \times 10^{-5}\ \mathrm{K}^{-1},\ \beta^2 = 4,\ \epsilon = 0.0168\,\mathrm{N\,m\,J}^{-1},$$
$$\theta_0 = 373.15\,\mathrm{K}\ \kappa = 386\,\mathrm{J\,K}^{-1}\,\mathrm{m}^{-1}\,\mathrm{s}^{-1},$$
$$h_{pl} = h_{cr} = 10\,\mathrm{W\,m}^{-2}\,\mathrm{K}^{-1}\mathrm{J\,K}^{-1}\,\mathrm{s}^{-1}, \lambda = 7.76 \times 10^{10}\mathrm{N\,m}^{-2},$$
$$\mu = 3.86 \times 10^{10}\,\mathrm{N\,m}^{-2},$$
$$\rho = 8954\,\mathrm{kg\,m}^{-3},\ \tau_0 = 0.025\,\mathrm{s},\ c_e = 383.1\,\mathrm{J\,Kg}^{-1}\,\mathrm{K}^{-1},\ T_0 = 293\,\mathrm{K},$$
$$c = 4.158 \times 10^3\,\mathrm{m\,s}^{-1}.$$

The nondimensional variations of temperature θ, displacement u, and thermal stresses σ_{rr}, σ_{zz}, σ_{rz} are computed numerically for first ten positive roots of transcendental equation (35) for radius $a = 1.0$ are $\nu_n = [0.2278,\ 3.8389,\ 7.0189,\ 10.1760,\ 13.3253,\ 16.4720,\ 19.6169,\ 22.7609,\ 25.9049,\ 29.0468]$.

5 Results and Discussion

Gaver–Stehfest algorithm [7, 8] has been applied to Eqs. (37)–(44) for inversion of Laplace transform to obtain the time-domain solutions for the fixed value $t = 0.1$ s. The numerically computed results are hereby plotted for $0 \leq r \leq 1$ fixing $z = 0.0$ and $-0.15 \leq z \leq 0.15$ with fixed $r = 0.5$ in radial and axial directions and shown by Figs. 1, 2, 3, 4, 5, 6, 7, 8, 9, and 10, respectively.

Figures 1 and 2 illustrate the nondimensional change in temperature θ inside the elastic body in radial and axial directions, respectively. It is seen from the figures that initially the magnitude of temperature is maximum for all the fractional orders and as radial or axial space increases the absolute temperature reduces. It can be seen that the absolute temperature is inversely proportional to the fractional order applied.

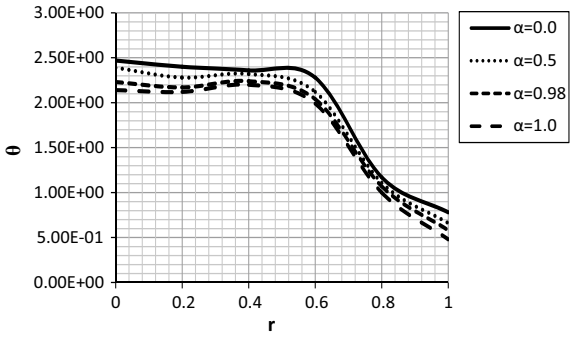

Fig. 1 Distribution of temperature θ in radial direction

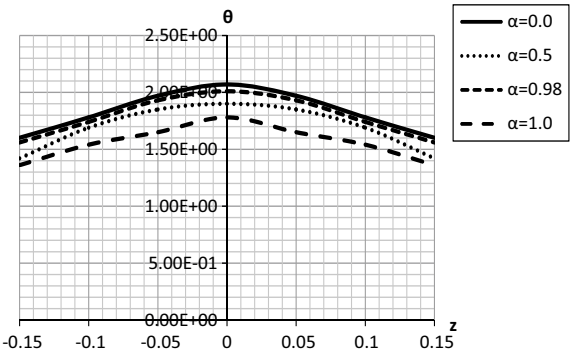

Fig. 2 Distribution of temperature θ in axial direction

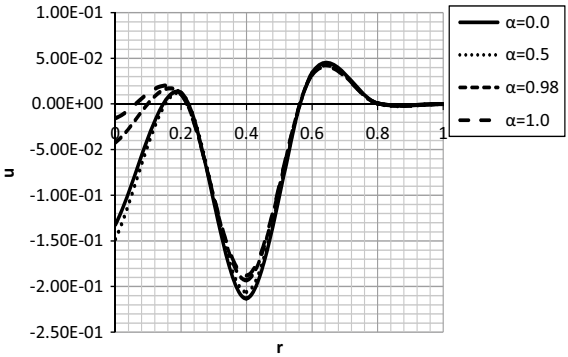

Fig. 3 Distribution of displacement u in radial direction

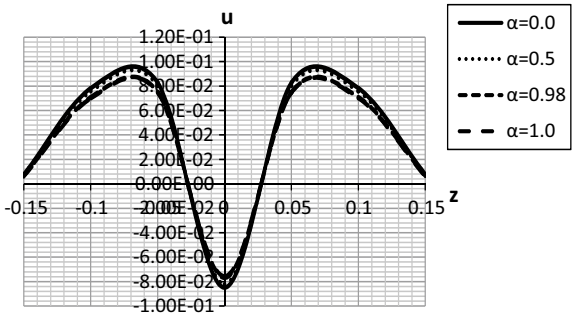

Fig. 4 Distribution of displacement u in axial direction

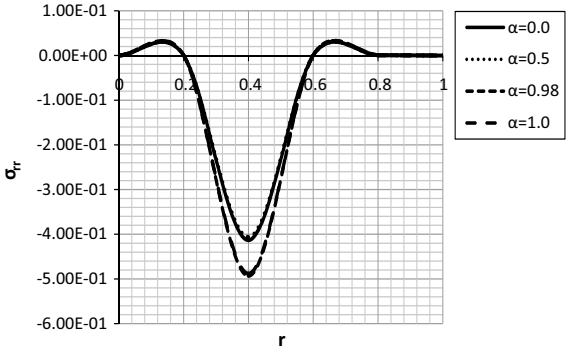

Fig. 5 Distribution of radial stress σ_{rr} in radial direction

Figures 3 and 4 exhibit the nondimensional displacement u inside the thick plate in radial and axial directions. The displacement is attaining positive and negative values as and when the space varies in both the sense and reaches zero at the extreme ends. One can note that as and when the values of fractional order α increase the peak of displacement decreases, or alternatively the change in displacement is inversely proportional to the fractional order α considered.

Figures 5 and 6 depict the nondimensional variations of radial thermal stresses σ_{rr} in radial and axial sense. Observing the results around $0.2 < r < 0.8$. Axially the

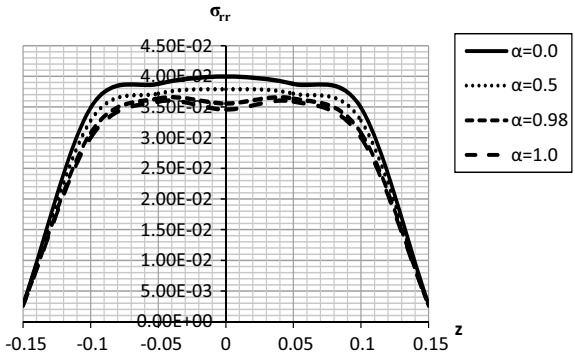

Fig. 6 Distribution of radial stress σ_{rr} in axial direction

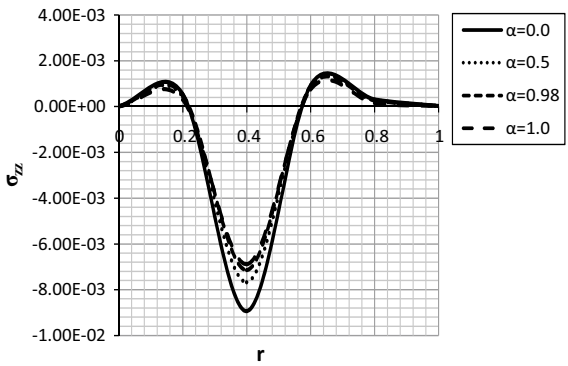

Fig. 7 Distribution of axial stress σ_{zz} in radial direction

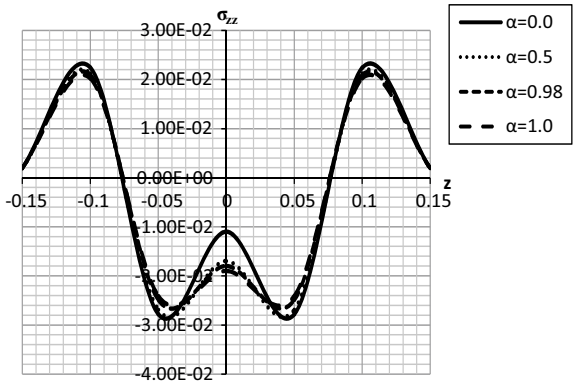

Fig. 8 Distribution of axial stress σ_{zz} in axial direction

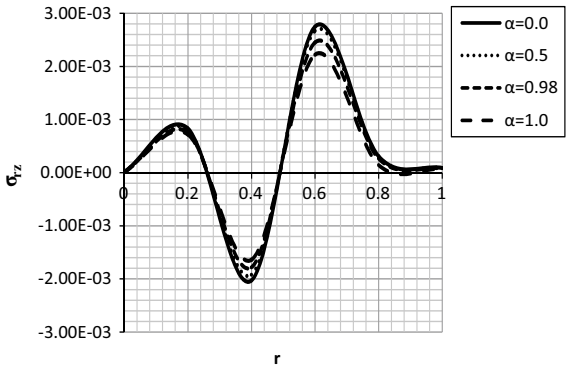

Fig. 9 Distribution of shear stress σ_{rz} in radial direction

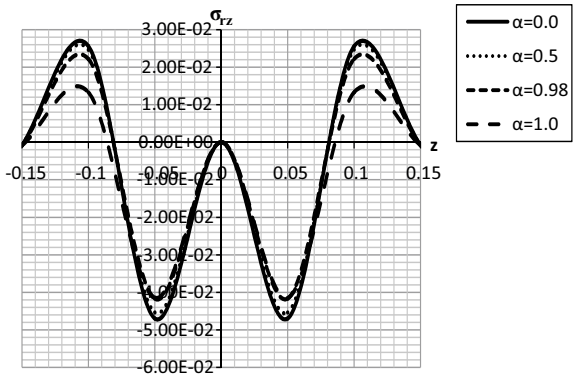

Fig. 10 Distribution of shear stress σ_{rz} in axial direction

stresses attain peak at middle plane $z = 0$ and attaining zero at both ends. It has been found that the radial stresses σ_{rr} are inversely proportional to the fractional order α.

Figures 7 and 8 show the plots of the nondimensional variations of axial stress σ_{zz} in radial and axial sense. The patterns of axial stresses show compressive and tensile behavior symmetrically. It has been found that the radial stresses σ_{zz} are inversely proportional to the fractional order α.

Figures 9 and 10 show the plots of the nondimensional variations of shear stress σ_{rz} in radial and axial sense. The patterns of shear stresses show compressive and tensile behavior symmetrically. It has been found that the radial stresses σ_{rz} are inversely proportional to the fractional order α.

From Figs. 1, 2, 3, 4, 5, 6, 7, 8, 9, and 10, one can see that whenever fractional order α approaches to zero the heat conduction equation (4) becomes parabolic and represents classical theory of thermoelasticity. Moreover, while fractional order α tends to unity, then the heat equation of this model becomes hyperbolic and expresses generalized thermoelasticity theory derived by Lord and Shulman [17].

6 The Concluding Remarks

In this manuscript, an attempt is made to investigate the thermal behavior of an elastic body in the form of a thick circular plate. Considering microstructural heat interactions due to the external heat flux applied to the body, a mathematical model has been designed in the context of fractional calculus and thermoelasticity theory and thermal-related parameters are obtained numerically and depicted graphically. The concluding remarks summarizing the entire work are given below:

1. As per generalized theory deduced by Lord and Shulman [17], due to the application of positive values of relaxation time τ_0 the heat conduction equation (4), it becomes hyperbolic for $\alpha = 1$ and hence the finite speed of thermal wave propagation has been attained.

2. The results obtained for temperature, displacement, and stresses are mathematically stable and satisfying all the initial and boundary conditions of the presented model.

3. Since the resulting expressions for thermal parameters obtained in Laplace domain are given in terms of hyperbolic functions that are multiplied to Bessel functions, they are integrable and of finite exponential orders. Therefore, it can be concluded that the method of inversion of Laplace transforms proposed by Gaver and Stehfest [10, 11] is convergent for the model and satisfies the stability criterion derived by Kunezentov [16].

4. Usually, the heat conduction models of thick circular plates are required to investigate the thermal changes when the plate is subjected to internal or external heating. The mathematical model presented in this manuscript investigates the thermal properties of a thick circular plate subjected to an axisymmetric external heat source. The finite speed of thermal waves has been achieved due to the application of one-relaxation time τ_0 in association with Caputo time fractional derivative of order $\alpha \in (0, 1)$. The presented model can further be investigated for dual- and triple-phase-lag heat conduction problems related to science and engineering. Following Cotterell and Perks [9], practically the presented heat conduction model is especially useful in solving the aerospace engineering problems.

5. According to this work, the fractional order α becomes a new investigator to categorize various materials as per their ability of heat conduction.

References

1. Povstenko YZ (2005) Fractional heat conduction equation and associated thermal stress. J Therm Stress 28:83–102. https://doi.org/10.1080/014957390523741
2. Povstenko YZ (2009) Thermoelasticity that uses fractional heat conduction equation. J Math Sci 162:296–305. https://doi.org/10.1007/s10958-009-9636-3
3. Caputo M (1967) Linear models of dissipation whose Q is almost frequency independent-II. Geophy J Int. 13:529–539. https://doi.org/10.1111/j.1365-246X.1967.tb02303.x
4. Sherief HH, El-Sayed A, El-Latief A (2010) Fractional order theory of thermoelasticity. Int J Solid Struct 47:269–275. https://doi.org/10.1016/j.ijsolstr.2009.09.034

5. Hussein EM (2015) Fractional order thermoelastic problem for an infinitely long circular cylinder. J Therm Stress 38:133–145. https://doi.org/10.1080/01495739.2014.936253
6. Tripathi JJ, Kedar GD, Deshmukh KC (2016) Dynamic problem of fractional order thermoelasticity for a thick circular plate with finite wave speeds. J Therm Stress 39:220–230. https://doi.org/10.1080/01495739.2015.1124646
7. Sherief HH, Raslan WE (2019) Fundamental solution for a line source of heat in the fractional order theory of thermoelasticity using the new Caputo definition. J Therm Stress 42(1):18–28. https://doi.org/10.1080/01495739.2018.1525330
8. Sherief, H. H., Hamza, F. A., El-latief Abd, A. M.: Wave propagation study for axisymmetric 2D problems of a generalized thermo-visco-elastic half space . J. Therm. Stresses. https://doi.org/10.1080/01495739.2019.1587326
9. Cotterell B, Parkes EW (1960) Thermal buckling Of circular plates. Ministry of Aviation, Aeronautical Research Council, Reports and memoranda No. **3245***, (1960). http://naca.central.cranfield.ac.uk/reports/arc/rm/3245.pdf
10. Gaver DP (1966) Observing stochastic processes and approximate transform inversion. Oper Res 14:444–459. https://doi.org/10.1287/opre.14.3.444
11. Stehfest H (1970) Algorithm 368, numerical inversion of Laplace transforms. Asson Comput Mach 13:47–49. https://doi.org/10.1145/361953.361969
12. Kilbas AA, Srivastava HM, Trujillo JJ (2006) Theory and applications of fractional differential equations. Elsevier, New-York
13. Pan I, Das S (2013) Intelligent fractional order systems and control: an introduction. Springer, New-York
14. Miller K, Ross B (1993) An introduction to the fractional calculus and fractional differential equations. Wiley, Inc, New York
15. Özisik MN (1968) Boundary value problems of heat conduction. International Textbook Company, Scranton, Pennsylvania
16. Kuznetsov A (2013) On the convergence of the Gaver-Stehfest algorithm. J Numer Anal 51:2984–2998. https://doi.org/10.1137/13091974X
17. Lord HW, Shulman Y (1967) A generalized dynamical theory of thermoelasticity. J Mech 15(5):299–309. https://doi.org/10.1016/0022-5096(67)90024-5

A Study on Free Vibration Behavior of Microbeam Under Large Static Deflection Using Modified Couple Stress Theory

Sujash Bhattacharya and Debabrata Das

Abstract The free vibration behavior of a statically deflected Timoshenko microbeam under uniformly distributed static load is studied based on modified couple stress theory. In the first step of the analysis, the beam configuration under large static deflection is obtained through a nonlinear static analysis in which the governing equations are derived employing minimum potential energy principle and incorporating von Karman geometric nonlinearity. In the subsequent step, the free vibration behavior of the statically deflected microbeam is investigated employing Hamilton's principle and incorporating the tangent stiffness of the statically deflected beam configuration. The solutions of the governing equations for both the steps are obtained by approximating the displacement fields following Ritz method. The model is validated using the available results in the literature for some reduced problems. The results for the first two vibration modes are presented in nondimensional frequency–amplitude plane for clamped, simply supported, and clamped–simply supported beams.

Keywords Microbeam · Timoshenko beam · Modified couple stress theory · Free vibration · Geometric nonlinearity

1 Introduction

With modern technological advancements, the use of micro- and nano-sized structural elements such as beams and plates is becoming evident in various engineering applications such as micro- and nano-electro-mechanical systems (MEMS and NEMS), vibration shock absorbers, atomic force microscopes, resonant testing equipments, electrostatically excited micro-actuators, micro-switches, etc. As a result, the scientists and engineers are attracted to this interesting and challenging field involving the experimental and theoretical study of microstructure-dependent behavior of beams and plates. Lam et al. [1] conducted experiments on micro-sized beams and showed that its bending rigidity and stiffness are higher than that predicted by

S. Bhattacharya · D. Das (✉)
Department of Mechanical Engineering, Jadavpur University, Kolkata 700032, India
e-mail: debabrata.das@jadavpuruniversity.in

D. Maity et al. (eds.), *Advances in Fluid Mechanics and Solid Mechanics*,
Lecture Notes in Mechanical Engineering,
https://doi.org/10.1007/978-981-15-0772-4_14

the classical beam theories. Over the past few years, various nonlocal and/or size-dependent theories were developed to capture the size effects of micro- and nano-sized beams, and modified couple stress theory (MCST) and strain gradient elasticity theory are the two major theories in this regard that are being widely considered by the researchers. Kong et al. [2] analytically investigated the size-dependent dynamic behavior of Euler–Bernoulli beam using MCST and employing Hamilton's principle. Based on MCST and Hamilton's principle, a microstructure-dependent Timoshenko beam model was developed by Ma et al. [3] using a variational formulation. Based on MCST, Asghari et al. [4] developed a nonlinear size-dependent Timoshenko beam model and presented results for static bending and free vibration of a hinged-hinged beam. Based on MCST, Dehrouyeh-Semnani and Nikkhah-Bahrami [5] carried out a parametric study to investigate the effect of size-dependent shear deformation on static bending, buckling and free vibration behavior of microbeams employing both classical and first shear deformation beam theories. Noori et al. [6] developed a higher order microbeam model to study the natural frequencies of vibration for different length-scale parameters and boundary conditions. In the current study, it is shown how Timoshenko microbeams dynamically behave when subjected to large static deflection, using MCST.

In the present work, the free vibration behavior of a statically deflected microbeam under uniformly distributed static load is studied based on MCST and the mathematical formulation is based on Timoshenko beam theory (TBT). This problem has been addressed for the first time through this work. In the first step of the problem, the beam configuration under large static deflection is obtained through a nonlinear static analysis in which the governing equations are derived employing minimum potential energy principle and incorporating von Karman geometric nonlinearity. In the subsequent step, the free vibration behavior of the deflected microbeam is investigated employing Hamilton's principle and incorporating the tangent stiffness of the statically deflected beam configuration. The solutions of the governing equations for both the steps are obtained by approximating the displacement fields following Ritz method. The results for the first two vibration modes are presented in nondimensional frequency–amplitude plane for clamped, simply supported, and clamped–simply supported beams.

2 Mathematical Formulation

A uniform beam with length L, width b, and thickness h is considered as shown in Fig. 1 where the x- and z- axes are along the axial and thickness directions of the beam. Considering TBT, the normal strain (ε_{xx}) and the shear strain (γ_{xz}) are given by

$$\varepsilon_{xx} = \frac{\mathrm{d}u}{\mathrm{d}x} - z\frac{\mathrm{d}\psi}{\mathrm{d}x} + \frac{1}{2}\left(\frac{\mathrm{d}w}{\mathrm{d}x}\right)^2 \tag{1a}$$

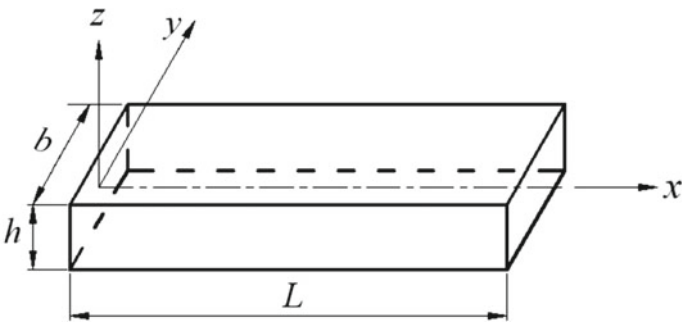

Fig. 1 Beam with dimensions and coordinate axes

$$\gamma_{xz} = \frac{\mathrm{d}w}{\mathrm{d}x} - \psi, \tag{1b}$$

where the term $\frac{1}{2}\left(\frac{\mathrm{d}w}{\mathrm{d}x}\right)^2$ accounts for von Karman-type geometric nonlinearity. Here, u and w are the axial and transverse displacement fields of the midplane and ψ is the rotation field of beam section about the midplane.

The governing equations for the static problem are derived employing the principle of minimum potential energy given by

$$\delta(U + V) = 0, \tag{2}$$

where U is the total strain energy, V is the potential energy of uniformly distributed load with intensity p (N/m), and δ is the variational operator.

Here,

$$U = U_{\mathrm{n}} + U_{\mathrm{s}} + U_{\mathrm{c}}, \tag{3}$$

where U_{n} is the normal strain energy, U_{s} is the shear strain energy, and U_{c} is the strain energy due to modified couple stress. According to MCST [3], the couple stress tensor ($\mathbf{m}$) is symmetric and the symmetric part of the curvature tensor ($\boldsymbol{\chi}$) is the only conjugate strain measure to contribute to the strain energy U_{c}. For the present one-dimensional problem involving beam, the only nonzero component of $\boldsymbol{\chi}$ is

$$\chi_{xy} = \frac{1}{2}\left(-\frac{\partial \psi}{\partial x} - \frac{\partial^2 w}{\partial x^2}\right). \tag{4}$$

The following one-dimensional constitutive relations [7] are employed to obtain the nonzero components of the classical stress tensor and the couple stress tensor: $\sigma_{xx} = E\varepsilon_{xx}, \sigma_{xz} = G\gamma_{xz}, m_{xy} = Gl^2\chi_{xy}$, where l is the material length-scale parameter, E is the Young's modulus, and G is the shear modulus given by $G = E/\{2(1+\upsilon)\}$ with υ being the Poisson's ratio. The various strain energies and work potential are derived to the form given below:

$$U_{\mathrm{n}} = \frac{EA}{2}\int_0^L \left[\left(\frac{\mathrm{d}u}{\mathrm{d}x}\right)^2 + \frac{1}{4}\left(\frac{\mathrm{d}w}{\mathrm{d}x}\right)^4 + \left(\frac{\mathrm{d}w}{\mathrm{d}x}\right)^2\left(\frac{\mathrm{d}u}{\mathrm{d}x}\right)\right]\mathrm{d}x + \frac{EI}{2}\int_0^L \left(\frac{\mathrm{d}\psi}{\mathrm{d}x}\right)^2 \mathrm{d}x, \tag{5a}$$

$$U_{\mathrm{s}} = \frac{kGA}{2}\int_0^L \left\{\left(\frac{\mathrm{d}w}{\mathrm{d}x}\right)^2 - 2\left(\frac{\mathrm{d}w}{\mathrm{d}x}\right)\psi + \psi^2\right\}\mathrm{d}x, \tag{5b}$$

$$U_{\mathrm{c}} = \frac{GAl^2}{8}\int_0^L \left\{\left(\frac{\mathrm{d}^2w}{\mathrm{d}x^2}\right)^2 + \left(\frac{\mathrm{d}\psi}{\mathrm{d}x}\right)^2 + 2\left(\frac{\mathrm{d}^2w}{\mathrm{d}x^2}\right)\left(\frac{\mathrm{d}\psi}{\mathrm{d}x}\right)\right\}\mathrm{d}x, \tag{5c}$$

$$V = -\int_0^L w(p\mathrm{d}x), \tag{5d}$$

where $A\,(= bh)$ and $I\,(= bh^3/12)$ are the cross-sectional area and area moment of inertia and k is the shear correction factor given by

$$k = \frac{5(1+\nu)}{6+5\nu}. \tag{6}$$

The displacement fields are approximated using Ritz method as follows:

$$u(x) = \sum_{i=1}^{nu} c_i\phi_i^u(x),\ w(x) = \sum_{i=nu+1}^{nu+nw} c_i\phi_{i-nu}^w(x),\ \psi(x) = \sum_{i=nu+nw+1}^{nu+nw+nr} c_i\phi_{i-nu-nw}^r(x), \tag{7}$$

where ϕ_i^u, ϕ_i^w, and ϕ_i^r are the set of orthogonal admissible functions and c_i is the set of unknown parameters which are to be determined. The lowest order admissible functions for clamped (CC), simply supported (SS), and clamped–simply supported (CS) beams are selected to satisfy the geometric boundary conditions [8]. Putting the expressions of assumed displacement fields given by (7) in (5a)–(5d) and applying Eq. (2), the governing equations are obtained as

$$\left[K_{ji}^T\right]\{c_i\} = \left\{f_j\right\}. \tag{8}$$

Considering $n1 = nu, n2 = nu + nw, n3 = nu + nw + nr$, the nonzero components of the total stiffness matrix $\left(\left[K_{ji}^T\right]\right)$ and the load vector $\left(\{f_j\}\right)$ are given below:

$$\left[K_{ji}^T\right]_{\substack{j=1,n1\\i=1,n1}} = EA\int_0^L \frac{\mathrm{d}\phi_i^u}{\mathrm{d}x}\frac{\mathrm{d}\phi_j^u}{\mathrm{d}x},$$

$$\left[K_{ji}^T\right]_{\substack{j=1,n1\\i=n1+1,n2}} = \frac{EA}{2}\int_0^L \left(\frac{\mathrm{d}w}{\mathrm{d}x}\right)\frac{\mathrm{d}\phi_{i-n1}^w}{\mathrm{d}x}\frac{\mathrm{d}\phi_j^u}{\mathrm{d}x}\mathrm{d}x,$$

$$\left[K_{ji}^T\right]_{\substack{j=n1+1,n2\\i=n1+1,n2}} = EA\int_0^L \left\{\left(\frac{\mathrm{d}u}{\mathrm{d}x}\right)\frac{\mathrm{d}\phi_{i-n1}^w}{\mathrm{d}x}\frac{\mathrm{d}\phi_{j-n1}^w}{\mathrm{d}x}\mathrm{d}x + \frac{1}{2}\int_0^L \left(\frac{\mathrm{d}w}{\mathrm{d}x}\right)^2\frac{\mathrm{d}\phi_{i-n1}^w}{\mathrm{d}x}\frac{\mathrm{d}\phi_{j-n1}^w}{\mathrm{d}x}\mathrm{d}x\right\}$$
$$+ kGA\int_0^L \frac{\mathrm{d}\phi_{i-n1}^w}{\mathrm{d}x}\frac{\mathrm{d}\phi_{j-n1}^w}{\mathrm{d}x}\mathrm{d}x + \frac{GAl^2}{4}\int_0^L \frac{\mathrm{d}^2\phi_{i-n1}^w}{\mathrm{d}x^2}\frac{\mathrm{d}^2\phi_{j-n1}^w}{\mathrm{d}x^2}\mathrm{d}x,$$

$$\left[K_{ji}^T\right]_{\substack{j=n1+1,n2\\i=n2+1,n3}} = -kGA\int_0^L \phi_{i-n2}^r\frac{\mathrm{d}\phi_{j-n1}^w}{\mathrm{d}x}\mathrm{d}x + \frac{GAl^2}{4}\int_0^L \frac{\mathrm{d}\phi_{i-n2}^r}{\mathrm{d}x}\frac{\mathrm{d}^2\phi_{j-n1}^w}{\mathrm{d}x^2}\mathrm{d}x,$$

$$\left[K_{ji}^T\right]_{\substack{j=n2+1,n3\\i=n1+1,n2}} = -kGA\int_0^L \frac{\mathrm{d}\phi_{i-n1}^w}{\mathrm{d}x}\phi_{j-n2}^r\mathrm{d}x + \frac{GAl^2}{4}\int_0^L \frac{\mathrm{d}^2\phi_{i-n1}^w}{\mathrm{d}x^2}\frac{\mathrm{d}\phi_{j-n2}^r}{\mathrm{d}x}\mathrm{d}x,$$

$$\left[K_{ji}^T\right]_{\substack{j=n2+1,n3\\i=n2+1,n3}} = EI\int_0^L \frac{\mathrm{d}\phi_{i-n2}^r}{\mathrm{d}x}\frac{\mathrm{d}\phi_{j-n2}^r}{\mathrm{d}x}\mathrm{d}x + kGA\int_0^L \phi_{i-n2}^r\phi_{j-n2}^r\mathrm{d}x$$
$$+ \frac{GAl^2}{4}\int_0^L \frac{\mathrm{d}\phi_{i-n2}^r}{\mathrm{d}x}\frac{\mathrm{d}\phi_{j-n2}^r}{\mathrm{d}x}\mathrm{d}x,$$

$$\left\{f_j\right\}_{j=1,n1} = 0, \left\{f_j\right\}_{j=n1+1,n2} = p\int_0^L \phi_{j-n1}^w\mathrm{d}x, \left\{f_j\right\}_{j=n2+1,n3} = 0. \tag{9}$$

Equation (8) is nonlinear involving unknown parameters c_i and solved by an iterative substitution method with successive relaxation. The solution provides the deflected configuration of the beam.

The governing equation for free vibration of the statically deformed microbeam is derived using Hamilton's principle given by

$$\delta\left(\int_{t_1}^{t_2}(T_k - U)dt\right) = 0, \tag{10}$$

where t is time and T_k is the kinetic energy of the microbeam which is given as

$$T_k = \frac{\rho A}{2} \int_0^L \left\{ \left(\frac{\mathrm{d}w}{\mathrm{d}t} \right)^2 + \left(\frac{\mathrm{d}u}{\mathrm{d}t} \right)^2 \right\} \mathrm{d}x + \frac{\rho I}{2} \int_0^L \left(\frac{\mathrm{d}\psi}{\mathrm{d}t} \right)^2 \mathrm{d}x, \tag{11}$$

where ρ is density of the material of the beam. For investigating the small amplitude free vibration behavior, the tangent stiffness of the deflected beam configuration is to be considered. Using the relationship $\left[K_{ji}^t\right] = \frac{\partial}{\partial c_i}\left\{F_j^{rs}\right\}$ [8], the elements of the tangent stiffness matrix are derived where $\left\{F_j^{rs}\right\}$ is the restoring force vector defined as

$$\left\{F_j^{rs}\right\} = \left[K_{ji}^T\right]\{c_i\}. \tag{12}$$

The linear components of the total and tangent stiffness matrices are same. The nonlinear components of $\left[K_{ji}^t\right]$ are as follows:

$$\begin{aligned}
\left[K_{ji}^t\right]_{\substack{j=1,n1 \\ i=n1+1,n2}} &= EA \int_0^L \left(\frac{\mathrm{d}w}{\mathrm{d}x} \right) \frac{\mathrm{d}\phi_{i-n1}^w}{\mathrm{d}x} \frac{\mathrm{d}\phi_j^u}{\mathrm{d}x} \mathrm{d}x, \\
\left[K_{ji}^t\right]_{\substack{j=n1+1,n2 \\ i=1,n1}} &= EA \int_0^L \left(\frac{\mathrm{d}w}{\mathrm{d}x} \right) \frac{\mathrm{d}\phi_i^u}{\mathrm{d}x} \frac{\mathrm{d}\phi_{j-n1}^w}{\mathrm{d}x} \mathrm{d}x, \\
\left[K_{ji}^t\right]_{\substack{j=n1+1,n2 \\ i=n1+1,n2}} &= EA \left[\int_0^L \left(\frac{\mathrm{d}u}{\mathrm{d}x} \right) \frac{\mathrm{d}\phi_{i-n1}^w}{\mathrm{d}x} \frac{\mathrm{d}\phi_{j-n1}^w}{\mathrm{d}x} \mathrm{d}x + \frac{3}{2} \int_0^L \left(\frac{\mathrm{d}w}{\mathrm{d}x} \right)^2 \frac{\mathrm{d}\phi_{i-n1}^w}{\mathrm{d}x} \frac{\mathrm{d}\phi_{j-n1}^w}{\mathrm{d}x} \mathrm{d}x \right].
\end{aligned} \tag{13}$$

The dynamic displacement and rotation fields are approximated as

$$u = \sum_{i=1}^{nu} d_i \phi_i^u(x) e^{\mathrm{i}\omega t}, \; w = \sum_{i=nu+1}^{nu+nw} d_i \phi_{i-nu}^w(x) e^{\mathrm{i}\omega t}, \; \psi = \sum_{i=nu+nw+1}^{nu+nw+nr} d_i \phi_{i-nu-nw}^r(x) e^{\mathrm{i}\omega t}, \tag{14}$$

where d_i is the set of unknown coefficients determining vibration mode shape, ω is the natural frequency of vibration, and $\mathrm{i} = \sqrt{-1}$. Using Eqs. (10) and (11) and the tangent stiffness matrix, and substituting the assumed displacement fields given by (14), the governing equation is derived as an eigenvalue problem as shown below:

$$\left[K_{ji}^t\right]\{d_i\} - \omega^2 \left[M_{ji}\right]\{d_i\} = 0, \tag{15}$$

where $\left[M_{ji}\right]$ is the mass matrix whose off-diagonal terms are zero. The elements of $\left[M_{ji}\right]$ are given as follows:

$$\left[M_{ji}\right]_{\substack{j=1,nu\\ i=1,nu}} = \rho A \int_0^L \phi_i^u \phi_j^u \mathrm{d}x, \left[M_{ji}\right]_{\substack{j=n1+1,n2\\ i=n1+1,n2}} = \rho A \int_0^L \phi_{i-n1}^w \phi_{j-n1}^w \mathrm{d}x, \left[M_{ji}\right]_{\substack{j=n2+1,n3\\ i=n2+1,n3}}$$
$$= \rho I \int_0^L \phi_{i-n2}^r \phi_{i-n2}^r \mathrm{d}x. \tag{16}$$

The solution of Eq. (15) gives the natural frequencies and the corresponding mode shapes.

3 Results and Discussion

The geometrically linear static deflection fields for different l/h values are compared with Ref. [7] for a simply supported Timoshenko beam under sinusoidally varying distributed load (of amplitude p) and it is shown in Fig. 2a. The natural frequencies of vibration for different h/l values for a simply supported Timoshenko beam are compared with Ref. [3] and it is shown in Fig. 2b. The comparison plots for Fig. 2b are generated by considering the three-dimensional form of constitutive relations as used in Ref. [3]. The comparison plots in Fig. 2 matches very well with the available results and thus validate the present model.

The results of the present study are presented in normalized frequency (ω/ω_1) versus static deflection amplitude ($w_{\max}/h$) plane where $w_{\max}$ is the maximum static deflection and ω_1 is the natural frequency of vibration for the first mode. The results are generated with the following values: $l = 17.6 \times 10^{-6}$ m, $E = 200$ GPa, $\nu = 0.30$, $\rho = 7850$ kg/m^3, $L/h = 20$, and $b/h = 2$. Figure 3a and b shows the frequency–amplitude plots for the first two modes of vibration for a CC beam, each corresponding to different h/l values. Similar plots corresponding to different h/l

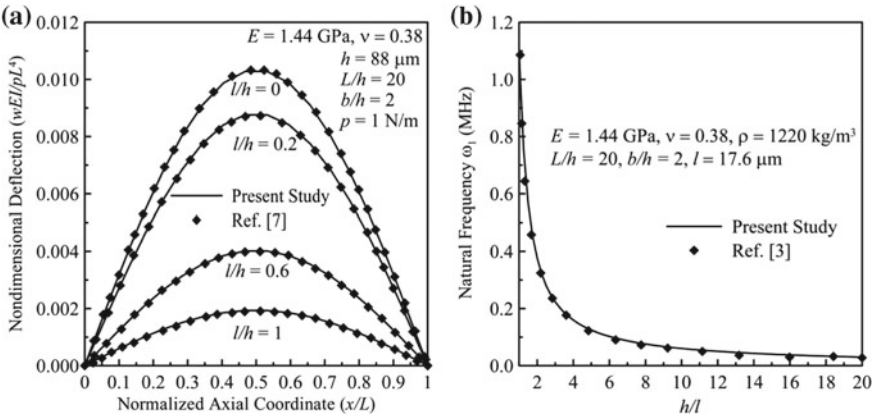

Fig. 2 Validation plots: **a** static deflection fields and **b** natural frequencies of vibration

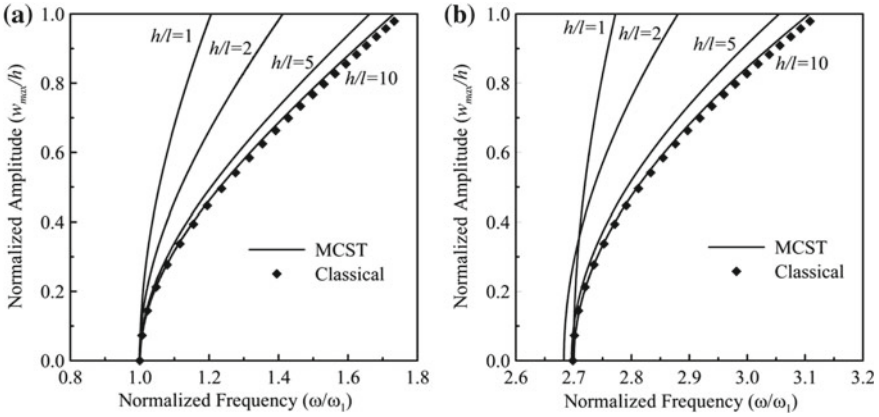

Fig. 3 Normalized frequency versus deflection amplitude plots for a CC beam: **a** first mode and **b** second mode

values are shown in Fig. 4a and b for the first two modes, respectively, for a SS beam and in Fig. 5a and b for the first two modes, respectively, for a CS beam. In each of the figures of Figs. 3, 4 and 5, the frequency–amplitude plots for a classical beam ($l = 0$) are also shown. The results show that with increase in the static deflection for any specific h/l ratio, the beam becomes more stiffer due to geometric stiffening action, thus making the frequency to increase. With increasing h/l ratio, the frequency–amplitude plots get more and more curved from the initial point, and this is true irrespective of the vibration modes and boundary conditions. It indicates that the beam stiffness increases when the thickness becomes comparable with the material length-scale parameter (decreasing h/l) and as a result the geometric stiffening effect due to large deflection becomes subdued. Further, it is observed that the behavior of a

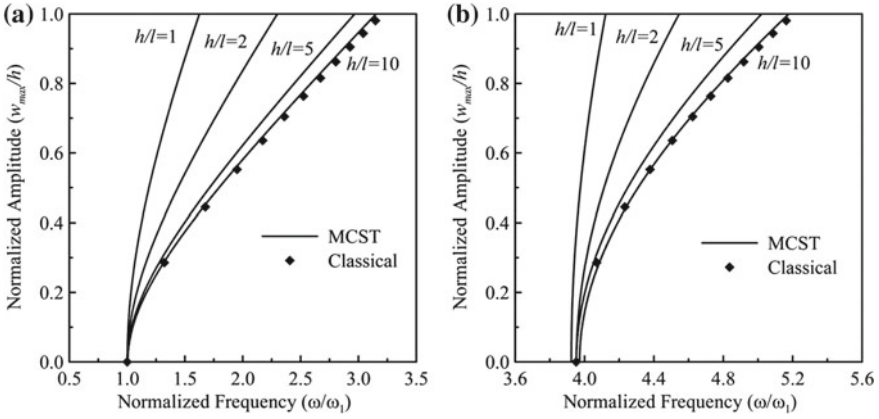

Fig. 4 Normalized frequency versus deflection amplitude plots for a SS beam: **a** first mode and **b** second mode

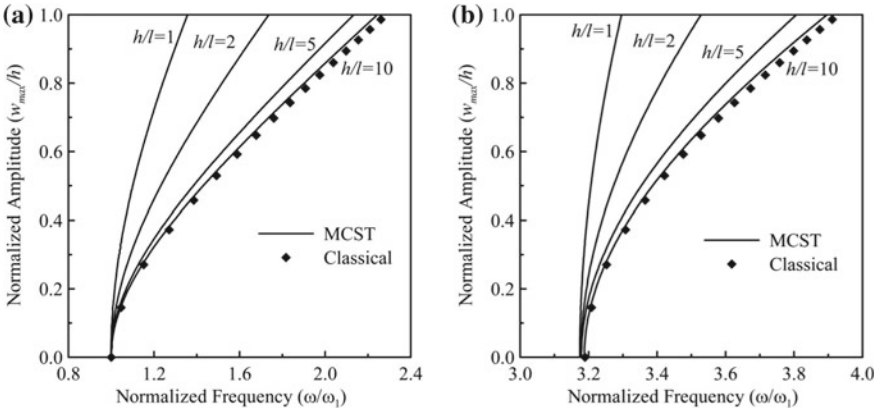

Fig. 5 Normalized frequency versus deflection amplitude plots for a CS beam: **a** first mode and **b** second mode

microbeam becomes almost identical to that of a classical beam when h/l becomes 10 or more. Figures 3, 4, and 5 show that with increase in the deflection level, a SS beam shows maximum increase in frequency, whereas a CC beam exhibits least increase in frequency, and a CS beam comes in between in this regard. Thus, the order of the beams with enhanced geometric stiffening is SS, CS, and CC.

4 Conclusions

The free vibration frequencies of a statically deflected Timoshenko microbeam under uniformly distributed static load are computed based on MCST. The results are presented in nondimensional frequency-static deflection amplitude plane for the first two vibration modes for clamped, simply supported, and clamped–simply supported microbeams. The results indicate that the beam stiffness increases when the thickness becomes comparable with the material length-scale parameter, and as a result the effect of geometric stiffening diminishes on the frequency–amplitude behavior. The size effect is found to disappear when the thickness is ten times or more of the material length-scale parameter.

References

1. Lam DCC, Yang F, Chong ACM, Wang J, Tong P (2003) Experiments and theory in strain gradient elasticity. J Mech Phys Solids 51:1377–1508. https://doi.org/10.1016/S0022-5096(03)00053-X
2. Kong S, Zhou S, Nie Z, Wang K (2008) The size-dependent natural frequency of Bernoulli–Euler micro-beams. Int J Eng Sci 46:427–437. https://doi.org/10.1016/j.ijengsci.2007.10.002

3. Ma HM, Gao XL, Reddy JN (2008) A microstructure-dependent Timoshenko beam model based on a modified couple stress theory. J Mech Phys Solids 56:3379–3391. https://doi.org/10.1016/j.jmps.2008.09.007
4. Asghari M, Kahrobaiyan MH, Ahmadian MT (2010) A nonlinear Timoshenko beam formulation based on the modified couple stress theory. Int J Eng Sci 48:1749–1761. https://doi.org/10.1016/j.ijengsci.2010.09.025
5. Dehrouyeh-Semnani AM, Nikkhah-Bahrami M (2015) The influence of size dependent shear deformation on mechanical behavior of microstructures-dependent beam based on modified couple stress theory. Compos Struct 123:325–336. https://doi.org/10.1016/j.compstruct.2014.12.038
6. Noori J, Fariborz SJ, Vafa JP (2016) A higher-order micro-beam model with application to free vibration. Mech Adv Mater Struct 23:443–450. https://doi.org/10.1080/15376494.2014.984090
7. Reddy JN (2011) Microstructure-dependent couple stress theories of functionally graded beams. J Mech Phys Solids 59:2382–2399. https://doi.org/10.1016/j.jmps.2011.06.008
8. Das D (2016) A new tangent stiffness based formulation to study the free vibration behavior of transversely loaded Timoshenko beam with geometric non-linearity. J Vib Control 24:1716–1727. https://doi.org/10.1177/1077546316668457

Fatigue Life Estimation of a Box Girder Bridge Using Coupled and Uncoupled Bridge–Vehicle Dynamics

Anjaly J. Pillai, Suvendu Parida and Sudip Talukdar

Abstract In the present paper, fatigue life of a steel box girder bridge has been evaluated by two approaches and the influencing parameters on fatigue life have been studied. In the first approach, the box girder bridge has been idealized as a Euler–Bernoulli beam and the coupled bridge–vehicle equations are developed. In the second approach, vehicle equations are first solved taking bridge as rigid. The pavement force found from the vehicle response and road roughness has been given as input in 3-D FEM model created in CSI Bridge. Fatigue life of the bridge component at the critical location has been found out using Miner approach and the stress time history from coupled and uncoupled schemes has been used for comparison purpose. The parameters which affect the fatigue life, i.e., velocity of the vehicle and road surface roughness are varied to observe the effect on fatigue life.

Keywords Fatigue life · Box girder bridge · Coupled scheme · Uncoupled scheme

1 Introduction

The interaction between the bridge and the movement of the vehicles is a coupled dynamic problem. Conventionally, majority of the research has been focussed on obtaining the bridge response by approximating the moving vehicle as a number of moving loads. The essential dynamic characteristics of the bridge are captured by the moving load model with sufficient accuracy. In this model, the effect of interaction between the bridge and the vehicle is ignored. Due to this reason, the moving load model works well for cases where the mass of the vehicle is smaller in relative to that of the bridge [1]. For cases where the mass of the vehicle cannot be ignored, the effect of interaction between bridge and vehicles should be considered.

In order to include the interaction between bridge and vehicles, the elastic effects of the tires and suspension mechanisms are modeled by springs and the damping effects of tires and suspension systems are modeled by dashpots [2, 3]. Therefore, a

A. J. Pillai (✉) · S. Parida · S. Talukdar
Department of Civil Engineering, Indian Institute of Technology Guwahati, Guwahati, India
e-mail: anjalypillai@iitg.ac.in

D. Maity et al. (eds.), *Advances in Fluid Mechanics and Solid Mechanics*,
Lecture Notes in Mechanical Engineering,
https://doi.org/10.1007/978-981-15-0772-4_15

multi-axle truck or tractor trailer can be represented as a number of discrete masses each supported by a set of spring and dashpot [1]. This dynamic interaction between vehicles and structures is analyzed by various researchers [2–5]. In addition, the bridge response significantly depends on the road surface roughness. This is modeled as a stationary Gaussian process which is generated by using certain power spectral density functions to take into account the randomness in nature [1]. The effects of vehicle-induced vibrations and the road surface roughness on bridge response have been studied by various researchers [5–8].

Therefore, the fatigue life of the bridge is affected by the factors mentioned above. Several authors have evaluated the fatigue life considering bridge–vehicle interaction. Rao and Talukdar [8] evaluated fatigue damage in continuous bridge girder based on the stress range frequency histogram. Vehicle-induced time history of maximum flexural stresses has been obtained by Monte Carlo simulation process and utilized to develop the stress range frequency histogram taking into consideration of the annual traffic volume. The cumulative damage index and the fatigue life of the bridge are calculated using the linear damage accumulation theory. Cai and Chen [9] presented the framework of dynamic analysis of coupled three-dimensional vehicle–bridge system. Zhang and Cai [10] evaluated the fatigue reliability assessment of existing bridges considering the random effects of vehicle speed and road-roughness condition. Wang et al. [11] have developed a new approach for fatigue design of steel bridges considering the effect of dynamic vehicle loading and truck overloading. The aim of the paper is to compare the fatigue life obtained from bridge–vehicle coupled and uncoupled dynamics and to examine the effect of vehicle speed and road roughness on fatigue life. The parameters which affect the fatigue life, i.e., velocity of the vehicle and the road surface roughness are varied to compare the same.

2 Road Surface Roughness

The road surface roughness which plays an important role in estimating the fatigue life is described as a stationary Gaussian random field characterized by its power spectral density (PSD) function [12]. The PSD function given by Yin et al. [13] has been used and is shown below:

$$S_{GG}(\Omega_s) = S_{GG}(\Omega_0)\frac{\Omega_0^2}{\Omega_s^2 + \Omega_L^2} \tag{1}$$

where $S_{GG}(\Omega_s)$ is the PSD function of road surface unevenness in m^2/c/m, $S_{GG}(\Omega_0)$ is the road-roughness coefficient in m^2/c/m, Ω_0 is the discontinuity frequency considered as $1/(2\pi)$ c/m, and Ω_L is the lower cut off frequency considered as 0.1 c/m [14].

The road-roughness coefficient as per ISO 8608:1995 for good, medium, and poor road conditions was considered as 64×10^{-6}, 256×10^{-6}, and 1024×10^{-6}, respectively [14].

3 Coupled Scheme

The box girder bridge has been idealized as Euler–Bernoulli beam and the coupled vehicle–bridge equations are developed. The vehicle model corresponds to a quarter car model as shown in Fig. 1.

The equation of motion for sprung mass is given by

$$m_s\ddot{z}_1 + c_s(\dot{z}_1 - \dot{z}_2) + k_s(z_1 - z_2) = 0 \tag{2}$$

The equation of motion for unsprung mass is given by

$$m_w\ddot{z}_2 + c_w\left(\dot{z}_2 - \dot{y} - \dot{h}\right) + k_w(z_2 - y - h) - c_s(\dot{z}_1 - \dot{z}_2) - k_s(z_1 - z_2) = 0 \tag{3}$$

The bridge response is assumed as superposition of the normal modes given as

$$y(x,t) = \sum_{j=1}^{\infty} \phi_j(x)\eta_j(t) \tag{4}$$

where $\phi_j(x)$ is the normalized mode shape in jth mode for simply supported beam. Substituting Eq. (4) in Eq. (3), we get

$$\begin{aligned} &m_w\ddot{z}_2 + (c_s + c_w)\dot{z}_2 + (k_w + k_s)z_2 - c_s\dot{z}_1 - k_s z_1 \\ &- c_w\sum_{j=1}^{\infty}\phi_j(x)\dot{\eta}_j(t) - \sum_{j=1}^{\infty} k_w\phi_j(x)\eta_j(t) = c_w\dot{h} + k_w h \end{aligned} \tag{5}$$

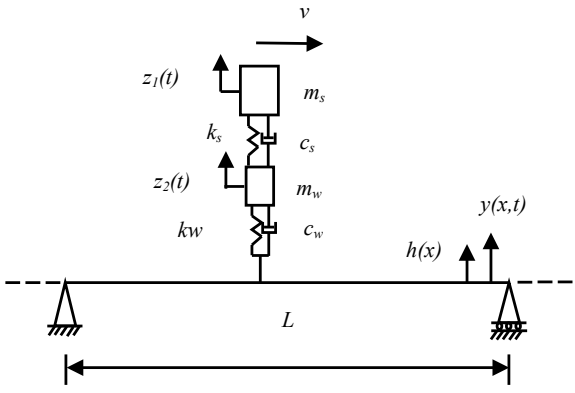

Fig. 1 Vehicle movement on bridge

The equation of motion for the bridge is given as

$$m_w\ddot{z}_2 + (c_s + c_w)\dot{z}_2 + (k_w + k_s)z_2 - c_s\dot{z}_1 - k_s z_1 - c_w\sum_{j=1}^{\infty}\phi_j(x)\dot{\eta}_j(t) - \sum_{j=1}^{\infty}k_w\phi_j(x)\eta_j(t) = c_w\dot{h} + k_w h \tag{6}$$

The equation of motion for the bridge is written considering modal expansion technique for linear system and in view of orthogonal nature of normal modes

$$\begin{aligned}\ddot{\eta}_j(t) + 2\xi\omega_j\dot{\eta}_j(t) + \omega_j^2\eta_j(t) - \frac{c_w}{M_j}\phi_j\{vt\}\dot{z}_2 - \frac{k_w}{M_j}\phi_j\{vt\}z_2 \\ = \frac{-k_w}{M_j}\phi_j\{vt\}h - \frac{c_w}{M_j}\phi_j\{vt\}\dot{h} - (m_s + m_w)g\phi_j\{vt\} \\ - \frac{c_w}{M_j}\int_0^L\left[\sum_{i=1}^{\infty}\phi_i(x)\dot{\eta}_i(t)\phi_j(x)\delta\{x - vt\} = dx\right] \\ - \frac{k_w}{M_j}\int_o^L\left[\sum_{i=1}^{\infty}\phi_i(x)\eta_i(t)\phi_j(x)\delta\{x - vt\}dx\right]; = j = 1, 2, \ldots\end{aligned} \tag{7}$$

In matrix form, the above equations can be written as

$$[M]\left\{\ddot{X}\right\} + [C]\left\{\dot{X}\right\} + [K]\{X\} = \{F(t)\} \tag{8}$$

where $[M]$, $[C]$, and $[K]$ are the mass matrix, damping matrix, and stiffness matrix containing vehicle and bridge degrees of freedom, respectively. The response consists of sprung mass displacement, unsprung mass displacement, and beam modes of vibration. The square matrices are of order (2 + n) where 2 corresponds to the vehicle degrees of freedom and n corresponds to the bridge vibration modes considered. The force vector $\{F(t)\}$ is given as

$$F(t) = \left\{0 \quad k_w h_m + c_w\dot{h}_m \quad Q_1(t) \quad Q_2(t)\ldots Q_k(t)\right\}^T \tag{9}$$

$$Q_k(t) = \frac{1}{M_k}\begin{pmatrix} k_w\left\{z_2(t) - \sum_{k=1}^{n}\phi_k(y)\eta_k(t) - h(x)\right\}\phi_k(y) \\ +c_w\left\{\dot{z}_2(t) - \sum_{k=1}^{n}\phi_k(y)\dot{\eta}_k(t) - \dot{h}(x)\right\}\phi_k(y) \\ -\{m_w + m_s\}g\phi_k(y)\end{pmatrix} \tag{10}$$

where M_k is the generalized mass, $\phi_k(y)$ denotes the mode shape function for simply supported beam, k_w is the tire stiffness, c_w is the damping of the tire, $\eta_k(t)$ is the bridge deflection considering the superposition of the normal modes, $h(x)$ is the road surface roughness at distance x from the left side of the beam consisting of road surface roughness, $h_r(x)$ and mean profile of the bridge, $h_m(x)$, m_w is the mass of the tire, m_s is the mass of the vehicle, $z_2(t)$ is the displacement of the unsprung mass, and $h_m(x)$ is the mean profile of the bridge as shown in Eq. (11).

$$h_m(x) = 0.01 \sin\left(\frac{\pi x}{L}\right) \tag{11}$$

The stress history has been obtained after deriving a closed-form expression of mean and covariance of the response given as

$$X_m(t) = \sum_{j=1}^{2n} u_{m+n,j} \sum_{s=1}^{n} u'_{js} \sum_{k=1}^{n} m'_{sk} \int_{-\infty}^{\infty} H_j(\omega, t) dS[F_k(\omega)];$$
$$m = 1, 2, 3, \ldots, n \tag{12}$$

$$E(X_m(t)) = \sum_{j=1}^{2n} u_{m+n,j} \sum_{s=1}^{n} u'_{js} \sum_{k=1}^{n} m'_{sk} \int_{-\infty}^{\infty} H_j(\omega, t) E\left[dS_{F_k}(\omega)\right];$$
$$m = 1, 2, 3, \ldots, n \tag{13}$$

$$I_{jk}(t) = \int_{-\infty}^{\infty} H_j(\omega, t) E\left[dS_{F_k}(\omega)\right] \tag{14}$$

$$K_{x_i x_k}(t_1, t_2) = \sum_{l=1}^{2n} \sum_{r=1}^{n} \sum_{p=1}^{2n} \sum_{s=1}^{n} \sum_{b=1}^{n} \sum_{w=1}^{n} \left[\begin{matrix} u_{i+n,l} u'_{l,r} \bar{m}_{r,s} u_{k+n,p} u'_{p,b} \bar{m}_{b,w} \\ \left\{ I_{s,b}(t_1, t_2) - I_{ls}(t_1) I_{pb}(t_2) \right\} \end{matrix} \right];$$
$$l, k = 1, 2, ..n \tag{15}$$

$$I_{s,b}(t_1, t_2) = \int_{-\infty}^{\infty} \int_{-\infty}^{\infty} H_l(\omega_1, t_1) H_p^*(\omega_2, t_2) \phi_{F_s F_b}(\omega_1, \omega_2) d\omega_1 d\omega_2 \tag{16}$$

$$\phi_{F_s F_b}(\omega_1, \omega_2) = \left\{ \begin{matrix} 0 \\ (k_t)^2 \phi_{h_R h_R}(\omega_1, \omega_2) + (c_t)^2 \phi_{\dot{h}_R \dot{h}_R}(\omega_1, \omega_2) \\ (k_t / M_k)^2 \phi_k(x_1) \phi_k(x_2) \phi_{h_R h_R}(\omega_1, \omega_2) \\ + (c_t / M_k)^2 \phi_k(x_1) \phi_k(x_2) \phi_{\dot{h}_R \dot{h}_R}(\omega_1, \omega_2) \end{matrix} \right\} \tag{17}$$

$$\phi_{h_R h_R}(\Omega_1, \Omega_2) = \phi_{h_R h_R}(\Omega_1) \delta(\Omega_1 - \Omega_2) \tag{18}$$

$$\phi_{\dot{h}_R \dot{h}_R}(\Omega_1, \Omega_2) = \Omega_1^2 \phi_{h_R h_R}(\Omega_1)\delta(\Omega_1 - \Omega_2) \tag{19}$$

In the above equation, u' denotes the inverse of the eigenvector matrix, u and m' denotes the inverse of mass matrix, $H_j(\omega, t)$ denotes the transient frequency response function [15], $\bar{m}$ indicates the inverse of mass matrix, $\phi_{F_s F_b}$ denotes the PSD function for force, $\phi_{h_R h_R}$ denotes the PSD function for road surface roughness given in Eq. (1), and $\phi_{\dot{h}_R \dot{h}_R}$ denotes the PSD function for derivative of road surface roughness.

The design stress obtained from the mean and standard deviation of the response using coupled iteration was given as input for estimating the fatigue life. The design stress considered was the addition of mean stress and two times the standard deviation of stress.

4 Uncoupled Iterative Scheme

First, the equation of motion for the vehicle is solved taking bridge as rigid. The pavement force is found out at discrete time step using vehicle response and road roughness. Thereafter, this force time history is applied to 3D FEM model of bridge to calculate bridge response. The bridge was modeled using beam element with a mesh size of 500 mm which is shown in Fig. 2. The length of the bridge considered was 30 m and the width of the bridge considered was 6 m. The pavement force along with the moving load was applied on the bridge to find out the response. Next, bridge response is added to road roughness and updated pavement force is calculated. This force is then applied to bridge model to obtain revised response. The process is repeated till convergence is achieved.

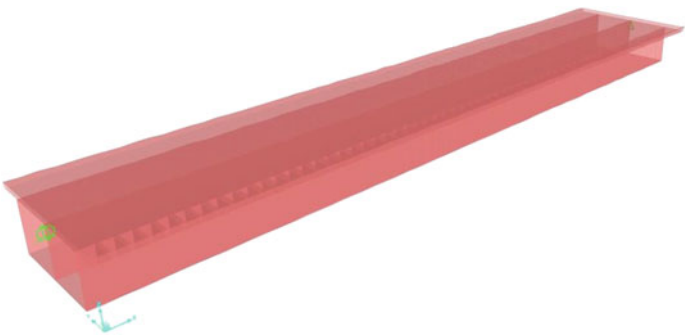

Fig. 2 Bridge model created in CSI Bridge

5 Results and Discussions

The stress history obtained from coupled scheme and uncoupled iteration scheme has been obtained for each category of road surface roughness, i.e., good, medium, and poor and also obtained by varying the vehicle forward velocity, i.e., 20, 40, and 60 km/h.

Fatigue life of the bridge component at critical location has been obtained using Miner approach where the stress time history from coupled and uncoupled schemes has been used for comparison.

The stress history plots using coupled and uncoupled schemes for 20, 40, and 60 km/h vehicle forward velocity are shown below in Figs. 3, 4, and 5, respectively.

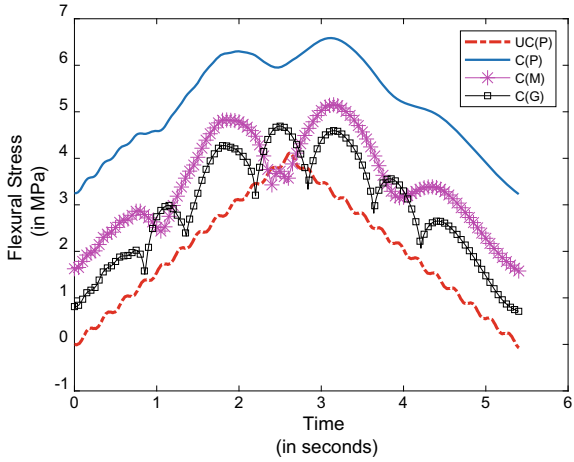

Fig. 3 Stress time history for fatigue life estimation for vehicle forward velocity 20 km/h

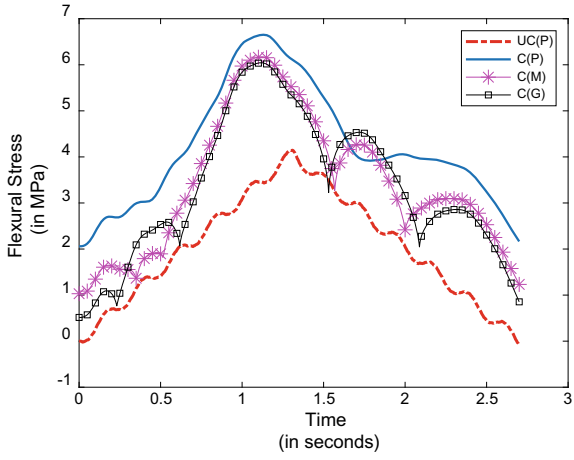

Fig. 4 Stress time history for fatigue life estimation for vehicle forward velocity 40 km/h

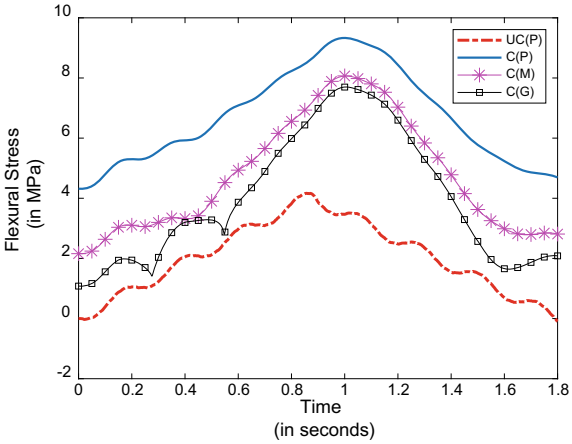

Fig. 5 Stress time history for fatigue life estimation for vehicle forward velocity 60 km/h

Table 1 Fatigue life comparison from coupled scheme and uncoupled scheme

Velocity of the vehicle (km/h)	Fatigue life (year) (coupled scheme)			Fatigue life (year) (uncoupled scheme)		
	Poor road	Medium road	Good road	Poor road	Medium road	Good road
20	497	510	535	273	273	273
40	157	197	274	Unchanged		
60	98	157	201	Unchanged		

Fatigue life calculated using Miner approach has been obtained for different velocities of the vehicle shown in Table 1.

In Figs. 3, 4, and 5, UC(P) denotes the stress time history obtained from uncoupled iteration scheme for poor road condition. C(P), C(M), and C(G) denote the stress time history obtained from coupled scheme for poor, medium, and good road conditions, respectively.

6 Conclusions

The following conclusions were made from the study:

1. It is observed that the fatigue life decreases as the condition of the road deteriorates since the dynamic force acting on the bridge will be more due to poor road surface as compared to a good road surface.
2. As the velocity of the vehicle increases, fatigue life is observed to decrease due to increase of low amplitude of flexural stress.

3. It also observed that uncoupled iterative scheme underestimates fatigue life without any sensitivity to the change of influencing factors.

References

1. Yang YB, Lin CW (2004) Vehicle-bridge interaction dynamics and potential applications. https://doi.org/10.1016/j.jsv.2004.06.032
2. Blejwas TE, Feng CC, Ayre RS (1979) Dynamic interaction of moving vehicles and structures. J Sound Vib 67:513–521. https://doi.org/10.1016/0022-460x(79)90442-5
3. Green MF, Cebon D (1997) Dynamic interaction between heavy vehicles and highway bridges. Comput Struct 62:253–264. https://doi.org/10.1016/s0045-7949(96)00198-8
4. Yang YB, Lin CW (2005) Vehicle-bridge interaction dynamics and potential applications. J Sound Vib 284:205–226. https://doi.org/10.1016/j.jsv.2004.06.032
5. Coussy O, Said M, van Hoove J-P (1989) The influence of random surface irregularities on the dynamic response of bridges under suspended moving loads. J Sound Vib 130:313–320. https://doi.org/10.1016/0022-460x(89)90556-7
6. Hwang E-S, Nowak AS (1991) Simulation of dynamic load for bridges. J Struct Eng 117:1413–1434
7. Pan T-C, Li J (2002) Dynamic vehicle element method for transient response of coupled vehicle-structure systems. J Struct Eng 128:214–223. https://doi.org/10.1061/(asce)0733-9445(2002)128:2(214)
8. Rao VG, Talukdar S (2003) Prediction of fatigue life of a continuous bridge girder based on vehicle induced stress history. Shock Vib 10:325–338
9. Cai CS, Chen SR (2004) Framework of vehicle-bridge-wind dynamic analysis. J Wind Eng Ind Aerodyn 92:579–607. https://doi.org/10.1016/j.jweia.2004.03.007
10. Zhang W, Cai CS (2012) Fatigue reliability assessment for existing bridges considering vehicle speed and road surface conditions. J Bridg Eng 17:443–453. https://doi.org/10.1061/(asce)be.1943-5592.0000272
11. Wang T-L, Liu C, Huang D, Shahawy M (2005) Truck loading and fatigue damage analysis for girder bridges based on weigh-in-motion data. J Bridg Eng 10:12–20. https://doi.org/10.1061/(asce)1084-0702(2005)10:1(12)
12. ISO 8608:1995. Mechanical vibration-road surface profiles reporting measured data
13. Yin X, Fang Z, Cai CS, Deng L (2010) Non-stationary random vibration of bridges under vehicles with variable speed. Eng Struct 32:2166–2174. https://doi.org/10.1016/j.engstruct.2010.03.019
14. Sun L, Kennedy TW (2002) Spectral analysis and parametric study of stochastic pavement loads. J Eng Mech 128:318–327. https://doi.org/10.1061/(asce)0733-9399(2002)128:3(318)
15. Nigam NC (1983) Introduction to random vibrations. The MIT Press Cambridge, Massachusetts

Size-Dependent Responses of Timoshenko Beam Incorporating the Strain Gradient Theories of Elasticity

Sai Sidhardh

Abstract This paper is concerned with the study of size effects over elastic response due to strain gradient elasticity (SGE). The general form of SGE with higher order gradients is simplified and either modified couple stress theory (MCST) or modified strain gradient theory (MSGT) models the size effects. An element-free Galerkin (EFG) model of the SGE response is obtained, and the algebraic governing equations of motion are derived here from the variational principles. Following validation, a comparison of the size effects exhibited by MCST and MSGT is carried out. The effect of each component of the higher gradients over the stiffness of the beam is also studied.

Keywords Strain gradient elasticity · Couple stress · Microstructure · Meshfree methods

1 Introduction

The microstructural effects over the elastic response of micro- and nano-dimensional structures have been noted through numerous theoretical and experimental studies. Considering the inefficacy of classical continuum theories, various forms of the higher order continuum theories have been proposed over the last century, in order to incorporate these size effects. The foremost of these being the works by Mindlin. However, owing to the complexity of these models, numerous simplified models have also been proposed.

In the current study, we intend to start from the generalized strain gradient elasticity (SGE) model presented by Mindlin and Eshel [1], and decompose the third-order strain gradient tensor to independent components corresponding to higher order gradients of the stretch and rotation variables. It will be shown that the prominent theories used in literature to analyze size effects like the modified couple stress theory

S. Sidhardh (✉)
Department of Mechanical Engineering, Indian Institute of Technology, Kharagpur 721302, West Bengal, India
e-mail: sidhu.sai1@iitkgp.ac.in

D. Maity et al. (eds.), *Advances in Fluid Mechanics and Solid Mechanics*, Lecture Notes in Mechanical Engineering,
https://doi.org/10.1007/978-981-15-0772-4_16

(MCST) [2] and the Lam's strain gradient theory [3], also referred to as the modified strain gradient theory (MSGT) [4], and are simplified models of this general theory. Following this, numerical models for the MCST and MSGT are derived, and a brief study on the effect of each higher order deformation mode on the size-dependent elastic response is carried out here.

Tensors (including vectors) are denoted using boldface symbols, with order of the tensor indicated. The comma notation is used to denote differentiation $\wedge$. For repeated indices, Einstein summation is observed, with respect to the standard Cartesian coordinates unless otherwise specified. The cross product is indicated by the $\wedge$.

2 Strain Gradient Elasticity

The internal energy $\mathcal{U}$ of an isotropic continuum over domain Ω can be written as [5]

$$\mathcal{U} = \int_{\Omega} \left(\mu ||sym \nabla \mathbf{u}||^2 + \frac{\lambda}{2} [tr \nabla \mathbf{u}]^2 + W_{sge}(D^2 \mathbf{u}) \right) dV \tag{1}$$

where λ and μ are the Lame coefficients of isotropic solids. The additional energy given by $W_{sge}(D^2\mathbf{u})$ may be attributed to SGE. Different models have been proposed corresponding to the variables chosen for the evaluation of this energy. Some of the important theories are as follows:

- Mindlin proposed three independent models over the choice of higher order gradients to evaluate W_{sge}: displacement gradients, strain gradients, or micro-rotations. They are [1]

$$\text{Form 1}: \quad \boldsymbol{\eta} = \nabla(\nabla \mathbf{u}); \quad \text{Form 2}: \quad \tilde{\boldsymbol{\eta}} = \nabla(\boldsymbol{\varepsilon}); \quad \text{Form 3}: \quad \tilde{\mathbf{k}} = \frac{1}{2} \nabla(\nabla \wedge \mathbf{u}) \tag{2}$$

In the Form-I or Form-II, the third-order tensor may be split into spherical, symmetric, and antisymmetric components [6], physically corresponding to dilatation gradient (div$\nabla \mathbf{u}$), deviatoric stretch gradient ($\tilde{\boldsymbol{\eta}}$), and curvature ($\boldsymbol{\chi}$). It must be noted that all the three independent components contribute to the gradient elastic response. However, ignoring one or more components, simplified versions of this generalized model may be derived.

- The curvature energy corresponding to MSGT is given as follows [3]:

$$W_{sge}(D^2\mathbf{u}) = \mu L_c^2 \left[a_0 \gamma_i \gamma_i + a_1 \hat{\eta}_{ijk} \hat{\eta}_{ijk} + a_2 \chi^s_{ij} \chi^s_{ij} \right] \tag{3}$$

where γ_i, $\hat{\eta}_{ijk}$, and χ^s_{ij} are the dilatation, deviatoric stretch gradients, and symmetric curvature tensor. They are defined as

$$\varepsilon_{ij} = \frac{1}{2}\left(u_{i,j} + u_{j,i}\right), \quad \gamma_i = u_{k,ki}, \ \chi^s_{ij} = \frac{1}{2}\left(\theta_{i,j} + \theta_{j,i}\right), \quad \text{where}\, \theta = \frac{1}{2}\nabla \wedge \mathbf{u}$$
$$\hat{\eta}_{ijk} = \frac{1}{3}\left(\varepsilon_{ij,k} + \varepsilon_{jk,i} + \varepsilon_{ik,j}\right) - \frac{1}{15}\left(\delta_{ij}\left(\varepsilon_{mm,k} + 2\varepsilon_{mk,m}\right)\right.$$
$$\left. + \ \delta_{jk}\left(\varepsilon_{mm,i} + 2\varepsilon_{mi,m}\right) + \delta_{ik}\left(\varepsilon_{mm,j} + 2\varepsilon_{mj,m}\right)\right) \tag{4}$$

L_c is the material characteristic length scale. In this theory, the higher order deformation energy due to antisymmetric component of curvature tensor $\boldsymbol{\chi}^a$ has been ignored.

- MCST is obtained from the MSGT model given above by further ignoring the effects of stretch gradients, $\boldsymbol{\gamma} = \mathbf{0}$ and $\tilde{\boldsymbol{\eta}} = 0$. The corresponding deformation energy is [2]

$$W_{sge}(D^2\mathbf{u}) = \mu L_c^2\left[\frac{\alpha_1}{4}\chi^s_{ij}\chi^s_{ij}\right] \tag{5}$$

3 MSGT Modeling

3.1 Constitutive Relations

The deformation energy corresponding to MSGT given in Eq. (3) may be expressed as

$$\mathcal{U} = \frac{1}{2}\int_{\Omega}\left(\boldsymbol{\sigma} : \boldsymbol{\varepsilon} + \mathbf{p}\cdot\boldsymbol{\gamma} + \mathbf{m} : \boldsymbol{\chi}^{\mathbf{s}} + \hat{\boldsymbol{\tau}}\dot{:}\hat{\boldsymbol{\eta}}\right) \mathrm{d}V \tag{6}$$

where the definitions for the strain and gradient tensor have been provided in Eq. (4). The constitutive relations for an isotropic solid considering MSGT can be given from Eq. (6) as

$$\sigma_{ij} = \lambda\varepsilon_{kk}\delta_{ij} + 2\mu\varepsilon_{ij}, \ p_i = 2\mu l_0^2\gamma_i, \ \hat{\tau}_{ijk} = 2\mu l_1^2\hat{\eta}_{ijk}, \ m_{ij} = 2\mu l_1^2\chi^s_{ij} \tag{7}$$

with l_0, l_1, and l_2 being the material length constants corresponding to the dilatation, deviatoric stretch, and symmetric rotation gradients, respectively.

3.2 Numerical Model

The components of the displacement vector **u** at any point in the domain of the beam (Ω) are given by the Timoshenko displacement field theory as follows:

$$u_1(x_1, x_3) = u_0(x_1) + x_3\phi_1(x_1), \quad u_2(x_1, x_3) = 0, \quad u_3(x_1, x_3) = w(x_1) \tag{8}$$

The column vector of generalized displacement coordinates for any point in Ω is as follows:

$$\{d\} = \{u_0 \quad w_0 \quad \phi_1\}^T \tag{9}$$

From the definitions given in Eq. (4), the evaluation of the components of the strain and strain gradient tensors is straightforward, and hence not presented here. The tensorial form of the constitutive relations given in Eq. (7) may be expressed in the matrix form as follows:

$$\{\sigma\} = [C]\{\varepsilon\}, \quad \{p\} = [R]\{\gamma\}, \quad \{\hat{\tau}\} = [S]\{\hat{\eta}\}, \quad \{m\} = [G]\{\chi^s\} \tag{10}$$

The strains, strain gradient vectors may be evaluated using nodal displacement vector $\{X\}$ as

$$\begin{aligned} \{\varepsilon\} &= [Z_0][B_t]\{X\}, \quad \left\{\chi^s\right\} = [Z_1][B_{Gt1}]\{X\} \\ \{\gamma\} &= [Z_2][B_{Gt2}]\{X\}, \quad \left\{\hat{\eta}\right\} = [Z_3][B_{Gt3}]\{X\} \end{aligned} \tag{11}$$

where the matrices $[Z_0], \ldots, [Z_3]$ provide the explicit interpolation of the strain and strain gradients across the x_3 and $[B_{(\bullet)}]$ are the matrices providing the approximation for gradients along x_1 present in the strain and higher order deformation vectors in terms of the nodal parameters for displacement coordinates. Further details regarding the interpolation function matrix $[N]$ (also referred to as shape functions) will be presented in the next section. The deformation energy $\mathcal{U}$ corresponding to MSGT as defined in Eq. (6) can now be written in terms of the strain, strain gradient, stress, and higher order stress vectors as

$$\mathcal{U} = \frac{1}{2}\iiint_{\Omega} \left(\{\varepsilon\}^T\{\sigma\} + \{\gamma\}^T\{p\} + \{\chi^s\}^T\{m\} + \{\hat{\eta}\}^T\{\hat{\tau}\}\right) dV \tag{12}$$

The total potential energy of the beam $\mathbf{\Pi}$, subjected to mechanical load $q(x_1)$ at the top surface ($x_3 = h/2$) is given as

$$\mathbf{\Pi} = \mathcal{U} - \int_0^L \left[q(x_1)u_3(x_1, h/2)\right] dx_1 \tag{13}$$

Applying the variational principle $\delta\mathbf{\Pi} = 0$, the algebraic governing equations of motion for the static bending response of a linear elastic isotropic beam using MSGT are derived to be

$$[K_{\mathrm{MSGT}}]\{X\} = \{F\} \tag{14}$$

$$[K_{\mathrm{MSGT}}] = \int_0^L \left([B_t]^T[D_t][B_t] + [B_{Gt1}]^T[D_{Gt1}][B_{Gt1}] + [B_{Gt2}]^T[D_{Gt2}][B_{Gt2}] + [B_{Gt3}]^T[D_{Gt3}][B_{Gt3}]\right)dx_1,$$

$$\{F\} = b\int_0^L \left([N]^T[0\ 1\ 0]^T q(x_1)\right)dx_1,\ [D_t] = b\int_{-h/2}^{h/2} [Z_0]^T[C][Z_0]dx_3,$$

$$[D_{Gt1}] = b\int_{-h/2}^{h/2} [Z_1]^T[G][Z_1]dx_3,\ [D_{Gt2}] = b\int_{-h/2}^{h/2} [Z_2]^T[R][Z_2]dx_3,$$

$$[D_{Gt3}] = b\int_{-h/2}^{h/2} [Z_3]^T[S][Z_3]dx_3,$$

The additional stiffness due to SGE added to the stiffness corresponding to the classical elasticity may be clearly noted from Eq. (16), with the energy added by each of the $[D_{Gt}]$ matrices corresponding to an independent mode of higher order deformation metric.

4 MCST Modeling

The deformation energy $\mathcal{U}$ for domain Ω of isotropic elastic solid evaluated using MCST is [2]

$$\mathcal{U} = \frac{1}{2}\int_{\Omega} \left(\boldsymbol{\sigma} : \boldsymbol{\varepsilon} + m : \chi^{\mathrm{s}}\right)dV \tag{15}$$

This theory may be considered to be a simplified model of the MSGT discussed above, by ignoring the hydrostatic and deviatoric stretch gradients. Thus, MCST may be obtained from MSGT by equating l_0 and l_1 to zero. Following this, the algebraic governing equations of motion for static bending response of a linear elastic isotropic beam under MCST are obtained as

$$[K_{\text{MCST}}]\{X\} = \{F\} \tag{16}$$

where $[K_{\text{MCST}}] = \int_0^L \left([B_t]^T[D_t][B_t] + [B_{Gt1}]^T[D_{Gt1}][B_{Gt1}]\right)dx_1$.

5 Weight and Shape Functions

At any point in the volume under study, the generalized displacement vector $\{d\}$ given in Eq. (9) can be interpolated in terms of the nodal displacement vector $\{X\}$ as follows:

$$\{d\} = [N]\{X\} \tag{17}$$

where $[N]$ is the shape function matrix derived using the EFG method. With explicit integrations being performed in the x_2 and x_3 (see Eq. (14)), the interpolation is necessary only in the x_1 direction. The nodal displacement vector $\{X\}$ has been developed using the EFG method [7], with nodes evenly distributed along the length of the beam, and their domain of influence chosen accordingly. A quadratic basis function supported by a quartic weight function is chosen for the moving least squares (MLS) approximation considering the $\mathbb{C}^1$ continuity requirements necessary for the evaluation of the strain gradients. The functions satisfying the above continuity may be obtained from the $\mathbb{H}^2$ Hilbert space defined over Ω. A detailed discussion on the derivation of shape functions is not presented here for the sake of brevity, please refer [8, 9].

6 Results and Discussions

For a numerical investigation of the EFG model developed above, the beam is considered to be made of a linear elastic, homogeneous, isotropic epoxy, with Young's modulus, $E = 1.44$ GPa, and Poisson's ratio $\upsilon = 0.38$. The geometric parameters of the beam L, h are varied to study the size dependence of the response, and are mentioned wherever necessary. The width of the beam b is always maintained at $2 \times h$. The material length scale parameters l_0, l_1 and l_2 are all taken to be equal: $l_0 = l_1 = l_2 = l$. The nondimensionalization of the displacements is performed as

$$\text{for distributed load:} \bar{w} = w\frac{1000EI}{q_0L^4}; \quad \text{for point load: } \bar{w} = w\frac{1000EI}{PL^3}$$

where I is the second moment of area $(= bh^3/12)$, q_0, and P are the amplitudes of the loads. To begin with, the numerical model developed in the preceding sections is

Table 1 Normalized $\bar{w}$ from EFG and analytical models [4, 10] for S-S beam under a uniform load (l varied)

h/l		$L = 10h$			$L = 100h$		
		CT	MCST	MSGT	CT	MCST	MSGT
1	Analytical	7.3006	2.2384	1.0760	6.9591	2.0949	0.759
	EFG	7.2985	2.2675	1.0779	6.955	2.1066	0.7587
	Abs. error (%)	0.029	1.300	0.177	0.059	0.558	0.040
10	Analytical	7.3006	7.1349	6.7703	6.9591	6.8011	6.4315
	EFG	7.2999	7.1386	6.7709	6.9568	6.8024	6.436
	Abs. error (%)	0.0096	0.052	0.009	0.033	0.019	0.070

validated with the corresponding analytical results [4, 10]. The normalized midplane displacements of a simply supported (S-S) beam under a uniformly distributed load $q(x_1) = q_0$ are presented in Table 1. A comparison of the numerical and analytical results corresponding to the static response of the size-dependent Timoshenko beam for different ratios of material and geometric length scales, h/l and L/h, respectively, illustrates the efficacy of the current numerical model for MCST and MSGT studies. From the table, the size dependence of elastic response for MCST and MSGT is illustrated by increasing $\bar{w}$ for reducing geometric dimensions h/l. This size dependence of the elastic response is not captured by the classical theory (CT), as noted from identical $\bar{w}$ for different h/l, given an aspect ratio L/h. Further, the $\bar{w}$ for MCST and MSGT approaching $\bar{w}$ of CT upon increasing dimensions (h/l) can be attributed to the decreasing ratio of deformation energy attributed to the gradient effects and classical strain energy, $W(D^2\mathbf{u})/W(D\mathbf{u}) << 1$ for large h/l, and thereby reducing size effects with increasing dimensions. Similar observations for the case of bending due to a point load (not presented here) indicate the intrinsic nature of SGE, and its relative invariability to the external load. A comparison of $\bar{w}$ for MCST and MSGT indicates, MSGT to be stiffer for all the cases considered here. This is due to increase in the stiffness of the beam with the additional deformation energy in MSGT corresponding to stretch gradients $(\gamma, \hat{\boldsymbol{\eta}})$, which is ignored for MCST. The normalized transverse displacement along the length of the beam due to a point load for different h/l is provided in Fig. 1a comparing the CT, MCST, and MSGT. The size-dependent nature due to SGE theories is clearly evident in the figure, with reducing difference of $\bar{w}$ across the theories with increasing dimensions, h/l. Further, $\bar{w}_{\mathrm{CT}} > \bar{w}_{\mathrm{MCST}} > \bar{w}_{\mathrm{MSGT}}$. From Sect. 2, the differences between CT, MCST, and MSGT are observed to be the additional terms added to the internal energy of the beam. Therefore, an analysis to compare the effect of each of these additional terms to the stiffness of the beam is also performed here. With l_0, l_1 and l_2 corresponding to dilatation, deviatoric stretch, and curvature gradient energies, different cases of zero and nonzero length scales are considered, and the normalized transverse displacement along the length in response to a point load is evaluated from Eq. (14) and presented in Fig. 1b. For example, $l_0 = l_1 = l_2 = 0$ corresponds to the classical elasticity, the choice of length constants for other cases are indicated in the figure. From the above parametric study, the

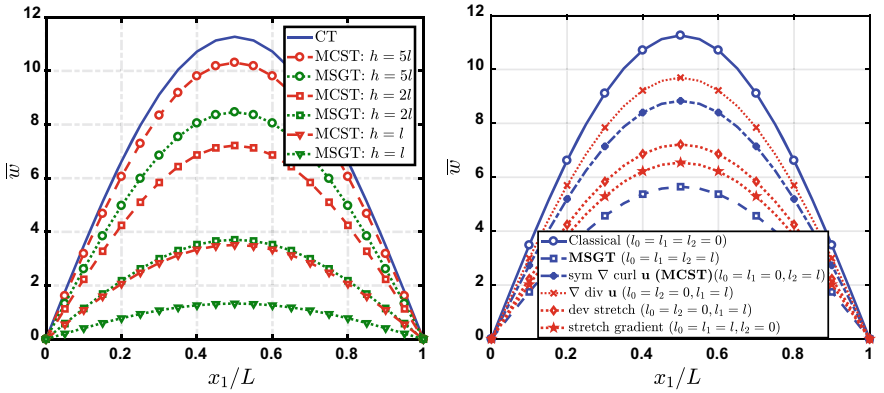

Fig. 1 Normalized transverse displacement of a S-S beam for point load ($L/h = 20$, $h = 50$ μm) comparing: (left) CT, MCST, MSGT for different h/l; (right) different components of SGE from Eq. (3) ($l = 17.6$ μm [3])

following order may be obtained for the size effects induced by each of the gradient terms available in the energy formulation provided in Eq. (3) over a beam bending:

$$\text{Size Effects:} \quad \text{CT} < \boldsymbol{\gamma} < \text{MCST}(\boldsymbol{\chi}) < \hat{\boldsymbol{\eta}} < \text{MSGT}$$

7 Conclusions

In this paper, the derivation of the simplified SGE theories from the generalized models has been studied. Following this, a numerical model for the size-dependent Timoshenko beam has been developed using EFG method, and validated with literature. The size-dependent response of microbeams due to effect of strain gradients is characterized by an additional deformation energy corresponding to these higher order gradients of the displacement field. The effect of SGE diminishes with increasing geometric dimensions, but it is significant in structures of the scale of material length constants. The size effects over the static response due to the MCST and MSGT are compared with CT here. Parametric studies indicate the significance of stretch gradients (hydrostatic and deviatoric) for the current study, thus illustrating the inadequacy of MCST for modeling gradient elastic response.

References

1. Mindlin RD, Eshel NN (1968) On first strain-gradient theories in linear elasticity. Int J Solids Struct 4(1):109–124
2. Yang FACM, Chong ACM, Lam DCC, Tong P (2002) Couple stress based strain gradient theory for elasticity. Int J Solids Struct 39(10):2731–2743
3. Lam DCC, Yang F, Chong ACM, Wang J, Tong P (2003) Experiments and theory in strain gradient elasticity. J Mech Phys Solids 51(8):1477–1508
4. Akgoz B, Civalek O (2013) A size-dependent shear deformation beam model based on the strain gradient elasticity theory. Int J Eng Sci 70:1–14
5. Ghiba I-D, Neff P, Madeo A, Munch I (2017) A variant of the linear isotropic indeterminate couple-stress model with symmetric local force-stress, symmetric nonlocal force-stress, symmetric couple-stresses and orthogonal boundary conditions. Math Mech Solids 22(6):1221–1266
6. Paolucci S (2016) Continuum mechanics and thermodynamics of matter. Cambridge University Press
7. Belytschko T, Lu YY, Gu L (1994) Element-free galerkin methods. Int J Numer Meth Eng 37(2):229–256
8. Sidhardh S, Ray MC (2018) Element-free galerkin model of nano-beams considering strain gradient elasticity. Acta Mech 229(2765). https://doi.org/10.1007/s00707-018-2139-x
9. Liu GR (2009) Meshfree methods: moving beyond the finite element method. CRC Press
10. Ma HM, Gao X-L, Reddy JN (2008) A microstructure-dependent timoshenko beam model based on a modified couple stress theory. J Mech Phys Solids 56(12):3379–3391

Dynamic Response of Axisymmetric Functionally Graded Viscothermoelastic Hollow Cylinder Due to Heat Sources by Using Series Solution

Himani Mittal and Dinesh Kumar Sharma

Abstract This paper represents the exact analysis of functionally graded viscothermoelastic hollow cylinder subjected to dynamic heat sources. The viscothermoelastic material is considered to be inhomogeneous due to easy power law. The outer and inner surfaces of cylinder are kept traction free and time-dependent heat flux is supplied on inner part of the body and outer part may be isothermal. The governing equations have been changed into ordinary differential equations due to time harmonics. Series solution for regular singular points has been applied to ordinary differential equations to represent deformation, temperature change, and traction analytically. Numerical computations have been applied to field functions and represented graphically for radial stress, temperature change, and displacement against time and thickness of cylinder. The present work has been deliberated for some special applications in the thermal environment as it controls the variations of tractions and deformations.

1 Introduction

The study of elastic and viscoelastic waves with cylindrical structures has many applications for functionally graded materials as they are helpful in controlling high variation of vibrations. The properties of these materials are not uniformly distributed across the whole material but depend on the position of the material. These materials are planned to have fluctuating chemical properties, changing thermal, mechanical, electromagnetic, and piezoelectric properties. Flugge [1] used various viscothermoelastic models for vibrating solids. Many problems in classical and nonclassical theories of thermoelasticity were described in detail by Dhaliwal and Singh [2]. According to Niino et al. [3], the functionally graded materials consisting of more

H. Mittal · D. K. Sharma (✉)
Department of Mathematics, School of Basic and Applied Sciences, Maharaja Agrasen University, Atal Shiksha Kunj, Baddi, Solan 174103, H.P, India
e-mail: dksharma200513@gmail.com

D. Maity et al. (eds.), *Advances in Fluid Mechanics and Solid Mechanics*,
Lecture Notes in Mechanical Engineering,
https://doi.org/10.1007/978-981-15-0772-4_17

than two different materials, having micro-structure across the volume of the material persuaded to have permanently varying spatial properties on macroscopic scales. Keles and Tutuncu [4] presented the forced and free vibrations of functionally graded transversely isotropic elastic cylinders and spheres in radial direction. Sharma et al. [5] have studied the free vibrations in rigidly fixed viscothermoelastic hollow sphere for uncoupled and coupled system of equations. Sharma et al. [6] have explored the stress-free functionally graded viscothermoelastic hollow sphere by using series solution in the framework of generalized thermoelasticity. Sharma [7] studied the spheroidal and toroidal vibrations in viscothermoelastic spherical curved plates in the framework of generalized thermoelasticity. Sharma et al. [8] presented the analytical and numerical solutions for dynamic response of transversely isotropic thermoelastic thick-walled hollow cylinder for time-dependent heat sources. Tripathi et al. [9] have critically studied the axisymmetric heat supply on thick plate of infinite extent in the context of diffusion thermoelasticity. Sherief and Allam [10] investigated the electromagnetic interactions for generalized thermoelastic solid cylinder. Sharma et al. [11] studied the dynamic problem for the viscothermoelastic semi-infinite cylinder in framework of five theories of generalized thermoelasticity. Sharma et al. [12] studied the forced thermal vibrations in functionally graded (FGM) viscothermoelastic hollow sphere under the action of heat sources. Neuringer [13] studied the Fröbenius method of series solution in which the indicial equation has complex roots.

In this paper, we consider dynamic functionally graded viscothermoelastic hollow cylinder under time-dependent dynamic heat sources. The Lord–Shulman (LS) [14] and Green–Lindsay (GL) [15] theories of generalized thermoelasticity have been used for modeling. The goal of this paper is to explore an analytical modeling for the realizing of field functions, i.e., stresses, temperature change, and displacement analytically and graphically.

2 Formulation of Problem

We consider a thermally conducting thick viscothermoelastic cylinder having outer radius ($\mathrm{K}\,a$, ($\mathrm{K} > 1$)) and inner radius a. The cylinder has been taken undisturbed in initial stage with the uniform temperature T_0. The domain for the cylinder is $a \leq r \leq \mathrm{K}\,a$. The solid is proposed to be axisymmetric hollow cylinder made up of functionally graded material. The components of displacement and temperature in cylindrical coordinates (r, θ, z) are expressed as $u_\theta = u_\varphi = 0$, $u_r = u\,(r, t)$ and $T\,(r, t)$. The governing equations for the homogeneous isotropic viscothermoelastic hollow cylinder/disk (Dhaliwal and Singh [3]) in the absence of body forces and heat sources are

$$\frac{\partial \sigma_r}{\partial r} + \frac{\sigma_r - \sigma_\theta}{r} = \rho \frac{\partial^2 u}{\partial t^2} \tag{1}$$

$$\frac{1}{r}\frac{\partial}{\partial r}\left(K\,r\,\frac{\partial T}{\partial r}\right)-\rho\,C_e\left(\frac{\partial}{\partial t}+t_0\frac{\partial^2}{\partial t^2}\right)T=T_0\beta^*\left(\frac{\partial}{\partial t}+t_0\delta_{1\,k}\frac{\partial^2}{\partial t^2}\right)\left(\frac{\partial\,u}{\partial r}+\frac{u}{r}\right) \tag{2}$$

where $\sigma_r = (\lambda^* + 2\mu^*)\frac{\partial u}{\partial r} + \lambda^*\frac{u}{r} - \beta^*\left(1 + t_1\delta_{2k}\frac{\partial}{\partial t}\right)T$

$$\sigma_\theta = \lambda^*\frac{\partial u}{\partial r} + \left(\lambda^* + 2\mu^*\right)\frac{u}{r} - \beta^*\left(1 + t_1\delta_{2k}\frac{\partial}{\partial t}\right)T \tag{3}$$

Since the material is considered functionally graded due to simple power law, we have

$$(\lambda^*,\ \mu^*, \rho,\ K,\ \beta^*) = \left(\lambda_0,\ \mu_0,\ \rho_e,\ K_0,\ \beta_0^*\right)\left(\frac{r}{a}\right)^\gamma \tag{4}$$

Here γ denotes the degree of inhomogeneity; σ_r and σ_θ are stress components; ρ_e is mass density; C_e is specific heat; K is thermal conductivity; λ^*, μ^*, and β^* are viscoelastic and viscothermoelastic constants.

$$\lambda_0 = \lambda_e\left(1+\alpha_0\frac{\partial}{\partial t}\right),\ \mu_0 = \mu_e\left(1+\alpha_1\frac{\partial}{\partial t}\right),\ \beta^* = \beta_e\left(1+\beta_0\frac{\partial}{\partial t}\right),$$

where

$$\beta_e = (3\lambda_e + 2\mu_e)\alpha_T,\ \beta_0 = \frac{(3\lambda_e\alpha_0 + 2\mu_e\alpha_1)\,\alpha_T}{\beta_e}$$

Here α_T is the coefficient of linear thermal expansion; λ_e and μ_e are Lame's constants;α_0, α_1, β_0 are viscoelastic and viscothermoelastic relaxation times; t_0, t_1 are relaxation time parameters; δ_{jk}; $(k = 1, 2)$ is Kronecker delta in which $j = 1$ and $j = 2$ are Lord–Shulman (LS) and Green–Lindsay (GL) theories of generalized thermoelasticity, respectively. Using Eqs. (3) and (4) in Eqs. (1) and (2), we get

$$\left.\begin{array}{c}\left(1+\delta_0\frac{\partial}{\partial t}\right)\left(\frac{\partial^2}{\partial r^2}+\frac{m_1}{r}\frac{\partial}{\partial r}\right)u+\frac{m_2^*}{r^2}u-\frac{\rho_e}{(\lambda_e+\mu_e)}\frac{\partial^2 u}{\partial t^2}\\ -\frac{\beta_e}{(\lambda_e+\mu_e)}\left(1+\beta_0\frac{\partial}{\partial t}\right)\left(1+t_1\delta_{2k}\frac{\partial}{\partial t}\right)\left(\frac{\partial}{\partial r}+\frac{\gamma}{r}\right)T=0\\ \frac{K_o}{T_0\beta_e}\left(\frac{\partial^2}{\partial r^2}+\frac{m_1}{r}\frac{\partial}{\partial r}\right)T-\frac{\rho\,C_e}{\beta_e T_0}\left(\frac{\partial}{\partial t}+t_0\frac{\partial^2}{\partial t^2}\right)T\\ -\left(1+\beta_0\frac{\partial}{\partial t}\right)\left(\frac{\partial}{\partial t}+t_0\delta_{2k}\frac{\partial^2}{\partial t^2}\right)\left(\frac{\partial u}{\partial r}+\frac{u}{r}\right)=0\end{array}\right\} \tag{5}$$

where $m_1 = \gamma + 1,\ m_2^* = \left[\lambda_0(\gamma - 1) - 2\mu_0\right]$

To remove the complexity of the equations, we introduce non-dimensional quantities given below:

$$\left.\begin{array}{c}X=\frac{r}{a},\tau=\frac{C_1 t}{a},U=\frac{u}{a},\varepsilon_T=\frac{T_0\beta_e^2}{\rho_e C_e(\lambda_e+2\mu_e)},\bar{\varepsilon}=\frac{T_0\beta_e}{(\lambda_e+2\mu_e)},\hat{\beta}_0=\frac{C_1}{a}\beta_0,\\ \delta_0=\hat{\alpha}_0+2\delta^2\left(\hat{\alpha}_1-\hat{\alpha}_0\right),(\tau_0,\tau_1)=\frac{C_1}{a}(t_0,t_1),(\hat{\alpha}_0,\hat{\alpha}_1)=\frac{C_1}{a}(\alpha_0,\alpha_1),\\ (\tau_X,\tau_\theta)=\frac{1}{\rho_e C_1^2}(\sigma_r,\sigma_\theta),\omega^*=\frac{C_e(\lambda_e+2\mu_e)}{K_0},\\ \Omega^*=\frac{a\omega^*}{C_1},C_1^2=\frac{(\lambda_e+2\mu_e)}{\rho_e},C_2^2=\frac{\mu_e}{\rho_e},\delta^2=\frac{C_2^2}{C_1^2},\end{array}\right\} \tag{6}$$

3 Boundary Conditions

The analysis of cylinder is supposed to be undisturbed both thermally and mechanically at initial stage. The non-dimensional initial conditions (after using nondimensional quantities) are

$$\frac{\partial U}{\partial \tau} = U = 0, \ \frac{\partial \theta}{\partial \tau} = \theta = 0 \text{ at } \tau = 0 \text{ and } 1 \leq X \leq \mathrm{K}; (\mathrm{K} > 1) \tag{7}$$

The inner surface $r = a$ of FGM cylinder has been assumed to be traction free ($\sigma_r = 0$) and all of a sudden this is applied to a time-dependent heat flux ($-K\,T_{,r} = q + t_0\dot{q} = q_0\,H(t),\ t > 0$) and outer radius ($r = \mathrm{K}a$) of this cylinder has been considered traction free ($\sigma_r = 0$) and isothermal conditions ($T = 0$). Hence, the respective thermal and mechanical boundaries are in non-dimensional form after using nondimensional quantities:

$$\begin{cases} \frac{\partial \theta}{\partial X} = -Q_0 H(\tau), \ \left(1 + \delta_0 \frac{\partial}{\partial \tau}\right)\frac{\partial U}{\partial X} + (1 - 2\delta^2)\left(1 + \alpha_0 \frac{\partial}{\partial \tau}\right)\frac{U}{X} \\ -\bar{\varepsilon}\left(1 + \beta \frac{\partial}{\partial \tau}\right)\left(1 + \tau_1 \frac{\partial}{\partial \tau}\right)\theta = 0 \text{ at } X = 1 \\ \theta = 0, \ \left(1 + \delta_0 \frac{\partial}{\partial \tau}\right)\frac{\partial U}{\partial X} + (1 - 2\delta^2)\left(1 + \alpha_0 \frac{\partial}{\partial \tau}\right)\frac{U}{X} \\ -\bar{\varepsilon}\left(1 + \beta \frac{\partial}{\partial \tau}\right)\left(1 + \tau_1 \frac{\partial}{\partial \tau}\right)\theta = 0 \text{ at } X = \mathrm{K} \end{cases} \tag{8}$$

where $Q_0 = \frac{q_0 a}{K_0 T_0}$, q_0 is constant.

4 Solution of Problem

Now substituting the non-dimensional quantities from Eq. (6) in Eq. (5), we get

$$\begin{cases} \left(1 + \delta_0 \frac{\partial}{\partial \tau}\right)\left(\frac{\partial^2}{\partial X^2} + \frac{m_1}{X}\frac{\partial}{\partial X}\right)U + \frac{m_2'}{X^2}U - \bar{\varepsilon}\left(1 + \hat{\beta}_0 \frac{\partial}{\partial \tau}\right)\left(1 + \tau_1 \delta_{2k} \frac{\partial}{\partial \tau}\right)\left(\frac{\partial}{\partial X} + \frac{\gamma}{X}\right)\theta = \frac{\partial^2 U}{\partial X^2} \\ \frac{\partial^2 \theta}{\partial X} + \frac{m_1}{X}\frac{\partial \theta}{\partial X} - \Omega^*\left(\frac{\partial}{\partial \tau} + \tau_0 \frac{\partial^2}{\partial \tau^2}\right)\theta = \frac{\varepsilon_T \Omega^*}{\bar{\varepsilon}}\left(1 + \hat{\beta}_0 \frac{\partial}{\partial \tau}\right)\left(\frac{\partial}{\partial \tau} + \tau_0' \frac{\partial^2}{\partial \tau^2}\right)\left(\frac{\partial}{\partial X} + \frac{1}{X}\right)U \end{cases} \tag{9}$$

where $m_2' = \left[\left(1 - 2\delta^2\right)\left(1 + \alpha_0 \frac{\partial}{\partial \tau}\right)\gamma - \left(1 + \hat{\delta}_0 \frac{\partial}{\partial \tau}\right)\right]$

Now introducing the time-harmonic vibrations from our earlier published paper Sharma et al. [6] and the transformation from Sharma et al. [8] as

$$U(X, \tau) = X^{\frac{-\gamma}{2}} V(X, \tau) e^{i\Omega\tau}; \ \theta(X, \tau) = X^{\frac{-\gamma}{2}} \Theta(X, \tau) e^{i\Omega\tau} \tag{10}$$

Using Eq. (10) in Eq. (9), we get

$$\nabla^2 V + \left(\frac{i\Omega}{\tilde{\delta}_0} - \frac{n^2}{X^2}\right)V + i\Omega m_3 \left(\frac{d}{dX} + \frac{\gamma}{2X}\right)\Theta = 0$$

$$\nabla^2\Theta + \left(i\Omega^2\Omega^*\tilde{\tau}_0 - \frac{\gamma^2}{4X^2}\right)\Theta + im_4\Omega^3\left(\frac{d}{dX} - \left(\frac{\gamma-2}{2}\right)\frac{1}{X}\right)V = 0 \tag{11}$$

where

$$\tilde{\tau}_0 = i\Omega^{-1} + \tau_0,\ \tilde{\alpha}_1 = i\Omega^{-1} + \hat{\alpha}_1,\ \tilde{\delta}_0 = i\Omega^{-1} + \delta_0,$$

$$\nabla^2 = \frac{1}{X}\frac{d}{dX}\left(X\frac{d}{dX}\right),\ n^2 = m_2 - \frac{\gamma^2}{4}$$

$$m_3 = \frac{\bar{\varepsilon}\,\tilde{\beta}_0\,\tilde{\tau}_0}{\tilde{\delta}_0},\ m_4 = \frac{\varepsilon_T\,\Omega^*\tilde{\beta}_0\,\tilde{\tau}_0'}{\bar{\varepsilon}},\ \tilde{\alpha}_0 = i\,\Omega^{-1} + \tilde{\alpha}_0,$$

$$\tilde{\beta}_0 = i\,\Omega^{-1} + \hat{\beta}_0,\ \tilde{\tau}_1 = i\,\Omega^{-1} + \tau_1\delta_{2k},\ \tau_0' = \tau_0$$

5 Series Solution

Since the differential Eq. (11) contains a regular singular point at $X = 0$, so we set up the matrix Frobenius method of series solution in Eq. (11) such that there exist one nontrivial solution which takes the form as

$$\begin{bmatrix} V \\ \Theta \end{bmatrix} = \sum_{k=0}^{\infty}\begin{bmatrix} A_K \\ B_K \end{bmatrix}X^{s+k} \tag{12}$$

Here s is an eigenvalue and A_k, B_k are the unknown coefficients. Substituting the solution assumed in Eq. (12) in Eq. (11) and on solving, we get

$$\sum_{k=0}^{\infty}\left(h_1(s+k)X^{-2} + h_2(s+k)X^{-1} + \begin{bmatrix} \frac{i\Omega}{\tilde{\delta}_0} & 0 \\ 0 & \Omega^*\Omega^2\tilde{\tau}_0 \end{bmatrix}\right)X^{s+k}\begin{bmatrix} A_K \\ B_K \end{bmatrix} = 0 \tag{13}$$

where $h_1(s+k) = \begin{bmatrix} (s+k)^2 - n^2 & 0 \\ 0 & (s+k) - \frac{\gamma^2}{4} \end{bmatrix}$, $h_2(s+k) = \begin{bmatrix} 0 & i\Omega m_3\left(s+k+\frac{\gamma}{2}\right) \\ i\Omega^*\Omega^3 m_4\left(s+k-\left(\frac{\gamma-2}{2}\right)\right) & 0 \end{bmatrix}$

Now taking the coefficients of the lowest power of X ($i.e.\ X^{s-2}$) equals to zero, we get

$$\begin{bmatrix} s^2 - n^2 & 0 \\ 0 & s^2 - \frac{\gamma^2}{4} \end{bmatrix}\begin{bmatrix} A_0(s_j) \\ B_0(s_j) \end{bmatrix} = 0 \tag{14}$$

For nontrivial solution, the roots of indicial equation from Eq. (14) are

$$s_1 = +n,\ s_2 = -n,\ s_3 = +\frac{\gamma}{2},\ s_4 = -\frac{\gamma}{2} \tag{15}$$

Here the roots s_1 and s_2 may be complex roots and s_3 and s_4 are real roots. The unknowns for the choice of indicial equation we choose as follows:

$$A_0(s_j) = \begin{cases} 1,\ j = 1, 2 \\ 0,\ j = 3, 4 \end{cases},\ B_0(s_j) = \begin{cases} 0,\ j = 1, 2 \\ 1,\ j = 3, 4 \end{cases} \tag{16}$$

Now taking the next lower power of X ($i.e.\ X^{s-1}$) equals to zero and after solving it, we get

$$\begin{bmatrix} A_1(s_j) \\ B_1(s_j) \end{bmatrix} = -\begin{bmatrix} 0 & E_{12}^1(s_j) \\ E_{21}^1 & 0 \end{bmatrix}\begin{bmatrix} A_0(s_j) \\ B_0(s_j) \end{bmatrix} \tag{17}$$

where $E_{12}^1(s_j) = \frac{i\Omega m_3\left(s_j+\left(\frac{\gamma+2}{2}\right)\right)}{\left(s_j+1\right)^2-n^2},\ E_{21}^1(s_j) = \frac{i\Omega^*\Omega^3 m_4\left(s_j+\left(\frac{4-\gamma}{2}\right)\right)}{\left(s_j+1\right)^2-\left(\frac{\gamma}{2}\right)^2}$

Continuing likewise and equating the like powers of the coefficients of X^{s+k} equal to zero, we get

$$h_1(s_j+k+2)\begin{bmatrix} A_{k+2}(s_j) \\ B_{k+2}(s_j) \end{bmatrix} + h_2(s_j+k+1)\begin{bmatrix} A_{k+1}(s_j) \\ B_{k+1}(s_j) \end{bmatrix} + \begin{bmatrix} \frac{i\Omega}{\delta_0} & 0 \\ 0 & \Omega^*\Omega^2\tilde{\tau}_0 \end{bmatrix}\begin{bmatrix} A_k(s_j) \\ B_k(s_j) \end{bmatrix} = 0; k = 0,\ 1,\ 2\ldots \tag{18}$$

On solving Eq. (18), the following recurrence relation has been obtained:

$$\begin{bmatrix} A_{k+2}(s_j) \\ B_{k+2}(s_j) \end{bmatrix} = -\left(\begin{bmatrix} 0 & h_{12}^k \\ h_{21}^k & 0 \end{bmatrix}\begin{bmatrix} A_{k+1}(s_j) \\ B_{k+1}(s_j) \end{bmatrix} + \begin{bmatrix} h_{11}^k & 0 \\ 0 & h_{22}^k \end{bmatrix}\begin{bmatrix} A_k(s_j) \\ B_k(s_j) \end{bmatrix}\right);\ k = 0,\ 1,\ 2\ldots \tag{19}$$

$$h_{11}^k = \frac{i\Omega}{\delta_0\left(\left(s_j+k+2\right)^2-n^2\right)},\ h_{22}^k = \frac{\Omega^*\Omega^2\tilde{\tau}_0}{\left(s_j+k+2\right)^2-\left(\frac{\gamma}{2}\right)^2},$$

where

$$h_{12}^k = \frac{i\Omega m_3\left(s_j+k+\left(\frac{\gamma+2}{2}\right)\right)}{\left(s_j+k+2\right)^2-n^2},\ h_{21}^k = \frac{i\Omega^3 m_4\left(s_j+k+\left(\frac{4-\gamma}{2}\right)\right)}{\left(s_j+k+2\right)^2-\left(\frac{\gamma}{2}\right)^2}$$

Substituting $k = 0$ in Eq. (19), we get

$$\begin{bmatrix} A_2(s_j) \\ B_2(s_j) \end{bmatrix} = -\begin{bmatrix} E_{11}^2(s_j) & 0 \\ 0 & E_{22}^2(s_j) \end{bmatrix}\begin{bmatrix} A_0(s_j) \\ B_0(s_j) \end{bmatrix} \tag{20}$$

where $E_{11}^2(s_j) = h_{12}^0(s_j)E_{21}^1(s_j) - h_{11}^0(s_j),\ E_{22}^2 = h_{21}^0(s_j)E_{12}^1(s_j) - h_{22}^0(s_j)$

Again substituting $k = 1$ in Eq. (19), we get

$$\begin{bmatrix} A_3(s_j) \\ B_3(s_j) \end{bmatrix} = \begin{bmatrix} 0 & E_{12}^3(s_j) \\ E_{21}^3(s_j) & 0 \end{bmatrix} \begin{bmatrix} A_0(s_j) \\ B_0(s_j) \end{bmatrix} \tag{21}$$

where $E_{12}^3(s_j) = h_{12}^1(s_j)E_{22}^2(s_j) - h_{11}^2(s_j)E_{12}^1(s_j)$, $E_{21}^3(s_j) = h_{21}^1(s_j)E_{11}^2(s_j) - h_{22}^1(s_j)E_{21}^1(s_j)$

Now continuing likewise, we obtain the unknowns $(A_{2k}(s_j),\ B_{2k}(s_j))'$ has similar form as $h_1(s_j + k)$ and $(A_{2k+1}(s_j),\ B_{2k+1}(s_j))'$ has same as $h_2(s_j + k)$. Hence

$$\begin{aligned} \begin{bmatrix} A_{2k}(s_j) \\ B_{2k}(s_j) \end{bmatrix} &= \begin{bmatrix} E_{11}^{2k}(s_j) & 0 \\ 0 & E_{22}^{2k}(s_j) \end{bmatrix} \begin{bmatrix} A_0(s_j) \\ B_0(s_j) \end{bmatrix}, \begin{bmatrix} A_{2k+1}(s_j) \\ B_{2k+1}(s_j) \end{bmatrix} \\ &= -\begin{bmatrix} 0 & E_{11}^2(s_j) \\ E_{11}^2(s_j) & 0 \end{bmatrix} \begin{bmatrix} A_0(s_j) \\ B_0(s_j) \end{bmatrix} \end{aligned} \tag{22}$$

where

$$\begin{aligned} E_{11}^{2k}(s_j) &= h_{12}^{2k-2}(s_j)E_{21}^{2k-1}(s_j) - h_{11}^{2k-2}(s_j)E_{11}^{2k-2}(s_j), \\ E_{22}^{2k}(s_j) &= h_{21}^{2k-2}(s_j)E_{12}^{2k-1}(s_j) - h_{22}^{2k-1}(s_j)E_{22}^{2k-1}(s_j) \\ E_{12}^{2k+1}(s_j) &= h_{12}^{2k-1}(s_j)E_{22}^{2k}(s_j) - h_{11}^{2k-1}(s_j)E_{11}^{2k-1}(s_j), \\ E_{21}^{2k+1}(s_j) &= h_{21}^{2k-1}(s_j)E_{11}^{2k}(s_j) - h_{22}^{2k-1}(s_j)E_{21}^{2k-1}(s_j) \end{aligned}$$

So, we can write

$$\begin{aligned} \begin{bmatrix} E_{11}^{2k}(s_j) & 0 \\ 0 & E_{22}^{2k}(s_j) \end{bmatrix} &\approx O\left(k^{-1}\right) \begin{bmatrix} i\Omega m_3 & 0 \\ 0 & i\Omega^3 m_4 \end{bmatrix}, \begin{bmatrix} 0 & E_{12}^{2k+1}(s_j) \\ E_{21}^{2k+1}(s_j) & 0 \end{bmatrix} \\ &\approx O\left(k^{-1}\right) \begin{bmatrix} 0 & i\Omega m_3 \\ i\Omega^3 m_4 & 0 \end{bmatrix} \end{aligned} \tag{23}$$

The sequence $\{h_k\}$ in the complex field converges $\left(\lim_{k\to\infty} h_k = h\right)$, if each of k component sequence converges. Introducing the above fact that both the matrices $\begin{pmatrix} E_{11}^{2k}(s_j) & 0 \\ 0 & E_{22}^{2k}(s_j) \end{pmatrix} \to 0$ and $\begin{pmatrix} 0 & E_{12}^{2k+1}(s_j) \\ E_{21}^{2k+1}(s_j) & 0 \end{pmatrix} \to 0$ as $k \to \infty$. This shows that the assumed sequences in solution (12) are uniformly and absolutely convergent. Hence, assumed sequences in solution (12) can be written as

$$\begin{aligned} \begin{bmatrix} V \\ \Theta \end{bmatrix} = \Bigg[I - \begin{bmatrix} 0 & E_{12}^1(s_j) \\ E_{21}^1(s_j) & 0 \end{bmatrix} x + \begin{bmatrix} E_{11}^2(s_j) & 0 \\ 0 & E_{22}^2(s_j) \end{bmatrix} x^2 \\ - \begin{bmatrix} 0 & E_{12}^3(s_j) \\ E_{21}^3(s_j) & 0 \end{bmatrix} x^3 + \ldots..\infty \Bigg] \begin{bmatrix} A_0(s_j) \\ B_0(s_j) \end{bmatrix} x^{s_j} \end{aligned} \tag{24}$$

Here I is identity matrix of order two. Hence, the series Eq. (12) and the derived series in Eq. (24) are analytic function and differentiated term by term. Thus, the general solution for Eq. (10) with the help of Eq. (24), we obtain

$$U(X,\tau)=\sum_{k=0}^{\infty}[h_{1k}e_{11}^{2k}(s_1)X^{s_1}+h_{2k}e_{11}^{2k}(s_2)X^{s_2} + h_{3k}e_{12}^{2k+1}(s_3)X^{s_3+1}+h_{4k}e_{12}^{2k+1}(s_4)X^{s_4+1}]X^{2k-\frac{\gamma}{2}}\left(e^{i\Omega\tau}\right) \tag{25}$$

$$\theta(X,\tau)=\sum_{k=0}^{\infty}h_{1k}e_{21}^{2k+1}(s_1)X^{s_1+1}+h_{2k}e_{21}^{2k+1}(s_2)X^{s_2+1} + h_{3k}e_{22}^{2k}(s_3)X^{s_3}+h_{4k}e_{22}^{2k}(s_4)X^{s_4}]X^{2k-\frac{\gamma}{2}}\left(e^{i\Omega\tau}\right) \tag{26}$$

where h_{1k}, h_{2k}, h_{3k} and h_{4k} are arbitrary constants to be determined. Applying time harmonics and transformation from Eq. (10) on the boundary conditions in Eq. (8), we obtain nondimensional transformed boundary conditions as

$$\left.\begin{array}{ll}\frac{d\theta}{dX}-\frac{\gamma}{2X}\theta=-Q^*, & \frac{dU}{dX}+\frac{1}{\tilde{\delta}_0}\left((1-2\delta^2)\tilde{\alpha}_0-\frac{\gamma}{2}\right)\frac{U}{X}-i\Omega m_3\theta=0, \text{ at } X=1\\ \theta=0, & \frac{dU}{dX}+\frac{1}{\tilde{\delta}_0}\left((1-2\delta^2)\tilde{\alpha}_0-\frac{\gamma}{2}\right)\frac{U}{X}-i\Omega m_3\theta=0, \text{ at } X=\mathrm{K}\end{array}\right\} \tag{27}$$

where $Q^*=Q_0H(\tau)$. Upon using Eqs. (25) and (26) in Eq. (27), we get following equations in matrix form as:

$$\left(h_{jk}\right)_{4\times1}=\left(E_{ij}\right)_{4\times4}^{-1}(C)_{4\times1} \tag{28}$$

where the matrix $C=\left(-Q^*\ 0\ 0\ 0\right)'$ and the elements of matrix E_{ij}; $(i,j=1,2,3,4)$ are given below:

$$E_{11}=(R_1^*+n)E_{11}^{2k+1}(n),\ E_{13}=\left(R_2^*+\gamma/2\right)E_{22}^{2k}(\gamma/2),$$
$$E_{21}=(2k+n+a^*)E_{11}^{2k}(n)+b^*E_{21}^{2k+1}(n)$$

$$E_{23}=\left(2k+\gamma/2+1+a^*\right)E_{12}^{2k+1}(\gamma/2)+b^*E_{22}^{2k}(\gamma/2),$$
$$E_{31}=E_{11}^{2k+1}(n)\mathrm{K}^{2k+1+n},\ E_{33}=E_{22}^{2k}(\gamma/2)\mathrm{K}^{2k+(\gamma/2)}$$

$$E_{41}=\left\{(2k+n+a^*)\frac{1}{\mathrm{K}}E_{11}^{2k}(n)+b^*E_{21}^{2k+1}(n)\right\}\mathrm{K}^{2k+n},$$
$$E_{43}=\left\{\left(2k+\frac{\gamma}{2}+1+a^*\right)\mathrm{K}E_{12}^{2k+1}\left(\frac{\gamma}{2}\right)+b^*E_{22}^{2k}\left(\frac{\gamma}{2}\right)\right\}\mathrm{K}^{2k+(\gamma/2)}$$

$$a^*=\left(1-2\delta^2\right)\frac{\tilde{\alpha}_0}{\tilde{\delta}_0}-\frac{\gamma}{2},\ b^*=\frac{i\bar{\varepsilon}\Omega\tilde{\beta}_0\tilde{\tau}_1}{\tilde{\delta}_0},\ R_1^*=2k+\frac{2-\gamma}{2},\ R_2^*=2k-\frac{\gamma}{2}$$

The elements E_{12}, E_{22}, E_{32}, E_{42} can be obtained from E_{11}, E_{21}, E_{31}, E_{41} by replacing n with $-n$ and the elements E_{14}, E_{24}, E_{34}, E_{44} can be obtained from E_{13}, E_{23}, E_{33}, E_{43} by replacing $\gamma/2$ with $-\gamma/2$. Equations (25)–(28) represent

formal solution of the problem. In this analysis, we have considered the periodic dynamic pressures as taken from Keles and Tutuncu [4]. For periodic pressure, we assume the function $H(\tau)$ as

$$Q^* = Q_0 H(\tau) = Q_0(1 - \cos \Omega \tau) \tag{29}$$

Deduction of results:

If the viscous effects and relaxation times are not considered, then the analysis is reduced to thermoelastic hollow cylinder. Also, if the thermal effects are ignored, then the analysis is reduced to elastic hollow cylinder.

6 Results and Discussions

For the authentication and validation of the analytical results, we need some numerical computations which are applied using MATLAB software tools. For numerical computations, we use copper material whose data has been acquired from our earlier published paper Sharma et al. [11]. The numerical computations have been considered by choosing the ratio of inner radius to outer radius by taking $\mathrm{K} = 2$ and distance $X = 1.5$ from the center of the cylinder. The numerical simulations for the variation of temperature, displacement, and radial stress are presented in Figs. 1, 2, and 3 versus normalized thickness and Figs. 4, 5, and 6 versus time for different values of inhomogeneous parameter γ.

Here the normalized thickness is defined as $(\eta^* = (X - 1)/(\mathrm{K} - 1);\ \mathrm{K} \neq 1)$ (here $0 \leq \eta^* \leq 1$). Figure 1 shows that the temperature change decreases with increasing values of η^*. The amplitude of temperature profile decreases due to inhomogeneity parameter and varies accordingly as the value of (γ) would be $\gamma = 0.65 < 0.35 < 0.0$ order. It is noticed from Fig. 2 that displacement (U) increases sharply to attain its maximum value between $0.3 < \eta^* < 0.5$ and decreases

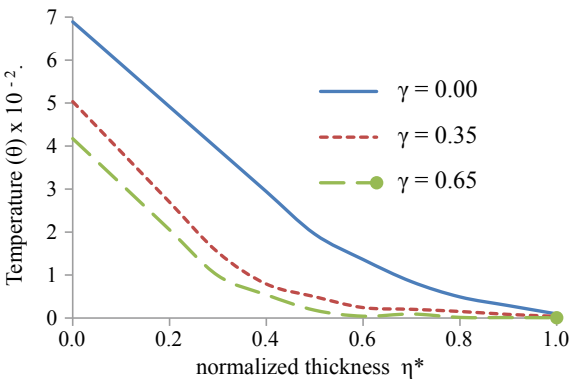

Fig. 1 Variation of temperature versus thickness

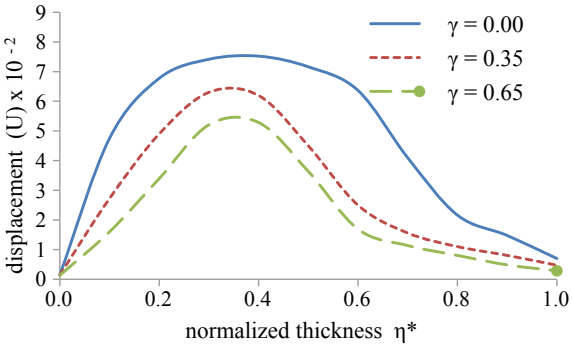

Fig. 2 Variation of displacement versus thickness

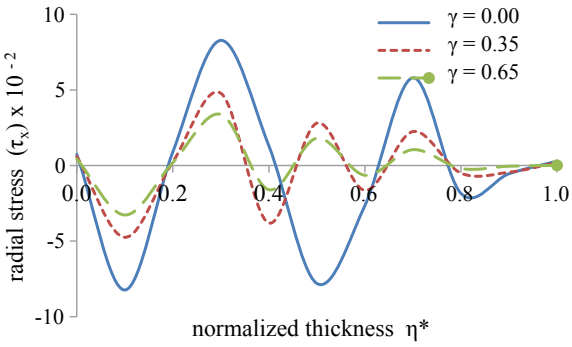

Fig. 3 Variation of radial stress versus thickness

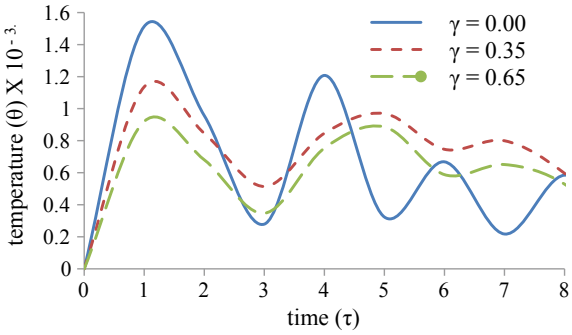

Fig. 4 Time history of temperature change

to become ultimately asymptotic with increasing value of (η^*). It is noted from Fig. 3 that the variation of radial stress (τ_X) is compressive initially, and achieves maximum variation at $\eta^* = 0.3$ and with increase in the value of η^* the variations go on decreasing and die out.

The field functions temperature, displacement, and radial stress in Figs. 4, 5, and 6 are noticed to vanish initially at $\tau = 0$, which clearly agree with our initial conditions as assumed in Eq. (7) of the problem. Figures 4, 5, and 6 show the patterns of field

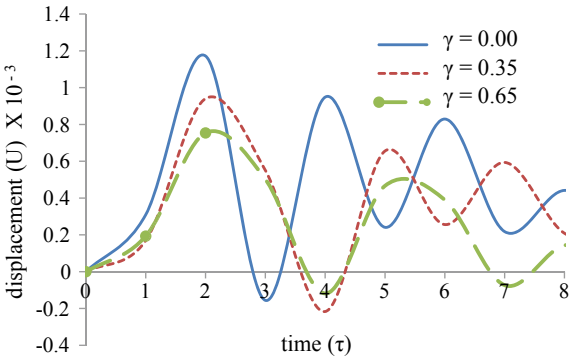

Fig. 5 Time history of displacement

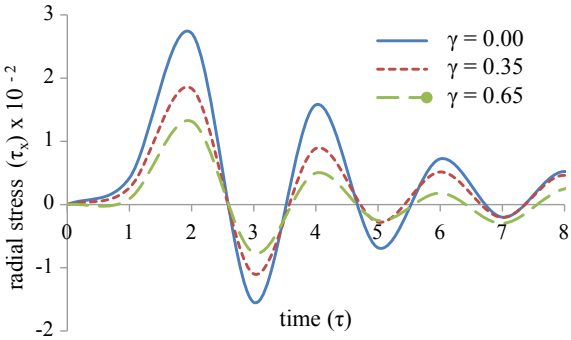

Fig. 6 Time history of radial stress

functions, i.e., temperature, displacement, and radial stress against nondimensional time in the disk made up of homogeneous material ($\gamma = 0$) and inhomogeneous material ($\gamma = 0.35,\ 0.65$) due to periodic heat flux dynamic pressure and $H(\tau)$ with $\Omega = 1.0$. Figure 4 has been presented for temperature change against nondimensional time. It is revealed from Fig. 4 that amplitudes of these quantities keep on interchanging with time for ($\gamma = 0,\ 0.35,\ 0.65$). The variation in magnitude of temperature in Fig. 4 is larger in homogeneous case, i.e., ($\gamma = 0$) rather than nonhomogeneous cases, i.e., ($\gamma = 0.35, 0.65$) and with increase in time the variation of temperature goes on decreasing.

Figure 5 represents the variation of radial stress versus time. It is observed from Fig. 5 that the behavior of quantities go on interchanging with time and has larger variation at $\tau = 2.0$ for all the values of γ and with increase in value of time the variation of amplitude of displacement go on decreasing. Figure 6 shows the variation of radial stress versus time. It is seen from Fig. 6 that the behavior of variations of radial stress is noted to be sinusoidal and with increase in time the variations of amplitude of stress go on decreasing. In Fig. 6, the peaks have been observed for radial stress at $\tau = 2.0$.

It can be concluded from all the figures that the variations are smaller for nonhomogeneous materials, i.e., ($\gamma = 0.35, 0.65$) in contrast with the larger variations

for homogeneous material, i.e., ($\gamma = 0$). Results in Figs. 4, 5, and 6 are consistent with (Keles and Tutuncu [4]) in the absence of thermal and viscous effects. It may also be observed that deformation and stress development may be examined (increased/decreased) as per requirement by increasing or decreasing the value of grading index γ.

7 Conclusions

The series solution for regular singular points has been implemented successfully to represent the axisymmetric vibrations of heat flux of viscothermoelastic hollow cylinders under dynamic pressure. With the help of grading parameter, the deformation, change in temperature, and traction can be examined as per requirement. The mechanical and thermal relaxation times have been observed to be significant in viscothermoelastic tractions, displacement, and temperature distributions. As the values of grading index parameter are increased, the variation is noted to be in decreasing behavior and the grading index parameter can be used as traction controller. The approach is well arranged and useful to represent the closed-form analytical solutions due to nonhomogeneity grading parameter for generalized theories of viscothermoelasticity. The results are consistent with (Keles and Tutuncu [4]) in the absence of thermal and viscous effects. The closed-form solutions have further scope for applied mechanics, applied mathematics, science, and engineering. The study may also find applications in industry as grading index helps to control the variation of high stress development.

Acknowledgements We both the authors are thankful to Late **Professor J. N. Sharma, NIT Hamirpur (HP) India** who has gone from this world for providing us the expertise, moral support, and kind guidance.

References

1. Flugge W (1967) Viscoelasticity. Blaisdell Publishing Company, Massachusetls, Toronto, London
2. Dhaliwal RS, Singh A (1980) Dynamic coupled thermoelasticity. Hindustan Publishing Corporation
3. Niino M, Hirai T, Watanabe R (1987) The functionally gradient materials. J Jpn Soc Compos Mater 13:257–264. https://doi.org/10.6089/jscm.13.257
4. Keles I, Tutuncu N (2011) Exact analysis of axisymmetric dynamic response of functionally graded cylinders (or disks) and spheres. J Appl Mech 78:061014–061017. https://doi.org/10.1115/1.4003914
5. Sharma JN, Sharma DK, Dhaliwal SS (2013) Free vibration analysis of a rigidly fixed viscothermoelastic hollow sphere. Indian J Pure Appl Math 44:559–586. https://doi.org/10.1007/s13226-013-0030-y

6. Sharma DK, Sharma JN, Dhaliwal SS, Walia V (2014) Vibration analysis of axisymmetric functionally graded viscothermoelastic spheres. Acta Mech Sin 30:100–111. https://doi.org/10.1007/s10409-014-0016-y
7. Sharma DK (2016) Free vibrations of homogenous isotropic viscothermoelastic spherical curved plates. Tamkang J Sci Eng 19:135–148. https://doi.org/10.6180/jase.2016.19.2.04
8. Sharma J, Sharma P, Mishra KC (2016) Dynamic response of functionally graded cylinders due to time-dependent heat flux. Meccanica 51:139–154. https://doi.org/10.1007/s11012-015-0191-3
9. Tripathi JJ, Kedar GD, Deshmukh KC (2016) Generalized thermoelastic diffusion in a thick circular plate including heat source. Alex Eng J 55:2241–2249. https://doi.org/10.1016/j.aej.2016.06.003
10. Sherief HH, Allam AA (2017) Electro–magneto interaction in a two-dimensional generalized thermoelastic solid cylinder. Acta Mech 228:2041–2062. https://doi.org/10.1007/s00707-017-1814-7
11. Sharma D, Mittal H, Sharma SR, Parkash I (2017) Effect of deformation on semi–infinite viscothermoelastic cylinder based on five theories of generalized thermoelasticity. Math J Interdiscip Sci 6:17–35. https://doi.org/10.15415/mjis.2017.61003
12. Sharma DK, Sharma SR, Walia V (2018) Analysis of axisymmetric functionally graded forced vibrations due to heat sources in viscothermoelastic hollow sphere using series solution. In: AIP conference proceedings, vol 1975, p 030010. https://doi.org/10.1063/1.5042180
13. Neuringer JL (1978) The Frobenius method for complex roots of the indicial equation. Int J Math Educ Sci Technol 9:71–77. https://doi.org/10.1080/0020739780090110
14. Lord HW, Shulman Y (1967) A generalized dynamical theory of thermoelasticity. J Mech Phys Solids 15:299–309. https://doi.org/10.1016/0022-5096(67)90024-5
15. Green A, Lindsay K (1972) Thermoelasticity. J Elast 2:1–7. https://doi.org/10.1007/BF00045689

Modeling of a Novel Lower Limb Exoskeleton System for Paraplegic Patients

Mrinal Gupta, Jyotindra Narayan and S. K. Dwivedy

Abstract This paper presents the design of a novel low-cost motorized wheelchair exoskeleton device to provide locomotive assistance and physical rehabilitation to paraplegic patients in the age group of 20–75 years. CAD modeling of different parts of the device has been completed using SOLIDWORKS software. Mathematical calculations are performed to estimate the torque requirements to drive rear wheels, and maximum torque requirement at knees in static condition. Static structural analysis of different parts of the mechanism is performed using ANSYS software for optimization and validation of the proposed design. The reduction in the overall mass of the mechanism is achieved by multi-use of actuators, where a single motor has been used for motion at more than one joints in the device. A mechanism is also designed to allow easy switching of power for the motors from one joint to the other. Further, to make the device eligible for use by people of different heights, adjustability in height of the mechanism has been achieved via the use of telescoping link mechanisms for legs of the device. The aim is to come up with a low-cost device which along with fulfilling the mobility requirements stays light, without compromising the strength and motion capabilities of the device.

Keywords Wheelchair exoskeleton · Paraplegic · Rehabilitation · Locomotive assistance · Structural analysis

M. Gupta · J. Narayan (✉) · S. K. Dwivedy
Department of Mechanical Engineering, IIT Guwahati, Guwahati 781039, India
e-mail: n.jyotindra@gmail.com

M. Gupta
e-mail: guptamrinal3822@gmail.com

S. K. Dwivedy
e-mail: dwivedy@iitg.ernet.in

D. Maity et al. (eds.), *Advances in Fluid Mechanics and Solid Mechanics*,
Lecture Notes in Mechanical Engineering,
https://doi.org/10.1007/978-981-15-0772-4_18

1 Introduction

Mobility is a fundamental element of an individual's daily life. Independence of motion allows a person to perform the basic daily needs of life. Unfortunately, medical conditions such as stroke, nerve injury, Parkinson's disease or even genetic disorders may cause damage to the nervous system of a person, subsequently leading him to lose his/her muscle function, and as a result the ability to move. Such a condition of inability to perform motion is known as paralysis. Majority of the cases of paralysis arise due to strokes. Estimates of 2015 show that India has a total of approximately 1.8 million cases of stroke annually [1], the number rising each year. Owing to their low incomes, the majority of these paralytic patients opt for manual wheelchairs as a means to restore their mobility. However, these pose a few limitations such as limited use on rough terrain, bruising on skin, and limited independent use by the elderly because of lack of sufficient body strength needed to drive the wheelchair. Thus, there is a need to develop a cheaper, more efficient solution in the form of a motorized wheelchair exoskeleton, which can restore mobility in a much better way, and simultaneously act as a means of rehabilitation, while keeping the overall cost less.

A wheelchair exoskeleton refers to an assistive mobility device used to provide assistance in locomotion to individuals suffering from limited physical mobility. It can be operated in two modes, one as a motorized wheelchair, allowing the individual to sit on a seat while steering himself/herself using a controller joystick to the point of destination. The second mode of the device is the exoskeleton mode. Instead of resting on the four wheels, the individual now stands on his/her feet with the help of a support mechanism, called the lower limb exoskeleton.

A great deal of research has been done in the field of exoskeleton and wheelchair design. A detailed study of some of these available exoskeleton devices, which include HAL, ALEX, LOPES, ReWalk, Lokomat, HyAWET has been performed. The Hybrid Assistive Limb (HAL) [2] is a battery operated lower limb exoskeleton device which uses DC servo motors and harmonic drive gears for hip and knee actuation. The Active Leg Exoskeleton (ALEX) [3] is a powered leg orthosis device which uses non-back drivable linear actuators at hip and knee joints. These linear actuators have built in encoders. In Lower Extremity Powered Exoskeleton (LOPES) [4], the robot moves parallel to the patient's body. Movements at joints have been achieved using Bowden cable driven series elastic actuators. ReWalk [5] is a wearable motorized suit developed by Argo Medical Technologies Inc. The device movements are controlled using changes in center of gravity of the person and device. Lokomat [6] is a robotic exoskeleton with a treadmill and body weight support system, manufactured by Hocoma AG, a Swiss company. Hybrid Assistive Wheelchair Exoskeleton (HyAWET) [7], designed by the Indian Institute of Technology Guwahati consists of an actuation mechanism for actuating multiple degrees of freedom with the help of minimum number of actuators. Other than a high cost factor, existing exoskeleton devices encounter certain other limitations, such as complex adjustment for use by individuals of different heights, large number of actuators in use, or lack of back

drivable motors at joints. Based on the literature review and evaluation of their merits and limitations, several design specifications related to dimensions of the parts, actuators, speed limits, weight and cost are decided to meet the design objectives.

In this paper, modeling of wheelchair exoskeleton system is described extensively in Sect. 2, using SOLIDWORKS software followed by formulation of torques required. Then, FEA analysis is performed in ANSYS workbench. In Sect. 3, results and discussions for finding the torque required at rear wheels and knee during sit to stand motion are carried out. Thereafter, in Sect. 4, the conclusions are drawn regarding the complete work covered for the exoskeleton system.

2 Modeling Description of the Wheelchair Exoskeleton System

2.1 SolidWorks Modeling

Computer-aided modeling of different parts of the wheelchair exoskeleton system is performed using SOLIDWORKS software. To make the device flexible for use by people of different heights, telescoping leg links are used both for the thigh and shank parts. Figure 1a shows the telescoping leg link mechanism. Back support consists of a vertical back that has been attached at the hip joints. Figure 1b shows the designed back support with all its components including a compartment for holding the batteries. In the wheelchair mode, the device consists of a back post, armrests, front and rear wheels, and the chassis. Two telescoping links, identical to the ones used for leg mechanism are used to complete a four-link closed-loop serial linkage. Figure 1c shows the four-link parallelogram chassis and how it transforms from wheelchair to exoskeleton mode.

Once the person starts to proceed into exoskeleton mode, the parallelogram starts to contract, with the top link moving up and the left and bottom link moving to contract along the straightening leg links too. The upward motion allows the rear wheels to rise and leave the ground and finally rise almost to the height of the knees, allowing the person to move in the exoskeleton mode. The front and rear wheels used in wheelchair design are shown in Fig. 1d.

Two linear actuators (one at each knee), as shown in Fig. 2a are being used at the leg links, with one point of attachment on the thigh link, and other on the shank link. These provide the required torque for motion at the knees. Two heavy-duty, back drivable DC motors are used to provide required torque and RPM to rear wheels for rotation while in wheelchair mode, and for the rotation of hip joints while in exoskeleton mode. Figure 2b shows the DC motor used for hip joint and rear-wheel actuation.

Figure 2c shows the gear, dog clutch, and belt based power transmission mechanism. The mechanism is designed in such a way that it could drive the hip joints in exoskeleton mode without engaging with the rear wheels during that operation, and also performs the vice-versa by actuating the rear wheels without any disturbance to the hip joints during the wheelchair mode. A moving gear sandwiched between two dog clutch devices allows fulfilling this purpose successfully.

Foot of the exoskeleton needs to be actuated for the exoskeleton to perform locomotion in accordance with the normal gait motion of a human body. To reduce the cost of actuators, a passively actuated mechanism is developed which can perform required motion at the ankle using angular motion from the knee as its reference. This multi-use of actuators allows reduction in overall cost associated with the device.

Based on the decided specifications, an appropriate design and CAD model of the mechanism is developed. Figure 3 shows the concerned design in its two modes, i.e., wheelchair mode and exoskeleton mode.

2.2 Calculation of Torque

Torque at Rear Wheels. Total force to drive the wheelchair is a sum of rolling force, the force required to move on inclined plane and force required to accelerate the device from rest to desired speed.

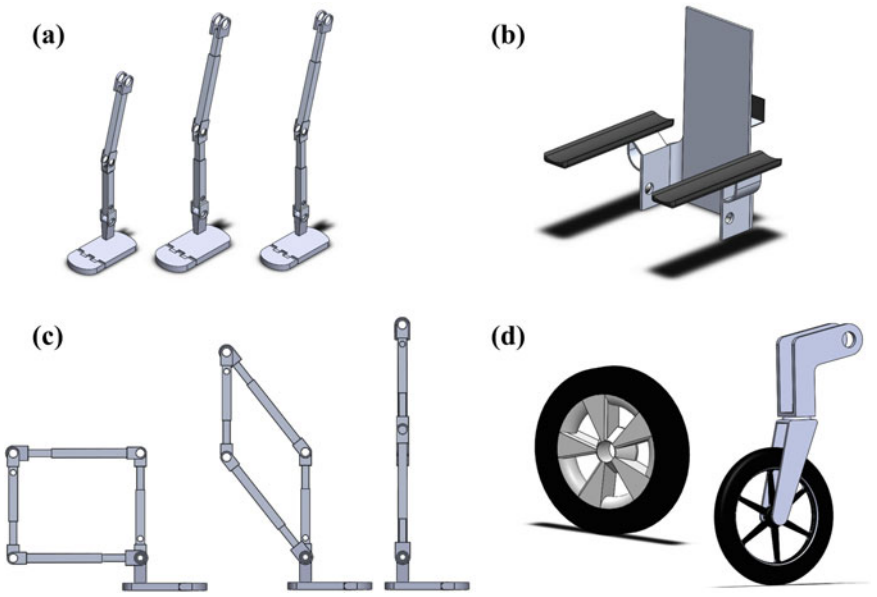

Fig. 1 CAD model of **a** telescoping leg links, **b** back support, **c** four-link mechanism and **d** front and rear wheels

$$F = F_R + F_I + F_A \tag{1}$$

where F is the total force, F_R is the rolling force, F_I is the force on an inclined plane and F_A is the force needed for acceleration.

$$F_R = M \times \mu_r \times g \tag{2}$$

where F_R is the rolling force, M is the total mass of device and human, μ_r is the coefficient of rolling resistance and g is acceleration due to gravity.

$$F_I = M \times sin(\alpha) \times g \tag{3}$$

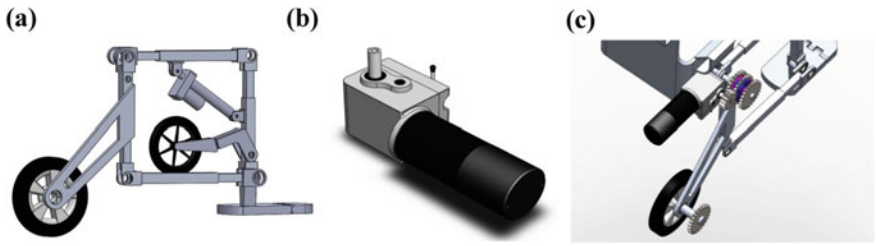

Fig. 2 CAD model of **a** linear actuators, **b** DC motor, **c** power transmission system

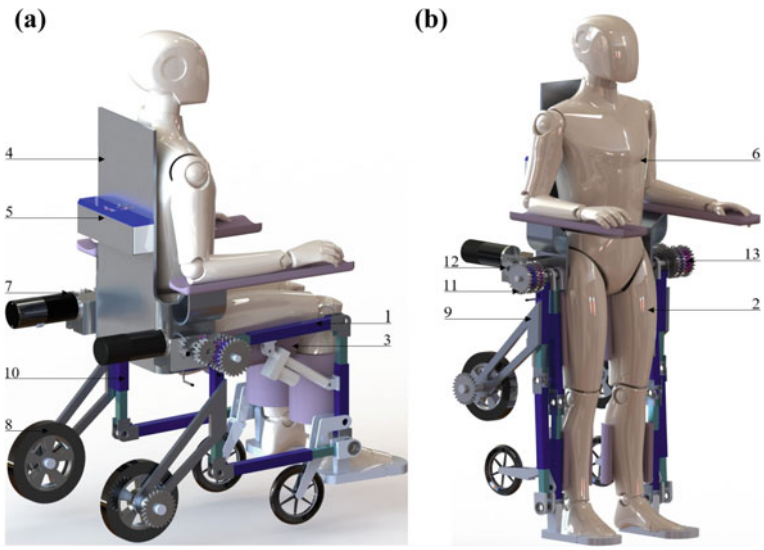

Fig. 3 Proposed design **a** Wheelchair mode, **b** Exoskeleton mode with labeled parts

where F_I is the force on an incline, M is the total mass, α is the incline angle and g is acceleration due to gravity.

$$F_A = M \times (v/t) \tag{4}$$

where F_A is the force required for acceleration, M is the total mass, v denotes final velocity and t is the time. Total torque needed at wheels is calculated using the product of total force with the radius of the wheel.

$$\tau = F \times r \tag{5}$$

where τ is total torque at wheels, F is the total force and r is the radius of the wheel.

Torque Required at Knee. Torque at the knees can be calculated using weights of device parts, and the location of their centers of gravity. The system can be divided into three sub-assemblies or systems for the calculation of torque at the knees. System 1 includes the thigh link, human thigh and support pad. System 2 has the back support, batteries and body trunk. System 3 includes the motor, rear wheel, and rear-wheel connector along with lower part of chassis, gears and the dog clutches. The equations for the mass of the three systems are illustrated below.

$$M_1 = m_1 + m_2 + m_3 \tag{6}$$

where M_1, m_1, m_2, and m_3 are masses of system 1, thigh link, human thigh, and support pad, respectively. As the mass of system 2 is distributed equally on both sides, it will be half the sum of individual masses.

$$M_2 = (m_4 + m_5 + m_6)/2 \tag{7}$$

where M_2, m_4, m_5, and m_6 are masses of system 2, back support, batteries, and human trunk, respectively.

$$M_3 = m_7 + m_8 + m_9 + m_{10} + m_{11} + m_{12} + m_{13} \tag{8}$$

where M_3, m_7, m_8, m_9, m_{10}, m_{11}, m_{12}, and m_{13}, respectively, denote the masses of system 3, motor, rear wheel, rear-wheel connector, lower part of chassis, driven gears, drive gear, and dog clutch mechanism. Total torque at the knee can be calculated using Eq. (9) given below:

$$\tau = (M_1 \times g \times d_1) + (M_2 \times g \times d_2) + (M_3 \times g \times d_3) \tag{9}$$

where τ is the torque at one knee, M_1, M_2, and M_3 are masses of systems 1, 2 and 3, respectively, g is acceleration due to gravity, and d_1, d_2, and d_3 are the distances of centers of masses of the three systems from the knee. Masses considered for the different components (m_1 *to* m_{13}) are in accordance with the labeling in Fig. 3.

2.3 Modeling Using FEM

Static structural analysis of different parts of the mechanism is performed using the ANSYS Workbench software. For analysis of the front-wheel connector, the base of the wheel is kept fixed while applying downward force at the connector joint. With a number of nodes and elements (BEAM4) at 25176 and 13456, respectively, maximum deformation of 0.79 mm is found in front-wheel connector, where it is attached to the parallelogram linkage, as shown in Fig. 4a. Figure 4b shows the equivalent von Mises stress which is quite less in the front-wheel connector as obtained from the analysis.

The link used for connecting the rear wheel with the parallelogram linkage is deformed by 0.30 mm at the junction of connector and linkage, as shown in Fig. 5a. These results are obtained by keeping the rear wheel joint fixed while applying a downward force at the junction between the connector and parallelogram chassis. The number of nodes and elements (BEAM4) are kept at 5565 and 2867 in this simple part. Figure 5b shows the equivalent von Mises stress result, far less than allowable stress, in the connector as obtained with the same imposed conditions.

The results of total deformation and equivalent stress in the parallelogram linkage are shown in Fig. 6a and b respectively. These are observed upon fixing the bottom joints of parallelogram chassis while applying downward force on top of the linkage. The number of nodes in the mesh is 33664 with a total of 6528 elements (BEAM4). A maximum deformation of 0.32 mm is observed in the top portion of the linkage. The aluminum alloy as a material is chosen for both the wheel connectors as well as the chassis of the wheelchair. The assistive pads of plastic material used to support thighs of the person have a higher deformation of 2.42 mm in the right side, as shown in Fig. 7a. The meshing in this padding generates 4301 nodes with 604 elements

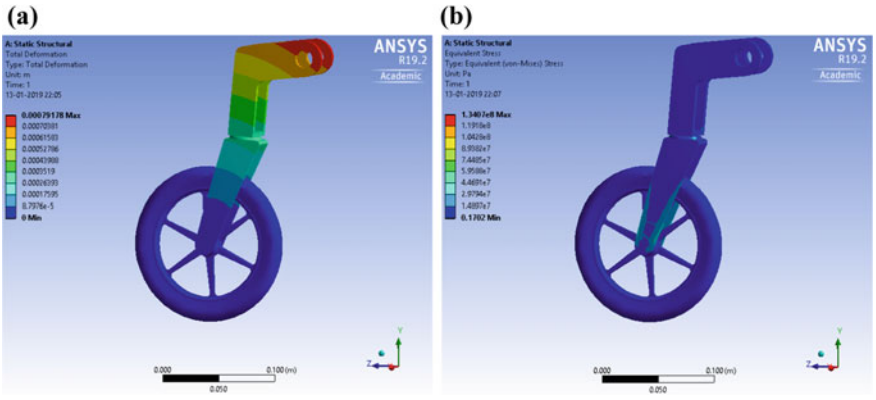

Fig. 4 Structural analysis of front-wheel connector **a** Total deformation, **b** Equivalent von Mises stress

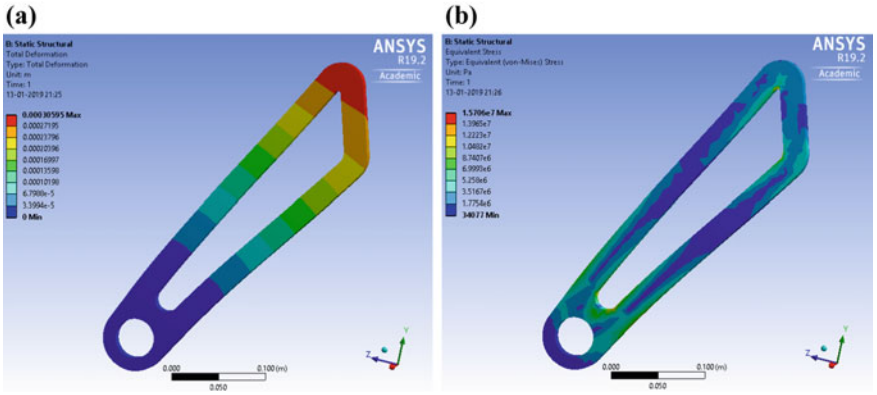

Fig. 5 Structural analysis of rear-wheel connector **a** Total deformation, **b** Equivalent von Mises stress

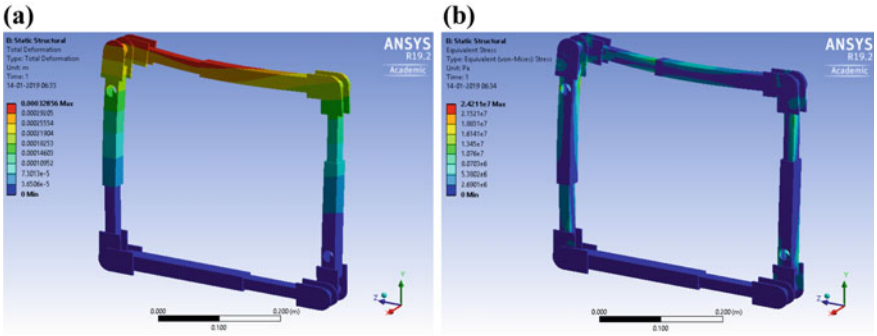

Fig. 6 Structural analysis of parallelogram chassis **a** Total deformation, **b** Equivalent von Mises stress

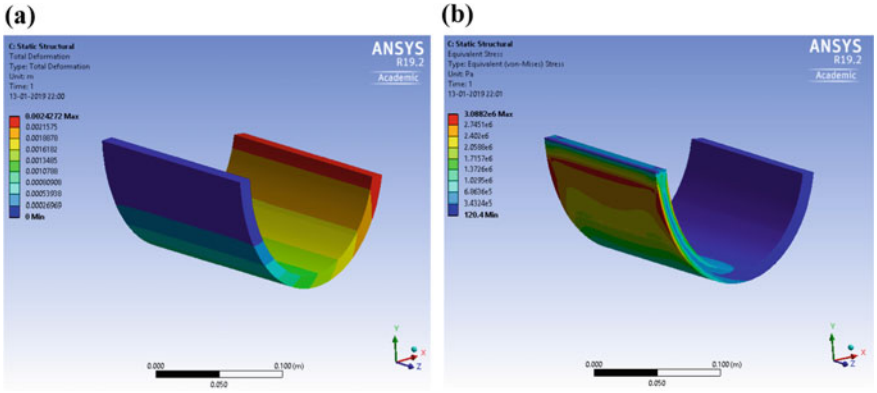

Fig. 7 Structural analysis of support pads **a** Total deformation, **b** Equivalent von Mises stress

(SOLID45). Figure 7b illustrates the equivalent stress, less than allowable stress, observed in the part, obtained with the left side of pad fixed to the parallelogram chassis.

3 Results and Discussions

3.1 *Torque Required at Rear Wheels During Sit to Stand Motion*

Considering an average human of mass 70 kg and the mass of wheelchair exoskeleton being ~18 kg calculated from the SolidWorks CAD model after assigning corresponding material properties to each component, the total mass of the device plus human becomes 88 kg. The considered design parameters are given in Table 1.

Using Eqs. (2)–(4),

$$F_R = 88 \times 0.01 \times 9.81 = 8.63 \text{ N} \tag{10}$$

$$F_I = 88 \times \sin(5^\circ) \times 9.81 = 75.24 \text{ N} \tag{11}$$

$$F_A = 88 \times (1.11/1) = 97.68 \text{ N} \tag{12}$$

Total force can be calculated using Eqs. (1), (10)–(12) as

$$F = 8.63 \text{ N} + 75.24 \text{ N} + 97.68 \text{ N} = 181.55 \text{ N} \tag{13}$$

Now using Eqs. (5) and (13) to calculate the total torque

$$\tau = 181.55 \text{ N} \times 0.115 \text{ m} = 20.88 \text{ N-m} \tag{14}$$

Hence, the torque required for the actuation of rear wheels during sit to stand motion is calculated as 20.88 N-m.

Table 1 Design parameters for torque estimation at rear wheels

Radius of rear wheel	115 mm
Desired speed of wheelchair exoskeleton in sitting configuration	1.11 m/sec
Desired acceleration time	1 s
Maximum incline angle (α)	5 degrees
Working surface	Concrete floor
Coefficient of rolling resistance	0.01

3.2 Torque Required at Knee During Sit to Stand Motion

Table 2 gives the percent weight proportions and characteristic length of different parts of the human body.

The masses of components of the wheelchair exoskeleton are calculated using SolidWorks after assigning corresponding material properties for each component. The masses of all involved components are given in Table 3.

Center of mass of the lower exoskeleton system consisting of rear wheel, wheel to chassis connector, gears and L shaped linkage is found to be at 0.51 m from the knee joint whereas for the system of back post, trunk, and battery case, it is found to be at 0.47 m. Moreover, considering a 70-kg person with height 1.75 m the length of the thigh is approximately 0.44 m, which gives the center of mass of thigh, thigh link and pad system at 0.293 m from knee joint. Masses of different systems are now calculated using the above-mentioned equations.

Using Eqs. (6)–(8),

Table 2 Fractional distribution of body weight and height of an average Indian human

Segment	Weight proportion in %	Characteristic length (m)
Head	8.23	0.29
Whole trunk	54.15	0.75
Total arm	5.335	0.45
Thigh	11.125	0.44
Lower leg	5.05	0.42
Foot	1.38	0.26

Table 3 Mass of different components involved in torque calculation

Component	Mass (kg)
Thigh link (m_1)	0.31
Human thigh (m_2)	7.787
Thigh support pad (m_3)	0.1
Back support (m_4)	0.8
Batteries (m_5)	5
Human trunk (m_6)	37.905
Motor (m_7)	2.0
Rear wheel (m_8)	0.5
Rear wheel connector (m_9)	0.413
Lower portion of chassis (m_{10})	0.56
Four driven gears (m_{11})	$4 \times 0.06 = 0.24$
Drive gear (m_{12})	0.06
Dog clutch mechanism (m_{13})	$4 \times 0.05 = 0.20$

$$M_1 = 0.31 + 7.787 + 0.1 = 8.197 \text{ kg} \tag{15}$$

$$M_2 = (0.8 + 5 + 37.905)/2 = (43.705/2) = 21.852 \text{ kg} \tag{16}$$

$$M_3 = 2.0 + 0.5 + 0.413 + 0.56 + 0.24 + 0.06 + 0.2 = 3.973 \text{ kg} \tag{17}$$

Now using Eqs. (9), (15)–(17) to calculate torque at one knee,

$$\begin{aligned}\tau =&(8.197 \times 9.81 \times 0.293) + (21.852 \times 9.81 \times 0.47) \\ &+ (3.973 \times 9.81 \times 0.51) = 144.19 \text{ N-m}\end{aligned} \tag{18}$$

Hence, torque required for the actuation of knee joints during sit to stand motion is calculated as 144.19 N-m.

4 Conclusions

In this paper, a novel motorized wheelchair exoskeleton has been proposed. The device has been modeled in SOLIDWORKS software. Thereafter, structural analysis has been done using ANSYS Workbench, which has given maximum deformations of 0.79 mm, 0.30 mm, 0.32 mm, and 2.42 mm in front-wheel, rear wheel connector, parallelogram chassis, and thigh paddings, respectively. Then, for a test case with an average human of 70 kg, torque requirements for the actuation of rear wheels and knee joints during sit to stand motion have been found out as 20.88 N-m and 144.19 N-m, respectively. The device successfully achieves adjustability in its size by use of telescoping links in the legs. Moreover, the use of a lesser number of motors for multiple actuations helps cutting down the overall cost associated with the device. The prototype, with the design analysis results and proper safety guidelines, will be a fine proposition to solve the problem of assistive wheelchair exoskeleton devices. Further, the dynamic analysis of the exoskeleton system for human gait with experimental validation will be carried out in the near future.

References

1. Patnaik L, Sahoo HS, Sahu T (2015) Awareness of the warning symptoms and risk factors of stroke among adults seeking health care from a rural hospital of India. Ann Indian Acad Neurol 18:487–488. https://doi.org/10.4103/0972-2327.165479
2. Lee S, Sankai Y (2002) Power assist control for walking aid with HAL-3 based on EMG and impedance adjustment around knee joint. In: IEEE international conference on intelligent robots and systems vol 2. pp 1499–1504. https://doi.org/10.1109/irds.2002.1043967

3. Banala SK, Kim SH, Agrawal SK, Scholz JP (2009) Robot assisted gait training with active leg exoskeleton (ALEX). Neural Sys Rehabil Eng 17(1):2–8. https://doi.org/10.1109/TNSRE.2008.2008280
4. Veneman JF, Kruidhof R, Hekman EE, Ekkelenkamp R, Van Asseldonk EH, Van Der Kooij H (2007) Design and evaluation of the LOPES exoskeleton robot for interactive gait rehabilitation. Neural Sys Rehabil Eng 15:379–386. https://doi.org/10.1109/TNSRE.2007.903919
5. ReWalk Robotics, ReWalk Personal 6.0. http://rewalk.com/rewalk-personal-3
6. Jezernik S, Colombo G, Keller T, Frueh H, Morari M (2003) Robotic orthosis lokomat: a rehabilitation and research tool. Neuromodulation Technol Neural Interface 6:108–115. https://doi.org/10.1046/j.1525-1403.2003.03017.x
7. Shankar T, Dwivedy SK (2015) A hybrid assistive wheelchair-exoskeleton. In: Proceedings of the international convention on rehabilitation engineering & assistive technology. Singapore Therapeutic Assistive and Rehabilitative Technologies (START) Centre

Characterization of Banana and Bagasse Fiber-Reinforced Hybrid Epoxy Composites

R. Prem Chand, Y. P. Ravitej and J. V. Shiva Mani Kanta

Abstract In this work, banana and bagasse fibers have been taken as reinforcement material because of its ease of availability and low cost. Initially, the density of the fibers are found using water displacement method. The fibers were treated by NaOH and NaCl solution of 5% concentration for good adhesion property. These are reinforced with the epoxy with Hardener—HY 951. The 20 and 30% of volume fraction of banana and bagasse fibers of equal proportions are taken for fabrication using hand lay-up method for the dimension 300 * 300 mm^2. Change in the volume fraction of FRC's changes the value of young's modulus by making the material more stiffer. The testing was carried out by the computer-integrated universal testing machine (UTM), which has the capacity of 100KN Kalpak software is used for the data acquisition the testing. The specimen is cut into as per ASTM D-3039 and ASTM D-790 standards for tensile test and flexural bending test, respectively. Tensile test and flexural bending tests are conducted on 20 and 30% of volume fraction of fibers (banana and bagasse). Results of tensile test and flexural bending test are obtained experimentally and compared each other, results reveal that fibers of 30% volume fraction make material stiffer and in turn increases the elasticity and UTS.

Keywords Tensile test · Computer-integrated universal testing machine · Flexural bending tests · Data acquisition · Weight reduction method

R. Prem Chand
Department of Mechanical Engineering, T John Institute of Technology, Bengaluru 560076, Karnataka, India

Y. P. Ravitej (✉) · J. V. Shiva Mani Kanta
Depatment of Mechanical Engineering, Dayananda Sagar University, Bengaluru 560068, Karnataka, India
e-mail: ravitejmtech@gmail.com

D. Maity et al. (eds.), *Advances in Fluid Mechanics and Solid Mechanics*,
Lecture Notes in Mechanical Engineering,
https://doi.org/10.1007/978-981-15-0772-4_19

1 Introduction

This work focuses on banana and bagasse fiber-reinforced hybrid epoxy composites. This will provide better properties by using naturally available fibers and deliver a better composite material for the advanced the composite world. The introduction of advanced epoxy resin matrix material's with high-performance reinforcement of the fibers of banana and bagasse, the penetration of the fibers as witnessed in the steady of expansion in uses and volume.

While increasing it has been resulted in expected as the costs reduction. For certain application, the use of natural fiber-reinforced composites rather than metals has a higher efficiency as well as the effect in its characteristics. The many materials when they are in a fibrous form shows very good strength property but to achieve these properties the fibers should be reinforced with the suitable matrix material. The density of cane bagasse as a composite of long particles and their internal adhesion as well as has verified their temperature until their decomposition and suggested their possible future utilization [1]. Bagasse reinforced composites having wider application in automotive and railway coaches and buses for public transport system keeping these characteristics and applications of Bagasse fiber has been selected to combine with Banana fibers in order to extract the better properties. Out of the available manufacturing process the hand lay-up technique is selected to prepare bagasse and banana fiber-reinforced hybrid composite by using epoxy with proper hardener. No work has been published on hybrid polymer matrix, to fill the void characterization of the banana and bagasse fiber-reinforced hybrid epoxy composites are obtained for different volume percentage combinations of fibers and results are correlated with each other.

2 Literature Survey

The usage of the bagasse wastes to prepare fiber-reinforced composites for commercial views and also discuss recent development of bagasse fiber-reinforced composite, processing methods and its applications [2] is investigated. The mechanical properties as per ASTM standards are investigated and stress–strain and deflection by using ANSYS software tests were conducted for different volume fractions and the results were compared. The authors suggested for hybrid composites by adding different fibers [3]. The mechanical behavior of hybrid natural composites samples were taken for different fibers with epoxy by using hand lay-up method for different weight fractions. Mechanical properties were evaluated according to ASTM standards and better results were obtained [4]. The hybridization process by incorporating synthetic fiber with natural fiber to get higher strength, better stiffness and also improvements in mechanical properties [5]. The mechanical properties of hybrid epoxy composites show better results in tensile, flexural, and impact compared with glass-reinforced composite and banana-reinforced composite. The banana fiber has

been treated with sodium hydroxide in order to increase the wettability. The results of treated and untreated banana fiber-reinforced composites were compared [6]. The tensile strength on the pseudo-stem woven fabric reinforced epoxy composite is increased by 90% compared to virgin epoxy [7]. Banana fibers are compared through their applications, use, and properties it has been concluded that banana fibers providing better chemical composition and properties by keeping the results obtained by the different tests. Banana fibers show high variability along with and between fibers. The standard deviation has been found to decrease with increasing diameters of fibers. The behavior of fibers also gives hint for the subsequent behavior as reinforcement in composites.

The above literature survey reveals that efficient hybridization of banana and bagasse is obtained which improves the properties of the material for the greater volume fraction of fibers for hybrid polymer matrix composites.

2.1 Calculation of Densities

Banana fibers are extracted by cutting into lengths into the convenient size and peeling by layer-wise. The individual sheaths were dried under sunlight for 2 weeks and again were soaked in water for 1 week. The sheaths were dried again and fibers were ripped off. The obtained banana fibers were checked for strength by using a single fiber strength method. Density calculation has been done for the individual fibers by using the water displacement method. In this method the displacement of the water after the addition of fiber into the water the density of fiber is determined. The weight of the fiber is noted down. The density calculation of banana fiber is shown in Table 1.

The Baggies fibers were extracted by crushing the sugarcane using the suitable machine the obtained residue were taken and dried in sunlight for one week. The dried residue was immersed in water for some time and then kept in the atmosphere by exposing for sunlight for one week. The stalks which are present in a residue were dried. The obtained residue is called Bagasse. In that, the fibers were extracted and preserved. Density calculation has been done for the bagasse the values have shown in Table 2. Out of the available manufacturing process, the hand lay-up technique is selected to prepare Bagasse and Banana fiber-reinforced hybrid composite by using epoxy with proper hardener. No work has been published on hybrid polymer

Table 1 Density test of banana fiber using the water displacement method

Sl. No	Mass of fiber	Initial reading	Final reading	Difference in volume	Density
1	2.1	50	51.8	1.5	1.35
2	2	49	50.5	1.4	1.32
3	2.5	52	53.9	1.9	1.3

Table 2 Density test of bagasse fiber using water displacement method

Sl. No	Mass of fiber	Initial reading	Final reading	Difference in volume	Density
1	2	40	41.6	1.6	1.25
2	2.2	42	43.7	1.7	1.29
3	2.5	44	46.1	2.1	1.1

matrix, to fill the void characterization of the banana and bagasse fiber-reinforced hybrid epoxy composites are obtained for different volume percentage combinations of fibers and results are correlated with each other.

3 Chemical Treatment

3.1 Alkali Treatment

Alkali treatment for natural fiber mercerization is applied in this method. It used for the treatment of natural fibers. This method provides good quality fibers. The mercerization process removes the natural and artificial impurities which are present in the fiber by that it improves the adhesion between fiber and matrix. The process reduces fiber diameter and improves aspect ratio. The alkali treatment gives better results in mechanical interlocking by increasing the surface roughness. The prepared fibers of banana and bagasse were immersed in the 5% concentration NaOH solution. Immersed fiber was soaked in the solution for 2 h, then the fibers were taken out form the solution and fibers were washed by the distilled water which is having the pH value 7. The fibers were washed neatly 4–5 times by using distilled in order to remove the NaOH solution which has been accumulated on the fiber surface. This process is used to remove the lignin content which is present in the fibers.

3.2 Saline Treatment

The distilled water was kept separately for one hour. The silane treatment has been done on fibers by that which provides fiber-matrix adhesion to stable properties of the composite. The sodium chloride pellets were dropped in a container which consists of water by that the 5% concentration of the silane solution has been prepared. The fibers were soaked separately in a silane solution and separately to 2 h in the solution. The fibers were taken out from the container after two hours and then washed with distilled water. These fibers were kept under sunlight for 1 week and dried.

After treatment (Alkaline + Saline), the weight loss was calculated from the equation.

$$\text{Weight loss} = [500 - 424/500] * 100$$

$$\text{Weight loss} = 15.2\%$$

W_0 and W_1 denote the weight of Natural fiber before and after (NaOH and NaCl) treatment, respectively.

4 Fabrication of Banana and Bagasse Fiber-Reinforced Hybrid Epoxy Composites

Banana and bagasse fibers were treated chemically by using NaOH and NaCl solutions, the fibers were dried to the sunlight. The dried fibers were collected and chopped to predetermine different lengths.

4.1 Calculation of Banana and Bagasse Fiber-Reinforced Hybrid Epoxy Composites

From the water displacement method, densities of banana and bagesse are shown below.

$$\begin{aligned}
&\text{Density of Banana fiber} = 1.35\ \text{g/cm}^3 \\
&\text{Density of Bagasse fiber} = 1.25\ \text{g/cm}^3 \\
&\text{Density of Epoxy (LY 556)} = 1.15\ \text{g/cm}^3 \\
&\text{Volume of the composite die} = \text{length} * \text{width} * \text{thickness} \\
&\text{Volume of the composite die} = 300 * 300 * 3\ \text{mm} = 270\ \text{cm}^3
\end{aligned} \tag{2}$$

4.1.1 Calculation for 20% Volume Fraction of Banana and Bagasse Fiber-Reinforced Hybrid Epoxy Composites

The calculations of 20% Volume composite is shown below.

$$\text{Vc} = \text{V Banana} * \text{V Bagasse} * \text{V Epoxy}$$

$$\text{m composite}/\rho\,\text{composite} = \text{m banana}/\rho\ \text{banana} * \text{m bagasse}/\rho\ \text{bagasse} * \text{m epoxy}/\rho\ \text{epoxy}$$

Mass of the banana fiber, bagasse fiber, and epoxy is taken 0.1, 0.1, and 0.8, respectively.

$$1/\rho_{\text{composite}} = 0.1/1.35 * 0.1/1.25 * 0.8/1.15$$
$$1/\rho_{\text{composite}} = 0.0741 * 0.08 * 0.6956$$
$$1/\rho_{\text{composite}} = 0.8497$$
$$\text{Density composite} = 1.176\ \text{g/cm}^3 \quad (2)$$

$$\text{Mass of composite mc} = \text{m composite} * \text{V composite}$$

From Eq. (1) and (2)

$$\text{Mass of composite mc} = 1.176 * 270$$

$$\text{Mass of composite mc} = 317.52\ \text{gms}$$

$$\text{Mass of composite mc} = 1.176 * 270$$

$$\text{Mass of composite mc} = 317.52\ \text{gms}$$

- **For volume fraction of 20%, volume fraction of banana and bagasse fiber-reinforced hybrid epoxy composites**

$$\text{Mass of total fiber} = 317.52 \times 20\%$$
$$\text{Mass of total fiber} = 63.504 \approx 64\ \text{gms}$$
$$\text{Mass of Banana fiber} = 32\ \text{gms}$$
$$\text{Mass of total fiber} = 63.504 \approx 64\ \text{gms}$$
$$\text{Mass of Banana fiber} = 32\ \text{gms}$$
$$\text{Mass of Bagasse fiber} = 32\ \text{gms}$$

- **For volume fraction of 30%, volume fraction of banana and bagasse fiber-reinforced hybrid epoxy composites**

$$\text{Vc} = \text{V Banana} + \text{V Bagasse} + \text{V Epoxy}$$

$$\text{M composite}/\rho\ \text{composite} = \text{M banana}/\rho\ \text{banana} + \text{M bagasse}/\rho\ \text{bagasse} + \text{M epoxy}/\rho\ \text{epoxy}$$

$$1/\rho_{\text{composite}} = 0.15/1.35 + 0.15/1.25 + 0.7/1.15$$
$$1/\rho_{\text{composite}} = 0.1111 + 0.12 + 0.6087$$

$$1/\rho_{composite} = 0.8398$$

$$\rho_{Composite} = 1.19\ g/cm^3$$

Massof composite mc $= \rho_{composite} \times V_{composite}$

Mass of composite mc $= 1.19 \times 270$

Mass of composite mc $= 321.3$ gms.

Mass of total fiber $= 321.3 \times 30\%$

Mass of total fiber $= 96$ gms.

Mass of Banana fiber $= 48$ gms.

Mass of Bagasse fiber $= 48$ gms.

4.2 Hand Lay-Up Method

Hand lay-up method is one of the preferred methods for the preparation of composite. Different fibers were taken for different lengths as well as different volume fraction. Initially, 5 mm length fibers were taken to prepare the composite for 20% volume fraction. The resin is prepared by using LY556 with suitable hardener HY 951 at proper proportions.

The well prepared mixed resin has been layered into the predetermined mold (specimen mold size is 300 * 300 * 3) mm. The chopped, both the fibers, banana and bagasse are then distributed randomly over the resin as per calculations. In the same way, the resin and the fibers were filled in the mold layer by layer. Then one more layer of resin is applied on the top surface of the mold then the suitable weight has been kept on the mold in order to avoid the shrinkage and the mold has been allowed for curing into the oven for 8 h. The process has been repeated for different fiber length with different volume fraction.

To prepare the hybrid composite plate the process used is hand lay-up process. Initially, in the hand lay-up process, the pre-mold is prepared according to the required dimensions of the composite plate. The Teflon tape is used for the boundary of the dimensions of the plate. The acetone is applied on the floor of the pre-mold surface and the mixture of fibers and resin are randomly distributed on the mold surface.

For the required dimension of thickness, the aluminum slab is placed on the top of the surface on the prepared die to remove the excess amount of resin and also to avoid the air bubbles in the mold. After removing the composite die the plate is kept in the woven for about 100 °C for 2 h and finished fabricated model is shown in Fig. 1.

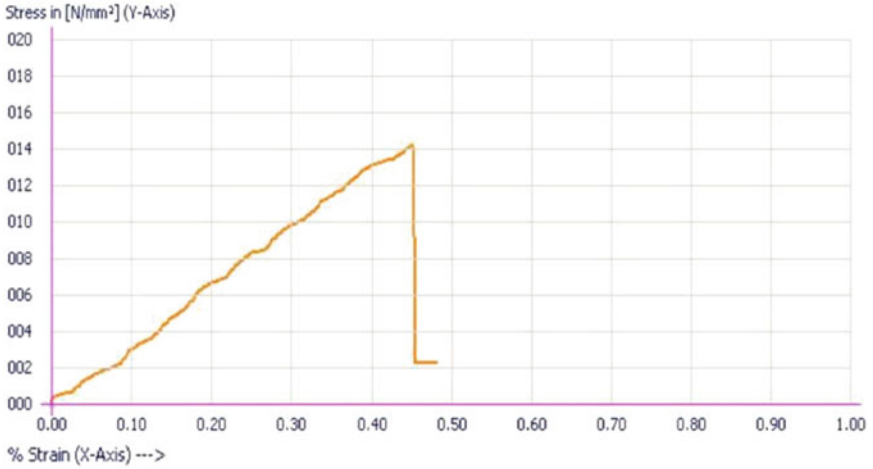

Fig. 1 Graph of stress versus strain for the tensile test

5 Results and Discussions

The obtained hybrid composite plates were cut according to ASTM composite standards for the characterizations. Some of the tests were conducted in order to characterize the mechanical properties. The testing was carried out by the computer-integrated universal testing machine (UTM) which has the capacity of 100KN Kalpak software is used for the data acquisition the testing.

5.1 Tensile Test

The desired dimension of specimen for mechanical testing was cut by the fabricated composite. Tensile strength of a material is the maximum amount of tensile stress that it can be taken before failure. Dog-bone type specimen is the commonly used specimen for tensile test. According to the ASTM D-3039, the tensile specimen was made and the dimension is shown in Table 3.

Table 3 The tensile specimen dimensions

Total length in (mm)	Span length in Mm	Width in mm	Thickness in mm
250	170	25	3

- **Calculation for Tensile Strength**

$$\text{Tensile Strength} = W/(b \times d)$$

where W, b and d are the ultimate failure load (N), mean width of sample (mm), and mean thickness of sample (mm), respectively.

$$\text{Tensile Strength} = W/(b \times d) = 645/(25 \times 3) = 8.60 \text{ MPa}$$

The tensile properties of the prepared specimen of ASTM D-3039 are tested, the stress and strain curve obtained is shown in Fig. 1.

The first specimen was 20% volume fraction specimen, where the specimen broke at the tip of the neck and the second shows the 30% volume fraction specimen where it as broke with maximum ultimate tensile strength by comparing to the 20% of volume fraction specimen. Also by comparing the experimental and theoretical, the percentage of error is less than 10%.

The above graph shows the results for stress versus strain in the tensile test, where the maximum stress is 14.15 MPa and the Strain is 0.48 for one of the tensile test which was carried out (Tables 4, 5, 6).

The results of the ultimate tensile strength versus volume fraction of the hybrid composite specimen, where the ultimate tensile strength for 20% of volume fraction is less compare to the volume fraction of 30%, results reveal that fibers of 30% volume fraction makes material stiffer and in turn increases the elasticity and UTS.

Table 4 Tensile test results

Sl. No.	Specimen composition	Peak load (N)	Ultimate tensile strength (MPa)
1	20%	436	9.08
2	30%	639	14.15

Table 5 Dimension for flexural bending test

Total length in (mm)	Span length in (mm)	Width in (mm)	Thickness in (mm)
125	100	12.5	3

Table 6 Results for flexural bending test

Sl. No.	Specimen composition	Peak load (N)	3 point flexural strength (MPa)
1	20%	46	48.94
2	30%	76	81.41

5.2 Flexural Bending Test (3 Point Bending Test)

The second test which we carried out was the three-point bending test that is the flexural test this was chosen because it requires less material and eliminates the need to accurately determine center point deflections with test equipment. According to the ASTM D-790, the test was carried out and the dimensions are given below.

5.2.1 Calculation for Flexural Strength

For the calculation of Flexural strength, the formula is given below

$$\text{Flexural Strength} = 3PL/2bh^2 = (3 \times 46 \times 80)/\left(2 \times 12.5 \times 3^2\right) = 49.06 \text{ MPa}.$$

The above specimen considering the ASTM D-790 was taken and kept in the UTM machine and the load was applied at the center point.

For the 20% of volume fraction, the flexural bending strength was 48.94 MPa and for the 30% of volume fraction, the flexural bending strength was 81.41 MPa as shown in the above graph. When the percentage of volume fraction is increased the better results were obtained in the above two tests. Also, the theoretical test was calculated and by observing both experimental and theoretical results for flexural test the percentage of error was calculated and it was less than 10%, results reveal that fibers of 30% volume fraction make material stiffer and in turn increases the elasticity and UTS.

6 Conclusion

The banana and bagasse Fiber-Reinforced Hybrid epoxy composite characteristics have been studied both the fibers were treated with 5% NaOH and 5% NaCl solutions. By that, the improved adhesion property has been observed. The fibers were reinforced into the epoxy resin by using the hand lay-up method. Test plates were obtained and were tested. The values which are obtained shows improved mechanical properties for larger volume fraction FRC's.

References

1. Ranadive Ananth G, Arun N, Lalitha P (2011) Bio-bleaching and bio-pulping of bagasse fiber using co-culture of trichoderma viridae and aspergillus glaucus fungi. Asian J Biosci 6: 128–130
2. Silva AJP, Lahr FAR, Christoforo AL (2012) Properties of sugarcane base to use in OSB. Int J Mater Eng, 50–56

3. Verma D, Gope PC, Maheshwari MK, Sharma RK (2012) Bagasse fiber composite a review. J Matter Environ Sci, 1079–1092. ISSN 2028-2508
4. Parndaman P, Jayaraman M (2015) Study on the mechanical properties of natural fibers reinforced hybrid composite. Int J Appl Eng Res 10: 12009–12019. ISSN 0973-4562
5. Tiwary M, Singh VK, Gope PC, Choudhary AK (2012) Evaluation of mechanical properties of bagasse-glass reinforced composite. J Mate Environ Sci, 171–184. ISSN 2028-2508
6. Balaji A, Karthekeyan B, Sundraj C (2015) Bagasse fiber-the future bio-composite material, a review. Int J CHEM Tech Res 7:223–233
7. Shashi Shankar P, Tirupathi Reddy K, Chandrashekar V (2014) Mechanical performance and analysis of banana fiber reinforced epoxy composites. Int J Recent Trends Mech Eng 1(4)

Crack Growth Simulation in Quasi-brittle Materials Using a Localizing Gradient Damage Model

Alok Negi and Sachin Kumar

Abstract Failure in quasi-brittle materials comes under an intermediate category of fracture failure, which includes different stages, i.e., micro-cracks nucleation, growth, and coalescence into a macroscopic crack. The different stages of failure result in a tension-softening structural response, which can be accurately modeled using the conventional gradient damage models. However, due to a constant interacting domain throughout the load history, conventional gradient damage models suffer from various drawbacks which limits their application to simulate the final stages of quasi-brittle failure process. In this contribution, the present work illustrates a thermodynamically consistent localizing gradient damage model, which successfully overcomes the drawbacks of conventional gradient damage models. The localizing gradient damage model uses an interaction function definition in the constitutive framework to take into account the diminishing nonlocal interactions, thus attaining a macroscopic crack in the form of a localized damage profile during the last stages of failure. The numerical accuracy of the model is tested against both mode-I and mode-II types of failure problems and compared with the experimental results.

Keywords Damage · Localizing gradient · Finite element · Quasi-brittle materials

1 Introduction

During the past few decades, failure simulation of a quasi-brittle fracture process has been a topic of interest among many researchers, due to their wide variety of applications in different engineering domains. Differing from the brittle materials, the quasi-brittle materials exhibit a tension-softening response, which can be simulated effectively with the help of discrete and smeared numerical approaches. In discrete approaches such as extended finite element method (XFEM) and cohesive crack

A. Negi (✉) · S. Kumar
Department of Mechanical Engineering, Indian Institute of Technology Ropar, Rupnagar 140001, Punjab, India
e-mail: aloknegi92@gmail.com

D. Maity et al. (eds.), *Advances in Fluid Mechanics and Solid Mechanics*,
Lecture Notes in Mechanical Engineering,
https://doi.org/10.1007/978-981-15-0772-4_20

models [1, 2], cracks are treated as discontinuous displacement fields and the principles of fracture mechanics are required to model the crack growth behavior. Whereas smeared approaches relies on the principles of continuum damage mechanics [3, 4] where cracks are treated as the diffused damage zones with a complete loss of stiffness. Both the approaches are effective enough to model the quasi-brittle fracture process with their own sets of advantages and disadvantages. Smeared approaches offer advantages in terms of prediction of initial cracks in the structure and are generally effective in multiple cracks scenarios, which can be a challenging task with discrete approaches. In the literature associated with smeared approaches, both local and nonlocal continuum damage models have been proposed for simulating the quasi-brittle fracture process. However, due to the strain-softening constitutive relations, the local damage models suffer from various drawbacks such as mesh-dependent results and pathological localization of damage. To overcome these drawbacks, the nonlocal damage models undergo a regularization process with the help of an internal length scale, which can be implemented either through gradient enhancement or integral enhancement [3, 5]. Even though these enhancements differ in their implementation approach, the gradient enhancement in the gradient damage models is equivalent to integral enhancement, when Green's function is used as the weight function in the integral type nonlocal damage models [4]. In the literature associated with nonlocal damage models, conventional gradient damage models with their excellent regularization capabilities are able to simulate the quasi-brittle fracture process. But due to the use of constant interaction domain, they still suffer from various issues such as incorrect damage initiation and spurious damage growth which can be observed during the final stages of failure [6]. The spurious damage growth behavior prevents the formation of a macroscopic crack which is an integral part of the quasi-brittle fracture process. Recently, based on a thermomechanical micromorphic framework, a localized gradient damage model is proposed in [7], which is successful in overcoming the drawbacks of the conventional gradient damage model. The localizing gradient damage model uses an evolving length scale definition in order to attain localized damage profiles during the final stages of softening.

2 Numerical Framework

The present numerical framework of the localized gradient damage model is based on a generalized thermomechanical micromorphic theory, where an additional micro-force balance equation needs to be satisfied. The localized gradient damage also employs a damage-based interaction function in the free energy statement, which results in an evolving interaction domain throughout the load history. This, in turn, prevents the spurious damage growth behavior, which is exhibited by the conventional gradient damage models. The free energy density function is assumed in such a way that a set of generalized stresses $\tilde{\sigma}$ and $\tilde{\boldsymbol{\xi}}$ are obtained, which fulfills an additional balance in the form of the micro-force balance equation, apart from the standard equilibrium equation. The free energy density function is expressed as

$$\psi = \frac{1}{2}(1-\omega)\boldsymbol{\varepsilon} : \mathbf{C} : \boldsymbol{\varepsilon} + \frac{1}{2}h\,(e-\tilde{e})^2 + \frac{1}{2}ghl^2\nabla\tilde{e}\cdot\nabla\tilde{e} \tag{1}$$

where $\mathbf{C}$ is the fourth-order elasticity tensor, ω is a damage variable which is responsible for the degradation in material stiffness, $\boldsymbol{\varepsilon}$ is the strain tensor, h is a coupling modulus, e is an equivalent strain variable characterizing macroscopic deformation, $\tilde{e}$ is a morphic variable characterizing microscopic deformation, g is an interaction function which captures the decrease in nonlocal interactions, and l is an internal length scale parameter. The constitutive relations including the modified stress–strain relation can be derived from the assumed free energy density statement by following the standard Coleman–Noll procedure [8]. The modified stress–strain relation along with the equivalent coupling stress $\tilde{\sigma}$ and moment stress $\tilde{\boldsymbol{\xi}}$ relations are expressed as

$$\boldsymbol{\sigma} = \frac{\partial\psi}{\partial\boldsymbol{\varepsilon}} = (1-\omega)\,\mathbf{C}\,\boldsymbol{\varepsilon} + h\,(e-\tilde{e})\frac{\partial e}{\partial\boldsymbol{\varepsilon}} \tag{2}$$

$$\tilde{\sigma} = \frac{\partial\psi}{\partial\tilde{e}} = h\,(\tilde{e}-e) \tag{3}$$

$$\tilde{\boldsymbol{\xi}} = \frac{\partial\psi}{\partial\nabla\tilde{e}} = ghl^2\nabla\tilde{e} \tag{4}$$

So apart from the standard equilibrium (given in Eq. (5)), a micro-force equilibrium (given in Eq. (6)) will be satisfied at each material point of the domain under consideration.

$$\nabla\cdot\boldsymbol{\sigma} = 0 \tag{5}$$

$$\tilde{\boldsymbol{\sigma}} = \nabla\cdot\tilde{\boldsymbol{\xi}} \quad \text{or} \quad \tilde{e} - e = \nabla\cdot\left(gl^2\nabla\tilde{e}\right) \tag{6}$$

3 Damage Characterization

A modified von Mises equivalent strain definition is used in the numerical examples for the characterization of deformation at the macroscopic scale [4],

$$e = \frac{s-1}{2s(1-2\nu)}I_1 + \frac{1}{2s}\left[\frac{(s-1)^2}{(1-2\nu)^2}I_1^2 + \frac{2s}{(1+\nu)^2}J_2\right]^{1/2} \tag{7}$$

where s is a sensitivity parameter which is the ratio between the compressive strength and tensile strength of the material, ν is the Poisson's ratio, I_1 is the first invariant of strain tensor and J_2 is the second invariant of the deviatoric strain tensor. The employed exponential damage evolution criteria are expressed as

$$\omega = \begin{cases} 0, & \kappa \leq \kappa_0 \\ 1 - \frac{\kappa_0}{\kappa}\{1 - \alpha + \alpha \exp[-\beta(\kappa - \kappa_0)]\}, & \kappa > \kappa_0 \end{cases} \tag{8}$$

where α accounts the residual strength of the material, β controls the softening behavior in structural response, κ is a history parameter that stores the latest maximum value of the nonlocal equivalent strain, and κ_0 is an initiation damage threshold. In the ensuing numerical examples, the damage initiation threshold is computed according to the relation $\kappa_0 = f_t / E$. The history parameter κ is governed by the Kuhn–Tucker relations, expressed as,

$$\dot{\kappa} \geq 0, \; f \leq 0, \; f\dot{\kappa} = 0 \tag{9}$$

where f is the damage loading function, given as,

$$f = \tilde{e} - \kappa \tag{10}$$

The interaction function used in the free energy statement governs the nonlocal interactions in the softening regime [7]. The interaction function depends on the current damage state and its value decreases exponentially with increasing damage. It is defined as

$$g = \frac{(1 - R)\exp(-\eta\omega) + R - \exp(-\eta)}{1 - \exp(-\eta)} \tag{11}$$

where η governs the rate of decreasing nonlocal interactions and R accounts for the residual nonlocal interactions. The material parameter $\eta = 1$ and a residual interaction value of $R = 0.005$ are used in the numerical examples.

4 Numerical Results and Discussion

To demonstrate the accuracy and performance of the localizing gradient damage model, both mode-I and mode-II type of failure problems are considered in our numerical analysis. MATLAB is used to simulate these problems where a standard Newton–Raphson scheme is employed to model the nonlinear response exhibited by the quasi-brittle structure. During the numerical implementation, displacement control analysis is chosen. The problem domain is discretized using quadrilateral elements (Q4 and Q8) with a total of 4 quadrature points within each element for the numerical integration. The first numerical problem relates to the mode-I failure in a three-point bending notched beam specimen. Since the specimen is only 13 mm thick in the out-of-plane direction, the localizing gradient model is modified as per the plane stress condition in our numerical analysis. The geometry and boundary conditions of the three-point bending limestone specimen are given in Fig. 1. The load is applied at the middle point of the specimen. The material parameters of the beam are taken

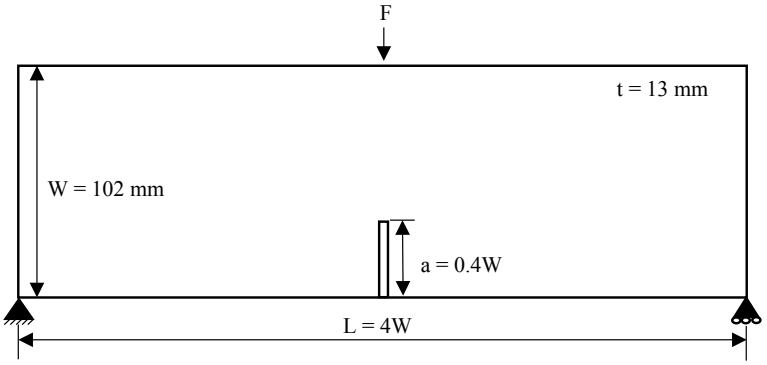

Fig. 1 Geometry structure and boundary conditions of a three-point bending limestone specimen

as those in [7, 8]: elastic modulus $E = 15{,}300$ MPa, tensile strength $f_t = 3.45$ MPa, Poisson's ratio $\upsilon = 0.15$, $h = E \times 10^{-9}$, internal length scale $l = 5.6$ mm, sensitivity parameter $s = 8$, residual strength parameter $\alpha = 0.99$, and softening parameter $\beta = 320$. The damage initiation threshold is taken as $\kappa_0 = f_t / E = 2.25 \times 10^{-4}$.

Figure 2 shows a comparison between the experimental and the numerical computed structural response of the limestone notched beam specimen. Based on the comparison, it can be noticed that the localizing gradient damage model is able to reproduce the experimental response quiet accurately throughout the load history. A similar peak load is attained and the model is able to capture the softening behavior of the specimen accurately.

The damage and nonlocal equivalent strain profile in front of the notch are illustrated in Fig. 3. For this purpose, three different loading points are considered in the load history in order to illustrate the evolution of damage and nonlocal equivalent in a more appropriate way. As per the damage profile illustrated in Fig. 3a, it can be noticed that the damage initiates from the notch and a localized damage profile is attained in the final loading steps. The damage propagates along the applied load in the subsequent loading steps. In contrast to the conventional damage model where

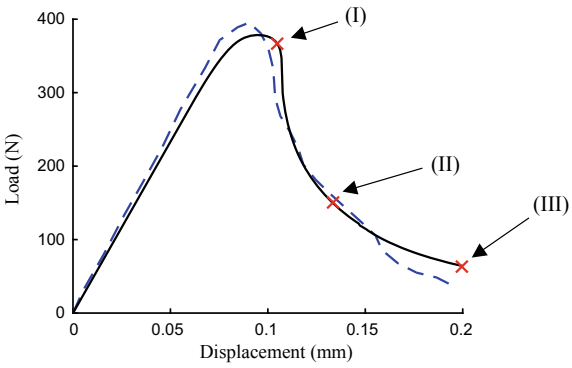

Fig. 2 Comparison between the experimental and numerical structural response [9, 10]

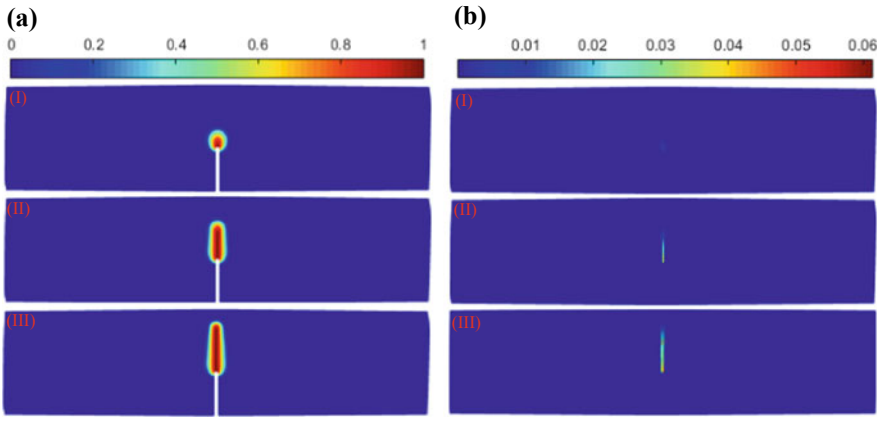

Fig. 3 **a** Damage profile (ω) and **b** nonlocal equivalent strain ($\tilde{e}$) profile for different loading steps using the localizing gradient damage model ($l = 5.6\,\text{mm}$)

damage tends to extend behind the notch, no spurious damage growth is observed around the notch area in the final stages of softening. Thus, the localizing gradient damage model is successful in delivering a localized macroscopic crack in the form of localized damage profile.

The next problem that is taken into consideration is the shear band failure which comes under the category of the mode-II type of failure problems. Shear band failure is commonly exhibited by many geo-materials when they are subjected to compressive loads and is an important problem for consideration. In this contribution, a shear ban specimen is taken into consideration which is subjected to a compressive load. Due to symmetry, only the half portion of the shear band specimen is modeled. The geometry and boundary conditions of the specimen are shown in Fig. 4. A defective

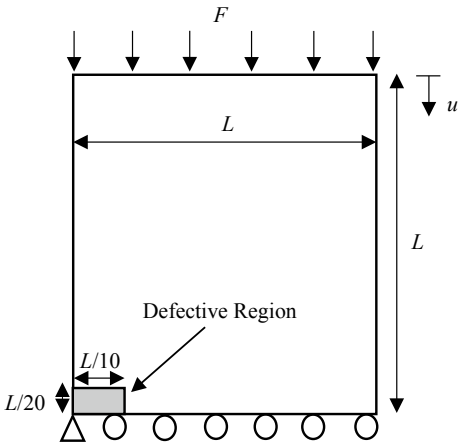

Fig. 4 Specimen under compressive load (shaded part indicates a defective region with a reduced damage initiation threshold)

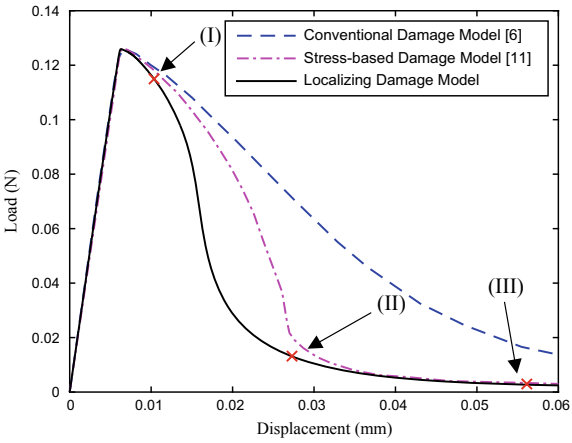

Fig. 5 Combined structural response using different models [6, 11]

region is set at the bottom left corner of the plate in order to initiate the damage propagation this region. The bottom end of the plate is fixed, while the top end of the plate is subjected to a compressive load. The material parameters are kept similar to that used in [9] are taken for the numerical simulation, i.e., elastic modulus $E = 20$ GPa, tensile strength $f_t = 2$ MPa, Poisson's ratio $\nu = 0.2$ and sensitivity parameter $s = 1$. The coupling modulus is taken as $h = E \times 10^{-9}$. The softening parameters are taken as $\alpha = 0.99$ and $\beta = 100$. A damage initiation threshold $\kappa_0 = f_t / E = 10^{-4}$ is chosen with a 50% reduction in the defective region. Plain strain condition is considered for the numerical simulation.

The combined structural response is shown in Fig. 5, which includes the structural response of the localizing gradient damage model, conventional model [6], and stress-based integral nonlocal damage model [11] from the literature. A similar length scale parameter $l = 2$ mm is chosen in all the models. On the basis of the combined structural response of different models, it can be noticed that nearly all the models have similar peak load capacity. However, due to nonlocal interactions over a constant domain, the conventional model (detailed in [6]) suffers from various drawbacks such as incorrect initiation of damage profile and spurious damage growth during the final stages of failure. Even the stress-based integral type nonlocal damage model (detailed in [11]) is not able to provide a smooth softening response for different mesh sizes, during the final stages of softening. In contrast, on the basis of damage (ω) and nonlocal equivalent strain ($\tilde{e}$) profiles illustrated in Fig. 6, it can be clearly noticed that the localizing gradient damage model is successful in providing a stationary shear band profile till the final stages of failure. The damage initiates correctly from the bottom left corner of the shear band specimen and an inclined shear band profile is observed in all the loading steps. No spurious damage growth perpendicular to shear band is observed during the final stages of softening. Instead a localized damage profile is observed along the initial shear band which characterizes a correct shear band failure.

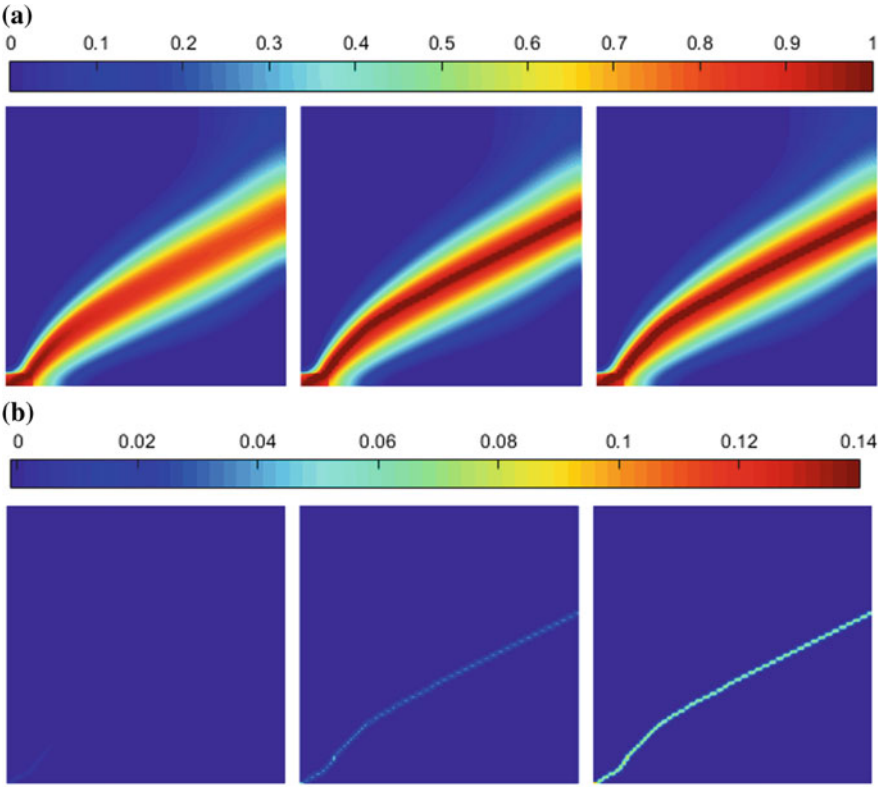

Fig. 6 **a** Damage profile (ω) and **b** nonlocal equivalent strain (ω) profile for different loading steps using the localizing gradient damage model ($l = 2$ mm)

5 Conclusions

Based on the obtained results of the mode-I problem, localizing gradient damage model is able to reproduce the experimental structural response with good accuracy. A narrow band of damage profile is observed during the final stages, which can be considered as a macroscopic crack. Additionally, no spurious damage growth is observed around the notch area and the crack propagates in accordance with the mode-I failure. In the case of mode-II shear band failure problem, a localized damage profile is observed along the initial shear band with no spurious damage growth during the final stages.

References

1. Kumar S, Singh IV, Mishra BK (2015) A homogenized XFEM approach to simulate fatigue crack growth problems. Comput Struct 150:1–22. https://doi.org/10.1016/j.compstruc.2014.12.008
2. Meschke G, Dumstorff P (2007) Energy-based modeling of cohesive and cohesionless cracks via X-FEM. Comput Methods Appl Mech Eng 196(21–24):2338–2357. https://doi.org/10.1016/j.cma.2006.11.017
3. Peerlings RD, De Borst R, Brekelmans WD, De Vree JHP (1996) Gradient enhanced damage for quasi-brittle materials. Int J Numer Meth Eng 39(19):3391–3403. https://doi.org/10.1002/(SICI)1097-0207(19961015)39:19%3c3391:AID-NME7%3e3.0.CO;2-D
4. Peerlings RHJ (1999) Enhanced damage modelling for fracture and fatigue. Doctoral dissertation, Technische Universiteit Eindhoven
5. Pijaudier-Cabot G, Bažant ZP (1987) Nonlocal damage theory. J Eng Mech 113(10):1512–1533. https://doi.org/10.1061/(asce)0733-9399(1987)113:10(1512)
6. Simone A, Askes H, Sluys LJ (2004) Incorrect initiation and propagation of failure in non-local and gradient-enhanced media. Int J Solids Struct 41(2):351–363. https://doi.org/10.1016/j.ijsolstr.2003.09.020
7. Poh LH, Sun G (2016) Localizing gradient damage model with decreasing interactions. Int J Numer Meth Eng 110(6):503–522. https://doi.org/10.1002/nme.5364
8. Coleman BD, Noll W (1963) The thermodynamics of elastic materials with heat conduction and viscosity. Arch Ration Mech Anal 13(1):167–178. https://doi.org/10.1007/bf01262690
9. Bažant ZP, Gettu R, Kazemi MT (1991) Identification of nonlinear fracture properties from size effect tests and structural analysis based on geometry-dependent R-curves. Int J Rock Mech Min Sci Geomech Abstr 28(1):43–51. https://doi.org/10.1016/0148-9062(91)93232-u
10. Khoramishad H, Akbardoost J, Ayatollahi M (2013) Size effects on parameters of cohesive zone model in mode I fracture of limestone. Int J Damage Mech 23(4):588–605. https://doi.org/10.1177/1056789513504319
11. Giry C, Dufour F, Mazars J (2011) Stress-based nonlocal damage model. Int J Solids Struct 48(25–26):3431–3443. https://doi.org/10.1016/j.ijsolstr.2011.08.012

Delamination Damage Analyses of Lap Shear Joints Made with Flat Fibre-Reinforced Polymer Composite Laminates Subjected to Transverse Load

Sumeet Kumar Pati, A. K. Pradhan and M. K. Pandit

Abstract In this work, initiation and growth of pre-embedded delamination in the adhesive-bonded lap shear joint (LSJ) made out of laminated fibre-reinforced polymer (FRP) considering flat geometry subjected to transverse load have been investigated. 3D nonlinear finite element technique has been employed to monitor the damage mechanism. The critical location to place the delamination has been obtained from the Tsai-Wu failure criterion. It is found to occur between the first and second layers of the bottom adherend of the Lap shear joint. Proper contact elements have been employed to avoid any interpenetration of delaminated surfaces. Interlaminar peel and shear stresses are obtained and found to be three dimensional in behavior. Virtual crack closure technique (VCCT) is used to determine the three components of strain energy release rates (SERR) with respect to sliding (Mode I), opening (Mode II) and cross sliding (Mode III) modes of failure. These values are found to be different along two delamination fronts which show the dissimilar nature of propagation of delamination.

Keywords Adhesive joints · Composites · Strain energy release rates (SERR) · Virtual crack closure technique (VCCT)

1 Introduction

Lap shear joints (LSJs) are used for strengthening fibre-reinforced polymer (FRP) composite of flat or curved structures. Delamination may exist in between the plies of the adherend of this type of joints. Delamination failure mode can be catastrophic, so their study needs to be done carefully. Major factors causing the onset of delamination are the high gradients of peel and shear stresses that occur in the interlaminar region. Higher values of these stresses can fasten the process of delamination. This delamination reduces the strength and stiffness of the overall structure. So these kinds

S. K. Pati (✉) · A. K. Pradhan · M. K. Pandit
School of Mechanical Sciences, Indian Institute of Technology Bhubaneswar, Bhubaneswar, Odisha, India
e-mail: sumeetpati94@gmail.com; skp17@iitbbs.ac.in

D. Maity et al. (eds.), *Advances in Fluid Mechanics and Solid Mechanics*, Lecture Notes in Mechanical Engineering,
https://doi.org/10.1007/978-981-15-0772-4_21

of structures need to be analysed properly and methods need to be devised to arrest or reduce the propagation of delamination.

Introduction of adhesives has been a gradual process, starting from the application of sticky products to producing the simple level of adhesives by general cooking methods, as mentioned by Adams [1]. The main full-fledged research about the adhesive bonding started with contributions from Volkersen, Goland, and Reissner [2, 3]. During loading, structures usually bend and loading becomes eccentric. This was not included by Volkersen [2]. But this void was filled by Goland and Reissner [3]. They also gave a two-dimensional analytical solution of peel and shear stress in single lap joints (SLJs). A study on the lap shear joint specimen with cracks along the interface was conducted by Brussat et al. [4]. They also gave some insights into a type of fracture called a mixed-mode method of fracture. Cheuk and Tong [5] investigated a Lap shear joint (LSJ) with an artificial crack pre-embedded in it. An experiment, as well as a nonlinear FEM study, was conducted to find the stress distribution and calculate the energy release rate at both the crack tips. Along with this they also obtained an analytical solution to that problem. Talreja [6] studied how the stiffness reduction is taking place due to transverse cracking in glass/epoxy composites. Rybicki and Kanninen [7] presented an efficient method of calculating the stress intensity factors. But the method was based on crack closure integral process. Panigrahi and Pradhan [8] investigated the out of plane stresses using 3D nonlinear FEM techniques in FRP. They investigated the effects on various delamination lengths. Sun and Tong [9] investigated crack propagation in a cylindrical aluminium structure, which was repaired by FRP. Kumar et al. [10] studied the delamination analysis in single lap pipe joint of FRP using FEM techniques. Xu and Li [11] developed an analytical model to predict stresses in a composite structure subjected to torsion. Baishya et al. [12] studied the failure analysis of laminated FRP composite subjected to pressure and torsion. Khan et al. [13] studied the fatigue delamination of the carbon fiber polymer matrix composite. Jayakrishna et al. [14] studied the health monitoring of polymer composites. Zhao et al. [15] simulated delamination problem in composite laminates using XFEM (extended finite element method) technique. Kumar et al. [16] studied delamination evolution in composites using modal analysis. Ipek et al. [17] studied the effect of delamination on the buckling behaviour of composites. Zhao et al. [18] introduced a stiffness reduction based model to study fatigue damage in composites. Ismail et al. [19] studied delamination using thermomechanical model. Li and Chen [20] proposed an extended cohesive damage model to predict delamination migration in laminated composites.

From the literature survey, it is found that most papers analysed adhesive joints using two-dimensional FEM. Further work needs to be done in the area of three-dimensional finite element methods. Mostly single lap joints were analysed in previous research works. So the area of lap shear joints needs to be explored more. Also, the transverse loading condition needs more attention as they have been seldom addressed.

The objective of the present work is to analyse the lap shear joint made out of FRP composite with pre-embedded delamination and subjected to transverse loading condition. Virtual crack closure method has been employed to determine the energy

release values. Tsai Wu failure criterion has been employed to locate the initiation of pre-embedded delamination. It is found to lie in the first two layers of the lower adherend. So, delamination is inserted in that location before the application of load. An effective FE simulation procedure has been used using proper contact elements to evaluate the peel and shear stresses. Materials, as well as dimensions used for analyses, have been chosen from Cheuk and Tong [5]. The current 3D nonlinear FEM has been employed to validate a 2D experimental result from Cheuk and Tong [5]. The results are found to be in accord with the existing work.

Following results were studied in this paper:

- Interlaminar peel and shear stress in the interface of adhesive and adherends and also along the two delamination fronts.
- Second, SERR values are analysed along the two delamination fronts.
- The direction of crack growth is determined based on SERR values.

2 Three-Dimensional Finite Element Modelling of the LSJ

The physical geometry of the lap shear joint used in the present research is shown in Fig. 1. The dimensions are taken as per Cheuk and Tong [5] model. The adherends used in the structure are made out of T300/934 carbon epoxy plain-woven prepreg [5]. Properties of individual layers or plies used in the adherends are mentioned in Table 1. Each adherend is composed of eight layers of plies. The orientation of each ply is zero degrees. And the thickness of each ply is of 0.215 mm. Though the adherends are orthotropic in nature the adhesive used is isotropic in its behaviour. FM 300-K of Cytek from Cheuk and Tong [5] has been used to join the adherends. Properties of adhesive taken from Cheuk and Tong [5] are mentioned in Table 2. The

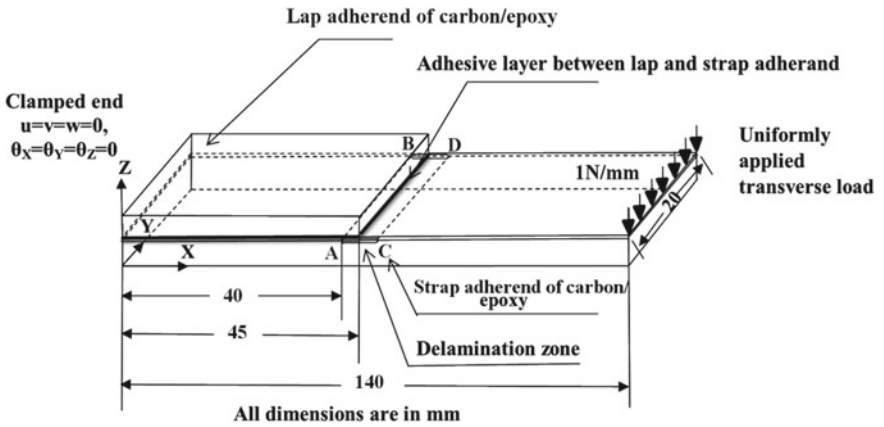

Fig. 1 Geometry of the lap shear joint (LSJ) made out of carbon/epoxy composite

Table 1 Properties of a ply of carbon epoxy plain-woven prepreg (Cheuk and Tong [5])

Elastic moduli, $E_x = E_y$	57.226 GPa
Transverse elastic modulus, E_z	4.800 GPa
Shear modulus, G_{xy}	4.481 GPa
Shear moduli, G_{xz} and G_{yz}	04.400 GPa
Poisson's ratio, ν_{xy}	0.050
Poisson's ratios, ν_{xz} and ν_{yz}	0.280

Table 2 Mechanical properties of FM 300-K (Cheuk and Tong [5])

Young's modulus, E	2.4 Gpa
Poisson's ratio, ν	0.32

thickness of the adhesive is kept equal to the ply thickness. The delamination used is symmetrical in nature. Delamination lengths used in the present analyses are 4, 6, 8 and 10 mm.

One end of the structure (Lap Shear Joint) is fixed and the other end is loaded with a uniformly distributed transverse load of 1 N/mm in the negative z-direction. The load is applied in equal steps along the width. The load magnitude and location of pre-embedded delamination have been decided from the Tsai-Wu failure criterion. Material non- linearity of adhesive has not been included in this research though geometric nonlinearity has been included as suggested by Cheuk and Tong [5].

ANSYS has been used to evaluate the stresses in the interface of lower adherend and adhesive and the stresses along two delamination fronts. Peel and out of plane shear stresses are found to be prominent as per the observations. SOLID 185 of layered type is used for the adherend and SOLID 185 of solid type is used for the adhesive.

3 Strain Energy Release Rates (SERR)

The three components of strain energy release rates (SERR) that is the mode I, mode II and mode III, calculated by Rybicki and Kanninen [7] using the virtual crack closure technique (VCCT) have been mentioned in the following equations:

$$G_I = \frac{1}{2\Delta A} Z_f [w_t - w_b] \tag{1}$$

$$G_{II} = \frac{1}{2\Delta A} X_f [u_t - u_b] \tag{2}$$

$$G_{III} = \frac{1}{2\Delta A} Y_f [v_t - v_b] \tag{3}$$

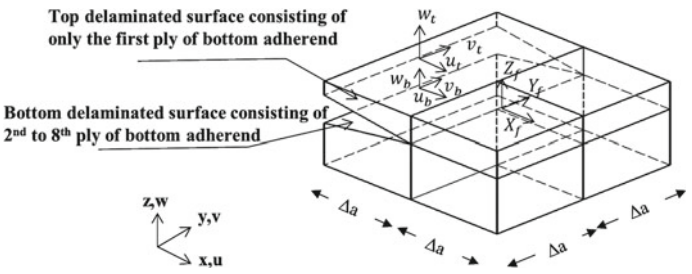

Fig. 2 SERR parameters shown in the geometrical configuration of the LSJ

where Z_f, X_f and Y_f denote the mode I, mode II and mode III forces, respectively, which are used to prevent the nodes to move along the delamination front. Here, $[u_t, v_t, w_t]$ and $[u_b, v_b, w_b]$ denote the displacements of the top and the bottom delaminated surfaces as shown in Fig. 2. ΔA is the virtual incremental failure area where ΔA can be expressed in the form of $\Delta A = \Delta a \times \Delta a$. Δa has been shown in Fig. 2.

4 Finite Element Analyses of the LSJ

4.1 Validation

Before doing the present research, an existing research paper in line with the present analyses has been validated. Research work of Cheuk and Tong [5] has been validated and found to be in good agreement. Here the material and dimensions used are the same as that of the present analyses. The current 3D FE technique is validated with the existing 2D FE technique. The peel stress plot obtained along the bond line interface has been shown in Fig. 3. Similarly, shear stresses along the bond line interface are plotted and found to be in good agreement with the existing paper. The above plots are also repeated for different delamination lengths and are validated with the existing paper.

4.2 Problem Definition

As the current 3D FE approach was validated, so it is applied to solve the current research work. Here the adhesive joint used is of lap shear type. The material and dimensions are as per Cheuk and Tong [5]. The present model has been shown in Fig. 1. The load applied is of uniform transverse type and the magnitude used is

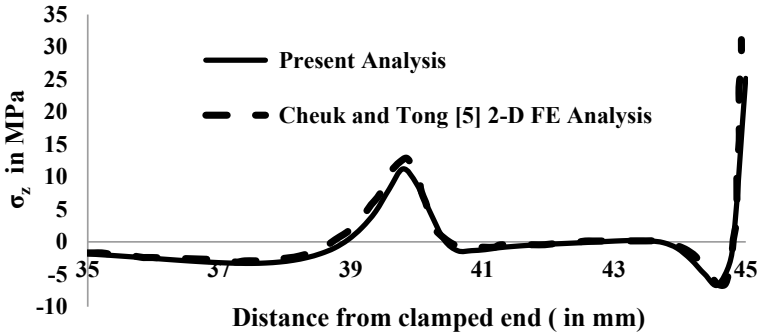

Fig. 3 Peel stress variation along the bond line interface of bottom adherend and adhesive with delamination of 10 mm

1 N/mm. The nonlinear effect of adhesive material has been neglected. But geometric nonlinearity has been included to get the results.

5 Results and Discussions

5.1 Bond Line Stress In-Between Adhesive and Bottom Adherend of Flat LSJ

Stress along the bond line interface plays a vital role in affecting the structural integrity of LSJ as a change in Young's modulus takes place at the interface. Both 3D and 2D plots have been obtained. 2D peel stress plot is shown in Fig. 4.

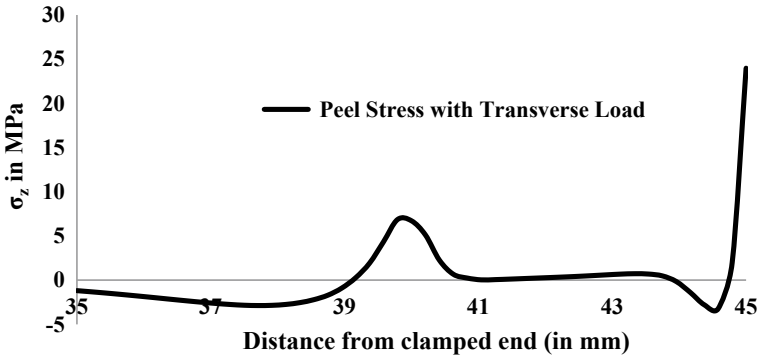

Fig. 4 Peel stress plot along the bond line interface with a transverse load of 1 N/mm and 10 mm delamination

From the plot, it is clear that peel stress value achieves peak at two locations, one at the overlapping end and the other near the delamination zone. Similarly, shear stress plots have also been obtained. The out of plane shear stresses have been found to be prominent than the in-plane shear stresses.

5.2 3D Variation of Stress In-Between Adhesive and Bottom Adherend of Flat LSJ

The 3D variation of peel and shear stresses has been found to study the variation of stresses along the width which was not possible through the 2D stress plots. The 2D plot variation along the delamination length has been found to be in line with the 3D plots.

From the 3D plots as shown in Figs. 5 and 6, it can be seen that the variation of peel and out of plane shear stress achieves two peaks, one near the crack or delamination zone and the other near the end where the load is applied.

5.3 Interlaminar Stresses Along Two Delamination Fronts

It is observed from Fig. 7 that the peel stress value is more in AB front than the CD. It signifies higher stress towards the stiffened side than the unstiffened one. It is also observed that peel stress value is maximum near the mid of the width. As

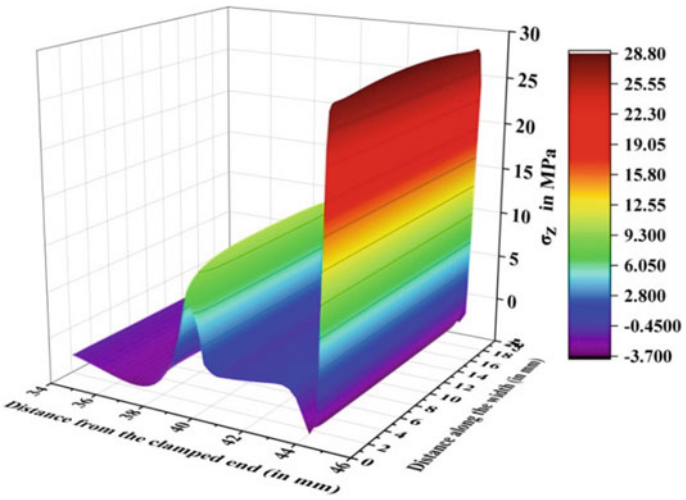

Fig. 5 Peel stress variation (σ_z) in between the adhesive and bottom adherend

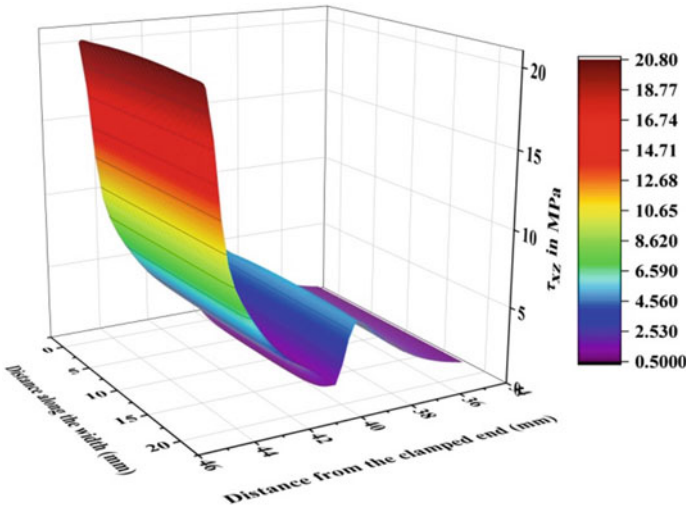

Fig. 6 Out of plane shear stress (τ_{xz}) variation in between the adhesive and bottom adherend

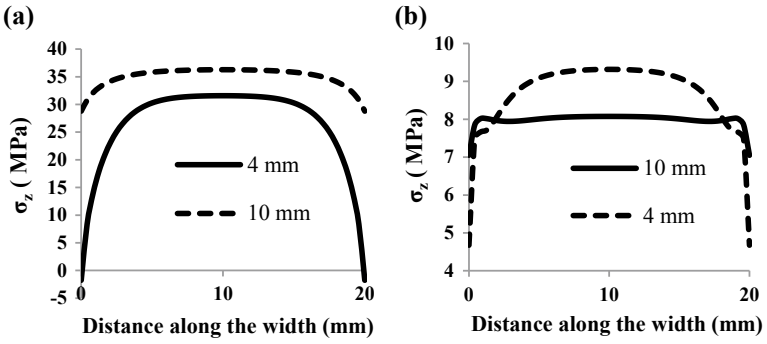

Fig. 7 Variation of peel stress along the width **a** AB front and **b** CD front

the delamination length is increased, peel stress value increases along the AB front while the opposite thing happens along the CD front.

5.4 Variation of SERRs Along the Delamination Fronts

From Fig. 8, it is observed that G_I value dominates along the AB front for 10 mm delamination length.

From Fig. 9, it is observed that G_{II} dominates along the CD front for 10 mm delamination length. So it can be concluded that there is a mixed-mode kind of

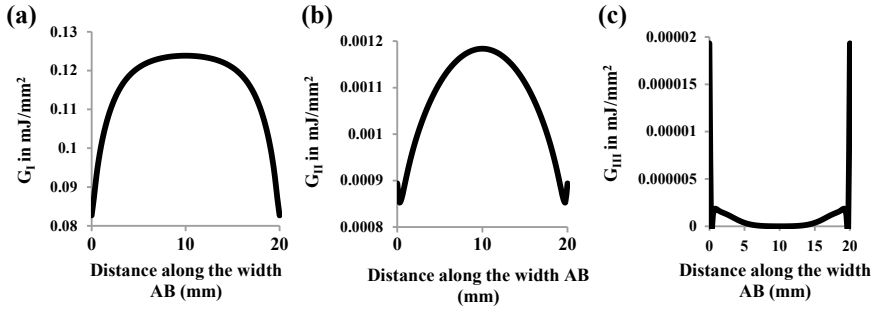

Fig. 8 Variation of SERR for 10 mm delamination length along AB. **a** G_I variation, **b** G_{II} variation, **c** G_{III} variation

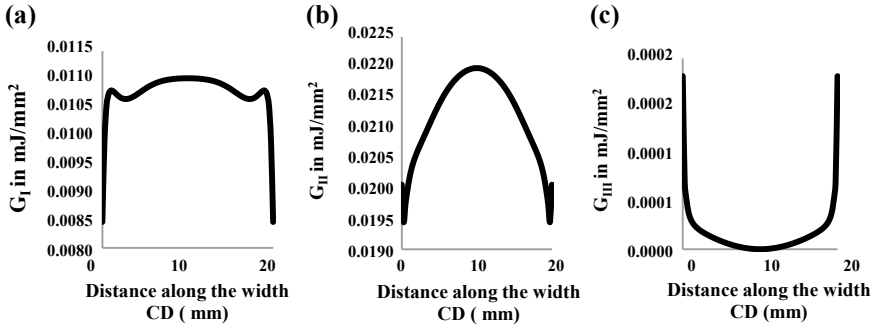

Fig. 9 Variation of SERR for 10 mm delamination length along CD. **a** G_I variation, **b** G_{II} variation, **c** G_{III} variation

failure. Variation of G_T has been shown in Fig. 10. It is observed from Fig. 10 that as we increase the delamination length, the G_T value increases along the AB front and it decreases along the CD front. So there would be a faster rate of propagation of the crack along the AB front or stiffened side of the LSJ.

6 Conclusion

Following conclusions have been drawn based on the 3D FE technique applied to the LSJ:

- Edge effect has been studied by using the 3D FEM technique. This has given an insight into the variation of stresses along the width.
- Based on the G_T values for different delamination lengths, it can be concluded that the rate of propagation of crack towards the stiffened side is more than the unstiffened side.

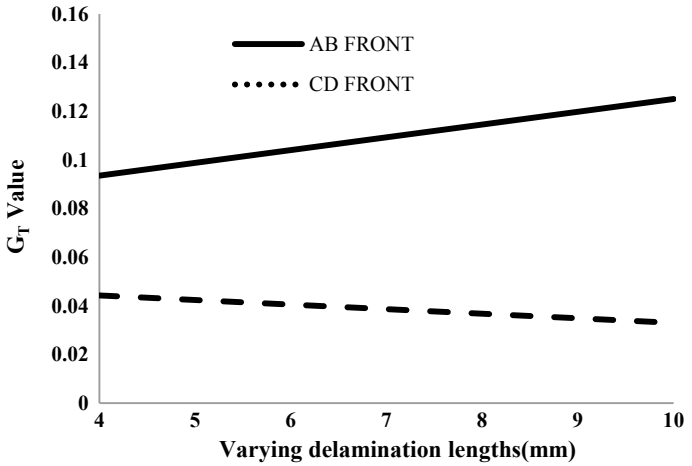

Fig. 10 Variation of G_T along two delamination fronts

- Mixed-mode failure of the Lap Shear Joint has been observed. Mode I has been found to be dominant towards the stiffened side and mode II towards the unstiffened side.
- Growth and propagation of delamination reduce the load-bearing capacity of the structure which needs to be prevented.
- The growth of delamination is not found to be symmetrical as the stress values are not identical along the two delamination fronts.

References

1. Adams RD (ed) (2005) Adhesive bonding: science technology and applications. CRC Press LLC, USA
2. Volkersen O (1938) Die Nietkraftverteilung in zugbeanspruchten Nietverbindungen mit konstanten Laschenquerschnitten. Luftfahrtfor schung. 15:41–47
3. Goland M, Reissner E (1944) The stresses in cemented joints. J Appl Mech 17:66
4. Brussat TR, Chiu ST, Mostovoy S (1977) Fracture mechanics for structural adhesive bonds (No. LR-28196). LOCKHEED-CALIFORNIA CO BURBANK. https://apps.dtic.mil/dtic/tr/fulltext/u2/a054023.pdf
5. Cheuk PT, Tong L (2002) Failure of adhesive bonded composite lap shear joints with embedded precrack. Compos Sci Technol 62(7–8):1079–1095. https://doi.org/10.1016/S0266-3538(02)00054-4
6. Talreja R (1985) Transverse cracking and stiffness reduction in composite laminates. J Compos Mater 19(4):355–375. https://doi.org/10.1177/002199838501900404
7. Rybicki E, Kanninen M (1977) A finite element calculation of stress intensity factors by a modified crack closure integral. Eng Fract Mech 9(4):931–938. https://doi.org/10.1016/0013-7944(77)90013-3

8. Panigrahi SK, Pradhan B (2007) Delamination damage analyses of adhesively bonded lap shear joints in laminated FRP composites. Int J Fracture 148(4):373–385. https://doi.org/10.1007/s10704-008-9210-x
9. Sun X, Tong L (2004) Curvature effect on fracture toughness of cracked cylindrical shells bonded with patches. AIAA J 42(12):2585–2591. https://doi.org/10.2514/1.2034
10. Kumar U, Kumar P, Noor MT, Das RR (2018) FEM based delamination damage analysis of bonded FRP composite pipe joints. ISSS J Micro Smart Syst 7(1):45–51. https://doi.org/10.1007/s41683-018-0022-6
11. Xu W, Li G (2010) Finite difference three-dimensional solution of stresses in adhesively bonded composite tubular joint subjected to torsion. Int J Adhes Adhes 30(4):191–199. https://doi.org/10.1016/j.ijadhadh.2009.12.007
12. Baishya N, Das RR, Panigrahi SK (2017) Failure analysis of adhesively bonded tubular joints of laminated FRP composites subjected to combined internal pressure and torsional loading. J Adhes Sci Technol 31(19–20):2139–2163. https://doi.org/10.1080/01694243.2017.1307498
13. Khan TA, Kim H, Kim HJ (2019) Fatigue delamination of carbon fiber-reinforced polymer-matrix composites. In: Failure analysis in bio composites, fibre-reinforced composites and hybrid composites. Woodhead Publishing, pp 1–28. https://doi.org/10.1016/B978-0-08-102293-1.00001-2
14. Jayakrishna K, Rajiyalakshmi G, Deepa A (2019) Structural health monitoring of fiber polymer composites. In: Structural health monitoring of biocomposites, fibre-reinforced composites and hybrid composites. Woodhead Publishing, pp 75–91. https://doi.org/10.1016/B978-0-08-102291-7.00005-8
15. Zhao L, Zhi J, Zhang J, Liu Z, Hu N (2016) XFEM simulation of delamination in composite laminates. Compos A Appl Sci Manuf 80:61–71. https://doi.org/10.1016/j.compositesa.2015.10.007
16. Kumar BA, Naidu SS, Varun C (2018) Delamination evolution of FRP composite plate using modal analysis. Int J Recent Technol Mech Electr Eng 5(5):60–64
17. Ipek G, Arman Y, Celik A (2018) The effect of delamination size and location to buckling behavior of composite materials. Compos B Eng 155:69–76
18. Zhao Y, Noori M, Altabey WA, Aval S, Wu Z (2018) A fatigue damage model for FRP composite laminate systems based on stiffness reduction. J Compos Mater
19. Ismail SO, Ojo SO, Dhakal HN (2017) Thermo-mechanical modelling of FRP cross-ply composite laminates drilling: delamination damage analysis. Compos B Eng 108:45–52
20. Li X, Chen J (2017) A highly efficient prediction of delamination migration in laminated composites using the extended cohesive damage model. Compos Struct 160:712–721

Dynamic Characteristics of Twisted Composite Panels—A Finite Element Study

K. S. Shivakumar Aradhya and S. Moorthi

Abstract This paper presents the details of the dynamic analysis of Laminated Composite Twisted Panels. The effects of different parameters such as the angle of twist, lamination angle, aspect ratio (plate width to thickness ratio) on the natural frequencies and mode shapes are considered. The FEM analysis was carried out using the front-end commercial software **ANSYS** (**Ver: 10.0**) (ANSYS(R) Help System, 2006 [1]) with its modal analysis capabilities. The Block Lanczos algorithm with subspace iteration technique was used in the extraction of natural frequencies and corresponding mode shapes. The first few natural frequencies and corresponding mode shapes were extracted for different combinations of angles of twist, lamination angles, and aspect ratios. The frequencies extracted are in good agreement with reported analytical solutions (Qatu and Leissa in Int J Mech Sci 33:927–940, 1991 [2]).

1 Introduction

Twisted cantilever panels have varied applications such as in wide-chord turbine blades, compressor blades, and impeller and fan blades, particularly in turbomachinery. This wide range of practical applications of these twisted panels requires a proper understanding of their dynamic characteristics for carrying out reliable designs. Structural elements like turbine blades, subjected to periodic forces may lead to parametric resonance due to a certain combination of forcing functions.

K. S. S. Aradhya (✉)
KCK Engineering Services & Consultancy, FEM & CFD Applications, A2-345 RMV Clusters (Phase I), LG Halli, RMV II Stage P.O., Bangalore 560094, India
e-mail: ksska@hotmail.com

S. Moorthi
Department of Mechanical Engineering (Post Graduate Studies), Kongu Engineering College, Perundurai, Erode 638052, Tamil Nadu, India

D. Maity et al. (eds.), *Advances in Fluid Mechanics and Solid Mechanics*,
Lecture Notes in Mechanical Engineering,
https://doi.org/10.1007/978-981-15-0772-4_22

Composite materials are being increasingly used in turbomachinery blades because of their high specific strength and stiffness, and these can be tailored through the variation of fiber orientation and stacking sequence to obtain an efficient design [3]. Thus, the parametric resonance characteristics of laminated composite twisted cantilever panels are of great importance in their engineering design, development, and applications.

Analytical solutions are seldom capable of accurately analyzing these types of problems because of the complex orthotropic nature of material and geometry. In such situations, recourse is taken to approximate numerical methods. The Finite Element Method (**FEM**) is the most commonly used numerical technique. The objectives of the present investigations are to review the literature related to Finite Element formulation of dynamic problems applied to orthographic laminated plates [4–6] and to carry out a parametric FEM analysis of Laminated Composite Twisted Panels. The effects of different parameters such as the angle of twist, lamination angle, aspect ratio (plate width to thickness) on the natural frequencies and mode shapes are considered. The front-end commercial software **ANSYS** [1] is utilized in the current studies.

2 Geometric Configuration of the Twisted Plate

Figure 1 shows the geometric configuration of the twisted cantilever plate with relevant nomenclature. The plate considered has a symmetric ply orientation [**θ/ − θ/θ**]. The ply orientation **(θ)** was varied from **0°** to **90°** in steps of **15°**. The angle of twist **Φ** is varied from **0°** to **45°** in steps of **15°**. The plate dimensions are **a = b = 0.1 m**. The two aspect ratios considered **are (a/h) = 20** and **100**.

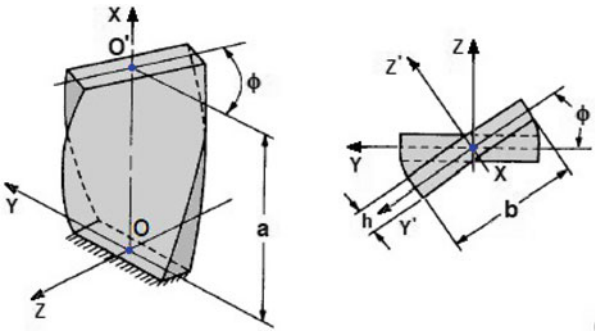

a: length of the plate; **b:** width of the plate; **h**: thickness of the plate; **ϕ**: angle of twist; **OXYZ:** Co-ordinate system at the fixed end; **O'X'Y'Z':** Co-ordinate system at the free end

Fig. 1 Geometric configuration of the twisted cantilever plate

3 Material Properties

The composite curved plate is assumed to be made of E-glass-epoxy composite system. The properties of the E-glass-epoxy composite are presented in Table 1.

Table 1 Material properties (E-glass epoxy composite)

Material property	Value
Modulus of elasticity	
E_{XX}	60.0×10^9 N/m^2
E_{YY}	24.8×10^9 N/m^2
E_{ZZ}	24.8×10^9 N/m^2
Modulus of rigidity	
G_{XY}	12×10^9 N/m^2
G_{YZ}	12×10^9 N/m^2
G_{XZ}	12×10^9 N/m^2
Poisson ratio ν	0.3
Density ρ	2324.76 Kg-mass/m^3
Volume fraction	
E-glass	83.26%
Epoxy	16.73%

4 Finite Element Analysis

1. **FEM Model**

The FEM meshes for different parametric studies were generated using the orthotropic 3D Shell elements (**SHELL99, ANSYS Ver: 10.0**). Figure 2 shows a typical FEM mesh for the twisted plate with ply angle $\boldsymbol{\theta} = \mathbf{45}^\circ$, thickness ratio $\mathbf{(a/h)} = \mathbf{20}$ and angle of twist $\boldsymbol{\Phi} = \mathbf{45}^\circ$.

The FEM mesh details are as follows:

Type of Element: **SHELL99**; No. of Elements = **400**; No. of Nodes: **1281**; No. of Degrees of Freedom per Node (**6**): **UX**, **UY**, **UZ** and **RX**, **RY**, **RZ**.

The mesh size (number of elements) was arrived at after carrying out a convergent study to get an optimum solution for each case considered.

2. **Boundary Conditions**

The fixed boundary conditions considered at the left end correspond to

$$\mathbf{UX = UY = UZ = RX = RY = RZ = 0}$$

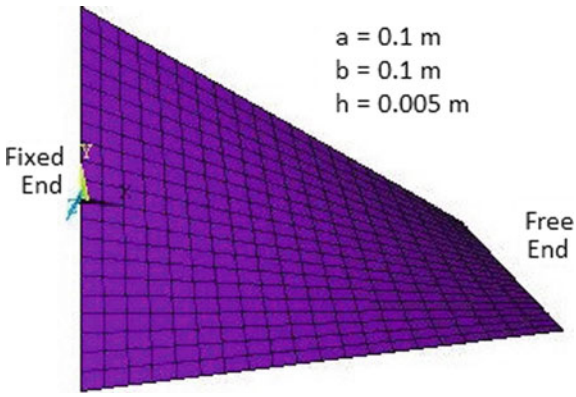

Fig. 2 Typical FEM shell model for the twisted plate

3. **FEM Analysis**

The problem was analyzed using the front-end commercial software **ANSYS** (**Ver: 10.0**) and adopting its modal analysis capabilities. The analysis was carried out on a desktop computer system having the following specifications:

Computer model: Pentium **4**; Operating System: **Windows XP**; System memory (**RAM**): **256 MB**; Hard disk size: **80 GB**.

5 Analytical Solution

Analytical solution for the reported investigations was obtained by Qatu and Leissa [2] using laminated shallow-shell theory and Ritz method. The relevant equation provided by them for the computation of natural frequency is

$$\mathbf{F_{ij}} = [\boldsymbol{\lambda_{ij}}/(\mathbf{2}\pi\mathbf{a}^2)] \times [\mathbf{E}_{11}\mathbf{h}^2/\boldsymbol{\rho}]^{0.5} \tag{1}$$

where $\boldsymbol{\lambda_{ij}}$ = Non-dimensional frequency; $\boldsymbol{\rho}$ = Mass density; $\mathbf{E_{11}}$= Modulus of elasticity; $\mathbf{h}$ = Thickness; $\mathbf{a}$ = Length of the plate.

6 Results and Discussion

The total investigation consists of fifty-six **(56)** sets of results, the first twenty-eight sets correspond to the aspect ratio **(a/h) = 20** and the remaining twenty-eight sets correspond to the other aspect ratio **(a/h) = 100**. In each case, the angle of twist $\boldsymbol{\phi}$ was varied from **0**° to **45**° in steps of **15**° and for each angle of twist $\boldsymbol{\phi}$, the ply orientation $\boldsymbol{\theta}$ was varied from **0**° to **90**° in steps of **15**°.

Tables 2 and 3 present typical comparisons of current investigation results with that of the analytical solutions obtained by Qatu and Leissa [2] for the first three natural frequencies. Table 2 corresponds to the results for aspect ratio **(a/h) = 20**, angle of twist **ϕ = 45°**, the ply orientation **θ** being varied from **0°** to **90°**. Similar results for **(a/h) = 100**, angle of twist **ϕ = 45°** (again the ply orientation **θ** being varied from **0°** to **90°**) are shown in Table 3.

Figures 3 and 4 represent typical mode shapes for plates with **(a/h) = 20** and **100**. Figure 3 presents the mode shapes for the untwisted plate **(ϕ = 0°)** and **(a/h) = 20**. The mode shapes correspond to the ply angle variation from **0°** to **90°** in steps of **30°** and for each ply angle, the first four mode shapes are shown. The mode shapes are shown in plan view and exhibit **w-displacement** (displacement along z-axis) dominance.

Similar mode shapes for **(a/h) = 100** and **ϕ° = 45°** are shown in Fig. 4. The mode shapes correspond to the ply angle variation from **0°** to **90°** in steps of **30°** and for each ply angle, the first four mode shapes are shown.

Table 2 Natural frequencies for **(a/h) = 20** and Angle of twist **Φ = 45°**

Ply angle θ	Mode shape					
	1		2		3	
	Ansys	Theory	Ansys	Theory	Ansys	Theory
0	398.03	351.73	1881.7	2022.8	1895.9	2522.7
15	382.51	338.39	1792.4	1949.16	1914.6	2516.49
30	343.03	304.77	1630.7	1763.8	1842	2432.56
45	299.5	566.62	1452	1553.47	1701.7	2264.87
60	269.88	239.38	1323.6	1402.73	1581.9	2121.04
75	257.38	227.3	1264	1333.29	1513.7	2043.53
90	254.67	224.7	1249.2	1316.16	1490.1	2018.12

Table 3 Natural frequencies for **(a/h) = 100** and Angle of twist **Φ = 45°**

Ply angle θ	Mode shape					
	1		2		3	
	Ansys	Theory	Ansys	Theory	Ansys	Theory
0	79.9	70.47	401.98	419.05	1174.5	1339.67
15	77.09	67.93	387.11	403.75	1161.4	1290.14
30	69.58	61.38	349.05	364.52	1099.3	1165.47
45	60.84	53.74	305.63	319.19	965.36	1023.72
60	54.53	48.1	274.45	236.27	870.74	920.76
75	51.75	45.58	260.48	271.39	828.72	873.51
90	51.12	45.02	257.3	268.02	819.34	862.53

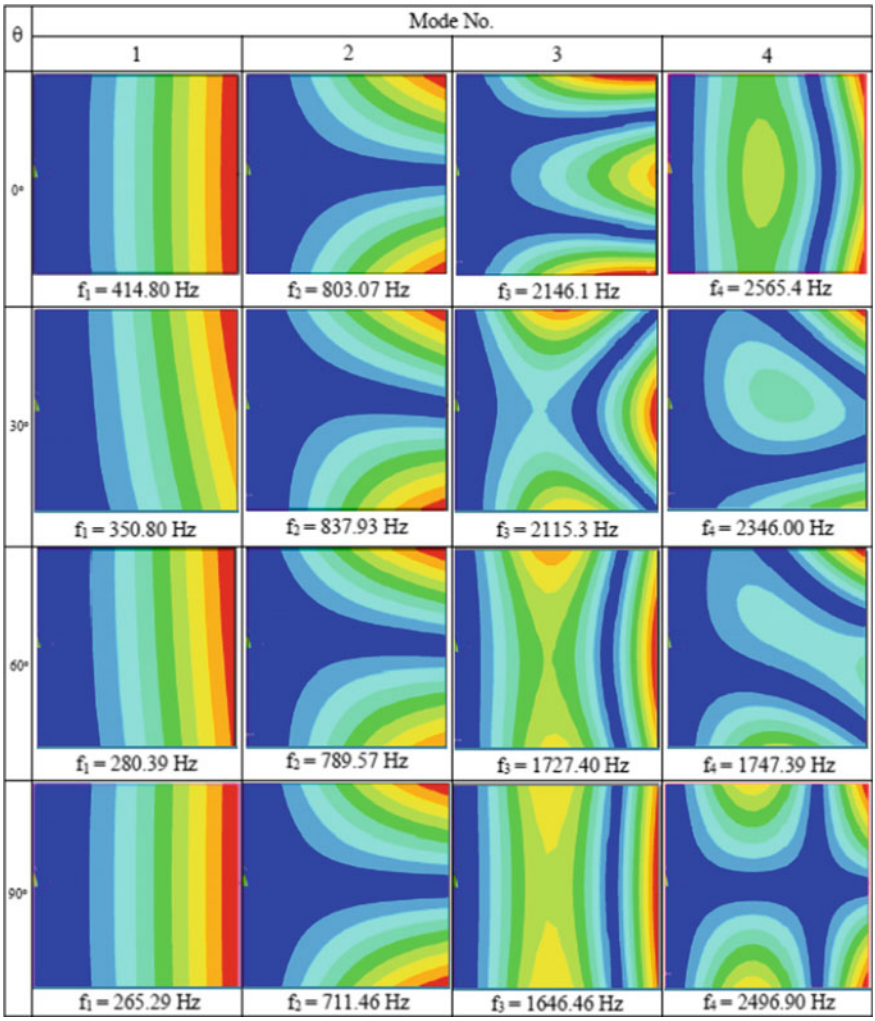

Fig. 3 Mode shapes for aspect ratio (a/h) = 20 and angle of twist $\phi = 0°$ (untwisted)

Consolidated results of the entire investigation are shown in Figs. 5 and 6. Figure 5 represents the variation of natural frequencies with respect to the angle of twist **(ϕ)** and for different ply orientations **(θ)** for a plate with an aspect ratio **(a/h) = 20**. Similar results for a plate with an aspect ratio **(a/h) = 100** are shown in Fig. 6.

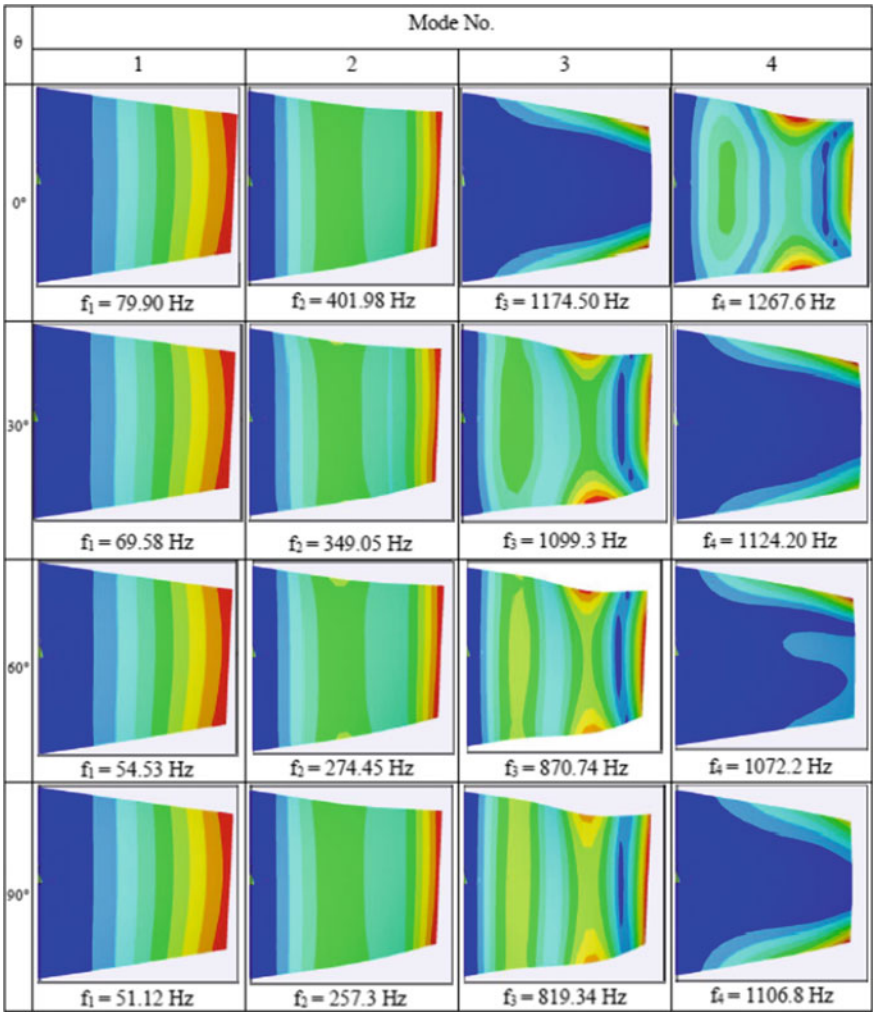

Fig. 4 Mode shapes for aspect ratio (a/h) = 100 and angle of twist $\phi = 45°$

7 Conclusions

1. For untwisted plate (Fig. 3) and when $\boldsymbol{\theta} = \mathbf{0}°$, the first four mode shapes are, in order, first span-wise bending mode (**1B**), first torsional mode (**1T**), first chord-wise bending mode (**1C**) and finally second bending mode (**2B**). For $\boldsymbol{\theta} = \mathbf{0}°$, there exists a material symmetry about the x-axis, and it is seen that the mode shapes are either symmetric or antisymmetric about the x-axis. As $\boldsymbol{\theta}$ increases, this symmetry/antisymmetry is lost. However, the material symmetry is recovered when $\boldsymbol{\theta}$ becomes $\mathbf{90}°$ and the mode shape is again either symmetric

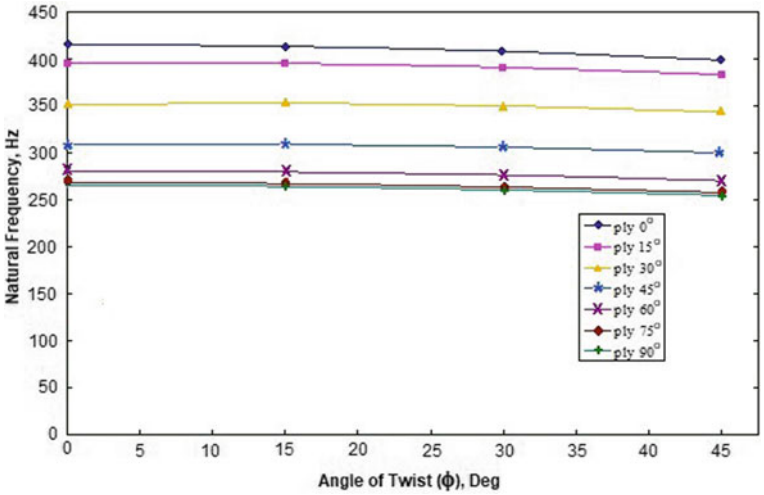

Fig. 5 Variation of natural frequencies with respect to the angle of twist (ϕ) and for different ply orientations (θ) for a plate with an aspect ratio (a/h) $=20$

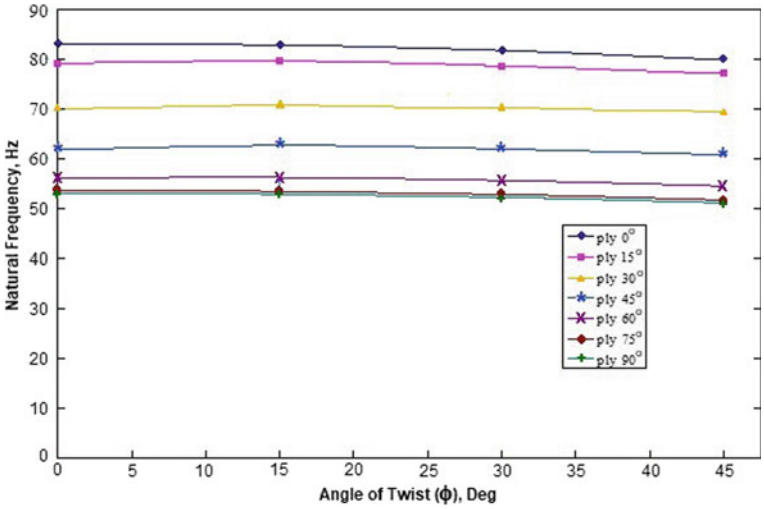

Fig. 6 Variation of natural frequencies with respect to the angle of twist (ϕ) and for different ply orientations (θ) for a plate with an aspect ratio (a/h) $= 100$

or antisymmetric. This observation is in concurrence with the results of Ref. [2].

2. When the plate starts to have an initial twist, the second mode shape does not remain as the torsional mode. For $\boldsymbol{\phi} = \mathbf{30}^\circ$ and $\mathbf{45}^\circ$, the second mode becomes second bending mode (**2B**).
3. The peak values of fundamental frequencies of the twisted plates are observed when the fibers are perpendicular to the clamped edge in all the cases studied.
4. For plates with higher aspect ratio [$\mathbf{(a/h) = 20}$], the second mode of vibration corresponds to the first torsional mode (**1T**).
5. For both the aspect ratios, $\mathbf{(a/h) = 20}$ and **100** and ply orientations varying from $\mathbf{0^0}$ to $\mathbf{90^0}$, the natural frequencies decrease with increasing angle of twist (Figs. 5 and 6).
6. For fiber angles between $\mathbf{0^0}$ and $\mathbf{90^0}$, the coupling between the modes exists, and the strength of the coupling increases both with increasing fiber angle and increasing and angle of twist.
7. Increasing in the angle of twist is found to decrease the fundamental frequency which corresponds to the first bending mode.
8. An analysis of the mode shapes shows that the second mode shape is not always the first torsional mode; it can be the second bending mode, especially for the plates with fibers parallel to the clamped edge ($\boldsymbol{\theta} = \mathbf{90}^\circ$).
9. The phenomenon of a certain mode-shape-changing gradually to a completely different mode shape as a certain parameter (fiber angle) changes is observed; more nodal lines tend to appear approximately parallel to the direction of the fibers.
10. The number of symmetric modes increases as the angle of twist increases, when $\boldsymbol{\theta} = \mathbf{90}^\circ$.
11. The results of the current investigation are in good agreement with reported analytical solutions [2], the maximum deviation being **12.5%**.
12. The accuracy of the results obtained permits one to conclude that the FEM method can be applied straightforwardly to investigate practical problems such as studying the vibration characteristics of laminated twisted cantilever plates. The method provides a quick means for the designer to assess the safety of the composite structures to withstand dynamic loads.

References

1. ANSYS(R) Help System (2006) Release 10.0
2. Qatu MS, Leissa AW (1991) Vibration studies for laminated composite twisted cantilever plates. Int J Mech Sci 33:927–940
3. Jones RM (1999) Mechanics of composite materials. In: International Student Edition. McGraw—Hill Kogakusha Limited, New Delhi
4. Ganapathi M, Varadan TK, Balamurugan V (1994) Dynamic stability of laminated composite curved panels using finite element method. J Comput Struct 53(2):335–342

5. Chen LW, Yang JY (1990) Dynamic stability of laminated composite plates by the finite element method. Compos Struct 36(5):845–851
6. Chen LW, Peng WK (1995) Dynamic stability of rotating blades with geometric non-linearity. J Sound Vib 187(3):421–433

Analytical Solution for Two-Dimensional Axisymmetric Thermoelastic Behavior in the Multilayer Composite Hollow Sphere

N. J. Wange, S. P. Pawar and M. N. Gaikwad

Abstract This article deals with an analytic solution of temperature distribution, displacement and stress distribution function for two-dimensional multilayered hollow spheres. The solution is obtained by using the separation of the variable method. Homogenous boundary conditions of the first or second kind can be applied on surfaces of $\theta =$ constant. However, homogeneous boundary conditions of the third kind (convection) are used in the r-direction. Under prescribed conditions, the temperature distribution, displacement and thermal stresses in the sphere are to be analyzed under the steady-state temperature field. The layers of the multilayer sphere are homogeneous and isotropic.

Keywords Composite hollow sphere · Temperature distribution · Displacement and thermal stresses · Steady state

1 Introduction

The temperature effect on thermal stresses in the composite regions consisting of several layers have numerous applications in engineering, Technology, manufacturing fields, etc. The increasing use of multilayer composite materials in engineering applications has resulted in considerable research activity in recent years. The use of composite materials of multilayer type has been tremendous in many engineering

N. J. Wange (✉)
Department of Mathematics, Datta Meghe Institute of Engineering, Technology and Research, Sawangi (Meghe), Wardha 442001, MS, India
e-mail: nitin.wange02@gmail.com

S. P. Pawar
Department of Mathematics, S. N. Mor and Smt. G. D. Saraf Science College, Tumsar, MS, India
e-mail: subhashpawar98@rediffmail.com

M. N. Gaikwad
Gopikabai Sitaram Gawande College, Umarkhed, MS, India
e-mail: adhimadhukar@gmail.com

D. Maity et al. (eds.), *Advances in Fluid Mechanics and Solid Mechanics*,
Lecture Notes in Mechanical Engineering,
https://doi.org/10.1007/978-981-15-0772-4_23

fields such as aerospace, automobiles, chemical and energy, civil and infrastructure, sports and recreation, biomedical engineering, and so on.

An understanding of thermally induced stresses in multilayer isotropic bodies is essential for a comprehensive study of their response due to exposure to a temperature field, which may, in turn, occur in service or during the manufacturing stages.

The Laplace transform technique is used by Carslaw and Jaeger [1], they discussed the infinite composite of two different medium and obtained the temperature distribution. They solved the transient boundary value problem of heat conduction in solids consisting of many parallel layers. In practice, if the number of layers is more than two, the inverse of the Laplace transform becomes quite difficult. The Adjoin-solution technique which has been introduced by Goodman [2] provides a method of solution to a large class of heat conduction problems in composite slabs from the solution but one adjoin problem. The primary disadvantage of the Adjoin-solution method is that only the solutions of the boundaries (i.e., interface) of the layers can be determined. Recently Tittle [3] introduced a technique for orthogonal expansion of functions over a one-dimensional multilayer region. The method essentially is an extension of Sturm–Liouville problem to the case of one-dimensional multilayer region and it has the advantage on other analytic methods is that its application to the solution of the boundary value problem of heat conduction is relatively simple. Bulavin and Kashcheev [4] used the method of separation of variables and orthogonal expansion of functions over a one-dimensional multilayer region to solve the transient heat conduction problem involving distributed volume heat sources in a multilayer region.

Recently, Vollbrech [5] discussed the stress in cylindrical and spherical walls subjected to internal pressure stationary heat flow. Kandil [6] has studied the effect of steady-state temperature and pressure gradient on the compound cylinder under high pressure and temperature. Ghosn and Sabbaghian [7] investigated a one-dimensional axisymmetric quasi-static coupled thermoelasticity problem. The solution technique uses the Laplace transform. The inversion to the real domain is obtained by means of Cauchy's theorem of residues. Sherif and Anwar [8] discussed the problem of infinitely long elastic circular cylinder whose inner and outer surfaces are subjected to a known temperature and are traction free. They have neglected both the inertia term and relaxation effects. Chen and Yang [9] discussed the thermal response of one dimensional quasi-static coupled thermoelastic problem of an infinitely long cylinder composed of two different materials. They applied the Laplace transform with respect to time and used the Fourier series and matrix operation to obtain the solution. Jane and Lee [10] considered the solution by using the Laplace transform and the finite difference method. The cylinder was composed of multilayer of different materials. They obtained a solution for the temperature and thermal stress distributions in a transient state. Lee [11] studied the one dimensional quasi-static coupled thermoelastic problem of the multilayered sphere with time-dependent boundary conditions is considered. The medium is without body forces and heat generation. Laplace transform and finite difference methods are used to obtain the solution of a wide range of transient thermal stresses.

The study of all above-cited papers and other referred literature on multilayer composites with different geometries reveals that results appearing with complexities such as space and time-dependent properties. In most of the articles, the authors have discussed the heat conduction problem only. In view of these findings, there is a need to quantify the conclusions regarding the effect of temperature asymmetry in fundamental problems where these multilayer composites are homogeneous and isotropic. Pawar et al. [12] discussed the problem where the temperature and thermal stresses are discussed under surface temperature asymmetry and heat generation and obtained analytic solution. Recently, Pawar et al. [13] discussed the problem where the steady temperature distribution and stress distribution function for one-dimensional three-layered sphere subjected to asymmetric surface temperature and internal heat generation is presented. The solutions are obtained and the effects on thermal stresses due to heat generation and surface temperature asymmetry parameter in the sphere are analyzed.

This article deals with an analytic solution of temperature distribution, displacement, and stress distribution function for two-dimensional multilayered steady-state hollow spheres. The solution is obtained by using the separation of the variable method, The radial and tangential displacement inside the sphere is discussed with the help of Goodier's displacement potential and Boussinesq harmonic functions.

2 Formulation of the Problem

This work deals with the two-dimensional axisymmetric thermoelastic problem of multilayer composite hollow sphere using the quasi-static approach. Composite n-layer sphere contains an inner region $r_0 \leq r \leq r_1$, middle region $r_1 \leq r \leq r_{n-1}$, and an outer region $r_{n-1} \leq r \leq r_n$ which are in perfect thermal contact. Homogeneous boundary conditions of the first and second kind are applied to the angular surfaces of $\theta = 0$ and $\theta = \varpi$. Third kind boundary condition set on the inner radial surface $i = 1, r = r_0$ and outer $i = n, r = r_n$ radial surfaces. Under these more realistic prescribed conditions the temperature distribution, displacement and thermal stresses in the sphere are to be analyzed under the steady-state temperature field. The layers of the multilayer sphere are homogeneous and isotropic, $k^{(i)}$, $(i = 1, 2, 3)$ are the thermal conductivities of material of these layers.

3 Heat Conduction Equation

Assume two-dimensional steady-state radial temperature field the heat conduction equation in the ith layer of the composite is given as [14].

$$\frac{\partial^2 T^{(i)}(r,\theta)}{\partial r^2} + \frac{2}{r}\frac{\partial T^{(i)}(r,\theta)}{\partial r} + \frac{1}{r^2 \sin\theta}\frac{\partial}{\partial \theta}\left(\sin\theta \frac{\partial T^{(i)}(r,\theta)}{\partial \theta}\right) = 0 \tag{1}$$

$$r_0 \le r \le r_n, r_{i-1} \le r \le r_i, 1 \le i \le n, 0 \le \theta \le \varpi, \varpi < \pi$$

Boundary, interface and initial conditions as
For the inner surface of the first layer ($i = 1$)

$$k^{(1)}\frac{\partial T^{(1)}(r_0,\theta)}{\partial r} + h^{(1)}T^{(1)}(r_0,\theta) = 0 \tag{2}$$

For outer surface of the nth layer ($i = n$)

$$k^{(n)}\frac{\partial T^{(n)}(r_n,\theta)}{\partial r} + h^{(n)}T^{(n)}(r_n,\theta) = 0 \tag{3}$$

For $\theta = 0$ surface ($i = 1, 2, 3 \ldots n$)

$$T^{(i)}(r,\theta = 0) = 0 \text{ or } \frac{\partial T^{(i)}(r,\theta = 0)}{\partial \theta} = 0 \tag{4}$$

For $\theta = \varpi$ surfaces ($i = 1, 2, 3 \ldots n$)

$$T^{(i)}(r,\theta = \varpi) = 0 \text{ or } \frac{\partial T^{(i)}(r,\theta = \varpi)}{\partial \theta} = 0 \tag{5}$$

For Inner interface of the ith layer $i = 2, 3 \ldots n$

$$T^{(i)}(r_{i-1},\theta) = T^{(i-1)}(r_{i-1},\theta) \tag{6}$$

$$k^{(i)}\frac{\partial T^{(i)}(r_{i-1},\theta)}{\partial r} = k^{(i-1)}\frac{\partial T^{(i-1)}(r_{i-1},\theta)}{\partial r} \tag{7}$$

For the outer interface of the ith layer $i = 1, 2, 3 \ldots n-1$

$$T^{(i)}(r_i,\theta) = T^{(i+1)}(r_i,\theta) \tag{8}$$

$$k^{(i)}\frac{\partial T^{(i)}(r_i,\theta,t)}{\partial r} = k^{(i+1)}\frac{\partial T^{(i+1)}(r_i,\theta,t)}{\partial r} \tag{9}$$

Initial condition is

$$T^{(i)}(r_i,\theta) = f^{(i)}(r,\theta) \tag{10}$$

4 Thermoelastic Problem

Two-dimensional problem of a spherical body, It is assumed that the body is deformed symmetrically with respect to the coordinate axis z. Making use of the spherical coordinate system (r, θ, ϕ), the force equilibrium equations in the directions of r and θ as [N. Noda].

$$\frac{\partial \sigma_{rr}^{(i)}}{\partial r} + \frac{1}{r}\frac{\partial \sigma_{\theta r}^{(i)}}{\partial \theta} + \frac{1}{r}\left(2\sigma_{rr}^{(i)} - \sigma_{\theta\theta}^{(i)} - \sigma_{\phi\phi}^{(i)} + \sigma_{\theta r}^{(i)}\cot\theta\right) + F_r^{(i)} = 0 \tag{11}$$

$$\frac{\partial \sigma_{r\theta}^{(i)}}{\partial r} + \frac{1}{r}\frac{\partial \sigma_{\theta\theta}^{(i)}}{\partial \theta} + \frac{1}{r}\left[\left(\sigma_{\theta\theta}^{(i)} - \sigma_{\phi\phi}^{(i)}\right)\cot\theta + 3\sigma_{r\theta}^{(i)}\right] + F_r^{(i)} = 0 \tag{12}$$

The constitutive equations in the spherical coordinate system, or the generalized Hooke's law as

$$\varepsilon_{rr}^{(i)} = \frac{1}{E^{(i)}}\left[\sigma_{rr}^{(i)} - \nu^{(i)}\left(\sigma_{\theta\theta}^{(i)} + \sigma_{\phi\phi}^{(i)}\right)\right] + \alpha^{(i)}\tau^{(i)} = \frac{1}{2G^{(i)}}\left(\sigma_{rr}^{(i)} - \frac{\nu^{(i)}}{1+\nu^{(i)}}\Theta^{(i)}\right) + \alpha^{(i)}\tau^{(i)} \tag{13}$$

$$\varepsilon_{\theta\theta}^{(i)} = \frac{1}{E^{(i)}}\left[\sigma_{\theta\theta}^{(i)} - \nu^{(i)}\left(\sigma_{rr}^{(i)} + \sigma_{\phi\phi}^{(i)}\right)\right] + \alpha^{(i)}\tau^{(i)} = \frac{1}{2G^{(i)}}\left(\sigma_{\theta\theta}^{(i)} - \frac{\nu^{(i)}}{1+\nu^{(i)}}\Theta^{(i)}\right) + \alpha^{(i)}\tau^{(i)} \tag{14}$$

$$\varepsilon_{\phi\phi}^{(i)} = \frac{1}{E^{(i)}}\left[\sigma_{\phi\phi}^{(i)} - \nu^{(i)}\left(\sigma_{rr}^{(i)} + \sigma_{\theta\theta}^{(i)}\right)\right] + \alpha^{(i)}\tau^{(i)} = \frac{1}{2G^{(i)}}\left(\sigma_{\phi\phi}^{(i)} - \frac{\nu^{(i)}}{1+\nu^{(i)}}\Theta^{(i)}\right) + \alpha^{(i)}\tau^{(i)} \tag{15}$$

$$\varepsilon_{r\theta}^{(i)} = \frac{1}{2G^{(i)}}\sigma_{r\theta}^{(i)} \tag{16}$$

where $\Theta^{(i)} = \sigma_{rr}^{(i)} + \sigma_{\theta\theta}^{(i)} + \sigma_{\phi\phi}^{(i)}$. Alternative forms are

$$\begin{aligned}
\sigma_{rr}^{(i)} &= 2\mu^{(i)}\varepsilon_{rr}^{(i)} + \lambda^{(i)}e^{(i)} - \beta^{(i)}\tau^{(i)} \\
\sigma_{\theta\theta}^{(i)} &= 2\mu^{(i)}\varepsilon_{\theta\theta}^{(i)} + \lambda^{(i)}e^{(i)} - \beta^{(i)}\tau^{(i)} \\
\sigma_{\phi\phi}^{(i)} &= 2\mu^{(i)}\varepsilon_{\phi\phi}^{(i)} + \lambda^{(i)}e^{(i)} - \beta^{(i)}\tau^{(i)} \\
\sigma_{r\theta}^{(i)} &= 2\mu^{(i)}\varepsilon_{r\theta}^{(i)}
\end{aligned} \tag{17}$$

where $e^{(i)} = \varepsilon_{rr}^{(i)} + \varepsilon_{\theta\theta}^{(i)} + \varepsilon_{\phi\phi}^{(i)}$

The components of strain for an axisymmetric deformation in the spherical coordinate system are

$$\varepsilon_{rr}^{(i)} = \frac{\partial u_r^{(i)}}{\partial r}$$
$$\varepsilon_{\theta\theta}^{(i)} = \frac{u_r^{(i)}}{r} + \frac{1}{r}\frac{\partial u_\theta^{(i)}}{\partial \theta}$$
$$\varepsilon_{\phi\phi}^{(i)} = \frac{u_r^{(i)}}{r} + \cot\theta \frac{u_\theta^{(i)}}{r}$$
$$\varepsilon_{r\theta}^{(i)} = \frac{1}{2}\left(\frac{1}{r}\frac{\partial u_r^{(i)}}{\partial \theta} + \frac{\partial u_\theta^{(i)}}{\partial r} - \frac{u_\theta^{(i)}}{r}\right)$$
$$e^{(i)} = \frac{\partial u_r^{(i)}}{\partial \theta} + 2\frac{u_r^{(i)}}{r} + \cot\theta \frac{u_\theta^{(i)}}{r} + \frac{1}{r}\frac{\partial u_\theta^{(i)}}{\partial \theta} \tag{18}$$

Substituting Eqs. (17) and (18) into Eqs. (11) and (12) Navier's equations of thermoelasticity for axisymmetric problems may be expressed as

$$\left(\lambda^{(i)} + 2\mu^{(i)}\right)\frac{\partial e^{(i)}}{\partial r} - \frac{2\mu^{(i)}}{r\sin\theta}\frac{\partial(\omega_\phi^{(i)}\sin\theta)}{\partial\theta} - \beta^{(i)}\frac{\partial \tau^{(i)}}{\partial r} + F_r^{(i)} = 0 \tag{19}$$

$$\left(\lambda^{(i)} + 2\mu^{(i)}\right)\frac{1}{r}\frac{\partial e^{(i)}}{\partial \theta} - \frac{2\mu^{(i)}}{r}\frac{\partial(r\omega_\phi^{(i)})}{\partial r} - \beta^{(i)}\frac{1}{r}\frac{\partial \tau^{(i)}}{\partial \theta} + F_\theta^{(i)} = 0 \tag{20}$$

where $\omega_\phi^{(i)} = \frac{1}{2r}\left[\frac{\partial(ru_\theta^{(i)})}{\partial r} - \frac{\partial u_r^{(i)}}{\partial \theta}\right]$

The solution of the Navier's equations without the body force for the axisymmetric problem in the spherical coordinate system can be expressed by the Goodier's thermoelastic displacement potential $\Phi^{(i)}$ and the Boussinesq harmonic functions $\varphi^{(i)}$ and $\psi^{(i)}$

$$u_r^{(i)} = \frac{\partial \Phi^{(i)}}{\partial r} + \frac{\partial \varphi^{(i)}}{\partial r} + r\cos\theta\frac{\partial \psi^{(i)}}{\partial r} - (3 - 4\nu^{(i)})\psi^{(i)}\cos\theta$$
$$u_r^{(i)} = \frac{\partial \Phi^{(i)}}{\partial r} + \left[\frac{\partial \varphi^{(i)}}{\partial r} + r\cos\theta\frac{\partial \psi^{(i)}}{\partial r} - (3 - 4\nu^{(i)})\psi^{(i)}\cos\theta\right]$$
$$u_r^{(i)} = \overline{u_r^{(i)}} + \overline{\overline{u_r^{(i)}}} \tag{21}$$

$$u_\theta^{(i)} = \frac{1}{r}\frac{\partial \Phi^{(i)}}{\partial \theta} + \frac{1}{r}\frac{\partial \varphi^{(i)}}{\partial \theta} + \cos\theta\frac{\partial \psi^{(i)}}{\partial \theta} - (3 - 4\nu^{(i)})\psi^{(i)}\sin\theta$$
$$u_\theta^{(i)} = \frac{1}{r}\frac{\partial \Phi^{(i)}}{\partial \theta} + \left[\frac{1}{r}\frac{\partial \varphi^{(i)}}{\partial \theta} + \cos\theta\frac{\partial \psi^{(i)}}{\partial \theta} - (3 - 4\nu^{(i)})\psi^{(i)}\sin\theta\right]$$
$$u_\theta^{(i)} = \overline{u_\theta^{(i)}} + \overline{\overline{u_\theta^{(i)}}} \tag{22}$$

where the component with a single bar is displacement with respect to $\Phi^{(i)}$ and component with double bar is displacement with respect to $\varphi^{(i)}$ and $\psi^{(i)}$. $G^{(i)}$, $\nu^{(i)}$ and $a_t^{(i)}$ are the shear modulus, Poisson's ratio, coefficient of thermal expansion for the material of multilayer hollow sphere. Functions must satisfy the equations as

$$\nabla^2\Phi^{(i)} = K^{(i)}\tau^{(i)}, \nabla^2\varphi^{(i)} = 0, \quad \nabla^2\psi^{(i)} = 0 \tag{23}$$

$$\nabla^2 = \frac{\partial^2}{\partial r^2} + \frac{2}{r}\frac{\partial}{\partial r} + \frac{1}{r^2}\frac{\partial^2}{\partial\theta^2} + \frac{1}{r^2}\cot\theta\frac{\partial}{\partial\theta}$$

$$K^{(i)} = \frac{1+\nu^{(i)}}{1-\nu^{(i)}}a_t^{(i)}$$

The strain components are represented as

$$\begin{aligned}
\varepsilon_{rr}^{(i)} &= \frac{\partial^2\Phi^{(i)}}{\partial r^2} + \frac{\partial^2\varphi^{(i)}}{\partial r^2} + r\cos\theta\frac{\partial^2\psi^{(i)}}{\partial r^2} - 2(1-2\nu^{(i)})\cos\theta\frac{\partial\psi^{(i)}}{\partial r}\\
\varepsilon_{\theta\theta}^{(i)} &= \frac{1}{r}\frac{\partial\Phi^{(i)}}{\partial r} + \frac{1}{r^2}\frac{\partial^2\Phi^{(i)}}{\partial\theta^2} + \frac{1}{r}\frac{\partial\varphi^{(i)}}{\partial r} + \frac{1}{r^2}\frac{\partial^2\varphi^{(i)}}{\partial\theta^2} + \cos\theta\frac{\partial\psi^{(i)}}{\partial r}\\
&\quad + \frac{1}{r}\cos\theta\frac{\partial^2\psi^{(i)}}{\partial\theta^2} + 2(1-2\nu^{(i)})\frac{1}{r}\sin\theta\frac{\partial\psi^{(i)}}{\partial r}\\
\varepsilon_{\phi\phi}^{(i)} &= \frac{1}{r}\frac{\partial\Phi^{(i)}}{\partial r} + \cot\theta\frac{1}{r^2}\frac{\partial\Phi^{(i)}}{\partial\theta} + \frac{1}{r}\frac{\partial\varphi^{(i)}}{\partial r} + \cot\theta\frac{1}{r^2}\frac{\partial\varphi^{(i)}}{\partial\theta}\\
&\quad + \cos\theta\frac{\partial\psi^{(i)}}{\partial r} + \frac{\cos^2\theta}{\sin\theta}\frac{1}{r}\frac{\partial\psi^{(i)}}{\partial\theta}\\
\varepsilon_{r\theta}^{(i)} &= \frac{\partial^2}{\partial r\partial\theta}\left(\frac{\Phi^{(i)}}{r}\right) + \frac{\partial^2}{\partial r\partial\theta}\left(\frac{\varphi^{(i)}}{r}\right) + (1-2\nu^{(i)})\sin\theta\frac{\partial\psi^{(i)}}{\partial r}\\
&\quad + \cos\theta\frac{\partial^2\psi^{(i)}}{\partial r\partial\theta} - 2(1-\nu^{(i)})\frac{1}{r}\cos\theta\frac{\partial\psi^{(i)}}{\partial\theta}
\end{aligned}$$

The stress components in the spherical coordinate system are represented in terms of three functions $\Phi^{(i)}$, $\varphi^{(i)}$ and $\psi^{(i)}$.

$$\begin{aligned}
\sigma_{rr}^{(i)} &= 2G^{(i)}\left[\frac{\partial^2\Phi^{(i)}}{\partial r^2} - K^{(i)}\tau^{(i)}\right]\\
&\quad + 2G^{(i)}\left[\frac{\partial^2\varphi^{(i)}}{\partial r^2} + r\cos\theta\frac{\partial^2\psi^{(i)}}{\partial r^2} - 2(1-\nu^{(i)})\cos\theta\frac{\partial\psi^{(i)}}{\partial r} + 2\nu^{(i)}\frac{1}{r}\sin\theta\frac{\partial\psi^{(i)}}{\partial\theta}\right]\\
\sigma_{rr}^{(i)} &= \overline{\sigma_{rr}^{(i)}} + \overline{\overline{\sigma_{rr}^{(i)}}}
\end{aligned} \tag{24}$$

$$\sigma_{\theta\theta}^{(i)} = 2G^{(i)}\left[\begin{array}{l}\dfrac{1}{r}\dfrac{\partial\Phi^{(i)}}{\partial r} + \dfrac{1}{r^2}\dfrac{\partial^2\Phi^{(i)}}{\partial\theta^2} + \dfrac{1}{r}\dfrac{\partial\varphi^{(i)}}{\partial r} + \dfrac{1}{r^2}\dfrac{\partial^2\varphi^{(i)}}{\partial\theta^2} + (1-2\nu^{(i)})\cos\theta\dfrac{\partial\psi^{(i)}}{\partial r} \\ \qquad + \dfrac{1}{r}\cos\theta\dfrac{\partial^2\psi^{(i)}}{\partial\theta^2} + 2(1-\nu^{(i)})\dfrac{1}{r}\sin\theta\dfrac{\partial\psi^{(i)}}{\partial\theta} - K^{(i)}\tau^{(i)}\end{array}\right]$$

$$\sigma_{\theta\theta}^{(i)} = 2G^{(i)}\left[\frac{1}{r}\frac{\partial\Phi^{(i)}}{\partial r} + \frac{1}{r^2}\frac{\partial^2\Phi^{(i)}}{\partial\theta^2} - K^{(i)}\tau^{(i)}\right] + 2G^{(i)}\left[\frac{1}{r}\frac{\partial\varphi^{(i)}}{\partial r} + \frac{1}{r^2}\frac{\partial^2\varphi^{(i)}}{\partial\theta^2} + (1-2\nu^{(i)})\cos\theta\frac{\partial\psi^{(i)}}{\partial r} + \frac{1}{r}\cos\theta\frac{\partial^2\psi^{(i)}}{\partial\theta^2} + 2(1-\nu^{(i)})\frac{1}{r}\sin\theta\frac{\partial\psi^{(i)}}{\partial\theta}\right]$$

$$\sigma_{\theta\theta}^{(i)} = \overline{\sigma_{\theta\theta}^{(i)}} + \overline{\overline{\sigma_{\theta\theta}^{(i)}}} \tag{25}$$

$$\sigma_{\phi\phi}^{(i)} = 2G^{(i)}\left[\begin{array}{l}\frac{1}{r}\frac{\partial\Phi^{(i)}}{\partial r} + \cot\theta\frac{1}{r^2}\frac{\partial\Phi^{(i)}}{\partial\theta} + \frac{1}{r}\frac{\partial\varphi^{(i)}}{\partial r} + \cot\theta\frac{1}{r^2}\frac{\partial\varphi^{(i)}}{\partial\theta} + (1-2\nu^{(i)})\cos\theta\frac{\partial\psi^{(i)}}{\partial r} \\ +\frac{1}{r}(\cos\theta\cot\theta + 2\nu^{(i)}\sin\theta)\frac{\partial\psi^{(i)}}{\partial\theta} - K^{(i)}\tau^{(i)}\end{array}\right]$$

$$\sigma_{\phi\phi}^{(i)} = 2G^{(i)}\left[\frac{1}{r}\frac{\partial\Phi^{(i)}}{\partial r} + \cot\theta\frac{1}{r^2}\frac{\partial\Phi^{(i)}}{\partial\theta} - K^{(i)}\tau^{(i)}\right] + 2G^{(i)}\left[\frac{1}{r}\frac{\partial\varphi^{(i)}}{\partial r} + \cot\theta\frac{1}{r^2}\frac{\partial\varphi^{(i)}}{\partial\theta} + (1-2\nu^{(i)})\cos\theta\frac{\partial\psi^{(i)}}{\partial r} + \frac{1}{r}(\cos\theta\cot\theta + 2\nu^{(i)}\sin\theta)\frac{\partial\psi^{(i)}}{\partial\theta}\right]$$

$$\sigma_{\phi\phi}^{(i)} = \overline{\sigma_{\phi\phi}^{(i)}} + \overline{\overline{\sigma_{\phi\phi}^{(i)}}} \tag{26}$$

$$\sigma_{r\theta}^{(i)} = 2G^{(i)}\left[\frac{\partial^2}{\partial r\partial\theta}\left(\frac{\Phi^{(i)}}{r}\right)\right] + 2G^{(i)}\left[\frac{\partial^2}{\partial r\partial\theta}\left(\frac{\varphi^{(i)}}{r}\right) + (1-2\nu^{(i)})\sin\theta\frac{\partial\psi^{(i)}}{\partial r} + \cos\theta\frac{\partial^2\psi^{(i)}}{\partial r\partial\theta} - 2(1-\nu^{(i)})\frac{1}{r}\cos\theta\frac{\partial\psi^{(i)}}{\partial\theta}\right]$$

$$\sigma_{r\theta}^{(i)} = 2G^{(i)}\left[\frac{\partial^2}{\partial r\partial\theta}\left(\frac{\Phi^{(i)}}{r}\right)\right] + 2G^{(i)}\left[\frac{\partial^2}{\partial r\partial\theta}\left(\frac{\varphi^{(i)}}{r}\right) + (1-2\nu^{(i)})\sin\theta\frac{\partial\psi^{(i)}}{\partial r} + \cos\theta\frac{\partial^2\psi^{(i)}}{\partial r\partial\theta} - 2(1-\nu^{(i)})\frac{1}{r}\cos\theta\frac{\partial\psi^{(i)}}{\partial\theta}\right]$$

$$\sigma_{r\theta}^{(i)} = \overline{\sigma_{r\theta}^{(i)}} + \overline{\overline{\sigma_{r\theta}^{(i)}}} \tag{27}$$

The mechanical boundary conditions on the traction free surfaces $r = r_0$ and $r = r_n$ are

$$\sigma_{rr}^{(i)} = 0 \quad \text{and} \quad \sigma_{r\theta}^{(i)} = 0 \tag{28}$$

Assuming the interface conditions as $i = 1, 2, 3, \ldots n-1$

$$\begin{aligned}\sigma_{rr}^{(i)}(r_i) &= \sigma_{rr}^{(i+1)}(r_i) \\ \sigma_{r\theta}^{(i)}(r_i) &= \sigma_{r\theta}^{(i+1)}(r_i) \\ \sigma_{\theta\theta}^{(i)}(r_i) &= \sigma_{\theta\theta}^{(i+1)}(r_i)\end{aligned} \tag{29}$$

5 Solutions

Heat Conduction

The separation of variables method is used to solve the problem.

$$T^{(i)}(r,\theta) = R^{(i)}(r)\theta^{(i)}(\theta) \tag{30}$$

$$\frac{d^2R^{(i)}(r)}{dr^2}\Theta^{(i)}(\theta) + \frac{2}{r}\frac{dR^{(i)}(r)}{dr}\Theta^{(i)}(\theta) + \frac{1}{r^2}R^{(i)}(r)\frac{d^2\Theta^{(i)}(\theta)}{d\theta^2} + \frac{\cot\theta}{r^2}R^{(i)}(r)\frac{d\Theta^{(i)}(\theta)}{d\theta} = 0$$

$$-r^2\left[\frac{R^{(i)''}(r)}{R^{(i)}(r)} + \frac{2}{r}\frac{R^{(i)'}(r)}{R^{(i)}(r)}\right] = \frac{\Theta^{(i)''}(\theta)}{\Theta^{(i)}(\theta)} + \cot\theta\frac{\Theta^{(i)'}(\theta)}{\Theta^{(i)}(\theta)} = -m(1+m) \tag{31}$$

where $m(1+m) = \left(\lambda_m^{(i)}\right)^2$

$$r^2R^{(i)''}(r) + 2rR^{(i)'}(r) - m(1+m)R^{(i)}(r) = 0$$

$$R_m^{(i)}(r) = a_m^{(i)}r^m + b_m^{(i)}r^{-(1+m)} \tag{32}$$

Application of the interface conditions (8)–(11) and boundary conditions (2)–(3) to the transverse eigenfunction $R_m^{(i)}(r)$. The matrix (2n × 2n) are as follows:

$$\begin{bmatrix}
c_{1in} & c_{2in} & 0 & 0 & \dots & 0 & 0 & 0 & 0 & \dots & 0 & 0 & 0 & 0 \\
x_{11} & x_{12} & x_{13} & x_{14} & \dots & 0 & 0 & 0 & 0 & \dots & 0 & 0 & 0 & 0 \\
y_{11} & y_{12} & y_{13} & y_{14} & \dots & 0 & 0 & 0 & 0 & \dots & 0 & 0 & 0 & 0 \\
\dots & \dots & \dots & \dots & \dots & \dots & \dots & \dots & \dots & \dots & \dots & \dots & \dots & \dots \\
0 & 0 & 0 & 0 & \dots & x_{i1} & x_{i2} & x_{i3} & x_{i4} & \dots & 0 & 0 & 0 & 0 \\
0 & 0 & 0 & 0 & \dots & y_{i1} & y_{i2} & y_{i3} & y_{i4} & \dots & 0 & 0 & 0 & 0 \\
\dots & \dots & \dots & \dots & \dots & \dots & \dots & \dots & \dots & \dots & \dots & \dots & \dots & \dots \\
0 & 0 & 0 & 0 & \dots & 0 & 0 & 0 & 0 & \dots & x_{i-1,1} & x_{i-1,2} & x_{i-1,3} & x_{i-1,4} \\
0 & 0 & 0 & 0 & \dots & 0 & 0 & 0 & 0 & \dots & y_{i-1,1} & y_{i-1,2} & y_{i-1,3} & y_{i-1,4} \\
0 & 0 & 0 & 0 & \dots & 0 & 0 & 0 & 0 & \dots & 0 & 0 & c_{1out} & c_{2out}
\end{bmatrix}
\begin{bmatrix} a_m^{(1)} \\ b_m^{(1)} \\ \dots \\ \dots \\ a_m^{(i)} \\ b_m^{(i)} \\ \dots \\ \dots \\ a_m^{(n)} \\ b_m^{(n)} \end{bmatrix}
=
\begin{bmatrix} 0 \\ 0 \\ \dots \\ \dots \\ 0 \\ 0 \\ \dots \\ \dots \\ 0 \\ 0 \end{bmatrix} \tag{33}$$

where

$$c_{1in} = k^{(1)}mr_1^{m-1} + h^{(1)}r_1^m$$

$$c_{2in} = -k^{(1)}(1+m)r_1^{-m-2} + h^{(1)}r_1^{-1-m}$$

$$x_{i1} = r_i^m \quad x_{i2} = r_i^{-1-m} \quad x_{i3} = -r_i^m \quad x_{i4} = -r_i^{-1-m}$$

$$y_{i1} = k^{(i)}mr_i^{m-1} \quad y_{i2} = k^{(i)}(-1-m)r_i^{-m-2} \quad y_{i3} = -k^{(i+1)}mr_i^{m-1}$$

$$y_{i4} = k^{(i+1)}(1+m)r_i^{-m-2}$$

$$c_{1out} = k^{(n)}mr_n^{m-1} + h^{(n)}r_n^m \quad c_{2out} = -k^{(n)}(1+m)r_n^{-m-2} + h^{(n)}r_n^{-1-m}$$

For heat flux to be continuous at the layer interfaces for all values of t.

$$\alpha^{(i)}\left(\lambda_m^{(i)}\right)^2 = \alpha^{(1)}\left(\lambda_m^{(1)}\right)^2, \quad \mathrm{i} = 1, 2, \dots n \tag{34}$$

In the above matrix equation, $\lambda_m^{(i)}(i \neq 1)$ maybe written in terms of $\lambda_m^{(1)}$ using the above equation. Subsequently, transverse eigen condition can be obtained by setting the determinant of the $(2n \times 2n)$ coefficient matrix equal to zero. And after that eigenvalue determined the constants $a_m^{(i)}$ and $b_m^{(i)}$.

The equation in $\Theta^{(i)}(\theta)$ can be written as

$$\frac{\Theta^{(i)''}(\theta)}{\Theta^{(i)}(\theta)} + \cot\theta \frac{\Theta^{(i)'}(\theta)}{\Theta^{(i)}(\theta)} = -m(1+m)$$
$$\Theta^{(i)''} + \cot\theta\Theta^{(i)'} + m(m+1)\Theta^{(i)} = 0 \tag{35}$$

By change of variable using $\mu = \cos\theta$

$$\Theta^{(i)'} = -\sin\theta \frac{d\Theta^{(i)}}{d\mu} \tag{36}$$

$$\Theta^{(i)''} = -\cos\theta \frac{d\Theta^{(i)}}{d\mu} + \sin^2\theta \frac{d^2\Theta^{(i)}}{d\mu^2} \tag{37}$$

Substituting Eqs. (36) and (37) in Eq. (35).

$$-\cos\theta \frac{d\Theta^{(i)}}{d\mu} + \sin^2\theta \frac{d^2\Theta^{(i)}}{d\mu^2} + \frac{\cos\theta}{\sin\theta}\left(-\sin\theta \frac{d\Theta^{(i)}}{d\mu}\right) + m(m+1)\Theta^{(i)} = 0 \tag{38}$$

$$(1-\mu^2)\frac{d^2\Theta^{(i)}}{d\mu^2} - 2\mu\frac{d\Theta^{(i)}}{d\mu} + m(m+1)\Theta^{(i)} = 0$$
$$\frac{d}{d\mu}\left[(1-\mu^2)\frac{d\Theta^{(i)}}{d\mu}\right] + m(m+1)\Theta^{(i)} = 0 \tag{39}$$

$$\Theta_m^{(i)}(\mu) = c_1 P_m^{(i)}(\mu) + c_2 Q_m^{(i)}(\mu)$$
$$\Theta_m^{(i)}(\mu) = c_1 P_m^{(i)}(\cos\theta) + c_2 Q_m^{(i)}(\cos\theta) \tag{40}$$

By using boundary conditions

$$Q_m^{(i)}(\cos 0) = Q_m^{(i)}(1) = \infty$$

Hence $c_2 = 0$

$$\Theta_m^{(i)}(\theta) = c_1 P_m^{(i)}(\cos\theta)$$

Hence

$$c_1 \neq 0, \Theta_m^{(i)}(\theta) = P_m^{(i)}(\cos\theta) \tag{41}$$

It is assumed that the solution of the problem is in the form of a series expansion of the derived eigenfunctions as follows such that

$$T^{(i)}(r,\theta) = \sum_{m=0}^{\infty} R_m^{(i)}(r)\Theta_m^{(i)}(\theta)$$

$$T^{(i)}(r,\theta) = \sum_{m=0}^{\infty} \left(a_m^{(i)} r^m + b_m^{(i)} r^{-m-1}\right) P_m^{(i)}(\cos\theta) \tag{42}$$

Initial temperature is $f^{(i)}$

6 Displacement Components

Displacement component corresponding to $\Phi^{(i)}$ and $\tau^{(i)}$

Therefore, the temperature change $\tau^{(i)}$ obtained as

$$\tau^{(i)} = T^{(i)}(r,\theta) - f^{(i)}$$

$$\tau^{(i)} = \sum_{m=0}^{\infty} \left(a_m^{(i)} r^m + b_m^{(i)} r^{-m-1}\right) P_m^{(i)}(\cos\theta) - f^{(i)} \tag{43}$$

The Goodier's thermoelastic displacement potential $\Phi^{(i)}$ satisfying the first of Eq. (25) is obtained as [15]

$$\Phi^{(i)} = K^{(i)} \left\{ -\frac{1}{6} f^{(i)} r^2 + \sum_{m=0}^{\infty} \left[\frac{1}{2(2m+3)} a_m^{(i)} r^{m+2} - \frac{1}{2(2m-1)} b_m^{(i)} r^{-m+1} \right] P_m^{(i)}(\cos\theta) \right\} \tag{44}$$

Displacement component corresponding to $\varphi^{(i)}$ and $\psi^{(i)}$

We have considered the problem of axisymmetric thermoelastic deformation in a hollow multilayer sphere. In this the coordinate variable θ is defined within the interval $0 \le \theta \le \pi$. The Legendre functions $P_m^{(i)}(\cos\theta)$ is considered as the fundamental solution of the Boussinesq harmonic functions $\varphi^{(i)}$ and $\psi^{(i)}$ for the axisymmetric case in the spherical coordinate system for $m = 0, 1, 2, 3 \ldots$ thus the displacement functions $\varphi^{(i)}$ and $\psi^{(i)}$ are represented by the series forms as [Noda].

$$\varphi_m^{(i)} = \sum_{m=0}^{\infty} \left(c_{1m}^{\prime(i)} r^m + c_{2m}^{\prime(i)} r^{-m-1}\right) P_m^{(i)}(\cos\theta) \tag{45}$$

$$\psi_m^{(i)} = \sum_{m=0}^{\infty} \left(d_{1m}^{\prime(i)} r^m + d_{2m}^{\prime(i)} r^{-m-1}\right) P_m^{(i)}(\cos\theta) \tag{46}$$

The displacements corresponding to the Goodier's thermoelastic potential functions $\Phi^{(i)}$ and the displacement functions $\varphi^{(i)}$ and $\psi^{(i)}$.

$$\overline{u_r^{(i)}} = K^{(i)}\left\{-\frac{1}{3}f^{(i)}r + \sum_{m=0}^{\infty}\left[\frac{m+2}{2(2m+3)}a_{im}r^{m+1} + \frac{m-1}{2(2m-1)}b_{im}r^{-m}\right]P_{im}(\cos\theta)\right\} \tag{47}$$

$$\begin{aligned}
\overline{\overline{u_r^{(i)}}} &= \frac{\partial}{\partial r}\left(\sum_{m=0}^{\infty}\left(c_{1m}^{'(i)}r^m + c_{2m}^{'(i)}r^{-m-1}\right)P_m^{(i)}(\cos\theta)\right) + r\cos\theta\frac{\partial}{\partial r}\left(\sum_{m=0}^{\infty}\left(d_{1m}^{'(i)}r^m + d_{2m}^{'(i)}r^{-m-1}\right)P_m^{(i)}(\cos\theta)\right)\\
&\quad - (3-4\nu^{(i)})\cos\theta\left(\sum_{m=0}^{\infty}\left(d_{1m}^{'(i)}r^m + d_{2m}^{'(i)}r^{-m-1}\right)P_m^{(i)}(\cos\theta)\right)\\
\overline{\overline{u_r^{(i)}}} &= \sum_{m=0}^{\infty}\left(c_{1m}^{'(i)}mr^{m-1} + c_{2m}^{'(i)}(-m-1)r^{-m-2}\right)P_m^{(i)}(\cos\theta)\\
&\quad + r\cos\theta\sum_{m=0}^{\infty}\left(d_{1m}^{'(i)}mr^{m-1} + d_{2m}^{'(i)}(-m-1)r^{-m-2}\right)P_m^{(i)}(\cos\theta)\\
&\quad - (3-4\nu^{(i)})\cos\theta\left(\sum_{m=0}^{\infty}\left(d_{1m}^{'(i)}r^m + d_{2m}^{'(i)}r^{-m-1}\right)P_m^{(i)}(\cos\theta)\right)\\
\overline{\overline{u_r^{(i)}}} &= \sum_{m=0}^{\infty}\left(c_{1m}^{'(i)}mr^{m-1} - c_{2m}^{'(i)}(m+1)r^{-m-2}\right)P_m^{(i)}(\cos\theta)\\
&\quad + \sum_{m=0}^{\infty}\left[(m-3+4\nu^{(i)})d_{1m}^{'(i)}r^m - (m+4-4\nu^{(i)})d_{2m}^{'(i)}r^{-m-1}\right]\\
&\quad \times \frac{1}{2m+1}\left[(m+1)P_{m+1}^{(i)}(\cos\theta) + mP_{m-1}^{(i)}(\cos\theta)\right]
\end{aligned} \tag{48}$$

where $\cos\theta P_m^{(i)}(\cos\theta) = \frac{1}{2m+1}\left[(m+1)P_{m+1}^{(i)}(\cos\theta) + mP_{m-1}^{(i)}(\cos\theta)\right]$

It can be seen from expression (48) that this is not suitable for solving practical boundary value problem because it contains three kinds Legendre functions with different orders $n-1, n, n+1$ under the summation signs. Two solve this problem we introduce new unknown constants given by

$$\begin{aligned}
c_{1m}^{'(i)} &= c_{1m}^{(i)} - (m-4+4\nu^{(i)})d_{1m-2}^{(i)}\\
c_{2m}^{'(i)} &= c_{2m}^{(i)} - (m+5-4\nu^{(i)})d_{2m+2}^{(i)}\\
d_{1m}^{'(i)} &= (2m+1)d_{1m-1}^{(i)}\\
d_{2m}^{'(i)} &= (2m+1)d_{2m+1}^{(i)}
\end{aligned}$$

The function $\varphi^{(i)}$ and $\psi^{(i)}$ reduce to

$$\varphi^{(i)} = \sum_{m=0}^{\infty}\left\{\left[c_{1,m}^{(i)} - (m-4+4\nu^{(i)})d_{1,m-2}^{(i)}\right]r^m + \left[c_{2,m}^{(i)} - (m+5-4\nu^{(i)})d_{2,m+2}^{(i)}\right]r^{-m-1}\right\}P_m^{(i)}(\cos\theta) \tag{49}$$

$$\psi^{(i)} = \sum_{m=0}^{\infty}\left[(2m+1)d_{1,m-1}^{(i)}r^m + (2m+1)d_{2,m+1}^{(i)}r^{-m-1}\right]P_m^{(i)}(\cos\theta) \tag{50}$$

Using new unknown constants (48) can be expressed as

$$\overline{\overline{u_r^{(i)}}} = \sum_{m=0}^{\infty}\left[mc_{1,m}^{(i)}r^{m-1} - (m+1)c_{2,m}^{(i)}r^{-m-2} + (m+1)(m-2+4\nu^{(i)})d_{1,m}^{(i)}r^{m+1} - m(m+3-4\nu^{(i)})d_{2,m}^{(i)}r^{-m}\right]P_m^{(i)}(\cos\theta)$$

Similarly the tangential displacement with respect to $\varphi^{(i)}$ and $\psi^{(i)}$

$$\overline{\overline{u_\theta^{(i)}}} = -\left(1-\mu^2\right)^{1/2}\sum_{m=1}^{\infty}\left[\begin{array}{l} c_{1,m}^{(i)}r^{m-1} + c_{2,m}^{(i)}r^{-m-2} + (m+5-4\nu^{(i)})d_{1,m}^{(i)}r^{m+1} \\ +(m-4+4\nu^{(i)})d_{2,m}^{(i)}r^{-m} \end{array}\right]\frac{m+1}{1-\mu^2}\left[\mu P_m^{(i)}(\mu) - P_{m+1}^{(i)}(\mu)\right]$$

The radial displacement and tangential displacement is obtained as

$$\begin{aligned} u_r^{(i)} &= K^{(i)}\left\{-\frac{1}{3}f^{(i)}r + \sum_{m=0}^{\infty}\left[\frac{m+2}{2(2m+3)}a_m^{(i)}r^{m+1} + \frac{m-1}{2(2m-1)}b_m^{(i)}r^{-m}\right]P_m^{(i)}(\cos\theta)\right\} \\ &\quad + \sum_{m=0}^{\infty}\left[\begin{array}{l} mc_{1,m}^{(i)}r^{m-1} - (m+1)c_{2,m}^{(i)}r^{-m-2} + (m+1)(m-2+4\nu^{(i)})d_{1,m}^{(i)}r^{m+1} \\ -m(m+3-4\nu^{(i)})d_{2,m}^{(i)}r^{-m} \end{array}\right]P_m^{(i)}(\cos\theta) \end{aligned} \tag{51}$$

$$\begin{aligned} u_\theta^{(i)} &= -K^{(i)}\left(1-\mu^2\right)^{1/2}\sum_{m=1}^{\infty}\left[\frac{1}{2(2m+3)}a_m^{(i)}r^{m+1} - \frac{1}{2(2m-1)}b_m^{(i)}r^{-m}\right]\frac{m+1}{1-\mu^2}\left[\mu P_m^{(i)}(\mu) - P_{m+1}^{(i)}(\mu)\right] \\ &\quad - \left(1-\mu^2\right)^{1/2}\sum_{m=1}^{\infty}\left[\begin{array}{l} c_{1,m}^{(i)}r^{m-1} + c_{2,m}^{(i)}r^{-m-2} + (m+5-4\nu^{(i)})d_{1,m}^{(i)}r^{m+1} \\ +(m-4+4\nu^{(i)})d_{2,m}^{(i)}r^{-m} \end{array}\right]\frac{m+1}{1-\mu^2}\left[\mu P_m^{(i)}(\mu) - P_{m+1}^{(i)}(\mu)\right] \end{aligned} \tag{52}$$

7 Thermal Stresses

The stress components corresponding to $\Phi^{(i)}$ and $\tau^{(i)}$

$$\overline{\sigma_{rr}^{(i)}} = 2G^{(i)}K^{(i)}\left\{\frac{2}{3}f^{(i)} + \sum_{m=0}^{\infty}\left[\frac{m^2-m-4}{2(2m+3)}a_m^{(i)}r^m - \frac{m^2+3m-2}{2(2m-1)}b_m^{(i)}r^{-m-1}\right]P_m^{(i)}(\cos\theta)\right\} \tag{53}$$

The stress components corresponding to $\varphi^{(i)}$ and $\psi^{(i)}$

$$\overline{\overline{\sigma_{rr}^{(i)}}} = 2G^{(i)}\sum_{m=0}^{\infty}\left[\begin{array}{l} m(m-1)c_{1,m}^{(i)}r^{m-2} - (m+1)(m+2)c_{2,m}^{(i)}r^{-m-3} \\ +(m+1)(m^2-m-2+2\nu^{(i)})d_{1,m}^{(i)}r^m + m(m^2+3m-2\nu^{(i)})d_{2,m}^{(i)}r^{-m-1} \end{array}\right]P_m^{(i)}(\cos\theta) \tag{54}$$

$$\begin{aligned} \sigma_{rr}^{(i)} &= 2G^{(i)}K^{(i)}\left\{\frac{2}{3}f^{(i)} + \sum_{m=0}^{\infty}\left[\frac{m^2-m-4}{2(2m+3)}a_m^{(i)}r^m - \frac{m^2+3m-2}{2(2m-1)}b_m^{(i)}r^{-m-1}\right]P_m^{(i)}(\cos\theta)\right\} \\ &\quad + 2G^{(i)}\sum_{m=0}^{\infty}\left[\begin{array}{l} m(m-1)c_{1,m}^{(i)}r^{m-2} - (m+1)(m+2)c_{2,m}^{(i)}r^{-m-3} \\ +(m+1)(m^2-m-2+2\nu^{(i)})d_{1,m}^{(i)}r^m + m(m^2+3m-2\nu^{(i)})d_{2,m}^{(i)}r^{-m-1} \end{array}\right]P_m^{(i)}(\cos\theta) \end{aligned} \tag{55}$$

$$\sigma_{\theta\theta}^{(i)} = 2G^{(i)}K^{(i)}\left\{\frac{2}{3}f^{(i)} + \sum_{m=0}^{\infty}\left[\begin{array}{l}\dfrac{1}{2(2m+3)}a_m^{(i)}r^m \\ \times\left\{(m+1)\dfrac{\mu}{1-\mu^2}\left[\mu P_m^{(i)}(\mu) - P_{m+1}^{(i)}(\mu)\right] - (m+1)^2 P_m^{(i)}(\mu)\right\} \\ +\dfrac{1}{2(2m-1)}b_m^{(i)}r^{-m-1} \\ \times\left\{-(m+1)\dfrac{\mu}{1-\mu^2}\left[\mu P_m^{(i)}(\mu) - P_{m+1}^{(i)}(\mu)\right] + (m-1)^2 P_m^{(i)}(\mu)\right\}\end{array}\right]\right\}$$
$$- 2G^{(i)}\sum_{m=0}^{\infty}\left[\begin{array}{l}m^2c_{1,m}^{(i)}r^{m-2} + (m+1)^2c_{2,m}^{(i)}r^{-m-3} + (m+1)(m^2+4m+2+2\nu^{(i)})d_{1,m}^{(i)}r^m \\ +m(m^2-2m-1+2\nu^{(i)})d_{2,m}^{(i)}r^{-m-1}\end{array}\right]P_m^{(i)}(\cos\theta)$$
$$+ 2G^{(i)}\sum_{m=1}^{\infty}\left[\begin{array}{l}c_{1,m}^{(i)}r^{m-2} + c_{2,m}^{(i)}r^{-m-3} + (m+5-4\nu^{(i)})d_{1,m}^{(i)}r^m \\ +(m-4+4\nu^{(i)})d_{2,m}^{(i)}r^{-m-1}\end{array}\right](m+1)\frac{\mu}{1-\mu^2}\left[\mu P_m^{(i)}(\mu) - P_{m+1}^{(i)}(\mu)\right] \tag{56}$$

$$\sigma_{\phi\phi}^{(i)} = 2G^{(i)}K^{(i)}\left\{\frac{2}{3}f^{(i)} + \sum_{m=0}^{\infty}\left[\begin{array}{l}\dfrac{1}{2(2m+3)}a_m^{(i)}r^m \\ \times\left\{-(m+1)\dfrac{\mu}{1-\mu^2}\left[\mu P_m^{(i)}(\mu) - P_{m+1}^{(i)}(\mu)\right] - (3m+4)P_m^{(i)}(\mu)\right\} \\ +\dfrac{1}{2(2m-1)}b_m^{(i)}r^{-m-1} \\ \times\left\{(m+1)\dfrac{\mu}{1-\mu^2}\left[\mu P_m^{(i)}(\mu) - P_{m+1}^{(i)}(\mu)\right] - (3m-1)P_m^{(i)}(\mu)\right\}\end{array}\right]\right\}$$
$$+ 2G^{(i)}\sum_{m=0}^{\infty}\left[\begin{array}{l}mc_{1,m}^{(i)}r^{m-2} - (m+1)c_{2,m}^{(i)}r^{-m-3} + (m+1)\left[m-2-2\nu^{(i)}(2m+1)\right]d_{1,m}^{(i)}r^m \\ -m\left[m+3-2\nu^{(i)}(2m+1)\right]d_{2,m}^{(i)}r^{-m-1}\end{array}\right]P_m^{(i)}(\cos\theta)$$
$$- 2G^{(i)}\sum_{m=1}^{\infty}\left[\begin{array}{l}c_{1,m}^{(i)}r^{m-2} + c_{2,m}^{(i)}r^{-m-3} + (m+5-4\nu^{(i)})d_{1,m}^{(i)}r^m \\ +(m-4+4\nu^{(i)})d_{2,m}^{(i)}r^{-m-1}\end{array}\right](m+1)\frac{\mu}{1-\mu^2}\left[\mu P_m^{(i)}(\mu) - P_{m+1}^{(i)}(\mu)\right] \tag{57}$$

$$\sigma_{r\theta}^{(i)} = -2G^{(i)}K^{(i)}\left(1-\mu^2\right)^{1/2}\sum_{m=1}^{\infty}\left[\frac{m+1}{2(2m+3)}a_m^{(i)}r^m + \frac{m}{2(2m-1)}b_m^{(i)}r^{-m-1}\right]\times\frac{m+1}{1-\mu^2}\left[\mu P_m^{(i)}(\mu) - P_{m+1}^{(i)}(\mu)\right]$$
$$- 2G^{(i)}\left(1-\mu^2\right)^{1/2}\sum_{m=1}^{\infty}\left[\begin{array}{l}(m-1)c_{1,m}^{(i)}r^{m-2} - (m+2)c_{2,m}^{(i)}r^{-m-3} \\ +(m^2+2m-1+2\nu^{(i)})d_{1,m}^{(i)}r^m - (m^2-2+2\nu^{(i)})d_{2,m}^{(i)}r^{-m-1}\end{array}\right] \tag{58}$$
$$\times\frac{m+1}{1-\mu^2}\left[\mu P_m^{(i)}(\mu) - P_{m+1}^{(i)}(\mu)\right]$$

unknown constants are determined by using boundary and interface conditions $\sigma_{rr}^{(i)} = 0$ and $\sigma_{r\theta}^{(i)} = 0$ at $r = r_0$ and $r = r_n$.

Assuming the interface conditions as $i = 1, 2, 3, \ldots n-1$.

$$\sigma_{rr}^{(i)}(r_i) = \sigma_{rr}^{(i+1)}(r_i)$$
$$\sigma_{r\theta}^{(i)}(r_i) = \sigma_{r\theta}^{(i+1)}(r_i)$$
$$\sigma_{\theta\theta}^{(i)}(r_i) = \sigma_{\theta\theta}^{(i+1)}(r_i)$$

8 Conclusion

In this paper, the exact analytical solutions are presented for displacement and thermal stresses with two-dimensional steady-state temperature distribution in the multilayer hollow sphere. The temperature distribution is obtained by solving the heat conduction equation by separation of variable method and using the condition of continuity at the interface to get required eigenvalues in the solution. Each layer of the spherical sphere is considered as isotropic and homogeneous. The components of displacement and thermal stress function has been discussed with the help of Goodier's displacement potential and Boussinesq harmonic functions as Noda et al. [16]. On determining temperature distribution function from the heat conduction equation, it is used as a known function. Furthermore, we have investigated the results on the basis of assumed boundary conditions and approach was purely mathematical. Obtained results are considered to be useful in the design of the smart multilayer spherical vessels. Also, results may be used in industrial furnace, nuclear reactors, chemical industry, turbines, spacecraft where multilayer materials are highly used.

References

1. Carslaw HS, Jaeger JC (1959) Conduction of heat conduction in solids, 2nd edn. Oxford University Press, London
2. Goodman TR (1961) The adjoin heat conduction problems for solids, ASTIA-AD, pp 254–769 (AFOSR-520)
3. Tittle CW (1965) Boundary value problems in composite medium: quasi orthogonal functions. J Appl Phys 36(4), 1486–1488
4. Bulavin PE, Kashcheev VM (1965) Solution of nonhomogeneous heat conduction equation for multilayer bodies. Int Chem Eng 5(1):112–115
5. Volbrecht H (1974) Stress in cylindrical and spherical walls subjected to internal pressure and stationary heat flow. Verfahrenstechnik 8:109–112
6. Kandil A (1975) Investigation of stress analysis under high pressure and temperature. M.S. Thesis, C.I.T. Helwan University, Egypt
7. Ghosn AH, Sabbaghian M (1982) Quasi-static coupled problem of thermoelasticity for cylindrical region. Therm Stress 5:299–313
8. Sherief HH, Anwar MN (1988) A problem in generalized thermoelasticity for an infinitely many annular cylinders. Int J Eng Sci 26:301–306
9. Chen CK, Yang YC (1986) Thermoelastic transient response of an infinitely long annular cylinder composed of two different materials. J Eng Sci 24:569–581
10. Jane KC, Lee ZY (1999) Thermoelastic transient response of an infinitely long multilayered cylinder. Mech Res Comm 26(6):709–718
11. Lee ZY (2004) Coupled problem of thermoelasticity for multilayered spheres with time dependent boundary conditions. J Mar Sci Technol 12(2):93–101
12. Pawar SP, Kedar GD, Deshmukh KC (2013) Effect of internal heat generation and temperature asymmetry in a hollow sphere and its thermal stresses. Int J Thermoelast 1(3), 1–5
13. Pawar SP, Wange N, Gaikwad MN (2018) Thermoelastic response to surface temperature asymmetry and internal heat generation parameters in a composite spherical body. Int J Math Arch 9(3), 1–10 (2018)
14. Ozisik MN (1968) Boundary value problems of heat conduction. International Textbook Co., Scranton, PA

15. Noda N, Hetnarski RB, Tanigawa Y (2003) Thermal stresses, 2nd edn. Taylor and Francis, New York
16. Noda N, Hetnarski RB, Tanigawa Y (2003) Thermal stresses, vol 2. Taylor and Francis, New York
17. Gaikwad MN, Wange NJ (2017) Analytical solution for three dimensional transient heat conduction in a multilayer sphere. Int J Math App (IJMAA) 5(2B):301–313

Investigation of Torsional Stability and Camber Test on a Meter Gauge Flat Wagon

Apurba Das and Gopal Agarwal

Abstract This paper presents the experimental study of the torsion test and camber test of a flat freight wagon. The freight wagon considered as open-type 40 ft. gauge flat wagon. The flat freight wagon comprises flat body structure and two bogies, where the flat surface used to transport containers, goods, wood logs, etc. HBM load cell of 50 T capacity is used to measure the force and deflection for experimental determination of the torsional and camber values. The test methodology and setup are established freight wagon testing. It is seen that the camber values are within the safe zone as per designed payload. The average torsional stiffness is 3.45×10^{10} KN mm^2/rad are seen considering the worst-case elevation with one side 20 mm and other three side elevations are zero.

Keywords Flat wagon · Torsional test · Camber test · Load cells · Deflection

1 Introduction

Flat wagon is considered as railway wagons having a flat, full-length, or deck (single or double decks for car transporters) with the superstructure. Various types of superstructures are provided depending on the type of goods to be carried. Other types of wagons like open wagons have side and end walls while the covered goods wagons have a fixed roof and sides. Flat wagons are primarily considered for the transportation of goods which are not affected by the weather. However, a special type of flat wagons can be covered completely by plastics or hoods to facilitate the transport of weather-affected products. The portion of the loading area of a flat wagon is fully open and easily accessible even for covered wagon after removing the cover. As per UIC flat wagons are generally divided into two segments. The first type is for ordinary goods wagons with category letters "*K*", "*O*", and "*R*" and the second type is for special goods wagons with category letters "*L*" and "*S*". The basic difference between these two types of the flat wagon is that the ordinary goods wagon always

A. Das (✉) · G. Agarwal
Mechanical Engineering Department, Jadavpur University, Kolkata 700032, India
e-mail: apurba.besu@gmail.com

D. Maity et al. (eds.), *Advances in Fluid Mechanics and Solid Mechanics*,
Lecture Notes in Mechanical Engineering,
https://doi.org/10.1007/978-981-15-0772-4_24

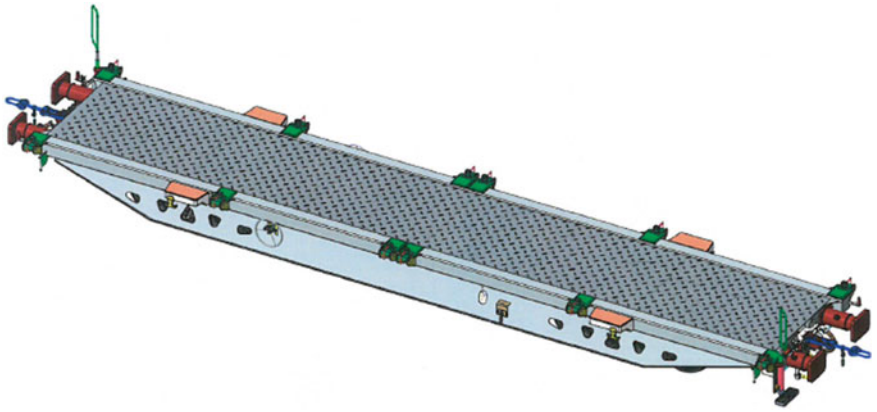

Fig. 1 Overview of the present 40-ft. container carrying flat wagon

consists of a flat deck which can be driven on, while the special goods wagon usually do not have a flat deck and these needs to be designed based on the special product to be carried on it. There are several variants with separate axles as well as bogie wagons [1] are available for both types of flat wagon. Flat wagons are the major stockholder in the goods wagon family. A typical statistics shown by the German carrier- DB in 1998 that flat wagons comprise 40% of the total goods carrying wagon [2] confirms this claim. The present container/goods carrying flat wagon (Fig. 1) can carry one 40 ft. standard container (12.2 m) or two 20 ft. (6.1 m) on top of another because considering the limited vertical clearance (maximum moving dimension) by respective railway authorities, even though they usually can carry the weight in two stacks. Apart from the conventional container some other typical goods can be transported using this flat wagon which include: vehicles, engines, large pipes, metal beams, wire coils, wire mesh, half-finished steel products, rails, sleepers and complete sections of railway track, gravel, sand, and other bulk goods with proper add-on attachment (hooks, side panels, etc.) to avoid the damage or loss of goods being transported. During the transportation of such a variety of products on the container carrying flat wagon, sometimes it is difficult to provide a uniform load on the wagon and sometimes the uneven distribution of the load becomes necessary while a combination of products or eccentrically loaded goods are being transported. Therefore, it is mandatory to prescribe the torsional limitation and the camber test data for uneven distribution of the load to avoid interference with bogie parts in dynamic loading condition for operational safety of the wagon [3, 4]. Camber is the vertical tilting of the flat portion of the floor of the flat wagon. When the flat portion tilts up direction at the middle and down direction at both ends the camber is considered as positive camber. On the other hand, when flat portion tilts in down direction at the middle and up direction at both ends, the camber is considered as negative camber. The sum of tilt is measured in degrees from the vertical position. Controlling the camber value is extremely necessary to restrict the influences the directional control and the

wheelset wear. High positive camber affects the outside of the wheel and it causes excessive premature wear on the suspension parts of the wagon. Whereas, high negative camber affects the inside of the wheel and it causes excessive premature wear on the suspension parts of the wheel. Camber of 1° or more will adversely affect the performance of the wagon [5]. In this present paper, the experimental torsional test, as well as camber test procedure, has been described and the experimental test data are captured in the data acquisition system. The outcomes of the test results are discussed, analyzed and mandatory recommendations are provided.

2 Wagon Specification and Experimental Setup

The container carrying meter gauge flat wagon is designed for carrying the maximum payload 54 ton and the tare weight (wagon weight in empty condition), hence the maximum gross load (wagon weight in fully loaded condition) is 68 ton. The material used for the wagon is S355J0 steels except for the top cover plate. The material used for the top cover plate is S355J0W, which is weather resistant steel as this top cover plate is exposed to rainwater. The other parametric data used for this wagon are tabulated in Table 1.

2.1 Experimental Setup for Torsion Test

The purpose of the torsional stiffness tests is to determine the framework of the trial program in accordance with the new freight wagon design policy as per EN 12663-2:2010 standard.

The flat wagon is placed on 4 load cell positioned as shown in Fig. 2. The HBM Data Acquisition System (MX840AQuntumX) is used to record the measured data [6]. The Force/displacement Sensor (Encardio Rite) of 50-ton capacity is used to measure the force and displacement values (Model No ELC-210A). The actual placement of the load cell and the data acquisition system under the wagon structure to capture the force and displacement are shown in Fig. 3. For torsion test, the wagon is

Table 1 Parametric specification of the present flat wagon

Overall length	13,140 mm
Bogie base	6940 mm
Height of buffering (buffers)	790 mm
Coupler height	780 mm
Estimated tare weight	14 tones
Maximum gross weight	68 tones
Bogie type	T17APB meter gauge bogie with 3.3 T weight

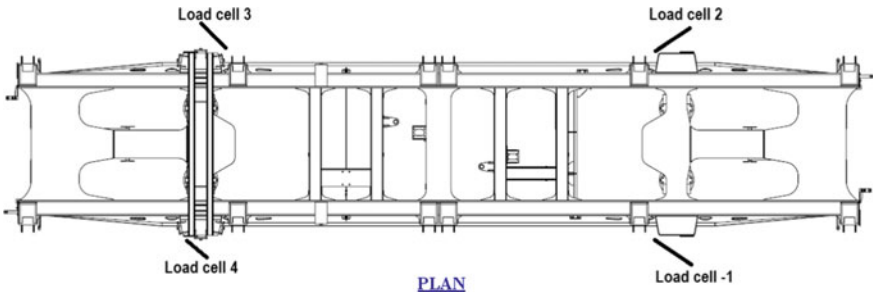

Fig. 2 Setup of load cell in the flat wagon

Fig. 3 Positioning of the load on the flat wagon with number 1–4

positioned under normal operating conditions in a lifting bench. The wagon without bogies is placed horizontally by its four lifting points (those at the pivot crossbars). The force sensor is placed under each of these points (shown in Fig. 3). Each of the support points are also provided with a vertical displacement sensor. For the first condition of the torsion test, one of the support points is then lifted and lowered with the help of hydraulic pressure jack. The four forces and displacement are measured and recorded. This similar operation is then carried out for each of the four support points (Table 2).

2.2 Experimental Setup for Camber Test

The purpose of the present camber tests is to determine the deflection of the solebar of the wagon in the loaded and unloaded condition in accordance to the new freight wagon design policy as per EN 12663-2:2010 standard. The solebar camber test value needs to be restricted within the 0.3% length of the bogie base (distance between two bogie centers). The wagon with bogie is placed on a flat railway shop ensuring

Table 2 Experimental results of the torsion test conducted

(Elevation)	(0 mm)	+5 mm	+10 mm	+15 mm	+20 mm	+15 mm	+10 mm	+5 mm	0 mm
Test 1: *Elevation variation on the load cell 1 data in ton*									
Load cell 1	2.487	2.967	3.367	3.77	4.192	3.779	3.368	2.937	2.482
Load cell 2	1.633	1.155	0.755	0.352	0	0.34	0.754	1.183	1.637
Load cell 3	1.688	2.16	2.553	2.95	3.373	2.962	2.555	2.132	1.685
Load cell 4	1.72	1.254	0.862	0.468	0	0.457	0.861	1.284	1.73
Sum=	7.528	7.536	7.537	7.54	7.565	7.538	7.538	7.536	7.534
Test 2: *Elevation variation on the load cell 2 data in ton*									
Load cell 1	2.484	2.039	1.625	1.282	1.28	1.2	1.645		2.1
Load cell 2	1.623	2.067	2.481	2.8	2.8	2.8	2.459	2.005	1.58
Load cell 3	1.694	1.259	0.8539	0.54	0.53	0.53	0.873	1.315	1.733
Load cell 4	1.721	2.155	2.564	2.891	2.89	2.89	2.546	2.097	1.678
Sum=	7.522	7.52	7.5239	7.513	7.5	7.42	7.523	7.517	7.518
Test 3: *Elevation variation on the load cell 3 data in ton*									
Load cell 1	2.485	2.929	3.35	3.8	4.181	3.79	3.348		2.915
Load cell 2	1.55	1.122	0.7	0.245	0	0.25	0.7	1.133	1.55
Load cell 3	1.747	2.182	2.599	3.05	3.428	3.04	2.597	2.169	1.747
Load cell 4	1.698	1.256	0.835	0.387	0	0.4	0.85	1.275	1.698
Sum=	7.48	7.489	7.484	7.482	7.609	7.48	7.495	7.492	7.48

(continued)

Table 2 (continued)

(Elevation)	(0 mm)	+5 mm	+10 mm	+15 mm	+20 mm	+15 mm	+10 mm	+5 mm	0 mm
Test 4: *Elevation variation on the load cell 4 data in ton*									
Load cell 1	2.488	2.078	1.668	1.267	1.25	1.256	1.68		2.091
Load cell 2	1.558	1.965	2.378	2.778	2.79	2.79	2.365	1.954	1.539
Load cell 3	1.75	1.347	0.943	0.554	0.541	0.542	0.955	1.355	1.766
Load cell 4	1.695	2.006	2.5	2.888	2.9	2.914	2.495	2.08	1.675
Sum=	7.491	7.396	7.489	7.487	7.481	7.502	7.495	7.48	7.488

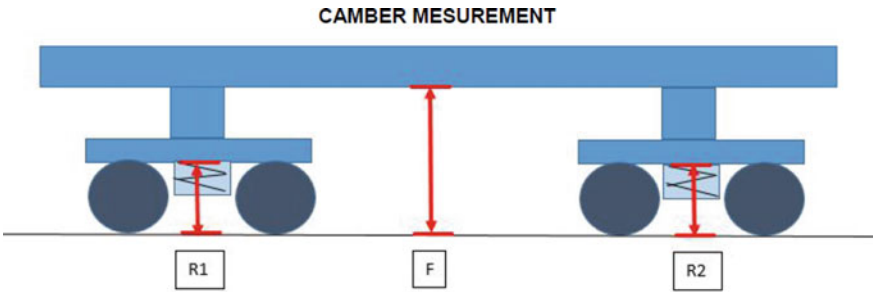

Fig. 4 Experimental setup for the camber test

the perfect horizontal condition with the help of spirit level. The distance from the left axle to the ground level ($R1$) and the distance from the right axle to the ground level ($R2$) as well as the distance of the wagon base from the ground level (F) at mid-position are measured and recorded both for empty (payload = 0) and loaded condition (payload = 58 ton) (Fig. 4).

3 Results and Discussion

3.1 Torsional Test Results

The torsional stiffness (Ct*) can be measured using the Eq. 1

$$\mathrm{Ct}^* = 2a.(2b_z)^2 \Delta F / h \tag{1}$$

where Ct* is the torsional stiffness in (KN mm^2/rad), $2a$ is the longitudinal distance between the measuring points in mm, corresponding approximately to the wheel-base, $2b_z$ = lateral distance of the axle suspensions mounted, ΔF = vertical force variation, h = displacement height, $\Delta F'/h'$: vertical stiffness at fulcrum in kN/mm. It corresponds to the slope of the linear part of the force curve as a function of the displacement. The forces are measured by a dynamometric chain. The sensor is conditioned by an acquisition unit. Filtering (with low-pass filter) and scanning are included in this package. It makes it possible to measure $\Delta F'$. The vertical displacement of the fulcrum is measured by a displacement measuring chain. The sensor is conditioned by the acquisition unit. Filtering (with low-pass filter) and scanning are included in this package. For the tests, the force and displacement measurements are synchronized. It makes it possible to measure h'. The initial value of load cell 1, 2, 3, and 4 after calibrating the wagon in perfect horizontal position are noted as 2.487 T, 1.633 T, 1.688 T, and 1.72 T, respectively. The torsional stiffness (Ct*) values for this specific wagon are calculated as presented in Table 3 (Fig. 5).

Table 3 Determination of average torsional stiffness (Ct*) in KN mm^2/rad from the torsion test

	Test 1	Test 2	Test 3	Test 4
$\Delta F'/h'$ in kN/mm	816.66	828	830.66	882
Average $\Delta F'/h'$ (kN/mm)	839.331			
$2a^*$ (mm)	6740			
$2b_z$ (mm)	2500			
Ct*(KN mm^2/rad)	3.45×10^{10}			

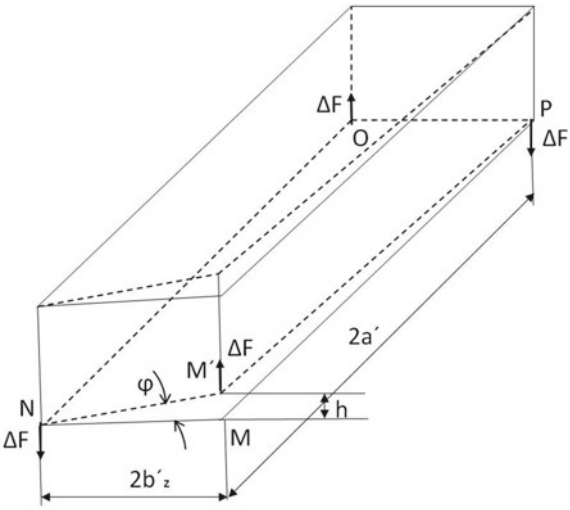

Fig. 5 Schematic diagram for torsional test parameter

4 Experimental Data and Calculation

(See Table 2).

4.1 Camber Test Results

This test consists to measure on the solebar the camber when the wagon is loaded and unloaded. After placing the wagon in the perfect horizontal condition, the camber value can be determined by Eq. 2.

$$\Delta F = (F0 - F1) - [(R10 - R11) + (R20 - R21)]/2 \tag{2}$$

where $R10$ and $R11$ is the distance from the left axle to the ground level in empty and loaded condition, respectively. $R20$ and $R21$ is the distance from the right axle to the ground level in empty and loaded condition, respectively. While $F0$ and $F1$ is

Table 4 Results and calculation of the Camber test data from the experiment

Left sensors (1,4)		Right sensors (2,3)	
Empty condition	Load condition	Empty condition	Load condition
F: 743 mm	$F1$: 689 mm	F: 766 mm	$F1$: 727 mm
$R1$: 854 mm	$R11$: 809 mm	$R1$: 882 mm	$R11$: 838 m
$R2$: 863 mm	$R21$: 819 mm	$R2$: 868 mm	$R21$: 836 mm
$\Delta F = 9.5$ mm		$\Delta F = 0$ mm	
Average $\Delta F = (9.5 + 0)/2 = 4.5$ mm			

The average camber value should be within 0.3% length of the bogie base (0.3% of 6940 mm = 21 mm) and for this case, it is within the limit

the distance of the wagon base from the ground level in empty and loaded condition, respectively (Table 4).

5 Conclusions

During this experimental setup and experimental process, a suitable methodology is established to determine the torsional stiffness and camber value of wagon due to unbalanced load or uneven fluctuations of load due to railway track or cant deficiencies. The following conclusions can be listed down from the present analysis.

(a) A general methodology for testing the torsional stiffness and camber value is established. This methodology can be used for other types of wagons such as hoper or tank wagons.
(b) This will act as a general guideline for the wagon manufacture to prescribe the worst-case camber and torsional stiffness data for the safe operation of the wagon avoiding the derailment phenomenon.
(c) This will help the designer to take care the interference due to camber and torsional instability due to unbalanced load distribution by the operating railways.
(d) The average torsional stiffness is 3.45×10^{10} KN mm^2/rad that is seen considering the worst-case elevation.
(e) For the present case, the torsional stiffness and camber are within the range for safe operation. The individual torsional stiffness for the case to case variation can be drawn from the table by interpolating the elevation data.

Acknowledgements The authors acknowledge the Titagarh Wagons Ltd (Hind Motor Division-Kolkata, India) and Titagarh Wagons AFR-Douai, France office for providing the testing facility and design data.

References

1. Commission Decision of 11 August 2006 Concerning the Technical Specification of Interoperability Relating to the Subsystem 'Traffic Operation and Management' of the Trans-European Conventional Rail System (Notified Under Document Number C (2006) 3593)
2. Bundesbahn Deutsche (1960) Güterwagen, Großbehälter. Straßenroller. Werbe- And AuskunftsamtFür den Personen- And Güterverkehr, Frankfurt (Main)
3. Santarremigia FE, Molero GD, Poveda-Reyes S, Aguilar-Herrando J (2018) Railway safety by designing the layout of inland terminals with dangerous goods connected with the rail transport system. Safety Science
4. Zhang Z, Dhanasekar M (2009) Dynamics of railway wagons subjected to braking/traction torque. Vehicle Syst Dyn 47(3):285–307
5. Kavitha C, Shankar SA, Karthika K, Ashok B, Ashok SD (2018) Active camber and toe control strategy for the double wishbone suspension system. J King Saud Univ Eng Sci
6. Sharma M, Mansuri I, Raval T, Sharma AL, Pradhan S (2016) Overview of data acquisition system for SST-1 diagnostics. Fusion Eng Des 15(112):872–876

Nonlinear Dynamic Buckling and Failure Study of Laminated Composite Plates Subjected to Axial Impulse Loads

Vasanth Keshav, S. N. Patel and Rajesh Kumar

Abstract In this paper, the nonlinear dynamic buckling of laminated composite plate is studied along with the failure of the plates. The balanced and symmetric cross-ply laminated composite plates are subjected to in-plane impulse compressive loads. The dynamic buckling load is calculated using Volmir's criterion. The nonlinear dynamic equations are solved using the finite element method. Imperfections are incorporated in the plate in order to simulate the actual behavior. The effect of imperfection, loading function, and duration of loading is studied. The first ply failure load for the plate is calculated to check the precedence of dynamic buckling and first ply failure. It is observed that the first ply failure for balanced and symmetric cross-ply laminated composite plates occurs after the plate has buckled due to dynamic impulse loads.

Keywords Dynamic buckling · Impulsive loads · In-plane loading · Laminated composite plates

1 Introduction

Laminated composite structures are being used for quite some time. Recently these structures are being used in civil engineering structures as well. Analyzing a large structure is time consuming, costly and in some cases, the desired output does not come. So, a part of the structure is taken up for analysis. Laminated composite plates are a part of a complex structure which, during its design life could be subjected to accidental loads as well. These loads could be suddenly applied due to various scenarios such as impact, fires, freezing, etc. When a laminated composite plate

V. Keshav · S. N. Patel (✉) · R. Kumar
Department of Civil Engineering, BITS Pilani, Pilani Campus, Pilani 333031, Rajasthan, India
e-mail: shuvendu@pilani.bits-pilani.ac.in

V. Keshav
e-mail: keshav.vasanth@gmail.com

R. Kumar
e-mail: rajesh.kr@pilani.bits-pilani.ac.in

D. Maity et al. (eds.), *Advances in Fluid Mechanics and Solid Mechanics*,
Lecture Notes in Mechanical Engineering,
https://doi.org/10.1007/978-981-15-0772-4_25

is subjected to such loads, it may not collapse, but can become unstable thereby affecting its neighboring components.

A lot of research has been carried out in the field of parametric instability, in which, the nature of the loads is vibrational. Prabhakara and Datta [1] studied the instability of plate with cutout subjected to tensile and compressive axial loads using finite element method. Chattopadhyay and Radu [2] studied the parametric instability of composite plates considering both rotary inertia and transverse shear. Sahu and Datta [3] studied the parametric instability of isotropic and laminated composite plates subjected to patch and point loads using finite element method. Pellicano [4] studied the parametric instability of imperfect cylinders using the analytical method. Chen et al. [5] studied the instability of composite plates subjected to biaxial and bending stress using first-order shear deformation theory. Dey and Ramachandra [6] studied the parametric instability of curved panels subjected to partial edge loading.

A few studies have been taken up in the area of dynamic buckling in which, the nature of loads is impulsive. Ari-Gur and Simonetta [7] studied the dynamic buckling of composite plates subjected to axial loads and reported that dynamic buckling loads can be lower than static buckling loads if the applied pulse frequency is near to the fundamental frequency of the plate. Petry and Fahlbusch [8] studied the dynamic buckling of isotropic thin plates subjected to in-plane loading and reported the effects of various parameters like aspect ratio, thickness, and imperfection. Kubiak [9] proposed a new criterion for calculating dynamic buckling load which takes into account components of inertia forces. Kowal-Michalska and Mania [10] calculated the dynamic buckling load of isotropic and orthotropic plates. Yang and Wang [11] calculated the dynamic buckling load of the isotropic plate with elastically restrained edges using Budiansky–Hutchinson criterion.

In the current study, the nonlinear dynamic load of the laminated composite plate is calculated using Volmir's criterion. According to Volmir's criterion, if the maximum dynamic displacement due to any loading function, loading duration, and loading amplitude, becomes equal to this thickness of the plate, then that load is considered as the dynamic buckling load. The effect of various parameters like loading function, imperfection, and loading duration is studied. The first ply failure of the plate is calculated to check whether the first ply failure is occurring before the plate is buckled due to dynamic impulse load. The study is carried out using the finite element method using ABAQUS/Explicit. Failure analysis can also be performed in the software by taking into account the reduction in stiffness due to ply failure. However, the current study focusses on dynamic buckling and hence regeneration of the stiffness matrix is not considered. The current study is numerical, some experiments are required for understanding the behavior in depth.

2 Theory and Formulation

The equation solved, and the theory is discussed in this section. In the current study, the nonlinear dynamic equation solved is given in Eq. 1. Where, $[M]$ is the mass matrix, $[K]$ the stiffness matrix, which is a function of deformations due to geometric

nonlinearity, $\{u\}$ the nodal displacement vector, $\{\dot{u}\}$ the nodal velocity vector and $\{\ddot{u}\}$ the nodal acceleration vector. $\{F(t)\}$ denotes the load vector. In the current study, the effect of damping is not considered.

$$[M]\{\ddot{u}\} + [C]\{\dot{u}\} + [K(\{u\})]\{u\} = \{F(t)\} \tag{1}$$

The Eq. 1 is solved in Finite element method using ABAQUS/Explicit. In ABAQUS/Explicit, thin shells (thickness <1/15 of characteristic length), are modeled using Kirchhoff shell theory. The panel is modeled using a general-purpose shell element S4R.

In ABAQUS/Explicit, the available failure criteria are Azzi-Tsai-Hill criterion, Maximum stress criterion, Maximum strain criterion, Tsai-Hill criterion, and Tsai-Wu criterion. Among these, Tsai-Hill criterion (Eq. 2) is considered, the equations of which are given in Sect. 22.2.3 of ABAQUS 6.13 user guide. In Eq. (2), σ_{11} is the stress in a normal direction, σ_{22} is the stress in the transverse direction, σ_{12} is the shear stress. X_t and X_c are the tensile and compressive strengths, respectively, in the normal direction, Y_t and Y_c are the tensile and compressive strengths in transverse direction and S is the shear strength. In accordance with the Tsai-Hill criterion, if $\sigma_{11} > 0$, $X = X_t$; otherwise, $X = X_c$. If $\sigma_{22} > 0$, $Y = Y_t$; otherwise, $Y = Y_c$.

$$FI = \frac{\sigma_{11}^2}{X^2} - \frac{\sigma_{11}\sigma_{22}}{X^2} + \frac{\sigma_{22}^2}{Y^2} + \frac{\sigma_{12}^2}{S^2} < 1 \tag{2}$$

The dynamic buckling criterion used is Volmir's criterion. The loss of stability for plate happens when the maximum deflection reaches a pre-set target displacement value [12]. This target transverse displacement value is set as the thickness of the plate for the current study.

3 Results

In this section, first the results of the convergence and validation study are presented and then the results of dynamic buckling study are discussed.

3.1 Convergence and Validation Study

3.1.1 Convergence and Validation Study of Static Buckling Load

In this section, the results of convergence and validation study are presented. A simply supported plate with material properties The materials properties presented by Narita and Leissa [13] are used. $E_1 = 138$GPa, $E_2 = 8.96$ GPa, $G_{12} = 7.1$ GPa, $\nu_{12} = 0.3$. These material properties correspond to Graphite/Epoxy plates. The geometric

properties considered are $a/b = 1$ and $a/h = 100$, where h corresponds to the thickness of the plate. The layup sequence is (45°/−45°/45°/−45°/45°) The geometry of the plate considered is shown in Fig. 1 and the boundary condition are shown in Fig. 2. The nondimensional static buckling loads are calculated for different mesh sizes and the converged mesh size is taken for the rest of the analysis. Equation 3 shows the nondimensional static buckling load. Figure 3 shows the nondimensional static buckling load versus mesh sizes and Table 1 shows the results of the current study compared with the results reported by Narita and Leissa [13].

$$\bar{P}_x = \frac{P_x a^2}{D_0} \tag{3}$$

where $D_0 = \frac{E_1 h^3}{12(1-\nu_{21}\nu_{12})}$

And, $\nu_{21} = \left(\frac{E_2}{E_1}\right)\nu_{12}$

Fig. 1 Geometry of the plate

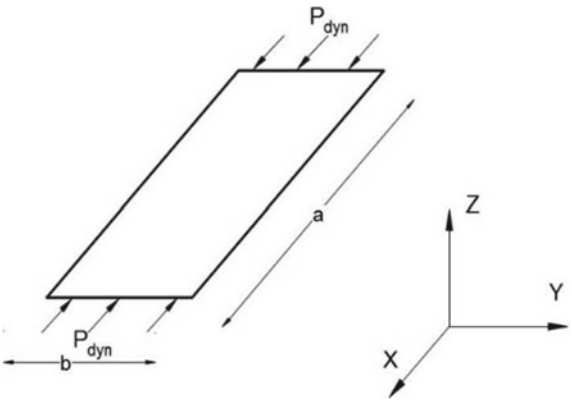

Fig. 2 Boundary conditions

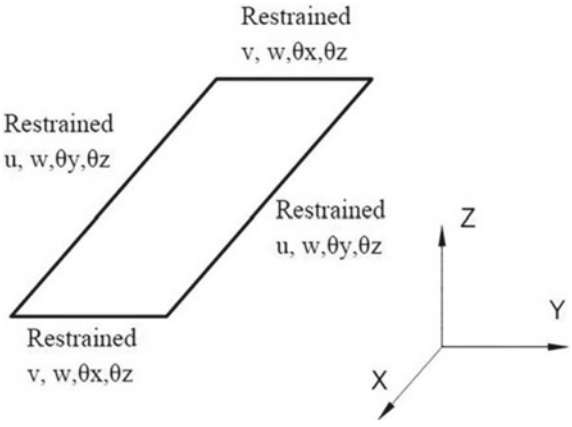

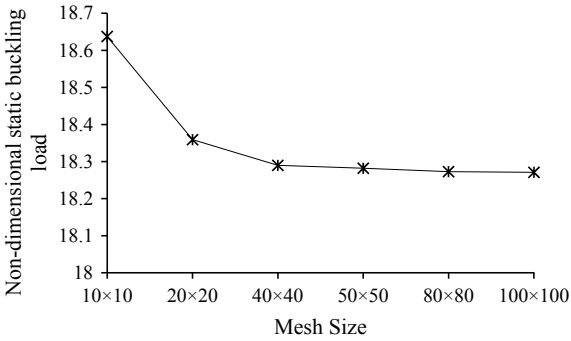

Fig. 3 Nondimensional static buckling load versus mesh sizes for the laminated composite plate with $a/b = 1$, $a/h = 100$, layup sequence (45°/−45°/45/°−45°/45°)

Table 1 Nondimensional static buckling load for laminated composited plate with layup sequence (45°/−45°/45°/−45°/45°)

Analysis	Nondimensional static buckling load
Present	18.282
Narita and Leissa [13]	18.66

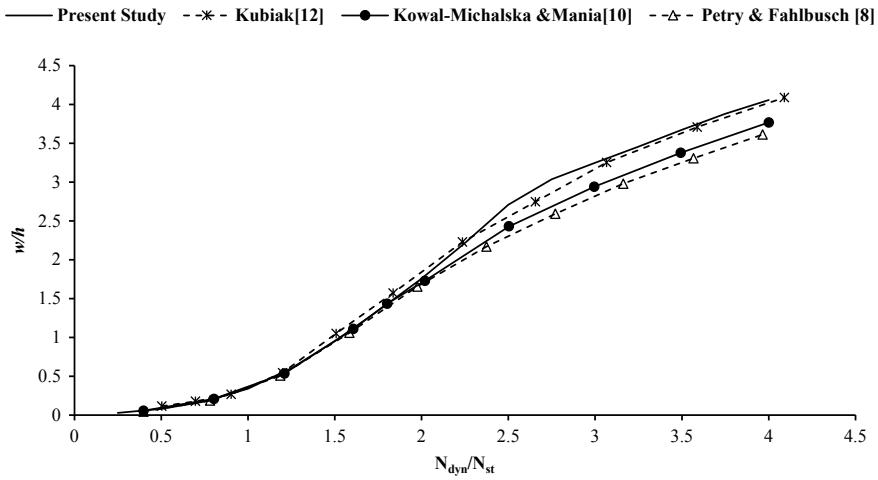

Fig. 4 w/*h* versus N_{dyn}/N_{st} for isotropic plate subjected to sinusoidal pulse load

From Fig. 3, it is seen that the results for mesh size 50 × 50 is converged and the same mesh size is used for the rest of the study. From Table 1, it is seen that the result of the present study match with the result of Narita and Leissa [13].

3.1.2 Validation of Dynamic Buckling Load for Isotropic Plate

In this section, the calculation of dynamic buckling load for an isotropic plate is validated using the result from the existing literature. An aluminum plate with geometric and material properties: $a/b = 1$, $h = 0.005$, imperfection $= 0.05\ h$; $E = 70$ GPa, $\nu = 0.3$, and $\rho = 2950$ kg/m^3. The imperfection is 5% of the plate thickness and the shape is the first buckling mode of the plate. Simply supported boundary conditions are used for the plate as shown in Fig. 2. The plate is loaded till its first natural period and the response is observed afterward also. The static buckling load of the plate is 43045 N/m and duration of loading is 0.043176 s. Sinusoidal loading function is shown in Fig. 5b is used. For various magnitudes of dynamic loads, the response is observed. Figure 4 shows the plot of w/h versus N_{dyn}/N_{st} for the current study compared with the analytical–numerical results of Kubiak [12], finite element results of Kowal-Michalska and Mania [10] and numerical results of Petry and Fahlbusch [8].

It is seen from Fig. 4 that the finite element results of the current study match with the analytical–numerical results of Kubiak [12].

3.2 *Dynamic Buckling Study of Balanced and Symmetric Cross-Ply Laminated Composite Plates*

In this section, the results of dynamic buckling study and effect of loading duration, loading function and imperfection is presented. The first ply failure load is also presented along with these studies. First, the static buckling load and the natural period of the plate is calculated using ABAQUS/Standard. Next imperfection is incorporated into the plate. The imperfection is a certain percentage of the thickness of the plate and the shape is the first buckling mode of the plate. The plate is loaded for a loading duration and the response is observed after the removal of the load as well. For various magnitudes of loads, the response of the plate is observed, and the dynamic buckling load is calculated. The material and geometric properties reported by Hinton et al. [14] are used. $a/b = 1$, $a/h = 100$; with $a = 0.1$ m. The

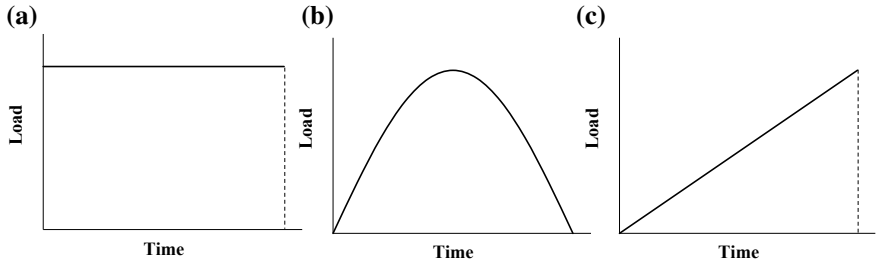

Fig. 5 **a** Rectangular loading function **b** Sinusoidal loading function **c** Triangular loading function

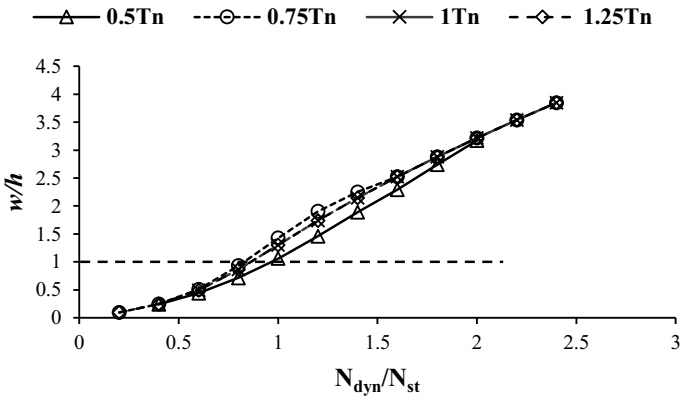

Fig. 6 w/h versus $N_{\text{dyn}}/N_{\text{st}}$ for composite plate with $a/b = 1$, $a/h = 100$ imperfection $= 0.2\ h$ subjected to rectangular loading function

material properties are $E_1 = 138\text{GPa}$, $E_2 = 11\text{GPa}$, $G_{12} = 5.5\text{GPa}$, $\nu_{12} = 0.28$, $X_T = 1500$ MPa, $X_C = 900$ MPa, $Y_T = 27$ MPa, $Y_C = 200$ MPa and $S_{12} = 80$ MPa. The layup sequence is (0°/90°/90°/0°). In the succeeding sections, the results of the effects of various parameters are presented.

3.2.1 Effect of Loading Duration

In this section, the effect of loading duration on dynamic buckling of the laminated composite plate is studied. The plate is loaded for T_b sec and the response is observed after the removal of load also. The natural frequency of the plate is calculated (T_n) and for various ratios of T_b/T_n the responses are observed. A laminated composite plate with material properties described above is subjected to rectangular pulse load (Fig. 5a). The static buckling load of the plate is 15951 N/m and the first natural period is 0.00284 s. Figure 6 shows the results of w/h versus $N_{\text{dyn}}/N_{\text{st}}$ for the laminated composite plate with $a/b = 1$, $a/h = 100$ imperfection $= 0.2\ h$.

From Fig. 6, it is seen that the converge after $T_b/T_n = 0.75$. Thus, the loading duration near the natural period of the plate is critical. It is also observed that the dynamic buckling load for all cases is lower than the static buckling load for the laminated composite plate with imperfection $0.2\ h$.

3.2.2 Effect of Loading Function

In this section, the effect of loading function on dynamic buckling load of a laminated composite plate is studied. Three types of loading functions are considered: rectangular (Fig. 5a), sinusoidal (Fig. 5b) and triangular (Fig. 5c). The laminated composite plate is loaded till its natural period. Figure 7 shows the plot of w/h versus

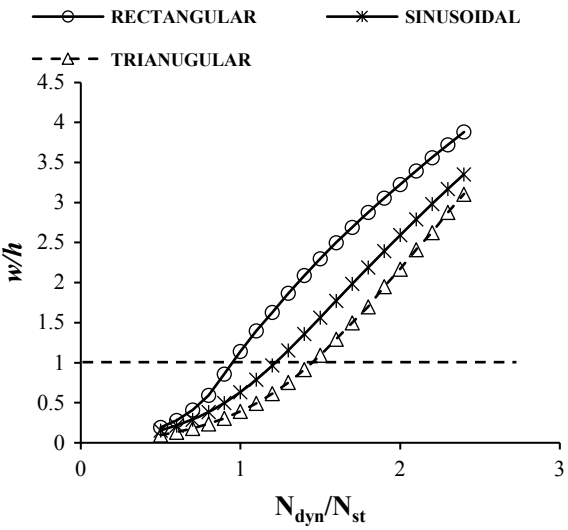

Fig. 7 w/h versus N_{dyn}/N_{st} for laminated composite plate with $a/b = 1$, imperfection $= 0.1\ h$, subjected to various loading functions

N_{dyn}/N_{st} for the laminated composite plate with $a/b = 1$, $a/h = 100$ imperfection $= 0.1\ h$. Figure 8 shows the plot of Failure index versus N_{dyn}/N_{st} for laminated composite plate with $a/b = 1$, $a/h = 100$ imperfection $= 0.1\ h$. The failure criterion used is Tsai-Hill criterion.

From Fig. 7, it is seen that the rectangular loading function is the most critical amongst the three since the area under the curve is the largest amongst the three loading functions considered. The dynamic buckling load for rectangular loading function is the only case where the dynamic buckling load is lower than the static

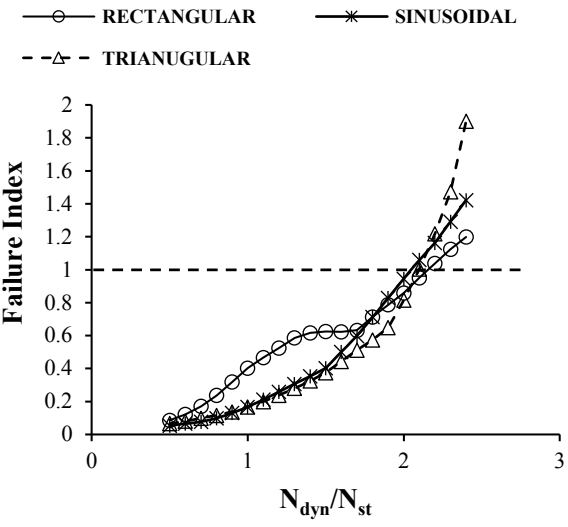

Fig. 8 Failure Index versus N_{dyn}/N_{st} for laminated composite plate with $a/b = 1$, imperfection $= 0.1\ h$, subjected to various loading functions

buckling load. It is observed from Fig. 8 that the first ply failure load for all the cases is higher than the dynamic buckling load. Hence, the first ply failure occurs after the laminated composite plate buckles due to dynamic pulse loads irrespective of the loading function used.

3.2.3 Effect of Imperfection

The effect of imperfection on dynamic buckling load is studied in this section. For all three types of loading functions, dynamic buckling load and first ply failure load are calculated. Four types of imperfection are considered: 0.05 h, 0.1 h, 0.15 h and 0.2 h which are percentages of the thickness of the plate and shape is the first buckling mode of the plate. The plate is loaded till its corresponding first natural period and the response is observed. Figures 9, 11 and 13 show the plot of w/h versus N_{dyn}/N_{st} for the laminated composite plate with $a/b = 1$, $a/h = 100$ for rectangular, sinusoidal and triangular loading functions, respectively. Figures 10, 12 and 14 show the plot

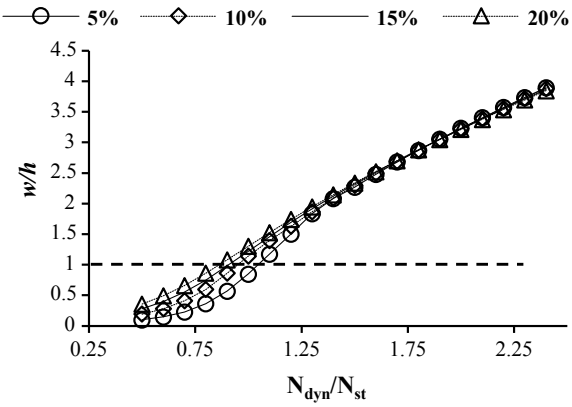

Fig. 9 w/h versus N_{dyn}/N_{st} for composite plate with $a/b = 1$, subjected to rectangular loading function for various percentages of imperfections

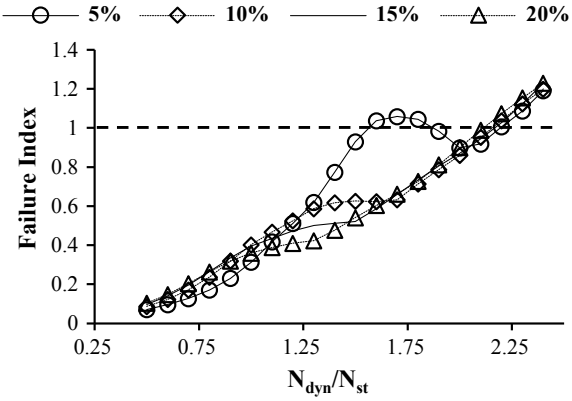

Fig. 10 Failure index versus N_{dyn}/N_{st} for composite plate with $a/b = 1$, subjected to rectangular loading function for various percentages of imperfections

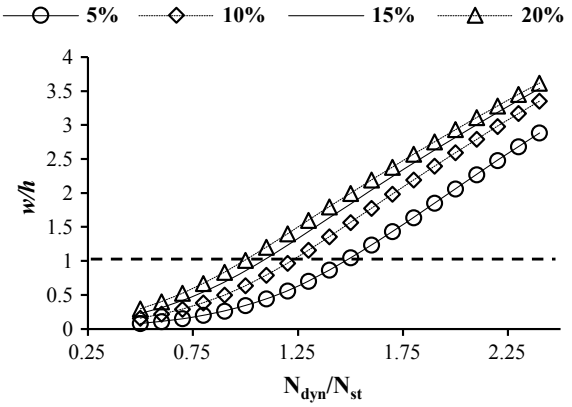

Fig. 11 w/h versus N_{dyn}/N_{st} for composite plate with $a/b = 1$, subjected to sinusoidal loading function for various percentages of imperfections

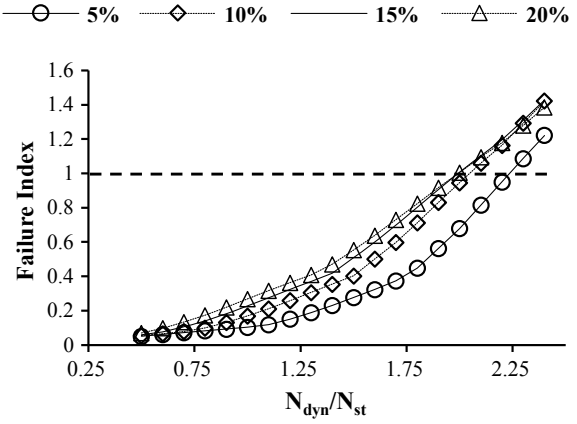

Fig. 12 Failure index versus N_{dyn}/N_{st} for composite plate with $a/b = 1$, subjected to sinusoidal loading function for various percentages of imperfections

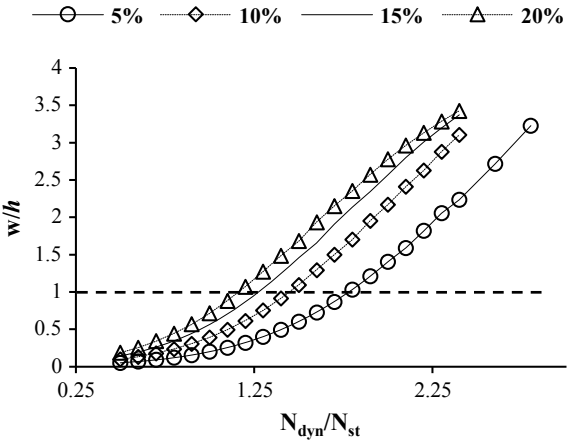

Fig. 13 w/h versus N_{dyn}/N_{st} for composite plate with $a/b = 1$, subjected to triangular loading function for various percentages of imperfections

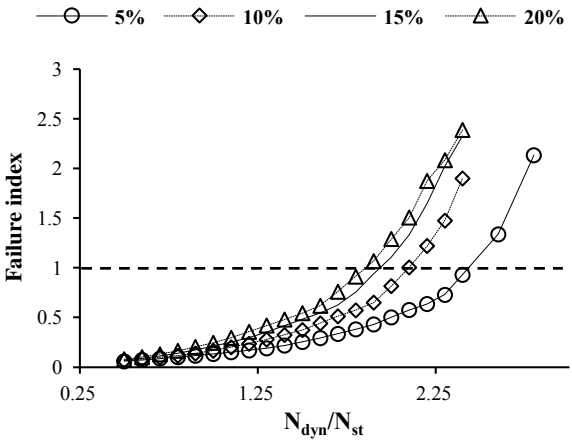

Fig. 14 Failure index versus N_{dyn}/N_{st} for composite plate with $a/b = 1$, subjected to triangular loading function for various percentages of imperfections

of Failure index versus N_{dyn}/N_{st} for laminated composite plate with $a/b = 1$, $a/h = 100$ for rectangular (Fig. 5a), sinusoidal (Fig. 5b) and triangular (Fig. 5c) loading functions, respectively, with respect to Tsai Hill criterion.

It is seen from the above figures that the dynamic buckling of a laminated composite plate occurs before the first ply failure load is reached. In the case of laminated composite plated subjected to rectangular loading function, the dynamic buckling load is lower than the static buckling load for imperfection values 0.1 *h*, 0.15 *h,* and 0.2 *h*. For sinusoidal loading function, the dynamic buckling load is equal to static buckling load for imperfection value 0.2 *h*. For all cases of loading functions and imperfection values, the first ply failure occurs at or beyond a ratio of $N_{dyn}/N_{st} = 2$. Figure 15 shows the deformed shape of the laminated composite plate with respect to maximum deflection, with maximum value occurring at the center of the plate, at a critical time when subjected to $N_{dyn}/N_{st} = 0.9$; the scale factor is 10. Figure 16 shows the deformed shape of the laminated composite plate with respect to failure index, with maximum value occurring at the center of the plate, at a critical time when subjected to $N_{dyn}/N_{st} = 0.9$; the scale factor is 10. Figure 17 shows the deformed shape of the laminated composite plate with respect to maximum deflection, with maximum value occurring at the center of the plate, at a critical time when subjected to $N_{dyn}/N_{st} = 2$; the scale factor is 5. Figure 18 shows the deformed shape of the laminated composite plate with respect to failure index, with maximum value occurring at the corners of the plate, at a critical time when subjected to $N_{dyn}/N_{st} = 2$; the scale factor is 5.

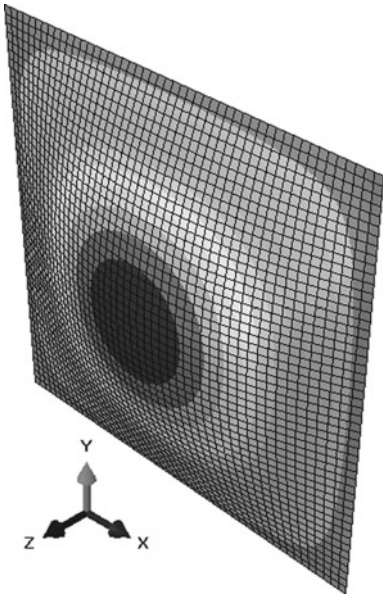

Fig. 15 Deformed composite plate showing maximum transverse deformation when subjected to rectangular loading with $N_{dyn}/N_{st} = 0.9$, at critical point of loading

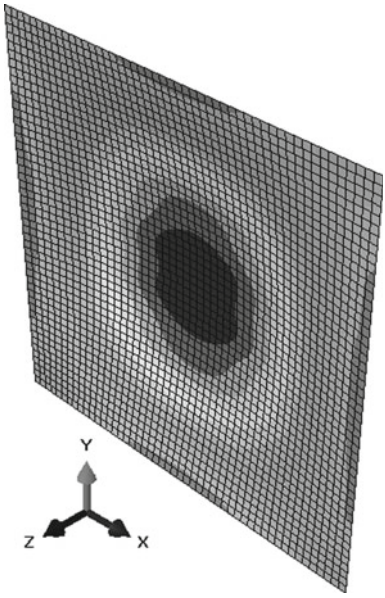

Fig. 16 Deformed plate showing failure index when subjected to rectangular loading with $N_{dyn}/N_{st} = 0.9$, at critical point of loading

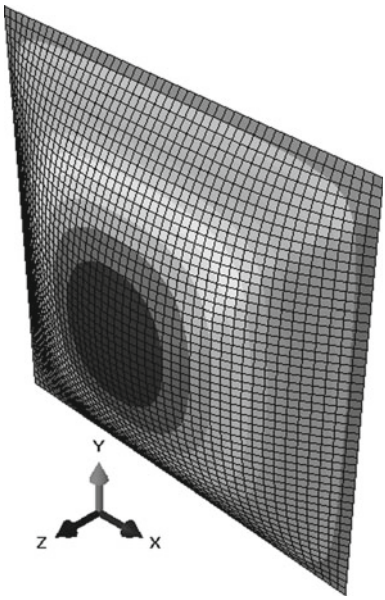

Fig. 17 Deformed composite plate showing maximum transverse deformation when subjected to rectangular loading with $N_{dyn}/N_{st} = 2$, at critical point of loading

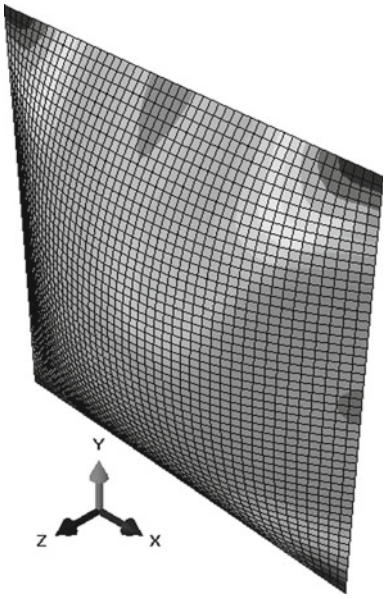

Fig. 18 Deformed plate showing failure index when subjected to rectangular loading with $N_{dyn}/N_{st} = 2$, at critical point of loading

4 Conclusions

From the current study, the following conclusions can be drawn for balanced and symmetric cross-ply laminated composite plates:

1. The dynamic buckling load for balanced and symmetric cross-ply laminated composite plates can be lower than static buckling load when subjected to impulsive compression of the rectangular loading function.
2. Among the three loading functions (rectangular, sinusoidal, and triangular), rectangular loading function is the most critical since the area under the curve is highest amongst the three.
3. Laminated composite plate, when subjected to axial impulsive loads, can lead to dynamic buckling when the loading duration is near to the first natural period of the plate.
4. Balanced and symmetric cross-ply laminated composite plate can withstand a dynamic pulse load for up to twice the static buckling load before the first ply failure occurs for the plate.

References

1. Prabhakara DL, Datta PK (1997) Vibration, buckling and parametric instability behaviour of plates with centrally located cutouts subjected to in-plane edge loading (tension or compression). Thin-Walled Struct 27(4):287–310. https://doi.org/10.1016/S0263-8231(96)00033-X
2. Chattopadhyay A, Radu AG (2000) Dynamic instability of composite laminates using a higher order theory. Comput Struct 77(5):453–460. https://doi.org/10.1016/S0045-7949(00)00005-5
3. Sahu SK, Datta PK (2000) Dynamic instability of laminated composite rectangular plates subjected to non-uniform harmonic in-plane edge loading. In: Proceedings of the institution of mechanical engineers, part G: journal of aerospace engineering. 214(5):295–312
4. Pellicano F (2009) Dynamic stability and sensitivity to geometric imperfections of strongly compressed circular cylindrical shells under dynamic axial loads. Commun Nonlinear Sci Numer Simul 14(8):3449–3462. https://doi.org/10.1016/j.cnsns.2009.01.018
5. Chen WR, Chen CS, Shyu JH (2013) Stability of parametric vibrations of laminated composite plates. Appl Math Comput 223:127–138. https://doi.org/10.1016/j.amc.2013.07.095
6. Dey T, Ramachandra LS (2014) Static and dynamic instability analysis of composite cylindrical shell panels subjected to partial edge loading. Int J Non-Linear Mech 64:46–56. https://doi.org/10.1016/j.ijnonlinmec.2014.03.014
7. Ari-Gur J, Simonetta SR (1997) Dynamic pulse buckling of rectangular composite plates. Compos B Eng 28(3):301–308. https://doi.org/10.1016/S1359-8368(96)00028-5
8. Petry D, Fahlbusch G (2000) Dynamic buckling of thin isotropic plates subjected to in-plane impact. Thin-Walled Struct 38(3):267–283. https://doi.org/10.1016/S0263-8231(00)00037-9
9. Kubiak T (2007) Criteria of dynamic buckling estimation of thin-walled structures. Thin-Walled Struct 45(10–11):888–892. https://doi.org/10.1016/j.tws.2007.08.039
10. Kowal-Michalska K, Mania RJ (2008) Some aspects of dynamic buckling of plates under in-plane pulse loading. Mech Mech Engineering 12(2):135–146
11. Yang B, Wang DY (2016) Dynamic buckling of stiffened plates with elastically restrained edges under in-plane impact loading. Thin-Walled Struct 107:427–442. https://doi.org/10.1016/j.tws.2016.06.019

12. Kubiak T (2013) Static and dynamic buckling of thin-walled plate structures, Springer, Switzerland. https://doi.org/10.1007/978-3-319-00654-3
13. Narita Y, Leissa AW (1990) Buckling studies for simply supported symmetrically laminated rectangular plates. Int J Mech Sci 32(11):909–924. https://doi.org/10.1016/0020-7403(90)90063-O
14. Hinton MJ, Kaddour AS, Soden PD (eds) (2004) Failure criteria in fibre reinforced polymer composites: the world-wide failure exercise. Elsevier. https://doi.org/10.1016/b978-0-080-44475-8.x5000-8

Adhesion Failure Analysis in Lap Shear Joint Specimen Subjected to Transverse Loading Made of Curved FGM

Pritam Kumar Kundu, Arun Kumar Pradhan and Mihir Kumar Pandit

Abstract Functionally Graded Materials (FGMs) are the variation of composition and structure over a volume which results in improvement of mechanical properties. Damage in adhesive-bonded FGM composite joints may generate in various forms like cohesive failure, adhesion failure, etc. This article deals with the loss of structural integrity of the Lap Shear Joint (LSJ) made with curved FGM adherends of Al_2O_3 and Nickel by quantifying adhesion failure propagation. This is performed by evaluation of the interfacial stresses and the three modes of Strain Energy Release Rate (SERR). The rate of propagation of the adhesion failure in the LSJ made with FGM panels subjected to transverse loading is evaluated by employing a three-dimensional nonlinear finite element analysis. The effect of overlap length on the LSJ made with curved adherends on the interfacial stresses and the three modes of SERR is computed. The use of FGM as adherend materials is found to be effective in reducing the peak values of interfacial stresses and the three modes of SERR.

Keywords Adhesive joints · FGM · Interfacial stress · Strain Energy Release Rates (SERR)

1 Introduction

Adhesive bonding techniques have been used successfully for joining different materials since an adhesive layer exhibit weight saving and a smooth load transfer between the adherends. Single-lap joints have found extensive use for testing adhesive properties and as a structural component.

The research about adhesive bonding started in the first half of the twentieth century, with the contributions of Goland and Reissner [1]. He presented a linear 2D analytical solution of the peel and shear stress distribution in SLJs made with composite adherends considering the effect of bending due to eccentric loading path and transverse vertical force at the joint ends. He has included large deflection of

P. K. Kundu (✉) · A. K. Pradhan · M. K. Pandit
School of Mechanical Sciences, Indian Institute of Technology, Bhubaneswar, Odisha, India
e-mail: pkk20@iitbbs.ac.in; pritam.kundu1993@gmail.com

D. Maity et al. (eds.), *Advances in Fluid Mechanics and Solid Mechanics*,
Lecture Notes in Mechanical Engineering,
https://doi.org/10.1007/978-981-15-0772-4_26

adherends in his formulation but considered that the adherend and thin adhesive are an integral part of the adherend. Hart-Smith [2] added to some useful information Goland and Reissner's [1] formulation by separately considering adhesive, upper adherend, and lower adherends. A new method has been developed by Zhao et al. [3] for determining bending moments at the overlap ends of SLJs. Along with that, they have also studied the effect of material, geometry, surface treatment, and environment on the shear strength of SLJs.

Thermomechanical loading of adhesively bonded tubular single-lap joint (SLJ) having functionally graded modulus was investigated by Apalak and Gunes [4] and Apalak et al. [5]. The material properties were graded along the thickness of the tube. Kumar [6] presented a mathematical approach to calculate the stress field in tubular functionally graded adhesive joint with an assumption of no shear stress variation along the thickness of the adhesive. The effective use of functionally graded adhesive in adhesively bonded joints, which reduces peel stress concentration near adherend discontinuities was studied by Scot et al. [7].

Hellen [8] proposed the Virtual Crack Extension Method (VCEM) to evaluate SERR to study the crack propagation characteristics. However, using this method the total SERR could only be calculated, but not the individual modes responsible for mixed-mode interlaminar fracture. Sahin and Taheri [9] used the SERR method for characterization and validation of the crack propagation in adhesive-bonded single-lap joint made with flat laminates.

As of now, literature dealing with the assessment of adhesion failure propagation in LSJs made with curved FGM adherends subjected to transverse loading are seldom available. In this research, 3D nonlinear FE analysis of LSJs made with curved FGM adherend panels are carried out. The lap and strap adherends are joined by an isotropic adhesive. Important aspects, such as the gradation of material properties of adherends have been considered in the FE analysis by material properties data inputs in the desired manner. As failure due to peel stress is significant and the interface region of strap and adhesive is found to have maximum peel stress so an embedded adhesion failure was given at the interface and crack was analyzed.

2 Three-Dimensional Finite Element Modeling of the LSJ

The geometry, loading, and boundary conditions of the LSJ specimen made with FGM curved panels and having pre-embedded adhesion failure at the bond line interface of adhesive and strap adherends is shown in Fig. 1. The thickness of the lap and strap adherends is 1 mm each. The inner radius of strap adherend is 71.6 mm. The angle of arc θ (shallowness angle) is taken to be 20° so that the width of strap adherend is equal to $w = 25.4$ mm. The thickness of the adhesive is taken to be 0.2 mm. A different dimension of circumferentially curved adhesion failure has been considered in the present analysis.

The material properties of the constituents of the FGM used for the adherend panels are given in Table 1 adopted from Apalak and Gunes [4]. Cytek make adhesive

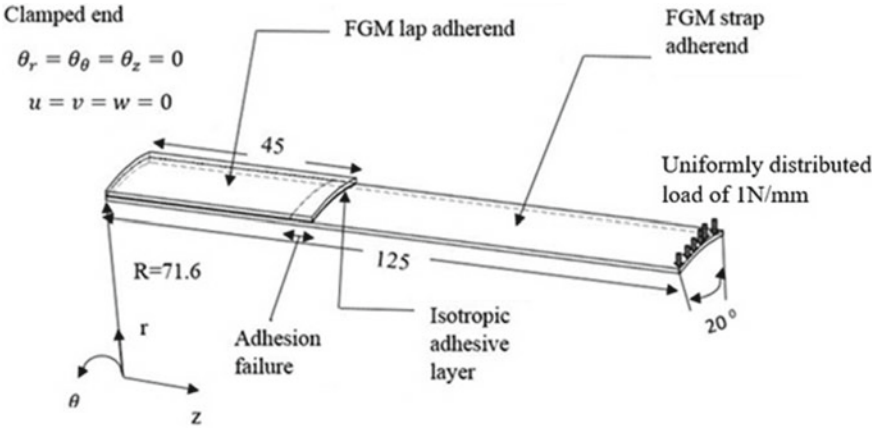

Fig. 1 Model of SLJ specimen subjected to transverse loading

Table 1 Material property of constituents in FGM [4]

Material property	Metal (Ni)	Ceramic (Al_2O_3)
Young's modulus	$E_m = 199.5$ GPa	$E_m = 393$ GPa
Poisson's ratio	$\upsilon_m = 0.3$	$\upsilon_c = 0.25$

Table 2 Material property of Adhesive [4]

Young's modulus	E = 2.4 GPa
Poisson's ratio	$\upsilon = 0.32$

FM 300 K is used for adhesive bonding between the lap and the strap FGM adherends and the material properties for the adhesive are given in Table 2.

The variation of E and υ follows the given expression for both lap and strap FGM adherends

$$E(z) = E_m + (E_c - E_m) \times (z/l_1)\text{^n for } 0 < z < l_1 \text{ and } l_1 = 45\text{ mm} \quad (1)$$

$$\upsilon(z) = \upsilon_m + (\upsilon_c - \upsilon_m) \times (z/l_1)\text{^n for } 0 < z < l_1 \text{ and } l_1 = 45\text{ mm} \quad (2)$$

$$\upsilon(z) = \upsilon_m + (\upsilon_c - \upsilon_m) \times (z/l_1)\text{^n for } z < l_1 < 1 \text{ and } l_1 = 125\text{ mm} \quad (3)$$

$$\upsilon(z) = \upsilon_c + (\upsilon_m - \upsilon_c) \times ((z - l_1)/(1 - l_1))\text{^n for } l_1 \le z \le 1; l_1 = 45\text{ mm}, l = 125\text{ mm} \quad (4)$$

3 Strain Energy Release Rate

The three modes of energy release rate are calculated by the virtual crack closure technique. The detailed expression is given below:

$$G_I = (1/2\Delta A)\, R_f\, [u_t - u_s] \tag{5}$$

$$G_{II} = (1/2\Delta A)\, Z_f\, [w_t - w_s] \tag{6}$$

$$G_{III} = (1/2\Delta A)\, \theta_f\, [v_t - v_s] \tag{7}$$

where Z_f, $R_{f,}$ and θ_f denote the opening, sliding, and tearing mode forces respectively which are required to hold the nodes at the tip of the crack front together to prevent it from growth and subsequent propagation as shown in Fig. 2. The different modes of failure are shown in Fig. 3.

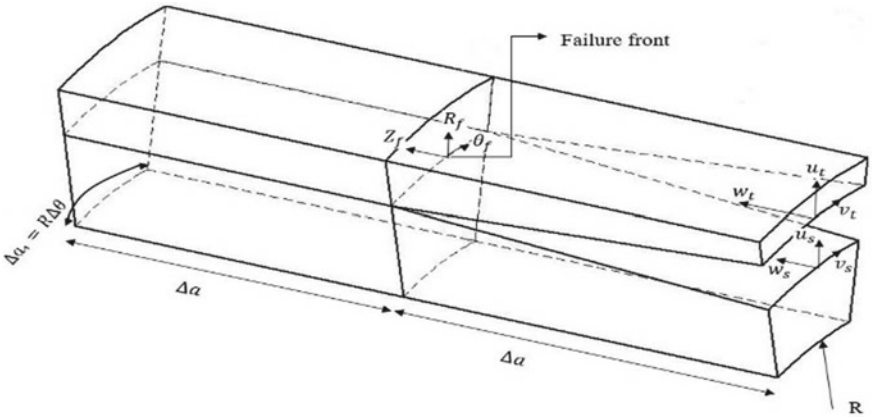

Fig. 2 Model of curved failure front for calculation of SERR by VCCT

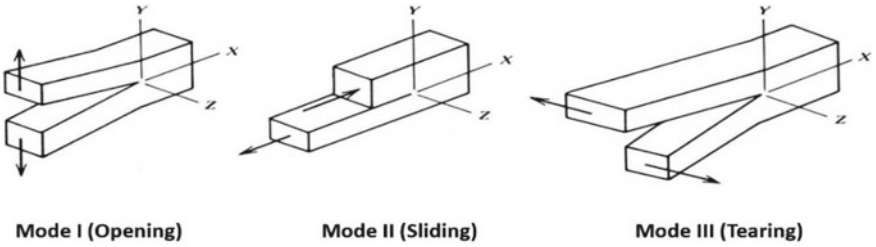

Fig. 3 Different modes of failure

4 Finite Element Modeling

4.1 Validation

For validation of results, a flat SLJ specimen with functionally graded adhesive having identical geometry, material, loading and boundary conditions as taken by Guin and Wang [10] has been analyzed using 8 nodded iso-parametric elements (SOLID185) of ANSYS 16.0. The geometry and boundary condition as used in the paper is shown in Fig. 4. Interfacial stresses have been evaluated in the present 3D FE method at the adhesive and adherend interfaces. Figure 5 shows a sample result for normalized peel stress along the entire overlap length.

4.2 Problem Definition

The approach was validated for flat FGM. So a similar analysis was done in this paper. This paper studies the stress distribution near the adhesion failure front in case of curved FGM subjected to transverse loading conditions. The dimensions and

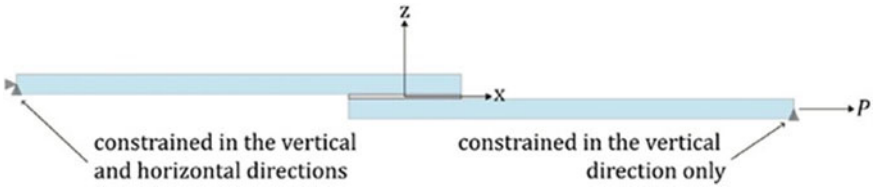

Fig. 4 Geometry and boundary conditions for Guin and Wang [10]

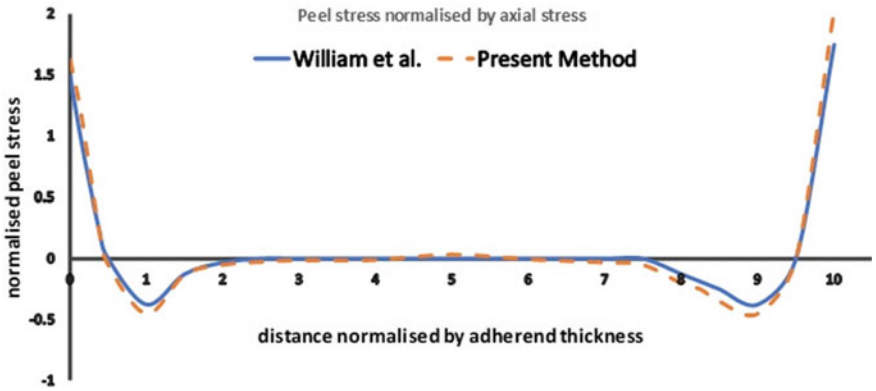

Fig. 5 Normalized peel stress versus normalized thickness for Guin and Wang [10]

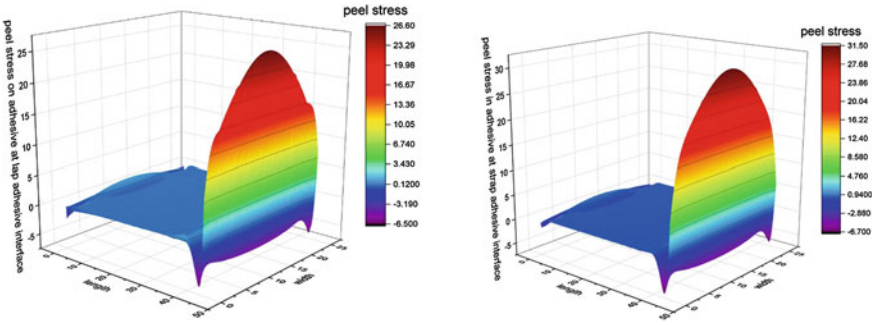

Fig. 6 3D peel stress distribution between lap-adhesive and strap-adhesive interface

loading conditions are given in Fig. 1. The present analysis is done for lap shear joint with one end clamped and other end loaded. The cohesive failure of adhesive is neglected in the present analysis. As seen in Fig. 6 the stress between the adhesive top surface and lap is less than the stress between adhesive bottom surface and strap. So an embedded adhesion failure is given at the location of maximum stress and the behavior of the crack is analyzed.

5 Results and Discussion

5.1 Interfacial Stress Along Failure Front

The plot of peel stress σ_r along the width for the transverse load is shown in Fig. 7. From the figure we can conclude that there is a peak in peel stress at the center of the width. Figure 8 represents the distribution of sliding stress which is in-plane shear stress. It also has a peak value at the center. The value of sliding stress is less as compared to peel stress. It corresponds to G_{II} mode of failure. From Fig. 8 which

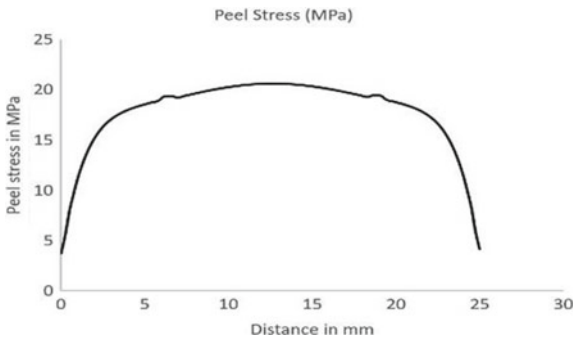

Fig. 7 Distribution of peel stress along the width

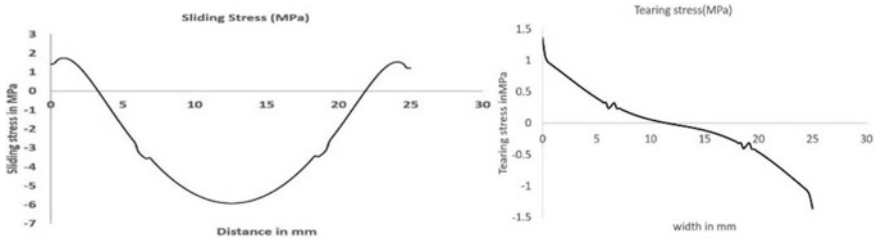

Fig. 8 Distribution of sliding stress and tearing stress along the width

represents the distribution of tearing stress along the failure front, we can conclude that the maximum value of tearing stress is far less than peel stress and sliding shear stress. This gives rise to the G_{III} mode of failure. So it also inferred that the value of G_{III} is insignificant with respect to G_I and G_{II} mode of failure.

5.2 Comparison of Different Adhesion Failure Length

It is observed that there is maximum stress at the adhesive and strap interface. It is evident from Fig. 6, so an intuitive adhesion failure is given at the interface to determine the behavior of the failure front in case of vertical loading. Figures 9 and 10 represents the values of strain energy release rate for curved FGM specimen along the width. It is clear that the values of strain energy release rate are highest at the mid of the width. This led to the conclusion that the crack will propagate more at the center as compared to the edges. Another inference which can be drawn from the above figures is that as the adhesion failure length increases the value of the strain energy release rate of different modes increases. So crack will propagate even faster.

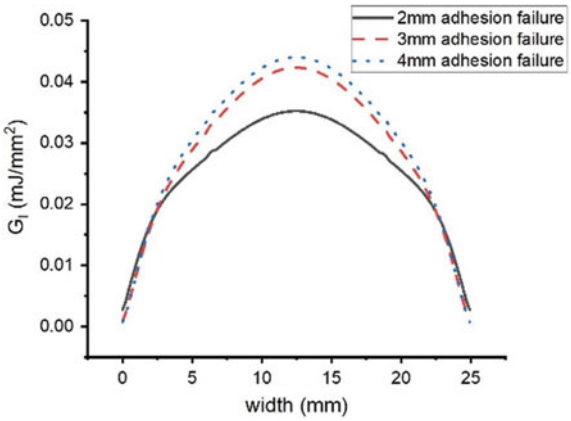

Fig. 9 Comparison of G_I along the width for 2 mm, 3 mm and 4 mm adhesion failure length

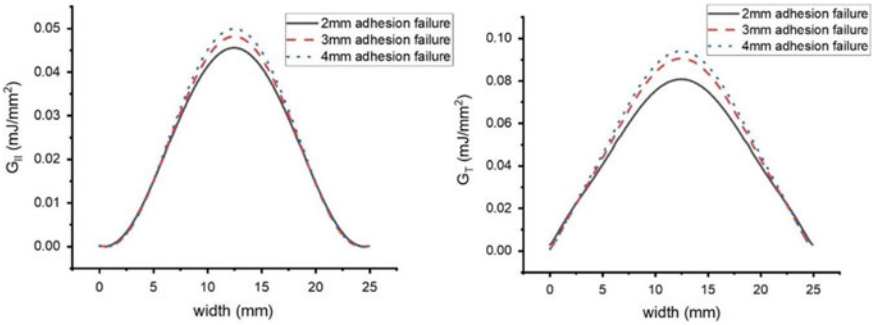

Fig. 10 Comparison of G_{II} and G_T along the width for 2 mm, 3 mm, and 4 mm adhesion failure length

Steps must be taken to reduce crack propagation. Stitching is one such operation, which is done to reduce crack propagation but it also leads to stress concentration.

5.3 Comparison of Coefficient for FGM Preparation

From Figs. 11 and 12, it is observed that with the increase in the coefficient for defining the FGM the value of G_I, $G_{II,}$ and G_T increases along the width.

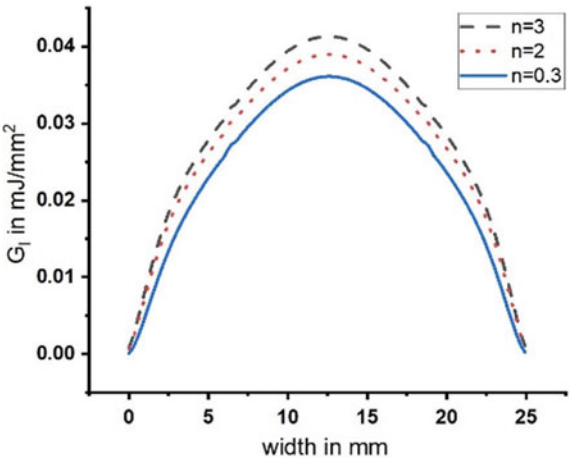

Fig. 11 Comparison of G_I along the width for different coefficients n = 0.3, 2, 3

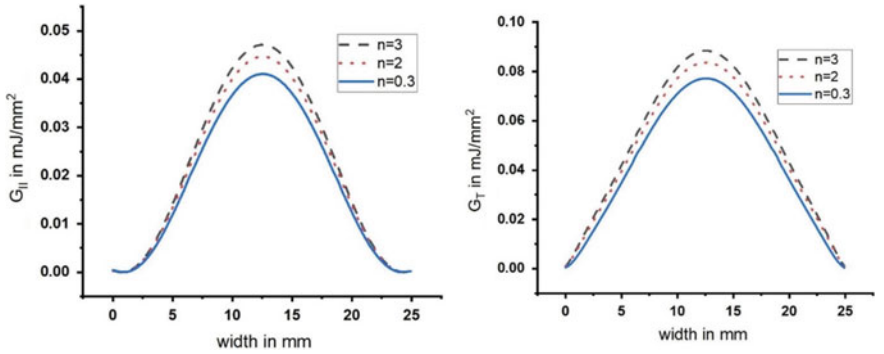

Fig. 12 Comparison of G_{II} and G_T along the width for different coefficients n = 0.3, 2, 3

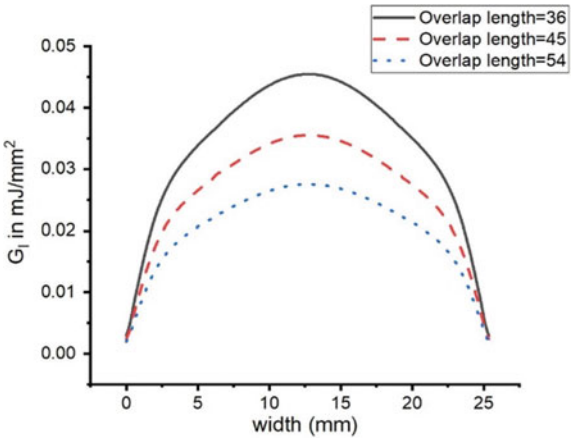

Fig. 13 Comparison of G_I along the width for different overlap lengths

5.4 Comparison of Varying Overlap Length

From Figs. 13 and 14, it is observed that with the increase in overlap length the value of all the energy release rate components decreases. It is an indication of the increase in peel, shear and tear strength of the component when subjected to transverse loading conditions.

6 Conclusion

Variation of stress along the width of the specimen are seldom reported. The stress variation needs to be done along the width to know in detail of the location of stress

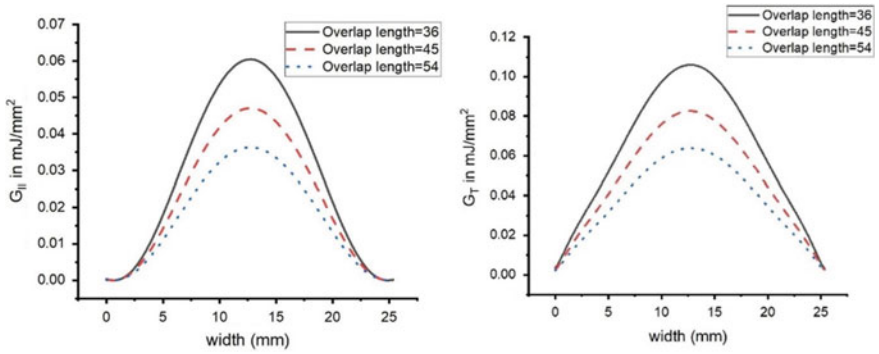

Fig. 14 Comparison of G_{II} and G_T along the width for different overlap lengths

concentration. So a 3D finite element analysis was done on the specimen and all the stress values were plotted along the width.

From the results obtained above, it was observed that there was a peak in the stress value at the center of the width. This proves that at the center of the width the opening is more as compared to at the edges. So we can conclude that the crack growth in the specimen is non-self-similar crack growth.

Values of peel stress and sliding stress were found to be significant with respect to tearing stress. So the value of G_I and G_{II} was more significant with respect to G_{III}. Hence the failure was not dominated by a single mode rather we observed a mixed-mode failure in FGM composite.

From the above figures, it was also observed that as the adhesion failure length increases there is a gradual and faster increase rate of SERR. Similar was the case for an increase in the exponential coefficient. This leads to a significant reduction in load-carrying capability. Steps must be taken to reduce this crack propagation. But with an increase in overlap length the adhesive area increases which lead to a decrease in different strain energy release components.

7 Future Scope

One assumption in the analysis is the adhesive is assumed to be brittle in nature. There is no cohesive failure occurring between layers of adhesive. This is followed by taking the thickness of adhesive very less as compared to adherend thickness. But in the real case, the adhesive may fail due to cohesive failure also. So a cohesive zone modeling for the given specimen needs to be done.

The analysis for the given problem statement is done only for static loading conditions while there are other dynamic loading conditions which are used in airplanes.

The LSJ beam thus generated may be subjected to harmonic and impact loading conditions also. Changing the loading conditions leads to specimen behaving differently which needs to be further analyzed.

Nowadays, functionally graded adhesives are also used to reduce the effect of peel stress and the interface. LSJ specimen with functionally graded adhesives (FGA) is also used in submarines and other marine applications which are subjected to continuous hygrothermal conditions. The effect of hygrothermal loading conditions on FGA still remains a vacant space which needs to be explored.

References

1. Goland M, Reissner E (1944) The stresses in cemented joints. J Appl Mech (7):17–27
2. Hart-Smith LJ (1973) Adhesive bonded single lap joints. 1 NASA CR112236 (9):227–235
3. Zhao X, Adams RD, da Silva LFM (2010) A new method for the determination of bending moments in single lap joints. Int J Adhes Adhes (30):63–71
4. Apalak MK, Gunes R (2005) Thermal residual stress analysis of Ni–Al2O3, Ni–TiO2, and Ti–SiC functionally graded composite plates subjected to various thermal fields. J Thermoplas Compos Mater (18):119–152
5. Apalak MK, Gunes R, Eroglu S (2007) Thermal residual stresses in an adhesively bonded functionally graded tubular single lap joint. Int J Adhes Adhes (27):26–48
6. Kumar S (2009) Analysis of tubular adhesive joints with a functionally modulus graded bond line subjected to axial loads. Int J Adhes Adhes (29):785–795
7. Scott ES, Anthony MW, Steven MA (2012) Functionally graded adhesives for composite joints. Int J Adhes Adhes (35):36– 49
8. Hellen TK (1975) On method of virtual crack extension. J Numer Methods Eng 9:187–207
9. Shahin K, Taheri F (2009) Deformations in adhesively bonded joints on elastic foundations. Compos Struct (90):130–140
10. Guin WE, Wang J (2016) Theoretical model of adhesively bonded single lap joints with functionally graded adherends. Eng Struct (124):316–332
11. Cheuk PT, Tong, L (2002) Failure of adhesive bonded composite lap shear joints with embedded precrack. Compos Sci Technol (62):1079–1095

A Gradient-Damage Model for Cyclic Behavior of Concrete

A. H. Monnamitheen Abdul Gafoor and D. Dinkler

Abstract The present paper elaborates a continuum formulation using a single loading surface that relates a unified equivalent strain with a history deformation parameter to characterize both the softening and hardening behaviors of the material. The history parameter governs the growth of damage. Two additional history parameters capture the crack-opening/closure effectively. The model further incorporates an implicit-gradient regularization to avoid numerical difficulties such as localization of deformation into a vanishing size and ill-posedness of the boundary value problem. Numerical results exhibit good agreement with experimental data under several tests. Finally, the paper demonstrates the localization of deformation due to a gradient-enhanced variable.

Keywords Isotropic damage · History parameter · Evolution law · Implicit-gradient

1 Introduction

Developments of continuum damage models to describe the deformation behavior and fracture mechanisms of various kinds of materials have been done with serious efforts. When the local continuum damage models are implemented into finite element programs, localization into a vanishing size and unacceptable mesh-dependent results are eventually caused due to strain-softening behavior of the material upon mesh refinement. Such numerical difficulties are overcome by adopting some regularization methods such as nonlocal integral method [1] or implicit/explicit gradient methods [2]. Thus, the advancements from local models to nonlocal models (either integral type or gradient type) make continuum damage mechanics a promising approach to study the deformation behavior of any material. In the field of civil engineering, concrete is a widely used construction material. But the

A. H. Monnamitheen Abdul Gafoor (✉) · D. Dinkler
Institute of Structural Analysis, Technische Universität Braunschweig, Brunswick, Germany
e-mail: a.abdul-gafoor@tu-braunschweig.de

D. Maity et al. (eds.), *Advances in Fluid Mechanics and Solid Mechanics*,
Lecture Notes in Mechanical Engineering,
https://doi.org/10.1007/978-981-15-0772-4_27

brittleness of concrete causes damage to the material by opening up tensile cracks and consequently leads to failure of structural components. Although there are several continuum models available to study the nonlinear deformation behavior of concrete, only a few models describe its deformation behavior including cyclic/dynamic effects, which are of particular interests in case of earthquakes or impact loadings. Therefore, it is essential to understand and to describe the mechanical behavior of concrete under various loadings such as monotonic, cyclic, and reverse loading conditions to ensure the safety of concrete structures.

Within the context of continuum damage mechanics, a macroscopic damage variable, which idealizes the internal changes of the material, describes the corresponding degradation in the material stiffness. A history deformation parameter, which is related to a local state of deformation, governs the growth of damage. The local state of deformation is usually measured by an effective stress, an equivalent stress, a damage energy release rate, and a damage equivalent strain [3]. Nonetheless, several models consider the damage equivalent strain such as Mazars strain [4], modified von-Mises strain [2] and cracking and crushing strains [5] as a driving force for the damage growth. These modifications in the measure of equivalent strains do not completely capture the initial elastic domain and ultimate stress domain. The numerical results show considerable differences, especially in bicompression and complex regions, while comparing with experiments [5]. Hence, the equivalent strain has to be defined appropriately to predict both the tensile and compressive behavior of concrete, as it becomes vital in the evolution of damage.

Therefore, the damage model proposed by the authors [6], which adopts a unified damage equivalent strain, is enabled to account for cyclic behavior of concrete in this paper. In order to ensure mesh-independent results and localization of deformation into a finite size, the implicit-gradient method [2] is incorporated as its linearization is straightforward.

2 Local Damage Modeling

According to local continuum damage theory, the nonlinear deformation behavior of the damaged concrete can be characterized by the constitutive relation, which is based on the assumption of energy equivalence principle as follows:

$$\boldsymbol{\sigma} = (1 - D)^2 \, \mathbb{H} : \varepsilon, \tag{1}$$

where $\boldsymbol{\sigma}$ is Cauchy stress tensor and $\boldsymbol{\varepsilon}$ is Almansi strain tensor; $\mathbb{H}$ is the fourth-order elasticity tensor of the undamaged material. D is an isotropic scalar damage introduced explicitly as a function of a history deformation parameter κ describing the severe most deformation that the material experienced during the load history. The explicit function proposed by the authors [3] reads as

$$D(\kappa) = 1 - \left[\frac{\kappa_0}{\kappa}\right]^{\beta_1} e^{-\beta_2\left[\frac{\kappa-\kappa_0}{\kappa_0}\right]}, \tag{2}$$

where κ_0 is an initial damage threshold used to set the initial elastic domain. The model parameters β_1 and β_2 are responsible for the initial growth of damage and the later damage growth. The range of D is given by $0 \leq D \leq 1$.

There must be a local state of deformation that drives the growth of damage, which is measured by the local equivalent strain ϵ. Although there are several definitions available for determining the local measure [3], a unified definition of damage equivalent strain is adopted in this work for describing both the tensile cracking as well as crushing failures, which is given by

$$\epsilon = \left(\alpha I_1 + \sqrt{3J_2} + \beta H \sigma_{\max}\right)/(1-\alpha)E, \tag{3}$$

where I_1 and J_2 are the invariants and $\sigma_{\max}$ is the maximum principal stress of predicted stress. H is a Heaviside function, which equals to 1 for all positive maximum principal stresses, otherwise equals to 0. α and β are dimensionless constants as defined in [7].

The expression (3) is inspired from the extended Lubliner-Lee failure criterion [7] and slightly transformed to express a damage criterion f conveniently in strain space. The relation between κ and ϵ is postulated by the damage criterion function f as follows:

$$f = \epsilon - \kappa. \tag{4}$$

Thus, the function f decides the possibility of damage evolution at a point of continuum. During the damage process, the evolution of the history parameter κ must always satisfy the Kuhn–Tucker loading/unloading conditions, which are mathematically expressed by

$$f \leq 0, \qquad \dot{\kappa} \geq 0, \qquad f\dot{\kappa} = 0, \tag{5}$$

where $(\dot{})$ represents the derivative of a variable with respect to time t. In addition, in order to characterize the unilateral/cyclic behaviors of concrete, two different history parameters κ_t and κ_c are introduced corresponding to tension and compression. Therefore, the history parameters κ_t, κ_c and κ are mathematically expressed as

$$\kappa_t = \mathrm{Sup}\left[\kappa_{0t}, \max\ \epsilon\right];\ \kappa_c = \mathrm{Sup}\left[\kappa_{0c}, \max\ \epsilon\right], \tag{6}$$

$$\kappa = \kappa_t H + \kappa_c (1 - H), \tag{7}$$

where κ_{0t} and κ_{0c} are the respective initial thresholds under tension and compression. κ_t and κ_c thereby describe the severe most deformation that the material experienced during the tensile load history and the compression load history respectively.

3 Gradient-Damage Formulation

As the damage growth in the present model is driven by the local equivalent strain ϵ, the nonlocal averaging procedure is applied to the local equivalent strain ϵ. Consequently, the nonlocal counterpart of ϵ is approximated by the partial differential equation called implicit-gradient equation [2] as follows:

$$\bar{\epsilon} - l_c^2 \nabla^2 \bar{\epsilon} = \epsilon, \tag{8}$$

where ∇^2 is the Laplacian operator and l_c is the characteristic internal length scale. The nonlocal equivalent strain $\bar{\epsilon}$, which represents the average of ϵ within the considered volume domain, describes the nonlocal behavior of the fracture process mechanism. The Eq. (8) must always be supplemented by an additional boundary condition. Therefore, the present work adopts a natural boundary condition at every point of the boundary as

$$\nabla \bar{\epsilon} \cdot \boldsymbol{n} = 0, \tag{9}$$

as it ensures that the average of nonlocal equivalent strain $\bar{\epsilon}$ over the entire domain equals that of its local counterpart ϵ [2]. Hence, in case of gradient-enhanced damage model, κ is related to the nonlocal equivalent strain $\bar{\epsilon}$ entering into the damage criterion (4) instead of its local counterpart.

4 Model Validations

In order to check the ability of the damage model in predicting the material behavior, the developed model has been implemented into an in-house finite element program called *codeBlue*. The nonlinear system of resulting equations has been solved by the Newton–Raphson method. The internal length scale l_c is chosen as 200 mm. Linear shape functions have been used for nonlocal equivalent strains. The adopted material and model parameters are provided in Table 1. The material parameters are taken from the work [7]. The model parameters β_1 and β_2 are calibrated using the uniaxial tensile and compressive tests.

Table 1 Material and model parameters used for validation

Material parameters	f_c (MPa) 27.6	f_t (MPa) 3.48	E (GPa) 31.7	ν (–) 0.2		
Model parameters	β_{1t} 0.85	β_{2t} 0.18	β_{1c} 0.0	β_{2c} 0.095	κ_{0t} f_c/E	κ_{0c} $10 f_t/3E$

First, a single 8-noded brick element of size 200 mm × 200 mm × 50 mm is analyzed under selected elementary tests such as direct cyclic tension and compression, and alternate tension-compression/reverse cyclic loading to evaluate the performance of the model. The displacement history is used to be cyclic with an increasing magnitude either in tensile or compressive direction as an imposed loading.

4.1 Cyclic Tension and Compression

The simulated stress–strain curves under direct cyclic tensile and compressive loading are depicted in Figs. 1 and 2, respectively. The model predictions agree fairly with the experimental curves [8, 9]. As observed, the softening behavior under tension is reasonably comparable with the experimental curves. Similarly, both the hardening and softening behaviors under compression are almost close to the experimental data. κ_t or κ_c grows monotonically, as every reloading follows the path of the

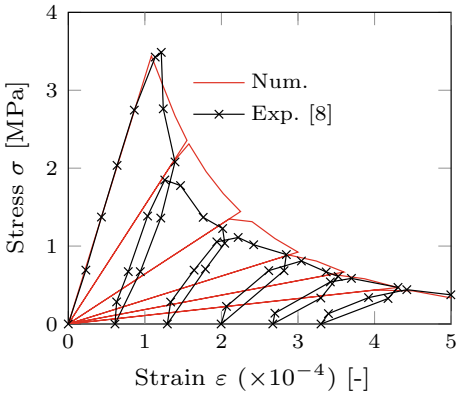

Fig. 1 Uniaxial cyclic tension

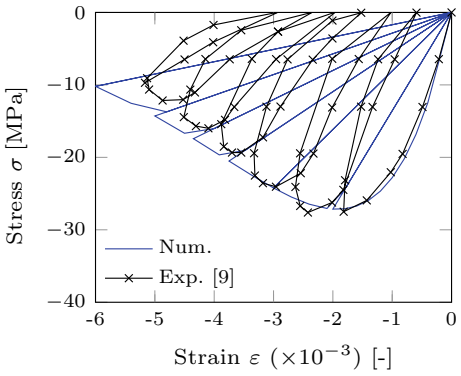

Fig. 2 Uniaxial cyclic compression

previous unloading. Consequently, the increase in the slopes of the unloading curves replicates the monotonic increase in damage under tension or compression. κ and D remain constant during unloading and thus the loading/unloading conditions (5) are satisfied. But the only discrepancy observed is that residual strains are not captured during unloading cycles since the model has not taken the inelastic evolution of strains into account.

4.2 Reverse Cyclic Tests

As can be seen in Fig. 3, κ_t or κ_c is monotonically increasing during tension-compression loading/unloading processes respectively. Subsequently, a monotonic increase in the effective damage D is also viewed in Fig. 4 under tension or compression. It is found that D becomes zero after the initial tensile loading (cycle 1) and then entering into the first phase of compression (cycle 2) with initial stiffness. But the accumulated D is recovered once the material experiences tension in reloading (cycle 3). Thus, the model describes the unilateral behavior quite well as it is observed from the Figs. 5 and 6 which display the actual and normalized stress curves of the model, respectively. Thereby, the numerical response agrees well with the experimental data [10] showing a full recovery of initial stiffness.

But the certain discrepancies observed are due to the fact that the permanent deformation is not captured as the present article is limited to elasticity based model. Nevertheless, the present model describes the loading and unloading behaviors and initial stiffness recovery of the material well.

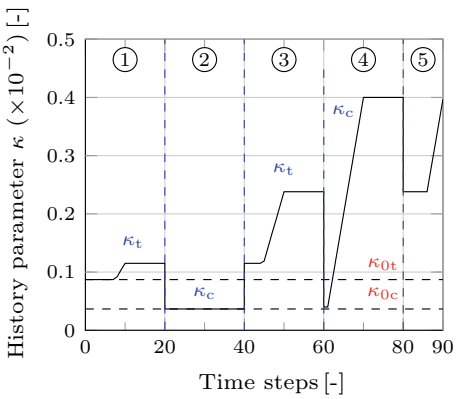

Fig. 3 History parameter evolution

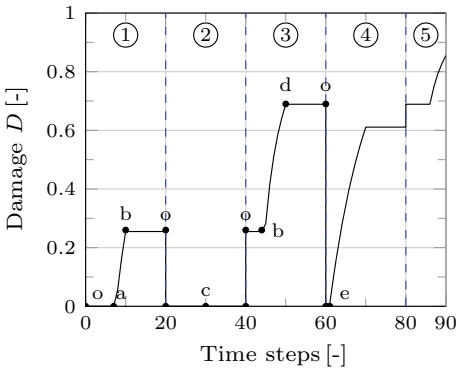

Fig. 4 Damage evolution

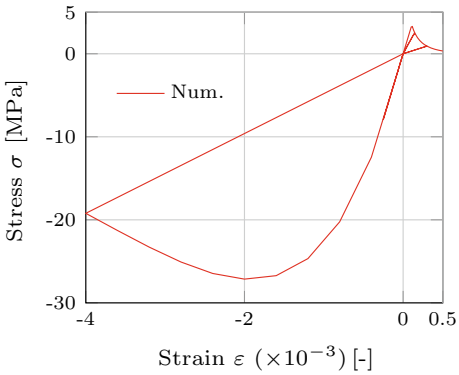

Fig. 5 Unilateral behavior

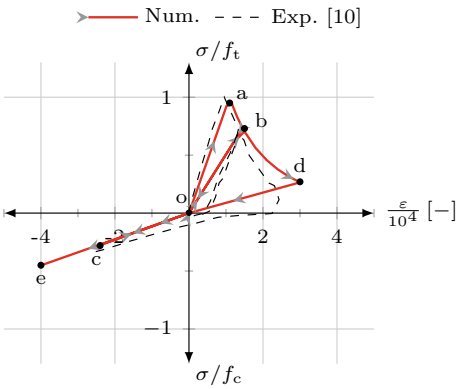

Fig. 6 Normalized behavior

4.3 Illustration of Nonlocal Phenomena

Second, a one-dimensional bar of size 100 mm × 10 mm × 10 mm with three different FE meshes ($n = 40, 80, 160$-solid elements discretized along the bar) is studied under tension in order to visualize the localization phenomena. An imperfection of 10 mm wide at the center of the bar is introduced. Two internal length values $l_c = \{5, 10\}$ mm. Mesh-independent solutions are achievable. The converged stress responses are illustrated in Fig. 7. The higher values of l_c lead to the increase in peak stress as noticed in Fig. 7 as well as the broader width of strain/damage localization as seen in Fig. 8 and vice versa. The distributions of local and nonlocal equivalent strains and damage over the length of the bar corresponding to three load steps are shown in Figs. 9 and 10, respectively. As realized, the finite width of localization of deformation or damage occurs and subsequent loading causes broadening of the localization band.

Thus, the maximum values of local equivalent strains and the smooth distribution of nonlocal strains replicate the formation of macro-crack and the existence of microstructural interactions in the bar, respectively.

5 Conclusions

The model has been developed using a unified equivalent strain that drives the evolution of effective damage. Two independent history parameters for tension and compression leads the proposed model to be able to describe the crack-opening/closure effects on micro-cracks under cyclic/reverse loadings. The model likewise captures the unilateral behavior of concrete with the initial stiffness recovery for the first compression loading by exhibiting good agreement with the experiments. Furthermore, the localization analysis demonstrates that the gradient-enhancement on the local

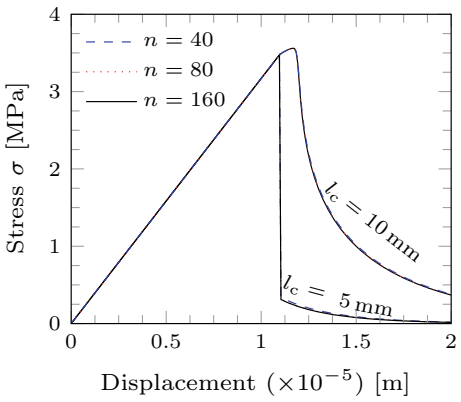

Fig. 7 Converged stress responses

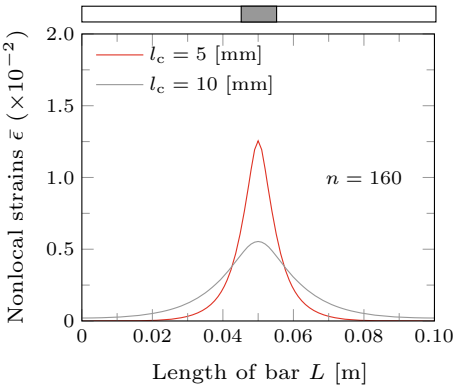

Fig. 8 Evolution of nonlocal strains

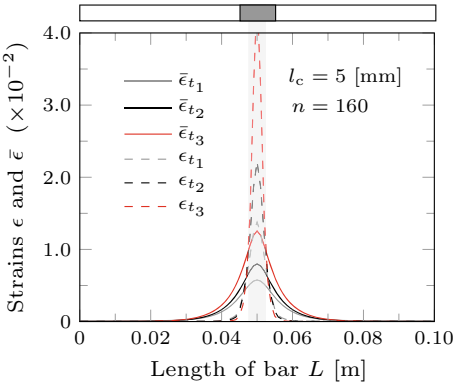

Fig. 9 Evolution of local/nonlocal strains

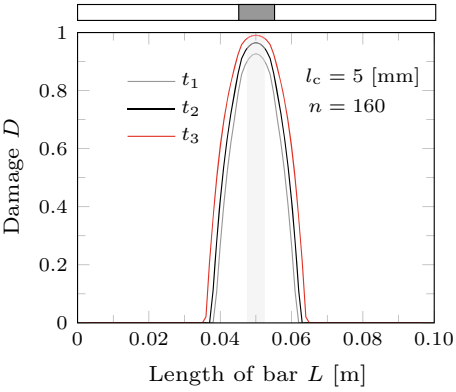

Fig. 10 Evolution of damage

equivalent strain yields physically meaningful and mesh-independent responses as the width of localization becomes finite. The maximum values of local strains and the smooth distribution of nonlocal strains replicate the macro-crack and the existence of micro-structural interactions in the bar respectively.

The model incorporating the permanent inelastic strains and the damage induced-anisotropy based on higher order tensors are underway and will be discussed in the forthcoming papers.

Acknowledgements The financial supports by DAAD (Research Grants, No.:57048249) and DFG (GRK 2075) are greatly acknowledged.

References

1. Bažant Z, Pijaudier-Cabot G (1988) Nonlocal continuum damage, localization instability and convergence. J Appl Mech 55(2):287–293
2. Peerlings R, De Borst R, Brekelmans W, Geers M (1998) Gradient-enhanced damage modelling of concrete fracture. Mech Cohesive-Frict Mater 3(4):323–342
3. Monnamitheen Abdul Gafoor AH, Dinkler D (2016) Influence of deformation history parameters on softening behaviour of concrete. PAMM 16(1):155–156
4. Mazars J, Pijaudier-Cabot G (1989) Continuum damage theory-application to concrete. J Eng Mech 115(2):345–365
5. Mazars J, Hamon F, Grange S (2015) A new 3d damage model for concrete under monotonic, cyclic and dynamic loadings. Mater Struct 48(11):3779–3793
6. Monnamitheen Abdul Gafoor AH, Dinkler D (2017) A model for coupled inelastic deformation and anisotropic damage behaviour of concrete. PAMM 17(1):241–242. https://doi.org/10.1002/pamm.201710090, https://onlinelibrary.wiley.com/doi/abs/10.1002/pamm.201710090
7. Lee J, Fenves G (1998) Plastic-damage model for cyclic loading of concrete structures. J Eng Mech 124
8. Gopalaratnam V, Shah S (1985) Softening response of plain concrete in direct tension. J Proc 82(3):310–323
9. Karsan I, Jirsa J (1969) Behavior of concrete under compressive loadings. J Struct Div 95(12):2543–2564
10. Mazars J, Berthaud Y, Ramtani S (1990) The unilateral behaviour of damaged concrete. Eng Fract Mech 35(4):629–635

Reductions of Bending Stresses and Wear in an Aerodynamic Involute Spur Gear Profile

Y. P. Ravitej, O. Abhilash and Naveen kumar

Abstract Gears are widely used in automobile and aerospace sectors. The most important duty of an engineer to design and manufacture of the transmission system of it. Gears normally fail stress concentrations and fatigue resulting in wear and tear of transmission elements like gears, pulleys, etc. This paper clears that by changing properties of material used for manufacturing of gears, by optimizing the gear, the stresses induced in the gears can be decreased modeling and analysis is carried out by CATIA and ANSYS workbench, respectively. It is seen that reduction in bending stresses is found in the above cases, are compared and correlated with each other.

Keywords Transmission elements · Aerospace sectors · Stress concentrations

1 Introduction

1.1 Transmission System

It is the system which contains power source and elements for transmission. It contains a system of gearbox, gear trains and gives the necessary amount of speed and torque from one shaft to another shaft. Gear ratios can be varied to obtain the desired speed.

1.2 Gear Technology

Gears are the important media for transmission of power from one shaft to other. Gear is classified based on shafts axis placement, speed, velocity ratio, etc. Due to the mating of the two teeth of the gear, two stresses are developed, viz., contact stresses

Y. P. Ravitej (✉) · O. Abhilash · N. kumar
Department of Mechanical Engineering, Dayananda Sagar University, Bangalore, India
e-mail: ravitejmtech@gmail.com

D. Maity et al. (eds.), *Advances in Fluid Mechanics and Solid Mechanics*,
Lecture Notes in Mechanical Engineering,
https://doi.org/10.1007/978-981-15-0772-4_28

and bending stresses. Contact stresses are developed at the contact point of the gears and bending stresses are developed at the root fillet of the gears. Contact stresses are calculated by Hertzian contact stresses and bending stresses are calculated by Levis bending stress equation.

1.3 Bending Stress

Bending stresses are developed at the root fillet of the gears. In the case of bending stresses, the gear tooth acts as a cantilever beam.

Yellampalli et al. [1] made a study on dynamic analysis of spur gear set. Methods for reduction of stresses involved in stresses mating of gears are discussed. Ravitej [2] explains the fabrication and analysis of composites structure helpful for composite gears.

In this paper, standard gear is design using CATIA and simulated using ANSYS workbench for the cases, i.e.,

(a) Different material properties
(b) Optimization.

2 Methodology

These are developed at the root fillet of the gear, which in turn reduces the life of the gears and to decrease the stresses induced the following are implemented.

- Changing the properties of the material,
- Optimization technique,
- Decreasing the root radius.

2.1 Gear Material Properties

Spur gear is designed by considering the parameters shown in Table 1.

Gear is modeled based on the design standards using CATIA 5 as shown in Fig. 1.

Three-dimensional gear model is modeled using CATIA v5, meshed and analyzed using ANSYS Workbench shown in Figs. 1 and 3, respectively. Load of 500 N acts on the face of the gear (Fig. 2).

Table 1 Gear design parameters

Sl. no.	Parameters	Values
1	Pressure angle	20°
2	Module	2
3	Addendum circle radius	32 mm
4	Pitch circle radius	30 mm
5	Dedendum circle radius	28.2 mm

Fig. 1 3D gear model

3 Results and Discussions

Results for different cases are discussed below.

3.1 Changing the Properties or Using Material with Different Properties

One way of decreasing the bending stresses is by changing the property if the gear, reduction of stresses for different materials is shown in the Figs. 4, 5, 6 and 7.

From the simulation analysis, it is concluded that by changing the properties of the gear material the bending stresses can be reduced which is less than the yield stress value of the material and is tabulated in Table 2.

Fig. 2 Details of meshing

Details of "Mesh"	
Defaults	
Physics Preference	Mechanical
Relevance	0
Sizing	
Use Advanced Size Fun...	Off
Relevance Center	Coarse
Element Size	Default
Initial Size Seed	Active Assembly
Smoothing	Medium
Transition	Fast
Span Angle Center	Coarse
Minimum Edge Length	0.437020 mm
Inflation	

Fig. 3 BC and analysis

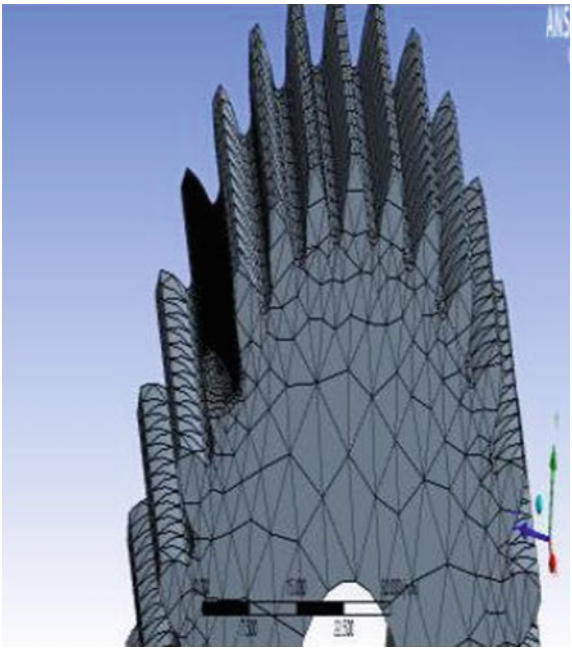

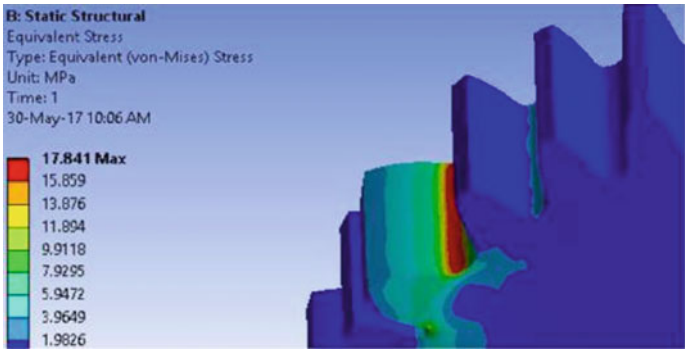

Fig. 4 Equivalent stress in structural steel

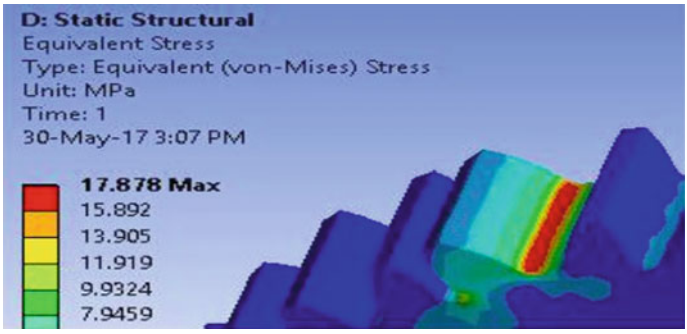

Fig. 5 Equivalent stress in titanium

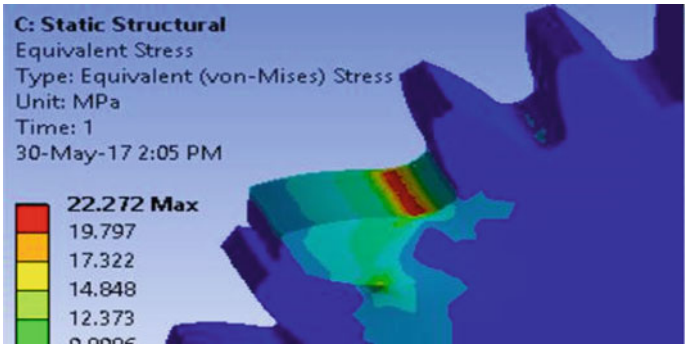

Fig. 6 Equivalent stress in stainless steel

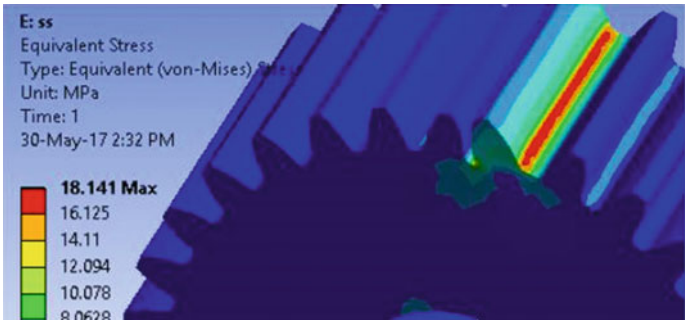

Fig. 7 Equivalent stress in aluminum

Table 2 Stress obtained by various materials

Material	Tensile yield stress (MPa)	Equivalent stress (MPa)
Aluminum	280	22.272
Stainless steel	207	18.141
Titanium	930	17.878
Structural steel	250	17.841

3.2 Optimization Technique

By optimization of the gear, bending stresses at the fillet can be decreased, for this instant structural steel is selected as the material for the analysis. 8 holes of 3 mm diameter are done on the specific positions, which decreases the weight of the gear and intern decreases the stress induced at the fillet shown in the Figs. 8 and 9.

Comparison of results is shown in Table 3.

From the above table, it is noticed that bending stress obtained by unoptimized gear is 17.841 MPa and bending stress obtained by optimized gear is 17.033 MPa.

3.3 By Decreasing the Root Radius

Root radius is an important factor that decides the stress intensity factor, root radius of gears 0.5 and 0.78 mm are designed and analyzed for structural steel as a material in mm. Results are discussed in Figs. 10 and 11.

Results are tabulated in Table 4.

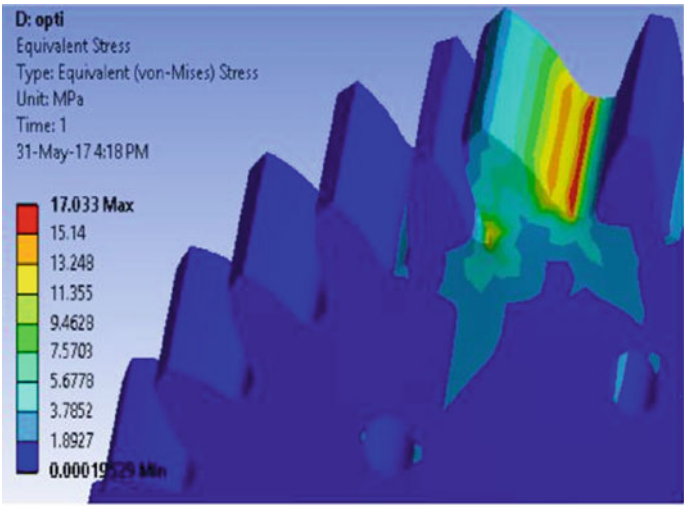

Fig. 8 Optimized gear

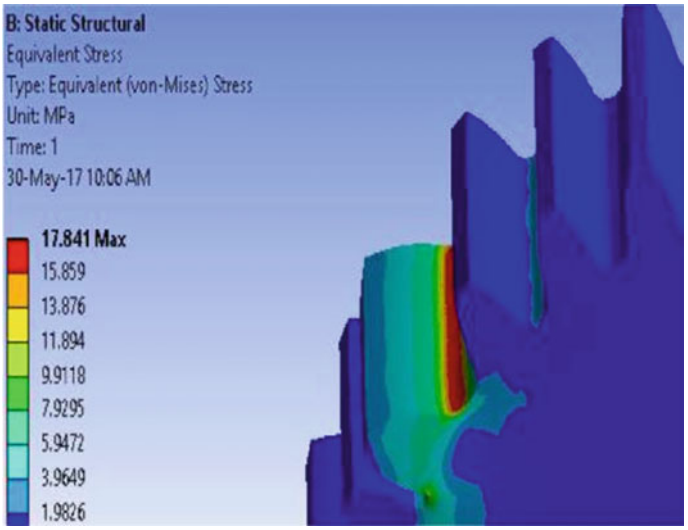

Fig. 9 Un-optimized gear

Table 3 Stress obtained by optimization by various materials

Un-optimized gear (MPa)	Optimized gear (MPa)	Difference (MPa)
17.841	17.033	0.808

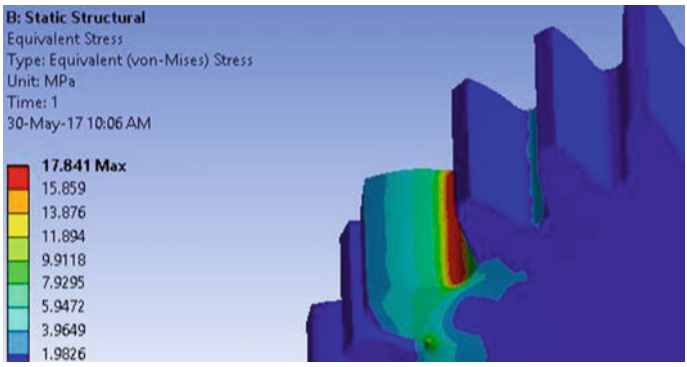

Fig. 10 Equi. stress result of radius 0.78 mm

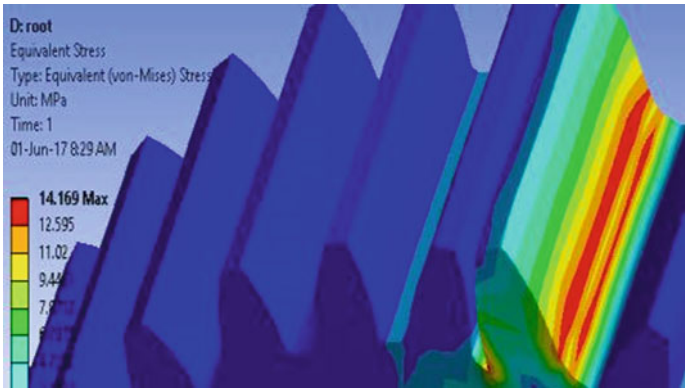

Fig. 11 Equi. stress result of root radius 0.5 mm

Table 4 Results of equivalent stress of different root radii

Root radius 0.5 mm	Root radius 0.78 mm	Difference (%)
14.169	17.841	0.2

4 Conclusion

It is concluded that by using different material properties, optimization and decrease of root radius bending stresses associated with the spur gear decreases. Hence wear and tear and stress concentration decreases.

References

1. Ravitej YP, Sandhya R, Nandeeshaiah BM (2016) Stress analysis of aero engine spur gear. Int J Innov Res Sci Eng Technol 5(9):797–802. ISSN (Online): 2319-8753
2. Ravitej YP, Swaroop V et al (2018) Finite element analysis of mild steel-rubber sandwich composite material. J Mater Sci Eng IOP Publ. Mater Sci Eng 376:012040. https://doi.org/10.1088/1757-899x/376/1/012040
3. Ristivojevic M, Lazovic T, Vencl A (2013) Studying the load carrying capacity of spur gear tooth flanks. Mech Mach Theory 59:125–137
4. Rincon AF, Viadero F, Iglesias M, Garcia P, de-Juan A, Sancibrian R (2013) A model for the study of meshing stiffness in spur gear transmissions. Mech Mach Theory 61:30–58
5. Karaveer V, Mogrekar A, Preman Reynolds Joseph T (2013) Modelling and finite element analysis of spur gear. Int J Curr Eng Technol 3(5). ISSN 2277-4106
6. Potghan D, Sharma S (2015) Finite element analysis of spur gearused in lathe headstock. Int J Eng Sci Res Technol 4(7). ISSN 2277-9655
7. Badithe M, Srikanth S, Bodapall J (2014) Stress and reduction analysis of a spur gear tooth. Int J Emerg Technol Adv Eng 4(3)

Probability of Failure of a Beam Subjected to Randomly Moving Loads

Alben Jose Kezhiyur, S. Talukdar and Anjaly J. Pillai

Abstract In the present paper, an analytical approach to study the deflection and dynamic stresses in a simply supported beam when traversed by randomly moving loads at a uniform speed whose inter-arrival time follows Poisson distribution has been developed. The magnitude of payloads has been assumed to follow a uniform distribution. Initially, the expression for deflection and dynamic stresses in a simply supported beam traversed by a constant force is developed by application of Fourier sine integral transformation followed by the method of Laplace–Carson integral transformation and further followed by Inverse Fourier transformation. The analytical expressions are found to obtain the deflection due to a set of loads which follow the Poisson distribution. The inter-arrival time between the payload is an important factor for the probability of failure as revealed from the analysis. The probability of failure increases when the interval of arrival time is decreased.

Keywords Moving load · Inter-arrival time · Probability of failure · Poisson distribution

1 Introduction

The general problem of transverse vibrations of beams resulting from the passage of moving loads is of considerable practical interest in the dynamics of structures. In most studies, the moving load has been regarded as deterministic. However, the moving forces acting on highway bridges are of random magnitude; moreover, they arrive at the span at random times. Consequently, the traffic load of a bridge is a random process. Vibrations of this kind, occurring mainly in bridges, have been the subject of studies for many years. Considering the practical importance of the topic, research has been carried out on the vibration of a beam due to randomly moving loads. The characterization of randomness can be done by different methods based on probability theory. Shinozuka et al. [1] had considered the inter-arrival time to be

A. J. Kezhiyur · S. Talukdar (✉) · A. J. Pillai
Department of Civil Engineering, Indian Institute of Technology, Guwahati, India
e-mail: staluk@iitg.ac.in

D. Maity et al. (eds.), *Advances in Fluid Mechanics and Solid Mechanics*,
Lecture Notes in Mechanical Engineering,
https://doi.org/10.1007/978-981-15-0772-4_29

following a gamma distribution. In this, the probability of trucks on the right and the left lane was computed assuming both are independent events. The random vibration of the beam when subjected to a random stream of moving forces was investigated by Fryba [2], Sniady [3], Sieniawska and Sniady [4] and Sniady et al. [5]. Chen et al. [6] developed the model in which the arrival of the vehicle follows a Poisson process. In the present paper, an analysis has been performed to study the maximum value, mean, and standard deviation of deflection and bending stresses developed at mid-span of a simply supported beam for a set of snapshot time intervals under randomly moving loads. The study is carried out considering the following cases (i) inter-arrival time between moving loads is considered to follow Poisson distribution (ii) magnitude of payloads is considered to follow a uniform distribution. An analytical expression developed has been used to generate each sample of ensemble corresponding to a set of random variables generated through the numerical process. A parametric study has been conducted to examine the mid-span response statistics and probability of failure.

2 Problem Formulation and Method of Solution

2.1 Dynamic Response

A Euler–Bernoulli beam model of uniform properties has been considered The beam behavior under a single constant moving load P is governed by the differential equation [7] as,

$$EJ\frac{\partial^4 v(x,t)}{\partial x^4} + \mu\frac{\partial v(x,t)}{\partial t} + 2\mu\omega_b\frac{\partial v(x,t)}{\partial t} = P\delta(x-ct) \tag{1}$$

where, EJ is flexural rigidity, μ is mass/length, ω_b is circular frequency of the damping of the beam, P is the constant load moving with velocity c, $v(x, t)$ is the beam deflection at point x at time t measured from the equilibrium position when beam is loaded by its self-weight. δ is a Dirac delta function. The simply supported boundary condition has been assumed for the beam. In the present paper, integral transform technique has been used which has wide applicability in moving load track interactions such as railway applications when track domain is infinite. Further, it has the advantage of converting differential equation to algebraic equation. To formulate the problem, we first define Fourier sine transform as

$$V(j,t) = \int_0^l v(x,t)\sin\frac{j\pi x}{l}dx \tag{2}$$

In Eq. (2), *V(j, t)* is the transform of original displacement *v(x, t)*, *j* is the harmonic number, *l* is the length of the beam. The next step is to multiply each term of Eq. (1) by *sin(jπx/l)*, then integrate using boundary conditions within the domain of beam which yields

$$\ddot{V}(j,t) + 2\omega_b \dot{V}(j,t) + \varpi_j^2 V(j,t) = (P/\mu)\sin\frac{j\pi c}{l}t \tag{3}$$

where

$$\varpi_j^2 = (j^4\pi^4/l^4)EJ/\mu \tag{4}$$

Now let us define Laplace–Carson integral [8] as

$$\bar{V}(j,s) = s\int_0^\infty V(j,t)\exp(-st)dt \tag{5}$$

Performing Laplace-transform integral on Eq. (3) and applying the initial conditions, one arrives after some algebraic manipulation

$$\bar{V}(j,s) = \frac{Pj\omega}{\mu}\frac{s}{(s^2 + j^2\omega^2)(s^2 + 2\omega_b s + \bar{\omega}_j^2)} \tag{6}$$

Taking inverse Fourier transforms and after rearrangement, finally, the expression of time-dependent response original coordinate in the spatial domain is given by

$$\begin{aligned} v(x,t) = {} & \tfrac{2Pl^3}{\pi^4 EJ}\sum_{j=1}^{\infty}\tfrac{1}{j^2[(j^2-\alpha^2)^2+4\alpha^2\beta^2]}[j^2(j^2-\alpha^2) \\ & \sin j\bar{\omega}t - \tfrac{j\alpha[(j^2-\alpha^2)-2\beta^2]}{(j^4-\beta^2)^{0.5}}\times \\ & \exp(-\omega_b t)\sin\varpi_j t - 2j\alpha\beta \\ & \{\cos j\bar{\omega}t - \exp(-\omega_b t)\cos\varpi_j t\}]\sin(j\pi x/l) \end{aligned} \tag{7}$$

where

$$\alpha = cl(\mu/\pi^2 EJ)^{0.5} \tag{8}$$

$$\beta = \omega_b(\mu l^4/\pi^4 EJ)^{0.5} \tag{9}$$

Figure 1 shows a simply supported beam traversed by a series of moving load. In the present study, a series of moving load which has randomness in load magnitude and inter-arrival time has been considered. In our problem, we denote t_s as snapshot time which is defined as the interval at which the beam response to the number of loads present on the beam is observed and the probability of failure is studied. Let

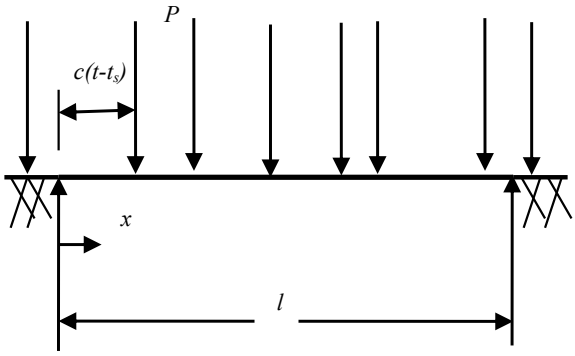

Fig. 1 Simply supported beam subjected to a series of moving loads

t be the time at which the load entered the beam. For the leading load as shown in Fig. 1, $t^{'} = 0$. The position of each load with reference to the origin is denoted by $c(t_s - t^{'})$.

The methodology adopted is that the inter-arrival time between two loads is considered to be a random variable which follows the Poisson distribution and so a set of random numbers which follow Poisson distribution are generated. The suitable snapshot time as interested can be chosen for the developing the ensemble. For each sample of a random number, response of the beam at mid-span subject to a series of the moving load is calculated using linear superposition of the response given by Eq. (7). Thus, performing repetitive calculation an ensemble consisting of N deflection time history can be created and statistical averaging across the ensemble yields mean and standard deviation of deflection.

2.2 Probability of Failure of Beam

In our problem, failure of the beam is attributed to the serviceability condition showing excessive deflection which hampers the performance of the structure. For estimation of probability, we take meantime history plus 2× standard deviation of the deflection of a slender beam. Let $X(t)$ be deflection history at mid-span. A threshold limit of the deflection is defined as X_m. A horizontal line X_m is drawn through the threshold value and then the corresponding time intervals Δt_i are measured for the regions which crosses the threshold limit. Hence, the probability of failure (P_f) is calculated [9] as

$$P_f = P(X > X_m) = \sum_{i=1}^{k} \Delta t_i / T \tag{10}$$

3 Results and Discussion

The present approach has been illustrated with the help of the following data:

Length of beam = 10 m; mass per unit length = 30 kg/m; Moment of inertia of beam section = 7×10^{-4} m^4. Modulus of elasticity of beam = 2.1×10^{11} N/m^2. The magnitude of vehicle load is taken randomly with uniform probability density function in the range of 80–300 kN. The snapshot time interval was considered 10–50 s for obtaining the result.

3.1 Effect of Damping Properties of Beam

The damping of the beam is included in the nondimensional parameter β. The mid-span deflection due to the series of moving load of uniform magnitude 200 kN with inter-arrival rate 2 s on the beam has been considered to examine the effect of damping. The mid-span deflection is nondimensionalized with respect to static deflection of single point load of the same magnitude and has been presented in Fig. 2. It is seen that only single wave is formed over the beam exhibiting lesser magnitude as nondimensional parameter β increases.

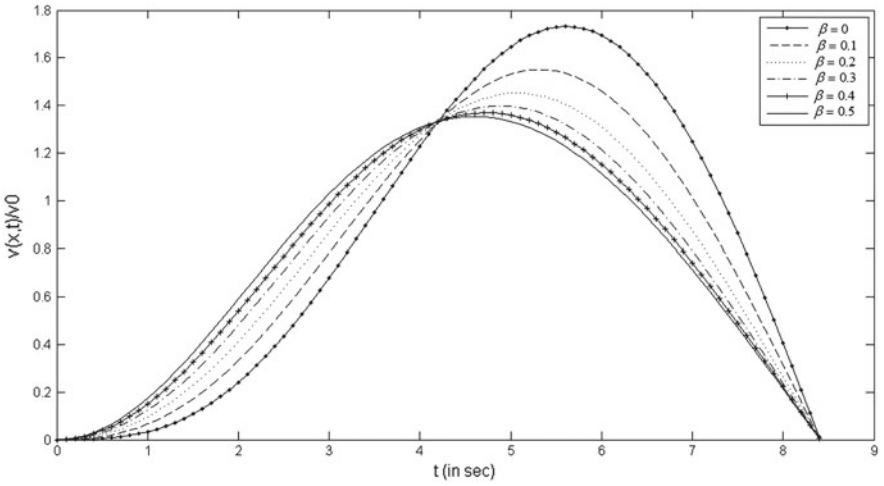

Fig. 2 Effect of beam damping on the mid-span deflection

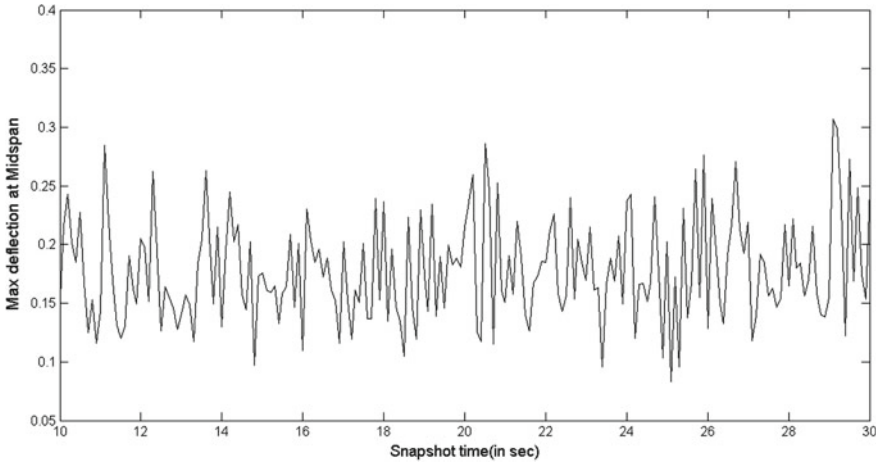

Fig. 3 Maximum deflection at mid-span of the beam for snapshot time 10–30 secs

3.2 Effect of Snapshot Time Interval on Mean and Standard Deviation of Peak Displacement

We define snapshot time as the interval at which the beam response to a number of loads present on the beam is observed and the probability of failure is studied. The snapshot time is taken from 10 to 30 s. The moving load arrival on the beam is assumed to follow Poisson's process. The mean arrival rate assumed for generating the result is taken 2. Figure 3 shows the peak value of mean displacement of the beam at mid-span while Fig. 4 presents the standard deviation of mid-span displacement. It is found that in the interval considered, the peak value is fluctuating; however, the largest value is noted at snapshot time 28 s. This may indicate a sufficient number of moving loads should pass along the beam for accumulating significant stress. The study thus remarks that for calculating the service life of a bridge, stress considered for single-vehicle passage may predict long service life while practically this may not happen in a busy bridge.

3.3 Probability of Failure

A parametric study has been done considering the mean of the Poisson random variable effect over the probability of failure of the beam for two different sets of snapshot intervals. This results in higher values of probability of failure. The probability of failure as obtained for 10–30 s snap-shot interval is 0.31 while the result for 10–50 s snap-shot interval is 0.39. The probability of failure is based on a threshold deflection limit of a steel beam, which is chosen as 50% more than permissible limit

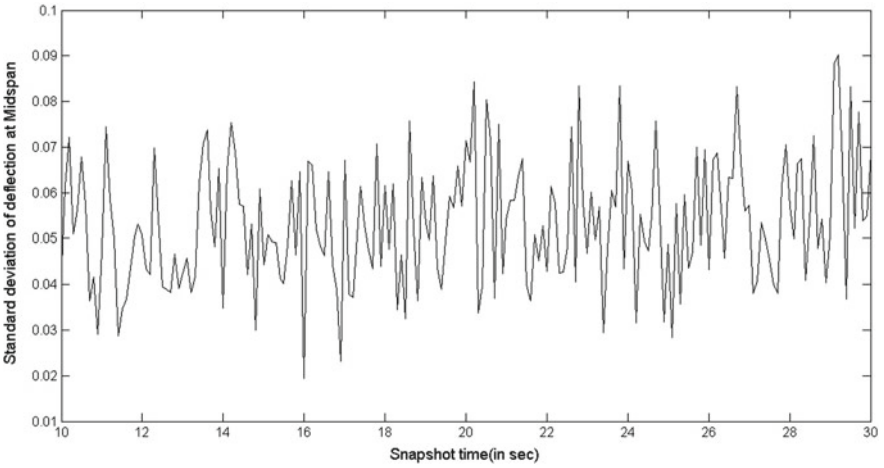

Fig. 4 Standard deviation of deflection at mid-span of beam for snap-shot time 10–30 s

for a steel beam as given in standard code of practice [10]. It is assumed that in the condition of the highly deformed profile, plastic hinge forms leading to the collapse of beam. As the mean value increases, the number of loads present on the beam at higher snapshot times increases which results in higher deflection values of the beam at those corresponding snapshot times.

4 Conclusion

In the present paper, an analytical expression for the dynamic response of a simply supported beam subject to a moving load randomly arriving on the beam at constant speed has been developed. The formulation is based on Fourier sine transform of original partial differential equation to the ordinary differential equation, which is again operated by Laplace–Carson integral transformation followed by the inverse transform. This procedure has applicability to beams of an infinite extent such as railroad track. The arrival rate of moving load has been considered to be a Poisson process. The maximum deflection of the beam at the mid-span has been taken to calculate the probability of failure by assuming certain threshold value of deflection, in which a steel beam starts to form plastic hinge leading to collapse. Beam damping has a significant effect on the peak displacement affecting the probability of failure. As the mean value of the Poisson variable decreases, the number of loads present on the beam increases which results in higher deflection values of the beam resulting in higher values of probability of failure.

References

1. Simulation of Multivariate and Multidimensional Random Processes (1971) M. Shinozuka. J Acoust Soc Am 49:357–368. https://doi.org/10.1121/1.1912338
2. Fryba L (1996) Dynamics of railway bridges. Academia Praha
3. Sniady P (1984) Vibration of a beam due to a random stream of moving forces with random velocity. J Sound Vib 97:23–33
4. Sieniawska R, Śniady P (1990) Life expectancy of highway bridges due to traffic load. J Sound Vib 140:31–38. https://doi.org/10.1016/0022-460x(90)90904-e
5. Śniady P, Biernat S, Sieniawska R, Zukowski S (2001) Vibrations of the beam due to a load moving with stochastic velocity. Probabilistic Eng Mech 16:53–59. https://doi.org/10.1016/s0266-8920(00)00007-2
6. Chen Y, Feng MQ, Tan C-A (2009) Bridge structural condition assessment based on vibration and traffic monitoring. J Eng Mech 135, 747–758 (2009). https://doi.org/10.1061/(asce)0733-9399(2009)135:8(747)
7. Paz (1985) Structural dynamics: theory and computation. CBS Publishers, New Delhi
8. Frýba L (1976) Non-stationary response of a beam to a moving random force. J Sound Vib 46:323–338. https://doi.org/10.1016/0022-460x(76)90857-9
9. Lin YK (1967) Probabilistic theory of structural dynamics. McGraw-Hill, New York
10. IS 800:2007: General Construction in Steel-Code of Practice. BIS, New Delhi

Numerical Simulation and Wind Tunnel Experiment on Pressure and Velocity Distribution Around the NACA0012 Airfoil for Optimising an Aerodynamic Model

Motahar Reza, Anindita M. Bhattacharyya, Deepak K. Sadangi and Aman Kumar

Abstract Airfoil design is a significant facet of aerodynamics. In this paper, optimise aerodynamic model for the NACA0012 airfoil shape has been studied based the wind tunnel experiment and numerical simulation using ANSYS. The velocity and pressure distribution around the NACA0012 airfoil has found by tests results which are compared with numerical simulation. Based on this experiment result, optimisations shape of the airfoil has been investigated.

Keywords Computational fluid dynamics (CFD) · Airfoil · Lift · Drag · NACA0012 · Lift coefficient · Drag coefficient

1 Introduction

Aerodynamics is a branch of science which deals with the analysis of flow over a body. By evaluation of CFD is an accurate method for solving the problem of aerodynamics. For the design of aircraft, the most important thing is to consider the airflow over the airfoil. Airfoil is defined as the cross section of a body that is placed in an airstream to generate useful aerodynamics force. A fixed-wing aircraft's wings, horizontal, and vertical stabilisers are built with airfoil-shaped cross sections, as are helicopter rotor blades Airfoil are also found in propellers, fans, compressors and turbines. Any object with an angle of attack in a moving fluid, such as a flat plate, a building, or the deck of a bridge, will generate an aerodynamic force (called lift)

M. Reza (✉)
Department of Mathematics, National Institute of Science and Technology, Berhampur 761008, India
e-mail: reza@nist.edu

A. M. Bhattacharyya
Department of Mathematics, Amity University, Kolkata, India

D. K. Sadangi · A. Kumar
Department of Mechanical Engineering, National Institute of Science and Technology, Berhampur 761008, India

D. Maity et al. (eds.), *Advances in Fluid Mechanics and Solid Mechanics*,
Lecture Notes in Mechanical Engineering,
https://doi.org/10.1007/978-981-15-0772-4_30

perpendicular to the flow. Airfoils are more efficient lifting shapes, able to create more lift (up to a point) and to generate lift with less drag.

Eleni et al. [1] evaluated the turbulence model for the simulation of the 2-D subsonic flow over NACA0012. Ghose et al. [2] investigated the flow characteristics over a symmetrical airfoil in a low-speed wind tunnel. Shih et al. [3] showed a new k-ε eddy—viscosity model. Safayet et al. [4] evaluated the analysis of NACA6409 and NACA4412 airfoil. Harris et al. [5] investigated 2-D aerodynamics characteristics of the NACA0012 airfoil. Goorjian and Guruswamy [6] evaluated transonic unsteady aerodynamic and aeroelastic calculation about airfoils and wings. The game theory based evolutionary algorithms (genetic algorithms) to optimize the lift coefficient the of an NACA0012 based airfoil has been investigated by Want et al. [7] and validated turbulence model on NACA0012 has been mentioned in the report of NAS Technical Report [8].

Motivation of this study is to examine the lift and drag characteristics of NACA0012 airfoil for symmetrical shape and it is having the same dimension of chamber line and cord line and it has been used in many constructions and engineering applications. Typical examples of such use of the airfoil are the B-17 flying fortress and Cessna 152 the helicopter Sikorsky S-61 SH-3 Sea King as well as horizontal and vertical axis wind turbine [1].

The objective of this paper is to study optimize aerodynamic model for airfoil NACA0012 shape based the wind tunnel experiment results and numerical simulation results using ANSYS. The velocity and pressure distribution around the NACA0012 airfoil has been examined based on wind tunnel experiments results which are compared with numerical solutions using Ansys based on finite volume scheme. Based on this improved numerical results, optimization shape NACA012 airfoil has been investigated and has been improved its performance through ANSYS software.

2 History of Airfoil

Based on measure needs airfoil profile was designed. One was the requirement of flight, and another was to develop a new concept of slender, sleek and efficient shapes. In the 1800s, the work on airfoil started with advancements continuing till today. Ackeret [9] first work on the airfoil and led the initial work on calculating the lift and drag on a supersonic airfoil. The flat plate was kept at angle of incidence to incoming airstreams, and the lift force was derived. After that, the curvature was applied to the leading edges of the flat plate and hence to avoid retardation of airspeed over it. Many researchers and aerodynamicists are made concentration on how the modified shapes and sizes of the aerofoil have to be used for their specific research tasks and application. In a type of research, gliders are an invention that inspiration to fly along with the air. If airflow passes over the wings from the leading edge, it needs control over the planes. This was achieved satisfactorily at first and then controlled with manual adjustments during flight. Great personalities who give their idea were Wilbur Wright, Horatio F Phillips and Otto Lilienthal etc. next to their

works, changes were made by National Physics Laboratory (NPL) and NACA in the 1930's with common names as the 4-digit and 5-digit series of airfoil after testing in the virtual wind tunnel at Langley Aeronautics Laboratory.

Present study is done on NACA0012 airfoil that is first family series of the airfoil in the history and it most commonly used for research purpose in most cases. In NACA0012 airfoil the centre of pressure remains constant at the upper and lower part of the airfoil. This reduces the problem of C_p variation with varying angle of attack of air over the airfoil.

3 Mathematical Model Analysis

The drag force is the aerodynamic force that opposes an aircraft's motion through the air is called drag. The lift force is the force that opposes the weight of an aeroplane in the sky.

The lift and drag equations are given by,

$$\mathrm{d}F_D = -P\mathrm{d}A\cos\theta + \tau\mathrm{d}A\sin\theta \tag{1}$$

$$\mathrm{d}F_L = -P\mathrm{d}A\sin\theta - \tau\mathrm{d}A\cos\theta \tag{2}$$

Now the drag force is,

$$F_D = \int \mathrm{d}F_D = \int(-P\cos\theta + \tau\sin\theta)\mathrm{d}A \tag{3}$$

And the lift force is,

$$F_L = \int \mathrm{d}F_L = -\int(P\sin\theta + \tau\cos\theta)\mathrm{d}A \tag{4}$$

Drag force and lift force can be written by using the coefficient of drag and coefficient of lift respectively.

$$F_D = \frac{1}{2}.\rho.A.V^2C_D \tag{5}$$

$$F_L = \frac{1}{2}.\rho.A.V^2.C_L \tag{6}$$

The lift phenomenon can also be expressed by using Bernoulli's equation. As per Bernoulli's equation for an incompressible steady flow; velocity increases if pressure decreases and vice versa. When air passes over an airfoil, pressure decreases as the continuous air flow from leading edge to the upper surface of the airfoil. Velocity increases in that area. On other hand pressure increases when the air passes through the bottom of the airfoil and velocity is decreased.

A distant region is formed between the fluid stream and the body due to liquid separation from a collection. This low-pressure region behind the body where backward force and recirculation occur is called separated region. If the divided area is vast, then drag is significant. Wake is defined as the region of air that arises behind the body around which the fluid flows and extends for some distance. It is the boundary layer that has separated from the rear of the body. Wake consists of vortices which are responsible for creating drag by creating negative pressure in that region. In bluff bodies, Wake doesn't occur. Aerodynamic model those have attack angle more than 15° there Wake can happen this known as stalling point. Drag and negative pressure become dominant from a stalling point.

Boundary layer separation depends on the Reynolds number. If Reynolds number is higher than there will be a greater tendency that the flow is turbulent. Reynolds number R_e is defined by,

$$R_e = \frac{\rho U x}{\mu} \tag{7}$$

where x is the thickness of the boundary layer where the current is laminar to turbulent.

For all the flows, the solver solves conservation equations for mass and momentum. Additional transport model is solver when the flow is turbulent. The equations for conservation of mass or continuity equation can be written as follows [1];

$$\frac{\partial p}{\partial t} + \nabla.(\rho\vec{u}) = S_m \tag{8}$$

Equation 8 represents the general form of the mass conservation equation which is valid for both compressible and incompressible flows. The source S_m is the mass added to the continuous phase from the dispersed second phase and any user-defined sources.

$$\frac{\partial}{\partial t}(\rho\vec{u}) + \nabla.(\rho\vec{u}\vec{u}) = -\nabla p + \nabla.(\bar{\bar{\tau}}) + \rho\vec{g} + \vec{F} \tag{9}$$

Equation 2 represents the conservation of momentum in an internal reference frame. Where p is the static pressure, $\rho\vec{g}$ and $\vec{F}$ are the gravitational and body force respectively. $\vec{F}$ is also contained other model-dependent source terms such as porous-media and user-defined sources. And $\bar{\bar{\tau}}$ is the stress tensor which is given by;

$$\bar{\bar{\tau}} = \mu\left[\left(\nabla\vec{u} + \nabla\vec{u}^t\right) - \frac{2}{3}\right]\nabla.\vec{u}I \tag{10}$$

where μ is the molecular viscosity, I is the unit tensor, and the second term on the right-hand side is the effect of volume dilation.

4 Numerical Methodology

In this study, ANSYS CFD version 14.5 is used to simulate high Reynolds number flow ($R_e = 3 \times 106$) past two-dimensional airfoil. Based on the chord length while the attack angle varied from $-5°$ to $5°$ then the flow is assumed as an incompressible flow. In steady state, the simulation was conducted. The airfoil mesh and geometry are shown in Fig. 1. The C-type mesh topology was chosen because it can minimize the skewness of a near wall mesh as the structured quadrilateral element has the advantages of a higher degree of control and accuracy, lower memory consumption and a faster convergence rate.

Three mesh configurations of 16,980, 57,140 and 78,488 cells were conducted for the grid independence test. The pressure coefficient versus distance of y-axis was plotted and analysed. The results show all the lines of both configurations are almost overlapped and there is no significant difference in between the 57,140 and 78488. These indicate that using more fine mesh does not improve the model prediction. Thus, meshing with a lower number of mesh cells does not sacrifice the solution accuracy.

Since the Central Processing Unit (CPU) time increases exponentially with the number of grids, the lower mesh cells, 57,140 were chosen. During CFD simulation less mesh cell reduce CPU time, which permits a significant amount of case to be run. The meshing gave a total of 19,325 nodes and had 10,075 elements, and the near wall of the airfoil is refined using the boundary layer as shown in Fig. 1. The boundary conditions for the airfoil are shown in Fig. 1. The airfoil was set to solid surfaces with no slip, and the top and bottom lines were set to the symmetrical boundary condition.

The outlet boundary condition was set to atmospheric pressure, and the inlet boundary was set to a velocity inlet of 30 m/s. The free stream temperature is 300 K. The Semi-Implicit Method for Pressure-Linked Equations (SIMPLE) scheme was selected for the pressure-velocity coupling while for spatial discretisation section,

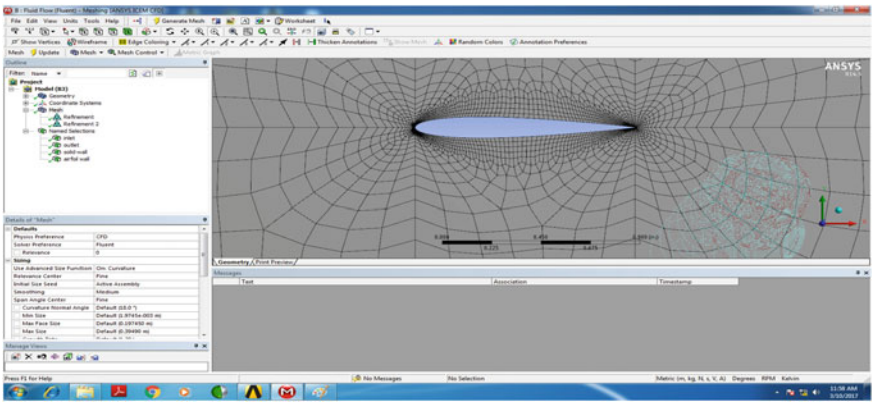

Fig. 1 The grid structure of airfoil 0012 using Ansys

the green-gauss node based was set. The second order upwind was used for the momentum, turbulent kinetic energy and turbulent dissipation rate to arrive at the best solution. Turbulences model from the viscous model which were Spalart-Allmaras, k-ε Realizable and k-ω SST were selected.

5 Experimental Results and Discussions

The experiment was carried out at NIST Research laboratory at a velocity of 30 m/s in an open circuit, suction type, and low-speed wind tunnel. The total length of the wind tunnel is about 6.8 m. Out of which blower section is 1.4 m long. The maximum height is approximately 1.5 m. The test section is of 30 cm × 30 cm cross section and 110 cm length with a thick plexiglass window. The suction side of a blower driven by a 1440 rpm 15 HP 440 V 50 cycles 3 phase AC motor is at the exit of the wind tunnel. The test section velocity is varied by turning the wheel of the sliding gate. The maximum speed of the wind tunnel is 70 m/s. in the experiment of the wind tunnel for the various angle of attack (−5° and 5°) the pressure difference at multiple points are given by the following tabulation, and from that table also we calculated the coefficient of lift.

From the Table 1, the lift coefficient can be calculated as,

$P_i = \rho g h_i$

$F_i = L_i \times \mathrm{B} \times P_i$

$\rho = 1000\,\mathrm{Kg/m^3}, g = 9.81,$

$h =$ manometric reading,

$L_i =$ Length of the strip $= 0.03$ m.

$B =$ Width of airfoil $= 0.2$ m.

Vertical component of each pressure force.

$F_n = F_i \times \mathrm{Cos}\theta_i$

$\theta_i =$ Angle at pressure force.

$\sum LF =$ Lift Force for $(0°) = 41419.65$ and Lift Force for $(40°) = 31765.27$

Coefficient of Lift $= FL/\rho.A.\frac{V^2}{2}$

$(A = 0.05\,\mathrm{m^2})$ Projected Area.

$(v = 30\,\mathrm{m/s})$ Velocity.

(For 0°) Coefficient of Lift $= 41419.65/\rho.A.\frac{V^2}{2} = 1.84087.$

(For 40°) Coefficient of Lift $= 31765.27/\rho.A.\frac{V^2}{2} = 1.41178.$

The analysis starts after visualisation of the output from the simulation process. The number of node and element set as 19,325 and 10,075 respectively. The result would be more accurate if the number of nodes and the feature could be increased in the mesh. By increasing the number of node and element, the finite element analysis can be performed more accurately.

Figure 2 shows that the lift performance of NACA0012 airfoil for the different angle of incidence from 0° to 30°. In Fig. 2 it is clear that coefficient of lift increases with increasing angle of incidence, but after reaching 25° the value of lift coefficient

Table 1 Experiment of the wind tunnel for the various angle of attack

(a) At pressure head 1–8									
Pressure head at a different point		1	2	3	4	5	6	7	8
Velocity (30 m/s)	The angle of attack (0°)								
P_i		444393	472842	479709	480690	478728	393381	441450	371799
F_i or F_n		2666.35	2837.05	2878.25	2884.14	2872.36	2360.2	2648.7	2230.79
For $\theta = 40°$ F_n		2047.05	2240.94	2263.48	2272.47	2277.01	1835.1	2182.3	1699.86

(b) At pressure head 9–15								
Pressure head at a different point		9	10	11	12	13	14	15
Velocity (30 m/s)	The angle of attack (0°)							
P_i		521892	500310	515025	517968	509139	404172	371799
F_i or F_n		3131.35	3001.86	3090.15	3107.80	3054.83	2425.03	2230.79
For $\theta = 40°$ F_n		2227.41	2195.85	2299.55	2344.64	2313.08	1857.68	1708.85

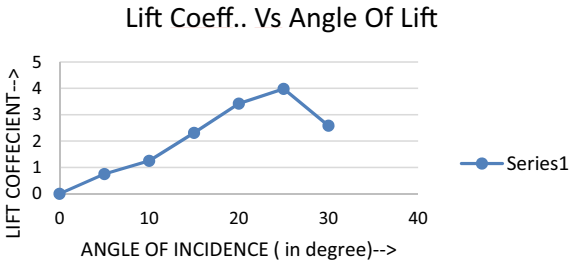

Fig. 2 Lift co-efficient versus angle of lift

decrease suddenly and goes on decreasing as per increasing angle of incidence. The condition at which the amount of lift coefficient starts to declines is known to be a stalling situation. Although the lift coefficient increases with angle of attack, the net effect is reduced efficiency for higher angle of attack. Hence another parameter is considered to know the performance, i.e. the ratio of lift to drag also is known as the coefficient of performance.

Figure 3 it is shown that the drag performance of NACA0012 airfoil, the drag coefficient increases when the angle of incidence goes on increasing. The lift and drag performance of NACA0012 airfoil for the different angle of incidence considered from 0° to 30°.

From the simulation, C_L and C_D were found for different angle of attack. Finally, the ratio of C_L and C_D was calculated in Fig. 4 in this figure the positive pressure was created at the lower surface while negative force act at the upper surface of the airfoil thus generating lift. Separation starts at the trailing edge thus forming Wake with negative pressure at that region.

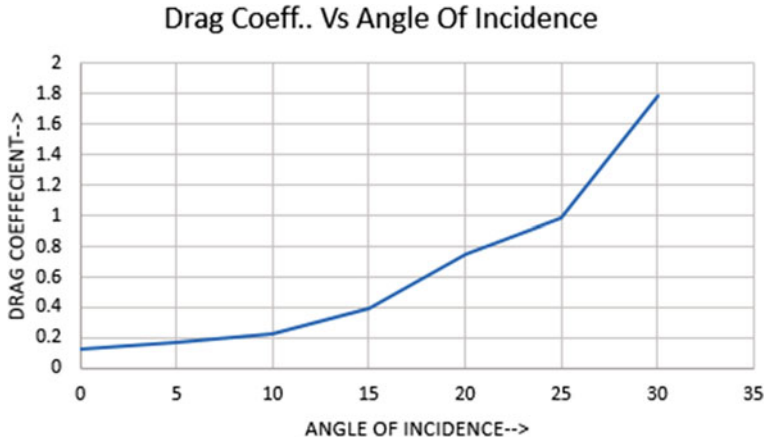

Fig. 3 Drag co-efficient versus angle of incidence

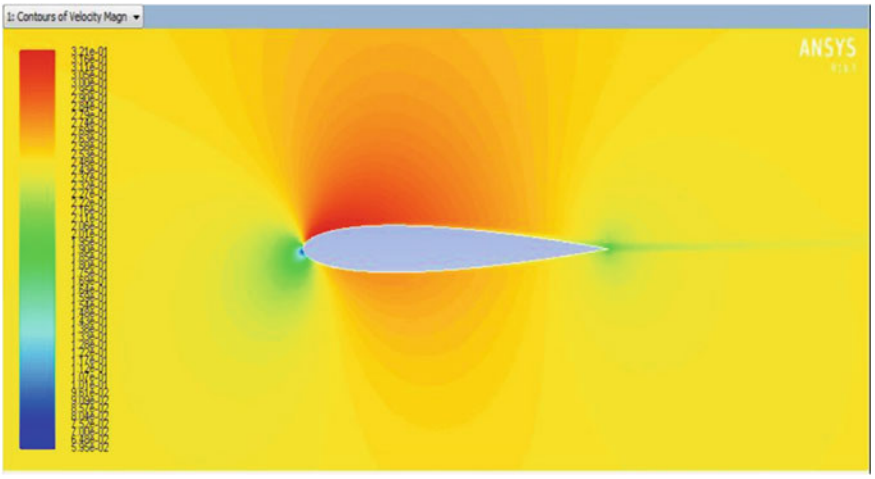

Fig. 4 Pressure distribution around an airfoil

6 Optimization of NACA-0012 Airfoil

The optimisation is defined as the technique through which we can change the shape of airfoil so that the drag force should be minimised and lift force should be maximised. We use ANSYS adjoint solver as an optimisation technique. In ANSYS adjoint solver we define three components, i.e. lift force, drag force and lift-drag ratio. First of all, we calculated the lift-drag ratio for the original shape is 12.15. Then we change the mesh around the airfoil by using mesh—morphing tool and then we again solved, and then we get the lift-drag ratio as 13.95. The optimised shape of the airfoil is displayed in Fig. 5.

7 Conclusions

In this paper, the experimental results and numerical simulation results are used to design a optimise airfoil shape using ANSYS software. It is noted from the observation that the lift to drag ratio is more than the original form of the airfoil. The optimisation of NACA-0012 L-D ratio increases from the original airfoil, i.e. 13.95. Hence, the lift force is maximised and drags force in minimised in our experiment. The airfoil shapes required a positive angle of attack to generate lift, but the cambered airfoil can generate lift at zero angles of attack. This "turning" of the air in the vicinity of the airfoil creates curved streamlines which results in lower pressure on one side and higher pressure on the other. This pressure difference is accompanied by a velocity difference, via Bernoulli's principle, so the resulting flow field about the airfoil has a higher average velocity on the upper surface than on the lower surface.

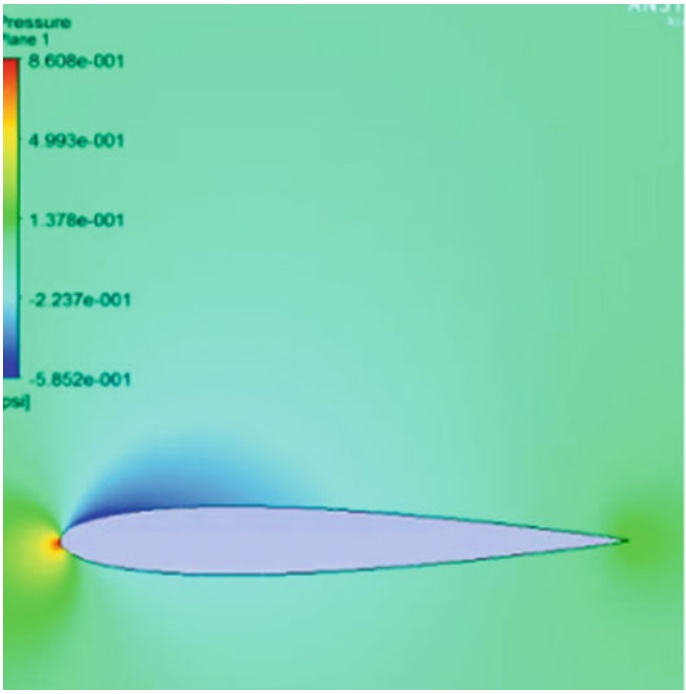

Fig. 5 Pressure distribution after optimising the shape of the airfoil

References

1. Eleni DC (2012) Evaluation of the turbulence model for the simulation of the flow over a NACA 0012 airfoil. J Mech Eng Res 4(3):100–111
2. Ghose P, Dewangan AK, Mitra P, Rout AK (2012) Experimental study of aero foil with wind tunnel setup. In: Recent advances in thermal engineering (RATE-2014), OSC-366/ 2012
3. Shih TH, Liou WW, Shabbir A, Zhu J (1995) A new k-ε eddy-viscosity model for high reynold number turbulent flows. National Aeronautics and space Administration, USA, pp 1–32
4. Hossain S, Raiyan MD, Ferdous M (2014) A comparative flow analysis of NACA 6409 AND NACA 4412 aerofoil. Int J Res Eng Technol 03:342–350
5. Harris CD (1981) Two-dimensional aerodynamic characteristics of the NACA0012 airfoil in the Langley 8-foot transonic pressure tunnel. NASA-TM-81927
6. Goorjian PM, Guruswamy GP (1988) Transonic unsteady aerodynamic and aeroelastic calculations about airfoils and wings. Comput Struct 30(4):929–936
7. Wang SF, Wu Y (2003) Hierarchical evolutionary algorithms and its application in transonic airfoil optimization in aerodynamics. Chin J Aeronaut 16:1–6
8. Rumsey C (2018) 2DN00: 2D NACA 0012 airfoil validation case. https://turbmodels.larc.nasa.gov/naca0012_val.html
9. Ackeret J (1925) Luftkrafte auf Flugel, die mit der grosserer als Schallgeschwindigkeit bewegt werden. Zeitschrift fur Flugtechnik und Motorluftschiffahrt 16:72–74